

# **Complex Petrogenesis of Lesser Antilles Arc Lavas: Insights From Mineral Chemistry**

Hannah Margaret Johnson BSc (Hons)

A thesis submitted for the degree of Doctor of Philosophy at the  
University of London.

Department of Earth Sciences

Royal Holloway College

University of London

September 2014

---

## **Declaration of Authorship**

---

I Hannah Margaret Johnson hereby declare that this thesis and the work presented in it is entirely my own. Where I have consulted the work of others, this is always clearly stated.

Signed

Date 18th September 2014

---

## Abstract

---

The Lesser Antilles arc is unusual in erupting high MgO lavas relative to many other volcanic arcs. This provides a rare opportunity to study early fractionating phases, such as olivine, with the aim of gaining insight into the early petrogenesis of these lavas as well as shallow level magmatic interactions and storage. Olivine, plagioclase and clinopyroxene crystals were studied from the central (Guadeloupe and Dominica) and southern (St. Vincent, Bequia, Petite Martinique, Carriacou and Grenada) islands of the arc in order to assess how deep (melting and source processes) and shallow (fractional crystallisation, crustal contamination and magma mixing) processes varied along arc strike.

Analysis of mineral crystals from the Lesser Antilles has shown significant variation in both textural and chemical signatures in crystal cargoes from the same lava. Multiple populations are observed in host lavas along the arc.

Geothermobarometric modelling showed the southern arc clinopyroxenes to have crystallised at higher temperatures and pressures (with the exception of the Bequia crystals) than those from further north. High forsterite olivines (up to Fo<sub>91</sub>) and high anorthite plagioclases (up to An<sub>96</sub>) indicate water is required in the melts, particularly in the south of the arc. Bimodal CaO, Al<sub>2</sub>O<sub>3</sub>, Cr, Y, Yb and in some cases Sc contents in the olivines suggest the disaggregation of cumulate xenoliths before assimilation into the host melts. Assimilation and magma mixing are also apparent in the plagioclase crystals, as are varying rates of ascent through the magmatic plumbing system. Effects of shallow level degassing or decompression are visible in the plagioclases and these processes could also be a suitable method for generating bimodal forsterite contents in the olivines from one Guadeloupe host lava.

Processes identified from the mineral phases show that petrogenesis in the Lesser Antilles is complex and varies along arc strike, with the southern islands potentially requiring more water in the melts and deeper crystallisation depths. In general, deeper processes are more prevalent to the south of the arc, with shallower processes dominating the north and centre.

---

# Table of Contents

---

<b>Declaration of Authorship.....</b>	<b>2</b>
<b>Abstract.....</b>	<b>3</b>
<b>List of Figures.....</b>	<b>10</b>
<b>List of Tables .....</b>	<b>21</b>
<b>List of Abbreviations .....</b>	<b>23</b>
<b>Acknowledgements .....</b>	<b>25</b>
<b>1 Introduction.....</b>	<b>26</b>
1.1 <i>Brief Overview of Arcs.....</i>	26
1.1.1 General Characteristics of Arc Magmas .....	28
1.2 <i>General Geology of the Lesser Antilles Arc.....</i>	28
1.2.1 Geological History .....	29
1.2.2 Strike and Dip of the Benioff Zone.....	30
1.2.3 Fore-arc Region and Accretionary Prism.....	30
1.3 <i>Rock Types and Cumulates .....</i>	31
1.4 <i>Changing Geochemistry of Lavas Along Arc Strike .....</i>	32
1.5 <i>Components of Lesser Antilles Arc Magmas .....</i>	35
1.5.1 Mantle Beneath the Lesser Antilles .....	35
1.5.2 Contribution from Subducting Slab .....	36
1.5.3 Sediment Being Subducted .....	37
1.5.4 Crustal Contamination .....	38
1.5.5 Contamination by Sediments at Source or in the Crust?.....	38
1.6 <i>What Makes the Lesser Antilles Arc Interesting to Study? .....</i>	39
1.7 <i>Project Aims.....</i>	41
1.8 <i>Thesis Overview.....</i>	42
<b>2 Mineral Chemistry Introduction .....</b>	<b>44</b>
2.1 <i>Introduction.....</i>	44
2.1.1 Reasoning for Analysing Minerals.....	44
2.1.2 Limitations of Using Mineral Chemistry in Conjunction with Whole Rock Chemistry .....	45
2.2 <i>Published Lesser Antilles Studies .....</i>	46

2.2.1	Findings of Published Studies.....	49
2.3	<i>Host Lavas</i> .....	53
2.3.1	Classification.....	53
2.3.2	Least Squares Fractional Crystallisation Modelling .....	54
2.3.3	Modal Phenocryst Proportions.....	56
2.4	<i>Analysis</i> .....	58
2.4.1	Crystal Mounts, Resin Blocks and Thick Sections .....	58
2.5	<i>Structure of Following Chapters</i> .....	61
<b>3</b>	<b>Olivine Chemistry</b> .....	<b>62</b>
3.1	<i>Introduction</i> .....	62
3.1.1	Importance of Analysing Olivine.....	62
3.1.2	Aims of Analysing Olivines in the Lesser Antilles.....	62
3.2	<i>Host Lavas</i> .....	63
3.3	<i>Olivine Petrography</i> .....	65
3.4	<i>Olivine Chemistry</i> .....	68
3.4.1	Forsterite Contents .....	68
3.4.2	CaO .....	69
3.4.3	Sc, V and TiO <sub>2</sub> .....	74
3.4.4	Zr.....	78
3.4.5	MnO .....	79
3.4.6	Y and Yb.....	80
3.4.7	Li.....	82
3.4.8	Cr and Ni.....	83
3.4.9	Al <sub>2</sub> O <sub>3</sub> .....	85
3.4.10	Incompatible trace element ratios - Zr/Y .....	86
3.4.11	Summary of LCO characteristics .....	87
3.4.12	Cumulate Xenoliths.....	87
3.4.13	δ <sup>18</sup> O Method.....	90
3.4.14	δ <sup>18</sup> O Results .....	95
3.5	<i>Discussion</i> .....	96
3.5.1	Equilibrium Olivines.....	97
3.5.2	Entrainment.....	103
3.5.3	Accumulation .....	104
3.5.4	Melt Composition .....	105
3.5.5	High Forsterite Olivines.....	111

3.5.6	Forsterite Bimodality in GU25 .....	113
3.5.7	$\delta^{18}\text{O}$ Discussion.....	114
3.5.8	Low Calcium Olivines .....	126
3.6	<i>Conclusions</i> .....	148
3.7	<i>Further Work</i> .....	150
<b>4</b>	<b>Plagioclase Chemistry.....</b>	<b>151</b>
4.1	<i>Introduction</i> .....	151
4.1.1	Importance of Analysing Plagioclase.....	151
4.1.2	Aims of Analysing Plagioclases in the Lesser Antilles.....	151
4.2	<i>Host Lavas</i> .....	152
4.3	<i>Plagioclase Petrography</i> .....	153
4.3.1	Guadeloupe .....	160
4.3.2	St. Vincent.....	160
4.3.3	Bequia .....	161
4.3.4	Sieve texturing and disequilibrium features in plagioclases .....	162
4.4	<i>Plagioclase Chemistry</i> .....	162
4.4.1	Anorthite Contents .....	163
4.4.2	Sr.....	166
4.4.3	K <sub>2</sub> O and Rb.....	169
4.4.4	Ba, Pb, La and Eu.....	171
4.4.5	Sm, Gd and Y .....	175
4.4.6	TiO <sub>2</sub> .....	178
4.4.7	MgO and Fe <sub>2</sub> O <sub>3</sub> .....	179
4.4.8	Spatial Variation in Plagioclase Chemistry.....	181
4.5	<i>Discussion</i> .....	187
4.5.1	Equilibrium Plagioclases.....	187
4.5.2	Degassing and Decompression at Shallow Levels.....	189
4.5.3	Plagioclase Response to Magma Ascent From Depth .....	193
4.5.4	Entrainment.....	197
4.5.5	Magma Mixing and Hybridisation.....	202
4.5.6	Accumulation .....	207
4.5.7	Melt Composition .....	207
4.5.8	Influence of Water and High Anorthite Plagioclases.....	211
4.5.9	Anorthite Bimodality in Guadeloupe Plagioclases .....	219
4.5.10	Sr and Ba Contents.....	222

4.5.11	Partition Coefficient Issues .....	227
4.6	<i>Conclusions</i> .....	230
4.7	<i>Further Work</i> .....	238
<b>5</b>	<b>Clinopyroxene Chemistry</b> .....	<b>239</b>
5.1	<i>Introduction</i> .....	239
5.1.1	Reasons for Analysing Clinopyroxene.....	239
5.1.2	Aims of Analysing Clinopyroxene in the Lesser Antilles.....	240
5.2	<i>Host Lavas</i> .....	240
5.3	<i>Clinopyroxene Petrography</i> .....	241
5.3.1	Guadeloupe .....	241
5.3.2	St. Vincent.....	242
5.3.3	Bequia .....	243
5.3.4	Carriacou.....	244
5.3.5	Grenada .....	245
5.4	<i>Clinopyroxene Chemistry</i> .....	246
5.4.1	Pyroxene Quadrilateral .....	246
5.4.2	Mg# .....	247
5.4.3	CaO .....	250
5.4.4	Al <sub>2</sub> O <sub>3</sub> , TiO <sub>2</sub> and V.....	250
5.4.5	MnO .....	252
5.4.6	Na <sub>2</sub> O.....	254
5.4.7	Cr and Ni.....	255
5.4.8	Sc.....	257
5.4.9	LREE - La, Ce and Nd.....	258
5.4.10	MREE - Sm, Eu, Gd and Dy .....	260
5.4.11	HREE - Er and Yb and Y.....	263
5.4.12	Hf and Zr.....	267
5.4.13	Li.....	269
5.4.14	Sr.....	270
5.4.15	Pb, Th, U, K <sub>2</sub> O, Ba, Rb and Nb .....	271
5.5	<i>Discussion</i> .....	275
5.5.1	Equilibrium Clinopyroxenes .....	275
5.5.2	Clinopyroxene Geothermobarometry.....	278
5.5.3	REE Partition Coefficient Calculations and Melt Back Calculation.....	283
5.6	<i>Issues with Partition Coefficients</i> .....	287

5.7	<i>Melt Evolution</i> .....	288
5.8	<i>Possible Entrainment or Magma Mixing</i> .....	290
5.9	<i>Depth of Melting</i> .....	291
5.9.1	Comparing Back Calculated Melt Depths to Whole Rock Melt Depths.....	295
5.10	<i>Conclusions</i> .....	297
5.11	<i>Further Work</i> .....	300
<b>6</b>	<b>Synthesis</b> .....	<b>301</b>
6.1	<i>Introduction</i> .....	301
6.2	<i>Whole Rock Pb Isotopes</i> .....	301
6.2.1	Pb Isotope Results.....	302
6.2.2	Pb Isotope Discussion .....	309
6.3	<i>Synthesis of Mineral Data</i> .....	314
6.3.1	Information from Each Phase .....	314
6.3.2	Comparison of Equilibrium Graphs .....	315
6.3.3	Comparison of Calculated Pressure and Temperatures.....	318
6.3.4	Comparing Processes and Populations.....	320
6.3.5	Effect of Fluid .....	325
6.3.6	Amphibole Fractionation?.....	326
6.4	<i>Overall Petrogenetic Model</i> .....	327
<b>7</b>	<b>Appendix 1 – Analytical Techniques</b> .....	<b>329</b>
7.1	<i>Sample Preparation</i> .....	329
7.1.1	Rock Crushing .....	329
7.1.2	Mineral Separation.....	329
7.2	<i>Thermal Ionisation Mass Spectrometry (TIMS)</i> .....	330
7.2.1	Cleaning Beakers .....	330
7.2.2	Sample Digestion .....	330
7.2.3	Making Columns.....	331
7.2.4	Column Chemistry .....	332
7.2.5	Bead Making.....	333
7.2.6	Sample Loading .....	333
7.2.7	Mass Spectrometry.....	333
7.2.8	Standard Reproducibility .....	334
7.2.9	Double Spike Pb Analysis.....	335
7.3	<i>Laser Ablation Inductively Coupled Plasma Mass Spectrometry (LA-ICP-MS)</i> .	338
7.3.1	Royal Holloway LA-ICP-MS System.....	338

7.3.2	Tuning .....	338
7.3.3	Laser Conditions and Settings.....	339
7.3.4	Mass Spectrometry.....	340
7.3.5	Standards.....	341
7.3.6	Data Processing.....	342
<b>8</b>	<b>Appendix 2 – Mineral Data .....</b>	<b>353</b>
	<b>References.....</b>	<b>355</b>

---

## List of Figures

---

Figure 1-1 Cross-section through the Lesser Antilles arc at St. Vincent and Barbados, modified from Westbrook et al. (1984). .....	27
Figure 1-2 Map showing the Lesser Antilles, modified from Carpentier et al. (2008) and Van Soest et al. (2002). The islands coloured in beige are ones from which data were obtained. The squares to the left of the name of the islands indicate which mineral phases were analysed from that island. Purple pentagons indicate the location of the sediment data detailed in Carpentier et al. (2008).....	29
Figure 1-3 Sr and Nd isotopic ratios from across the Lesser Antilles arc, modified from Macdonald et al. (2000). Data from Macdonald et al. (2000) and references therein. ....	33
Figure 1-4 Summary of Pb isotopic data from Lesser Antilles arc lavas compared to lavas from other intra-oceanic arc settings, modified from Carpentier et al. (2008). Data from Carpentier et al. (2008) and references therein. ....	34
Figure 1-5 Summary diagram showing principal changes along arc strike (Carpentier <i>et al.</i> , 2008, Macdonald <i>et al.</i> , 2000, Westbrook <i>et al.</i> , 1984, White & Dupre, 1986). Legend for map is as in Figure 1-2.....	40
Figure 2-1 TAS diagram showing the host lavas from which the analysed minerals were sampled. Modified from Le Bas et al. (1986). The red line represents the division between alkaline and sub-alkaline rocks suggested by MacDonald (1968).....	53
Figure 2-2 K <sub>2</sub> O versus SiO <sub>2</sub> graph showing all of the host lavas from which minerals were analysed. ....	54
Figure 2-3 Results of least squares fractional crystallisation modelling, as shown by the black lines. Legend for the four smaller graphs is the same as for the larger SiO <sub>2</sub> against MgO upper graph.....	55
Figure 2-4 Olivine crystal showing measurements used to calculate % distance from rim... 61	61
Figure 3-1 Olivine in GU1 showing evidence of resorbed edges and embayments. PPL is shown on the left hand side and XPL on the right. ....	65
Figure 3-2 Olivines in SV19 showing Fe oxide alteration. The larger olivines only show the alteration around the rims of the crystals, whereas the smaller crystals show pervasive alteration throughout the minerals. ....	66
Figure 3-3 Olivines in SV42. The larger olivine shows iddingsite alteration around the margins, with a smaller, skeletal olivine fully altered to iddingsite to the right of this crystal. ....	66
Figure 3-4 Skeletal and elongate olivines in CA3. The olivines also show chlorite alteration along cracks in the crystals. ....	67
Figure 3-5 Highly altered olivine in 6259. Aside from the iddingsite alteration, disequilibrium features are apparent in the form of partially resorbed edges and embayments. ....	67
Figure 3-6 Forsterite contents measured in the olivines. The y axis is arranged by latitude, with the most northern islands at the top and the southern islands at the bottom. Different islands are shown as different colours and are separated by dashed lines. ....	68
Figure 3-7 CaO contents in the Lesser Antilles olivines. The dashed line represents a CaO concentration of 0.11 wt% which has been used as the upper limit for the determination of the LCO, based on histogram data (Figure 3-8).....	70

Figure 3-8 Histogram showing a bimodal distribution in calcium contents by frequency. The overlaid line shows the kernel density estimation. The dashed line shows 0.11 wt% CaO...	71
Figure 3-9 Variations in CaO contents across olivine crystals. The upper graph shows the absolute concentrations (with the dashed line representing 0.11 wt%) whereas the lower graph shows the ratio of CaO contents in the rims relative to the cores (the solid line represents a ratio of 1, with analyses plotting higher than this being more enriched than the cores and analyses below being depleted relative to the cores). It can be seen, particularly in the lower graph, that CaO contents increase towards the rims of the crystals. ....	73
Figure 3-10 Sc and V contents in the Lesser Antilles olivines, showing the LCO (overlain by the small black crosses) to have slightly lower Sc and V concentrations at a given forsterite content than the higher CaO olivines. ....	74
Figure 3-11 TiO <sub>2</sub> contents in the olivines. The LCO (overlain by the small black crosses) show the lowest TiO <sub>2</sub> concentrations, however several LCO crystals show similar contents to the normal CaO olivines. ....	77
Figure 3-12 Concentrations of Zr in the LCO (small black crosses) and the higher CaO olivines, showing the two populations to have comparable Zr contents at a given forsterite content. ....	78
Figure 3-13 MnO and forsterite contents in the olivines, showing no discernible depletion in MnO in the LCO (overlain by the small black crosses). ....	79
Figure 3-14 Y and Yb concentrations in the olivines. The LCO are shown by small black crosses and exhibit slightly lower Y and Yb concentrations than the higher CaO olivines at a given forsterite content. ....	81
Figure 3-15 Li contents in the Lesser Antilles olivines, the LCO are shown as small black crosses. ....	82
Figure 3-16 Ratios between Li concentrations across olivines and with the core analysis for the olivines analysed in thick section. The dashed line represents a ratio of 1, with values greater than one indicating higher Li contents than the core analysis. ....	83
Figure 3-17 Cr concentrations in the olivines. The majority of the LCO (small black crosses) show lower Cr contents at a given forsterite contents, generally under 100 ppm. ....	84
Figure 3-18 Ni concentrations in the olivines against forsterite content showing the LCO as small black crosses. ....	85
Figure 3-19 Al <sub>2</sub> O <sub>3</sub> concentrations in the olivines, showing the LCO (overlain by small black crosses) to have lower alumina contents at a given forsterite content. In addition, the higher CaO olivines show decreasing Al <sub>2</sub> O <sub>3</sub> contents with decreasing forsterite contents whereas the LCO show increasing Al <sub>2</sub> O <sub>3</sub> with decreasing forsterite content. ....	86
Figure 3-20 Zr/Y ratios in the olivines, the LCO (shown by small black crosses) exhibit much higher Zr/Y ratios (up to 11). ....	87
Figure 3-21 Thick section photographs of the cumulate olivines hosted within xenoliths in each host lava in PPL. ....	88
Figure 3-22 Olivines in 6001 (upper photograph) 6004 (lower photograph) found within the host lava surrounding the cumulate xenoliths, taken in PPL. ....	90
Figure 3-23 IMF versus Forsterite content for the standard data analysed at the start of the day on 22/03/13. The gradient and intercept of the trendline are used in the calculation of the IMF correction for that day (Equation 3-2). ....	91
Figure 3-24 San Carlos data analysed on 22/03/13. The upper graph shows the IMF corrected data and shows a decrease in $\delta^{18}\text{O}$ which may be a result of instrumental drift. The lower graph shows the same San Carlos data after a drift correction (Equation 3-5) has been	

applied to the IMF corrected data. The dashed lines represent a $\delta^{18}\text{O}$ value of 5.3‰. Error bars show 1sd.....	94
Figure 3-25 IMF correction for 13/08/13. There is a larger range in IMF for the fayalite data than for the Fo <sub>90.3</sub> olivine. ....	95
Figure 3-26 Forsterite contents of the analysed olivines against the IMF and drift corrected $\delta^{18}\text{O}$ data. Solid line represents mantle olivine value of 5.18‰ with the dashed lines representing the $\pm 0.28\%$ error on the mantle olivine value (Mattey <i>et al.</i> , 1994). Average forsterite contents have been used if more than one LA-ICP-MS analysis has been performed on the same crystal. Low calcium olivines are shown as symbols outlined in red. ....	96
Figure 3-27 Forsterite compositions of olivines analysed against the forsterite content of olivine calculated to be in equilibrium. The area between the lines represents where the olivines are in equilibrium with their whole rock, within error of the Roeder and Emslie (1970) partition coefficient. More primitive olivines plot below the lines and potentially accumulative olivines plot above the lines. The LCO are shown as black dashes.....	98
Figure 3-28 $\Delta$ parameter used to show offset of olivines from equilibrium olivine against CaO content. The LCO are shown as dark green diamonds. 0 on the y axis represents equilibrium with the host lava assuming a $K_D$ of 0.3 (Roeder & Emslie, 1970).....	100
Figure 3-29 Forsterite contents in the analysed olivines compared to those calculated to be in equilibrium with the whole rock if the LCO are assumed to have been entrained into the host lava.....	101
Figure 3-30 Comparison between calculated hypothetical equilibrium olivine compositions for GU25 the observed forsterite contents of the analysed crystals. The hollow diamonds show where the HFG and LFG plot if neither population is removed. The solid dark blue diamonds represent where the LFG would plot if the HFG were removed and the light blue diamonds depict where the HFG would plot if the LFG were removed from the whole rock. ....	102
Figure 3-31 Whole rock and calculated melt MgO and CaO compositions. The higher CaO olivines are shown as black diamonds, with the LCO depicted as green diamonds. The hollow grey symbols are all the available whole rock compositions determined for Lesser Antilles lavas from the islands from which olivines were analysed. The whole rock compositions of the host lavas from which the olivines analysed by LA-ICP-MS originated are shown as solid grey symbols with a black outline (Thirlwall, unpublished data).....	107
Figure 3-32 Calculated approximations for partition coefficients for the analysed olivines using both the whole rock composition as a proxy for melt (solid symbols) and the calculation provided by Jurewicz and Watson (1988a) using forsterite content (hollow symbols). Also shown are published partition coefficients for Ca into olivine in basalts, taken from the GERM partition coefficient database (Beattie, 1994, Dunn, 1987, Higuchi & Nagasawa, 1969, Kloecke & Palme, 1988, Leeman & Scheidegger, 1977). The Dunn (1987) and Beattie (1994) partition coefficients were derived experimentally whilst the remaining published coefficients are from phenocryst-matrix studies. ....	108
Figure 3-33 Ratios of olivine CaO contents to recalculated whole rock CaO compositions after CaO held in olivine, clinopyroxene and plagioclase had been removed using Equation 3-13. ....	110
Figure 3-34 Forsterite contents (black diamonds) and CaO concentrations (hollow diamonds) in the Feig <i>et al.</i> (2006) olivines against melt water contents. The regression lines through each series show the increase in Fo contents and decrease in CaO concentrations as water content increases. ....	111

Figure 3-35 Melt water contents based on the regression line through the Feig et al. (2006) olivines for the higher CaO and LCO analysed in Lesser Antilles host lavas. Both groups also show an increase in forsterite contents with increasing theoretical melt water contents. .....	112
Figure 3-36 Modelled changes in olivine $\delta^{18}\text{O}$ with decreasing forsterite content of the olivines as a result of fractional crystallisation. The coloured lines represent fractional crystallisation of assemblages as shown in the legend. The LCO are outlined in red. ....	116
Figure 3-37 Changes in olivine $\delta^{18}\text{O}$ when the average mineral assemblage calculated during least squares fractional crystallisation modelling is removed from the CA13 whole rock $\delta^{18}\text{O}$ . This trend is shown by a grey line. ....	118
Figure 3-38 Variation in whole rock $\delta^{18}\text{O}$ calculated from the $\delta^{18}\text{O}$ of the respective olivine phenocrysts. ....	119
Figure 3-39 Results of adding sediment compositions from Carpentier et al. (2009) to the DMM composition of Workman and Hart (2005) using the increment method. Unit 3 from Site 144 is a black shale unit which has been suggested to be responsible for anomalous Pb isotopic results for the Lesser Antilles in the literature (Carpentier <i>et al.</i> , 2008, Carpentier <i>et al.</i> , 2009). Tick marks show 5% increments. Red outlines are around the LCO. ....	120
Figure 3-40 Variations in olivine $\delta^{18}\text{O}$ with subducted sediment and crust addition. Solid lines represent mixing with the Davidson (1985) mantle endmember, dashed lines represent mixing with the Davidson (1985) MORB endmember. Crust composition [1] also from Davidson (1985), [2] subducted sediment and crust compositions from Thirlwall et al. (1996). Lower graph is a close up of the upper graph. ....	122
Figure 3-41 $\delta^{18}\text{O}$ compared to Li/Yb ratios in the olivines. The LCO are outlined in red. .	124
Figure 3-42 $\delta^{18}\text{O}$ contents plotted against CaO concentrations in the olivines. The LCO are outlined in red, with the dashed line representing 0.11 wt% CaO (the upper limit of the LCO). ....	125
Figure 3-43 CaO contents and forsterite contents of the LCO and the higher CaO Lesser Antilles olivines compared to mantle olivine data from Kamenetsky et al. (2006), De Hoog et al. (2010) and Hirano et al. (2004). The dashed line represents a CaO content of 0.11 wt%. .....	127
Figure 3-44 Cr concentrations and CaO contents of the LCO and mantle olivine data. ....	128
Figure 3-45 CaO and $\text{Al}_2\text{O}_3$ contents of the LCO, the non-LCO and the De Hoog et al. (2010) mantle xenolith olivines. ....	129
Figure 3-46 CaO and forsterite contents of the Parkinson et al. (2003) olivines compared to the LCO, showing the lower forsterite olivines of Parkinson et al. (2003) having higher CaO contents more comparable to those in the non-LCO. ....	130
Figure 3-47 Ni and CaO concentrations in the Hirano et al. (2004) mantle xenocryst olivines compared to the LCO. The Hirano et al. (2004) olivines show higher Ni contents at a given CaO content than many of the LCO. ....	131
Figure 3-48 Graphs showing how the cumulate xenolith olivines and olivines in the host lavas containing the cumulate xenoliths compare to the LCO and non LCO. ....	136
Figure 3-49 CaO and forsterite contents of the LCO and the Kamenetsky et al. (2006) olivines, showing that the LCO have comparable CaO contents but lower forsterite contents. .....	137
Figure 3-50 Cr concentrations and forsterite contents in the Kamenetsky et al. (2006) olivines and the LCO. The Kamenetsky et al. (2006) olivines show higher Cr concentrations at a given forsterite content than the LCO. ....	138

Figure 3-51 CaO and forsterite contents of the LCO and non-LCO compared to the Walter (1998) olivines. ....	140
Figure 3-52 CaO and forsterite contents in the Hellebrand et al. (2002) olivines compared to the LCO and non-LCO. The Hellebrand et al. (2002) olivines have comparable CaO contents to the LCO.....	141
Figure 3-53 Al <sub>2</sub> O <sub>3</sub> contents in the Hellebrand et al. (2002) olivines compared to the LCO, showing that the Hellebrand et al. (2002) olivines are comparable to the LCO in terms of alumina contents. ....	142
Figure 3-54 Comparison of the LCO with boninite olivines (SOBOLEV & DANYUSHEVSKY, 1994). ....	143
Figure 3-55 Cr concentrations in the LCO and the boninite olivines analysed by Sobolev and Danyushevsky (1994). ....	143
Figure 3-56 Sr/Y ratios of the host lavas compared to the percentage of analysed olivine crystals from each host lava that are classified as LCO.....	145
Figure 3-57 Overall summary of olivine petrogenesis in the Lesser Antilles. LCO are represented by pale green hexagons.....	149
Figure 4-1 Plagioclase phenocrysts photographs taken from the thick section of GU25, all photographs are shown in plane polarised light. Laser pits are visible as small circles, as highlighted in A. A shows the subhedral nature of the plagioclases and shows evidence of disequilibrium features, such as the sieve texture present within the phenocrysts. B shows further alteration in the core of the crystal. ....	160
Figure 4-2 Analysed plagioclase phenocrysts (identifiable by the circular laser pits) in SV19 (A and B) and SV20 (C and D) under plane polarised light. A shows extensive disequilibrium features in the core of a crystal in SV19. B shows a second SV19 phenocryst with much less evidence of disequilibrium in the core of the crystal but some stepwise corrosion is apparent around the rim. The darker brown colour present is the ablation blanket resulting from the LA-ICP-MS analysis. C and D show examples of spot locations when multiple analyses are undertaken in a single crystal. Both C and D show plagioclases with a different pattern of disequilibrium to that seen in the SV19 crystals. The cores are relatively fresh, with intermediate bands of extensive sieve texturing which are adjacent to unaltered rims. ....	161
Figure 4-3 Plagioclase phenocrysts in plane polarised light from BQ19. A shows a relatively fresh crystal with slight corrosion around the margins of the crystal. B shows a plagioclase phenocryst with a sieve texture apparent, particularly around the margins of the crystal. The crystal in the top right of the field represents the largest extent of disequilibrium features seen in the Bequia thin sections. ....	162
Figure 4-4 Analysed plagioclase crystals shown on an An-Ab-Or ternary plot by island... 163	163
Figure 4-5 Anorthite contents in all the analysed plagioclases. The y axis is ordered with host lavas from the centre of the arc at the top and host lavas from the south at the bottom of the axis. Each island is shown as a different colour and is separated by a dashed line. ....	164
Figure 4-6 Sr concentrations against anorthite contents for the analysed plagioclase crystals. Two GU25 crystals are not shown but lie at An <sub>41</sub> and An <sub>43</sub> with Sr concentrations of 1678 and 1694 ppm respectively. ....	167
Figure 4-7 K <sub>2</sub> O and Rb concentrations versus anorthite contents. Negative values appear on the Rb graph as concentrations were so low as to approach detection limits for the LA-ICP-MS.....	169
Figure 4-8 Ratios of the interquartile ranges of concentrations for the measured elements between those crystals with >An <sub>90</sub> and all the plagioclase crystals. ....	170

Figure 4-9 Ba, Pb, La and Eu concentrations versus anorthite content in the analysed plagioclases in crystal mounts, thick sections and resin blocks.....	173
Figure 4-10 Sm, Gd and Y concentrations in the analysed plagioclases, with Y representing the HREE contents of the Lesser Antilles plagioclases .....	176
Figure 4-11 Eu anomalies in the analysed plagioclases.....	177
Figure 4-12 TiO <sub>2</sub> contents versus anorthite contents in the analysed plagioclases.....	178
Figure 4-13 MgO and Fe <sub>2</sub> O <sub>3</sub> concentrations in the Lesser Antilles plagioclases. ....	180
Figure 4-14 Anorthite variation across crystals from SV20 (A) and one crystal from BQ19 (B). The laser sites are colour graded with the highest An contents being the strongest colours and the lowest An contents being the weakest shades. It can be seen that the anorthite contents do not vary smoothly particularly in the SV20 crystals. K/Ti was used as an indication of fluid involvement, with K being fluid mobile and Ti fluid immobile.....	183
Figure 4-15 An contents of the analysed plagioclases plotted against the Ca/K+Na+Ca ratio for the whole rocks from which they originated. Samples labelled with TS are thick section analyses, RB are resin block analyses and the remainder are crystal mounted plagioclases. The Guadeloupe samples originate from the centre of the arc and the St. Vincent and Bequia samples are from the south of the arc. The regression line shows a weak positive trend between the sampled plagioclases and the whole rock composition, although the R <sup>2</sup> value suggests this may not be statistically robust. ....	188
Figure 4-16 Petrographic evidence of shallow level degassing and/or decompression in crystal BQ19-1. The blue box shows the location of the close up shown in the right hand photograph. Resorption of the crystal edges and fine sieve texturing can be seen in more detail in the larger scale image.....	190
Figure 4-17 Variations in anorthite content between cores and rims of crystals in the thick section analyses. The dashed line represents An/An <sub>core</sub> = 1.0, analyses plotting below this line have lower anorthite contents than the cores of the respective crystals.....	192
Figure 4-18 Photograph of SV20-5 showing fine sieve texturing and breakdown and resorption of the crystal edge. ....	192
Figure 4-19 Results from Putirka (2008) modelling using the analysed plagioclase crystals in crystal mounts, thick section and resin blocks. ....	195
Figure 4-20 Putirka (2008) modelling for the thick section analyses, separated by population. ....	196
Figure 4-21 Methods of generating compositionally different cores and rims in plagioclases through magmatic plumbing. Modified from Davidson et al. (2007).....	198
Figure 4-22 Heavily sieved zones seen in two populations from differing lavas from St. Vincent. Photograph A shows SV19-3 and does not exhibit a fresher core region. Photograph B shows SV20-3 which has fresher material preserved in the core. Whilst the rim material appears fresher there is still evidence of some resorption of the crystal edges, possibly caused by shallow level degassing/decompression. ....	199
Figure 4-23 Anorthite contents in both populations from SV20. SV20-a is the population thought to be antecrysts whereas SV20-b may originate from the host melt. The upper graph shows the absolute anorthite contents in the core and rim analyses. The lower graph shows the anorthite contents relative to the core value of each crystal.....	200
Figure 4-24 Concentrations of a compatible, LILE, HFSE and REE element across the analysed populations in SV20. The grey rectangle shows the approximate potential point of entrainment during growth of the crystals. ....	201
Figure 4-25 Examples of synneusis in SV20 (A) and BQ19 (B), possibly as a result of self convective magma mixing in shallow magma chambers prior to eruption.....	204

Figure 4-26 GU25-3 which is in population GU25-b. The core shows coarse sieving (likely to be a result of decompression) followed by three finely sieved zones which may result from magma mixing.....	205
Figure 4-27 Anorthite content (solid symbols) and Sr concentration (hollow symbols) variation across two crystals from population BQ19-a, which is thought to show evidence of magma mixing. The dashed lines on the photographs and graph represent the locations of the sieve texturing numbered in the photographs. ....	206
Figure 4-28 Whole rock graphs for selected elements and element ratios against MgO content to show fractional crystallisation of olivine, clinopyroxene and plagioclase in the lavas from which the analysed plagioclases originate. Hollow grey symbols represent whole rock analyses from the same islands that the plagioclases were sampled from (squares: Guadeloupe, diamonds: St. Vincent and triangles: Bequia; Thirlwall, unpublished data). Individual sample legends are as shown in the upper left graph.....	209
Figure 4-29 La/Y ratios of the thick section plagioclase analyses versus % distance from the rim of the crystals.....	211
Figure 4-30 Observed analysed plagioclase compositions plotted against the whole rock (WR) CaO/Na <sub>2</sub> O ratios from which they were sampled. Partition coefficients used are from Sisson and Grove (1993). The dashed lines represent plagioclases in equilibrium using the published $K_D^{Ca-Na}$ for each water content, at a given whole rock CaO/Na <sub>2</sub> O ratio. ....	213
Figure 4-31 K/Y and Ba/Y ratios in the analysed plagioclases against anorthite content. ..	214
Figure 4-32 Whole rock (WR) CaO/Na <sub>2</sub> O and Al <sub>2</sub> O <sub>3</sub> /SiO <sub>2</sub> ratios (Thirlwall, unpublished data) compared to the analysed plagioclase anorthite compositions. The legend for the lower graph is as shown in the upper diagram. ....	216
Figure 4-33 Variations in anorthite content relative to the core analysis in the plagioclase thick section data.....	217
Figure 4-34 Variations in modelled temperature with anorthite content using the Putirka (2008) and Bindeman et al. (2008) models. The Bindeman et al. (2008) model is not designed for use above An <sub>80</sub> , illustrated by the grey rectangle and is shown by the dashed line. ....	218
Figure 4-35 An contents (solid symbols) and Sr concentrations (hollow symbols) ratioed to the core analyses for both GU25 populations against % distance from the rim. ....	220
Figure 4-36 La concentrations with % distance from rim in the GU25 thick section analyses. ....	221
Figure 4-37 Concentrations of Ba and Sr in the analysed plagioclases ratioed with the whole rock concentrations compared to analysed plagioclase anorthite contents. The dashed black lines represent the partition coefficients calculated using Blundy and Wood (1991), with the solid black line using temperatures calculated from the analysed plagioclases using the Bindeman et al. (1998) equation. The grey ellipse shows a group of plagioclases with unexpectedly low $[Sr]_{Plag}/[Sr]_{WR}$ at a given anorthite content.....	224
Figure 4-38 Lesser Antilles plagioclase data compared to the partition coefficient trend of Ren et al. (2003), represented by the dashed line, showing a more suitable gradient than that seen using the Blundy and Wood (1991) partition coefficient equations. ....	227
Figure 4-39 $[Sr]_{Plag}/[Sr]_{WR}$ calculated for the analysed plagioclases against anorthite content. The dashed lines represent the Blundy and Wood (1991) $K_D^{Sr}$ at 500°C and 1500°C. Annotations show the effect of possible processes affecting the system which may move the analysed crystals away from the Blundy and Wood (1991) lines. The coloured arrows and matching processes in the text box to the right indicate the direction in which the	

plagioclases would be shifted as a result of the processes discussed below, the length of the arrows bears no significance. ....	228
Figure 4-40 Schematic representation of processes occurring throughout the Lesser Antilles arc observed in analysed plagioclases. Temperature estimates are calculated from Putrika (2008).....	237
Figure 5-1 Clinopyroxenes shown in PPL from GU20 (left hand side photographs) and GU25 (right hand side photograph). ....	242
Figure 5-2 Crystal GU25-1 shown in thick section in PPL showing zoning. The circular structures are the pits ablated during LA-ICP-MS analysis.....	242
Figure 5-3 Fine scale inclusions within a clinopyroxene from SV20 seen in PPL. Again, the circles present show the location of the LA-ICP-MS spots. ....	243
Figure 5-4 Glomerocryst in SV3, shown in PPL in the left hand photograph and XPL in the right hand photograph. ....	243
Figure 5-5 Clinopyroxene BQ19-1 (left hand side) and another unanalysed crystal from BQ19 (right hand side) photographed in PPL. Zoning is apparent in BQ19-1 (as are the LA-ICP-MS sites). Fine scale inclusions are seen in the clinopyroxene bordering the plagioclase crystal in the centre of the right hand side photograph. ....	244
Figure 5-6 Glomerocryst in CU28 in PPL (left hand side) and XPL (right hand side). The clinopyroxenes are small, with the overall size of the glomerocryst being less than 1 mm across in size. Also shown in the lower right quadrant of the photographs is a clinopyroxene exhibiting sector twinning in XPL. ....	244
Figure 5-7 Clinopyroxene crystal from CA3 photographed in PPL (left hand photograph) and XPL (right hand photograph). The crystal shows evidence of breaking down at the crystal margins. Zoning is also seen in the XPL photograph, with the core area showing a different birefringence colour to the outer margins. In addition, there are at least two small plagioclase laths within the clinopyroxene crystal.....	245
Figure 5-8 Clinopyroxene crystal from 468 photographed in PPL (left hand side) and XPL (right hand side). Cleavage is well defined in this crystal and can be seen particularly well in PPL.....	245
Figure 5-9 Pyroxene quadrilateral (upper graph) and an excerpt from a pyroxene quadrilateral (lower graph) showing the locations of the Lesser Antilles clinopyroxenes after calculation of endmembers. ....	247
Figure 5-10 Mg# numbers of the clinopyroxene crystals, including crystal mount, thick section and resin block analyses. Islands are ordered by latitude on the y axis. Each island is shown as a different colour. ....	248
Figure 5-11 Variation in Mg# with % distance from the rim. 100% distance from the rim indicates the core analysis.....	249
Figure 5-12 Ratio of $Mg\#/Mg\#_{Core}$ against % distance from the rim for the GU25 and SV20 thick section analyses. Cores plot at a $Mg\#/Mg\#_{Core}$ ratio of 1, as indicated by the dashed line. As a result, analyses plotting above this line show a higher Mg# number than the core and those below the line have lower Mg# than the core. ....	249
Figure 5-13 CaO contents of the clinopyroxenes analysed from Lesser Antilles host lavas during this study. Crystal mount, thick section and resin block analyses are all shown.....	250
Figure 5-14 $Al_2O_3$ , $TiO_2$ and V concentrations in the Lesser Antilles clinopyroxenes in comparison to the Mg# of the crystals. ....	251
Figure 5-15 MnO contents in the clinopyroxenes, against Mg#. ....	253
Figure 5-16 Excerpt from Figure 5-15 showing $>Mg\#_{75}$ on the x axis. The CA3 clinopyroxenes are shown in blue and the 468 crystals are shown in orange.....	254

Figure 5-17 Concentrations of Na <sub>2</sub> O in the clinopyroxenes. ....	254
Figure 5-18 Concentrations of Cr and Ni in the Lesser Antilles clinopyroxenes plotted against Mg#.....	256
Figure 5-19 Sc concentrations plotted against the Mg# of the Lesser Antilles clinopyroxenes. ....	257
Figure 5-20 Concentrations of the LREE in the clinopyroxenes, plotted against Mg#. ....	259
Figure 5-21 MREE concentrations plotted against Mg# in the Lesser Antilles clinopyroxenes.....	262
Figure 5-22 HREE concentrations measured in the Lesser Antilles clinopyroxenes, plotted against Mg#.....	264
Figure 5-23 REE profiles of the clinopyroxenes. Each graph shows a different island, with the shaded areas representing the range in concentrations normalised to the values of Nakamura (1974) with individual dashed lines representing discrete clinopyroxene analyses. The two CA3 crystals shown by solid lines on the Carriacou graph exhibit different trends to the remaining CA3 clinopyroxenes.....	265
Figure 5-24 Eu anomalies in the clinopyroxenes, the upper graph shows the Eu/Eu* ratio in relation to chondrite normalised La/Sm ratios whilst the bottom graph shows the Eu anomalies compared to Mg#. The dashed line at 1 on both graphs represents no anomaly, with those crystals below exhibiting negative anomalies and those above positive anomalies. ....	266
Figure 5-25 Concentrations of Hf and Zr in the clinopyroxenes. ....	268
Figure 5-26 Li concentrations in the Lesser Antilles clinopyroxenes, plotted against Mg#.....	269
Figure 5-27 Sr concentrations in the analysed clinopyroxenes plotted against Mg#.....	270
Figure 5-28 % Relative uncertainties on each oxide/element measured in the clinopyroxenes. The elements being discussed in this section of the results are coloured in black.....	271
Figure 5-29 Concentrations of Pb, Th, U, K <sub>2</sub> O, Ba, Rb and Nb in the clinopyroxenes plotted against Mg#.....	274
Figure 5-30 1/Mg# for each clinopyroxene analysis plotted against 1/Mg# for the respective host lava. The coloured lines show where clinopyroxenes in equilibrium with the whole rock Mg# would plot based on a partition coefficient of 0.28±0.08 (Putirka, 2008). The area above the upper error limit is suggested to be a potentially more accumulative field, with the area below the lower error limit being more primitive than the whole rock composition. The numbers above and below each host lava show the whole rock MgO contents. ....	275
Figure 5-31 Equilibrium graph replotted with melt Mg# if all clinopyroxene phenocrysts in the host lavas are assumed to be accumulated. Hollow symbols show 1/WR Mg# and the solid symbols show the recalculated melt Mg#. ....	278
Figure 5-32 Pressures and temperatures of crystallisation for the Lesser Antilles clinopyroxenes calculated using the equations contained in Putirka (2008). ....	280
Figure 5-33 Calculated crystallisation temperatures and pressures using equations contained in Putirka (2008), which rely solely on the compositions of the clinopyroxenes. ....	281
Figure 5-34 Pressure and temperature variations across crystals analysed in thick section from GU25 and SV20. ....	282
Figure 5-35 Graph showing the average anhydrous and hydrous partition coefficients calculated from Wood and Blundy (1997) and Wood and Blundy (2002). ....	284
Figure 5-36 Calculated melt compositions showing an LREE (La), MREE (Sm) and HREE (Yb). The two CA3 crystals with conflicting REE patterns to the remainder of the clinopyroxenes from this host lava are indicated by the blue squares. ....	287

Figure 5-37 La concentrations in clinopyroxenes from BQ19. Blue diamonds are analyses in between the core and the rims in BQ19-1, with rim analyses from this crystal being light blue. Orange diamonds are analyses intermediate between core and rim from BQ19-2, with light orange being rims. Dark green diamond is a BQ19-3 core analysis with light green being rims.....	289
Figure 5-38 Dy/Yb <sub>N</sub> and La/Yb <sub>N</sub> ratios of the melt compositions back calculated using the partition coefficients of Wood and Blundy (1997) and Wood and Blundy (2002). The upper graph shows all the compositions whilst the lower shows more detail of the lower La/Yb <sub>N</sub> ratios.....	292
Figure 5-39 Comparison of the average La/Yb <sub>N</sub> and Dy/Yb <sub>N</sub> ratios of the back calculated melt compositions (hollow symbols) with the whole rock ratios (solid symbols). The GU20, GU25 and CA3 whole rock data was obtained using the isotope dilution technique (Appendix 1). REE data not available for GU26. ....	295
Figure 6-1 Pb isotopic ratios of Lesser Antilles lavas compared to the DMM value of Salters and Stracke (2004), used by Carpentier et al. (2008) (hollow diamond), local DMM compositions taken from PetDb ( <a href="http://www.earthchem.org/petdb">http://www.earthchem.org/petdb</a> ) (solid black diamonds) and the Northern Hemisphere Reference Line (Hart, 1984) (black line). The bulk sediment compositions analysed by Carpentier et al. (2008) are shown by hollow squares.....	306
Figure 6-2 $\Delta 7/4$ and $\Delta 8/4$ of the Lesser Antilles whole rocks. DMM (Salters & Stracke, 2004) symbols are as in Figure 6-1, as are the sediments (Carpentier <i>et al.</i> , 2008). The NHRL (Hart, 1984) is represented by a solid black line. Dashed lines represent linear regression through the Dominica (a representative island from the north and centre of the arc) and Grenada (a representative island from the south of the arc) data and are labelled on the lower graph. ....	308
Figure 6-3 Lesser Antilles $\Delta 8/4$ values against $^{206}\text{Pb}/^{204}\text{Pb}$ ratios. Also shown are both the bulk and the individual unit sediment compositions of Carpentier et al. (2008). DMM compositions are also shown (Salters & Stracke, 2004). ....	310
Figure 6-4 Mixing line between Site 144 bulk sediment compositions and the shale unit from Site 144 (Unit 3) (Carpentier <i>et al.</i> , 2008). DMM data is from PetDB, with the hollow diamond representing the composition of DMM from Salters and Stracke (2004). ....	312
Figure 6-5 $^{87}\text{Sr}/^{86}\text{Sr}$ and $^{143}\text{Nd}/^{144}\text{Nd}$ of Lesser Antilles lavas (Thirlwall, unpublished data) against the $^{206}\text{Pb}/^{204}\text{Pb}$ ratios from this study and Thirlwall (unpublished data). Also shown are mixing lines between the average local DMM composition (from PetDB) and the local sediments (Carpentier <i>et al.</i> , 2008, Carpentier <i>et al.</i> , 2009). Markers on the mixing lines show 5% increments of sediment addition. ....	313
Figure 6-6 Olivine diagram is Figure 3-28, clinopyroxene diagram is 5-30 and plagioclase diagram is Figure 4-15. It should be noted that both the olivine and clinopyroxene diagrams use the inverse of Fo content and Mg# respectively, whilst the plagioclase diagram uses actual anorthite contents. As such, the field above the line on the first two graphs represents the potentially accumulative region, whilst the field below is the more primitive region whereas the reverse is true for the plagioclase diagram.....	317
Figure 6-7 Comparison of pressures and temperatures of clinopyroxenes and plagioclases from the same host lavas. Solid symbols are calculated from plagioclases and hollow symbols are calculated from clinopyroxenes. ....	319
Figure 6-8 Textural examples of magma mixing (left hand picture, crystal from GU25) and entrainment (right hand picture, crystal from SV20). ....	322
Figure 6-9 Sr concentrations and An contents in core analyses in the BQ19-a and BQ19-b populations.....	323

Figure 6-10 La/Yb <sub>N</sub> against Dy/Yb <sub>N</sub> graph showing the bimodality observed in CA3 between the populations exhibiting differing REE profiles. ....	324
Figure 6-11 Overall petrogenetic models for the north and centre of the arc and the south of the arc, including examples of populations which show the processes highlighted. ....	328
Figure 7-1 Reproducibility of SRM987 <sup>87</sup> Sr/ <sup>86</sup> Sr and Dilute Aldrich <sup>143</sup> Nd/ <sup>144</sup> Nd standards during the period of analysis. Solid lines represent the mean value for each standard and dotted lines represent 2sd. ....	335
Figure 7-2 <sup>206</sup> Pb/ <sup>204</sup> Pb ratios measured on the SRM981 double spike during the period of study. Solid black line shows the mean ratio measured during the study with the dotted lines representing 2sd. ....	337
Figure 7-3 LA-ICP-MS analysis of an olivine from BQ19 showing a significant Ba peak at the end of the analysis. The Ba peak was removed as this clearly represents included material and not the olivine itself. ....	350

---

## List of Tables

---

Table 1-1 Summary of rock types found in each section of the arc, with sections being based on seismic subdivisions (Macdonald <i>et al.</i> , 2000, Wadge & Shepherd, 1984).....	31
Table 2-1 Summary table of studies which have analysed mineral phases in the Lesser Antilles.....	48
Table 2-2 Results of least squares fractional crystallisation modelling with parent and daughter whole rock compositions used at each stage detailed in the left hand column. Ol is olivine, cpx is clinopyroxene, plag is plagioclase and mt is magnetite. Sums of squares of residuals are shown in the right hand column and are acceptable for each stage apart from 262 to CU109 and particularly CU109 to SV19.....	56
Table 2-3 Percentage modal proportions of the phenocryst phases and groundmass point counted in the host lavas analysed by LA-ICP-MS. Thin sections were not available for the host lavas shaded grey in the table.....	58
Table 3-1 Host lava names, locations, whole rock MgO, modal olivine proportions based on point counting (1500 counts) and number of olivines analysed from each host lava as crystal mounts (n CM) and in situ in thick sections (n TS). No thin section was available for DM11A and 6264 so no point counting data were obtained for these two host lavas.....	64
Table 3-2 Olivines analysed in host lavas containing cumulate xenoliths. n is the number of each type of olivine analysed.....	88
Table 3-3 Host lava name and locations with numbers of crystals analysed in each sample block. Forsterite contents are from LA-ICP-MS analysis. Numbers in brackets show the number of the crystals which can be deemed LCO based on their CaO contents derived from LA-ICP-MS analysis. Forsterite range is the range in the olivines analysed for $\delta^{18}\text{O}$ only... 93	93
Table 3-4 CA13 thick section analyses, showing forsterite contents and CaO concentrations relative to distance from the rims of the crystals.....	134
Table 4-1 Sample name and origin of host lavas from which plagioclase crystals were analysed. Also shown is the modal proportion of plagioclase in the host lavas based on point counting data (1500 counts per thin section). No thin section was available for BQMT3. n refers to the number of plagioclases analysed by the differing methods, where CM stands for crystal mounts, TS thick sections and RB resin blocks.....	153
Table 4-2 Summary of plagioclase populations analysed in crystal mounts. The plagioclases being referred to are circled in white in the photographs if more than one phenocryst is present. The populations are referred to by letter following the sample number in which they were seen.....	157
Table 4-3 Summary of plagioclase populations analysed in the thick sections. The plagioclases being referred to are circled in white if multiple crystals are present in the photographs. The populations are referred to as a or b following the sample number in which they were seen.....	159
Table 4-4 Anorthite ranges in the thick section analyses separated by population (determined by textural analysis as shown in Table 4-3). Within each population, the whole range of anorthite contents is shown before being subdivided into core, intermediate and rim analyses.....	165

Table 4-5 Core and rim ranges of the elements analysed separated by population for the thick section plagioclases. No successful analyses of cores of crystals from SV19-b were obtained. Concentrations of trace elements are in ppm and oxides are in wt% .....	186
Table 4-6 Modal proportions of phenocryst phases in the whole rocks from which the plagioclases were analysed based on point counting data. 1500 counts per sample were used. ....	208
Table 4-7 Processes affecting each population of plagioclases identified in the thin sections analysed. Numbers on the photographs and diagrams correspond to those of the listed processes for each population and represent the order in which these processes are thought to have occurred. ....	236
Table 5-1 Sample names and locations of the host lavas from which the clinopyroxenes were analysed. Also shown are the modal proportions of clinopyroxene in each host lava ascertained from point counting data (1500 counts per thin section) and the whole rock MgO content. n shows the number of clinopyroxene crystals analysed using each method, where CM are crystal mount analyses, TS are thick sections and RB are from resin blocks. It should be noted that n represents the number of discrete clinopyroxene crystals analysed in each host lava rather than the total number of analyses undertaken. ....	241
Table 6-1 Double spike Pb data from Lesser Antilles whole rocks. Also shown are Sr and Nd isotope ratios measured on the RHUL TIMS. Analyses in italics are those of Thirlwall (unpublished data).....	305
Table 6-2 Pressure and temperatures calculated for the Lesser Antilles clinopyroxenes (Nimis, 1995, Nimis & Taylor, 2000, Putirka, 2008) and plagioclases (Putirka, 2008). No plagioclases were analysed from Carriacou and Grenada.....	318
Table 7-1 Laser settings used for each mineral phase analysed using the LA-ICP-MS. ....	339
Table 7-2 Integration times used for each phase. The olivine method was fine tuned during the study, as such there are several methods shown for this phase. ....	341

---

## List of Abbreviations

---

<b>cpx</b>	clinopyroxene
<b>DMM</b>	depleted MORB mantle
<b>HFG</b>	high forsterite group
<b>HFSE</b>	high field strength elements
<b>HREE</b>	heavy rare earth elements (Dy-Lu)
<b>IMF</b>	instrumental mass fractionation
<b>K<sub>D</sub></b>	partition coefficient
<b>LA-ICP-MS</b>	laser ablation inductively couple plasma mass spectrometry
<b>LCO</b>	low calcium olivines
<b>LFG</b>	low forsterite group
<b>LILE</b>	large ion lithophile elements
<b>LREE</b>	light rare earth elements (La-Sm)
<b>Ma</b>	million years before the present
<b>MC-ICP-MS</b>	multi collector inductively coupled plasma mass spectrometry
<b>MORB</b>	mid ocean ridge basalt
<b>MREE</b>	middle rare earth elements (Eu-Dy)
<b>NHRL</b>	Northern Hemisphere Reference Line (Hart, 1984)
<b>ol</b>	olivine
<b>opx</b>	orthopyroxene
<b>plag</b>	plagioclase
<b>ppm</b>	parts per million
<b>REE</b>	rare earth elements (La-Lu)
<b>TAS</b>	total alkali silica

<b>TIMS</b>	thermal ionisation mass spectrometry
<b>wt%</b>	weight percentage

---

## Acknowledgements

---

This thesis is dedicated to my Grandmother, Joan Johnson, who was an inspirational woman and one of the most intelligent people I have ever met. Her unwavering belief in my ability was amazing and I hope that I have made her proud.

The following people have been indispensable in the completion of this study. Firstly, my supervisors, Christina Manning and Matthew Thirlwall. This thesis has benefited enormously from the help, advice, support and constructive criticism I have received. I am truly grateful for the amount of time and energy that has gone into improving this thesis and getting it to the point of submission. Further thanks must go to the technical staff at Royal Holloway. Kevin D'Souza for providing use of the optics lab and taking photos of crystal mounts and thick sections and always being a friendly face to chat to. Neil Holloway for his seemingly endless patience in preparing my samples for analysis. I also need to thank John Craven and the Edinburgh Ion Microprobe Facility for providing essential help and advice during the acquisition of the oxygen isotope data. NERC are also thanked for providing the funding that allowed me to carry out these analyses. The Research Committee at Royal Holloway must also be acknowledged for providing the funds for numerous hours of LA-ICP-MS time.

I also need to thank all the postgrads who I have befriended during my time here, several of whom I now consider close friends, particularly my part of room 201, past and present. It has been great to be able to have a tea break, relax and laugh with people who can offer a more rational perspective in times of stress and demonstrate that finishing a thesis is possible!

The most important thanks must go to my family. My grandparents have been so supportive and encouraging, not just during my PhD, but throughout my life and I am lucky to have them. My family: Mum, Dad and Tom. There is no way I would have got this far and been the person I am today without you. I can't really express effectively how much you mean to me but your love and support throughout this process has been tremendous and unwavering and I would not have got close to finishing this thesis without you. I am privileged to call you my family.

I also need to thank James France. Again, it is difficult to put into words how much he has helped throughout this process in so many ways. He has been patient, kind, caring, loving and endlessly supportive even when things got difficult. Having you in my life has been the greatest achievement of this whole PhD process and I could not have done this without you.

---

# 1 Introduction

---

## 1.1 Brief Overview of Arcs

Volcanic arcs form as a consequence of subduction where one plate is subducted beneath another. As both plates involved in the formation of the Lesser Antilles arc are oceanic, it is deemed an intra-oceanic subduction zone. Subduction is important as a mechanism of recycling material back into the mantle, creating heterogeneities in the upper mantle (Anderson, 2006, Tatsumi & Eggins, 1995, Tatsumi & Kogiso, 2003). Heterogeneities result from the addition of subducted components to the mantle. Such additions include the downgoing crust and sediments overlying this (Tatsumi & Kogiso, 2003). In addition, the downgoing lithosphere is cold and thus helps to encourage convection in the mantle (Macdonald *et al.*, 2000). Eruption of arc lavas also builds continental crust (Tatsumi & Eggins, 1995, Tatsumi & Kogiso, 2003).

Macdonald *et al.* (2000) present an overview of published arc magmagenesis models (Arculus, 1994, Pearce & Peate, 1995, Tatsumi & Eggins, 1995) in 5 stages. Firstly, amphibolite dehydrates in the downgoing slab at around 50-60 km depth, causing the transfer of supercritical fluid phases to the overlying mantle wedge ( $\pm$  the melting of sedimentary material on the slab). This causes amphibole to form due to the hydrous conditions now present in the wedge. Peridotite bearing amphibole is then subducted further until 110 km, where the amphibole is no longer stable. The hydrous phases are released and transferred to the mantle wedge. Partial melting results from the lowering of the solidus caused by the introduction of fluids and volatiles. Diapirism occurs with the lower density melts rising through the denser wedge material. Melting continues through adiabatic decompression and the diapirs reaching hotter mantle away from the cold slab. The subduction of the slab creates a drag force, which pulls the less denser diapir material back towards the slab via convection. Resulting volcanism occurs above the shallow corner zone of the wedge, where the partial melts collect (Macdonald *et al.*, 2000).

Figure 1-1 shows an example of arc structure, via a cross-section of the Lesser Antilles arc in the vicinity of St. Vincent and Barbados (Westbrook *et al.*, 1984).

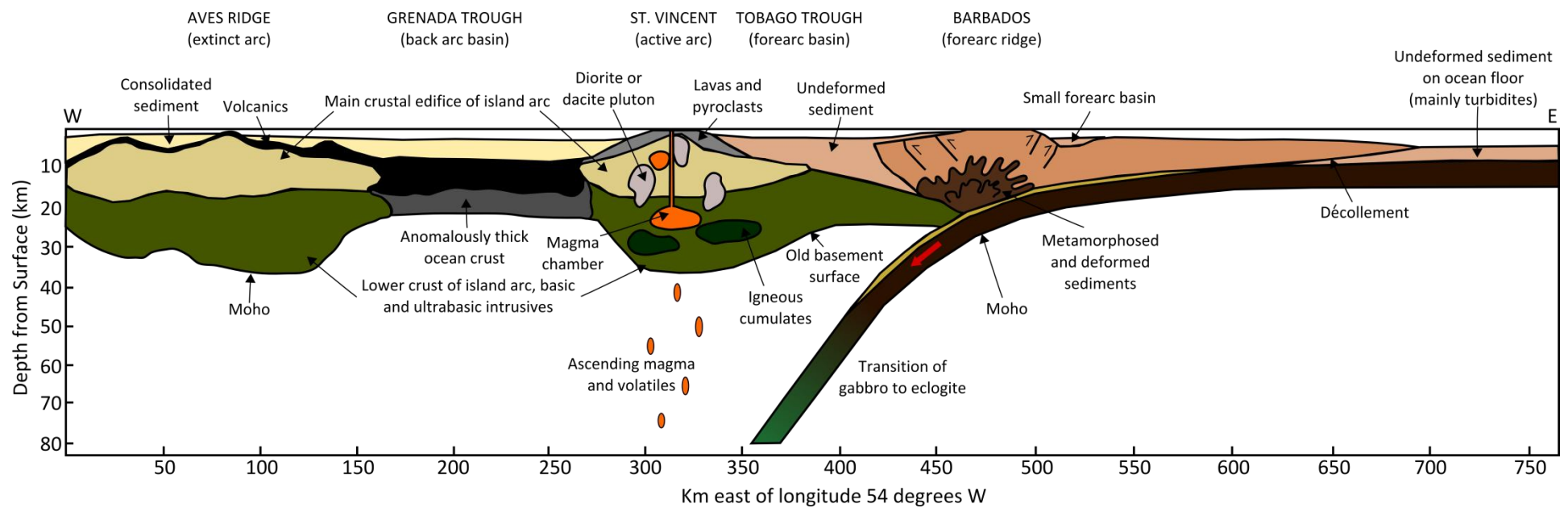


Figure 1-1 Cross-section through the Lesser Antilles arc at St. Vincent and Barbados, modified from Westbrook et al. (1984).

### **1.1.1 General Characteristics of Arc Magmas**

There are three principal common features of arc magmas (Macdonald *et al.*, 2000), with each arc then having its own individual characteristics, Tatsumi and Eggins (1995) commented that each arc system is different.

- High water contents
- High oxidation states
- LILE enrichment compared to LREE, HFSE and Th contents

Pichavant and Macdonald (2003) suggested in general there are up to four components to primitive basalts generated in arc settings:

- The mantle wedge
- Aqueous fluid
- Subducted sediment
- Shallow crustal sediment

Components thought to be contributing to the Lesser Antilles arc are discussed in section 1.5.

## **1.2 General Geology of the Lesser Antilles Arc**

The Lesser Antilles arc is an intra-oceanic arc formed by the westward subduction of the North American plate beneath the Caribbean plate, currently at a rate of approximately 2cm/year, although previously this figure was thought to be 4 cm/year (Leat & Larter, 2003, Macdonald *et al.*, 2000). This is a relatively low figure in terms of global arc convergence rates, which have been shown to extend up to 24 cm/year in the northern Tonga-Kermadec arc (Leat & Larter, 2003). Leat and Larter (2003) suggest that rates of between 5 and 13 cm/year are more conventional. The Lesser Antilles arc also shows low rates of magma production compared to other convergent zones, such as Central America, suggesting that the slow convergence rate of the arc as a possible cause (Wadge, 1984). The rate of convergence is four times higher in Central America compared to the Lesser Antilles, with production rates estimated to be an order of magnitude greater than in the Lesser Antilles

(Wadge, 1984). The active part of the Lesser Antilles extend from Saba in the north to Grenada in the south (Figure 1-2).

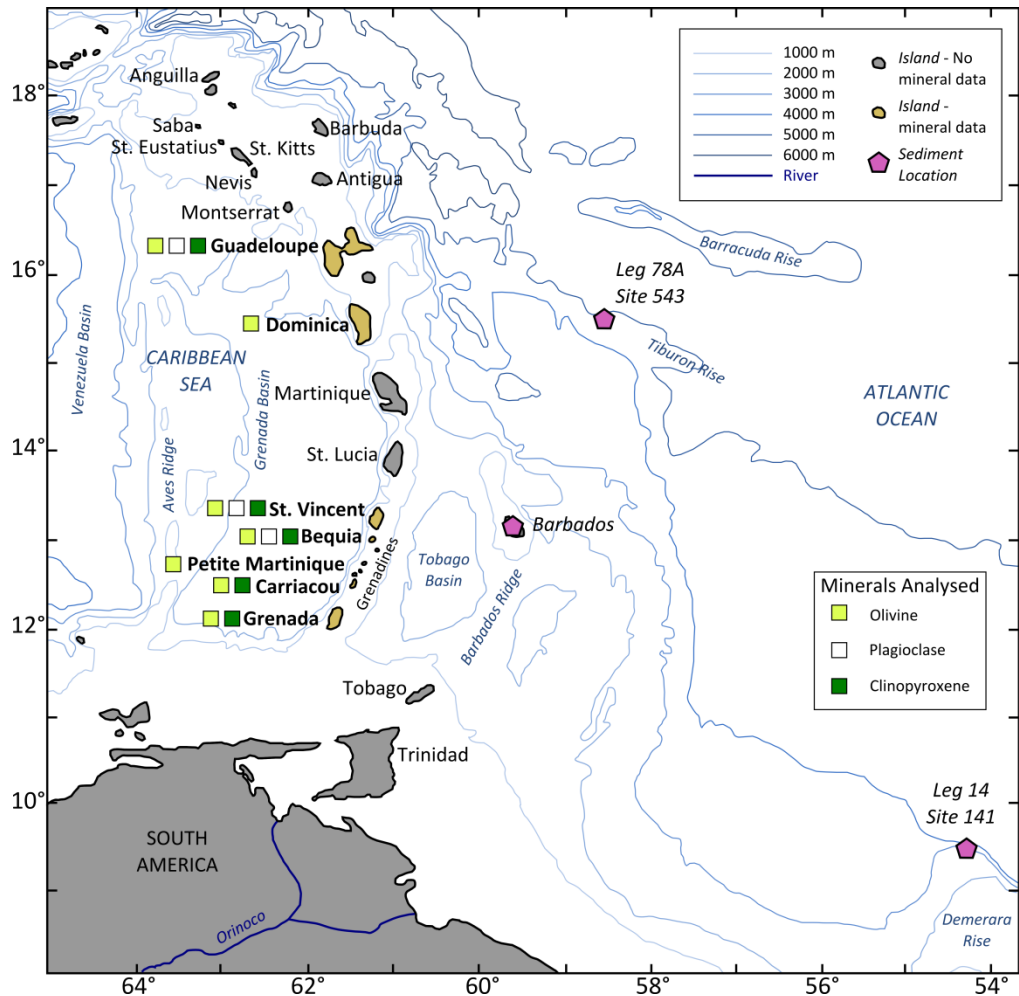


**Figure 1-2** Map showing the Lesser Antilles, modified from Carpentier et al. (2008) and Van Soest et al. (2002). The islands coloured in beige are ones from which data were obtained. The squares to the left of the name of the islands indicate which mineral phases were analysed from that island. Purple pentagons indicate the location of the sediment data detailed in Carpentier et al. (2008).

### 1.2.1 Geological History

Subduction began when the Caribbean plate moved eastwards from its original location in the Pacific and collided with the North American and South American plates. This resulted in the formation of the now extinct Aves Ridge between 88-59 Ma (Bouysse, 1984, Bouysse *et al.*, 1990, Macdonald *et al.*, 2000, Neill *et al.*, 2011). Following this, in the Palaeocene to early Eocene, volcanism stopped and the Grenada Basin opened, as described by Neill *et al.* (2011) and references therein.

Rollback of the subduction zone occurred, shifting the volcanic front to form the Lesser Antilles arc in its current location (Neill *et al.*, 2011).

### ***Bifurcation of the Arc***

During the Miocene, there was a shift in volcanism westwards, as noted by Westbrook *et al.*, (1984) and references therein. Bifurcation of the arc occurred at 9 Ma (Baker, 1984), originating at Martinique and affecting the islands to the north (Bouysse *et al.*, 1990). The two branches of the arc have been named as follows: the 'Limestone Caribbees' are those now inactive islands (and parts of islands) to the east and the 'Volcanic Caribbees' are located on the current front of active volcanism to the west (Bouysse, 1984). Baker (1984) provides date ranges for the activity of each branch of the arc, with the Limestone Caribbees being active between 38-10 Ma and the Volcanic Caribbees commencing volcanism from 7.7 Ma and continuing until the present day. The southern part of the arc has been active since the Eocene.

### **1.2.2 Strike and Dip of the Benioff Zone**

Wadge and Shepherd (1984) conducted a study based on earthquake seismicity in the Lesser Antilles region and concluded that both the strike and dip of the Benioff zone beneath the arc changes from north to south. From Martinique northwards, the Benioff zone dips at 60-50° and trends NNW. The southern section from St. Lucia and southwards shows a dip of 50-45°, however at the southernmost reaches of the arc, the Benioff zone shows a vertical dip (the change in dip occurring beneath Grenada) (Wadge & Shepherd, 1984). The zone trends NNE in the southern section.

### **1.2.3 Fore-arc Region and Accretionary Prism**

The Lesser Antilles arc is accretionary, with material being built up since the Eocene (Speed & Larue, 1982, Westbrook *et al.*, 1988), although most modern arcs are non-accretionary (Leat & Larter, 2003). The dimensions of the fore-arc change from north to south, both in width and depth. To the north, the sequence is both narrower and deeper, being 8 km deep (Chase & Bunce, 1969) and 150 km wide (Macdonald *et al.*, 2000). In the south of the arc, the fore-arc is 450 km wide and hosts the accretionary complex known as the Barbados Ridge (Carpentier *et al.*, 2009).

Barbados forms the surface expression of the accretionary prism (Macdonald *et al.*, 2000). The trench in the north of the arc is thought to be over 6 km deep, whereas in the south the trench is completely filled with the fore-arc sequence, which is up to 20 km thick (Van Soest *et al.*, 2002).

A décollement exists between sediment being scraped off the descending slab and being accreted and that which remains with the slab during subduction (Plank & Langmuir, 1993). In the Lesser Antilles, this occurs at a depth of around 200 m (Macdonald *et al.*, 2000, Plank & Langmuir, 1993). The material which is not being subducted needs to be taken into consideration when modelling sediment contribution to the parent melts, as the accreted material will have no effect on melt composition.

### 1.3 Rock Types and Cumulates

Table 1-1 shows a summary of igneous rocks found in the arc (Macdonald *et al.*, 2000). Basalts are much more dominant in the southern part of the arc than the central and northern parts. Petrologically, the northern and central sections exhibit more evolved lavas although some basalt is still present.

<b>Region</b>	<b>Extent</b>	<b>Rock Types</b>
<b>Northern</b>	Saba to Montserrat	Dominantly andesite, some basalt, dacite, rare rhyolite.
<b>Central</b>	Guadeloupe to St. Lucia	Dominantly andesite, some basalt, dacite, rare rhyolite.
<b>Southern</b>	St. Vincent to Grenada	Dominantly basalt and basaltic andesite, some andesite, rare dacite.

**Table 1-1 Summary of rock types found in each section of the arc, with sections being based on seismic subdivisions (Macdonald *et al.*, 2000, Wadge & Shepherd, 1984).**

In addition to eruptive products, the Lesser Antilles is also host to many cumulates, with examples being found across the arc on every island bar Nevis and Guadeloupe (Arculus & Wills, 1980, Macdonald *et al.*, 2000). The cumulates have been extensively studied, showing compositional and textural differences (Arculus & Wills, 1980, Coulon *et al.*, 1984, Parkinson *et al.*, 2003, Stamper *et al.*, 2014, Tollan *et al.*, 2012). Minerals found in cumulates include amphibole, plagioclase,

clinopyroxene, orthopyroxene, olivine, magnetite, biotite, quartz, ilmenite and apatite, with proportions being changeable (Arculus & Wills, 1980, Macdonald *et al.*, 2000).

#### **1.4 Changing Geochemistry of Lavas Along Arc Strike**

Brown *et al.* (1977) first noted the change composition of magmas along arc strike, noting a trend of tholeiitic compositions in the north of the arc, calc-alkaline compositions in the central section and alkaline compositions in the south of the arc. Davidson and Wilson (2011) pointed out that once more detailed studies of individual volcanic centres were undertaken, large ranges in magmatic composition can also be observed at this scale, suggesting that the trend proposed by Brown *et al.* (1977) is oversimplified. Nonetheless, the magmas with MgO contents of >8 wt% MgO are exclusively observed in the south of the arc (Davidson & Wilson, 2011). This study has analysed olivines (a mineral requiring reasonable MgO contents in the melt) from whole rocks from Guadeloupe and Dominica, but these were sampled from host lavas with 4-6 wt% MgO and 5 wt% MgO respectively. MgO contents of olivine host lavas from the south of the arc extended up to 17 wt%.

Macdonald *et al.* (2000) and references therein show there is relatively smooth transition from lower K<sub>2</sub>O whole rock contents at a given SiO<sub>2</sub> in the north of the arc through to higher K<sub>2</sub>O compositions in the south of the arc, with Macdonald *et al.* (2000) specifically showing the K<sub>2</sub>O contents of the Grenada lavas relative to those seen in northern and central islands.

White and Dupre (1986) report wide variations in isotopic compositions of lavas in the Lesser Antilles. The <sup>87</sup>Sr/<sup>86</sup>Sr and <sup>143</sup>Nd/<sup>144</sup>Nd ratios measured by White and Dupre (1986) were also compared by the authors to oceanic island values and were shown to overlap with oceanic island basalts. White and Dupre (1986) deemed the signatures of the Lesser Antilles lavas to be "enriched", more so than the signatures of most other island arcs. <sup>143</sup>Nd/<sup>144</sup>Nd isotope ratios decrease from north to south (Carpentier *et al.*, 2008), whilst the <sup>87</sup>Sr/<sup>86</sup>Sr ratios show a more complicated trend, with the central islands showing an extensive range in values (Figure 1-3).

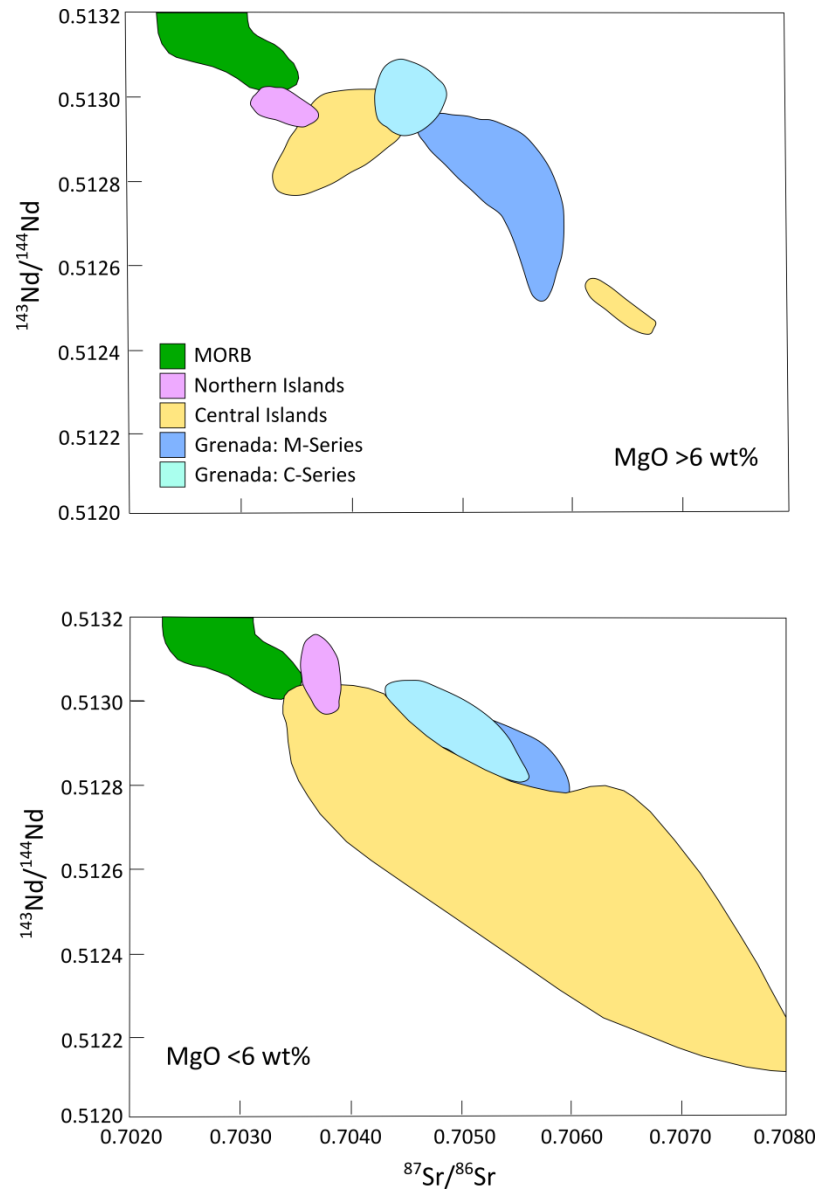


**Figure 1-3 Sr and Nd isotopic ratios from across the Lesser Antilles arc, modified from Macdonald et al. (2000). Data from Macdonald et al. (2000) and references therein.**

The Pb isotopic composition of the arc lavas have been a topic of note in many papers published about the Lesser Antilles (Carpentier *et al.*, 2008, Carpentier *et al.*, 2009, Macdonald *et al.*, 2000, White & Dupre, 1986, White *et al.*, 1985). The principal point of interest is that in the south of the arc (from Martinique to Grenada, Carpentier *et al.*, 2009), the Pb isotope ratios extend to very radiogenic values (Carpentier *et al.*, 2008, Carpentier *et al.*, 2009, White & Dupre, 1986, White *et al.*, 1985) and are the highest observed in intra-oceanic arcs (Carpentier *et al.*, 2008) Figure 1-4. Pb isotopic ratios extend up to 20.16 ( $^{206}\text{Pb}/^{204}\text{Pb}$ ) and 15.85 ( $^{207}\text{Pb}/^{204}\text{Pb}$ ) (White & Dupre, 1986). The unusually radiogenic Pb isotope ratios have been attributed to the sediments being subducted in this region of the arc, either solely

(Labanieh *et al.*, 2010, Turner *et al.*, 1996, White & Dupre, 1986) or in conjunction with crustal contamination (Davidson, 1985, Davidson, 1986, Davidson, 1987, Davidson & Harmon, 1989, Smith *et al.*, 1996, Thirlwall & Graham, 1984, Thirlwall *et al.*, 1996). Sediments will be discussed more in section 1.5.2.

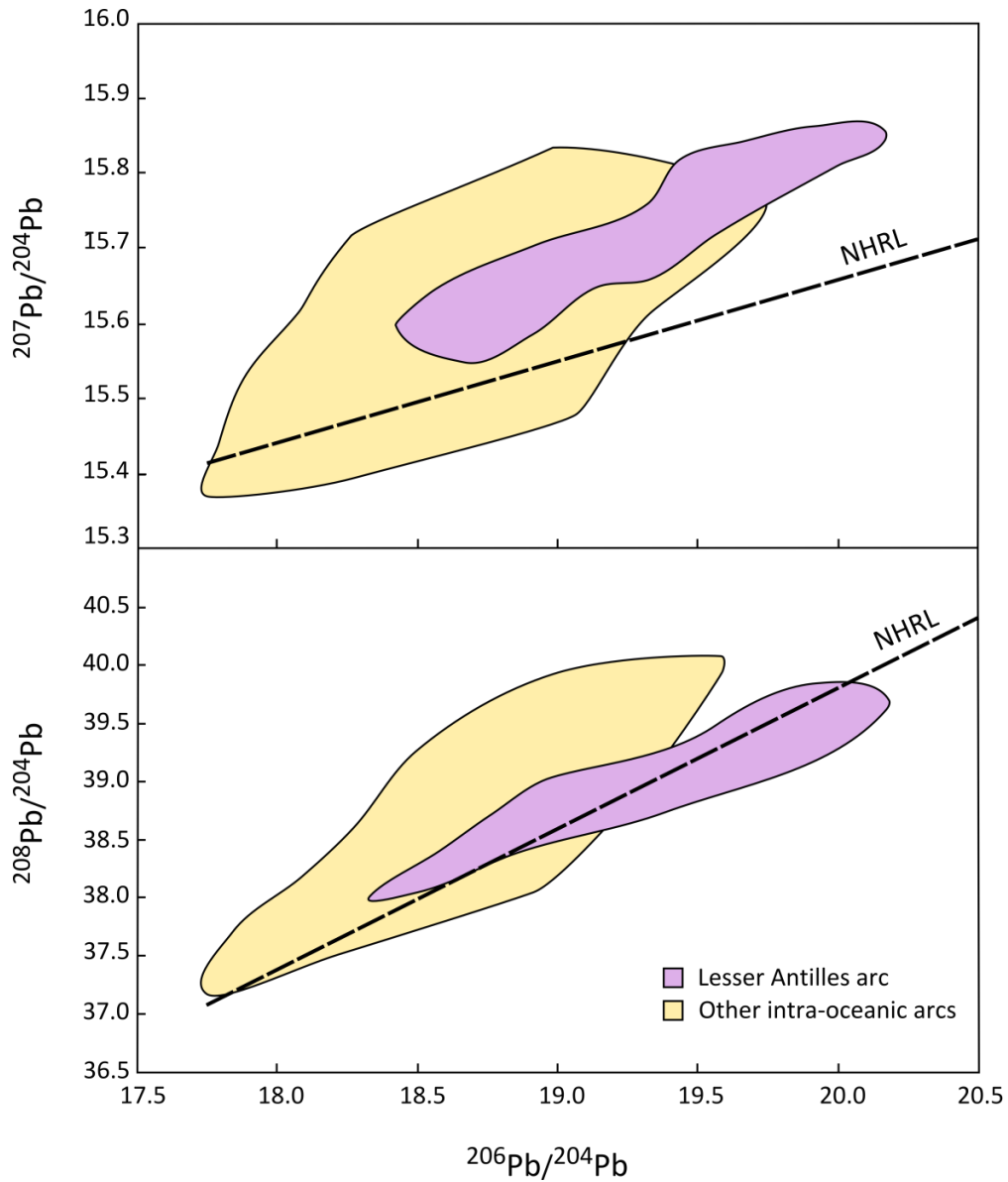


**Figure 1-4 Summary of Pb isotopic data from Lesser Antilles arc lavas compared to lavas from other intra-oceanic arc settings, modified from Carpentier *et al.* (2008). Data from Carpentier *et al.* (2008) and references therein.**

Broadly speaking, in the north of the Lesser Antilles arc, the lavas are comparable to other oceanic island arcs, whilst in the south the isotopic compositions do not resemble conventional arc data, being more 'crust-like' (Labanieh *et al.*, 2012, Labanieh *et al.*, 2010, White & Dupre, 1986).

Of the basaltic lavas found on Grenada, two main suites can be identified: the M-series and the C-series (Hawkesworth *et al.*, 1979, Thirlwall & Graham, 1984). Differentiation between the two uses the relationship between CaO and MgO in the lavas, the M-series exhibit lower CaO contents at a given MgO compared to the C-series. The C-series also show much higher proportions of augite than the M-series (Thirlwall & Graham, 1984). The authors concluded that the C-series lavas originated from picritic parents before undergoing assimilation fractional crystallisation (AFC). The M-series evolved from picritic parents without the addition of crustal material (Thirlwall *et al.*, 1996).

## **1.5 Components of Lesser Antilles Arc Magmas**

The arc magmas of the Lesser Antilles require three principal components in the mantle wedge: an N-MORB type source, at least one type of hydrous fluid (possibly up to three, Bouvier *et al.*, 2008) and sediment material (possibly from partial melting of subducted sediments) (Macdonald *et al.*, 2000, Thirlwall *et al.*, 1996, Turner *et al.*, 1996). The proportions of these contributors vary along arc strike, with sediment being more dominant in the south of the arc than the north (Macdonald *et al.*, 2000). After generation of the primary magmas in the mantle wedge, many are then thought to be affected by crustal contamination. The sub-sections below provide further details on these components.

### **1.5.1 Mantle Beneath the Lesser Antilles**

The mantle beneath the Lesser Antilles arc is thought to be of an N-MORB composition (Bouvier *et al.*, 2008, Macdonald *et al.*, 2000). General characteristics of the whole rocks are given by Macdonald *et al.* (2000) as follows (relative to MORB): the LREE and LILE are enriched and the HREE, MREE, HFSE are depleted, Ti/V ratios are lower and LILE/LREE ratios are higher. The authors suggested this could be resolved either by the lavas being derived from mantle sources with heterogeneous depletion in incompatible trace elements or by starting with an N-MORB source which is subsequently enriched in both LREE and LILE, potentially by fluids. The LREE and LILE enrichment is thought to result from a contribution from the downgoing slab. If this contribution is in the form of a fluid, the degree of partial melting may be increased by the lowering of the solidus. The

latter theory appears to agree with the findings of Bouvier et al. (2008) who proposed a three stage contamination by varying fluids in order to explain their melt inclusion compositions. However, the findings of Davidson (1996) (based on Zr/Nb ratios) could suggest that the former argument is true and the mantle wedge is heterogeneous, with some areas being enriched and others being depleted. Macdonald et al. (2000) proposed that this is supported by the low Ti/V ratios.

Overall, Macdonald et al. (2000) and references therein outline the mantle source to be heterogeneous N-MORB, with subsequent enrichment of LILE and LREE from the addition of a slab derived component (such as fluid). Degree of melting is thought to be higher than MORB to generate the primary magmas (Macdonald *et al.*, 2000).

REE concentrations in the lavas provide information on potential sources. When the magmas have high MgO, with the literature suggesting contents of above of 6 wt% MgO to be adequate (Macdonald *et al.*, 2000, Thirlwall *et al.*, 1994a), it is thought that the effects of fractional crystallisation are effectively filtered out.

Arc magmas can be subdivided based on their Ce/Yb ratios (Hawkesworth *et al.*, 1993a, Hawkesworth *et al.*, 1993b). Most island arcs exhibit only one group of magmas, either high or low Ce/Yb. However, the Lesser Antilles is unusual in that both Ce/Yb groups are present in the arc, suggesting either differing sources or partition coefficients and/or degree of partial melting (Macdonald *et al.*, 2000).

### **1.5.2 Contribution from Subducting Slab**

LREE and LILE enrichment of arc lavas is thought to result from a contribution from the slab (Macdonald *et al.*, 2000). This can be in the form of a fluid component, e.g. released during the dehydration of the subducted altered oceanic crust or from a partial melt of the slab and/or sediments, or potentially a combination of both. Partial melting of sediments has been proposed by Hawkesworth et al. (1997) to be responsible for increased Th/Ce ratios and less radiogenic  $^{143}\text{Nd}/^{144}\text{Nd}$  ratios in the island arcs of the Aeolian Islands, the Philippines and Indonesia. A further possibility is the bulk addition of sediment to the mantle wedge through delamination (Macdonald *et al.*, 2000).

The fluid component in the Lesser Antilles is thought to be dominantly water (with a 10:1 ratio to CO<sub>2</sub>) (Macdonald *et al.*, 2000, Peacock, 1990, Stolper & Newman, 1994), with potentially higher Cl concentrations that seen in other arcs worldwide, based on melt inclusion data (Bouvier *et al.*, 2008, Bouvier *et al.*, 2010, Devine & Sigurdsson, 1995, Heath *et al.*, 1998a, Young *et al.*, 1998). Macdonald *et al.* (2000) also suggested that fluids would have high H<sub>2</sub>S contents as a result of breaking down sulphides hosted in the descending slab materials.

The potential for slab melting is effectively ruled out by Macdonald *et al.* (2000) on the basis of the findings of (Davies & Stevenson, 1992, Nichols *et al.*, 1994, Peacock, 1996, Peacock *et al.*, 1994). The latter suggest that in order for slab melting to occur, the downgoing lithosphere needs to be both hot and young. Given that the subducting North American plate in the Lesser Antilles is between Jurassic and Cretaceous in age, it is likely to be too old and cold to undergo melting.

However, partial melting of sediments on the subducting slab has been suggested to contribute to high Ta/Zr ratios in Grenada whole rocks (Turner *et al.*, 1996).

### **1.5.3 Sediment Being Subducted**

The type and thickness of sediment being subducted with the North American plate changes along arc strike. Thicker sequences of terrigenous sediment are subducted to the south of the arc, as a result of this section's proximity to the South American continent. Material eroded from the Guyana Highland (part of the South American craton) is transported principally by the Orinoco River (Carpentier *et al.*, 2008, Carpentier *et al.*, 2009, Macdonald *et al.*, 2000, Westbrook *et al.*, 1984, White & Dupre, 1986, White *et al.*, 1985). Westbrook *et al.* (1984) also suggest some sediment transport via the Amazon River, which has its mouth further to the south than the Orinoco, emptying directly into the Atlantic Ocean off the east coast of Brazil. Moving northwards along arc strike and away from the South American continent, the volume of terrigenous material decreases. The sediment subducted is more pelagic in nature than in the south of the arc. The sediment pile is thought to be 10 km thick to the south of the arc and less than 1 km thick in the north (Carpentier *et al.*, 2008, Carpentier *et al.*, 2009, Westbrook *et al.*, 1984).

In addition to the geochemical zoning observed in the lavas, the sediments on the downgoing North American plate are also thought to change composition from north to south (White *et al.*, 1985). Studies on sediment compositions have largely involved analysing sediment sampled from Site 543 (Plank & Langmuir, 1993, White *et al.*, 1985) and Site 144 of the DSDP (Carpentier *et al.*, 2008, Carpentier *et al.*, 2009). In addition, the Carpentier *et al.* (2008, 2009) analysed sediment sampled from Barbados. Locations from which sediments have been analysed are shown on Figure 1-2. Carpentier *et al.* (2008) found that the Nd and Pb isotopic compositions of sediments mirror the changes observed in the lavas by White and Dupre (1986). The Pb isotope ratios get more radiogenic further to the south, with this change being attributed to the subduction of black shale sequences (found in the Site 144 sediments) comprising part of the downgoing sediment load in the south of the arc (Carpentier *et al.*, 2008, Carpentier *et al.*, 2009).

#### **1.5.4 Crustal Contamination**

This is evident through the inclusion of metamorphic xenoliths in many of the arc lavas. Assimilation fractional crystallisation has been suggested as a key process by several authors (Bezard *et al.*, 2014, Davidson, 1985, Davidson & Wilson, 2011, Davidson, 1986, Davidson, 1987, Davidson & Harmon, 1989, Smith *et al.*, 1996, Thirlwall & Graham, 1984, Thirlwall *et al.*, 1996, Van Soest *et al.*, 2002), based in part on  $\delta^{18}\text{O}$  results. The effects of crustal contamination have been particularly well studied on Martinique (Davidson, 1985, Davidson & Wilson, 2011, Davidson, 1986, Davidson, 1987, Davidson & Harmon, 1989). However, other authors dispute the importance of AFC, such as Devine and Sigurdsson (1995), who found little evidence for the process in the same series of lavas as those studied by Thirlwall *et al.* (1996). Overall, crustal assimilation is thought to play an important role in the central islands of the arc (with the exception of St. Vincent) but not in the northern islands; as previously mentioned, the importance of AFC processes in Grenada is subject to debate (Macdonald *et al.*, 2000).

#### **1.5.5 Contamination by Sediments at Source or in the Crust?**

Whilst there has been debate in favour of both mechanisms, as of yet no overall conclusion has been made as to whether Lesser Antilles arc lavas are being

contaminated dominantly by sediments in the mantle wedge or by crustal assimilation (Macdonald *et al.*, 2000). Both methods have been suggested to be able to generate some of the more extreme whole rock isotopic compositions that set the Lesser Antilles lavas apart from those from other oceanic arcs. Macdonald *et al.* (2000) proposed that as a very general test, the Sr and Nd isotopic ratios could be used to suggest where sediment contamination had occurred. An Sr ratio of  $^{87}\text{Sr}/^{86}\text{Sr} > 0.706$  coupled with an Nd ratio of  $^{143}\text{Nd}/^{144}\text{Nd} < 0.5127$  was put forward as an indicator that the lava had been contaminated in the crust (Macdonald *et al.*, 2000). However, crustal contamination should also increase  $\delta^{18}\text{O}$ , whereas adding fluid from the subducting slab to the mantle source is not thought to greatly alter oxygen isotope compositions (Davidson & Harmon, 1989). When oxygen isotope ratios are used in combination with  $^{87}\text{Sr}/^{86}\text{Sr}$  ratios, the shape of mixing curves between source and contaminant endmembers can be used to suggest whether contamination is occurring in the crust or at source (James, 1981). Whole rock  $\delta^{18}\text{O}$  can be changed from magmatic values during low temperature hydration and secondary alteration and thus careful correction is required to obtain meaningful interpretations (Macdonald *et al.*, 2000).

## **1.6 What Makes the Lesser Antilles Arc Interesting to Study?**

The presence of high MgO basaltic lavas in the Lesser Antilles is unusual for an intra-oceanic island arc (Macdonald *et al.*, 2000). As a result, the Lesser Antilles provides an excellent opportunity to study near primary melts in an island arc setting as basalts are found across the whole arc, though primarily in the southern islands (Macdonald *et al.*, 2000). Using minerals in particular provides an excellent window into petrogenesis before fractionation can alter the composition of the melt as phases that crystallise early (such as olivine) can be studied and compared to later crystallising minerals.

The Lesser Antilles show wide variations in the whole rocks along arc strike, both isotopically and compositionally, as first noted by Brown *et al.* (1977). This will be explored further in section 1.3 and is one of the most notable features of the arc.

Macdonald *et al.* (2000) comment that as arc crust thickens, magmas of basaltic composition pond and require fractionation to lower density and permit ascent

through the crust. Average crustal thickness beneath the Lesser Antilles is 30 km (White & Dupre, 1986). Studying minerals allows further insight into this process, as crystals formed at different times and in different parts of the magmatic plumbing system can show different characteristics. This information is lost when looking at only homogenised whole rock compositions. Given that basaltic magmas can be rare in arc settings, the Lesser Antilles provide an excellent location to use mineral chemistry to probe the processes occurring within the plumbing system.

Figure 1-5 shows a summary of the varying trends along arc strike.

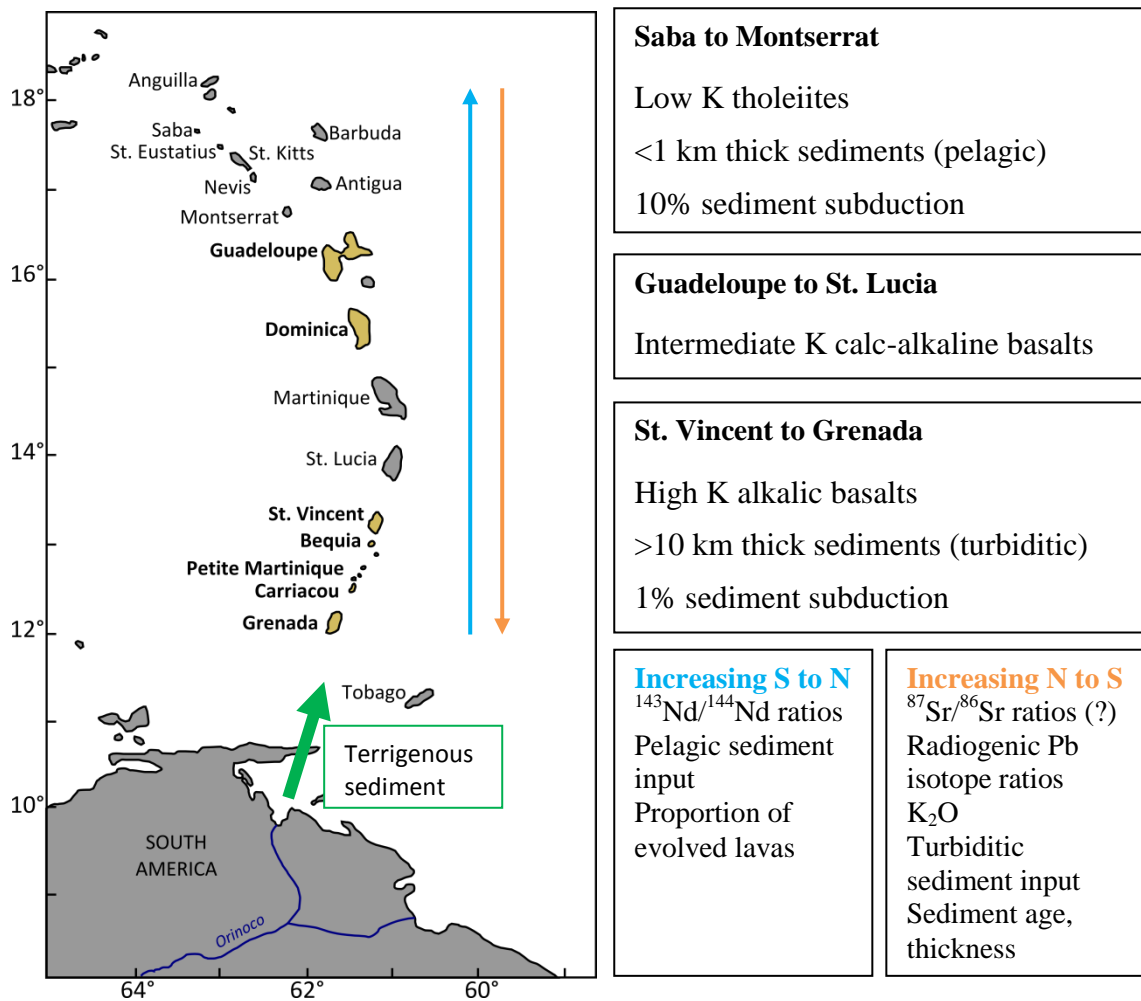


Figure 1-5 Summary diagram showing principal changes along arc strike (Carpentier *et al.*, 2008, Macdonald *et al.*, 2000, Westbrook *et al.*, 1984, White & Dupre, 1986). Legend for map is as in Figure 1-2.

Variation in the whole rock chemistry is seen in  $^{143}\text{Nd}/^{144}\text{Nd}$  ratios,  $^{88}\text{Sr}/^{87}\text{Sr}$  ratios, U/Th ratios,  $\text{K}_2\text{O}$  and MgO concentrations from the south to the north of the arc (Macdonald *et al.*, 2000, White & Dupre, 1986). It is suggested in the literature that these variations in part arise from varying degrees and types of sediment input along

the arc strike (Carpentier *et al.*, 2008, Carpentier *et al.*, 2009), with terrigenous sediment being incorporated in greater degrees in the south of the arc than the pelagic material thought to be contributing in the north.

## 1.7 Project Aims

The principal aim of this project is to use mineral chemistry to disentangle petrogenetic processes occurring within the Lesser Antilles and develop an overall model of petrogenesis, with information on how this changes along arc strike and provide further insight into the unusual chemistries observed in the arc. In addition, there are the following supplementary aims:

- Provide a comprehensive mineral dataset covering the Lesser Antilles island arc.
- Use this data to observe processes occurring in the magmatic plumbing systems in which the minerals were formed.
- Couple the mineral data with whole rock geochemical and isotopic data to provide insights into the petrogenesis of the Lesser Antilles island arc lavas.
- Test the hypothesis of Carpentier *et al.* (2008) as to the source of the unusual Pb isotopic ratios.
- Attempt to constrain better endmembers involved in mixing between the mantle sources and sediment input along arc strike.

Whilst numerous whole rock studies have been undertaken, few have studied multiple mineral phases from islands across the arc. Recently, Bezard *et al.* (2014), noted the need for a mineral-scale study to shed further light specifically on assimilation. Detailed mineral analysis is also important because it allows the processes occurring within the arc system to be studied, tying textural and geochemical information together to bolster understanding of what happens to melts between formation and eruption. Being able to observe variations in minerals can add a different perspective e.g. on where sediment is being added to the arc. If material is added at source into the mantle wedge, this would affect all subsequently crystallising minerals. If sediment is being assimilated, there may be evidence of changes in melt compositions back calculated from the mineral analyses and

potentially textural differences. Chapter 2 fully explains the benefits of mineral analysis. The textural and compositional data can also be combined with whole rock isotopic data to observe if there are any correlations between isotopic ratios and populations of minerals. This study can further the literature both in terms of the scale of mineral analysis and using this data to try and answer questions posed by the distinctive isotopic ratios of many whole rocks from the arc in combination with high precision double spike Pb data.

## **1.8 Thesis Overview**

Below is a brief summary of the information contained in the following chapters.

### *Chapter 2*

This provides an introduction into the benefits of using mineral chemistry. An overview of published mineral data obtained from the Lesser Antilles is given. Information pertinent to the mineral data chapters is also given, such as classification of the host lavas, point counting data, a method summary and an explanation of parameters used on thick section data to quantify location of analysis sites within the crystals.

### *Chapters 3, 4 and 5*

These chapters comprise the studies of each individual mineral phase targeted in this study. Information as to what insights each mineral phase can provide, results, identification of discrete populations, comparison to other Lesser Antilles ( $\pm$  other arc) data and a discussion on processes and petrogenesis is provided in each chapter. Chapter 3 concerns olivine, Chapter 4 plagioclase and Chapter 5 clinopyroxene.

### *Chapter 6*

This chapter synthesises all the mineral information gleaned, combining evidence from the discrete mineral phases to give a more complete view of petrogenesis in the Lesser Antilles. In addition, this chapter comprises the whole rock isotopic data and models based on Sr, Nd and Pb isotope ratios. This is then combined with the

mineral study to form an overall model of Lesser Antilles arc petrogenesis and how and why this changes along strike of the arc.

---

## 2 Mineral Chemistry Introduction

---

### 2.1 Introduction

#### 2.1.1 Reasoning for Analysing Minerals

Recent research (Bezard *et al.*, 2014, Davidson *et al.*, 2007b) has shown the benefit of analysing minerals over bulk rock in constructing petrogenetic histories of lavas. Significant heterogeneity can be preserved in crystal cargoes allowing better understanding of the processes that have occurred from melt to eruption. Analysis of multiple populations can also allow insights into processes over wider pressure-temperature conditions. Zoned minerals represent changes in the crystallising conditions and analysis of individual chemical zones alongside investigation of the type of boundary (sharp, diffusion, resorbed etc.) can allow significant information to be gained from a single mineral.

This makes mineral analysis a powerful tool in deciphering the processes and melt compositions contributing to the overall petrogenesis of a lava. Furthermore, targeting minerals allows for the observation of potential heterogeneities between crystals. Thus, multiple populations may be identified in individual lavas, providing insights into how these populations originate, combine and travel through the magmatic plumbing system.

Different mineral phases can record numerous processes happening throughout petrogenesis and as such each phase targeted serves a different purpose to this end.

Olivine was analysed as this is commonly the first forming phase from a melt. As a result it can record the early petrogenetic history of a melt, before fractional crystallisation has affected the melt chemistry and may give insights into potential source melt compositions.

Plagioclase records textural and geochemical information from numerous processes, such as magma mixing, entrainment, decompression of melts during ascent and degassing at shallow levels. This information can be tracked across single crystals, giving insights into what has happened to these minerals en route to the surface.

Clinopyroxene is particularly useful for geothermobarometry, giving an indication of whether pressure and temperature conditions for clinopyroxene crystallisation are consistent both within host lavas and, at a larger scale, along the arc. REE profiles from clinopyroxenes are also useful for providing insights into the trace element chemistry of potential parent melts, through back calculation following partition coefficient estimation.

### **2.1.2 Limitations of Using Mineral Chemistry in Conjunction with Whole Rock Chemistry**

Minerals in the host lavas may not necessarily have crystallised from the melt in which they are found. Mineral populations have been split into three broad categories in this study: phenocrysts, antecrysts and xenocrysts. Phenocrysts are those minerals that appear to have crystallised in equilibrium with the host melt at some point during its evolution and then been erupted whilst resident in the same melt. Antecrysts (Davidson *et al.*, 2007b) are minerals which have been crystallised from a melt related to the host melt but not the melt in which the crystals were erupted. For example, the melt may have originated from a similar source but followed a different evolutionary path through the magmatic plumbing system. Antecrysts are explored more fully in Chapter 3. Xenocrysts are those crystals that have been erupted in the host lava but show no relation to this melt, such as crystals entrained from the mantle.

Because minerals are a product of specific conditions and/or time periods in the petrogenesis of the melt, the whole rock is essentially a combination (and thus homogenisation) of many chemical compositions representing different stages in the evolution of the melt. Entrainment of crystal cargoes from cumulate bodies, wall rock etc. will also affect the chemistry of the whole rock. Some of these populations may not necessarily be related to the melt in which they reside, but whole rock compositions will include these crystals.

As a result, throughout this study it has been found that comparing mineral chemistry to that of the whole rock often results in discrepancies. Overall, it is more useful to consider the minerals (and any back calculated melt compositions) separately to the whole rocks. In each chapter, mineral compositions have been

compared to the whole rock compositions as a matter of course and this often confirms the lack of relationship between the two.

Whilst whole rocks obviously have a part to play in understanding the petrogenesis of lavas, mineral analysis provides a much more detailed window into the journey from partial melt to erupted lava.

## **2.2 Published Lesser Antilles Studies**

There have been numerous studies on minerals from the Lesser Antilles arc (Arculus, 1978, Arculus & Wills, 1980, Cawthorn *et al.*, 1973, Coulon *et al.*, 1984, Davidson & Wilson, 2011, Heath *et al.*, 1998b, Parkinson *et al.*, 2003, Pichavant & Macdonald, 2007, Pichavant *et al.*, 2002a, Pichavant *et al.*, 2002b, Stamper *et al.*, 2014, Tollan *et al.*, 2012, Toothill *et al.*, 2007, Turner *et al.*, 2003, Van Soest *et al.*, 2002, Vannucci *et al.*, 2007). However, with the exception of the Arculus and Wills (1980), Davidson and Wilson (2011) and Van Soest *et al.* (2002) studies, these publications focus on minerals from a single island only (Table 2-1).

Analysis of multiple phases from islands across the arc using the same technique allows for easy comparison of compositions observed both within discrete host lavas and across islands. None of the previous studies have analysed olivine, clinopyroxene and plagioclase in numerous islands. Therefore this study can provide comparable data across the arc from multiple phases giving a more complete picture of petrogenesis along the arc.

<b>Study</b>	<b>Location</b>	<b>Olivine</b>	<b>Plagioclase</b>	<b>Clinopyroxene</b>	<b>Notes</b>
<b>Arculus (1978)</b>	Grenada	✓		✓	
<b>Arculus and Wills (1980)</b>	Lesser Antilles	✓	✓	✓	Cumulates
<b>Cawthorn et al. (1973)</b>	Grenada	✓		✓	
<b>Coulon et al. (1984)</b>	Martinique	✓	✓	✓	Xenoliths
<b>Davidson and Wilson (2011)</b>	St. Eustatius, Martinique	✓	✓	✓	
<b>Devine and Sigurdsson (1995)</b>	Kick 'Em Jenny			✓	
<b>Heath et al. (1998)</b>	St. Vincent	✓	✓	✓	
<b>Parkinson et al. (2003)</b>	Grenada	✓	✓	✓	Xenoliths
<b>Pichavant and Macdonald (2007)</b>	St. Vincent	✓	✓	✓	
<b>Pichavant et al. (2002a)</b>	Martinique	✓	✓	✓	
<b>Pichavant et al. (2002b)</b>	St. Vincent	✓		✓	
<b>Stamper et al. (2014)</b>	Grenada	✓	✓	✓	Cumulates and xenoliths
<b>Tollan et al. (2012)</b>	St. Vincent	✓	✓	✓	Cumulates
<b>Toothill et al. (2007)</b>	St. Kitts	✓		✓	
<b>Turner et al. (2003)</b>	Martinique	✓	✓	✓	

<b>Study</b>	<b>Location</b>	<b>Olivine</b>	<b>Plagioclase</b>	<b>Clinopyroxene</b>	<b>Notes</b>
<b>Van Soest et al. (2002)</b>	Lesser Antilles	✓		✓	
<b>Vannucci et al. (2007)</b>	Grenada	✓		✓	Xenoliths

**Table 2-1 Summary table of studies which have analysed mineral phases in the Lesser Antilles.**

Arculus (1978), Arculus and Wills (1980) and Tollan et al. (2012) studied minerals from cumulate blocks. Another three studies analysed minerals hosted in mantle xenoliths (Coulon *et al.*, 1984, Parkinson *et al.*, 2003, Vannucci *et al.*, 2007). Stamper et al. (2014) analysed minerals from both various cumulate lithologies and mantle xenoliths from Grenada.

Primarily these studies focus on major element data, with only Turner et al. (2003) and Vannucci et al. (2007) providing trace element data. Heath et al. (1998b) conducted a U and Th concentration and isotopic study on lavas and mineral separates from St. Vincent. Turner et al. (2003) built upon this study and provided U and Th data for mineral separates from both St. Vincent and Martinique, additionally providing Ba concentrations for two of the analysed plagioclase crystals and one olivine crystal. Thus this study significantly expands the amount of trace element data available for minerals in the Lesser Antilles. Trace element data is important to provide information on potential parent melts and ratios of these elements can be taken to see through the effects of fractional crystallisation. Furthermore, differing populations can be better constrained by studying their trace element chemistry in addition to the major elements. Elements such as Sr and Ba are important in plagioclase, whilst REE concentrations can be measured in clinopyroxenes and used to model melting depths.

$\delta^{18}\text{O}$  studies on a variety of mineral separates have been undertaken by Davidson and Wilson (2011) (St. Eustatius and Martinique), Tollan et al. (2012) (St. Vincent) and Van Soest et al. (2002) (Saba, Statia, Montserrat, Guadeloupe, Martinique, St. Vincent, Grenadines, and Grenada).

### **2.2.1 Findings of Published Studies**

Below are brief summaries of the findings of each published Lesser Antilles study which analysed mineral phases, subdivided into lavas, xenoliths and cumulates. Some studies overlap and have analysed more than one type of rock, these will be mentioned as required in each section.

## *Lavas*

This section will describe the findings of studies which analysed minerals in lavas, and is ordered from south to north geographically, starting with Grenada.

Cawthorn et al. (1973) conducted experiments to try and replicate the crystallisation sequences they observed in the Grenada calc-alkaline suite. The authors concluded that intermediate pressure crystallisation of amphibole under hydrous conditions was necessary to generate the lavas seen (Cawthorn *et al.*, 1973). This study was followed by work by Arculus (1978), which comprised a thorough investigation of the mineralogy and petrology of lavas from Grenada, with the author suggesting that the juxtaposition of alkalic and calc-alkalic characteristics of the rocks found on Grenada warranted further study.

Water contents of around 2 wt% are estimated to be required in the crystallisation of lavas from Kick 'Em Jenny, to the north of Grenada (Devine & Sigurdsson, 1995), although these may have been as high as 5 wt%. Assimilation of amphibole bearing crust was also proposed by the authors.

Heath et al. (1998b) do not require amphibole crystallisation in order to generate the lavas they studied from St. Vincent. The authors find conflicting evidence for melt water contents prior to eruption, ranging from >3 wt% to anhydrous conditions. Heath et al. (1998b) suggest little crustal contamination was involved in the petrogenesis of the lavas, however, they do suggest that both subducted sediment and basaltic crust make a contribution (Heath *et al.*, 1998b). Pichavant et al. (2002b) agreed that water contents may be low (~2 wt% H<sub>2</sub>O) but suggested that this may be a result of more hydrous melts undergoing crystallisation on ascent, resulting in much of the erupted material to be hosted in drier melts. The St. Vincent samples studied by Pichavant et al. (2002b) were also thought to be possibly representative of a melt originating in the subarc mantle. More broadly speaking, the study proposed that differing mantle melt compositions are the explanation behind chemically distinct suites in the arc (Pichavant *et al.*, 2002b). Later work by Pichavant and Macdonald (2007) also corroborated the findings of Heath et al. (1998b) that amphibole is not involved in the petrogenesis of primitive lavas. Melt water contents were thought to be between 2-5 wt% (Pichavant & Macdonald, 2007), variations

were postulated to arise from differing water contents in different parts of the mantle wedge.

Turner et al. (2003) observed that cumulate storage times in Martinique are much longer than those for magma differentiation (by up to three orders of magnitude). Furthermore, they suggested that the presence of glomerocrysts observed in arc lavas may be a result of the breakdown and inclusion of cumulate material in host melts (mainly by the injection of new magma) (Turner *et al.*, 2003). Pichavant et al. (2002a) proposed that basaltic liquids with water contents of >5-6 wt% (and corresponding low temperatures of  $\leq 1050$  °C) were responsible for feeding the Mont Pelée magma chamber. Van Soest et al. (2002) suggested that crustal contamination is more pervasive in the south of the arc than the north, with sediment proposed to be the contaminant, their isotope studies on phenocrysts indicate little crustal contamination in the newer volcanic centres on Martinique, in contrast to the findings of previous studies of the older centres (Davidson, 1986, Davidson & Harmon, 1989).

Davidson and Wilson (2011) studied lavas from Martinique and St. Eustatius, which required the crystallisation of amphibole in both cases. However, amphibole was usually absent from the erupted mineralogy and thus its fractionation was deemed 'cryptic' by the authors. Inferred differing parental melt compositions are attributed to variation in the mantle sources, with an increase subducted sediment contribution in the Martinique lavas (Davidson & Wilson, 2011).

Toothill et al. (2007) analysed lavas from St. Kitts and found that little assimilation of crustal material was required to generate the lavas. Instead they suggest that sediment input was to the mantle source. A melt water content of 2 wt% is proposed (Toothill *et al.*, 2007). Toothill et al. (2007) also commented on the prevalence of mineral inclusions, inferring that this either required the crystals hosting them to be antecrysts or old crystals.

### ***Xenoliths***

Xenoliths include both basaltic xenoliths and mantle xenoliths.

Coulon et al. (1984) studied basaltic xenoliths from Martinique and concluded that these represented magma mixing between calc-alkaline basaltic melts and melts of a

more andesitic to dacitic composition. Mixing took place after the former had ponded and begun crystallisation in a shallow magma chamber, before being intruded by the latter. It was noted that phenocryst transfer between xenolith and host lava (and vice versa) occurred (Coulon *et al.*, 1984).

Xenoliths from Parkinson *et al.* (2003) are thought to represent the sub-arc mantle and show evidence of interaction with a low-silica melt, in addition, some of this mantle is shown to be oxidised. Vannucci *et al.* (2007) built on this study and suggested that the metasomatism observed in the Grenada xenoliths occurred in several stages during thickening of the arc crust.

### *Cumulates*

Cumulates as described below are inferred to be a product of fractional crystallisation within the magmatic plumbing system.

Arculus and Wills (1980) noted the wide range of cumulate mineralogies and phase abundances in the Lesser Antilles arc, whilst noting the dominant phases were plagioclase and amphibole. Water was suggested to play an important role, with cumulate plagioclases showing higher An contents than their analysed phenocryst plagioclases (Arculus & Wills, 1980). Cumulates from St. Vincent analysed by Tollan *et al.* (2012) show variable degrees of H<sub>2</sub>O are required but do not show evidence of crustal assimilation. It is suggested that the cumulates originate from ~5 km deep magma chambers (Tollan *et al.*, 2012). Stamper *et al.* (2014) documented all the cumulate types found on Grenada and constrained the pressure conditions for their formation to 0.2-0.5 GPa (deeper than the St. Vincent cumulates due to the thicker oceanic lithosphere beneath Grenada). The cumulates were found to be notably different from those documented in St. Vincent (Stamper *et al.*, 2014). They suggested that plutonic fragments could be included in erupted material as a result of explosive eruptions. In addition, their study of lavas showed that the M-series of Grenada are formed at greater depths (~1.4-1.8 GPa) than the C-series (~0.2 GPa) (Stamper *et al.*, 2014).

## 2.3 Host Lavas

### 2.3.1 Classification

On a TAS diagram (Le Bas *et al.*, 1986) the host lavas range from sub-alkaline picrobasalts to basaltic andesites (with CU109 lying almost on the border between basaltic andesite and andesite) (Figure 2-1). The majority of the host lavas are basaltic in composition. All the host lavas with the exception of BQ19 appear as sub-alkaline according to the classification of MacDonal (1968). BQ19, CA13 and 6103 lie on the dividing line between sub-alkaline and alkaline.

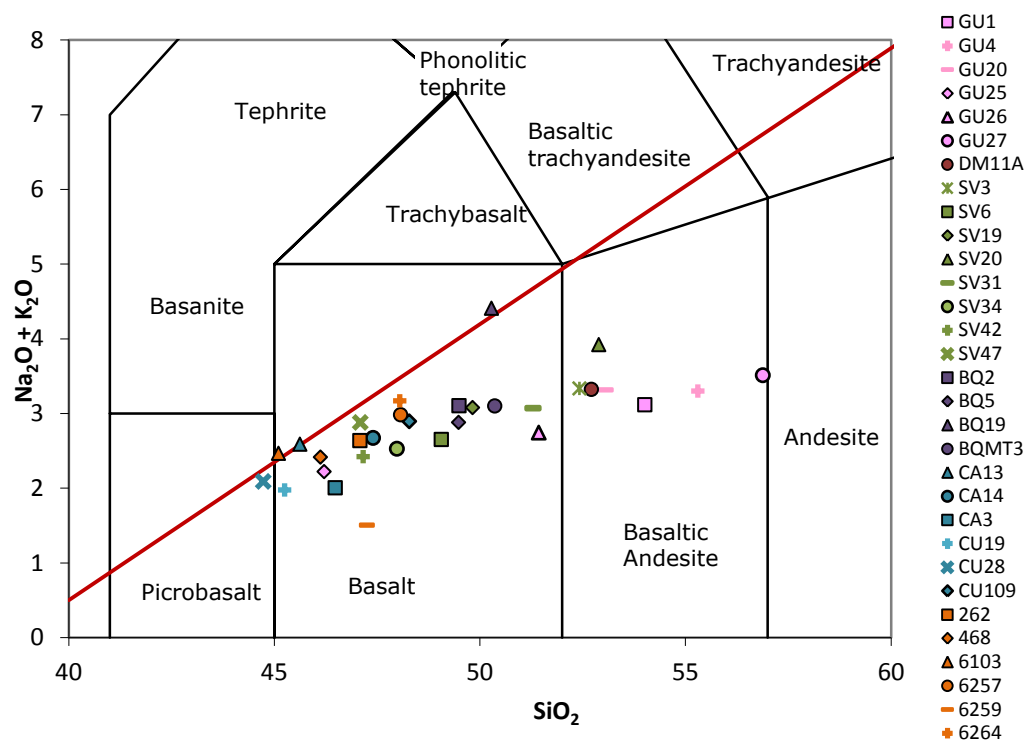


Figure 2-1 TAS diagram showing the host lavas from which the analysed minerals were sampled. Modified from Le Bas *et al.* (1986). The red line represents the division between alkaline and sub-alkaline rocks suggested by MacDonal (1968).

Figure 2-2 shows  $\text{K}_2\text{O}$  plotted against  $\text{SiO}_2$  for the host lavas. The majority of the host lavas plot in the calc-alkaline field with several lavas lying in the island arc tholeiite field.

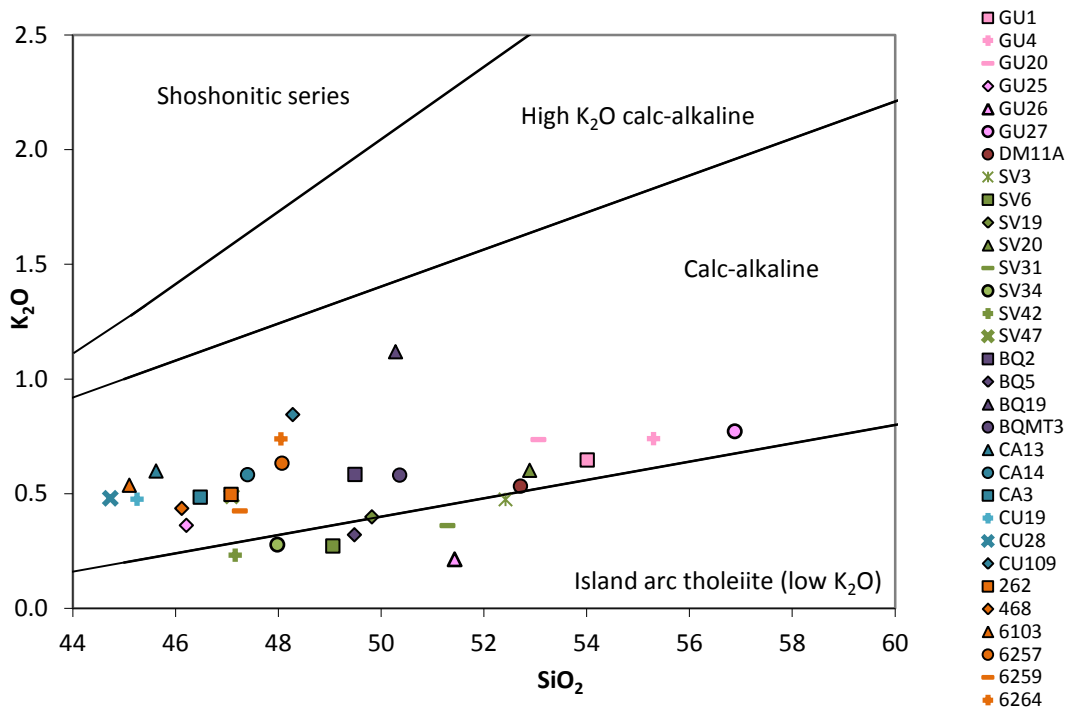


Figure 2-2 K<sub>2</sub>O versus SiO<sub>2</sub> graph showing all of the host lavas from which minerals were analysed.

### 2.3.2 Least Squares Fractional Crystallisation Modelling

Fractional crystallisation modelling was performed to gain an insight into the mineral assemblages crystallising as whole rock MgO contents decrease. The whole rock compositions used were those of host lavas from which any mineral had been analysed as part of this study. A least squares approach was used where the sum of the squares of the residuals was used as an indication of how viable the model was. Four phases were input into the model (olivine, plagioclase, clinopyroxene and magnetite). For this number of phases a sum of squares of <0.2 is thought to be acceptable. The mineral compositions used during the modelling were those calculated to be in equilibrium with the whole rock compositions at each stage. Figure 2-3 shows the results of the modelling for five different major elements.

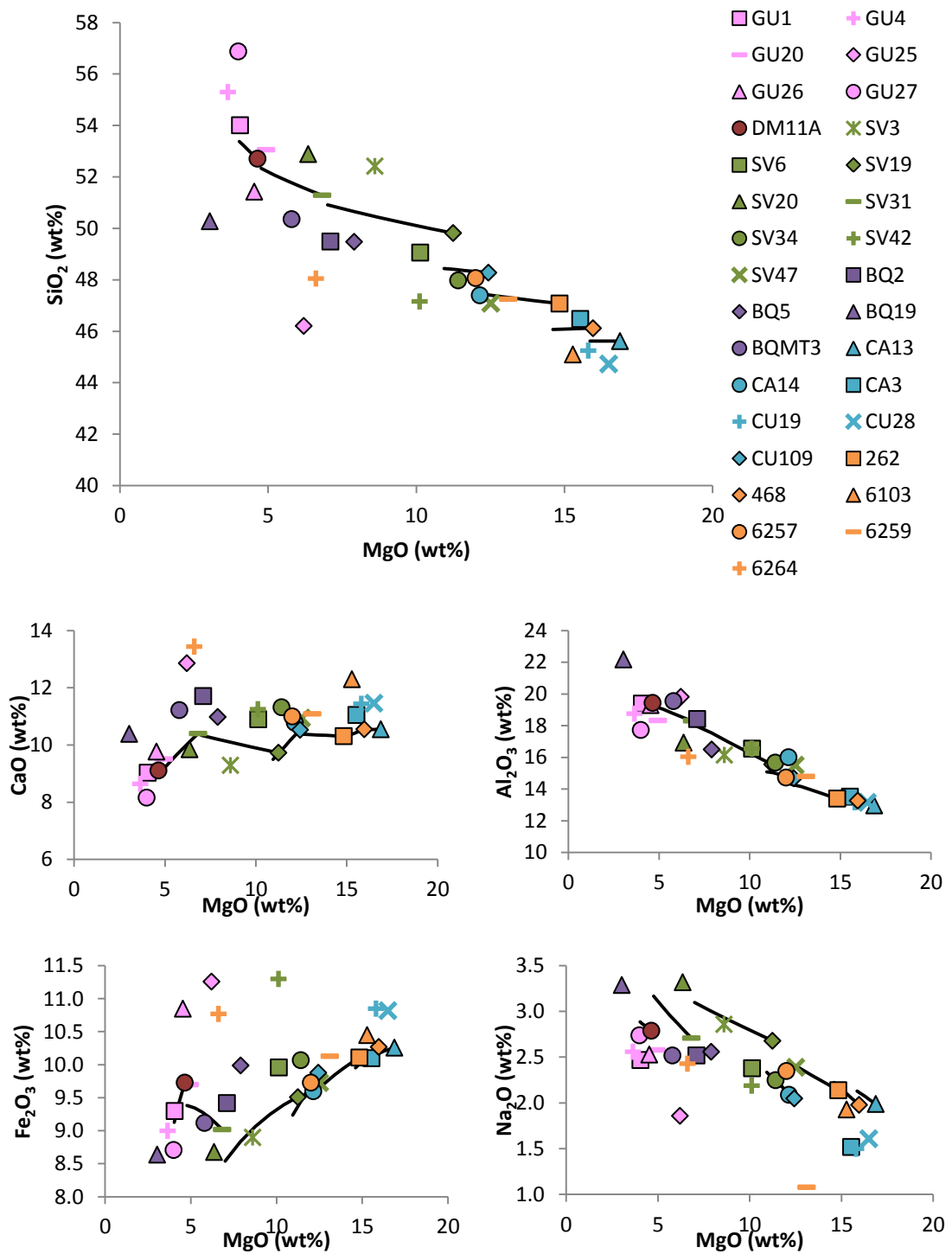


Figure 2-3 Results of least squares fractional crystallisation modelling, as shown by the black lines. Legend for the four smaller graphs is the same as for the larger SiO<sub>2</sub> against MgO upper graph.

The mineral assemblages removed during the modelling are shown in Table 2-2 below.

	<b>% Ol</b>	<b>% Cpx</b>	<b>% Plag</b>	<b>% Mt</b>	<b><math>\Sigma r^2</math></b>
<b>CA13 to 468</b>	4.5	5.8	3.3	0.8	0.1
<b>468 to 262</b>	6.7	5.4	7.4	1.8	0.1
<b>262 to CU109</b>	7.6	4.8	3.1	1.3	0.3
<b>CU109 to SV19</b>	4.5	8.8	6.6	2.1	0.6
<b>SV19 to SV31</b>	9.9	4.3	-1.5	0.6	0.2
<b>SV31 to DM11A</b>	4.0	9.0	8.8	0.5	0.2
<b>DM11A to GU1</b>	2.4	-0.1	5.6	1.0	0.2

**Table 2-2 Results of least squares fractional crystallisation modelling with parent and daughter whole rock compositions used at each stage detailed in the left hand column. Ol is olivine, cpx is clinopyroxene, plag is plagioclase and mt is magnetite. Sums of squares of residuals are shown in the right hand column and are acceptable for each stage apart from 262 to CU109 and particularly CU109 to SV19.**

Overall the modelling results are reasonable although it is worth bearing in mind that the whole rocks are taken from different edifices and different islands. As a result the whole rocks are unlikely to be derived from a single parent undergoing fractional crystallisation as this model may suggest. Consequently the least squares modelling is very much an oversimplification but does give some indication of the phases that may be crystallising as MgO decreases.

### **2.3.3 Modal Phenocryst Proportions**

Point counting was carried out on each host lava from which minerals were analysed. 1500 counts were used per host lava, these data were then converted to percentages. Table 2-3 shows the modal proportions of phenocrysts in each of the host lavas.

<b>Sample</b>	<b>Ol %</b>	<b>Cpx %</b>	<b>Plag %</b>	<b>Opx %</b>	<b>Oxides %</b>	<b>Groundmass %</b>
<b>GU1</b>	1.2	3.8	30.3	0.0	1.1	63.7
<b>GU4</b>	0.0	9.3	24.1	0.0	0.4	69.7
<b>GU20</b>	2.8	8.2	24.1	1.5	0.4	63.0
<b>GU25</b>	5.8	5.2	44.1	0.0	0.8	44.0
<b>GU26</b>	2.4	6.3	27.9	0.0	2.9	60.4
<b>GU27</b>	1.1	1.4	29.1	4.4	0.9	63.2
<b>DM11A</b>						
<b>SV3</b>	10.5	4.2	15.3	2.1	0.3	67.5
<b>SV6</b>	9.1	1.0	0.0	2.0	1.0	87.0
<b>SV19</b>	13.1	13.3	9.1	0.0	1.7	62.7
<b>SV20</b>	3.2	15.5	22.5	0.0	2.4	56.6
<b>SV31</b>	3.9	5.6	31.1	0.0	0.5	58.9
<b>SV34</b>	21.1	1.9	0.4	0.0	0.4	76.2
<b>SV42</b>	15.1	0.1	0.0	0.0	1.9	82.8
<b>SV47</b>	10.0	8.1	0.6	3.1	8.5	69.8
<b>BQ2</b>	3.9	16.6	32.3	0.0	0.1	47.0
<b>BQ5</b>	6.0	21.0	30.2	0.0	0.5	42.3
<b>BQ19</b>	2.6	2.1	43.1	0.0	0.5	51.7
<b>BQMT3</b>						
<b>CA13</b>	31.5	0.2	0.0	0.0	0.1	68.2
<b>CA14</b>	21.4	2.9	3.2	0.0	1.3	71.3
<b>CA3</b>	20.7	7.4	0.0	0.0	0.0	71.9
<b>CU19</b>	20.4	5.3	0.0	0.0	1.6	72.7
<b>CU28</b>	17.0	3.9	0.0	0.0	2.3	76.7

<b>Sample</b>	<b>Ol %</b>	<b>Cpx %</b>	<b>Plag %</b>	<b>Opx %</b>	<b>Oxides %</b>	<b>Groundmass %</b>
<b>CU109</b>	13.2	18.1	0.0	0.0	1.7	66.9
<b>262</b>	20.9	13.7	13.3	0.0	0.3	51.8
<b>468</b>	11.0	9.7	0.0	0.0	3.4	76.0
<b>6103</b>	11.1	7.4	0.0	0.0	1.7	80.0
<b>6257</b>	8.8	3.0	14.1	1.9	2.0	70.2
<b>6259</b>	17.9	9.4	0.2	0.0	3.7	68.8
<b>6264</b>						

**Table 2-3 Percentage modal proportions of the phenocryst phases and groundmass point counted in the host lavas analysed by LA-ICP-MS. Thin sections were not available for the host lavas shaded grey in the table.**

## **2.4 Analysis**

The minerals were analysed at Royal Holloway, University of London, using the LA-ICP-MS system, as described by Müller et al. (2009) and utilising the technique of Thirlwall et al. (in prep). Full details are available in **Appendix 1**. The key benefit of this technique is that major and trace element data can be obtained from a single spot, thus the same material is being sampled for both. In addition, the method is fast and efficient, permitting hundreds of analyses being able to be performed in a single day of analysis without compromising precision.

### **2.4.1 Crystal Mounts, Resin Blocks and Thick Sections**

Minerals were mounted three ways: in crystal mounts, resin blocks and thick sections.

Crystal mounts were made by picking minerals between 250 µm and 1 mm in size from cleaned non-magnetic fractions of each host lava. These were then mounted on 1 inch circular glass slides. The slides were then covered with approximately 10 mm of epoxy resin, before polishing to remove the glass to expose the crystals and provide a flat surface for analysis. All the crystal mount analyses are assumed to be analyses of the cores of the crystals, with the laser being targeted at the centre of the

crystals. Whilst it is assumed that any rim material overlying the cores was either broken off, or polished off, this cannot be confirmed. The advantages of this method are that over 200 crystals can be placed on a single mount. This increases the speed of analysis as, in the RHUL LA-ICP-MS system, two of these crystal mounts can be loaded with two standard mounts at once. This reduces the number of sample changes required during a day of analysis and increases the number of analyses that can be performed during the day. The main disadvantage of this technique is that no petrographic information is preserved and due to the epoxy resin, the mount cannot be viewed under a petrologic microscope following analysis. Also, whilst analyses are assumed to be cores, it is not known explicitly whether crystals or crystal fragments have been mounted.

As a result, thick section and resin blocks were employed as these allowed for the in-situ analysis of crystals. Both the thick sections and resin blocks permitted multiple sites to be analysed in a single phenocryst whilst preserving spatial information. Resin blocks were made by placing ~30  $\mu\text{m}$  thick slices of the host lava onto circular 1 inch glass mounts, before covering with epoxy resin and polishing as for the crystal mounts. Whilst this method did preserve spatial information, not all the petrographic detail was kept (again as a result of the epoxy resin inhibiting the use of a microscope). The resin blocks were studied under a binocular microscope but this did not allow for the observation of XPL characteristics. Furthermore, no scaled photographs could be taken as the binocular microscope used did not allow for the superimposition of a scale bar.

Thick section (~30  $\mu\text{m}$ ) analysis proved to be the most successful technique for combining petrographic, textural, spatial and compositional information. As the thick sections could be viewed under a microscope before analysis, specific areas of crystals could be identified and targeted (such as texturally different areas). Crystal margins could also be clearly identified which aided with positioning of laser spots close to the rims of crystals. This allowed for greater understanding of how chemical compositions were changing across crystals and whether rim compositions differed to those measured in the cores. In the resin blocks, it was often unclear where the crystal margins really were (and so where to aim the laser close to the crystal edges).

Although fewer host lavas could be analysed during a day (as only one thick section could be mounted in the LA-ICP-MS system at a time), the ability to combine

information as a result of using this method far outweighed the negatives. Combining petrographic and geochemical evidence provides critical information on processes that have affected the minerals prior to eruption. It allows for easier identification of discrete populations in the host lavas. By studying these processes and populations, much more detailed information on the petrogenesis of the lavas can be obtained.

### *Quantifying Core and Rim Analyses*

In the thick section analyses, material was ablated at several sites across the crystals. In order to try and numerically quantify cores and rims, and to provide easier comparison of equivalent sites in different populations and host lavas, the following equation was used (Equation 2-1).

#### **Equation 2-1**

$$\% \text{ Distance from rim} = \frac{\text{Distance from crystal rim to laser site}}{\text{Distance from crystal rim to core laser site}} \times 100$$

The core laser site is deemed to be the laser site analysed nearest to the core of the crystal in question. The minimum distance between this and the rim of the crystal provides the denominator in Equation 2-1 (Figure 2-4). The smallest distance between the crystal rim and the desired laser site was then measured and used as the numerator. Although this method of determining site location within crystals may not be flawless (for example, the method does not take into account the difference in size of the analysed crystals), it at least provides an approximate means of determining which analyses are rims, intermediates and cores.

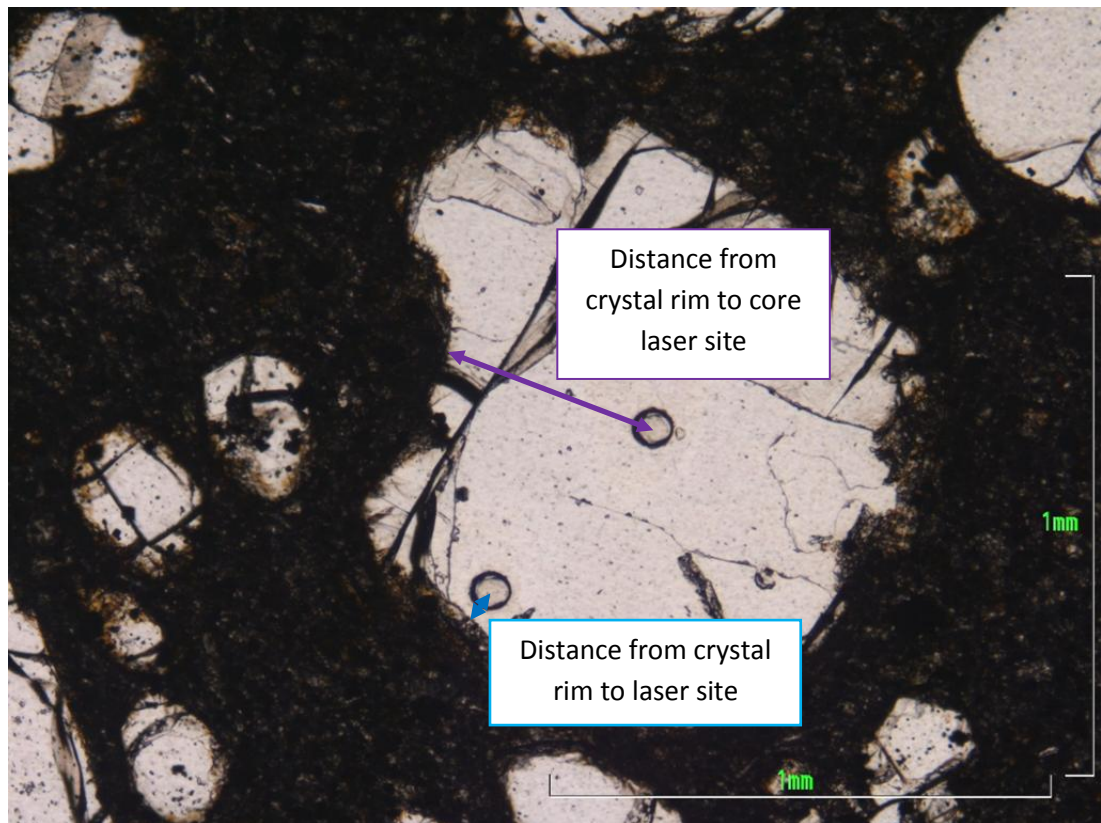


Figure 2-4 Olivine crystal showing measurements used to calculate % distance from rim.

## 2.5 Structure of Following Chapters

The following three chapters deal with olivine, plagioclase and clinopyroxene chemistry. They are designed to discuss their respective mineral phases alone and as such, interpretations combining observations from two or more minerals will be presented in Chapter 6 rather than the discrete mineral chapters. Each chapter should be able to be read in isolation (or with reference to this chapter).

---

## 3 Olivine Chemistry

---

### 3.1 Introduction

#### 3.1.1 Importance of Analysing Olivine

Olivine generally comprises the first crystallising phase of a magnesian rich melt. As such, high forsterite olivines provide an excellent insight into a melt composition before it is significantly altered by shallow level processes such as extensive fractional crystallisation and accumulation (Ford *et al.*, 1983).

Primitive basalts and basaltic andesites are rare in intra-oceanic subduction settings and thus high forsterite olivines are also unusual. Consequently, the presence of high magnesian lavas in the Lesser Antilles island arc provides a valuable opportunity to study primitive olivines (up to Fo<sub>91</sub>) in an oceanic subduction environment.

This study comprises analyses of olivines from seven of the Lesser Antilles islands throughout the arc. The olivines were analysed using LA-ICP-MS analysis coupled with a new processing technique (Thirlwall *et al.*, in prep) (**Appendix 1**). Lavas from Guadeloupe and Dominica represent the central section of the arc and lavas from St. Vincent, Bequia, Carriacou, Petite Martinique (the latter three islands being part of the Grenadines) and Grenada taken from the south of the arc.

#### 3.1.2 Aims of Analysing Olivines in the Lesser Antilles

##### *Aims*

- To provide an extensive new dataset for major and trace element data in olivines from the Lesser Antilles.
- To provide  $\delta^{18}\text{O}$  data on some of these olivines to provide information about sources and potential sediment input to the host lavas.
- To observe if there are any heterogeneities in the olivine chemistries, either within individual host lavas and/or between host lavas from different islands.

- Observe any discrete olivine populations and identify any potential antecrysts or xenocrysts.
- To provide information on sources and early petrogenetic processes as olivine is one of the first phases to crystallise.
- To start to develop a petrogenetic model for the Lesser Antilles which will be embellished with the plagioclase and clinopyroxene data.

### 3.2 Host Lavas

Olivines from 22 host lavas were analysed using LA-ICP-MS. Table 3-1 shows the islands from which the host lavas originated, whole rock MgO and the number of crystals analysed (in both crystal mounts and thick sections). The islands are listed in order of decreasing latitude, with the most northerly islands at the top and the southernmost at the bottom. The host lavas were point counted (where thin sections were available) to obtain modal proportions of olivine found in each lava (Table 3-1). Point counting was undertaken using 1500 counts per host lava. During point counting it was not possible to differentiate between any discrete olivine populations. Thus the modal proportion for the olivine phase encompasses all phenocryst olivine as one fraction.

Basalts and basaltic andesites with high MgO (generally >6 wt% MgO) were targeted in order to obtain sufficient quantities of olivine and to ensure that these provided a good insight into early processes. For the islands of Guadeloupe, Dominica and Bequia, melt MgO contents are generally lower than in the south, resulting in fewer olivine bearing host lavas to choose from. As a result, for these islands some host lavas were chosen based largely on how much phenocryst olivine they contained.

<b>Host Lava</b>	<b>Island</b>	<b>Modal Ol (%)</b>	<b>Whole Rock MgO (wt%)</b>	<b>n CM</b>	<b>n TS</b>
<b>GU1</b>	Guadeloupe	1.2	4.05	24	-
<b>GU25</b>	Guadeloupe	6.4	6.20	17	7
<b>DM11A</b>	Dominica	-	4.64	21	-

<b>Host Lava</b>	<b>Island</b>	<b>Modal Ol (%)</b>	<b>Whole Rock MgO (wt%)</b>	<b>n CM</b>	<b>n TS</b>
<b>SV6</b>	St.Vincent	9.1	10.13	25	-
<b>SV19</b>	St.Vincent	13.1	11.24	25	13
<b>SV20</b>	St.Vincent	3.2	6.35	25	8
<b>SV34</b>	St.Vincent	21.1	11.41	26	-
<b>SV42</b>	St.Vincent	15.1	10.11	26	-
<b>SV47</b>	St.Vincent	10.0	12.51	21	-
<b>BQ2</b>	Bequia	3.9	7.10	25	-
<b>BQ5</b>	Bequia	6.0	7.90	19	-
<b>BQ19</b>	Bequia	2.6	3.03	25	-
<b>CA13</b>	Petite Martinique	31.5	16.87	24	18
<b>CA14</b>	Petite Martinique	21.4	12.14	19	3
<b>CA3</b>	Carriacou	20.7	15.53	22	-
<b>CU109</b>	Carriacou	13.2	12.43	43	-
<b>262</b>	Grenada	20.9	14.83	47	-
<b>468</b>	Grenada	11.0	15.96	33	-
<b>6103</b>	Grenada	11.1	15.28	20	-
<b>6257</b>	Grenada	8.8	12.00	19	-
<b>6259</b>	Grenada	17.9	13.10	44	-
<b>6264</b>	Grenada	-	6.61	20	-

**Table 3-1 Host lava names, locations, whole rock MgO, modal olivine proportions based on point counting (1500 counts) and number of olivines analysed from each host lava as crystal mounts (n CM) and in situ in thick sections (n TS). No thin section was available for DM11A and 6264 so no point counting data were obtained for these two host lavas.**

### 3.3 Olivine Petrography

All the lavas were porphyritic and showed phenocryst olivine, with several also exhibiting clinopyroxene and plagioclase phenocrysts; orthopyroxene was noted in some lavas. Groundmasses were mainly composed of plagioclase and oxides with accessory olivine and/or clinopyroxene in most cases.

Petrographically the olivines varied both between islands and between lavas. Olivines originating from the central islands (Guadeloupe and Dominica) showed varying degrees of iddingsite alteration. These olivines were up to 1.5mm in size and were subhedral to anhedral. Evidence of disequilibrium was seen in both host lavas from Guadeloupe although this was more extensive in GU1. These features include partially resorbed edges and embayments (Figure 3-1).

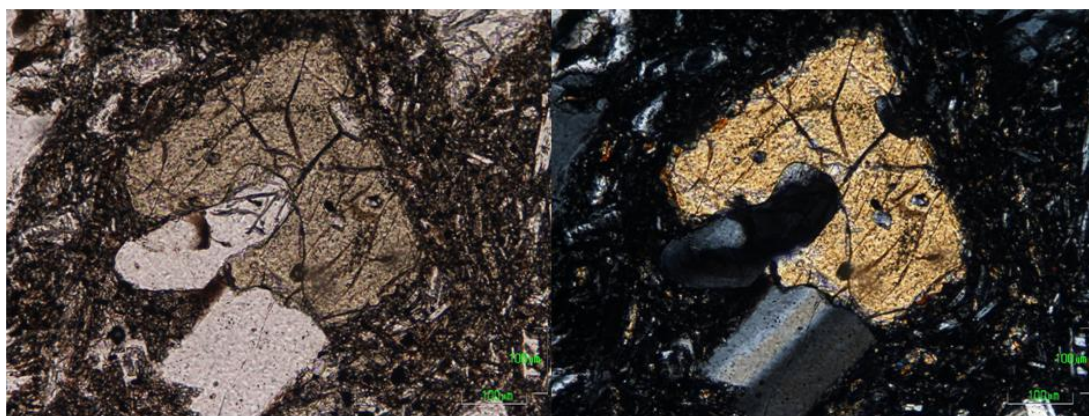


**Figure 3-1 Olivine in GU1 showing evidence of resorbed edges and embayments. PPL is shown on the left hand side and XPL on the right.**

The olivines from the more central part of the Lesser Antilles arc (St. Vincent and Bequia) were also generally subhedral to anhedral (with a few euhedral olivines present in SV47) but were larger than those seen in the central islands (up to 3mm in size). Olivines from Bequia showed high degrees of iddingsitisation with disequilibrium features present. Most of the St. Vincent olivines display iddingsite alteration, although none was observed in samples SV20 and SV47. In addition to the iddingsite, SV19 and SV34 show extensive alteration of olivine to iron oxide (Figure 3-2), commonly around the margins of the crystals but also pervasively through the olivines.

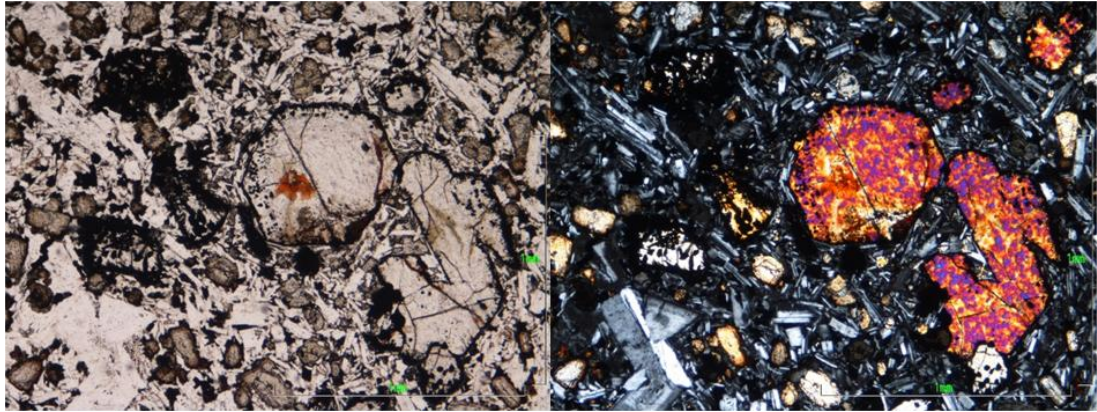


**Figure 3-2 Olivines in SV19 showing Fe oxide alteration. The larger olivines only show the alteration around the rims of the crystals, whereas the smaller crystals show pervasive alteration throughout the minerals.**

These lavas appear to exhibit two populations of olivines, with one showing some iron oxide alteration and a second showing at least 50% alteration in the olivines. Disequilibrium features are present throughout the St. Vincent olivines, with olivines in some of host lavas exhibiting much higher degrees of disequilibrium than others. The St. Vincent lavas also showed skeletal olivines and/or more elongate olivines than seen in the central lavas (Figure 3-3).

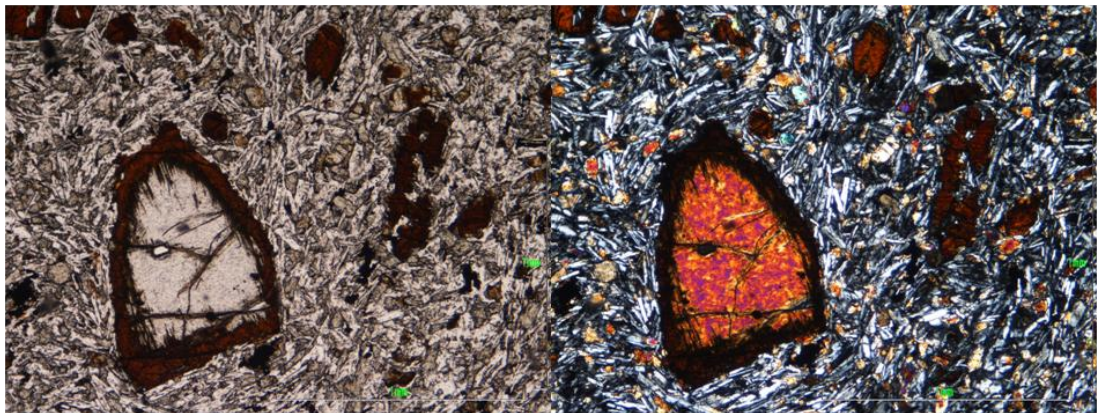


**Figure 3-3 Olivines in SV42. The larger olivine shows iddingsite alteration around the margins, with a smaller, skeletal olivine fully altered to iddingsite to the right of this crystal.**

The southern arc olivines (originating from Carriacou, Petite Martinique and Grenada) are smaller than those from the central section, being up to 2mm in size. Again the crystals are subhedral to anhedral. The Carriacou and Petite Martinique lavas exhibit elongate olivines and skeletal olivines. There is little alteration to iddingsite but the olivines do show alteration to chlorite which is not seen elsewhere in the arc (Figure 3-4).

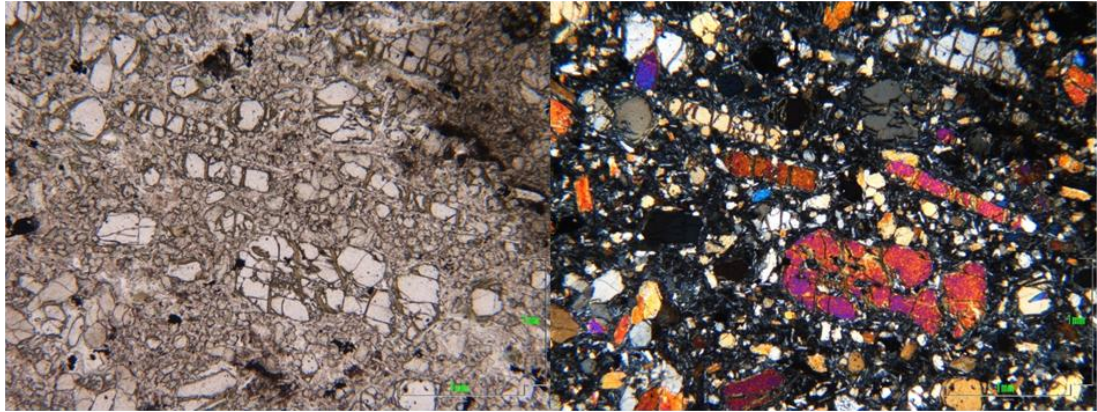


**Figure 3-4 Skeletal and elongate olivines in CA3. The olivines also show chlorite alteration along cracks in the crystals.**

Disequilibrium features such as resorption and embayments are again present in these olivines. The Grenada lavas show different alteration both to the Carriacou and Petite Martinique olivines and to each other. Samples 468, 6103 and 6257 show little evidence of any alteration whereas 6259 shows iddingsite alteration (to a lesser extent than seen further north). 262 shows alteration not seen anywhere else. A highly birefringent material is present in cracks in the olivines. All the Grenada olivines exhibit disequilibrium features, although these are most extensive in 262, 6257 and particularly 6259 (Figure 3-5). In general the Grenada olivines show less evidence of disequilibrium than the central arc olivines and the other southern arc olivines. Elongate olivines are present in most of the Grenada lavas with 262 showing some skeletal olivines as well.

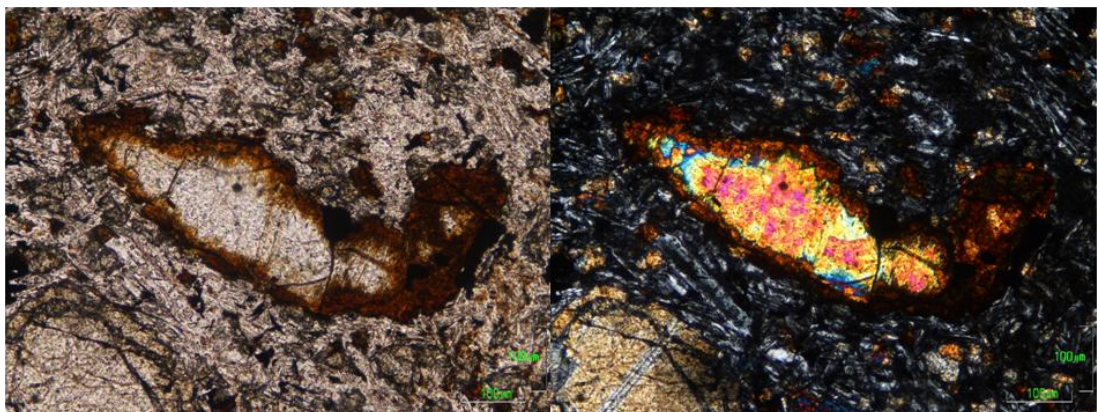


**Figure 3-5 Highly altered olivine in 6259. Aside from the iddingsite alteration, disequilibrium features are apparent in the form of partially resorbed edges and embayments.**

### 3.4 Olivine Chemistry

#### 3.4.1 Forsterite Contents

The forsterite contents in the olivines range from Fo<sub>50</sub> to Fo<sub>91</sub> (Figure 3-6). The lowest forsterite contents are found in Bequia. There is no obvious correlation between the latitude of the island from which the olivines were sampled and forsterite content. GU25 shows bimodality in forsterite contents, with a lower forsterite group (LFG) at Fo<sub>72-73</sub> and a higher forsterite group (HFG) at Fo<sub>82-84</sub>. Several other host lavas show one or two isolated crystals at higher or lower forsterite contents than the bulk of the olivines from that lava (such as SV20 and CA13), but these are not thought to be statistically significant.

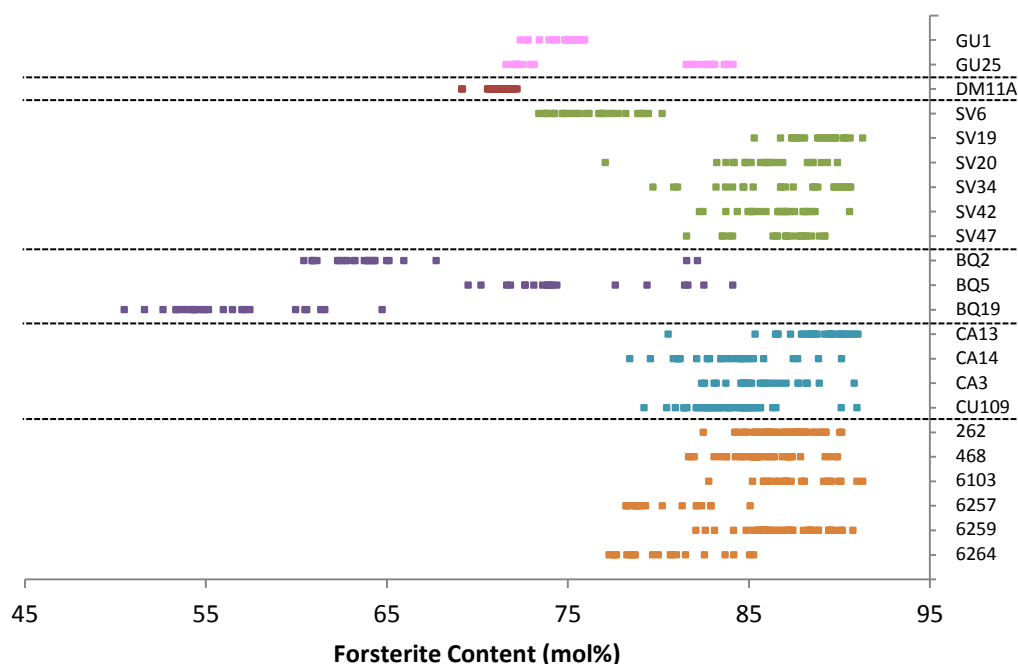


**Figure 3-6** Forsterite contents measured in the olivines. The y axis is arranged by latitude, with the most northern islands at the top and the southern islands at the bottom. Different islands are shown as different colours and are separated by dashed lines.

Olivines from Guadeloupe and Dominica (excluding the bimodal GU25) generally show small ranges in forsterite contents within both GU1 (4 mol%) and DM11A (3 mol%). The range in the lower forsterite group GU25 is 1 mol% and 2 mol% in the higher group.

In contrast, host lavas from St. Vincent show ranges in forsterite content up to 13 mol% (SV20). Furthermore, there is a range in forsterite contents of Fo<sub>73-91</sub> (18

mol%) for all the olivines from St. Vincent, with SV6 exhibiting lower forsterite contents ( $\text{Fo}_{73-80}$ ) than the other host lavas from St Vincent.

The widest ranges in olivine forsterite contents both within individual host lavas and across all the olivines from one island are found in Bequia, with a 22 mol% range in BQ2 (including two crystals offset to higher Fo contents than the majority of the olivines from this host lava), a 15 mol% range in BQ5 and a 14 mol% range in BQ19. Overall, Fo contents of  $\text{Fo}_{84-50}$  result in a range of 34 mol% in the Bequia olivines. As observed in St. Vincent, one of the host lavas contains olivines with lower forsterite contents than the remaining two from this island; BQ19 shows a range of  $\text{Fo}_{65-50}$  compared to  $\text{Fo}_{82-60}$  and  $\text{Fo}_{84-69}$  in BQ2 and BQ5 respectively.

Host lavas from Carriacou, Petite Martinique and Grenada all show similar forsterite contents and comparable ranges in forsterite contents. All olivines analysed from these latter three islands (the light blue and orange symbols in Figure 3-6) exhibit Fo contents between  $\text{Fo}_{77-91}$  (a range of only 14 mol%). Ranges of forsterite contents within individual host lavas from these islands range from 7 mol% to 12 mol%.

### **3.4.2 CaO**

The olivines show bimodality in CaO contents. Many of the olivines show low CaO concentrations at a given forsterite content compared to the majority of the olivines (at forsterite contents  $>\text{Fo}_{80}$ ). Whilst there are two groups evident, there is no clear distinction between the lower CaO olivines and the higher olivines, rather a continuum exists between the two (Figure 3-7).

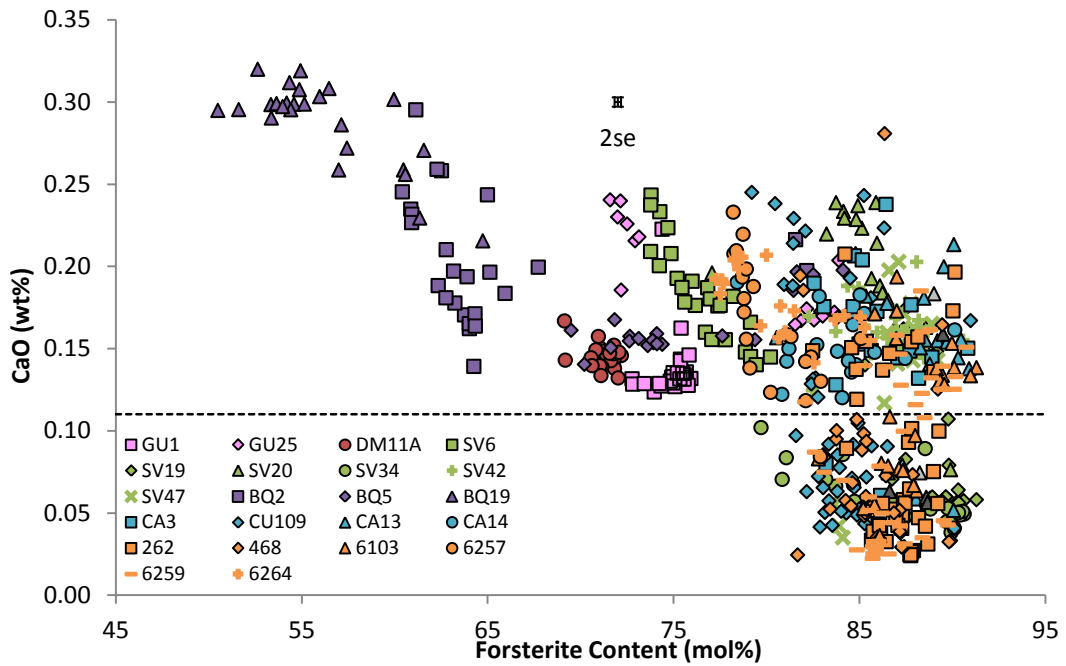


**Figure 3-7 CaO contents in the Lesser Antilles olivines. The dashed line represents a CaO concentration of 0.11 wt% which has been used as the upper limit for the determination of the LCO, based on histogram data (Figure 3-8).**

Kamenetsky et al. (2006) observed a similar continuum between higher and lower calcium olivine populations and used a relatively arbitrary value of 0.15 wt% to separate their groups. In order to identify a suitable value to use as discriminator between the higher and lower calcium olivines in this study (to allow for easy distinction between the groups in the following discussion), a histogram was plotted of the CaO contents of olivines  $>Fo_{80}$ . The kernel density estimation was then overlain using the PAST software package (Hammer *et al.*, 2001) (Figure 3-8). This method was also used to ensure that the bimodality was statistically apparent.

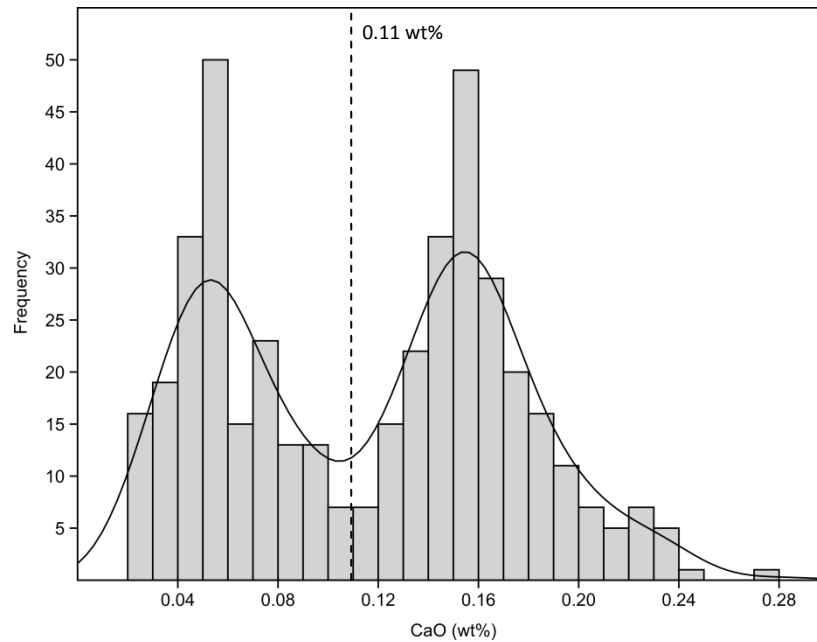


**Figure 3-8 Histogram showing a bimodal distribution in calcium contents by frequency. The overlaid line shows the kernel density estimation. The dashed line shows 0.11 wt% CaO.**

Figure 3-8 shows two clear peaks; the dashed line represents 0.11 wt% CaO, which falls in the centre of the minima. Based on the histogram data, olivines with CaO concentrations of 0.11 wt% or below have been termed 'low calcium olivines' (LCO). The LCO have CaO contents of 0.02 to 0.11 wt% (over a range in forsterite contents of  $Fo_{80-91}$ ); the higher CaO olivines exhibit contents of 0.12 to 0.32 wt% CaO over a forsterite range of  $Fo_{50-91}$ . Over the forsterite range of the LCO ( $Fo_{80-91}$ ), the higher CaO olivines show CaO concentrations of 0.12 to 0.25 wt%.

The LCO are found in several islands from the south of the arc: St. Vincent, Petite Martinique, Carriacou and Grenada. Although Bequia is located south of St. Vincent, no LCO were found in the three host lavas from this island. No LCO were found in the host lavas from Guadeloupe and Dominica in the centre of the arc, although this may be a result of the LCO only being found in more primitive lavas (however, SV20 from St. Vincent does contain LCO and only has a whole rock MgO content of 6.35 wt%, lower than some of the Bequia lavas which exhibit no LCO).

The presence of the LCO results in large ranges in CaO at given forsterite contents at  $Fo_{>80}$ . Of the host lavas from the islands containing LCO olivines, only SV34 does not show any non-LCO crystals. Five host lavas with olivines exhibiting greater than  $Fo_{80}$  show no LCO - GU25, BQ5, SV42, CA14 and 6264. 468 shows the largest range in CaO contents with olivines exhibiting between 0.024 and 0.281 wt%,

encompassing the whole range of CaO concentrations at forsterite contents over Fo<sub>80</sub> over a range of 4 mol%.

In general the olivines within each host lava show increasing CaO contents as forsterite content decreases. However, these trends vary in steepness, for example SV6 exhibits a range in CaO of 0.108 wt% over 6 mol% Fo whereas SV42 shows a CaO range of 0.078 wt% over a larger forsterite range of 9 mol%. GU1, BQ5 and CA14 also exhibit shallower trends than the majority of the host lavas.

Below Fo<sub>80</sub> the olivines are predominantly from host lavas originating from Guadeloupe, Dominica and Bequia, with the one exception to this being SV6. The latter again shows a relatively large range in CaO contents (0.145-0.243 wt%) over a small forsterite range (6 mol%). GU25 exhibits both a lower and higher forsterite group, the LFG exhibiting comparable CaO concentrations to those seen in SV6 at a given forsterite content. However, the BQ5 crystals at similar forsterite contents show ~0.5 wt% lower CaO contents than the SV6 and GU25 olivines. Additionally, the BQ5 olivines do not exhibit an increase in CaO as forsterite content decreases, in contrast to SV6 and the lower forsterite GU25 crystals. This relatively constant CaO content with changing forsterite content is also seen in GU1 and DM11A at similar Fo contents to BQ5. GU1 olivines show marginally lower CaO concentrations to BQ5 while DM11A crystals are approximately 0.2 lower than BQ5 olivines at a given forsterite content. The lowest forsterite olivines are seen in BQ19 (Fo<sub>50-65</sub>) and BQ2 (Fo<sub>60-68</sub>). Both of these host lavas show dramatic increases in CaO concentrations of 0.104 wt% (BQ2) and 0.156 wt% (BQ19). BQ19 olivines exhibit the highest CaO contents of the sampled olivines (up to 0.320 wt%).

Olivines from 5 of the host lavas were analysed in situ in thick sections. These lavas were GU25 (Guadeloupe), SV19 and SV20 (St. Vincent), CA13 and CA14 (Petite Martinique). Of these host lavas, 3 showed LCO - CA13, SV19 and SV20. Analysis of in situ crystals allows for the comparison of core and rim sites to observe how olivine composition varies across the crystals.

### Core and Rim Analyses

The thick section analyses show that CaO contents in general increase from cores to rims in the olivines (Figure 3-9). However, low CaO contents are found in both cores and rims of crystals.

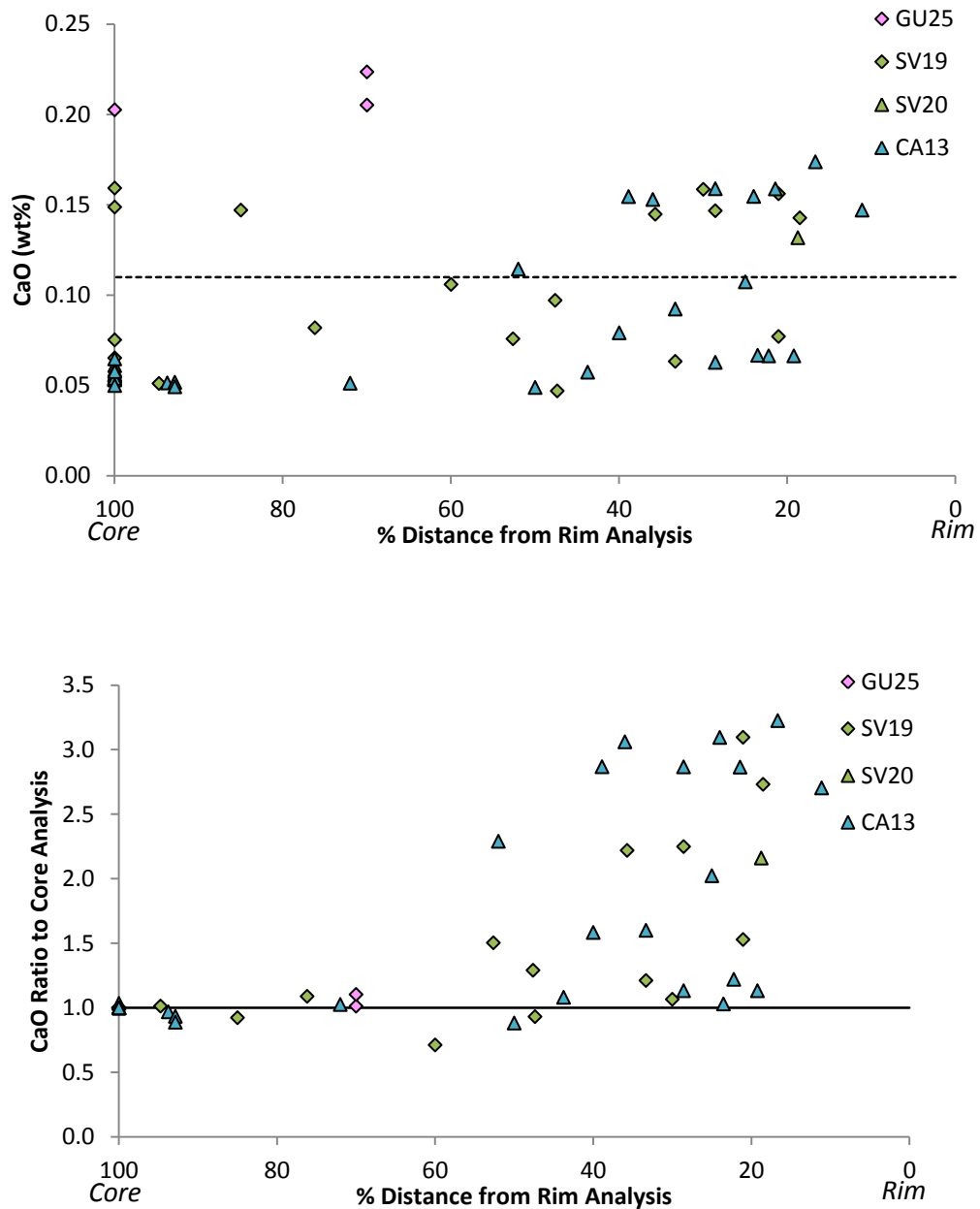


Figure 3-9 Variations in CaO contents across olivine crystals. The upper graph shows the absolute concentrations (with the dashed line representing 0.11 wt%) whereas the lower graph shows the ratio of CaO contents in the rims relative to the cores (the solid line represents a ratio of 1, with analyses plotting higher than this being more enriched than the cores and analyses below being depleted relative to the cores). It can be seen, particularly in the lower graph, that CaO contents increase towards the rims of the crystals.

### 3.4.3 Sc, V and TiO<sub>2</sub>

TiO<sub>2</sub>, Sc and V concentrations generally increase with decreasing forsterite content. However, Sc and V concentrations in many of the LCO are also lower than those in the higher CaO Lesser Antilles olivines at a given forsterite content (Figure 3-10), which is not seen in the TiO<sub>2</sub> contents (Figure 3-11).

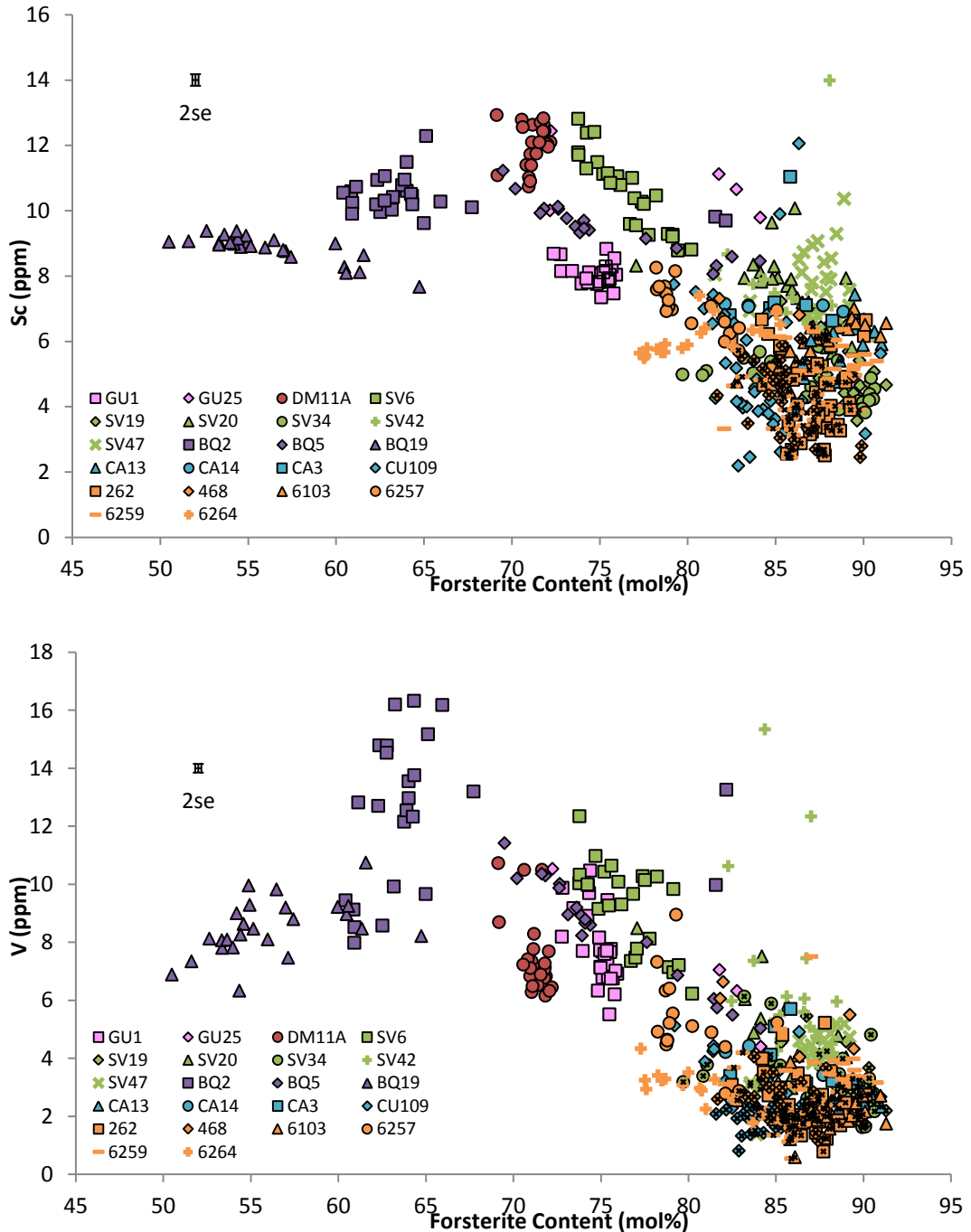


Figure 3-10 Sc and V contents in the Lesser Antilles olivines, showing the LCO (overlain by the small black crosses) to have slightly lower Sc and V concentrations at a given forsterite content than the higher CaO olivines.

Olivines from several of the host lavas show positive correlations between Sc or V concentrations and forsterite content. DM11A and 6264 show positive trends in Sc contents. BQ2 and BQ19 exhibit positive correlations for V concentrations.

There is a large range in Sc contents at forsterite contents  $>Fo_{80}$ , however, this is largely due to the LCO generally having lower Sc contents at a given forsterite content than the olivines with relatively higher CaO. The higher CaO olivines exhibit Sc contents of between 3.3 and 14.0 ppm over a range of forsterite contents of  $Fo_{80-91}$  whereas the LCO show contents of 2.2 to 7.2 ppm Sc over the same range of forsterite contents.

There are still large ranges in Sc present in some individual host lavas at  $>Fo_{80}$ , e.g. SV19 exhibits a twofold increase in Sc (an absolute range of 3.6 ppm) over a forsterite range of 6 mol%. SV47 crystals exhibit higher Sc contents than the majority of olivines from other host lavas at a given forsterite content (by between 4.8-10.4 ppm), this is not seen in the CaO data.

In contrast to the CaO data, the olivines from BQ19 do not show the highest Sc concentrations. At a given forsterite content, the BQ2 olivines exhibit ~1 ppm higher Sc than the BQ19 crystals. In addition, the DM11A olivines show higher Sc contents than both the BQ5 and GU1 data at comparable forsterite contents and exhibit among the highest Sc values (up to 12.9 ppm). As a result, the DM11A show similar Sc concentrations to SV6 (despite being at slightly lower Fo contents) which was not observed in the CaO data.

Between  $Fo_{65-80}$ , SV6 and DM11A exhibit the highest Sc contents at a given forsterite content, higher than those seen in BQ5 and GU1. One GU25 analysis has a comparable Sc concentration to the DM11A crystals with comparable forsterite contents. There is a 4.5 ppm range in contents between all of the olivines at this forsterite range, similar to that observed in the higher Fo content olivines. Below  $Fo_{65}$  there are only two host lavas from Bequia present, with BQ2 showing 25% higher concentrations of Sc than BQ19.

V contents are similar to the Sc concentrations - the majority of the host lavas show increasing V concentrations as forsterite content decreases and the LCO generally exhibit lower concentrations than their higher CaO counterparts. However, in

contrast to the Sc data, the range in concentrations at a given forsterite content is larger as Fo content decreases to Fo<sub>60</sub>.

At higher forsterite contents (over Fo<sub>80</sub>) the SV47 olivines show slightly higher V concentrations compared to the other host lavas at a given forsterite content, as in the Sc data. In contrast to the Sc data however, the higher forsterite olivines do not show as large a range in V contents within a host lava as BQ2.

The LCO V concentrations range between 0.5 and 6.1 ppm at Fo<sub>80-91</sub>, whilst the higher CaO olivines exhibit contents of 1.8 to 15.3 ppm. The V contents of the two populations agree best at Fo<sub>89-91</sub>. At Fo<sub>89-91</sub> the olivines show concentrations of 1.6 to 4.8 ppm (LCO) and 1.7 to 5.5 ppm (higher CaO olivines).

At Fo<sub>65-80</sub>, the DM11A olivines exhibit V concentrations more similar to GU1 than SV6 (in contrast to the Sc data). The BQ5 crystals show comparable V contents to the GU1 olivines at a given forsterite content. As observed in the Sc data, the SV6 crystals exhibit the highest contents of V at this forsterite range.

At lower forsterite contents (<Fo<sub>65</sub>), there is some overlap in the V concentrations of BQ2 and BQ19 at a given Fo content, however the BQ19 olivines show a smaller range in V, with the concentration of V in the BQ2 crystals varying by a factor of 1.9 at invariant Fo compared to a factor of 1.6 in the BQ19 analyses. The BQ2 olivines also exhibit the highest V concentrations analysed (up to 16.3 ppm).

As for the Sc and V data, TiO<sub>2</sub> concentrations increase with decreasing forsterite content in the majority of the host lavas. However, GU1 shows a trend of decreasing TiO<sub>2</sub> as Fo contents decrease. Above Fo<sub>65</sub>, the olivines from all the host lavas show similar concentrations of TiO<sub>2</sub> at a given forsterite content.

Over a forsterite range of Fo<sub>80-91</sub> the lowest TiO<sub>2</sub> concentrations are found in the LCO (Figure 3-11), however there are numerous low calcium crystals which show comparable TiO<sub>2</sub> contents to the higher calcium olivines. The LCO TiO<sub>2</sub> concentrations lie between 0.0011 and 0.0102 wt% compared to 0.0034 and 0.0139 wt% (higher CaO olivines). In contrast to the V contents, the LCO at higher forsterite contents (Fo<sub>89-91</sub>) show more distinct differences when compared to the higher CaO olivines at the same forsterite content, being approximately 0.002 wt% lower on average than the higher CaO olivines.

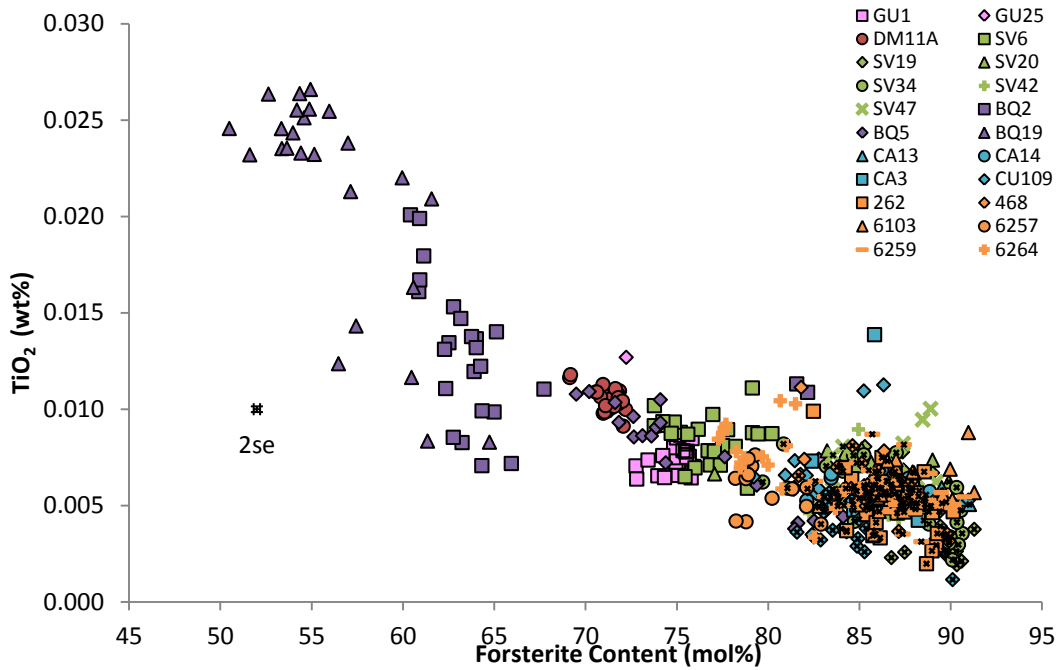


**Figure 3-11 TiO<sub>2</sub> contents in the olivines. The LCO (overlain by the small black crosses) show the lowest TiO<sub>2</sub> concentrations, however several LCO crystals show similar contents to the normal CaO olivines.**

Comparable concentrations in the LCO and higher CaO olivines result in a comparatively smaller range at high forsterite contents than observed in the Sc and V data. CU109 has the largest range at a given forsterite content at  $>Fo_{80}$  of 0.008 wt% (an increase by a factor of 4.2). Additionally, SV47 displays comparable TiO<sub>2</sub> contents to those seen in the other olivines at a given forsterite content rather than the higher concentrations previously observed in Sc and V.

At  $Fo_{65-80}$ , the olivines show comparable ranges and concentrations of TiO<sub>2</sub> at a given forsterite content, with the exception of one crystal from GU25 which shows 14% higher TiO<sub>2</sub> than the highest DM11A olivine at invariant Fo.

At lower forsterite contents ( $<Fo_{65}$ ), BQ2 and BQ19 show extensive ranges in TiO<sub>2</sub>, both of which are higher than most of those seen at  $>Fo_{80}$  (factors of 2 and 2.5 at a given forsterite content respectively). In addition, the concentrations measured in these olivines extend to much higher levels than the remaining crystals (up to 0.02659 wt% in BQ19 and 0.02009 wt% in BQ2; the highest value recorded outside of these two host lavas is 0.01387 wt%). In contrast to the Sc and V data, BQ19 exhibits higher concentrations of TiO<sub>2</sub> than BQ2.

### 3.4.4 Zr

Below  $Fo_{80}$ , Zr concentrations in the olivines generally increase as forsterite contents decrease (as seen in the previously discussed elements), with the exception of DM11A which exhibits a positive correlation. At higher forsterite contents, there is no obvious correlation with decreasing Fo contents. However, there is more scatter in the data than seen in the CaO,  $TiO_2$ , Sc and V data, particularly at  $>Fo_{80}$ . This may be a result of sampling inclusions within the olivines.

Zr concentrations in the LCO and the higher CaO olivines are comparable at a given forsterite content (Figure 3-12). The LCO have Zr contents of 0.0025 to 0.0839 ppm at  $Fo_{80-91}$  compared to 0.0018 to 0.1704 ppm (higher CaO olivines) over the same forsterite range. Both olivine populations show consistent Zr contents across the Fo range, showing no change in compatibility with evolution of the melt.

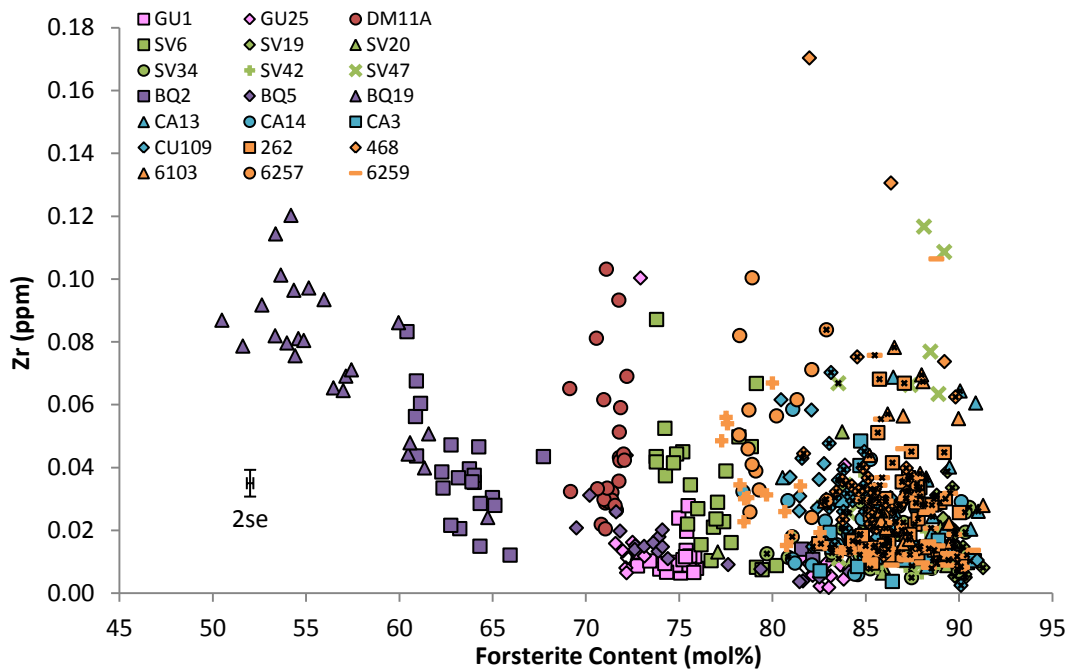


**Figure 3-12 Concentrations of Zr in the LCO (small black crosses) and the higher CaO olivines, showing the two populations to have comparable Zr contents at a given forsterite content.**

At forsterite contents lower than  $Fo_{80}$ , there are large ranges in Zr concentrations at invariant Fo (e.g. factors of 5.0 in DM11A, 3.1 in BQ2 and 1.9 in BQ19). The BQ19 olivines again show higher Zr contents than the BQ2 olivines, as seen in the CaO and  $TiO_2$  data. The DM11A olivines also replicate the  $TiO_2$  data in that they exhibit higher concentrations of Zr than the BQ5 crystals at a given forsterite content.

At higher forsterite contents, the olivines predominantly show increasing Zr contents with decreasing Fo within the host lavas. One exception to this is 262 which appears to exhibit a positive correlation. Large ranges in Zr at a given forsterite content are present, however, these may be a function of the aforementioned potential inclusion data.

### 3.4.5 MnO

The host lavas all show increasing MnO concentrations in the olivines as forsterite content decreases (Figure 3-13). This is in contrast to the previous elements where at least one host lava exhibits a positive correlation.

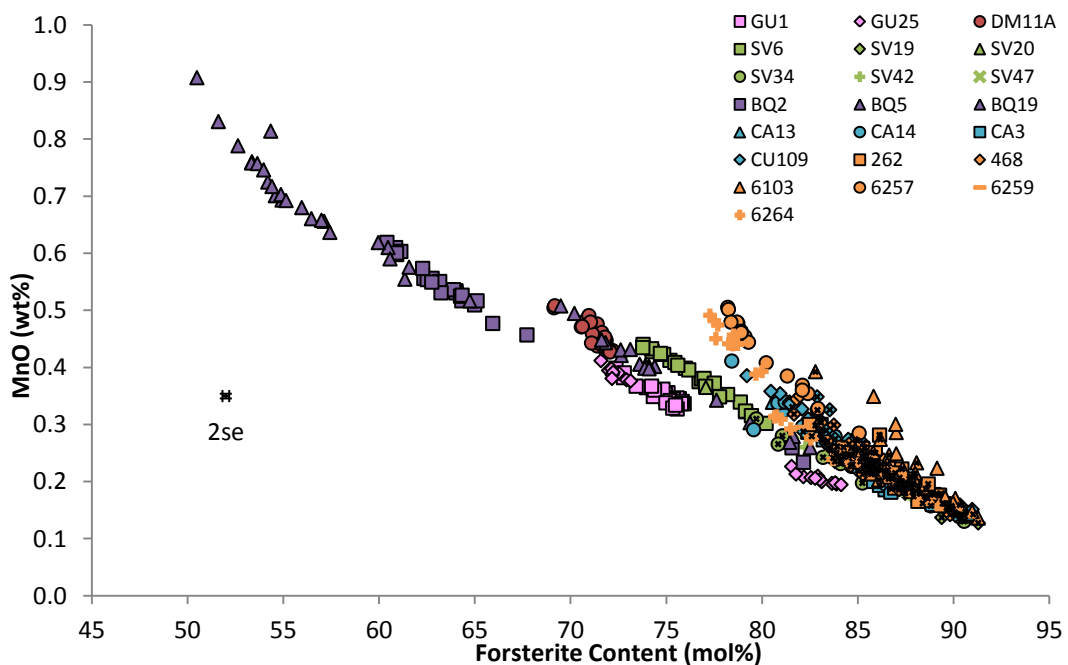


Figure 3-13 MnO and forsterite contents in the olivines, showing no discernible depletion in MnO in the LCO (overlain by the small black crosses).

The correlations exhibit much less scatter than any of the previously discussed elements. The gradients of the trends seem to vary. The highest forsterite olivines (>Fo<sub>75</sub>) from Carriacou, Petite Martinique and Grenada show a steeper increase in MnO as forsterite contents reduce than those crystals from St. Vincent and Guadeloupe at invariant Fo. At ~Fo<sub>75</sub> the St. Vincent olivines show higher MnO concentrations than those from Bequia and Guadeloupe. However, the Bequia (and Dominica) olivines show steeper trends than the St. Vincent crystals. At lower forsterite contents (below Fo<sub>65</sub>) the Bequia olivines show similar trajectories to the St. Vincent olivines.

MnO concentrations in the LCO and the higher CaO olivines show no discrepancies between the two populations at Fo<sub>80-91</sub>. The LCO exhibit MnO contents of between 0.001 and 0.007 wt% and the higher CaO olivines show concentrations of 0.001 to 0.009 wt% MnO (Figure 3-13).

The different gradients observed may be due to variations in the partitioning behaviour of MnO between olivine and the melt. The Mn partition coefficient has been shown to be affected by melt composition and temperature, with temperature having more of an effect if melt compositions are basaltic in nature (as melt composition influences the partition coefficient more as melts get more silicic) (Watson, 1977). As temperatures decrease, Mn becomes more compatible in olivine (Watson, 1977). Therefore, the variations seen in Figure 3-13 may be due to lower temperatures in those host lavas with steeper gradients (such as those from Grenada) than those with shallower gradients (for example those from St. Vincent).

#### **3.4.6 Y and Yb**

Y and Yb contents also show increases with decreasing Fo content, suggesting that these elements become slightly more compatible as MgO contents in the melt decline (Figure 3-14). Between Fo<sub>75-85</sub>, Several host lavas show large ranges in Y and particularly Yb with small changes in Fo content. 6257 shows a factor of 6.9 increase in Yb (a range of 0.23 ppm) over 7 mol% Fo, SV6 a factor of 7.9 (0.22 ppm) over 6 mol% and BQ2 a factor of 9.3 (0.24 ppm) over 7 mol%.

At high forsterite contents (over Fo<sub>85</sub>) the ranges in both Y and Yb are relatively small, excluding several anomalously high appearing analyses that may result from sampling inclusion material. The majority of the olivines at these Fo contents lie between 0 and 0.1 ppm Y and 0 and 0.04 ppm Yb.

These elements also exhibit LCO contents slightly lower than those seen in the higher CaO olivines. Over a forsterite range of Fo<sub>80-91</sub>, Y concentrations are 0.003 to 0.243 ppm in the LCO (0.018 to 0.384 ppm in the higher CaO olivines) and Yb concentrations are 0.002 to 0.062 ppm (0.007 to 0.120 ppm).

Y and Yb concentrations in DM11A, GU1 and BQ5 are all lower than SV6 at a given forsterite content as seen in the CaO, V, Sc and Zr data.

The highest concentrations of both Y and Yb are found at lower forsterite contents, in the BQ19 olivines (up to 0.38 ppm and 1.2 ppm respectively compared to up to 0.03 ppm Y and 0.12 ppm Yb in the olivines  $>Fo_{90}$ ).

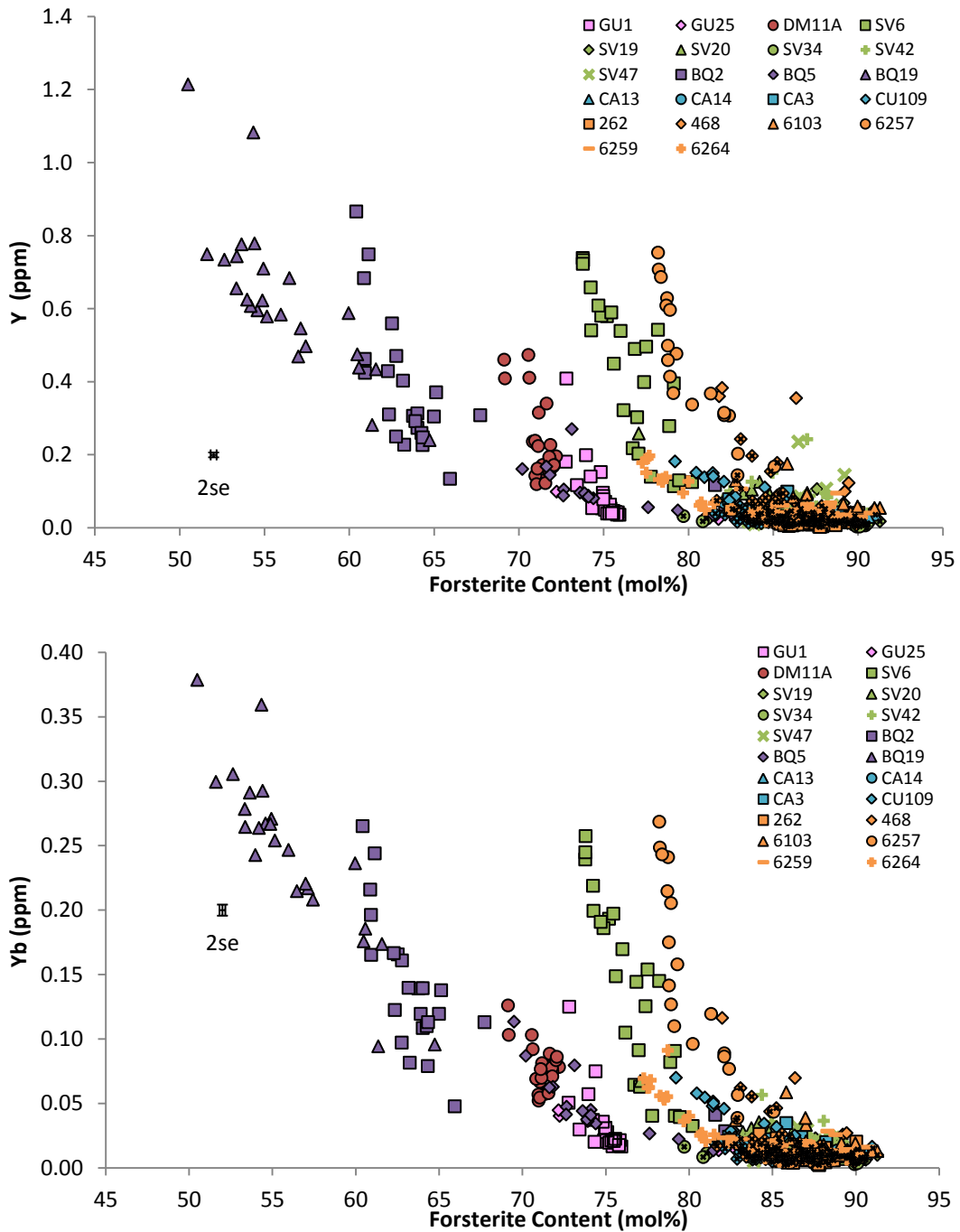
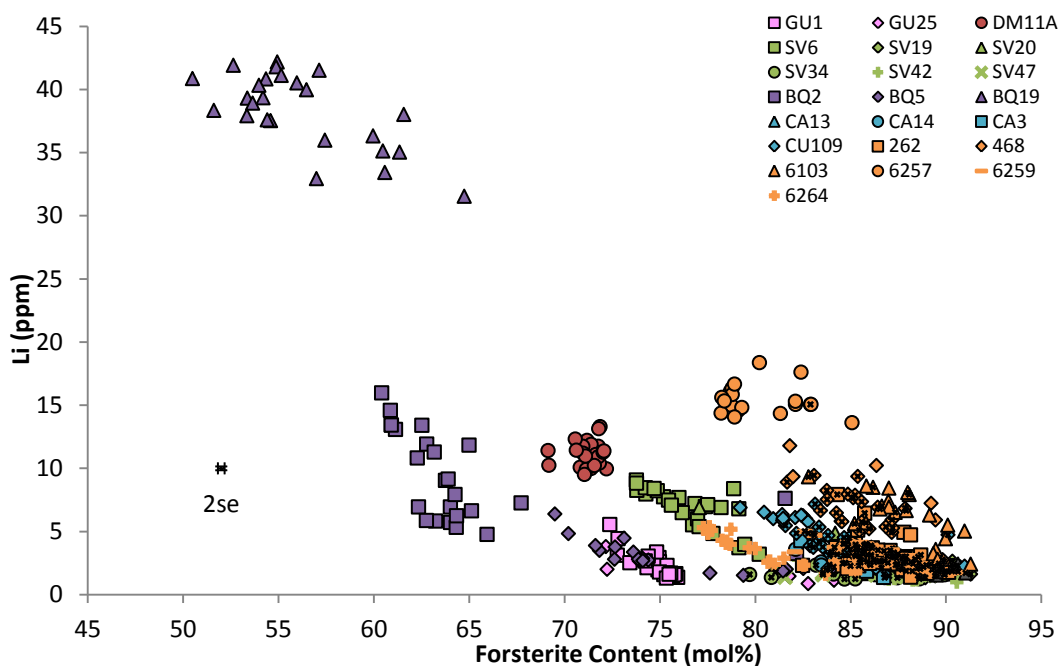


Figure 3-14 Y and Yb concentrations in the olivines. The LCO are shown by small black crosses and exhibit slightly lower Y and Yb concentrations than the higher CaO olivines at a given forsterite content.

### 3.4.7 Li

The Li contents of the olivines exhibit similar trends to those seen in the Y and Yb data (Figure 3-15), although the trends show shallower gradients. In addition, the BQ19 crystals plot at much higher Li concentrations than olivines from the other host lavas (32-42 ppm in the BQ19 crystals compared to a maximum of 18 ppm in the remaining olivines, at least 78-133% higher) (Figure 3-15).



**Figure 3-15** Li contents in the Lesser Antilles olivines, the LCO are shown as small black crosses.

At  $>Fo_{80}$ , there is more spread in the data than observed for Y and Yb. 468 and 6103 show  $\sim 1.5$  ppm higher Li contents at invariant Fo than the majority of olivines, which was not observed in the Y and Yb data. The LCO show comparable Li concentrations to those seen in the higher CaO olivines at a given forsterite content, with the LCO having concentrations of 1.35-15.06 ppm compared to 0.99-18.38 ppm in the higher CaO olivines at  $Fo_{80-91}$ . At  $\sim Fo_{80}$ , the 6257 crystals exhibit higher Li contents at a given forsterite content than olivines from other host lavas.

Between  $Fo_{70-80}$ , SV6 shows several olivines lying on a shallower trend than the other host lavas at comparable Li and Fo contents, with this trend being more similar to that exhibited by BQ5. The DM11A olivines also show relatively higher Li concentrations than Y or Yb contents in that they are approximately 4 ppm higher than the GU1 and BQ5 olivines at a given forsterite content.

At approximately Fo<sub>60-65</sub>, BQ2 also shows a large range in Li contents, with a factor of 3.4 increase (an absolute range of 11.2 ppm), in agreement with the large variations seen in these olivines in Y and Yb concentrations.

Lithium is thought to diffuse through olivine at approximately an order of magnitude faster than Fe and Mg (Chakraborty, 2010). Transects across crystals could indicate whether the olivines have been affected by diffusion if concentrations increase towards the rims. Figure 3-16 shows the ratios of Li concentrations across the crystals compared to their respective core analyses, where the distance from rim analysis parameter is as defined in Chapter 2. Increases in Li concentrations towards the rim of crystals are most evident in the St. Vincent thick section olivines, with CA13 also demonstrating some increase with distance from the core potentially indicating diffusion. However, Li contents in the GU25 olivines appear to show no change in concentration across the crystals. Unfortunately, no Bequia crystals were analysed in thick section and thus it cannot be determined if the much higher Li concentrations in the BQ19 olivines compared to crystals from other host lavas are a direct result of diffusion.

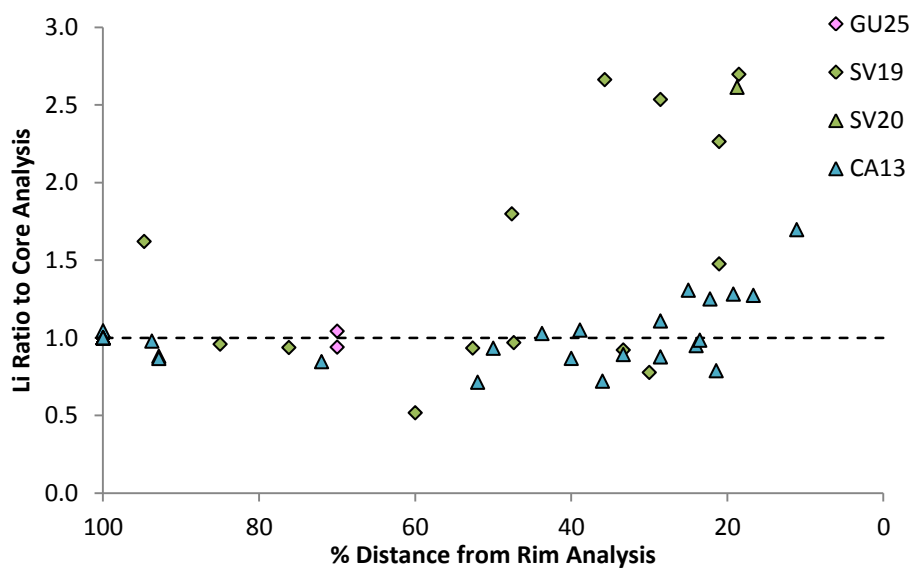


**Figure 3-16 Ratios between Li concentrations across olivines and with the core analysis for the olivines analysed in thick section. The dashed line represents a ratio of 1, with values greater than one indicating higher Li contents than the core analysis.**

### 3.4.8 Cr and Ni

Cr and Ni concentrations in the olivines decrease with increasing fractionation. Cr concentrations in the LCO are lower than those in the higher CaO olivines at a given

forsterite content (Figure 3-17), particularly above Fo<sub>86</sub>. The majority of the LCO have Cr concentrations under 100 ppm, although a few of the LCO crystals show Cr concentrations which are comparable to those of the higher CaO olivines at a given forsterite content. Several LCO olivines with forsterite contents over Fo<sub>87</sub> exhibit Cr concentrations over 100 ppm. The higher CaO olivines have Cr contents between 4 and 395 ppm over a forsterite range of Fo<sub>80-91</sub> whilst the LCO have a range of 3 to 324 ppm (including those olivines with uncharacteristically high Cr concentrations).

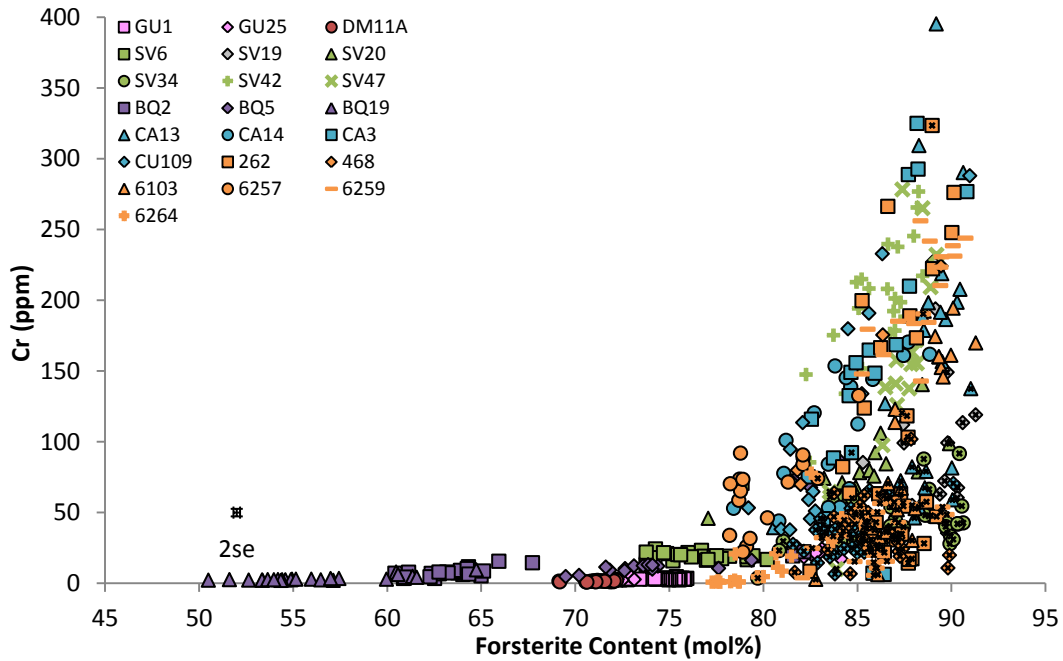


**Figure 3-17 Cr concentrations in the olivines. The majority of the LCO (small black crosses) show lower Cr contents at a given forsterite contents, generally under 100 ppm.**

At higher forsterite contents (>Fo<sub>80</sub>) large ranges in Cr contents at a given forsterite content within host lavas are observed (e.g. 59-395 ppm Cr at approximately Fo<sub>90</sub> in CA13, a factor of 6.7). Below Fo<sub>80</sub>, little variation is seen in the Cr contents of the olivines as forsterite contents decrease.

The LCO have Ni contents of 8 to 100 ppm over a range of Fo<sub>80-91</sub> where the higher CaO olivines exhibit concentrations of 2 to 69 ppm over the same forsterite range (Figure 3-18). There are some LCO at Fo<sub>89-91</sub> which show slight Ni concentration differences compared to the higher CaO olivines, these LCO have higher concentrations by approximately 20 ppm on average. Not all the LCO show these elevated Ni concentrations. Some of the LCO at Fo<sub>89-91</sub> compare very favourably with the higher CaO olivines.

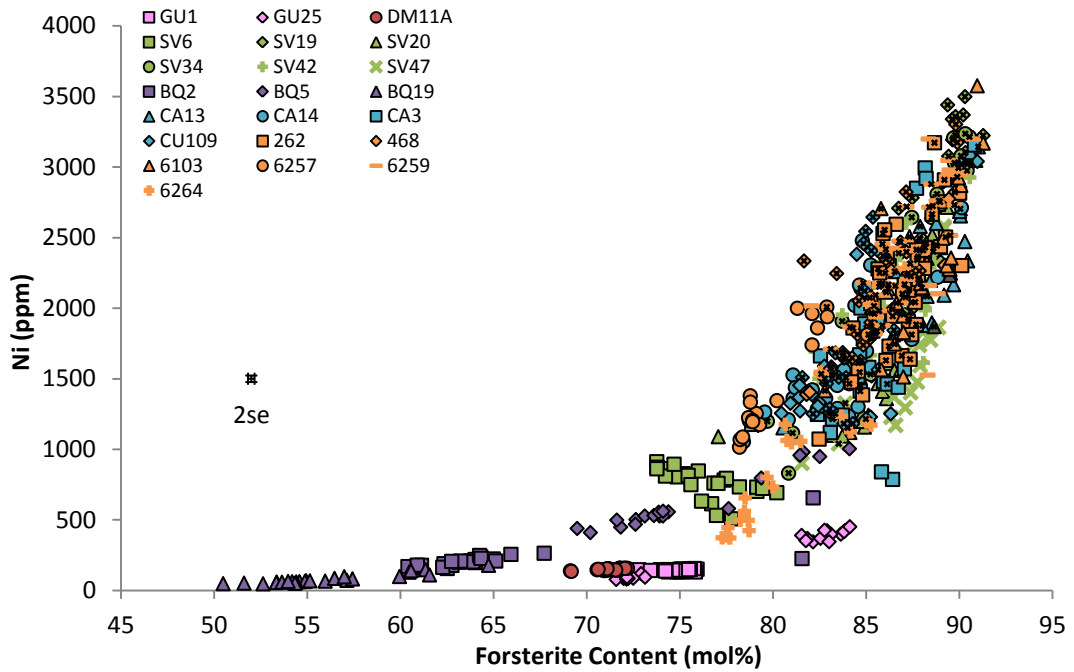


**Figure 3-18 Ni concentrations in the olivines against forsterite content showing the LCO as small black crosses.**

Large ranges in Ni content are also apparent at higher forsterite contents at invariant Fo contents, such as a 1.7 fold increase (a range of 1428 ppm) in SV19 at Fo<sub>88-89</sub>. In contrast to the Cr data however, at forsterite contents below Fo<sub>75</sub>, there is an obvious decrease in Ni with melt evolution. The higher forsterite GU25 group exhibit ~500 ppm lower Ni concentrations than the other olivines at a given forsterite content. Additionally, the GU1, lower forsterite GU25 and DM11A olivines all show approximately 300 ppm lower (but similar) Ni concentrations than the BQ5 crystals at a comparable forsterite content. The former group appear to lie off trend to the bulk of the Lesser Antilles data.

The SV6 olivines are unusual in that they show a negative trend rather than decreasing Ni as forsterite contents decrease. There also appear to be two gradients within this host lava that are outside of the 2se, as observed in the Li data. The olivines from 6264 exhibit a steeper trend than that shown in the BQ5 crystals at similar Ni concentrations.

### 3.4.9 Al<sub>2</sub>O<sub>3</sub>

Al<sub>2</sub>O<sub>3</sub> data is available for much fewer of the olivines, as this analysis was only included for the last batch of olivines analysed (Figure 3-19). Alumina contents in

the higher CaO olivines decrease with decreasing forsterite contents. The LCO do not show any clear trend. Additionally, the LCO generally show much lower concentrations of  $\text{Al}_2\text{O}_3$  over a range of  $\text{Fo}_{86-91}$  than the higher CaO olivines (three LCO crystals approach the concentrations of the higher CaO olivines). LCO alumina contents are 0.0039 to 0.0160 wt% at  $\text{Fo}_{86-91}$ , whereas the higher CaO olivine exhibit concentrations between 0.0148 and 0.0259 wt%.

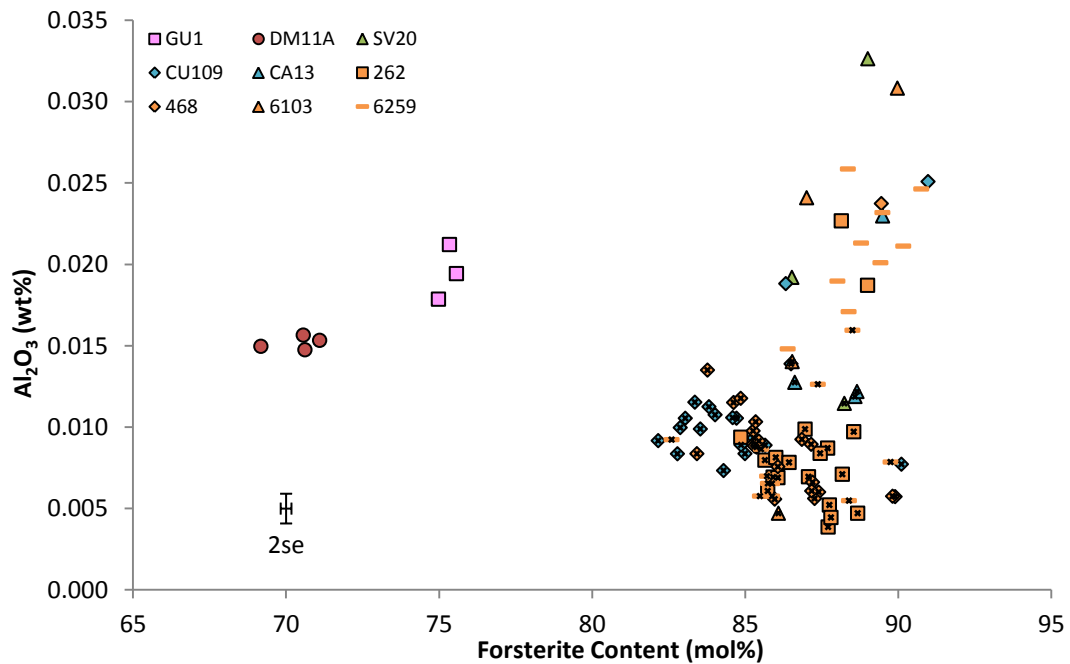


Figure 3-19  $\text{Al}_2\text{O}_3$  concentrations in the olivines, showing the LCO (overlain by small black crosses) to have lower alumina contents at a given forsterite content. In addition, the higher CaO olivines show decreasing  $\text{Al}_2\text{O}_3$  contents with decreasing forsterite contents whereas the LCO show increasing  $\text{Al}_2\text{O}_3$  with decreasing forsterite content.

The olivines from DM11A and GU1 between  $\text{Fo}_{69-76}$  show similar  $\text{Al}_2\text{O}_3$  contents to the non-LCO crystals at higher ( $>\text{Fo}_{85}$ ) forsterite contents.

### 3.4.10 Incompatible trace element ratios - Zr/Y

The LCO exhibit very high Zr/Y ratios compared to the higher CaO olivines (Figure 3-20). As Zr/Y should not be influenced by fractional crystallisation, this provides information on the differences in the sources of the two olivine populations. The LCO Zr/Y values range from 0.14 to 11.08 whereas the higher CaO olivines show much lower values of 0.07 to 1.73. The highest Zr/Y ratios in the LCO are found at a forsterite range of  $\text{Fo}_{86-88}$ .

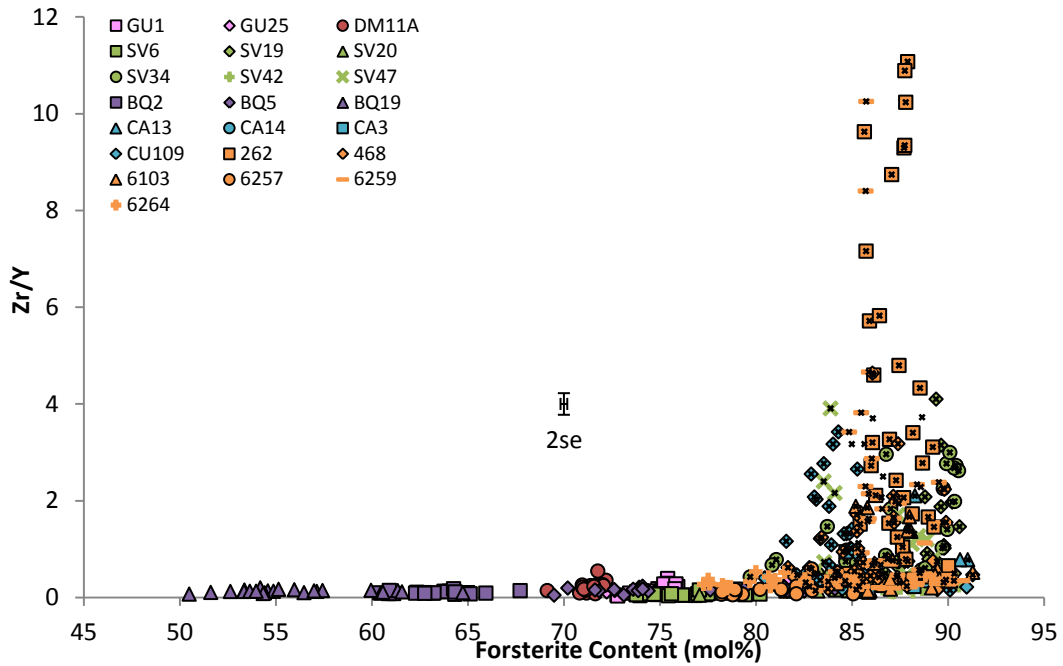


Figure 3-20 Zr/Y ratios in the olivines, the LCO (shown by small black crosses) exhibit much higher Zr/Y ratios (up to 11).

Non-LCO crystals generally show low Zr/Y ratios of  $<1$ , particularly at forsterite contents lower than  $FO_{80}$  where the ratios do not exceed 0.4.

### 3.4.11 Summary of LCO characteristics

- Low CaO contents ( $<0.11$  wt%) at a given forsterite content compared to the other analysed Lesser Antilles olivines.
- Low  $Al_2O_3$  contents at a given forsterite content.
- Low Cr concentrations at a given forsterite content.
- Low Y and Yb concentrations at a given forsterite content.
- Low Sc in some cases (e.g. in the LCO from St. Vincent).
- High Zr/Y ratios (up to 11).

### 3.4.12 Cumulate Xenoliths

Cumulate xenoliths hosted in two lavas from Grenada were also targeted as part of this study. In each case both olivines from within the xenolith and in the surrounding host lava were analysed. 20 crystals were examined from host lava 6001 and 14 from

host lava 6004. All the olivines pertaining to the cumulate xenoliths were analysed in situ in thick section. Table 3-2 shows the number of olivines analysed (both in the xenolith and in the surrounding host lava) and the forsterite ranges of each discrete group.

Host Lava	Olivine Type	n	Fo Range (mol%)
6001	Cumulate xenolith	15	85-87
6001	Host lava	5	86-88
6004	Cumulate xenolith	8	90-91
6004	Host lava	6	82-90

**Table 3-2 Olivines analysed in host lavas containing cumulate xenoliths. n is the number of each type of olivine analysed.**

### *Petrography*

The cumulate xenolith olivines appear different in each host lava (Figure 3-21). The left hand picture shows olivines in thick section in host lava 6001, the right hand picture olivines in 6004.

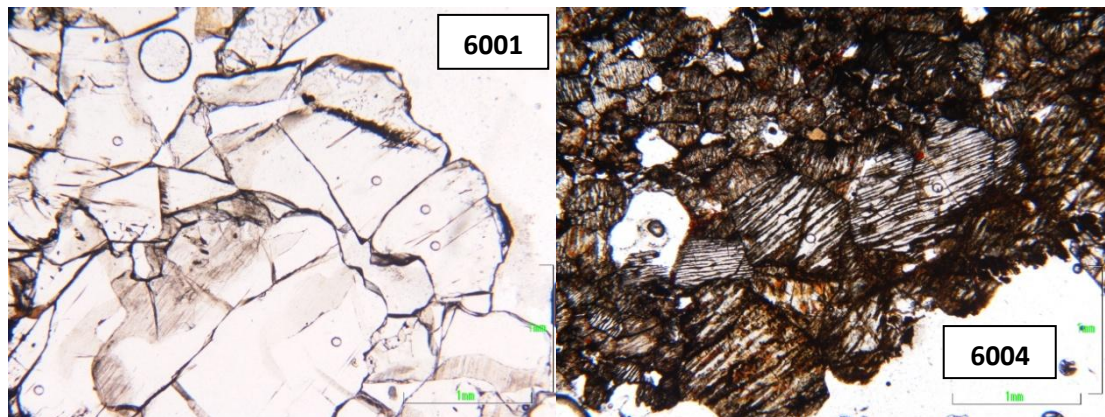
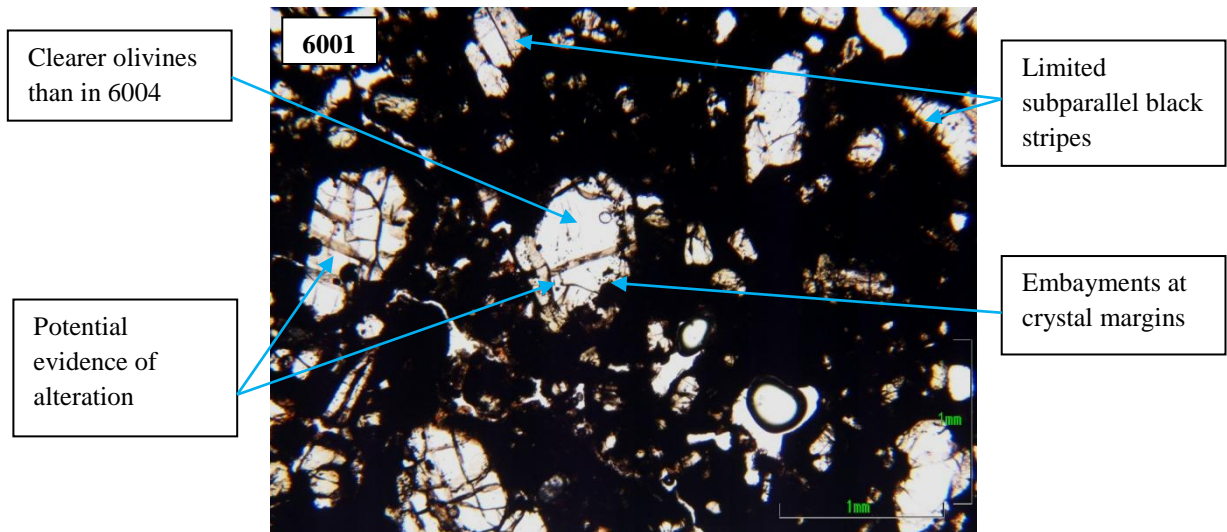


**Figure 3-21 Thick section photographs of the cumulate olivines hosted within xenoliths in each host lava in PPL.**

Crystal sizes of the cumulate olivines are similar in each host lava, extending up to 2 mm. This is in contrast to the plutonic cumulates detailed by Arculus and Wills (1980) but may be similar to the 'cognate inclusions' described in the same paper, with the latter being described by the authors as 'crystal clots' that may be a product

of magma mixing. The 6001 olivines are subhedral to anhedral and appear relatively clear, with some small black lines extending partway across some crystals; these may be Fe-Ti oxides or exsolution lamellae. However, the 6004 crystals (whilst also appearing subhedral to anhedral) are extensively cross-cut by sub-parallel black lines (which are also thicker than those observed in the 6001 olivines), giving an overall 'stripy' appearance to these olivines. Further to this, most crystals also show iddingsitisation, both along the crystal margins and associated with the black lines.

The olivines with the groundmass of the host lava appear similar and in some cases show petrographic evidence of being in disequilibrium with the surrounding melt composition, particularly in host lava 6004 (Figure 3-22). The features that could indicate disequilibrium include embayments at the crystal margins and crystal edges which show evidence of resorption.



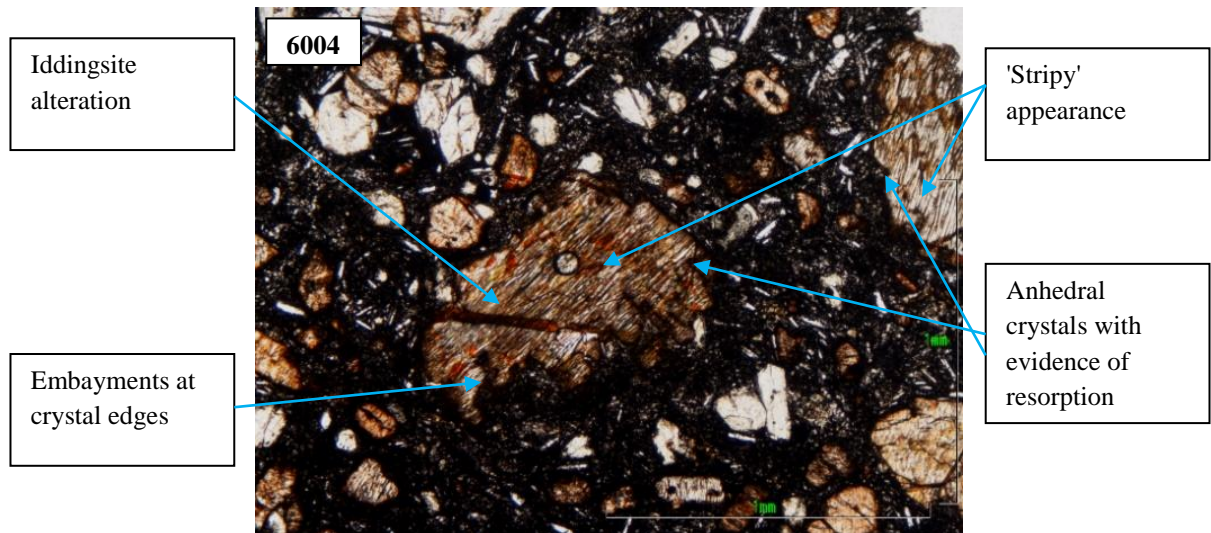


**Figure 3-22 Olivines in 6001 (upper photograph) 6004 (lower photograph) found within the host lava surrounding the cumulate xenoliths, taken in PPL.**

Given the similarities between the cumulate xenolith olivines and the olivine phenocrysts found in the host lavas, coupled with evidence that the phenocrysts do not always appear to be in equilibrium with their respective groundmasses, it can be reasonably assumed that at least some of the phenocryst olivines originated from the cumulate body. Thus there is petrographic evidence of disaggregation of the cumulates in these two host lavas.

### 3.4.13 $\delta^{18}\text{O}$ Method

#### *Analytical Method*

$\delta^{18}\text{O}$  analyses were undertaken at the Ion Microprobe Facility at the University of Edinburgh over three days in March and August 2013. Olivine crystal mounted separates from 6 islands (Guadeloupe, Dominica, St. Vincent, Carriacou, Petite Martinique and Grenada) were analysed by SIMS (using a  $\text{Cs}^+$  ion beam) on the Cameca 1270.  $\delta^{18}\text{O}$  analysis of the samples is important as this is one of the only isotopic systems that can be successfully measured in olivine. Olivine crystals were mounted in epoxy resin blocks along with an  $\text{Fo}_{90.2}$  San Carlos standard (as used for the LA-ICP-MS analyses) and an  $\text{Fo}_{90.3}$  San Carlos standard (provided by the Ion Microprobe Facility for  $\delta^{18}\text{O}$  analysis). The crystal mounts were then sputter coated with gold prior to analysis.

Point analyses were carried out using a spot size of 20µm with a distance of at least 35µm between each point. Efforts were made to avoid analysing spots close to holes or bubbles in the mount to avoid charging the sample. Samples were standardised and instrumental mass fractionation corrected using a regression through forsterite and fayalite standards (e.g. Figure 3-23) run at the beginning of each day. Instrumental mass fractionation (IMF) was calculated using Equation 3-1.  $^{18}\text{O}/^{16}\text{O}$  San Carlos is the accepted value for this ratio in the San Carlos olivine standard used and is 0.0020158.

**Equation 3-1**

$$IMF = \left( \frac{^{18}\text{O}/^{16}\text{O} \text{ Measured} - ^{18}\text{O}/^{16}\text{O} \text{ San Carlos}}{^{18}\text{O}/^{16}\text{O} \text{ San Carlos}} \right) \times 1000$$

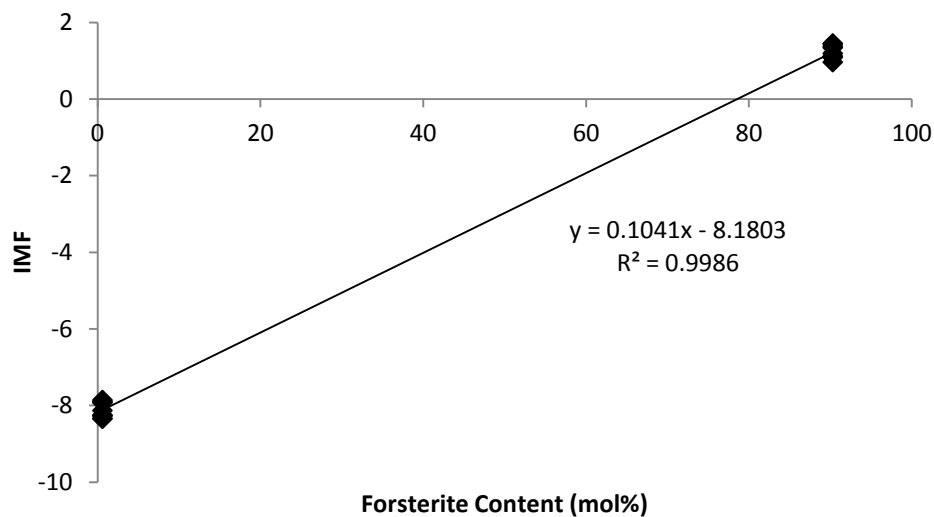


**Figure 3-23 IMF versus Forsterite content for the standard data analysed at the start of the day on 22/03/13. The gradient and intercept of the trendline are used in the calculation of the IMF correction for that day (Equation 3-2).**

IMF correction for each analysis was based on the forsterite content of the analysed material and the equation of the regression line for the day of analysis (Equation 3-2). The IMF corrections were then used to correct the measured  $^{18}\text{O}/^{16}\text{O}$  ratios using Equation 3-3.

**Equation 3-2**

**IMF Correction**

$$= Fo \text{ content} \times \text{Gradient of regression line} - \text{Intercept of regression line}$$

**Equation 3-3**

$$^{18}\text{O}/^{16}\text{O} \text{ Corrected} = \frac{^{18}\text{O}/^{16}\text{O} \text{ Measured}}{(\text{IMF Correction}/1000) + 1}$$

The corrected  $^{18}\text{O}/^{16}\text{O}$  ratios were then used in the calculation of  $\delta^{18}\text{O}$  (Equation 3-4), where  $\delta^{18}\text{O}$  is the ratio of  $^{18}\text{O}/^{16}\text{O}$  of the sample in relation to Standard Mean Ocean Water (SMOW) expressed in per mil.

**Equation 3-4**

$$\delta^{18}\text{O}_{\text{IMF Corrected}} = \left( \frac{^{18}\text{O}/^{16}\text{O} \text{ Corrected}}{^{18}\text{O}/^{16}\text{O} \text{ SMOW}} - 1 \right) \times 1000$$

6 points were analysed per sample crystal and sample-standard bracketing was used to assess instrumental drift throughout the day. Data for each point was corrected using Equation 3-1 through to Equation 3-4 before an average and standard deviation was calculated for each crystal. Forsterite content for each olivine was input from pre-existing LA-ICP-MS data. In instances where crystals had been analysed twice on the laser (as a check for reproducibility), an average of the forsterite contents was used.

Olivines from ten host lavas were analysed. 4 crystals were analysed from each lava, with the exception of SV47, from which 6 crystals were targeted (Table 3-3). The bracketed numbers in the table show the number of the analysed crystals which are classified as LCO based on LA-ICP-MS determined CaO contents.

<b>Analysis Date</b>	<b>Island</b>	<b>Host Lava</b>	<b>Number of Crystals (LCO)</b>	<b>Forsterite Range (mol%)</b>
13/08/13	Guadeloupe	GU1	4 (0)	74.98-75.56
13/08/13	Dominica	DM11A	4 (0)	69.18-71.10
13/08/13	St. Vincent	SV20	4 (1)	86.52-89.00
22/03/13	St. Vincent	SV47	6 (3)	83.55-87.90
12/08/13	Petite Martinique	CA13	4 (3)	86.62-89.49
22/03/13	Petite Martinique	CA14	4 (0)	80.82-89.48
22/03/13	Carriacou	CA3	4 (1)	82.80-89.52

<b>12/08/13</b>	Grenada	468	4 (4)	83.77-85.34
<b>12/08/13</b>	Grenada	6103	4 (2)	86.08-89.97
<b>22/03/13</b>	Grenada	6257	4 (0)	78.24-82.10

**Table 3-3 Host lava name and locations with numbers of crystals analysed in each sample block. Forsterite contents are from LA-ICP-MS analysis. Numbers in brackets show the number of the crystals which can be deemed LCO based on their CaO contents derived from LA-ICP-MS analysis. Forsterite range is the range in the olivines analysed for  $\delta^{18}\text{O}$  only.**

*Drift Correction*

The San Carlos olivine data shows a consistent decrease in  $\delta^{18}\text{O}$  during the course of the March analysis day (Figure 3-24). All analysed crystals were given an 'analysis number' to illustrate at what point they were analysed during the day. A linear regression was put through the data, the gradient and intercept of this line were then used to drift correct the San Carlos data (Figure 3-24) and the sample data using Equation 3-5 (where A Number is the analysis number). The accepted value for  $\delta^{18}\text{O}$  for the San Carlos olivine standard analysed is 5.3‰ and is shown in Figure 3-24 as a dashed line.

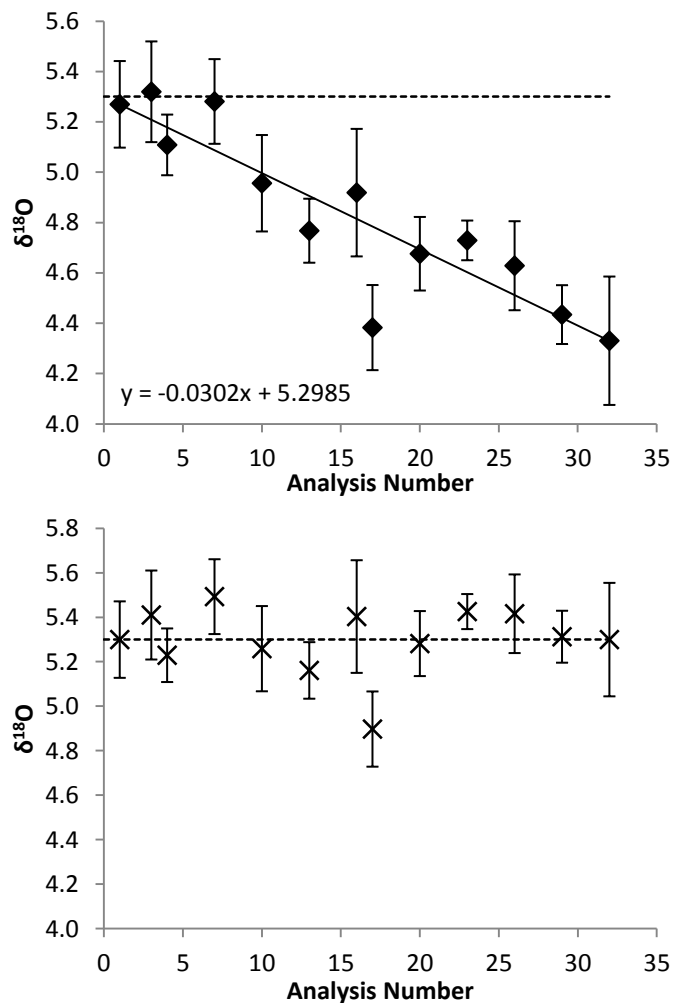


Figure 3-24 San Carlos data analysed on 22/03/13. The upper graph shows the IMF corrected data and shows a decrease in  $\delta^{18}\text{O}$  which may be a result of instrumental drift. The lower graph shows the same San Carlos data after a drift correction (Equation 3-5) has been applied to the IMF corrected data. The dashed lines represent a  $\delta^{18}\text{O}$  value of 5.3‰. Error bars show 1sd.

Equation 3-5

$$\begin{aligned} \delta^{18}\text{O}_{\text{Drift Corrected}} &= \delta^{18}\text{O}_{\text{IMF Corrected}} \\ &+ (\delta^{18}\text{O}_{\text{San Carlos}} - (-0.0302 \times A \text{ Number}) + 5.2985) \end{aligned}$$

The same correction was applied to the data from the remaining two analysis days.

### ***IMF Correction***

The IMF correction is based only on two standards, due to a lack of suitable standards intermediate to Fo<sub>0.6</sub> and Fo<sub>90.3</sub> (Figure 3-23). This introduces some limitations on the validity of the correction. It is assumed that there is a linear relationship between the two standards but without a standard with an intermediate forsterite content this has not been proven. Additionally, there can be a wider range in the IMF for the Fo<sub>0.6</sub> olivine than the Fo<sub>90.3</sub> olivine (Figure 3-25). Thus the gradient and intercept of the regression line (and thus the corrections based upon it) may have a significant error.

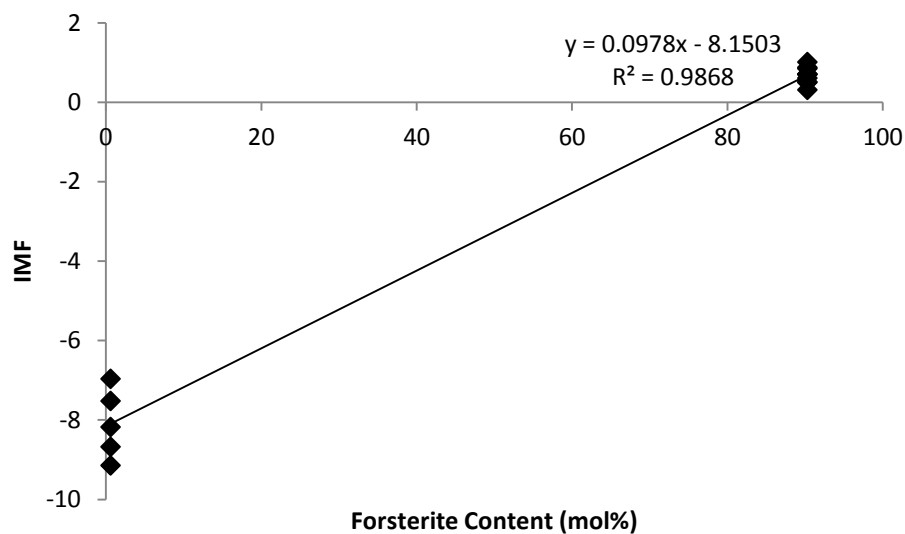


**Figure 3-25 IMF correction for 13/08/13. There is a larger range in IMF for the fayalite data than for the Fo<sub>90.3</sub> olivine.**

### **3.4.14 $\delta^{18}\text{O}$ Results**

The olivine  $\delta^{18}\text{O}$  data were compared to both olivine LA-ICP-MS data and the whole rock isotopic data of the host lavas.

#### ***Forsterite contents and $\delta^{18}\text{O}$***

Some of the host lavas show a trend of increasing  $\delta^{18}\text{O}$  with decreasing forsterite content (Figure 3-26). These lavas are SV20, SV47, CA3, CA13, CA14, 6103 and 6257.

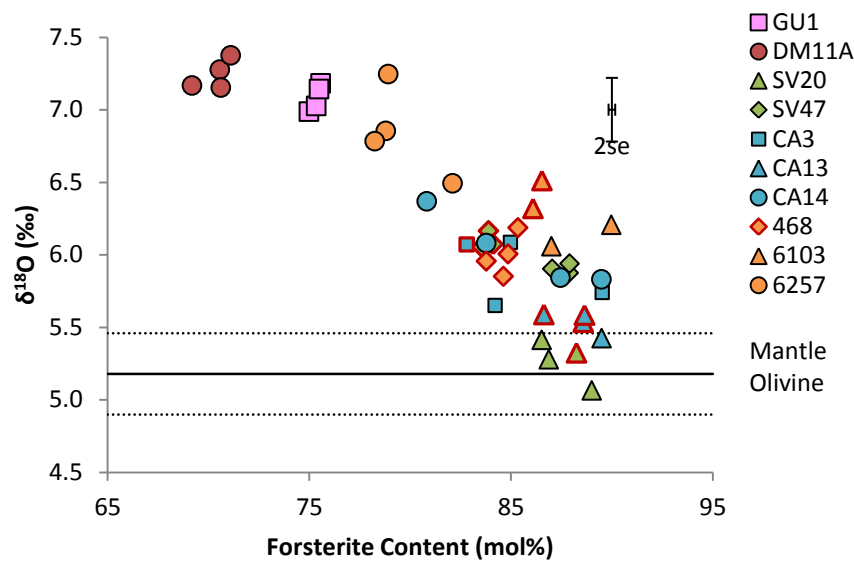


**Figure 3-26** Forsterite contents of the analysed olivines against the IMF and drift corrected  $\delta^{18}\text{O}$  data. Solid line represents mantle olivine value of 5.18‰ with the dashed lines representing the  $\pm 0.28\%$  error on the mantle olivine value (Matthey *et al.*, 1994). Average forsterite contents have been used if more than one LA-ICP-MS analysis has been performed on the same crystal. Low calcium olivines are shown as symbols outlined in red.

The negative correlation seen between the forsterite contents of the analysed olivines and their  $\delta^{18}\text{O}$  contents may be a result of instrumental mass fractionation which is not being adequately corrected for by the IMF correction. However, without further evidence to show that the trend is definitely an artefact of the correction method, it is assumed that the results are valid and that the correlation observed is real.

Davidson and Wilson (2011) analysed several olivines from Statia (in the northern part of the arc) for  $\delta^{18}\text{O}$  by laser ablation. The Statia olivines exhibited  $\delta^{18}\text{O}$  contents between 5.0-5.3‰. The most northerly islands analysed as part of this study (Guadeloupe and Dominica) are further south than Statia but show IMF corrected  $\delta^{18}\text{O}$  values of 6.99-7.18‰ (GU1) and 7.15-7.37‰ (DM11A). It is interesting to note however, if the data is not IMF corrected these values drop to 5.48-5.73‰ (GU1) and 5.08-5.48‰ (DM11A), which is much more comparable to the findings of Davidson and Wilson (2011).

### 3.5 Discussion

Olivines were analysed in order to gain insights into early petrogenetic processes occurring in the Lesser Antilles arc. The presence of the low calcium olivines alone

shows that petrogenesis is not a simple process in the Lesser Antilles. The questions of the origin of the LCO and how they came to be erupted in the host melts are important to try and answer to understand better what is happening at lower crustal and upper mantle levels in the arc. Further to this, the unusually low CaO concentrations and high forsterite contents in the higher CaO olivines also warrant investigation. The isotopic data obtained can also shed light on the conundrum of sediment addition in the arc through modelling the effects of adding varying sediment types and trying to test where these sediments were added.

Those traits that are common between both the higher CaO olivines and the LCO (e.g. whether the olivines are in equilibrium with their whole rock compositions and the high forsterite contents of some of the crystals) will be discussed first. Then the petrogenesis of the LCO will be discussed separately to the processes affecting the higher CaO olivines.

### **3.5.1 Equilibrium Olivines**

Before discussing potential processes affecting the petrogenesis of the olivines it is important to try and ascertain if the crystals are in equilibrium with their host melts. However, as noted in Chapter 2, whole rocks are essentially a homogenisation of groundmass and phenocryst phases which do not take into account whether these phenocrysts originate from the melt in which they reside. Both antecrysts and xenocrysts may be present in the whole rock despite not being direct products of the host melt. These populations will then affect the whole rock composition e.g. by increasing Mg# if significant amounts of olivine and/or clinopyroxene have been entrained. Given the high phenocryst proportions in many of the host lavas coupled with the wide ranges in forsterite contents observed (and the presence of a discrete LCO population), it would appear unlikely that the olivines are in equilibrium with their host lavas.

The petrography of the olivines is detailed in section 3.3. Features which suggest that the olivines are not in equilibrium with the host rocks are commonplace, including resorption of crystal edges, embayments and alteration (to iddingsite, iron oxide and chlorite).

However, it is worth investigating this numerically in order to observe if any of the crystals approach equilibrium. In addition, the method used may give an indication as to whether the non-equilibrium olivines show potential evidence of originating from more primitive lavas or possible accumulation into the host lavas. Forsterite contents of olivines which would be in equilibrium with the whole rocks compositions were calculated using a partition coefficient for  $Fe^{2+}/Mg^{2+}$  of  $0.30 \pm 0.03$  from Roeder and Emslie (1970) as defined in Equation 3-6.

**Equation 3-6**

$$K_{D_{Fe-Mg}}^{ol-melt} = \frac{(Fe^{2+}/Mg^{2+})_{ol}}{(Fe^{2+}/Mg^{2+})_{melt}}$$

The  $Fe_2O_3/FeO$  ratios used to estimate how much of the total whole rock FeO was  $Fe^{2+}$  were those recommended by Middlemost (1989) based on the whole rock's location on a TAS (Le Bas *et al.*, 1986) plot. Figure 3-27 shows where the analysed olivines plotted in relation to the calculated equilibrium olivines, with the area between the lines being in equilibrium. Most of the olivines plot above the equilibrium lines, suggesting they may be accumulative. The olivines below the equilibrium lines may be more primitive than their whole rock compositions.

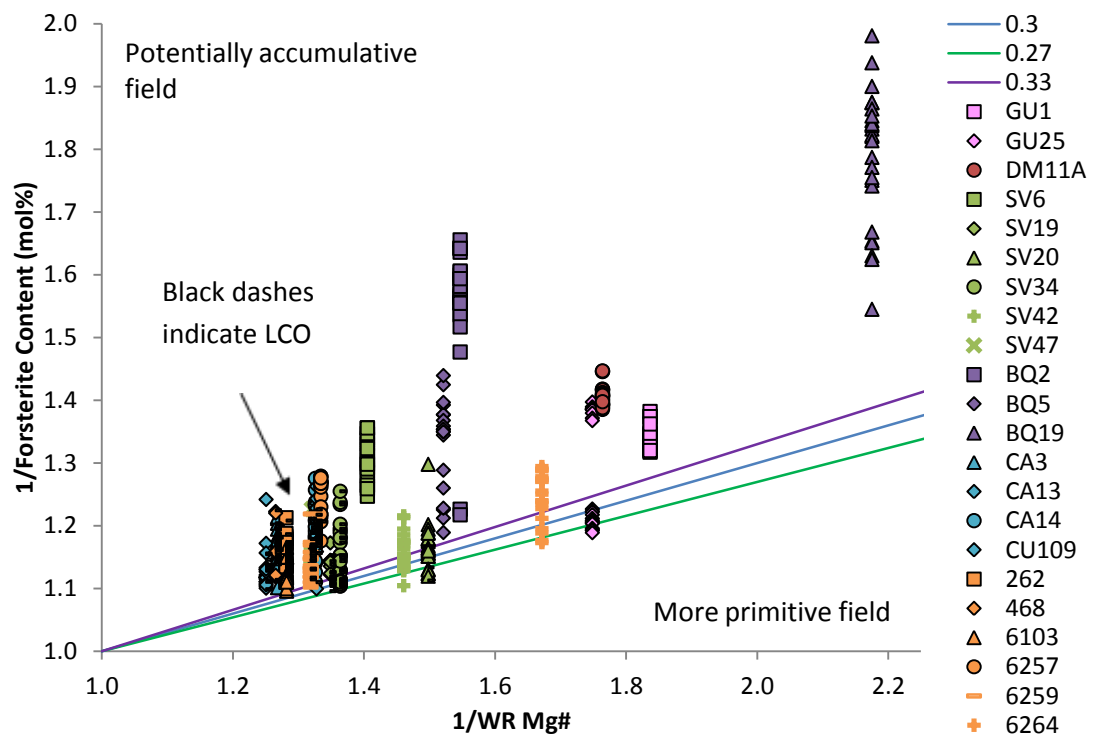


**Figure 3-27** Forsterite compositions of olivines analysed against the forsterite content of olivine calculated to be in equilibrium. The area between the lines represents where the olivines are in equilibrium with their whole rock, within error of the Roeder and Emslie (1970) partition

**coefficient. More primitive olivines plot below the lines and potentially accumulative olivines plot above the lines. The LCO are shown as black dashes.**

Figure 3-27 shows that the LCO do not lie on a separate trend to the normal CaO olivines when compared to the calculated equilibrium olivine for each whole rock. The majority appear to plot in the potentially accumulative field but several appear to be in equilibrium with their whole rocks. Additionally, SV20 shows two LCO plotting in the more primitive field.

In order to show the discrepancies between the calculated equilibrium olivines and measured forsterite contents of the analysed crystals, a delta parameter was defined using Equation 3-7 and Equation 3-8. In Equation 3-7, 0.3 is the gradient of the 0.3  $K_D$  line from Figure 3-27 (Roeder & Emslie, 1970) and 0.7 is the intercept.

**Equation 3-7**

$$\text{Equilibrium } 1/Fo = (0.3 \times 1/WR MgO) + 0.7$$

**Equation 3-8**

$$\Delta \text{Equilibrium Olivine} = 1/Fo - \text{Equilibrium } 1/Fo$$

Figure 3-28 further shows that there is no trend between calcium concentrations in the olivines and plotting in equilibrium with the host lava. The LCO show similar offsets from the calculated equilibrium olivines for their respective host lavas the higher CaO crystals. Figure 3-28 also reinforces how many of the olivines (both low and higher CaO) plot in the potentially accumulative field compared to those that may be more primitive.

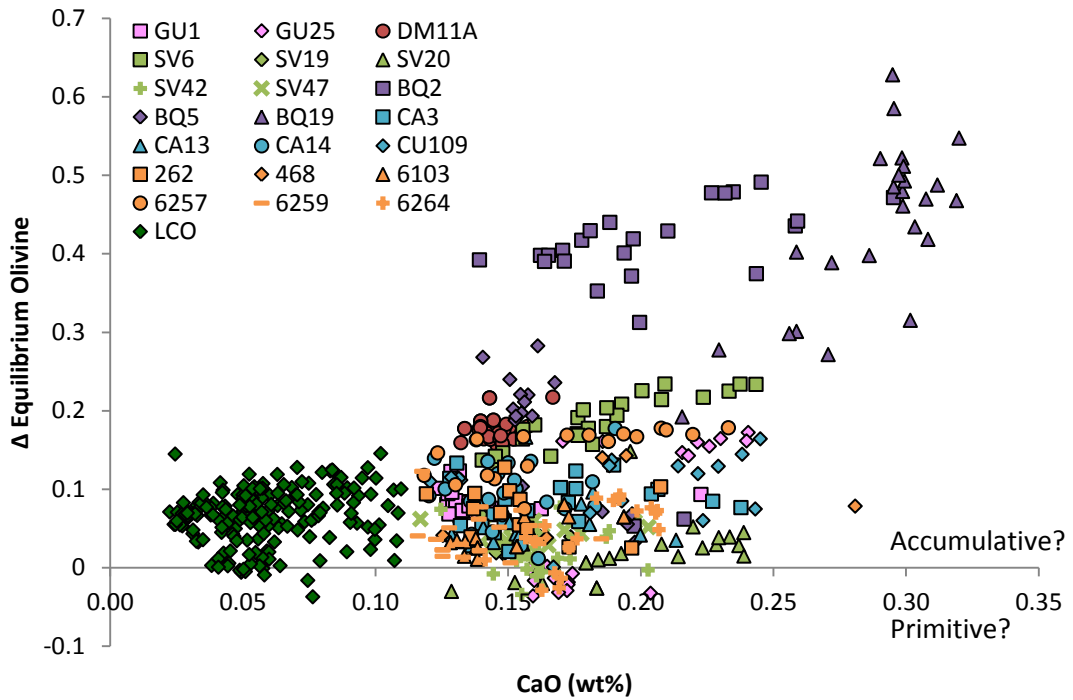
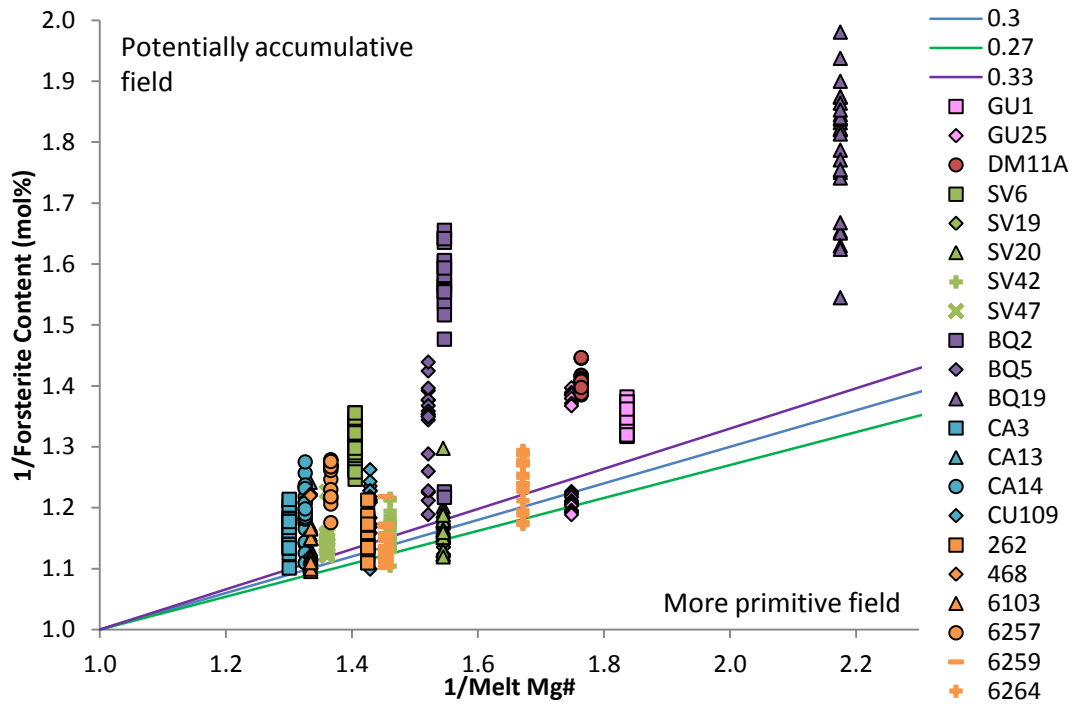


Figure 3-28  $\Delta$  parameter used to show offset of olivines from equilibrium olivine against CaO content. The LCO are shown as dark green diamonds. 0 on the y axis represents equilibrium with the host lava assuming a  $K_D$  of 0.3 (Roeder & Emslie, 1970).

If it is assumed that the LCO have been entrained into the host rock and were not crystallised from the host lava, this would change the Mg# of the whole rock. Consequently, removal of the LCO may increase the 1/WR Mg# of the host lava. Table 3-1 shows the percentage of the whole rocks attributed to phenocryst olivine based on point counting data. The proportions of the olivines from each host lava that are LCO were calculated by dividing the number of LCO by the total number of analysed olivines. New melt Mg# for the host lavas was then calculated by removing the LCO from the whole rock compositions. Replotting Figure 3-27 with the LCO removed can test if the presence of the LCO is responsible for the remaining olivines from LCO bearing host lavas appearing to lie out of equilibrium with the whole rock composition in Figure 3-27 (Figure 3-29).



**Figure 3-29 Forsterite contents in the analysed olivines compared to those calculated to be in equilibrium with the whole rock if the LCO are assumed to have been entrained into the host lava.**

Figure 3-29 shows that even with the LCO removed, the remaining olivines do not all plot in equilibrium, although olivines from 262 and 6259 are shifted closer to the equilibrium lines. SV34 does not appear on Figure 3-29 as all the olivines analysed in this host lava were LCO.

Host lavas without LCO present also do not plot in equilibrium, this is particularly evident in BQ19 and DM11A. Therefore even if the LCO are entrained and are artificially reducing the 1/WR Mg# ratio, other processes must be in effect to fully explain the apparent disequilibrium between the forsterite contents of the analysed olivines and the whole rock.

In order to test if the removal of either the LFG or HFG would result in the remaining population being in equilibrium with the resulting melt, Figure 3-27 was replotted after having calculated the effects of population removal on the Mg# of potential melts (Figure 3-30).

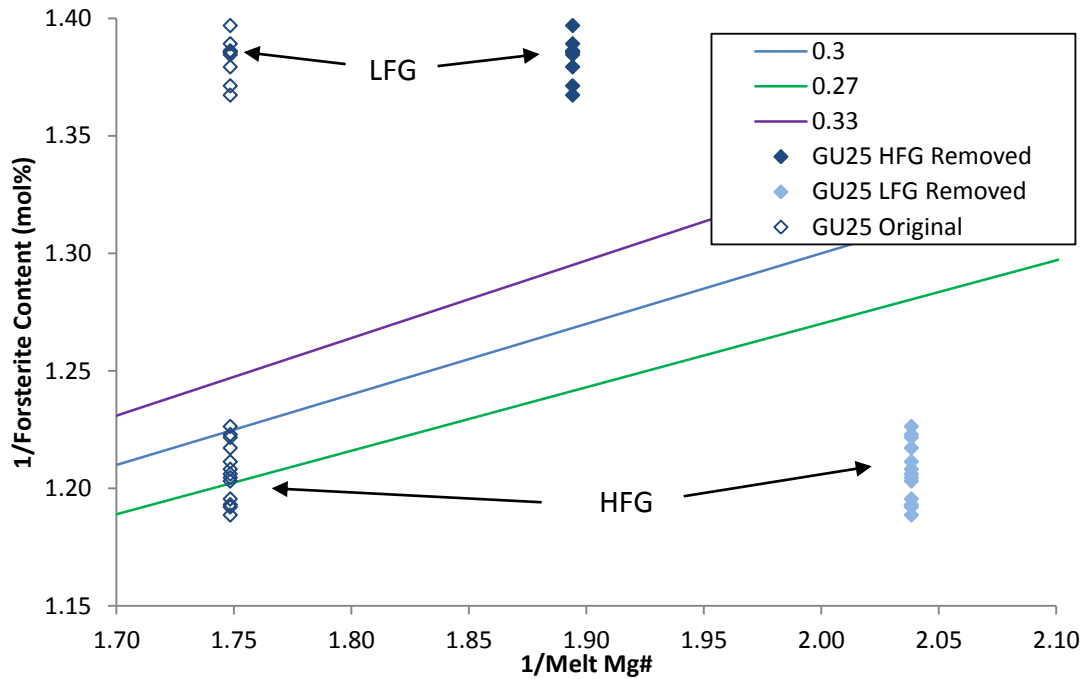


**Figure 3-30 Comparison between calculated hypothetical equilibrium olivine compositions for GU25 the observed forsterite contents of the analysed crystals. The hollow diamonds show where the HFG and LFG plot if neither population is removed. The solid dark blue diamonds represent where the LFG would plot if the HFG were removed and the light blue diamonds depict where the HFG would plot if the LFG were removed from the whole rock.**

Figure 3-30 shows that removing either population from the GU25 whole rock does not result in all of the HFG or LFG lying in the equilibrium area between the upper and lower error limits on the Roeder and Emslie (1970) partition coefficient. In fact, in the case of the HFG, the crystals are displaced further away from the equilibrium area. If the LFG are not removed, 4 of the HFG lie within equilibrium, however, with the LFG assumed to be entrained, only 2 crystals are in equilibrium. The LFG are shifted nearer to the equilibrium zone, but only fractionally.

Therefore, the olivines do not appear to be in equilibrium with their host lavas in the majority of cases, as expected given that the whole rock compositions are a combination of both any mineral phases present as phenocrysts and the groundmass. As demonstrated by the LCO, host lavas can contain multiple populations which may not originate from the host lava. Unless compositions are corrected for all of these populations, it is unlikely that phenocryst minerals will appear in equilibrium. Whilst the crystals appear to be accumulative in the most part, further investigation is required to confirm this.

### 3.5.2 Entrainment

There are no obvious petrographic differences between any of the olivines found within individual lavas. This makes it harder to identify if any of the crystals have been entrained into the host lavas after having been crystallised from a differing parent melt as only geochemical evidence can be used. Whilst the LCO have obviously different chemistry to the remaining olivines, they will be dealt with in a separate section.

GU25 is bimodal in terms of forsterite content. Compositions of the HFG and LFG are comparable with the olivines from the other host lavas at a given forsterite content for all the elements analysed, with the exception of MnO (Figure 3-13) and Ni (Figure 3-18). The HFG exhibit approximately 500 ppm lower Ni concentrations and 0.05 wt% MnO. The compositional similarities suggest that it is unlikely that the GU25 populations have been crystallised from different sources. They may have originated from a single parent melt that has evolved through fractional crystallisation or a single source that has undergone different degrees of partial melting. The former instance requires either a break in olivine crystallisation or for any crystallised olivines to have fractionated from the host melt and thus not have been erupted, resulting in a lack of olivines with forsterite contents between the HFG and LFG.

Whilst removing either population does not place the other in equilibrium (Figure 3-30), it is still possible that one has been entrained and there are other factors influencing the olivines lying out of equilibrium. Of the two populations, it would seem more likely that the HFG is the population that has been entrained as removing this moves the LFG closer to equilibrium.

Thick section analysis of in situ GU25 olivines was undertaken but was limited by the extent of iddingsite alteration apparent in the crystals found in this host lava. As a result, good analyses were only possible on three rims of olivines and 6 smaller olivine cores. This does not permit comparison between cores and rims or further investigation of whether forsterite contents increase or decrease across crystals.

### 3.5.3 Accumulation

Accumulation is the crystallisation of olivines from a melt that then settle out of the melt and congregate at the base of the magma chamber. Accumulation of olivines could explain the discrepancies between the calculated forsterite contents of equilibrium olivines and the observed forsterite contents of the crystals analysed (Figure 3-27). If crystallised olivines accumulate in a magma reservoir, this will increase the Mg# of the whole rock, thus meaning that the Fo content of the olivines is lower than that of the hypothetical equilibrium olivine. High olivine phenocryst proportions (Table 3-1) would support accumulation. Of the St. Vincent lavas, SV20 shows the lowest olivine phenocryst population (3.2%) and does not appear to plot in the more accumulative field, ranging from the equilibrium area to the more primitive field. The remaining host lavas from St. Vincent have between 9.1-21.1% olivine phenocrysts. SV42 has 15.1% olivine but does not plot in the accumulative field on Figure 3-27.

The Carriacou and Petite Martinique lavas show high modal proportions of olivine, between 13.2-31.5%, with 13.2% being found in CU109. The latter host lava exhibits some olivines within the equilibrium area, unlike the remaining Carriacou and Petite Martinique host lavas. These high proportions could support some degree of accumulation having occurred. In the Grenada host lavas, olivine modal proportions of between 8.8 and 20.9% were observed (although no thin section was available for 6264). As seen in the Carriacou host lavas, some of the Grenada olivines extend into the equilibrium area on Figure 3-27, in 6103 and 6259. However, 6259 has the second highest olivine phenocryst proportion of the Grenada host lavas at 17.9%, suggesting there is no definitive correlation between modal olivine proportion and how far from the equilibrium area the olivines plot in Figure 3-27.

The Bequia crystals all plot in the accumulative field but show low modal olivine proportions of 2.6-6.0%. However, BQ2 and BQ5 have high modal clinopyroxene proportions (16.6% and 21.0% respectively). As clinopyroxene is also a magnesian phase, it is possible that increased clinopyroxene concentrations could have caused the host rock to have an elevated Mg# relative to the observed forsterite contents of the olivines. BQ19 only has 2.1% clinopyroxene but is the furthest removed from the equilibrium area on Figure 3-27.

As seen in Figure 3-30, the LFG from GU25 appear to plot in the accumulative field and if either the LFG or the HFG were accumulated, this would affect the whole rock Mg#. There is no petrographic evidence to differentiate between the two populations so it is not obvious which (if either) population was not crystallised from the host lava. However, accumulation alone does not explain the bimodality seen in GU25. No thin section was available for DM11A so no point counting could be undertaken, consequently it cannot be ascertained if there is an excess of magnesian rich phases to support the possibility of accumulation.

Given that there is no real correlation between modal proportion of olivine phenocrysts and where the crystals plot on Figure 3-27 (as demonstrated by low modal proportions of olivine in the Bequia lavas coupled with definite upward offset from the equilibrium zone defined by the Roeder and Emslie, 1970  $K_D$  values), it appears unlikely that accumulation is a key process in the petrogenesis of Lesser Antilles lavas.

### **3.5.4 Melt Composition**

Published partition coefficients can be used to reconstruct melt compositions. However, partition coefficients between olivine and melt can be affected by numerous parameters, such as temperature, pressure, melt water contents and oxygen fugacity. Thus finding a suitable value can be challenging. A rough approximation of partition coefficients can be calculated from the data by using the whole rock composition and concentrations in the olivines and then these can be compared to published values, however, as previously established, few of the crystals are in equilibrium with their host melts. The most applicable  $K_D$  values may be those where olivine composition is used to determine partition coefficients, such as those of Jurewicz and Watson (1988a), detailed below.

#### ***Back Calculated Melt Compositions***

Given the bimodality in the CaO data, the concentrations of CaO expected in the melts responsible for crystallising both populations (the LCO and the higher CaO olivines) were calculated. Partition coefficients for CaO were calculated for each

olivine using the equation published by Jurewicz and Watson (1988a) (Equation 3-9).

**Equation 3-9**

$$K_D = \{(-0.08 \pm 0.015)(\%Fo) + (9.5 \pm 0.2)\}$$

The equation was used as follows in the calculation (Equation 3-10).

**Equation 3-10**

$$K_D = \{(-0.08)(\%Fo) + (9.5)\}$$

Melt compositions were then calculated by using the  $K_D$  values determined from Equation 3-10 and the concentrations of CaO measured in the olivines using Equation 3-11. The latter equation is a general formula for calculating the concentration (x) of an element/oxide (i) in a melt using the partition coefficient between melt and olivine for that element/oxide ( $K_D^i$ ).

**Equation 3-11**

$$x_{Melt}^i = \frac{x_{Olivine}^i}{K_D^i}$$

In the same way, the MgO content of the melt compositions were also calculated using Equation 3-11, but in this instance a partition coefficient of 2.94 was used (Beattie, 1994).

Figure 3-31 shows both the calculated melt compositions for the higher CaO olivines and the LCO in addition to the whole rock compositions analysed in Lesser Antilles lavas from the same islands as those from which the olivines were sampled.

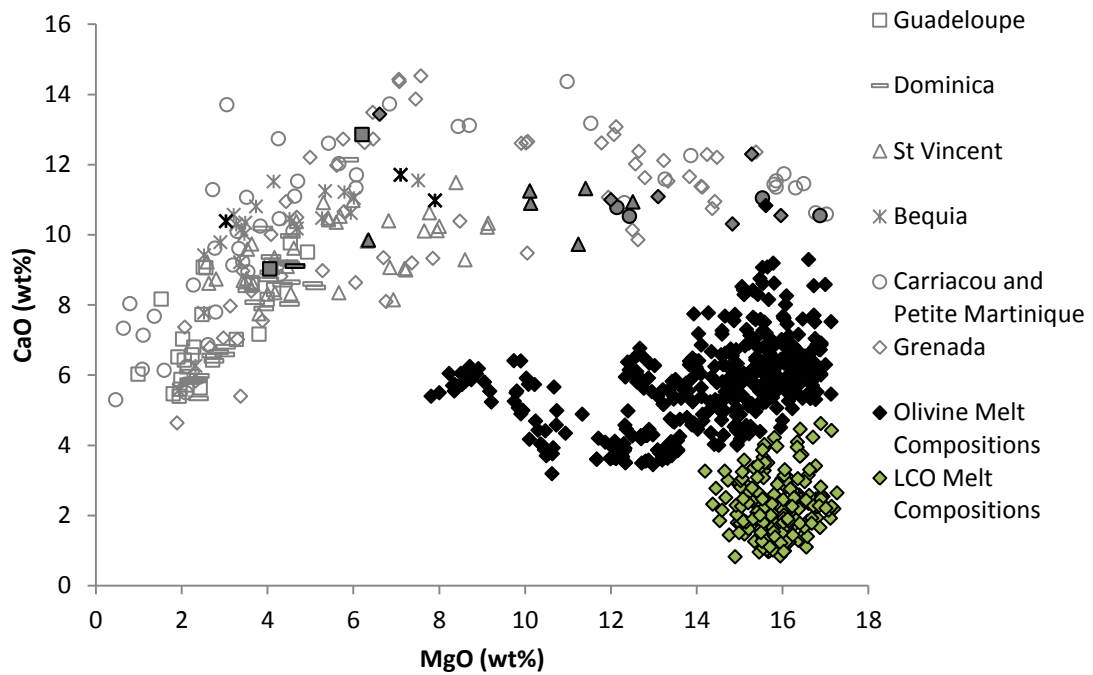


**Figure 3-31 Whole rock and calculated melt MgO and CaO compositions. The higher CaO olivines are shown as black diamonds, with the LCO depicted as green diamonds. The hollow grey symbols are all the available whole rock compositions determined for Lesser Antilles lavas from the islands from which olivines were analysed. The whole rock compositions of the host lavas from which the olivines analysed by LA-ICP-MS originated are shown as solid grey symbols with a black outline (Thirlwall, unpublished data).**

The CaO contents calculated for melt composition for both olivines populations in Figure 3-31 are lower than those measured in the whole rocks. There is one lone melt composition calculated from a higher CaO olivine that exhibits a similar CaO content to the whole rock analyses at 15.6 wt% MgO and 10.8 CaO. In particular it is noteworthy that the LCO show very low CaO melt compositions (0.83-4.62 wt% CaO).

MgO compositions for the calculated melts lie within range of those observed in the whole rock analyses, albeit with some of the host lavas exhibiting lower whole rock MgO contents than suggested by the calculated melt compositions.

The method used is fairly crude, in order for more accurate melt compositions to be derived, less porphyritic host lavas would be required. Aphyric samples with phenocryst olivine alone would permit the measurement of both olivine composition and a more homogenous groundmass composition to use in lieu of a homogenised whole rock composition to compare the calculated melt compositions to. An aphyric groundmass would be a much more suitable proxy for melt, not least because using the whole rock composition means that the calculated melt compositions are being

compared to a material which also contains olivine (and thus the CaO hosted by olivine). As Table 3-1 shows, some of the host lavas have high modal olivine proportions which would contribute significantly to their overall whole rock CaO concentrations.

The method does not take into account other phenocryst phases that may also be hosting olivine, such as clinopyroxene, which may have fractionated simultaneously with olivine. As a result, the parent melts may have had higher CaO concentrations but the CaO contained in other phases is not being considered.

### Estimated Partition Coefficients

Using a variation on Equation 3-11 (Equation 3-12), rough approximations of partition coefficients between the olivines and the whole rock compositions (as a crude proxy for melt compositions) can be calculated (Figure 3-32).

#### Equation 3-12

$$\sim K_D^{Ca} = \frac{[Ca]_{Olivine}}{[Ca]_{Whole\ Rock}}$$

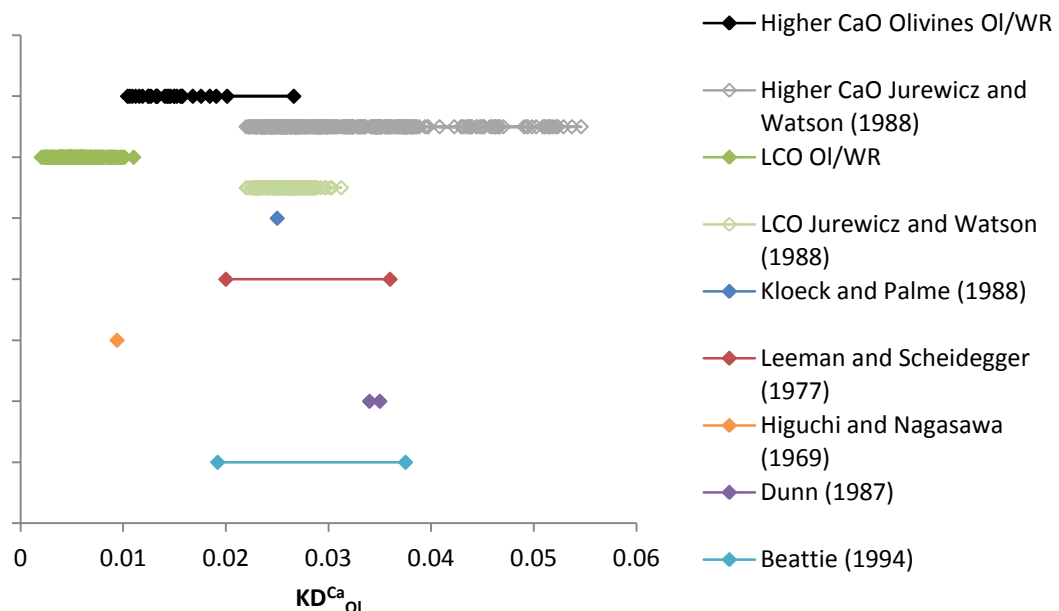


**Figure 3-32** Calculated approximations for partition coefficients for the analysed olivines using both the whole rock composition as a proxy for melt (solid symbols) and the calculation provided by Jurewicz and Watson (1988a) using forsterite content (hollow symbols). Also shown are published partition coefficients for Ca into olivine in basalts, taken from the GERM partition coefficient database (Beattie, 1994, Dunn, 1987, Higuchi & Nagasawa, 1969, Kloeck & Palme, 1988, Leeman & Scheidegger, 1977). The Dunn (1987) and Beattie (1994) partition

coefficients were derived experimentally whilst the remaining published coefficients are from phenocryst-matrix studies.

Figure 3-32 shows that the partition coefficients calculated from the Jurewicz and Watson (1988a) equation compare reasonably well with the published values, particularly at higher forsterite contents (lower  $K_D$  values). However, the published values are for basaltic compositions and several of the host lavas are basaltic andesites. This may partly explain why some of the lower forsterite olivines exhibit higher than expected  $K_{DS}$ .

Figure 3-32 is further evidence that using whole rock compositions as melt proxies for their mineral cargoes is unreliable. This is particularly evident when comparing the Jurewicz and Watson (1988a)  $K_D$  values for the LCO to the  $[Ca]_{Olivine}/[Ca]_{WR}$  ratios. The latter only overlap with one of the published values (that of Higuchi and Nagasawa, 1969).

In order to try and make the whole rock compositions represent the melt compositions better, calculations were performed to remove the CaO contributions from the olivines and also any plagioclase or clinopyroxene present. This was done using the modal proportions of these phases obtained from point counting (Table 2-3) and the average CaO content of each phase in the host lavas in Equation 3-13. Equation 3-13 shows the calculation for olivine, the calculation is the same for clinopyroxene and plagioclase using their respective modal proportions and average CaO contents. Given that the point counting data are an estimation of modal proportion and using an average concentration of CaO also introduces a source of error, this method is by no means perfect but should provide a better composition to ratio the olivine CaO concentrations to than that of the whole rock.

**Equation 3-13**

*WR CaO with Ol Removed*

$$= \frac{(WR\ CaO\ (Modal\ Proportion\ Ol \times Average\ Ol\ CaO))}{(1 - Modal\ Proportion\ Ol)}$$

The calculations were done on any host lava where all the phases present had been analysed, in the case of GU25, SV20, BQ19 and CA3 this was olivine, clinopyroxene and plagioclase and in the case of 468 and 6103 no plagioclase was present so only olivine and clinopyroxene were removed. The CaO concentrations of

the olivines were then ratioed to their respective recalculated whole rock compositions (Figure 3-33).

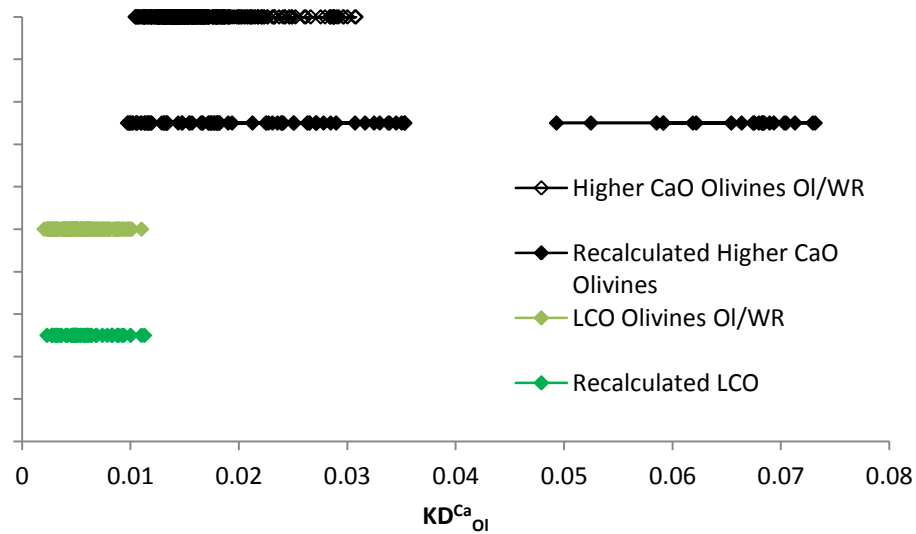


**Figure 3-33 Ratios of olivine CaO contents to recalculated whole rock CaO compositions after CaO held in olivine, clinopyroxene and plagioclase had been removed using Equation 3-13.**

Figure 3-33 shows little variation in the LCO approximate  $K_D$  values, however the higher CaO olivines show two distinct groups, one extending to much higher values than those using the original whole rock composition. The latter group are the olivines from BQ19, which has a high proportion of plagioclase (43.1%), thus removing this phase dramatically lowers the CaO concentration of the recalculated whole rock composition to 4 wt% CaO compared to the original 10.4 wt% CaO. This highlights another potential source of error in the method, the timing of the crystallisation of each phase. By removing all the phases it is assumed that the CaO held in each was not part of the melt co-existing with the olivines at the time of their formation. However, if the plagioclases crystallised after the olivines (as would be expected), this CaO would have been available as part of the melt when the olivines were being formed and thus would not need removing. Therefore without knowing when the clinopyroxenes and plagioclases crystallised relative to the olivines, it is hard to accurately constrain what to remove from the whole rock composition to best approximate a suitable melt composition. Given the varying sources of error with using both the whole rock composition and the recalculated whole rock compositions, the method of using a ratio of  $[x]_{\text{Olivine}}/[x]_{\text{WR}}$  was not pursued further for the olivines.

### 3.5.5 High Forsterite Olivines

Forsterite contents in some of the Lesser Antilles olivines are very high (up to Fo<sub>91</sub>). As seen in Figure 3-27, many of these high forsterite content olivines are not in equilibrium with their whole rock compositions, plotting in the potentially accumulative field. This suggests that the forsterite content of the equilibrium olivines based on the whole rock compositions are higher than those of the observed in the analysed olivines.

#### *Influence of Water and High Forsterite Olivines*

Given that the Lesser Antilles is an intra-oceanic subduction zone, it is highly likely that water will have had an effect on petrogenesis. Macdonald *et al.* (2000) and references therein provide information on estimated water contents in Lesser Antilles melts. Near primary basaltic melts are thought to have between 1-2 wt%, basaltic andesites 3% and silicic melts 5-6 wt% (Macdonald *et al.*, 2000). Feig *et al.* (2006) conducted crystallisation experiments over varying pressure and temperature conditions using four different water contents in a basaltic system. Their results showed that with increasing water contents, forsterite content of crystallising olivine increases (Figure 3-34), noting an increase of ~12 mol% at 1100°C and 200 MPa between dry and water saturated runs (Feig *et al.*, 2006).

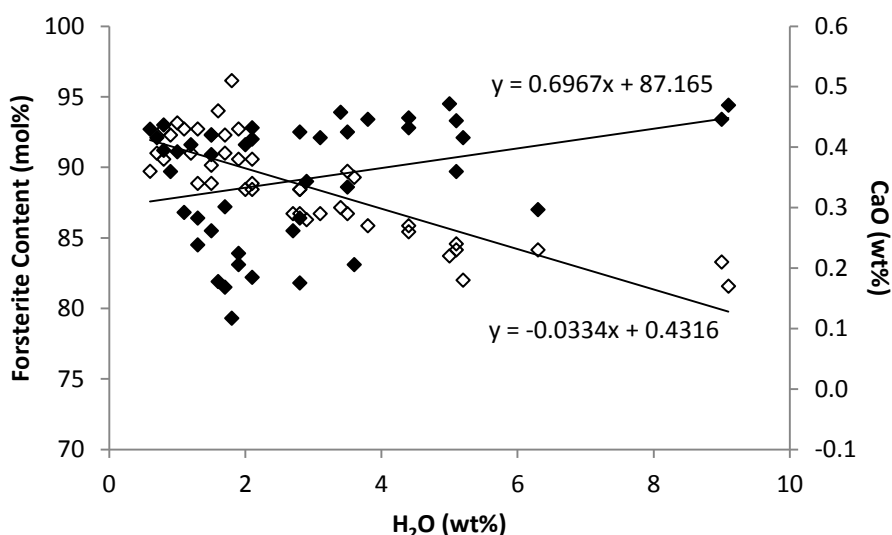


Figure 3-34 Forsterite contents (black diamonds) and CaO concentrations (hollow diamonds) in the Feig *et al.* (2006) olivines against melt water contents. The regression lines through each series show the increase in Fo contents and decrease in CaO concentrations as water content increases.

However, many of the olivines analysed by Feig et al. (2006) have high forsterite contents ( $>F_{090}$ ) even at low water contents ( $<1$  wt% melt  $H_2O$ ), although the trends are scattered.

Feig et al. (2006) suggest that part of the reasoning for increasing melt water contents resulting in higher forsterite olivines is the increase in melt fraction caused by the elevated water contents lowering the solidus. They also suggest increases in the  $Fe^{2+}/Mg$  ratio of the melt to be caused by increases in oxygen fugacity due to higher water contents, prompting more forsteritic olivine crystallisation (Feig *et al.*, 2006).

#### ***Overall Lower Calcium Contents in Lesser Antilles Olivines***

Figure 3-34 also shows that CaO contents decrease with increasing water contents. The CaO concentrations in the Lesser Antilles olivines range from 0.02 wt% to 0.32 wt% (although the LCO will be dealt with in a separate discussion). The higher CaO olivines show contents between 0.12 wt% to 0.32 wt%.

As a rough estimate of water contents, the regression through the Feig et al. (2006) olivines was used to calculate melt water contents based on the CaO concentrations in the analysed Lesser Antilles olivines (Figure 3-35).

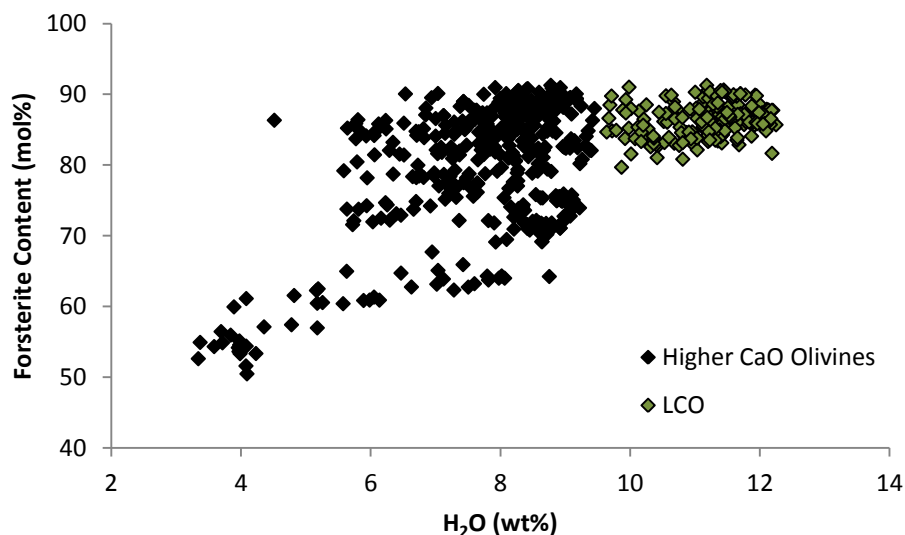


**Figure 3-35 Melt water contents based on the regression line through the Feig et al. (2006) olivines for the higher CaO and LCO analysed in Lesser Antilles host lavas. Both groups also show an increase in forsterite contents with increasing theoretical melt water contents.**

Figure 3-35 shows that the water contents calculated by using the Feig *et al.* (2006) regression are very high, particularly when compared to the published values (Macdonald *et al.*, 2000 and references therein). Thus it may be more sensible to view Figure 3-35 as a qualitative figure rather than quantitative, it implies that the LCO would require higher melt water contents than the higher CaO olivines.

Water contents in the Lesser Antilles melts undoubtedly play a role in the petrogenesis of the lavas. Melt water contents of at least 1 wt% for the arc lavas have been suggested previously (Macdonald *et al.*, 2000) and seem to provide at least a partial explanation as to the high forsterite contents and low calcium concentrations observed in the olivines. Water contents alone however do not provide a reasonable explanation for the bimodality in CaO seen as forsterite contents are similar between both populations and increased melt water contents for the LCO should prompt even higher Fo contents.

### **3.5.6 Forsterite Bimodality in GU25**

The HFG and LFG in GU25 are discrete populations, with a 9 mol% interval between the two groups. Petrographically, these groups could not be distinguished as the analysed thick section olivines all exhibited forsterite contents within the LFG bracket.

One possibility for explaining the discrepancy between the two groups is degassing of the melt. Degassing alters the volatile (including water content) of the melt. As seen within section 3.5.4, water content has been shown to have an effect on the forsterite content of crystallising olivines. If increased water contents promote crystallisation of higher forsterite content olivine (Feig *et al.*, 2006), degassing of the melt could then reduce Fo contents of olivines crystallising after degassing has occurred. This would appear to be the most likely solution for the forsterite bimodality apparent in the GU25 olivines. Pre-degassing crystallisation could have formed the HFG, with the LFG being crystallised after degassing had occurred (this could also explain the lack of transitional forsterite contents between the two that may be expected if the crystals were resident in the same host melt for a sufficient length of time). Lower CaO contents in the HFG appear to support this (Feig *et al.*, 2006). Additionally, one crystal from the LFG was analysed in thick section and

showed consistent forsterite contents between Fo<sub>71-72</sub> across the mineral, suggesting that the LFG do not have higher forsterite cores rimmed by lower forsterite material.

However, what is unclear is why this process would only affect one of the host lavas. Bimodality in forsterite contents is not seen in any of the other host lavas which were studied but degassing is not a rare process in the Lesser Antilles, as shown in Chapter 3 in the plagioclase textures.

### 3.5.7 $\delta^{18}\text{O}$ Discussion

#### *Fractional Crystallisation*

Removing crystal phases from the melt can affect the  $\delta^{18}\text{O}$  of the remaining melt (Davidson, 1985). Melt composition and temperature can also affect the fractionation factor between olivines and the melt, changing the  $\delta^{18}\text{O}$  value of olivines crystallising from a melt (Zhao & Zheng, 2003, Zheng, 1993, Zheng, 1999). However, it is thought that the fractionation factor increases as temperature decreases, meaning fractionation of oxygen isotopes is liable to be low at the temperatures that the host lavas were crystallised (Davidson *et al.*, 2005). Modelling was undertaken to observe if the increases in  $\delta^{18}\text{O}$  with decreasing forsterite contents could result from fractional crystallisation or to confirm that fractional crystallisation is not a suitable method of generating the observed trends. In order to do this, the whole rock composition of sample CA13 was used as a parent in a fractional crystallisation model. This composition was chosen as it is the most primitive of the host lavas from which olivines were analysed for oxygen. The assemblage removed was varied and included olivine  $\pm$  clinopyroxene  $\pm$  plagioclase  $\pm$  magnetite. Compositions of the minerals removed were those calculated to be in equilibrium with the whole rock compositions and varied accordingly as crystallisation progressed.

The changing whole rock compositions obtained were then used to calculate the  $\delta^{18}\text{O}$  of the olivines in equilibrium at each stage of the fractional crystallisation. The  $\delta^{18}\text{O}$  modelling followed the increment method outlined in the literature (Zhao & Zheng, 2003, Zheng, 1993, Zheng, 1999) and comprised the following basic steps:

- Calculating the oxygen isotope indices ( $I^{18}\text{O}$ ) of CA13 and the subsequent melt compositions produced by the fractional crystallisation model.
- Calculating the thermodynamic oxygen isotope factors ( $10^3\ln\beta$ ) of both the whole rocks and olivines (relative to quartz at a given temperature).
- Calculating the oxygen isotope fractionation factors ( $10^3\ln\alpha$ ) between the olivines and the whole rocks (also known as the  $\Delta$  parameter).

Chemical compositions were used in the modelling as opposed to CIPW normative minerals as the parents are volcanic rocks, in line with the recommendations of Zhao and Zheng (2003).

$I^{18}\text{O}_{\text{WR}}$  was calculated using Equation 3-14, where X is the mole fraction of oxygen in the mineral compared to the whole rock and  $I^{18}\text{O}$  is as given in Zhao and Zheng (2003).

**Equation 3-14**

$$I^{18}\text{O}_{\text{WR}} = \sum X_{\text{oxide}} \times I^{18}\text{O}_{\text{oxide}}$$

The  $10^3\ln\beta$  of quartz (used as a reference material) was then calculated at the temperature required (Equation 3-15). A temperature of 780°C (1053K) was used (Labanieh *et al.*, 2012).

**Equation 3-15**

$$10^3\ln\beta_{\text{quartz}} = 11.83 \times 10^6 / T^2$$

The  $10^3\ln\beta$  of the whole rock compositions were then calculated using Equation 3-16.

**Equation 3-16**

$$10^3\ln\beta_{\text{WR}} = I^{18}\text{O}_{\text{WR}} \times 10^3\ln\beta_{\text{quartz}}$$

The  $10^3\ln\beta$  values for the olivines were calculated after first calculating the oxygen isotope index of the mineral (Equation 3-17) before calculating the thermodynamic oxygen factors for the olivines (Equation 3-18). The  $I^{18}\text{O}$  for forsterite and fayalite were obtained from Zheng (1993) and Zheng (1999).

**Equation 3-17**

$$I^{-18} O_{olivine} = ((Fo/100) \times I^{-18} O_{Fo}) + ((1 - (Fo/100)) \times I^{-18} O_{Fa})$$

**Equation 3-18**

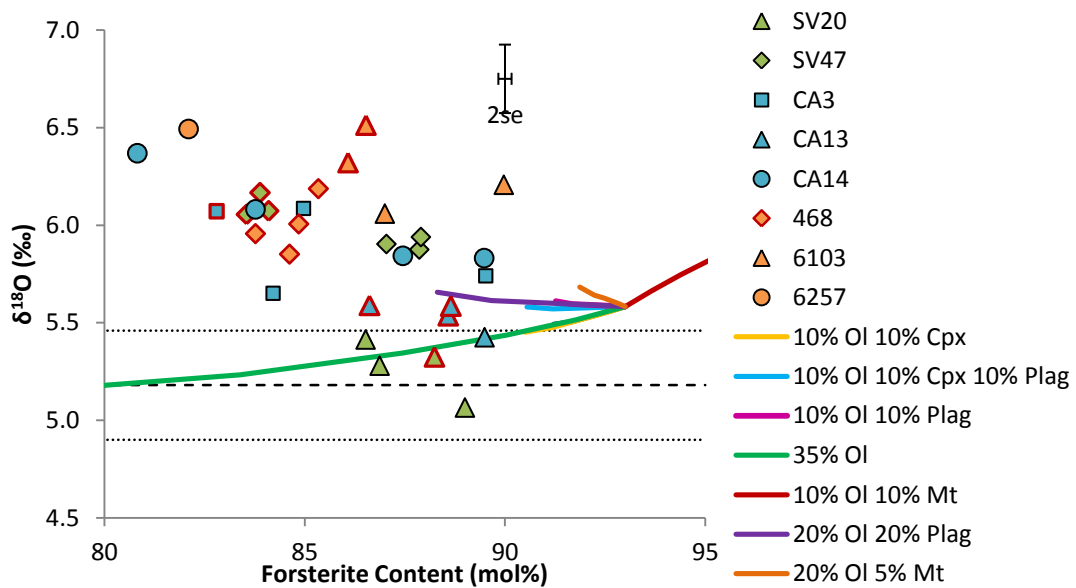
$$10^3 \ln \beta_{olivine} = I^{-18} O_{olivine} \times 10^3 \ln \beta_{quartz}$$

The fractionation factor between the whole rock and the crystallising olivines was calculated using Equation 3-19.

**Equation 3-19**

$$10^3 \ln \alpha_{olivine-WR} = 10^3 \ln \beta_{olivine} - 10^3 \ln \beta_{WR}$$

The fractionation factor was then applied to a whole rock value of 5.93‰ (equal to the  $\delta^{18}O$  of the most primitive olivine from CA13 plus 0.5‰ to convert this value to a rough whole rock  $\delta^{18}O$ ) to investigate how  $\delta^{18}O$  of olivine in equilibrium with the modelled melt compositions varies with fractionation. The results are shown in Figure 3-36.



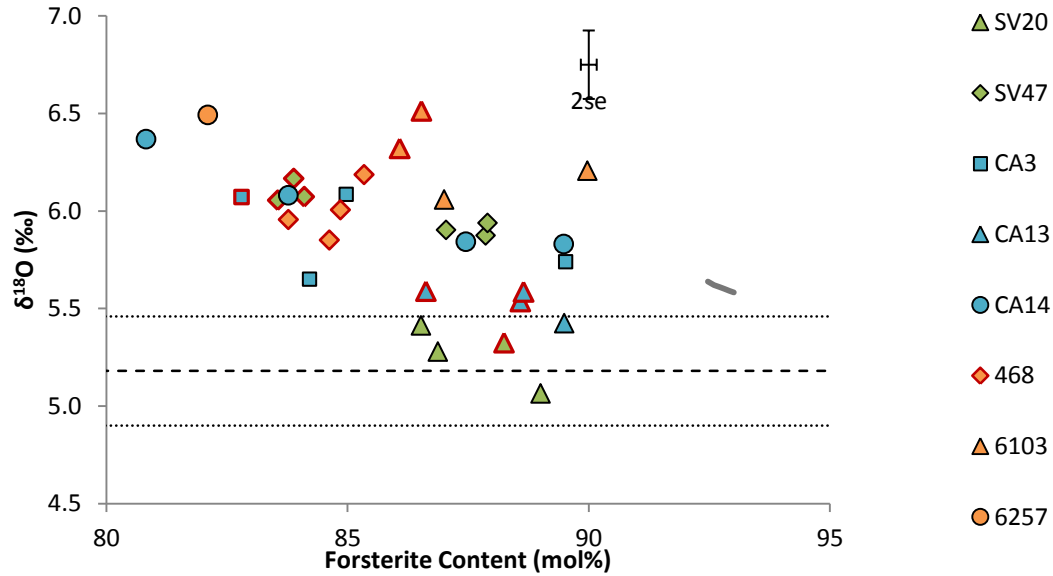
**Figure 3-36 Modelled changes in olivine  $\delta^{18}O$  with decreasing forsterite content of the olivines as a result of fractional crystallisation. The coloured lines represent fractional crystallisation of assemblages as shown in the legend. The LCO are outlined in red.**

Figure 3-36 shows that fractionating olivine alone will not increase the  $\delta^{18}O$  of olivines crystallising at a lower forsterite content. Clinopyroxene also has very little effect on  $\delta^{18}O$ . However, both plagioclase and magnetite are capable of increasing the  $\delta^{18}O$  of olivine. Equal amounts of magnetite and olivine is not a suitable assemblage as this increases forsterite content as well as  $\delta^{18}O$ . Adding a smaller

volume of magnetite than olivine produces a more suitable trend. The main issue with magnetite fractionation is that this is unlikely to occur until the whole rock composition has an MgO content of around 5 wt%. At MgO contents as low as this, using the partition coefficients of Roeder and Emslie (1970), the forsterite contents of any equilibrium olivine crystallising should be at a maximum of Fo<sub>72</sub>. The olivines analysed during the study show increasing  $\delta^{18}\text{O}$  contents with decreasing forsterite content at forsterite contents over Fo<sub>72</sub>, suggesting that magnetite should not be fractionating simultaneously.

The trend produced by fractionating equal amounts of olivine and plagioclase ( $\pm$  clinopyroxene) could explain the negative correlation between  $\delta^{18}\text{O}$  and forsterite content. When compared to the point counting data however, six of the host lavas analysed for  $\delta^{18}\text{O}$  have less than 3.5% plagioclase (CA3, CA13, CA14, 468, 6103 and SV47). In particular, CA3, CA13, 468, 6103 and SV47 exhibit less than 1% plagioclase in thin section. It therefore seems unlikely that plagioclase crystallisation should have a substantial effect on  $\delta^{18}\text{O}$ . Potentially if plagioclase were fractionating and settling out of the melt (and thus not being erupted) this could account for the  $\delta^{18}\text{O}$  variation but this does not seem likely.

In order to further test the theory that fractional crystallisation could have affected the  $\delta^{18}\text{O}$  of the olivines analysed, the average mineral assemblage calculated from least squares fractional crystallisation modelling (Chapter 2) was removed from the approximate CA13 whole rock  $\delta^{18}\text{O}$  composition (Figure 3-37). The average mineral assemblage comprised 6% olivine, 5% clinopyroxene, 5% plagioclase and 1% magnetite. Ideally this modelling would have been done in stages, with different assemblages being removed from the respective whole rock compositions used in the fractional crystallisation modelling with decreasing MgO. However, not all of the whole rocks used in the model had olivines analysed for  $\delta^{18}\text{O}$  which could be converted to an approximate whole rock composition. The model only holds for increments between parent and daughter compositions up to 4 wt% MgO and not all the whole rocks with olivines analysed for  $\delta^{18}\text{O}$  were within this range of each other.



**Figure 3-37 Changes in olivine  $\delta^{18}\text{O}$  when the average mineral assemblage calculated during least squares fractional crystallisation modelling is removed from the CA13 whole rock  $\delta^{18}\text{O}$ . This trend is shown by a grey line.**

Despite the limitations of using an average composition, it can be seen that the assemblage of minerals crystallising in the Lesser Antilles whole rocks produces a very small change in  $\delta^{18}\text{O}$  that does not explain the changes observed in the Lesser Antilles olivines.

Davidson (1985) analysed whole rock  $\delta^{18}\text{O}$  from several islands in the Lesser Antilles (St. Kitts, Redonda, Martinique and St. Lucia). The author concluded that the wide ranges in  $\delta^{18}\text{O}$  observed (+5.8‰ to +11.5‰) could not be satisfactorily explained solely by fractional crystallisation. Whilst the range in the olivine  $\delta^{18}\text{O}$  is not as large (being +5.07‰ to +7.37‰), it would appear that fractional crystallisation is not a suitable method of generating the trend between  $\delta^{18}\text{O}$  and forsterite content, in agreement with Davison (1985).

The fractionation factors between the olivines and the whole rocks were calculated using the same method, but changing the parent composition to the host rock of each respective crystal, so CA3 crystals used the whole rock composition of CA3 as the parent, SV47 crystals used the whole rock composition of SV47 etc. This allowed the calculation of the whole rock  $\delta^{18}\text{O}$  from the  $\delta^{18}\text{O}$  of the olivines, to observe changes in the whole rock  $\delta^{18}\text{O}$  with crystallisation. This method also showed varying increases in  $\delta^{18}\text{O}_{\text{WR}}$  with decreasing forsterite content of the olivines (Figure 3-38).

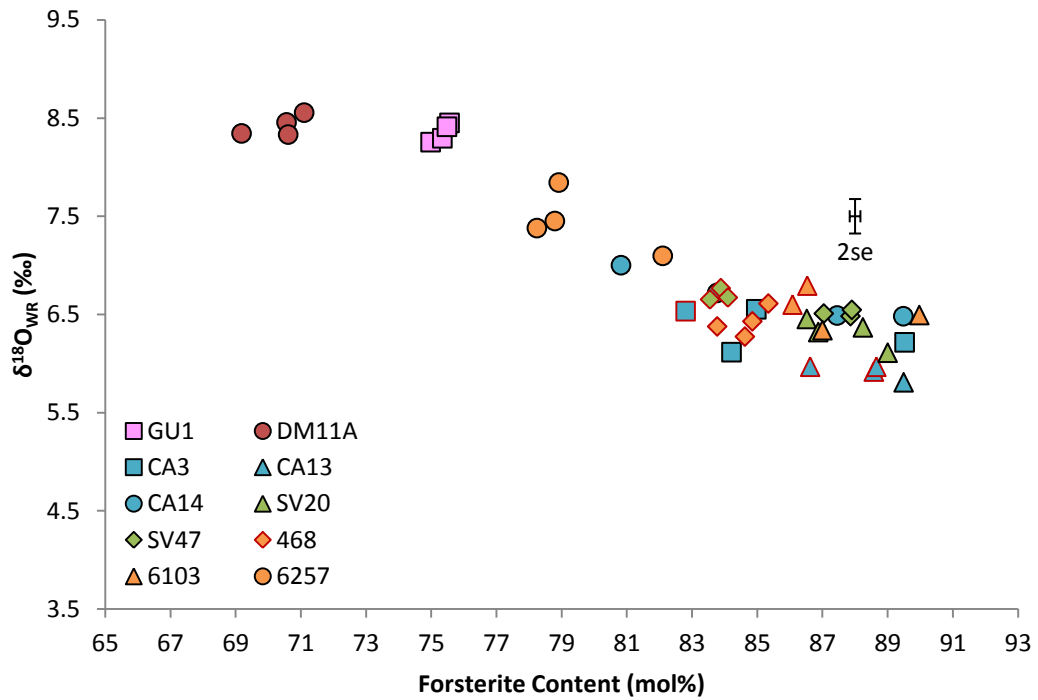


**Figure 3-38** Variation in whole rock  $\delta^{18}\text{O}$  calculated from the  $\delta^{18}\text{O}$  of the respective olivine phenocrysts.

### *Sediment*

Sediment addition has been shown to increase the  $\delta^{18}\text{O}$  of melts (e.g. James, 1981). Modelling was utilised to ascertain if adding sediments to the DMM composition of Workman and Hart (2005) could produce an increase in  $\delta^{18}\text{O}$  in the olivines in equilibrium with the new melt compositions and whether the trend seen in the analysed olivines could be replicated (Figure 3-39). Sediment compositions used were those provided by Carpentier et al. (2009).

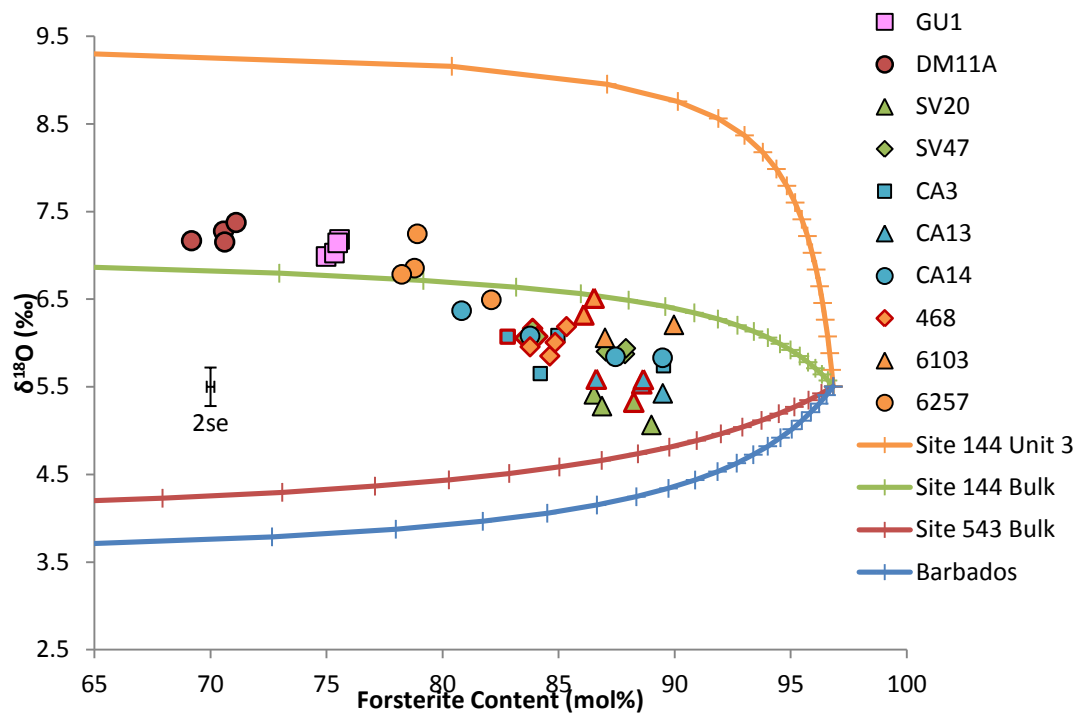


**Figure 3-39** Results of adding sediment compositions from Carpentier *et al.* (2009) to the DMM composition of Workman and Hart (2005) using the increment method. Unit 3 from Site 144 is a black shale unit which has been suggested to be responsible for anomalous Pb isotopic results for the Lesser Antilles in the literature (Carpentier *et al.*, 2008, Carpentier *et al.*, 2009). Tick marks show 5% increments. Red outlines are around the LCO.

Figure 3-39 shows that whilst adding sediment from Site 144 can increase the  $\delta^{18}\text{O}$  of olivines crystallising from the melt, the shape of the modelled curve still does not show the same trajectory as that observed. Furthermore, the volume of sediment required to approach the compositions of the olivines is unrealistically high and would have an overwhelming effect on the Sr, Nd and Pb isotope compositions of the whole rocks, which is not observed. Adding sediment from Site 543 and Barbados either causes olivine  $\delta^{18}\text{O}$  to decrease with decreasing forsterite content of the hypothetical equilibrium olivine. Thus it would appear that adding these particular sediments to the host melts is not a suitable mechanism for generating the negative correlation.

The olivine  $\delta^{18}\text{O}$  was then plotted against the whole rock  $^{87}\text{Sr}/^{86}\text{Sr}$  ratio for each host lava (Figure 3-40). James (1981) suggested that the shape of mixing curves between a mantle endmember and sediments on this type of graph can indicate if the sediment is being added at source or is the result of crustal contamination. Concave trends are thought to represent sediment addition to the source, with convex trends reflecting later stage crustal contamination. However, one caveat of this method is that the

curves are largely determined by the concentration of Sr in the source. Higher Sr contents in the source compared to the sediment leads to convex curves, lower Sr concentrations in the source prompt concave trends. If the source is a peridotite, it is likely to have very low Sr concentrations, thus the material being added will almost always have higher Sr contents. Figure 3-40 shows that the central island olivines (from GU1 and DM11A) are within error of mixing between the Davidson (1985) mantle endmember and the subducted sediment composition of Thirlwall et al. (1996).

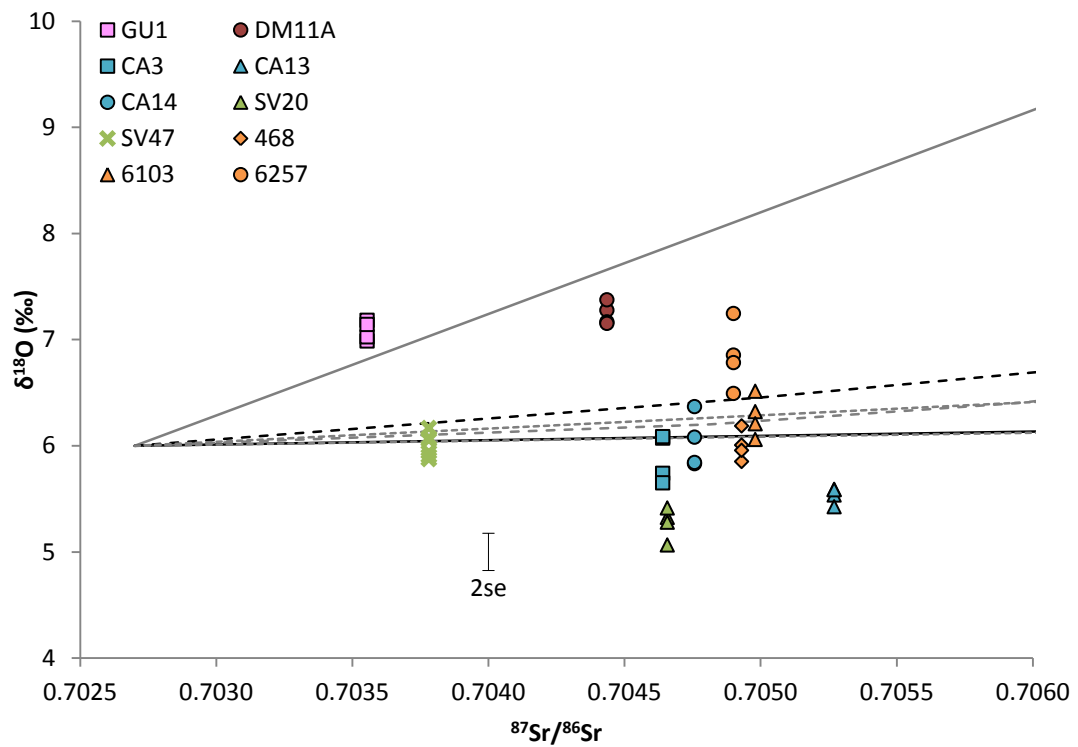
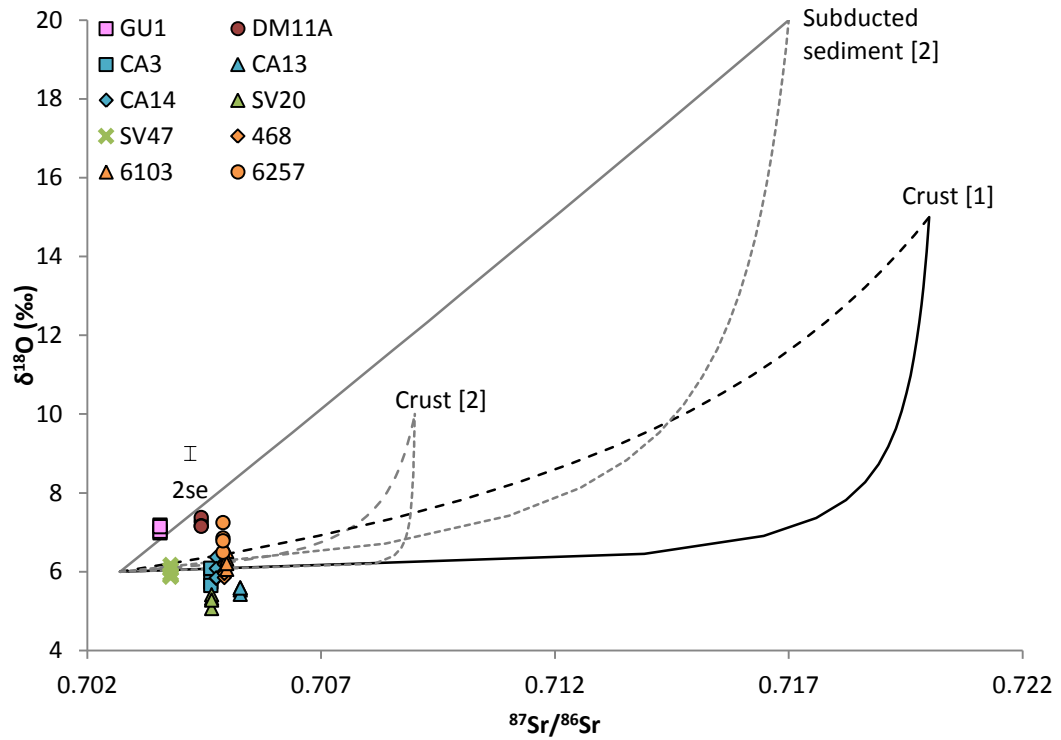


Figure 3-40 Variations in olivine  $\delta^{18}\text{O}$  with subducted sediment and crust addition. Solid lines represent mixing with the Davidson (1985) mantle endmember, dashed lines represent mixing with the Davidson (1985) MORB endmember. Crust composition [1] also from Davidson (1985), [2] subducted sediment and crust compositions from Thirlwall et al. (1996). Lower graph is a close up of the upper graph.

However, olivines from the remaining host lavas (with the exception of those from CA13 and SV20) are in error of MORB mixing with both the subducted sediment and crustal compositions as well as the mantle endmember mixing with both crustal compositions. It is therefore hard to distinguish what mixing is occurring, particularly as less than 5% of any sediment or crust is being added to the source.

Adding the subducted sediment composition of Thirlwall et al. (1996) to the Davidson (1985) mantle endmember may be a valid explanation for the high  $\delta^{18}\text{O}$  values observed in the Guadeloupe and Dominica olivines. However, whole rock  $^{87}\text{Sr}/^{86}\text{Sr}$  ratios have been used in the modelling, meaning that all the  $\delta^{18}\text{O}$  values from individual host lavas plot at the same values on the x axis, which is clearly a limitation of using this technique.

Similar modelling was undertaken by Davidson (1985) using whole rock isotopic compositions from Statia, St. Kitts and Redonda in the north of the Lesser Antilles and Martinique and St. Lucia in the centre of the arc. The author concluded that fractional crystallisation was not a suitable method of generating the correlations observed between  $\delta^{18}\text{O}$  and  $^{87}\text{Sr}/^{86}\text{Sr}$  ratios. Instead, Davidson (1985) favoured contamination, proposed to be between a MORB source and sediments in the form of continental cratonic material. However, in contrast to the data from this study, the author found that entrainment of the contaminant occurred as melts were ascending.

### *Fluid*

Bouvier et al. (2008) analysed  $\delta^{18}\text{O}$  contents in melt inclusions hosted in olivine in St. Vincent basalts. The latter study also utilised SIMS analysis, in contrast to that of Davidson and Wilson (2011). Bouvier et al. (2008) found a wide range in  $\delta^{18}\text{O}$  contents of 3.2-10.1‰. This is a much larger range than observed in Figure 3-26. Bouvier et al. (2008) suggested a three stage contamination of the source was necessary to explain the compositions of the varying types of melt inclusions they observed. The authors suggested that variable fluid enrichment of the source resulted in differing parental magma compositions, resulting in a wide range in olivine  $\delta^{18}\text{O}$ . The three contaminant fluids were thought to be a seawater like fluid, a fluid formed as a result of the dehydration of altered oceanic crust and a fluid produced by the dehydration of terrigenous sediments (with Bouvier et al., 2008 advocating the involvement of the black shales described by Carpentier et al., 2008).

The olivine data procured during this study does not show such extensive ranges within islands. Even though olivines were analysed rather than melt inclusions, olivines originating from the same host lavas show good consistency in  $\delta^{18}\text{O}$  (with most olivines lying in error of others from the same lava) which does not suggest that such extensive modification of  $\delta^{18}\text{O}$  values has occurred as postulated by Bouvier et al. (2008).

Li/Yb ratios were used as an indicator of fluid (with Li being a fluid mobile element and Yb being a fluid immobile HREE) (Figure 3-41). There is no obvious correlation between  $\delta^{18}\text{O}$  and Li/Yb ratio. GU1 and DM11A exhibit the highest  $\delta^{18}\text{O}$  contents but exhibit amongst the lowest Li/Yb ratios. Conversely, the olivines with the highest Li/Yb ratios (>400) exhibit intermediate  $\delta^{18}\text{O}$  contents of 6.17-6.51‰.

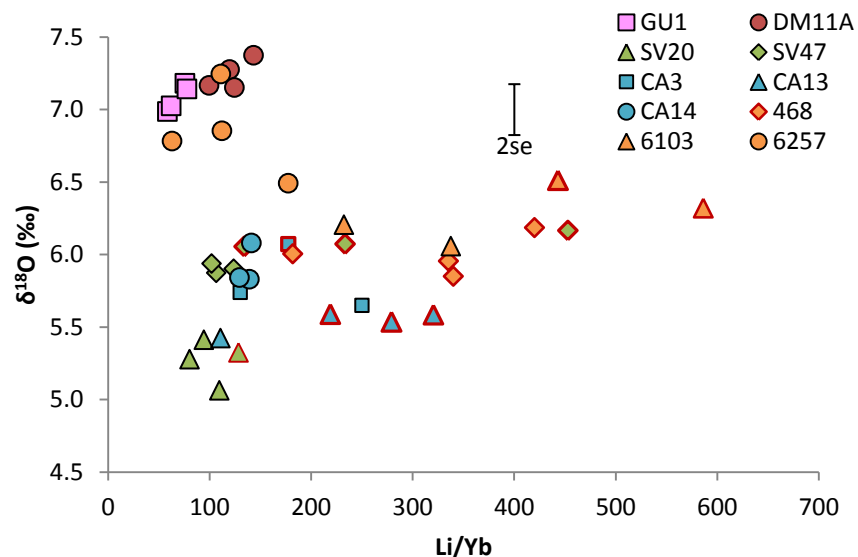


**Figure 3-41  $\delta^{18}\text{O}$  compared to Li/Yb ratios in the olivines. The LCO are outlined in red.**

It is possible that fluid has had an effect on the  $\delta^{18}\text{O}$  contents measured. However, without further accompanying trace element data (such as La, Sm, B, S, F and Cl, as analysed by Bouvier et al., 2008) it is hard to establish if there is a relationship between fluid mobile elements and  $\delta^{18}\text{O}$ . Ba concentrations in the olivines are available but are close to detection limits of the LA-ICP-MS and as such have large 2se.

### $\delta^{18}\text{O}$ in the LCO

Two of the main reasons for analysing  $\delta^{18}\text{O}$  in the olivines were to investigate whether the LCO had a) a different source to the normal calcium olivines and b) whether the LCO had  $\delta^{18}\text{O}$  contents that would support their being mantle xenocrysts. Figure 3-42 shows that there is no discernible difference between the  $\delta^{18}\text{O}$  of the LCO and the normal calcium olivines. Therefore if the LCO do have a different source, it is isotopically similar in terms of oxygen isotope ratios. In addition, as observed in Figure 3-26, most of the LCO do not show  $\delta^{18}\text{O}$  contents low enough to be classified as mantle values.

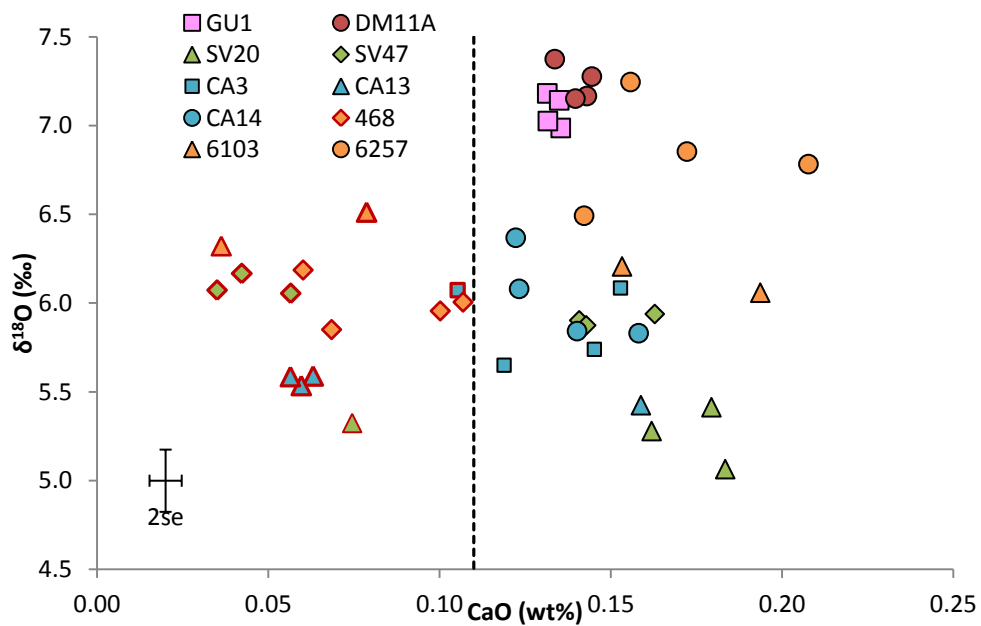


**Figure 3-42**  $\delta^{18}\text{O}$  contents plotted against CaO concentrations in the olivines. The LCO are outlined in red, with the dashed line representing 0.11 wt% CaO (the upper limit of the LCO).

Diffusion may represent a mechanism of increasing the  $\delta^{18}\text{O}$  of the LCO above mantle values, if they were resident in the host lava for a significant period of time. However, oxygen has been shown to diffuse slowly in olivine, especially when compared to Fe-Mg (Chakraborty, 2010, Farver, 2010). In addition, the LCO in both SV47 and 6103 show higher  $\delta^{18}\text{O}$  contents than their coexisting higher calcium counterparts, suggesting diffusion is not a likely resolution and that there is insufficient isotopic evidence to support the theory that the LCO are mantle xenocrysts.

### *$\delta^{18}\text{O}$ Conclusions*

The modelling suggests that fractional crystallisation, sediment addition or fluid addition in isolation are not suitable methods of replicating the observed trend between forsterite content and  $\delta^{18}\text{O}$ .

If the trend is at least in part a result of the limitations with the IMF correction, it is difficult to accurately constrain the effect of any of these processes on olivine  $\delta^{18}\text{O}$  when compared to forsterite content. Removing the IMF correction from the data results in values of +4.83‰ to +6.13‰, in contrast to +5.07‰ to +7.37‰ with it applied, which is a significant change. Whilst a correction for instrumental mass fractionation is certainly required, without knowing how accurate this correction is, quantitative modelling is challenging.

Assuming the trend is real, it would appear that the  $\delta^{18}\text{O}$  values observed in the olivines could be generated by addition of sediment and/or crustal material to the mantle source. However, Davidson (1985) proposed that little geophysical evidence is present for continental crustal material in the basement of the Lesser Antilles. Fractional crystallisation may have an effect on the  $\delta^{18}\text{O}$  contents of the olivines but is not solely responsible for generating the trend. Fluid addition may also play a role. If GU1 and DM11A are discounted there is a trend of increasing  $\delta^{18}\text{O}$  with increasing Li/Yb. However constraining the chemical compositions of potentially suitable fluids requires knowledge of more parameters than just  $\delta^{18}\text{O}$ .

### **3.5.8 Low Calcium Olivines**

Low calcium olivines have been noted in arc settings previously, for example in work by Elburg et al. (2006a), Elburg et al. (2006b) and Kamenetsky et al. (2006). None of these works provide a suitable solution to their petrogenesis however. This is particularly true of the LCO in the Lesser Antilles as they appear in the same host lavas as higher CaO olivines.

The low calcium olivines (LCO) originate from a different source to that of the normal CaO olivines, as is evident from their differing trace element compositions at a given forsterite content. This discussion examines the possibility of their being mantle xenocrysts, disaggregated from cumulate bodies or a result of melting of a different source and what this source could be.

### Mantle Xenocrysts

Published mantle olivine xenocryst data such as De Hoog et al. (2010) and Hirano et al. (2004) show that mantle olivine can exhibit sufficiently low CaO contents so as to be comparable with the LCO, which have a range in CaO contents of 0.02-0.11 wt% (Figure 3-43).

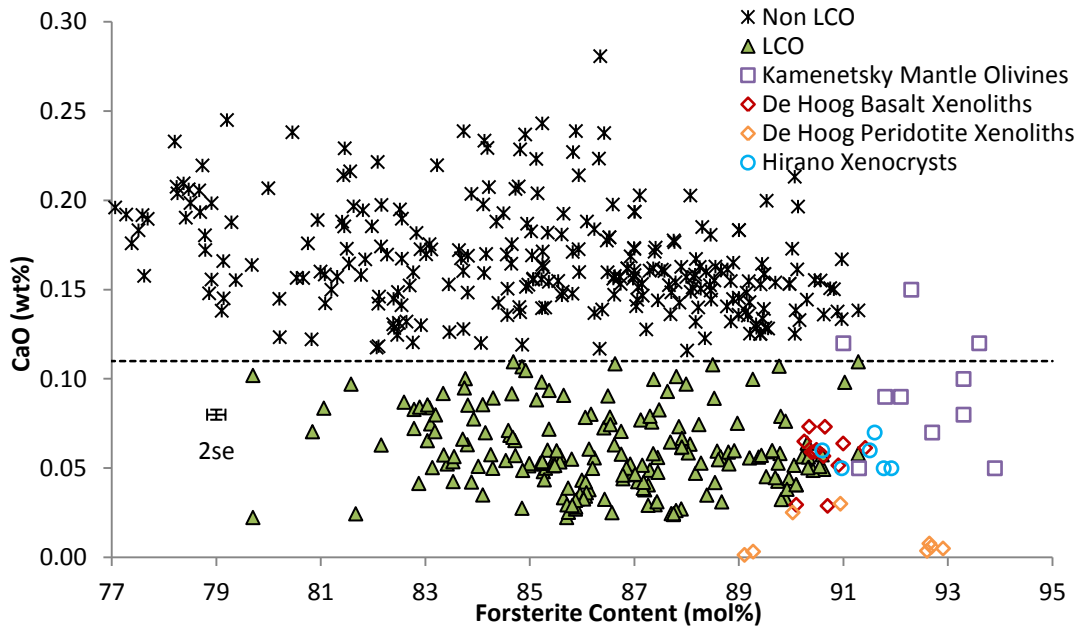


**Figure 3-43** CaO contents and forsterite contents of the LCO and the higher CaO Lesser Antilles olivines compared to mantle olivine data from Kamenetsky et al. (2006), De Hoog et al. (2010) and Hirano et al. (2004). The dashed line represents a CaO content of 0.11 wt%.

Hirano et al. (2004) reported olivine xenocrysts from alkali basalts dredged from the north of the Japan Trench, occurring concurrently with groundmass olivine. CaO contents in the xenocrystal olivine are 0.05-0.07 wt% (at Fo<sub>91-92</sub>), covering part of the LCO CaO concentration range, but at a higher forsterite content than the LCO (Fo<sub>80-91</sub>). De Hoog et al. (2010) presented data from a range of mantle olivines from xenoliths from basalts and orogenic peridotites, the olivines originating from a variety of peridotite compositions; garnet harzburgites, garnet lherzolites, spinel lherzolites and spinel garnet lherzolites. The LCO CaO contents are most comparable to the spinel lherzolites (Figure 3-43), which have CaO contents of 0.001 to 0.073 wt% (at Fo<sub>89-91</sub>), with the remaining De Hoog et al. (2010) lithologies all having CaO contents of less than 0.01 wt%. CaO contents of the LCO would suggest that they could plausibly be mantle xenocrysts entrained in the host magma (which was then responsible for crystallising the remaining higher CaO Lesser Antilles olivines); a scenario proposed by Hirano et al. (2004) as a suitable mechanism for

their findings of groundmass olivines juxtaposed with megacryst xenocryst olivines of a different chemical composition (groundmass olivines  $FO_{81-88}$ ,  $CaO >0.10$  wt%; xenocryst olivines  $FO_{91-92}$ ,  $CaO <0.08$  wt%).

Although CaO contents in the LCO and mantle olivines are comparable, Cr concentrations in the LCO are less convincing. De Hoog et al. (2010) provide Cr data for their olivines (Hirano et al. (2004) do not), the spinel lherzolites of De Hoog et al. (2010) show a range in Cr concentrations of 9 to 120 ppm, but Cr concentrations in the mantle olivines appear slightly too high for the majority of the LCO at a given CaO content (Figure 3-44). This suggests that the melt from which the LCO were derived had a lower Cr concentration than the spinel lherzolites and that the LCO may not be mantle xenocrysts. This is compounded by the  $Al_2O_3$  data for the LCO. Figure 3-45 shows CaO and  $Al_2O_3$  contents in the LCO and the De Hoog et al. (2010) mantle olivines; the LCO have lower  $Al_2O_3$  at a given CaO content by up to 0.06 wt%  $Al_2O_3$  (LCO  $Al_2O_3$  0.004 to 0.016 wt% and De Hoog et al. (2010) spinel lherzolite olivine  $Al_2O_3$  0.001 to 0.031 wt%).

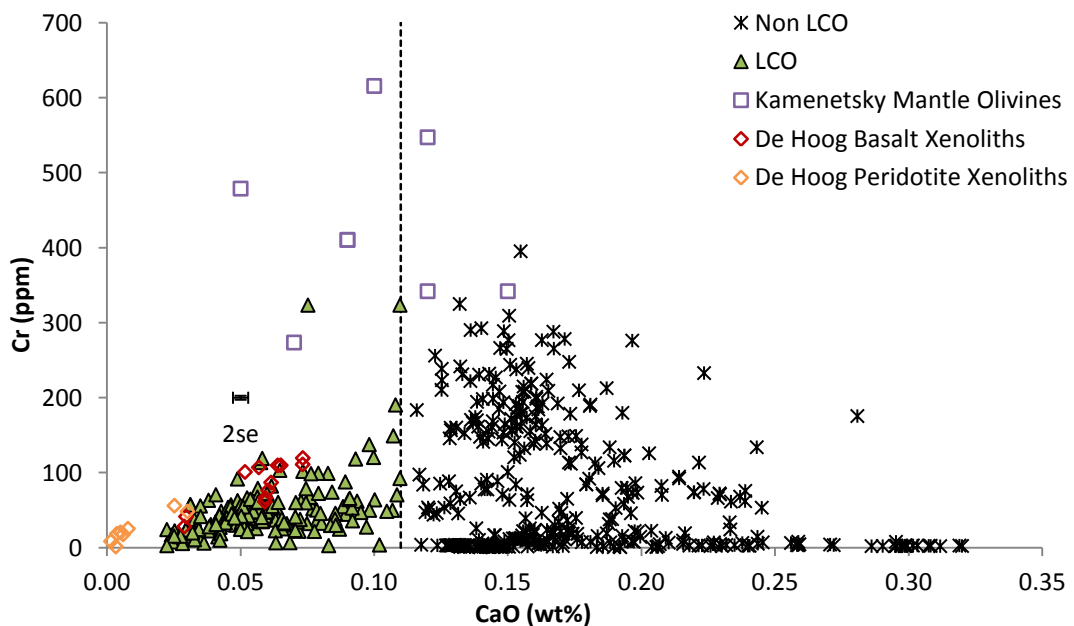
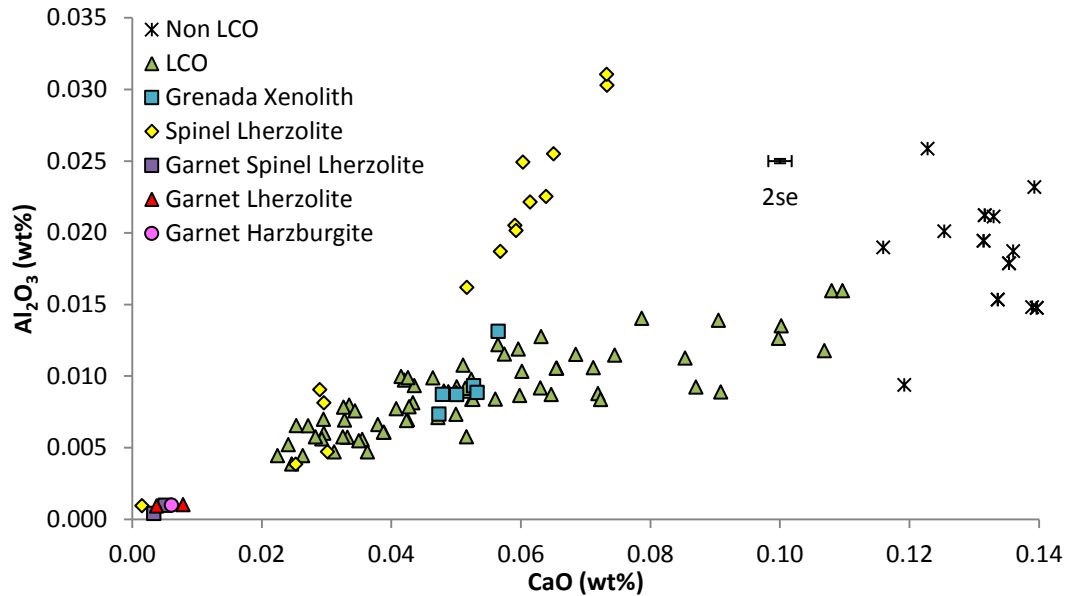


Figure 3-44 Cr concentrations and CaO contents of the LCO and mantle olivine data.



**Figure 3-45** CaO and Al<sub>2</sub>O<sub>3</sub> contents of the LCO, the non-LCO and the De Hoog et al. (2010) mantle xenolith olivines.

The most compelling evidence against the LCO being mantle xenocrysts is their forsterite contents. Mantle olivine has been suggested to have an average forsterite content of 90 mol% (Sato, 1977), with the Hirano et al. (2004) xenocryst olivines and the De Hoog et al. (2010) spinel lherzolite olivines having forsterite ranges of Fo<sub>91-94</sub> and Fo<sub>89-91</sub> respectively. In contrast, the LCO have forsterite contents of Fo<sub>80-91</sub>. Whilst the high forsterite values seen are unusual for an arc setting, many of the LCO do not have forsterite contents high enough to suggest a mantle source, with an average of Fo<sub>86</sub>.

Parkinson et al. (2003) reported a series of 13 peridotites xenoliths from Grenada, including harzburgites and dunites. Lherzolites are also present in alkali olivine basalts in Grenada but mainly represent reacted harzburgites (Parkinson *et al.*, 2003). Several of the xenoliths show varying degrees of interaction with the host magma. The Parkinson et al. (2003) olivines show forsterite contents of Fo<sub>88-92</sub>, but, in contrast to the De Hoog et al. (2010) and Hirano et al. (2004) mantle olivines, some olivines (associated with reacted orthopyroxene) from one xenolith showing extensive reaction with the surrounding melt (G11) show a range in forsterite contents of Fo<sub>80-83</sub> (Figure 3-46).

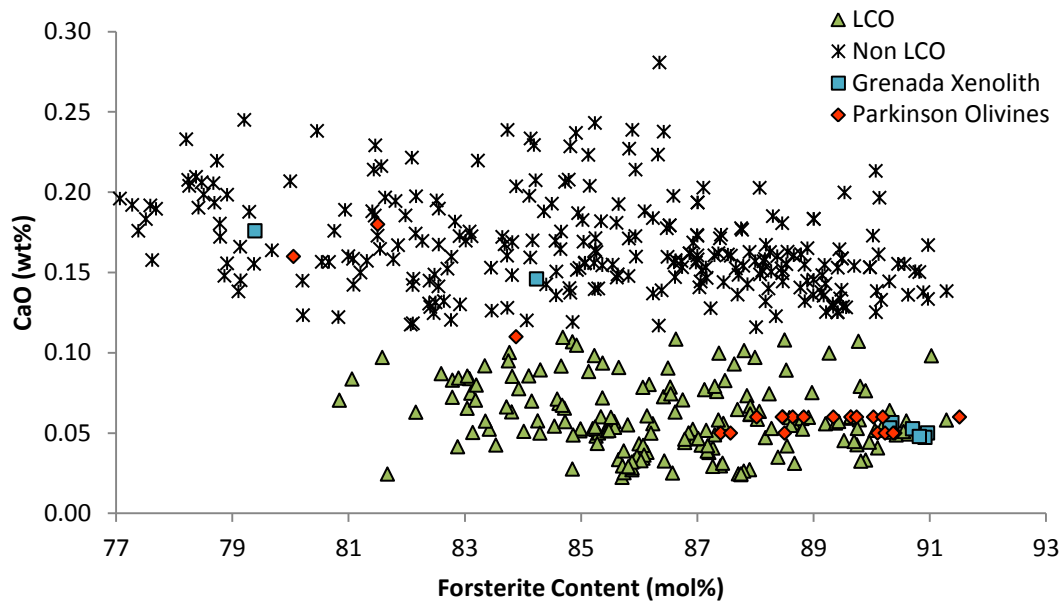


**Figure 3-46** CaO and forsterite contents of the Parkinson et al. (2003) olivines compared to the LCO, showing the lower forsterite olivines of Parkinson et al. (2003) having higher CaO contents more comparable to those in the non-LCO.

This forsterite range is comparable with the lowest values of the range exhibited by the LCO (Fo<sub>80-91</sub>), although the xenolith olivines only occupy a total range of 3 mol% forsterite compared to the 11 mol% shown by the LCO. Parkinson et al. (2003) show that these lower forsterite olivines exhibit higher CaO contents than those from olivines with higher forsterite contents (0.11 to 0.18 wt% at Fo<sub>80-83</sub> compared to <0.05 wt% at Fo<sub>88-92</sub>). Therefore it could appear plausible that the range in both forsterite contents and the continuum in CaO observed in the LCO may be a representation of increasing degrees of interaction between the LCO crystals and their host melts. Unfortunately, Parkinson et al. (2003) do not provide data for Al<sub>2</sub>O<sub>3</sub>, Cr, Sc, Y or Yb so the other defining chemical characteristics of the LCO cannot be assessed in their xenoliths.

Diffusion could provide an explanation as to why the LCO exhibit lower forsterite contents. Hirano et al. (2004) noted that their xenocryst olivines were surrounded by reaction rims (around 0.1 mm) showing increasing CaO and ‘infrequently’ decreasing forsterite contents towards the margin of the crystal, suggesting interaction between the xenocrysts and the host melt. If the LCO are mantle xenocrysts and were diffusion to have affected them, it is possible that the forsterite contents in the LCO could have begun to re-equilibrate with the surrounding melt. The low CaO and Cr signatures could have been preserved as these elements have

been shown to diffuse through olivines more slowly than Mg and Fe (Coogan *et al.*, 2005, Jurewicz & Watson, 1988b, Petry *et al.*, 2004) and Ca to diffuse more slowly than trace elements such as Ni (Chakraborty, 2010, Dohmen *et al.*, 2007, Petry *et al.*, 2004). Coogan *et al.* (2005) report diffusion coefficients around 1 order of magnitude lower for Ca than Fe and Mg in olivines at a temperature of 900°C and an  $fO_2$  of  $10^{-12}$  bar. This is consistent with our findings of lower CaO in the cores of the LCO. However, residence in a lower Mg/Fe melt over a significant period of time may result in homogenisation of the forsterite contents of the LCO and produce a narrow range in equilibrium with the host melt. The range in forsterite contents is much larger in the LCO (11 mol%) than the Hirano *et al.* (2004) mantle xenocrysts (3 mol%), the Parkinson *et al.* (2003) mantle olivines (3 mol%) or the De Hoog *et al.* (2010) spinel lherzolite olivines (2 mol%). Whilst Hirano *et al.* (2004) noted a range in forsterite contents of Fo<sub>81-91</sub> in the reaction rims of the crystals, the centres of the megacryst mantle olivines, where the CaO contents are lowest, were shown to be much more homogenous (Fo<sub>91-92</sub>). The cores of the xenocrysts described by Hirano *et al.* (2004) also show elevated NiO contents compared to the groundmass olivines, whereas the LCO do not show anomalously higher NiO concentrations compared to the higher CaO olivines (Figure 3-47).

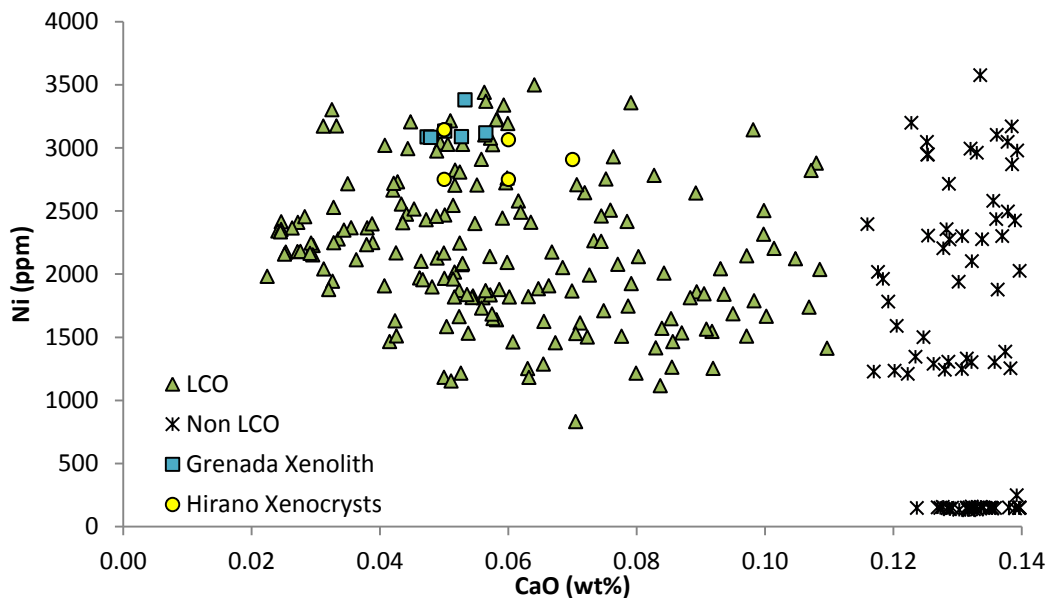


**Figure 3-47 Ni and CaO concentrations in the Hirano *et al.* (2004) mantle xenocryst olivines compared to the LCO. The Hirano *et al.* (2004) olivines show higher Ni contents at a given CaO content than many of the LCO.**

Ablation spots across several larger olivine crystals in a thick section of CA13 (from Carriacou) show little difference between the forsterite content at the centre of the crystal and the margin, in fact several show fractionally higher forsterite content at the rim than in the centre (Table 3-4). This suggests little diffusion has occurred as forsterite contents should be affected more rapidly by diffusion than CaO content (Jurewicz & Watson, 1988b). The smaller LCO crystals analysed in the same thick section show lower forsterite contents on average than the larger LCO phenocrysts, with an average of Fo<sub>87</sub> compared to Fo<sub>90</sub> for the smaller and larger olivine crystals respectively.

<b>Crystal Number</b>	<b>% Distance from Rim</b>	<b>Distance from Rim (mm)</b>	<b>Fo (mol%)</b>	<b>CaO (wt%)</b>
CA13 L1	100	0.41	91.1	0.053
CA13 L1	94	0.38	91.1	0.051
CA13 L1	44	0.18	91.1	0.057
CA13 L1	25	0.10	91.2	0.107
CA13 L2	100	0.34	89.2	0.059
CA13 L2	19	0.06	89.2	0.066
CA13 L3	100	0.36	90.6	0.055
CA13 L3	93	0.33	90.9	0.052
CA13 L3	93	0.33	90.8	0.049
CA13 L3	50	0.18	90.7	0.049
CA13 L3	29	0.10	90.2	0.159
CA13 L3	29	0.10	90.9	0.063
CA13 L3	21	0.08	90.8	0.159
CA13 L4	100	0.23	89.0	0.056
CA13 L4	100	0.23	89.0	0.054
CA13 L4	22	0.05	88.9	0.066
CA13 L4	11	0.03	89.0	0.147
CA13 L5	100	0.46	86.8	0.054
CA13 L5	39	0.18	88.9	0.155
CA13 L5	17	0.08	88.6	0.174
CA13 L6	100	0.32	90.1	0.050
CA13 L6	72	0.23	90.2	0.051
CA13 L6	52	0.17	90.6	0.114

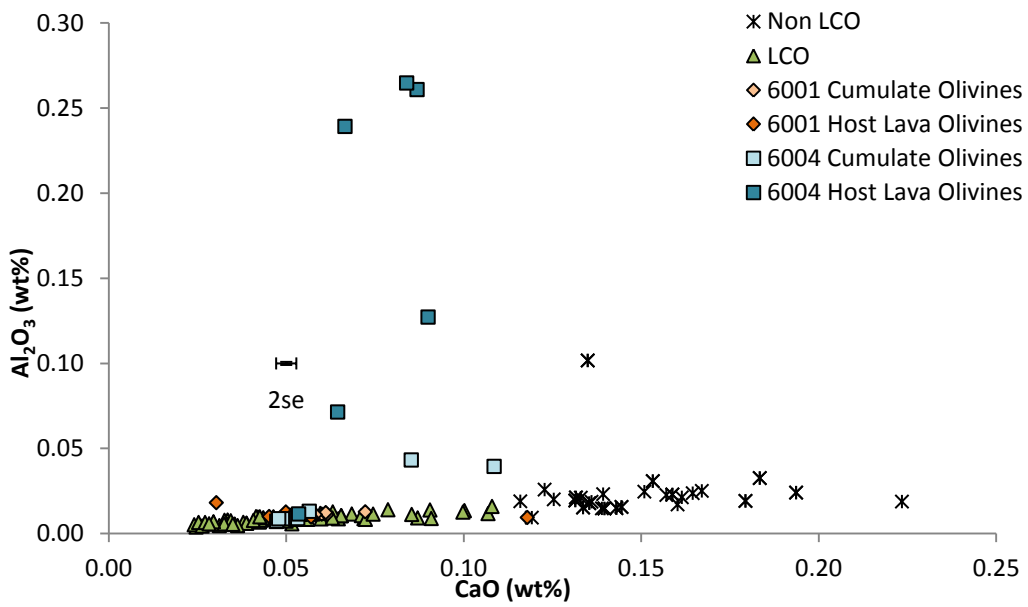
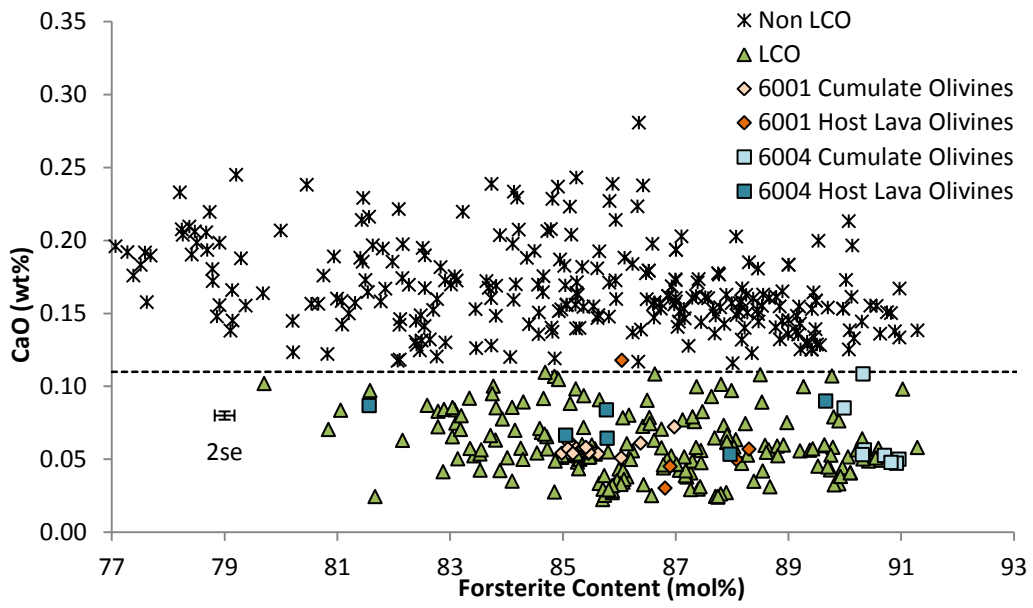
<b>Crystal Number</b>	<b>% Distance from Rim</b>	<b>Distance from Rim (mm)</b>	<b>Fo (mol%)</b>	<b>CaO (wt%)</b>
CA13 L6	40	0.13	90.2	0.079
CA13 L6	36	0.12	89.9	0.153
CA13 L6	24	0.08	89.8	0.155
CA13 L7	100	0.44	89.6	0.065
CA13 L7	24	0.10	89.7	0.067
CA13 L8	100	0.31	88.1	0.058
CA13 L8	33	0.10	88.5	0.092

**Table 3-4 CA13 thick section analyses, showing forsterite contents and CaO concentrations relative to distance from the rims of the crystals.**

Therefore it seems unlikely that the LCO are mantle xenocrysts, independent of whether they were merely entrained and then erupted relatively shortly afterwards (precluding diffusion) or were resident in the host melt for a sufficient period of time to allow interaction and/or diffusive behaviour to occur. Although CaO contents agree, low Cr and in particular low Al<sub>2</sub>O<sub>3</sub> and forsterite contents do not agree with the mantle olivine data published by Hirano et al. (2004) and De Hoog et al. (2010). Additionally, the profiles of spots across individual olivine crystals show that forsterite contents do not seem to have been modified by significant diffusion.

#### ***Disaggregation of crustal cumulate xenoliths***

As seen in section 3.4.12, there is evidence of cumulate xenolith disaggregation in the two Grenada host lavas containing cumulate material. When compared to the low calcium olivines, it can be seen that the cumulate olivines have very similar chemistry to the LCO (Figure 3-48), with the exception of some Al<sub>2</sub>O<sub>3</sub> contents in 6004 olivines (although this may be a result of sampling some of black stripe material observed in thick section).



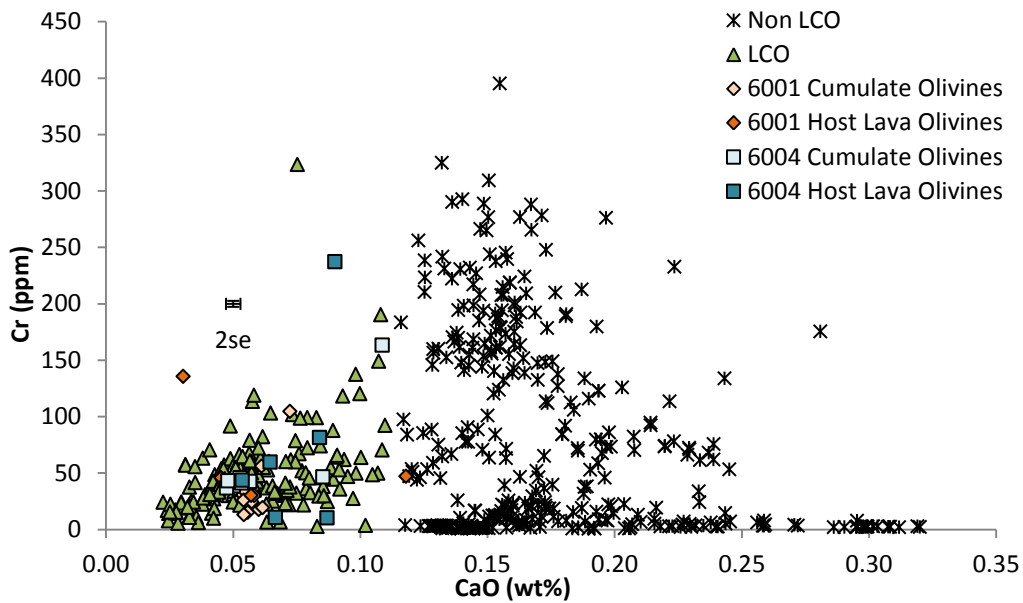


**Figure 3-48** Graphs showing how the cumulate xenolith olivines and olivines in the host lavas containing the cumulate xenoliths compare to the LCO and non LCO.

Furthermore, the cumulate olivines extend across nearly the whole range of LCO forsterite contents, particularly when the olivines in the host lavas (which may have originated from the cumulate bodies) are considered.

Given the chemical similarities between the cumulate xenolith olivines and the olivine phenocrysts in the host lavas containing the cumulates, this would support the petrographic evidence that crystals from the cumulate xenoliths could have become separated from the cumulate and entrained in the host melt. Figure 3-48 suggests that it is possible that the LCO represent these disaggregated olivine crystals.

However, even if the LCO are cumulate olivines which have disaggregated from their xenolith bodies, this still does not explain why their CaO, Al<sub>2</sub>O<sub>3</sub> and other trace elements are so low. The following section examines possible sources which could have produced the distinctive chemistry of the LCO.

***Melting of a different source***

*Other reported low calcium olivines*

Kamenetsky et al. (2006) discussed olivines with similarly low calcium contents (0.02-0.15 wt% CaO compared to 0.02-0.11 wt% in the Lesser Antilles LCO)

(Figure 3-49) from several arcs across the world (Indonesia, the Solomon Islands, Kamchatka and the Valu Fa Ridge). Kamenetsky et al. (2006) also saw a continuum between those olivines being designated as ‘low Ca’ and ‘high Ca’ (with their threshold of 0.15 wt% being described as ‘tentative’).

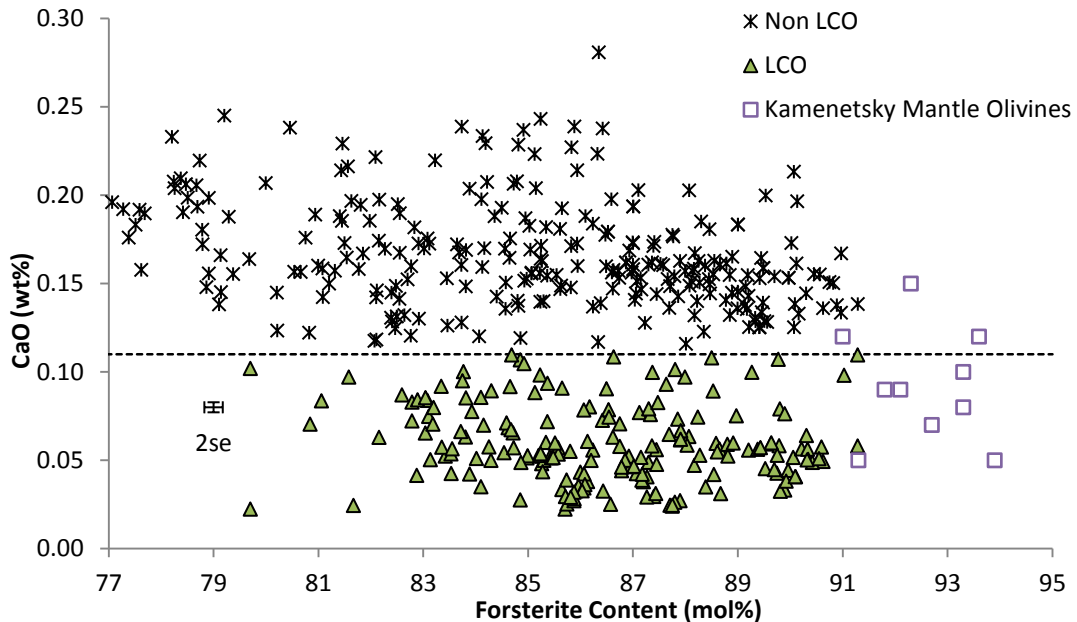


**Figure 3-49** CaO and forsterite contents of the LCO and the Kamenetsky et al. (2006) olivines, showing that the LCO have comparable CaO contents but lower forsterite contents.

Kamenetsky et al. (2006) proposed that there were contrasting melts present in the magmatic system, each crystallising a discrete population of olivines. These populations were then combined by magma mixing. The mixing of the melts allowed diffusion and overgrowth of higher Ca rims on the low CaO olivines to occur and thus create the continuum between the low and high Ca olivine populations (Kamenetsky *et al.*, 2006). The range of CaO contents reported by Kamenetsky et al. (2006) agrees with that seen in the Lesser Antilles olivines. In addition the lowest CaO concentrations were found in the cores of the crystals. However, the forsterite contents of the LCO do not correlate with those discussed by Kamenetsky et al. (2006). The Kamenetsky et al. (2006) olivines span a forsterite range of Fo<sub>90-94</sub>, while the Lesser Antilles LCO occupy a range of Fo<sub>80-91</sub>. The forsterite contents have been modified by diffusion, as suggested by Kamenetsky et al. (2006). However, in order to reduce the forsterite contents sufficiently, the LCO would either have to have been resident in the host melt for a longer period of time than those discussed by Kamenetsky et al. (2006) or the host melt would have to have had a lower Mg/Fe

ratio than those encountered by Kamenetsky et al. (2006). The former is unlikely as longer residence times should increase homogeneity, whereas the LCO have a forsterite range of 11 mol%, compared to 4 mol% reported by Kamenetsky et al. (2006). Additionally, the thick section analyses show little evidence of any diffusion having occurred, with similar forsterite contents in the cores and rims of the crystals. The LCO also show lower Cr at a given forsterite content than the higher CaO olivines (Figure 3-50), with the LCO concentrations ranging from 3-190 ppm and the higher CaO olivines ranging from 5-395 ppm over a forsterite range of Fo<sub>80-91</sub>. The Kamenetsky et al. (2006) olivines show Cr concentrations more similar to the higher Cr contents of the higher CaO olivines (274-616 ppm at Fo<sub>90-94</sub>). Kamenetsky et al. (2006) do not provide any information on the melts from which their low Ca olivines crystallised except to say that the melts must have had low Ca and high SiO<sub>2</sub> contents. It seems plausible that theoretically the LCO may be a result of the mixing of two or more melts in the magmatic plumbing system, each contributing a different population of olivines. This could have potentially have been followed by diffusion and/or overgrowth of the higher CaO olivine, as described by Kamenetsky et al. (2006); although the data suggest this did not occur. This does not preclude magma mixing as the melts could have been mixed and then erupted before any overgrowth or diffusion had time to occur.

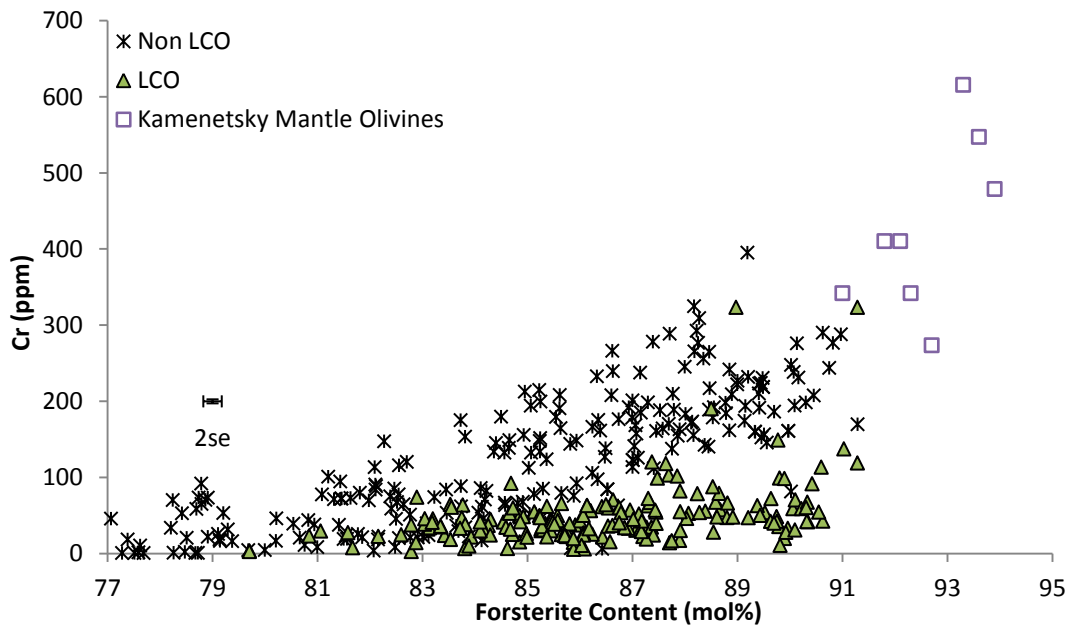


**Figure 3-50** Cr concentrations and forsterite contents in the Kamenetsky et al. (2006) olivines and the LCO. The Kamenetsky et al. (2006) olivines show higher Cr concentrations at a given forsterite content than the LCO.

### *Residual garnet?*

The LCO must have originated from a relatively primitive melt in order to have crystallised olivines up to Fo<sub>91</sub>. The LCO are also depleted in Cr, Al, Y, Yb and in some cases Sc, which may suggest melting in the presence of residual garnet. If garnet was present in the source, the HREE, Cr and Al would be withheld in the garnet during melting, producing a parent melt depleted in these elements. It should be possible to observe garnet presence in the Y/Yb ratios of the olivines, with high Y/Yb ratios indicating garnet involvement, unfortunately the size of the uncertainties in the Y and Yb data are too large to provide conclusive evidence to support this hypothesis.

However, melting in the presence of residual garnet does not explain the lower CaO concentrations of the LCO, as CaO should not be preferentially held in the garnet and thus the CaO content of the melt would be similar to that which crystallised the higher CaO olivines. Walter (1998) conducted melting experiments on garnet peridotite and reported the composition of co-existing olivine. The Walter (1998) olivines have CaO contents of 0.13 to 0.34 wt% (over a range of Fo<sub>90-95</sub>), at least 0.02 wt% higher than the upper threshold of 0.11 wt% CaO of the LCO (Figure 3-51). In addition, melts produced during the Walter (1998) experiments were also analysed and showed CaO contents of 4.27 to 10.92 wt%. If a partition coefficient for CaO into olivine in basalts of 0.028 (averaged from Beattie, 1994 ) is used, even the 4.27 wt% Walter (1998) melt does not allow for the crystallisation of the LCO, with a calculated concentration of CaO in olivine being 0.121 wt%.

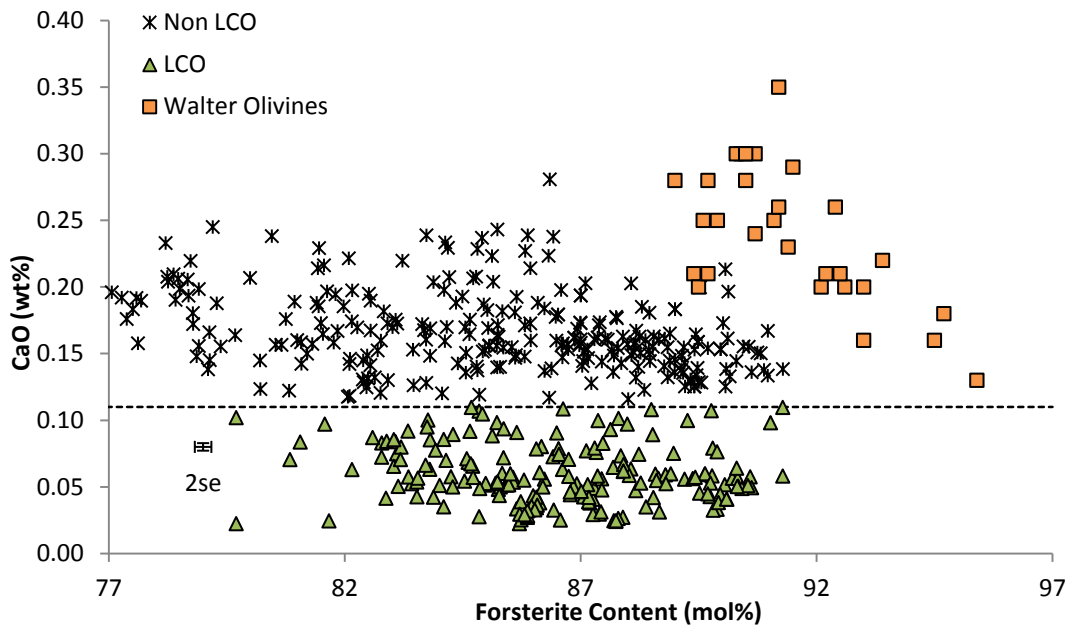


**Figure 3-51** CaO and forsterite contents of the LCO and non-LCO compared to the Walter (1998) olivines.

Further evidence is that low calcium olivines as reported here and by Kamenetsky et al. (2006) only appear to be found in arc settings. Were the LCO simply to be a product of melting with garnet present, it would seem likely that other volcanic settings should be capable of producing such olivines. There is little evidence in the literature that low calcium olivines exist in any other volcanic environments aside from arcs. Therefore, whilst residual garnet may be a factor in the LCO crystallisation, it is unlikely that this alone is responsible for their unusual geochemistry.

*Refractory harzburgite?*

A refractory garnet harzburgite could provide the source for the LCO. The garnet component could account for the low HREE, Al and Cr but the refractory nature of the harzburgite could also accommodate the low CaO content required of the LCO parent melt. Hellebrand et al. (2002) reported mineral data from several residual abyssal peridotites, with the MREE/HREE ratios of the analysed clinopyroxenes showing that at least some melting must have occurred in the garnet stability field. Olivines analysed by Hellebrand et al. (2002) showed CaO contents ranging from 0.02 to 0.10 wt%, which agrees well with the LCO CaO contents of 0.02 to 0.11 wt% (Figure 3-52).

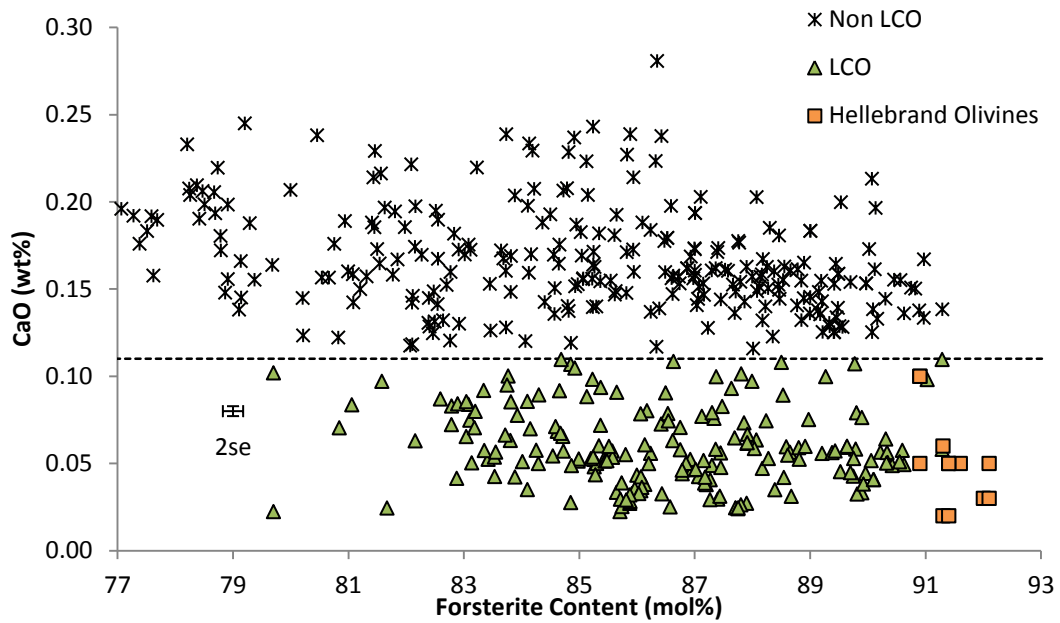


**Figure 3-52 CaO and forsterite contents in the Hellebrand et al. (2002) olivines compared to the LCO and non-LCO. The Hellebrand et al. (2002) olivines have comparable CaO contents to the LCO.**

The  $\text{Al}_2\text{O}_3$  contents of the Hellebrand et al. (2002) also show a good correlation with the LCO, ranging from 0.00 to 0.03 wt%, compared to 0.00 to 0.02 in the LCO (Figure 3-53). The forsterite contents again show a much smaller range ( $\text{Fo}_{91-92}$ ) and only agree with the highest forsterite olivines of the LCO ( $\text{Fo}_{80-91}$ ). No trace element data are available for the olivines, but the accompanying Hellebrand et al. (2002) clinopyroxene data do show depleted HREE concentrations so it is possible that the olivine would also exhibit depletions in these elements, although the degree of depletion cannot be quantified.

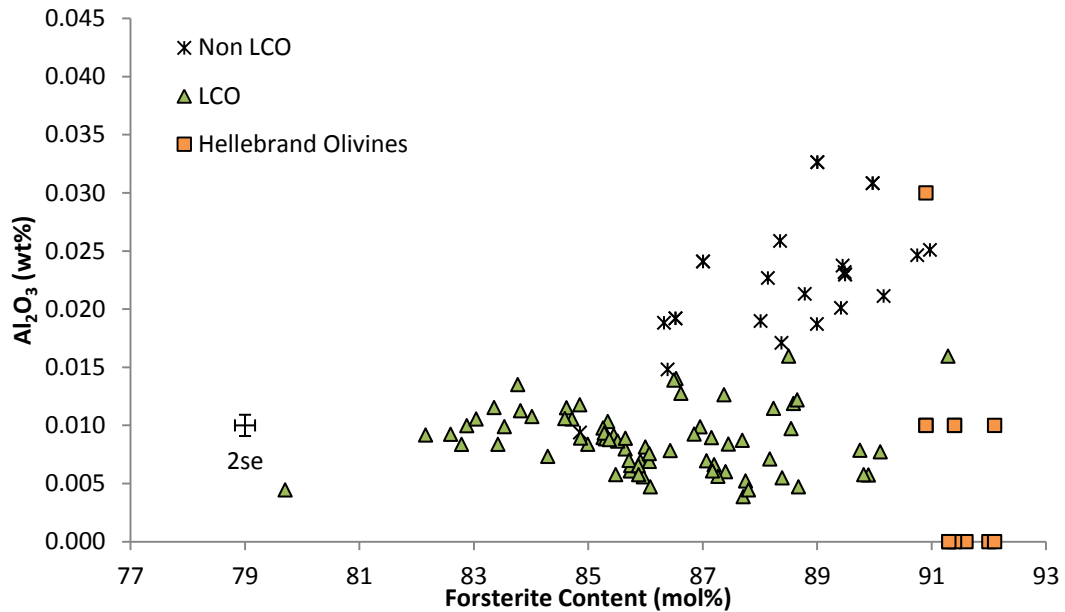


**Figure 3-53** Al<sub>2</sub>O<sub>3</sub> contents in the Hellebrand et al. (2002) olivines compared to the LCO, showing that the Hellebrand et al. (2002) olivines are comparable to the LCO in terms of alumina contents.

*Boninite like genesis?*

It may be unlikely that refractory garnet harzburgites would melt. Melting of metasomatised mantle is thought to produce boninites (Falloon *et al.*, 2008) which could show similar compositions to melting refractory harzburgite. Sobolev and Danyushevsky (1994) suggested that highly refractory peridotites are the source of the compatible elements derived from the mantle in boninites. Generally speaking boninites have high MgO contents and are relatively enriched in LREE, but are depleted in non-fluid mobile HREE as well as Al<sub>2</sub>O<sub>3</sub>. They can either be high or low in terms of CaO contents (Kamenetsky *et al.*, 2002, SOBOLEV & DANYUSHEVSKY, 1994, TAYLOR *et al.*, 1994). Olivines crystallising in boninites commonly have high forsterite contents (Fo<sub>92-94</sub>) (Kamenetsky *et al.*, 2002). In order to see if the LCO could originate from a boninite like melt composition, the data were compared to the boninite olivines of Sobolev and Danyushevsky (1994) (Figure 3-54).

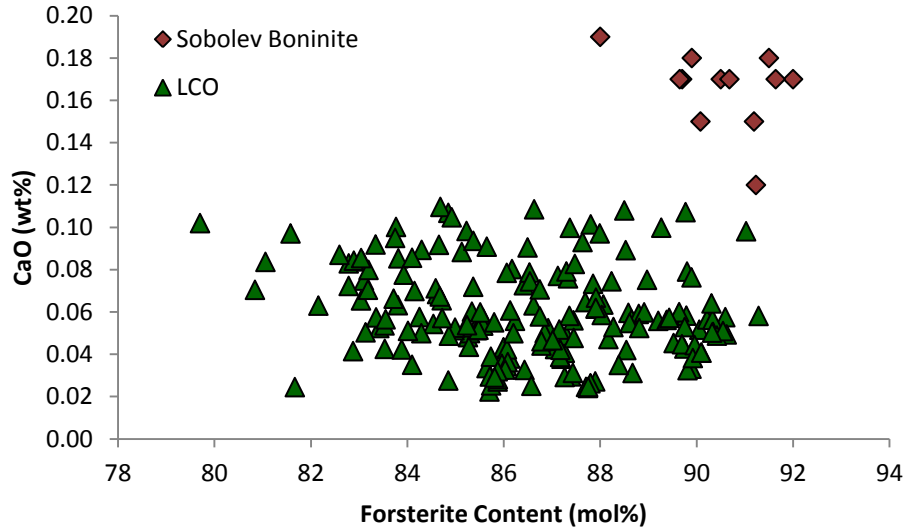


**Figure 3-54 Comparison of the LCO with boninite olivines (SOBOLEV & DANYUSHEVSKY, 1994).**

Figure 3-54 shows that the boninite olivines do not have CaO contents as low as the LCO. It may be that there are olivines found in boninites with lower CaO concentrations than those of Sobolev and Danyushevsky (1994) which has not been published. The forsterite contents of the LCO do overlap with the boninite olivines but they also extend to much lower Fo contents. To further test if the boninite olivines are a viable explanation of the LCO, the Cr contents were compared to the LCO, given that these are unusually low in the LCO compared to the higher CaO olivines (Figure 3-55).

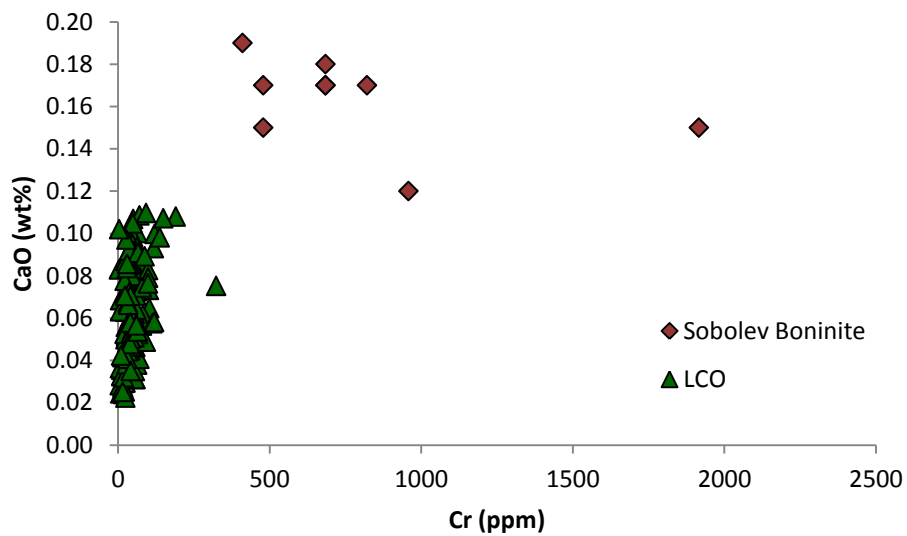


**Figure 3-55 Cr concentrations in the LCO and the boninite olivines analysed by Sobolev and Danyushevsky (1994).**

Figure 3-55 shows that the boninite olivines do not show sufficiently low Cr concentrations to be comparable to the LCO. Given this coupled with the higher CaO concentrations and smaller range in forsterite contents, it appears that the LCO are not the product of boninite like petrogenesis.

#### *Slab melting?*

Assuming a partition coefficient of 0.028 (Beattie, 1994) for CaO in olivine in basalts, the LCO parent melts would require CaO contents of 0.79 to 3.87 wt%. These values suggest a more evolved parent melt, such as a dacite. More evolved melts could also explain the lower Cr concentrations seen in the LCO at a given forsterite content compared to the higher CaO olivines. Klemme et al. (2002) (and references therein) have noted that siliceous melts can be generated by the melting of the subducting slab (basalt altered to garnet amphibolite and/or eclogite), producing melts with between 63 to 74 wt% silica. Defant and Drummond (1990) introduced the term adakite to describe rocks related to the subduction of oceanic lithosphere less than 25 Ma old. Adakites also typically show Y and Yb depletions (Castillo, 2006, Rapp *et al.*, 2003), indicating the presence of garnet which could explain some of the chemical characteristics of the LCO.

Klemme et al. (2002) and references therein suggest that slab melts should be enriched in TiO<sub>2</sub>, a feature not observed in the LCO. It is therefore likely that if the LCO are related to slab melting, a Ti bearing phase such as rutile must be present in the residue to account for the HFSE concentrations seen in the LCO, as suggested by Kelemen et al. (1993) and McDonough (1991). This HFSE depletion is often noted in adakites (Castillo, 2006).

Sr/Y ratios could be used to investigate the involvement of slab melting in the petrogenesis of the LCO, with high Sr/Y indicating the presence of garnet and absence of plagioclase in the melting assemblage and thus likely slab involvement (Garrison & Davidson, 2003, Rapp *et al.*, 2003, Rapp *et al.*, 1999). However, the uncertainties in the Sr and Y data for the LCO are too large to obtain useful information from the Sr/Y ratios of the LCO. Sr/Y ratios of the whole rocks in which the LCO were found also show no discernible trend between occurrence of LCO crystals and Sr/Y (Figure 3-56), on the contrary, many of the whole rocks with higher Sr/Y exhibit few LCO crystals.

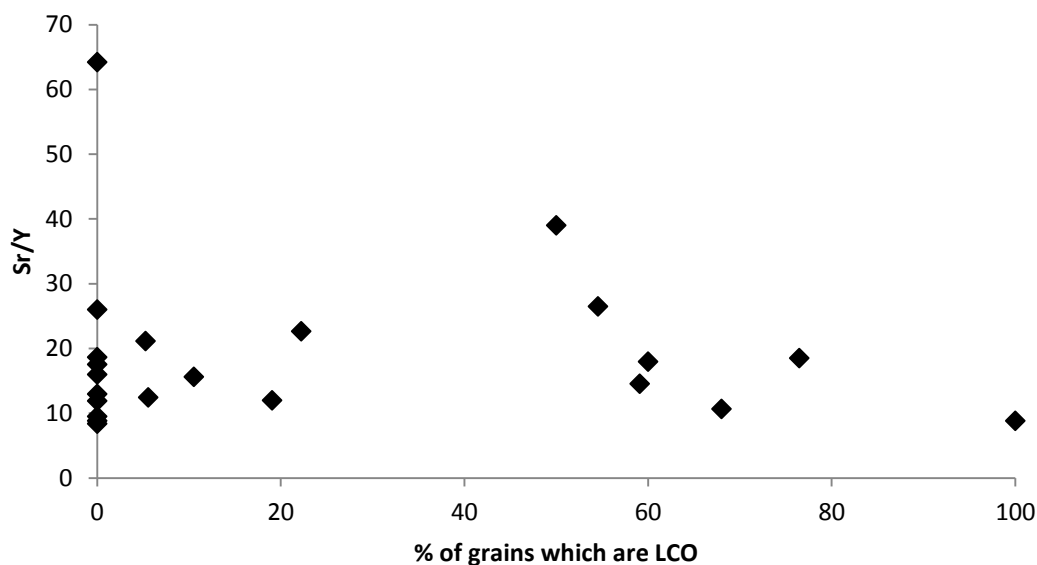


**Figure 3-56 Sr/Y ratios of the host lavas compared to the percentage of analysed olivine crystals from each host lava that are classified as LCO.**

There are other major issues with the notion that the LCO could have been crystallised from a melt generated by the melting of subducted metamorphosed basalt. Firstly, adakites are characterised by high  $\text{Al}_2\text{O}_3$  contents (Castillo, 2006, Garrison & Davidson, 2003, Klemme *et al.*, 2002, Rapp *et al.*, 1999). The LCO show very low  $\text{Al}_2\text{O}_3$  contents (0.004 to 0.016 wt%  $\text{Al}_2\text{O}_3$ ), suggesting that a melt with high levels of alumina (with adakites having an alumina content over 15 wt%, Castillo, 2006) cannot be a suitable parent melt for the Lesser Antilles LCO. The principal problem with a slab melt parent for the LCO is that dacitic melts should not crystallise olivine. Castillo (2006) suggested that adakites have MgO contents of less than 3 wt%. Lesser Antilles host lavas with MgO contents this low have rarely been shown to crystallise olivine e.g. Davidson and Wilson (2011); Macdonald *et al.* (2000).

*Slab melt interaction with peridotite?*

Rapp *et al.* (1999) suggested that high Mg# adakites were not simply a result of slab melting but that the high  $\text{SiO}_2$  melts generated from partial melting of the subducted lithosphere then infiltrated the overriding mantle wedge to form hybrid melts from which the high Mg# adakites were then derived. This could supply a potential mechanism for the formation of the LCO if reaction with peridotite could raise the MgO content of the slab melt sufficiently to crystallise olivine.

Rapp et al. (1999) conducted experiments in which adakitic melts were allowed to interact with peridotite in order to study melt rock reactions. The results of these experiments showed that mixing with peridotite caused increases in MgO, FeO and TiO<sub>2</sub> whilst decreasing SiO<sub>2</sub> and Al<sub>2</sub>O<sub>3</sub>. In addition, CaO contents for the products of the experiments were in the range of 1.98 to 2.25 wt% (Rapp *et al.*, 1999), which could be sufficiently low to be capable of crystallising olivines with similar CaO concentrations to those seen in the LCO. Kelemen et al. (1993) agreed that reaction between slab melts and peridotite should increase Mg# of the melt, but also proposed that the Ni and Cr concentrations in the melt would increase also. The LCO have lower Cr contents than the higher CaO olivines and comparable Ni concentrations at a given forsterite content, which could suggest that slab melt and peridotite interaction is not a suitable mode of petrogenesis for the LCO.

Furthermore, Rapp et al. (1999) agreed with Sekine and Wyllie (1982a, 1982b) that even though the melt rock reactions increase MgO, olivine is not crystallised from the hybrid magma. The inability for slab derived melts, either with or without peridotite interaction, to exhibit sufficiently high MgO contents to crystallise olivine may present a fundamental flaw in the theory that the LCO may have been derived by melting of the subducting oceanic lithosphere.

However, Sobolev et al. (2007) proposed that eclogite derived high silica melts mix with the mantle wedge peridotite to produce olivine-free pyroxenite. They analysed olivine phenocrysts in erupted basalts to investigate the degree of recycled crustal material involved in mid-ocean ridge, ocean island and continental basalts by assessing the amount of the hybrid pyroxenite melt involved in the petrogenesis of the olivines. Sobolev et al. (2007) suggested that these hybrid melts would be depleted in Mg, Mn and Ca but enriched in Si and Ni. Based on the work of Eggins (1992), they thought that with adiabatic decompression, the melts would become olivine saturated. However, if the Sobolev et al. (2007) mechanism was involved in the petrogenesis of the LCO, the Ni concentrations in the LCO should show enrichment and the MnO contents should appear lower than the higher CaO Lesser Antilles olivines. Figure 3-13 and Figure 3-18 show that neither of these scenarios are realised in the LCO data. Thus while Sobolev et al. (2007) provide a method for crystallising olivines from melts with a slab component, it appears unlikely that the LCO were derived in this way.

Further to the work done by Sobolev et al. (2007), Lambart et al. (2012) suggested that the precipitation of olivine from peridotite pyroxenite hybrid melts is dependent on silica activity of the pyroxenite melt interacting with the peridotite, based on experiments where a known quantity of pyroxenite liquid was added to a known volume of peridotite. Where silica activity is high, olivine will dissolve and orthopyroxene will be precipitated; however, where silica activity is low, olivine will crystallise while orthopyroxene undergoes dissolution (Lambart *et al.*, 2012). In addition to this, Lambart et al. (2012) proposed that garnet is stable at lower pressures in pyroxenite than in peridotite, consequently mixtures of peridotite and pyroxenite can produce melts with a garnet signature (as seen in the LCO) at lower pressures than would be expected from purely peridotite melts.

### ***LCO Summary***

The LCO show distinctive geochemical characteristics, their juxtaposition with higher CaO olivines in the same host lavas implying a differing petrogenesis for each population before mixing prior to eruption.

Comparison with published data shows that the LCO are unlikely to be mantle xenocrysts, with forsterite contents being lower than reported values but with little evidence of Fe and Mg diffusion evident which could have offered a mechanism for lowering the forsterite contents.

However, chemical similarities between the LCO and the analysed cumulate xenolith olivines hosted in two lavas from Grenada suggest that the LCO may be disaggregated cumulate crystals entrained into the melts then responsible for crystallising the higher CaO olivines.

HREE depletion, coupled with low Al<sub>2</sub>O<sub>3</sub> contents imply that the LCO were crystallised from a melt in equilibrium with residual garnet. However, garnet alone does not explain the low CaO contents of the LCO. The Hellebrand et al. (2002) olivines agree well with the CaO and Al<sub>2</sub>O<sub>3</sub> concentrations of the low calcium olivines which suggests that a refractory garnet harzburgite source could be partly responsible for the generation of the LCO. The published data for olivines derived from refractory garnet harzburgite melts show higher forsterite contents than those seen in the LCO.

Material from melted subducted oceanic lithosphere does not seem to have contributed to the petrogenesis of the LCO based on the expected chemistry such melts would exhibit. Whole rock Sr/Y ratios in particular show little correlation with the frequency of LCO in the host lavas.

Therefore, it is proposed that the LCO have been crystallised from a melt formed in the presence of residual garnet, potentially from a refractory garnet harzburgite source. The presence of garnet in the source implies that these melts were generated at depth, in the garnet stability field. The reasoning behind the relatively low forsterite contents in the LCO is unclear.

### **3.6 Conclusions**

High forsterite contents and low CaO concentrations in the Lesser Antilles arc olivines are likely to be in part a result of increased melt water contents due to the intra-oceanic subduction zone setting. Forsterite bimodality in GU25 is suggested to be a result of degassing of the melt. This would result in lower Fo contents due to a change in oxygen fugacity affecting the  $\text{Fe}^{2+}/\text{Mg}$  ratio of the host melt.

There are two discrete populations of olivines present, which have been defined in this study based on their CaO contents, although they also exhibit lower Y, Yb, Cr,  $\text{Al}_2\text{O}_3$  and in some cases Sc concentrations. It is suggested that the LCO population are disaggregated cumulate xenoliths which are then incorporated into the host melts responsible for crystallising the remaining olivines. These cumulates crystallised from CaO poorer melts which may have had higher water contents than those suggested by Macdonald et al. (2000) and references therein. In addition, clinopyroxene in the cumulates may also be a repository for the depleted elements. However, the higher CaO crystals do not show such depletions in the elements noted even though some of the host lavas also have clinopyroxene phenocrysts present. Variations across crystals may result from material crystallising from the melts in which the LCO are entrained, around LCO cores.

Figure 3-57 provides a schematic overview of petrogenetic processes affecting the composition and crystallisation of olivine phenocrysts in the Lesser Antilles island arc.

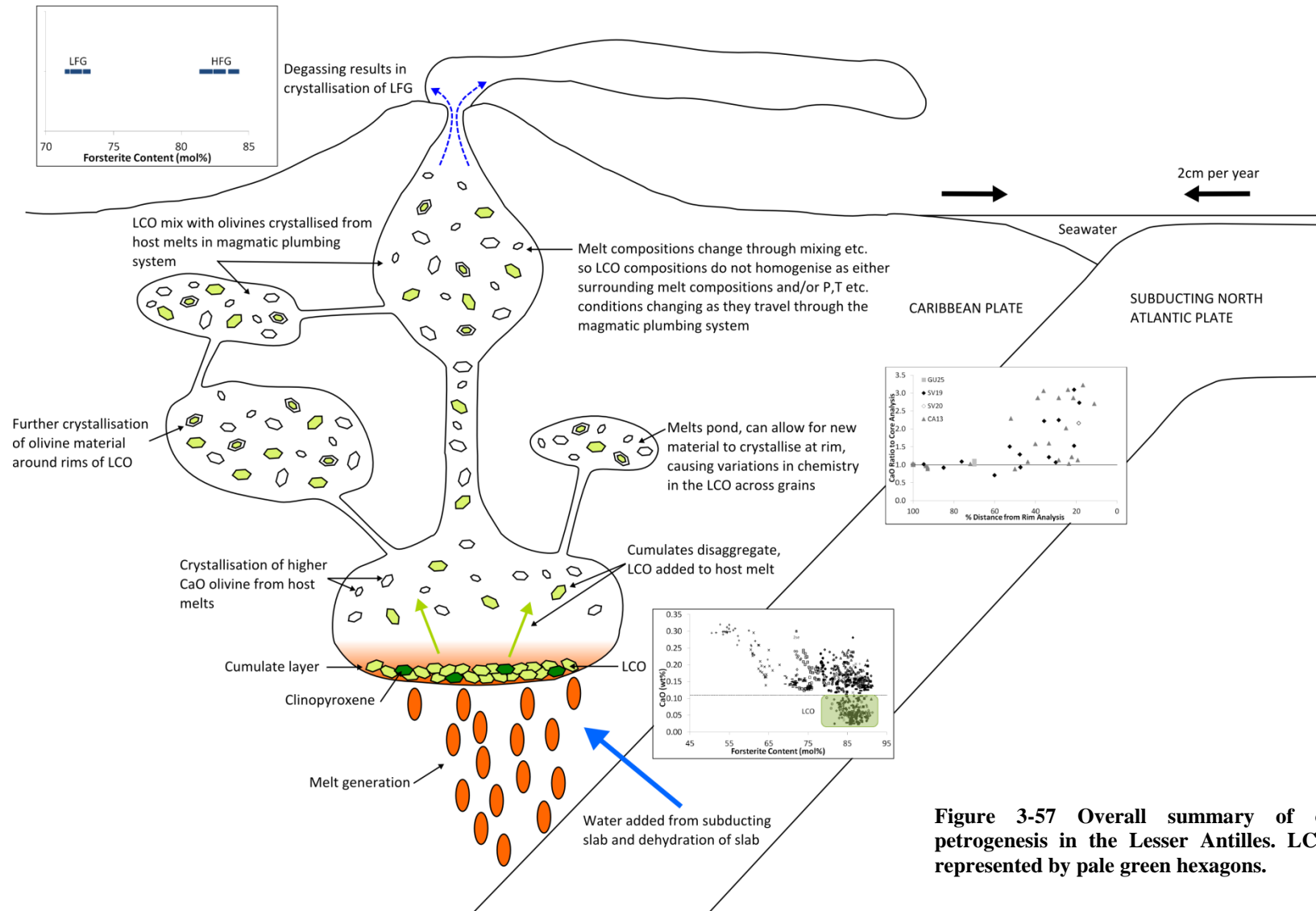


**Figure 3-57 Overall summary of olivine petrogenesis in the Lesser Antilles. LCO are represented by pale green hexagons.**

### 3.7 Further Work

- The study would benefit from more accurately constrained partition coefficients, particularly for CaO and forsterite contents. This may be achieved by conducting phenocryst-matrix pair analyses on Lesser Antilles lavas with more aphyric groundmasses and phenocryst olivine alone.
- Studies of melt inclusions trapped within olivines would provide valuable information on potential parental melt compositions of both the higher CaO olivines and the LCO.
- Volatile studies on these melt inclusions could also provide information on melt water contents. This could then permit comparison of water contents in both populations to get a more definitive answer as to if water contents are significantly different in both populations.
- Analysis of more cumulate xenoliths, not only from Grenada but other islands in the arc would expand the dataset. Xenoliths from islands which do not contain LCO would be of particular interest, as this would allow investigation as to whether the low calcium olivine crystals are present. Were they to be apparent in cumulates, this would pose interesting questions as to why some cumulate bodies disaggregate in the southern section of the arc and others may not.

---

## 4 Plagioclase Chemistry

---

### 4.1 Introduction

#### 4.1.1 Importance of Analysing Plagioclase

Plagioclases provide a vital insight into shallow level petrogenetic processes affecting ascending melts and are very sensitive to changes in melt composition. In the case of tholeiites (as seen in the northern section of the Lesser Antilles island arc), plagioclase should crystallise before clinopyroxene. The reverse is true in more alkalic and calc-alkalic melts, as found in the southern section of the arc. Zoning of plagioclases can provide more detailed information as fluctuating melt compositions are recorded throughout the growth of individual crystals. In addition, petrogenetic processes can be observed in microtextural variations in plagioclases (Renjith, 2013, Viccaro *et al.*, 2010), providing insights into how the plagioclases have travelled through the magmatic plumbing systems prior to eruption.

Differences in plagioclase compositions within single lavas could suggest the presence of multiple crystal populations (and thus potentially different parental melts for these populations). Such bimodalities have been observed in the olivines analysed in the Lesser Antilles island arc (Chapter 2) with the identification of the low calcium olivines.

With suitable partition coefficients, the melt compositions from which the plagioclases crystallised can be calculated. Additionally the composition of plagioclases expected to be in equilibrium with the whole rock chemistry can be estimated. Discrepancies between the hypothetical equilibrium plagioclases and the analysed compositions can point to whether the crystals could be a result of accumulation or if they appear to be more primitive than the hypothetical equilibrium plagioclase.

#### 4.1.2 Aims of Analysing Plagioclases in the Lesser Antilles

This study is unique in that it provides both major and extensive trace element data from plagioclases across the arc. Previously, no studies have compared plagioclase

data between multiple islands. In addition, in situ analyses using thick sections have been undertaken, allowing the investigation of spatial relationships within crystals. The latter allows detailed petrogenetic histories of zoned crystals to be pieced together.

Trace elements analysed include TiO<sub>2</sub>, Rb, Sr, Y, Pb, Ba, La, Sm, Eu and Gd. Nb was analysed as a measure of contamination of plagioclases by inclusions, as concentrations of niobium in the crystals should be negligible.

### *Aims*

- To provide a new dataset incorporating major and trace element data for plagioclases from multiple islands in the Lesser Antilles.
- To observe any heterogeneities in plagioclase chemistry both within individual lavas and along strike of the arc.
- To undertake a textural analysis of the crystals analysed.
  - To provide information on shallow level processes affecting the ascending melts.
  - To provide possible insights into volatile contents of the host melts as these were not measured as part of the study.
- To complement the olivine dataset and thus provide a more detailed and rounded insight into the petrogenesis of the lavas.

## **4.2 Host Lavas**

156 plagioclase crystals were sampled from 12 lavas from 3 islands in the Lesser Antilles (4 lavas each from Guadeloupe, St. Vincent and Bequia). Table 4-1 shows the host lava names, locations and modal plagioclases proportions (based on point counting data using 1500 points per thin section). All the host lavas showed at least 9% modal plagioclase (although no thin section was available for BQMT3). The plagioclases were analysed using LA-ICP-MS as crystal separates mounted in epoxy resin blocks, thick sections and resin blocks (where a slice of rock approximately 30µm thick, similar to the thick sections, was mounted into a 1 inch epoxy resin

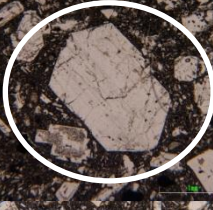
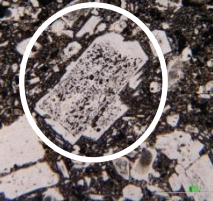
disc). Table 4-1 also provides the numbers of crystals analysed and how the crystals were mounted.

<b>Host Lava</b>	<b>Island</b>	<b>Modal Plag (%)</b>	<b>Whole Rock MgO (wt%)</b>	<b>n CM</b>	<b>n TS</b>	<b>n RB</b>
<b>GU1</b>	Guadeloupe	30.3	4.05	11	-	-
<b>GU4</b>	Guadeloupe	24.1	3.64	10	-	-
<b>GU25</b>	Guadeloupe	44.9	6.20	14	7	-
<b>GU27</b>	Guadeloupe	29.1	3.99	9	-	-
<b>SV3</b>	St.Vincent	15.3	8.60	-	-	9
<b>SV19</b>	St.Vincent	9.1	11.24	10	7	-
<b>SV20</b>	St.Vincent	22.5	6.35	8	6	-
<b>SV31</b>	St.Vincent	31.1	6.82	-	-	14
<b>BQ2</b>	Bequia	32.3	7.10	10	-	-
<b>BQ5</b>	Bequia	30.2	7.90	10	-	-
<b>BQ19</b>	Bequia	43.1	3.03	10	11	-
<b>BQMT3</b>	Bequia	N/A	5.79	10	-	-

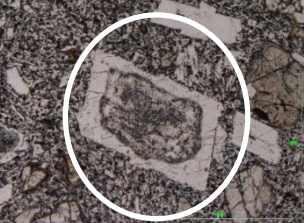
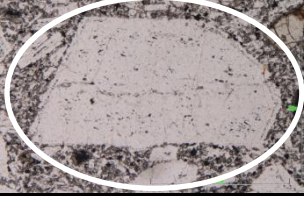
**Table 4-1 Sample name and origin of host lavas from which plagioclase crystals were analysed. Also shown is the modal proportion of plagioclase in the host lavas based on point counting data (1500 counts per thin section). No thin section was available for BQMT3. n refers to the number of plagioclases analysed by the differing methods, where CM stands for crystal mounts, TS thick sections and RB resin blocks.**

### **4.3 Plagioclase Petrography**

Thin sections of the host lavas from which plagioclases were analysed in crystal mounts and resin blocks were studied and in all but one case at least two populations were observed (Table 4-2). Where crystals were analysed in situ in thick sections, photographs of the analysed crystals were taken. Within each of the thick sections, two populations of plagioclases were evident. Table 4-3 provides a summary of the plagioclase populations observed in the thick sections.

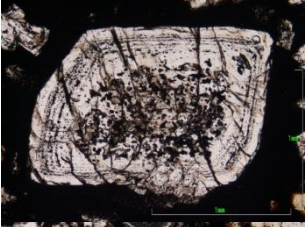
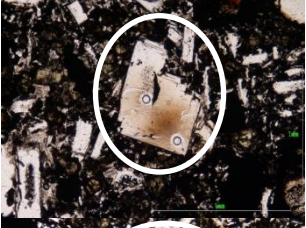
Type	Largest Crystal Size (mm)	Textures	Picture
GU1 a	3.5	Patchy cores. Rims appear relatively fresh Edges do not appear resorbed.	
GU1 b	3	Relatively fresh crystals. Zoning apparent in XPL. Edges do not appear resorbed. Some crystals appear dusty.	
GU1 c	3	Cores relatively fresh but rounded. Zoning visible in XPL. Varying extents of dense sieve texturing adjacent to fresher rim material. Edges do not appear to be resorbed.	
GU4 a	3	Heavily resorbed cores. Rim material appears fresher. Partial resorption of crystal edges.	

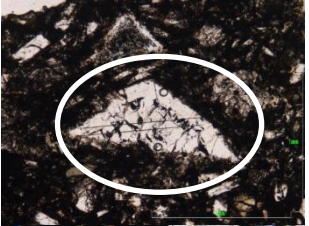
<b>GU4 b</b>	4	Relatively fresh crystals, although most appear dusty. Zoning seen in some crystals in XPL. Slight evidence of resorption within crystals and partial resorption apparent at crystal edges.	
<b>GU4 c</b>	4	Cores appear patchy. Surrounded by heavily corroded regions of varying extent. Rim material appears fresher. Edges show evidence of resorption.	
<b>GU27 a</b>	2.5	Relatively fresh but dusty crystals. Zoning apparent in XPL. Slight resorption in cores of crystals. Little resorption seen at edges of crystals.	
<b>GU27 b</b>	2	Heavily corroded cores. Rims appear much fresher and zoned under XPL. Crystal edges do not appear resorbed.	

<b>SV3 a</b>	4	Heavily corroded cores. Some cores appear fresher. Zone of fresher appearing material towards rims of crystals. Crystal edges appear slightly resorbed.	
<b>SV3 b</b>	3	Crystals appear fresher. Slight evidence of resorption within some crystals. Zoning apparent in XPL. Edges appear partially resorbed.	
<b>SV31 a</b>	2.5	Fresh appearing but rounded cores surrounded by heavily corroded zone. Crystal edges show evidence of resorption.	
<b>SV31 b</b>	2	Fresher appearing crystals. Some slight evidence of resorption towards cores of crystals. Small zone of resorbed material adjacent to crystal rims. Edges appear resorbed.	

BQ2 a	1.5	Cores fresh but rounded. Heavily corroded zone adjacent to fresher rim material. Crystal edges resorbed.	
BQ2 b	3	Cores relatively fresh. Some cores show slight resorption. Sieved zone adjacent to rims. Rims appear fresher. Crystal edges partially resorbed.	
BQ5 a	4	Patchy cores. Slight zoning seen under XPL. Crystals extensively cracked. Edges do not appear resorbed.	

**Table 4-2 Summary of plagioclase populations analysed in crystal mounts. The plagioclases being referred to are circled in white in the photographs if more than one phenocryst is present. The populations are referred to by letter following the sample number in which they were seen.**

Type	Crystal Size Range	Zoning	Textures	Picture
<b>GU25 a</b>	2	Normal zoning.	Relatively fresh cores. Sieve textures towards rim. Rims fresh. Partially resorbed edges.	
<b>GU25 b</b>	4	Normal zoning.	Heavily resorbed cores. Concentric sieve textures towards rim. Rims fresher. Resorbed edges.	
<b>SV19 a</b>	3	Normal zoning.	Relatively fresh crystals. Some have dusty zones towards the rims. Edges partially resorbed.	
<b>SV19 b</b>	3	Reverse zoning.	Heavily corroded cores. Rims fresh. Edges partially resorbed.	

<b>SV20 a</b>	3	Oscillatory where intermediate sites are present, overall reverse zoning.	Relatively fresh cores, some dusty and sieved zones present. Zone of heavy corrosion adjacent to rim. Rims fresher. Partially resorbed edges.	
<b>SV20 b</b>	3	Normal zoning.	Sieve texture in core and in concentric zones towards crystal edges. Edges very resorbed.	
<b>BQ19 a</b>	4	Varies between little variation, oscillatory and normal zoning. Overall normal zoning.	Some sieve textures evident in cores. Extensive sieve textures adjacent to fresher rim material. Edges very resorbed.	
<b>BQ19 b</b>	4	Little variation or normal zoning.	Relatively fresh crystals, cores generally dusty. Edges resorbed.	

**Table 4-3 Summary of plagioclase populations analysed in the thick sections. The plagioclases being referred to are circled in white if multiple crystals are present in the photographs. The populations are referred to as a or b following the sample number in which they were seen.**

### 4.3.1 Guadeloupe

The four lavas from Guadeloupe contain both phenocryst and groundmass plagioclase (although the latter is fine and no groundmass plagioclase has been separated and included in the crystal mounts). All the lavas have phenocrysts up to approximately 3mm in size, with GU4 and GU27 also exhibiting some larger crystals (up to 4mm). The plagioclases are primarily subhedral, although some more anhedral examples are present in GU4. GU25 shows some small, near euhedral crystals. The majority are lath shaped and display some disequilibrium features, most commonly sieve textures (Figure 4-1).

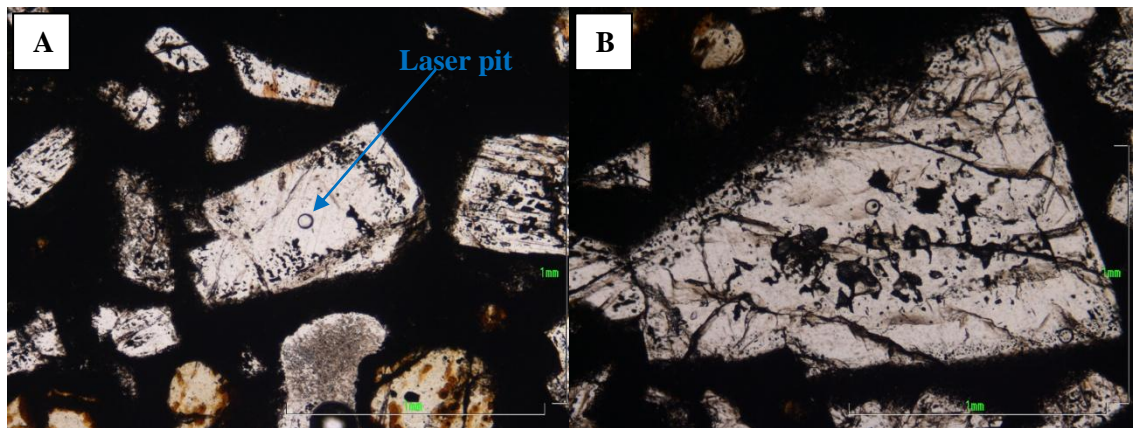


**Figure 4-1 Plagioclase phenocrysts photographs taken from the thick section of GU25, all photographs are shown in plane polarised light. Laser pits are visible as small circles, as highlighted in A. A shows the subhedral nature of the plagioclases and shows evidence of disequilibrium features, such as the sieve texture present within the phenocrysts. B shows further alteration in the core of the crystal.**

### 4.3.2 St. Vincent

The St. Vincent plagioclases are up to 4mm in size. The host lavas show coarser groundmass than those from Guadeloupe. The plagioclases are subhedral and many display disequilibrium features similar in nature to, but more extensive than, those in the Guadeloupe lavas (Figure 4-2). All of the St. Vincent host lavas contain both plagioclases exhibiting extensive disequilibrium features and fresher appearing crystals. The fresher crystals in SV20 also exhibit zoning in some cases.

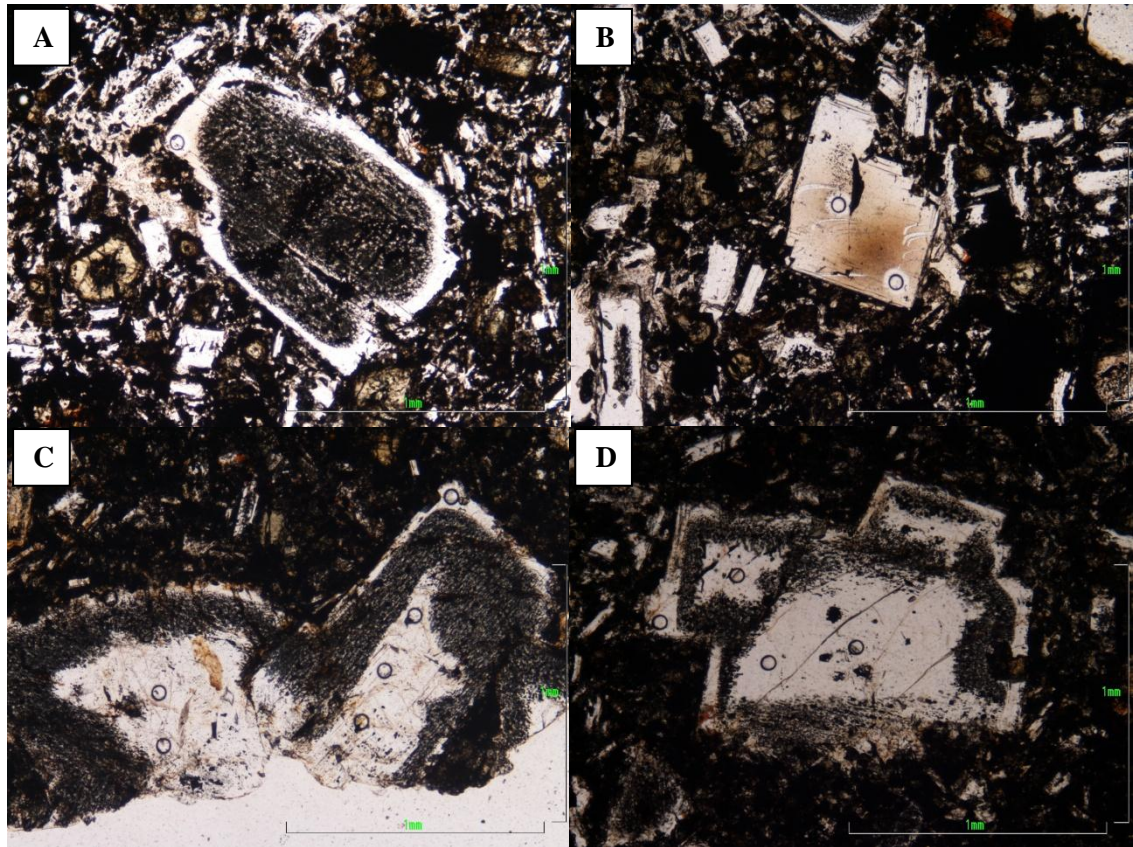


**Figure 4-2** Analysed plagioclase phenocrysts (identifiable by the circular laser pits) in SV19 (A and B) and SV20 (C and D) under plane polarised light. A shows extensive disequilibrium features in the core of a crystal in SV19. B shows a second SV19 phenocryst with much less evidence of disequilibrium in the core of the crystal but some stepwise corrosion is apparent around the rim. The darker brown colour present is the ablation blanket resulting from the LA-ICP-MS analysis. C and D show examples of spot locations when multiple analyses are undertaken in a single crystal. Both C and D show plagioclases with a different pattern of disequilibrium to that seen in the SV19 crystals. The cores are relatively fresh, with intermediate bands of extensive sieve texturing which are adjacent to unaltered rims.

### 4.3.3 Bequia

The plagioclase phenocrysts present are up to 4mm in size, with groundmass plagioclase being fine, as in the Guadeloupe thin sections. The phenocrysts are primarily subhedral. The Bequia plagioclases show much less evidence of disequilibrium than the St. Vincent crystals (Figure 4-3) but do still show sieve textures in several crystals (as in the Guadeloupe lavas). Very little zoning is seen in the crystals.

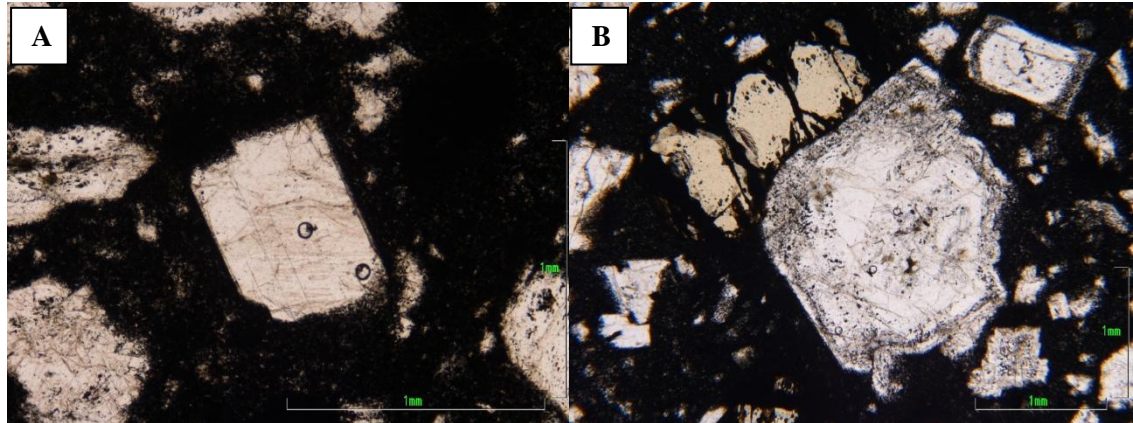


**Figure 4-3 Plagioclase phenocrysts in plane polarised light from BQ19. A shows a relatively fresh crystal with slight corrosion around the margins of the crystal. B shows a plagioclase phenocryst with a sieve texture apparent, particularly around the margins of the crystal. The crystal in the top right of the field represents the largest extent of disequilibrium features seen in the Bequia thin sections.**

#### **4.3.4 Sieve texturing and disequilibrium features in plagioclases**

Several of the populations show sieve texturing and/or disequilibrium features, often in conjunction with a fresher looking rim zone. Published work has shown that plagioclase textures can provide insights into processes occurring in the system prior to eruption (Renjith, Viccaro *et al.*, 2010). As there are texturally distinct groups present in each host lava, discrete populations have been identified based on petrography.

In order to clarify the type of sieve texturing being discussed, coarse sieving will be defined as that having individual inclusions of over 0.01 mm whilst fine sieving will be defined as inclusions of less than 0.01 mm.

Other disequilibrium features include resorption of crystal edges (Figure 4-1, particularly in photograph B), where the plagioclase material at the rims is not in equilibrium with the host melt and thus starts to break down. This produces the ragged edge textures seen in the majority of the populations.

### **4.4 Plagioclase Chemistry**

An Ab-An-Or ternary plot is shown in Figure 4-4. Guadeloupe plagioclases show compositions ranging from andesine to anorthite, with the majority of the crystals being anorthite or labradorite. The majority of St. Vincent plagioclases form a continuum between anorthite and andesine. There are however two analyses from St.

Vincent which are oligoclase in composition. The Bequia plagioclases range from anorthite to bytownite, with the majority being anorthitic. Orthoclase contents in the plagioclases are low (all crystals are composed of less than 5% orthoclase).

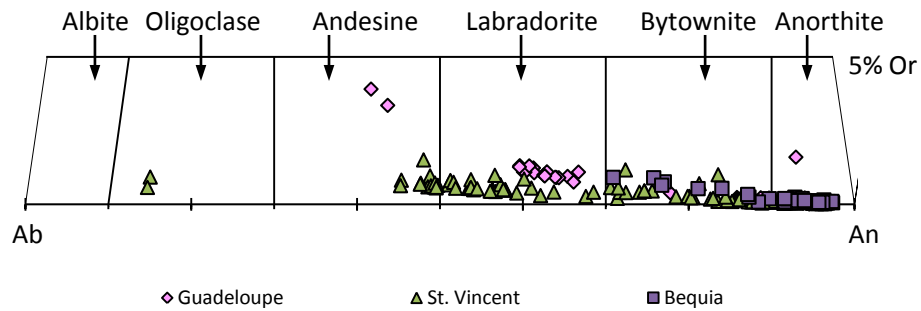


Figure 4-4 Analysed plagioclase crystals shown on an An-Ab-Or ternary plot by island.

#### 4.4.1 Anorthite Contents

The Lesser Antilles plagioclases analysed as part of this study show a range in An contents of  $An_{41-97}$  across the three islands sampled, which is roughly comparable to published values from Mount Pelée, Martinique ( $An_{51-91}$ ) (Pichavant et al., 2002) and plagioclases found in both xenoliths and accompanying host lavas analysed by Coulon et al. (1984) ( $An_{50-92}$ ). The Lesser Antilles plagioclases analysed as a part of this study extend to much higher anorthite contents than the Parkinson et al. (2003) range ( $An_{49-82}$ ). Arculus and Wills (1980) noted a range in anorthite contents of  $An_{36-100}$  in cumulates and inclusions, exhibiting a larger range than seen in the plagioclases analysed during this study. In contrast, Tollan et al. (2012) recorded compositions between  $An_{85-95}$ , also in cumulates.

There is no obvious correlation between plagioclase anorthite content and the latitude from which the host lava originated (Figure 4-5). In general, the Guadeloupe plagioclases extend to both high (up to  $An_{96}$ ) and low anorthite contents (down to  $An_{41}$ ). Very nearly the entire An content range observed in the Lesser Antilles is seen in the Guadeloupe plagioclases ( $An_{41-96}$  in Guadeloupe,  $An_{41-97}$  across all the host lavas). A comparable range in anorthite contents is shown by the St. Vincent

plagioclases ( $An_{45-92}$ ), but the highest An contents are 4 mol% lower than those measured in Guadeloupe. Similarly high anorthite contents to the Guadeloupe data are exhibited by the Bequia plagioclases (up to  $An_{97}$ ) but the range in An contents is lower than that seen in Guadeloupe, with  $An_{71}$  being the lowest value measured.

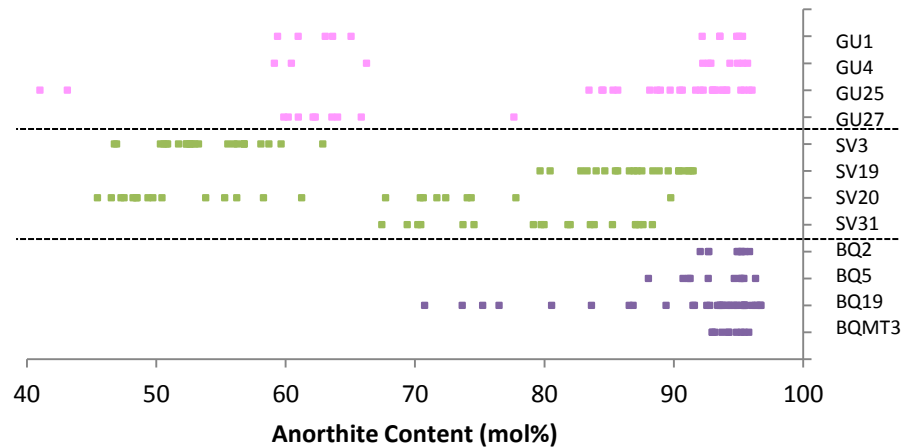


**Figure 4-5 Anorthite contents in all the analysed plagioclases. The y axis is ordered with host lavas from the centre of the arc at the top and host lavas from the south at the bottom of the axis. Each island is shown as a different colour and is separated by a dashed line.**

Plagioclases from three of the four Guadeloupe lavas analysed showed bimodalities in anorthite content. GU1 has a very high anorthite content group of between  $An_{92-95}$  (7 crystals) and another lower anorthite group of  $An_{59-65}$  (3 crystals). The higher and lower anorthite groups of GU4 lie at  $An_{92-96}$  (12 crystals) and  $An_{59-66}$  (2 crystals) respectively. The higher and lower anorthite groups from GU1 and GU4 plot at very similar An contents. GU25 has a group at similarly high anorthite contents ( $An_{85-96}$ ) but the lower group lies between  $An_{41-43}$ . However, the latter group is made up of only two analyses of the 14 crystals analysed for this host lava. Sample GU27 predominantly shows plagioclases between  $An_{60-66}$ , although there is a single phenocryst from this lava exhibiting  $An_{78}$ .

The St. Vincent lavas do not show bimodalities in anorthite content, however, SV20 does exhibit a large range in plagioclase compositions ( $An_{47-90}$ ). SV19 has a smaller range in anorthite content of  $An_{80-92}$  but exhibits much higher anorthite contents than those seen in the former St. Vincent sample (with the exception of one  $An_{90}$  analysis in the SV20 thick section). SV31 plagioclases show relatively high anorthite contents, with analyses between  $An_{67-88}$ . SV3 shows lower An contents between  $An_{47-63}$ .

The Bequia lava plagioclases all show very high anorthite contents (BQ2 An<sub>92-96</sub>, BQ5 An<sub>88-96</sub>, BQ19 An<sub>71-97</sub> and BQMT3 An<sub>93-96</sub>). The ranges observed for BQ2, BQ5 and BQMT3 are much lower than those seen elsewhere in the arc. The lower anorthite values observed in the BQ19 plagioclases all originate from the rims of crystals analysed in thick section.

Using the thick section analyses it is possible to couple An variations with pre-determined textural populations (Table 4-4). However, due to the problems identifying textures (and thus populations) in the crystal mount and resin block plagioclases these observations are made on thick section crystals only, consequently n is smaller.

<b>Population (Table 4-2)</b>	<b>An Range All (mol%)</b>	<b>An Range Core (mol%)</b>	<b>An Range Intermediate (mol%)</b>	<b>An Range Rim (mol%)</b>
<b>GU25-a</b>	89-95	94-95	-	89-91
<b>GU25-b</b>	83-95	88-95	-	83-86
<b>SV19-a</b>	83-91	83-91	-	84-86
<b>SV19-b</b>	80-87	-	-	80-87
<b>SV20-a</b>	45-74	45-68	47-54	70-74
<b>SV20-b</b>	72-90	90	-	72-74
<b>BQ19-a</b>	74-96	91-96	87-95	74-93
<b>BQ19-b</b>	71-96	87-95	93-95	71-96

**Table 4-4 Anorthite ranges in the thick section analyses separated by population (determined by textural analysis as shown in Table 4-2). Within each population, the whole range of anorthite contents is shown before being subdivided into core, intermediate and rim analyses.**

The majority of the populations analysed in thick section agree with Pichavant et al. (2002a) and Coulon et al. (1984) in that the highest An contents are found in the cores of the crystals. However, reverse zoning, as also observed in some crystals by Arculus and Wills (1980) and Tollan et al. (2012), is apparent in SV20-a. In terms of anorthite variation across crystals, Tollan et al. (2012) comment on very low fluctuations in An content between cores and rims (less than 1 mol% An), whereas the thick section data from this study show ranges up to 22 mol%.

The thick section analyses from GU25 show higher An contents in the cores than in the rims of the plagioclases in both populations. There is no bimodality present in the GU25 thick section analyses. Rim analyses were performed on the thick section crystals and no anorthite contents as low as the two crystals seen in the crystal mounts were observed. This suggests that the two low An crystal mount analyses are evidence of bimodality and do not merely reflect lower anorthite contents at the rims of crystals.

Anorthite content in both St. Vincent host lavas are comparable in crystal mounts and thick sections. In SV19-a the core analyses show a larger range in anorthite content than the rim analyses (with the rim An contents being within the range observed in the cores). Due to the corrosion in the cores of the SV19-b crystals, only rim analyses were obtained. The SV19-b crystals show similar anorthite contents to those seen in SV19-a. The SV20-a plagioclases analysed in thick section show higher An contents at the rims than in the cores of the crystals. However, population SV20-b shows the reverse, with the lone core analysis being at An<sub>90</sub> and the rims exhibiting contents of An<sub>72-74</sub>.

The range of An contents for BQ19 is much larger in the thick section plagioclases (An<sub>71-96</sub>) compared to that of the separates (An<sub>90-97</sub>). The lower anorthite contents (<An<sub>88</sub>) in the thick section analyses are rim analyses. Thus it is possible that the true variation in An contents in the remaining Bequia lava plagioclases is higher but only cores have been analysed in the separates. Both populations show similar ranges in anorthite contents.

#### **4.4.2 Sr**

If whole rock bulk  $K_D^{Sr}$  does not exceed 1, published partition coefficients suggest that plagioclase Sr contents should increase with decreasing anorthite contents (Bédard, 2006, Bindeman & Davis, 2000, Bindeman *et al.*, 1998, Blundy & Wood, 1991).

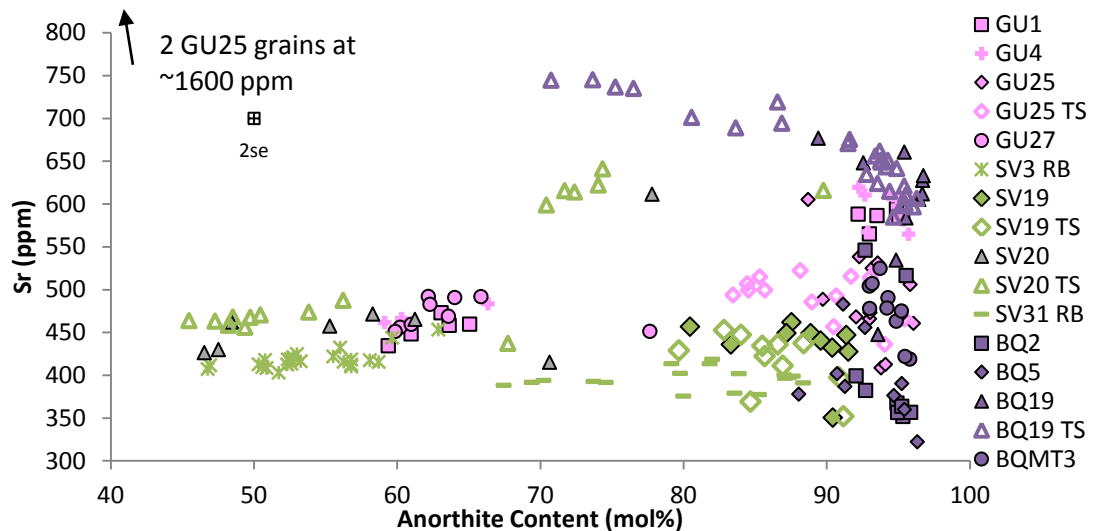


**Figure 4-6 Sr concentrations against anorthite contents for the analysed plagioclase crystals. Two GU25 crystals are not shown but lie at  $An_{41}$  and  $An_{43}$  with Sr concentrations of 1678 and 1694 ppm respectively.**

Figure 4-6 shows that the majority of the Lesser Antilles plagioclase populations do not follow this trend. At high anorthite contents ( $>An_{90}$ ) there is a large range in Sr (322-675 ppm) at essentially invariant An. The high anorthite crystals are predominantly from Bequia and Guadeloupe. Bequia plagioclases encompass the whole 322-675 ppm range, with Sr variation in individual lavas of between 94 ppm and 161 ppm. The Guadeloupe crystals show a smaller range in Sr concentrations between 409-620 ppm at  $>An_{90}$ . GU25 exhibits a similar Sr range to that seen in high anorthite Bequia plagioclases and lies at intermediate Sr. The variation in GU1 and GU4 are smaller at 29 and 54 ppm respectively. The St. Vincent crystals from SV19 exhibit an Sr range of 351-447 ppm at high anorthite contents.

At  $An < 90$  there are two main trends - a high Sr trend which shows increasing Sr with decreasing anorthite content (mainly BQ19 thick section analyses) and a low Sr trend which exhibits little overall Sr variation as An content decreases. However, individual host lavas at low Sr show distinct trends, commonly of decreasing Sr.

In contrast to the majority of the Bequia lavas, BQ19 shows a large range in An content extending down to  $An_{71}$ . The lower anorthite plagioclases are found in the thick section analyses only and are confined to the lower anorthite rims of crystals (all analyses  $<An_{88}$  in BQ19 being rim analyses). The BQ19 plagioclases show increasing Sr as anorthite contents decrease (below  $An_{90}$ ). The thick section analyses from GU25 extend to lower An ( $An_{95-83}$ ) than the majority of the GU25 crystal

mount plagioclases. There are two anomalously low anorthite GU25 crystals at An<sub>43-41</sub> with very high (~1600 ppm) Sr concentrations. The GU25 thick section analyses do not show an associated change in Sr as anorthite content decreases. GU1 and GU4 exhibit populations with the lower anorthite groups showing similar ranges in An content (An<sub>66-59</sub>) and Sr (434-483 ppm) with clear positive correlations between anorthite content and Sr concentration. GU27 is not bimodal but shows similar anorthite (An<sub>66-60</sub>) and Sr contents (451-492 ppm) to the lower anorthite GU1 and GU4 plagioclases.

At high anorthite contents, SV19 shows relatively constant Sr concentrations (approximately 500 ppm) between An<sub>92-80</sub>, as does SV31 between An<sub>88-67</sub> (approximately 400 ppm). The SV3 and most SV20 crystal mount analyses appear similar in terms of anorthite content (An<sub>63-47</sub> and An<sub>61-47</sub> respectively) and Sr concentrations (403-453 ppm and 426-472 ppm). These crystals also exhibit similar Sr at a given anorthite content to the lower anorthite Guadeloupe plagioclases. The SV20 thick section analyses are bimodal in terms of both anorthite content and Sr concentrations. The lower anorthite group of SV20 show similar anorthite contents to the SV3 and SV20 crystal mount analyses but show slightly higher Sr concentrations (456-488 ppm). This group is composed of core and intermediate analyses. The higher anorthite (An<sub>74-70</sub>) SV20 group is mainly composed of rim analyses and shows much higher Sr contents than the other plagioclases from St. Vincent at a similar anorthite content (50% higher). In addition, the higher anorthite group show a trend of decreasing Sr with decreasing anorthite content, in contrast to the lower anorthite group which show relatively consistent Sr concentrations.

Overall it can be seen that Guadeloupe and Bequia are dominated by high anorthite (>An<sub>90</sub>) plagioclases with large ranges in Sr. St. Vincent is mainly composed of lower anorthite plagioclases and shows negative correlations between An content and Sr. Greater variations in both anorthite content and Sr concentrations are seen in the thick section analyses due to both core and rim material being targeted.

### 4.4.3 K<sub>2</sub>O and Rb

K<sub>2</sub>O and Rb are both alkali metals and hence show similar trends against anorthite content (Figure 4-7).

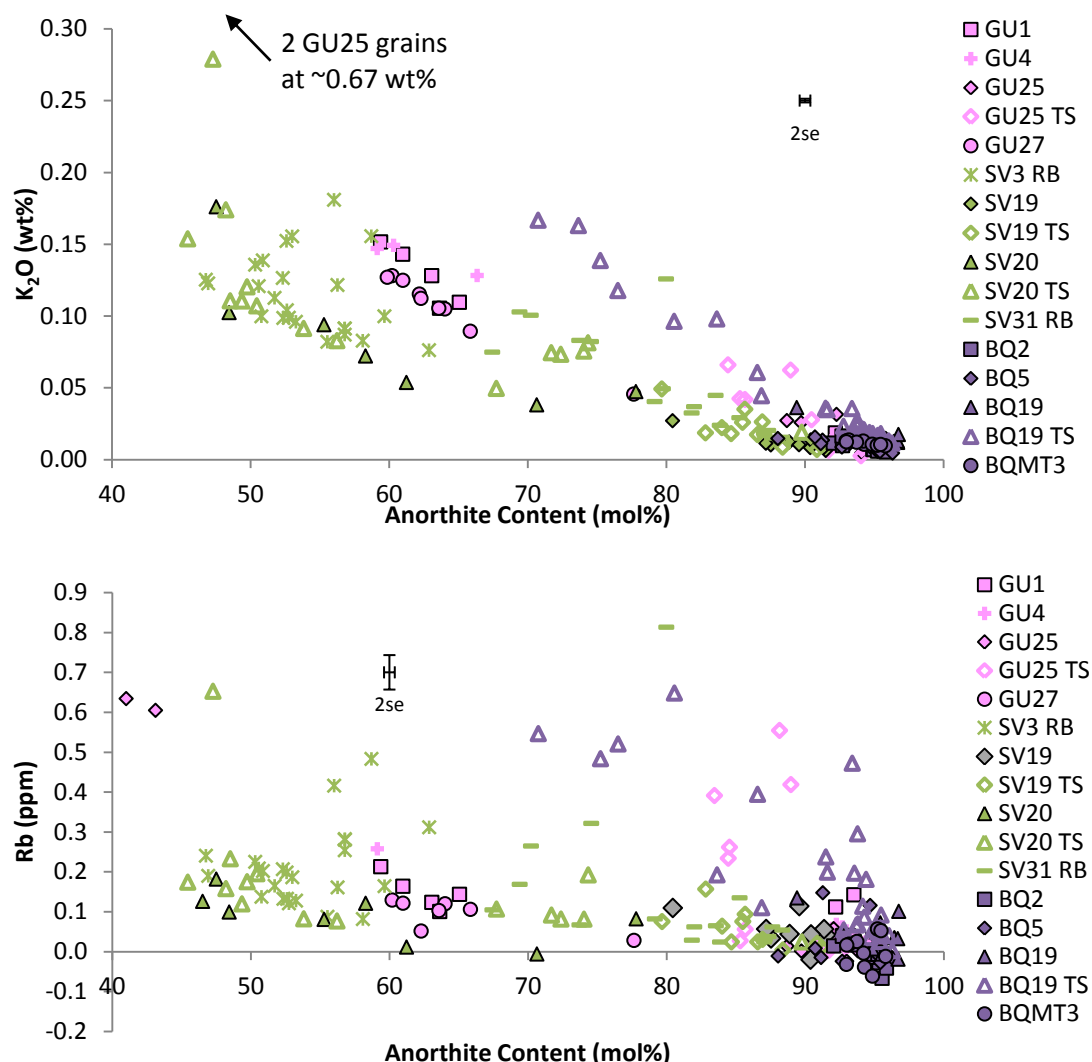


**Figure 4-7 K<sub>2</sub>O and Rb concentrations versus anorthite contents. Negative values appear on the Rb graph as concentrations were so low as to approach detection limits for the LA-ICP-MS.**

Absolute concentrations of Rb are lower than those of K<sub>2</sub>O, with relative uncertainty in the Rb measurements being 17 times greater than for K<sub>2</sub>O. As a result, there is a greater degree of scatter in the Rb graph than in both the Sr and K<sub>2</sub>O graphs. In addition, with the Rb concentrations in some plagioclases being so low, detection limit issues occur, giving rise to apparent negative concentrations of Rb (Figure 4-7). Therefore, despite data appearing with negative concentrations, these are considered to be analytical artefacts and will not be considered further. In contrast to the Sr

analyses, the ranges observed in K<sub>2</sub>O and Rb at high anorthite contents (>An<sub>90</sub>) are smaller (0.005-0.018 wt% K<sub>2</sub>O and 0-0.15 ppm Rb in the Bequia crystal mounts). In order to compare the relative size of the ranges in the analysed elements at >An<sub>90</sub> successfully, the influence of absolute concentration needed to be removed. To do this, the ranges of the analysed elements at An<sub>90</sub> were ratioed to the ranges observed across the whole anorthite range. Firstly, to eliminate outliers, the interquartile range of the data for each element analysed was calculated across the whole anorthite range. The interquartile range was then calculated for only the plagioclases with anorthite contents >An<sub>90</sub>. The two ranges were then ratioed, as in Equation 4-1.

**Equation 4-1**

$$> An_{90} \text{ Range/All An Range} = \frac{\text{Interquartile Range } > An_{90}}{\text{Interquartile Range All An}}$$

Figure 4-8 shows how the relative size of the ranges in measured concentrations in the high anorthite plagioclases varies between elements. The Sr data exhibit the largest range at >An<sub>90</sub> of all the elements measured, whereas K<sub>2</sub>O shows the smallest ratio.

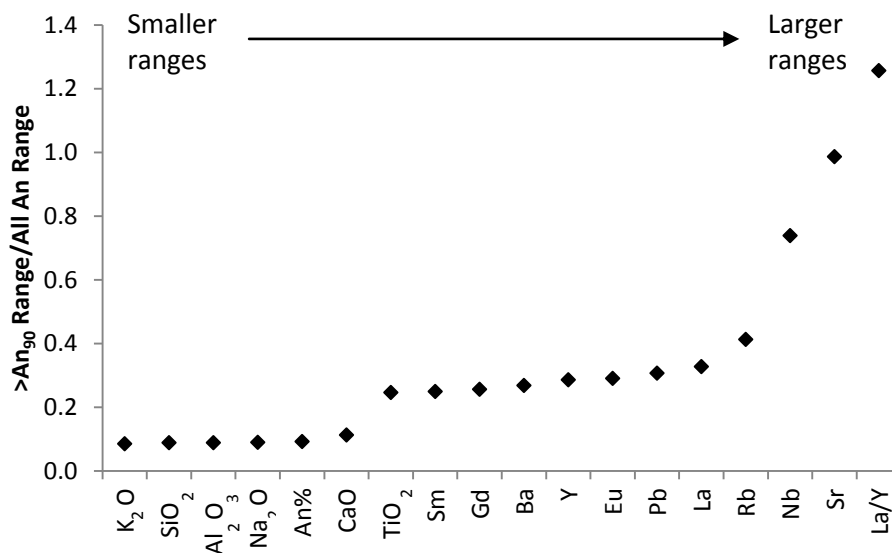


**Figure 4-8 Ratios of the interquartile ranges of concentrations for the measured elements between those crystals with >An<sub>90</sub> and all the plagioclase crystals.**

The BQ19 rim analyses (<An<sub>88</sub>) exhibit higher K<sub>2</sub>O and Rb than the St. Vincent plagioclases at constant An. In addition, all the plagioclase populations, with the exception of the higher anorthite group from the SV20 thick section, exhibit clear correlations of increasing K<sub>2</sub>O and Rb with decreasing anorthite content. The higher

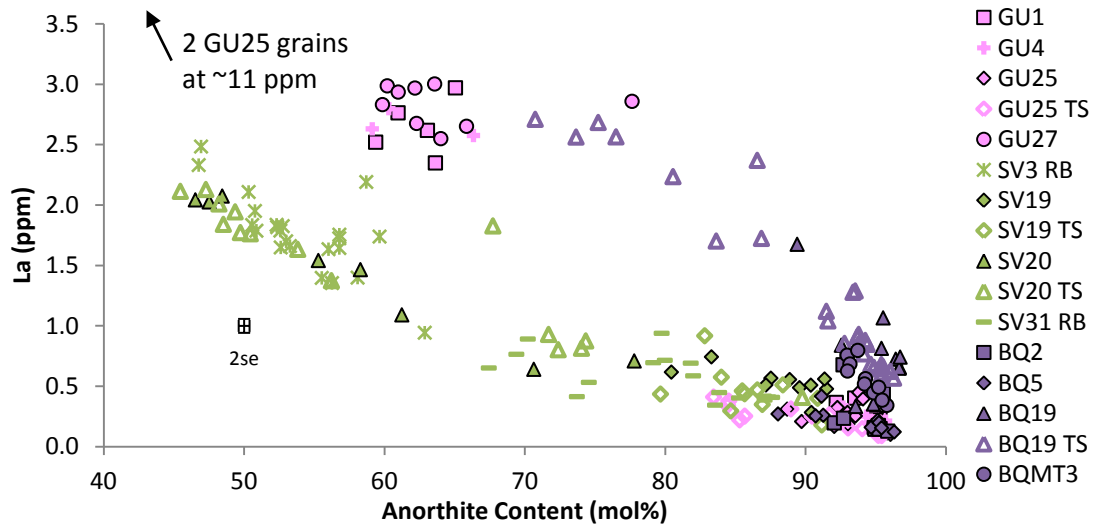
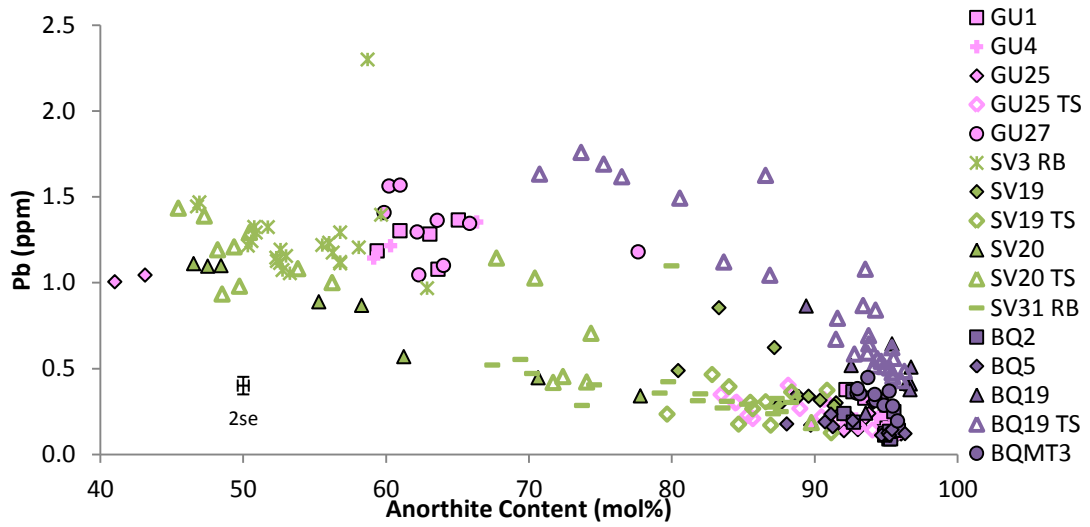
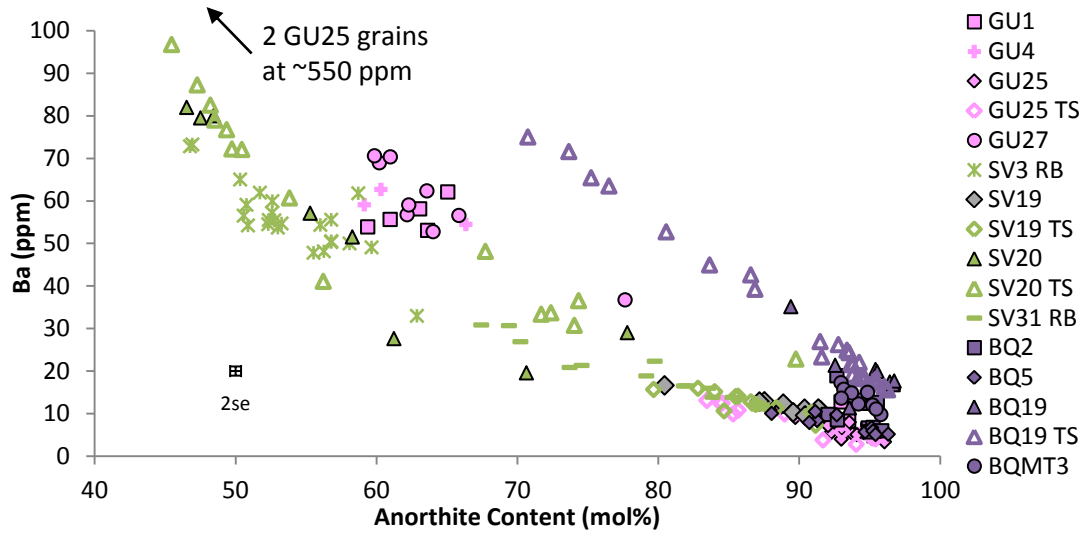
SV20 thick section group shows minimal change in K<sub>2</sub>O with a decrease in anorthite content above An<sub>50</sub> but does show an increase in Rb.

In terms of the lower anorthite populations (SV3, SV20, GU27 and the lower An groups of GU1 and GU4), Guadeloupe plagioclases generally show higher concentrations of K<sub>2</sub>O and Rb at a given anorthite content than the St. Vincent crystals. As observed in the Sr data, the An<sub>41-43</sub> plagioclases from GU25 show apparently anomalously high K<sub>2</sub>O contents; whilst their Rb concentrations are higher than the majority of the St. Vincent analyses at a similar anorthite content (0.62 and 0.73 wt% compared to ~0.16 wt%) they are comparable to the low An BQ19 thick section analyses at approximately 0.6 ppm.

K<sub>2</sub>O contents of plagioclases published by Parkinson et al. (2003), Pichavant et al. (2002a) and Coulon et al. (1984) are comparable to those in the Lesser Antilles plagioclases analysed as part of this study at a given anorthite content. Over the range in anorthite contents observed in the plagioclases analysed in this study (An<sub>45-97</sub>), the Parkinson et al. (2003) plagioclases exhibit a range in K<sub>2</sub>O of <0.05-0.27 wt%, the Pichavant et al. (2002a) crystals show K<sub>2</sub>O contents of 0-0.17 wt% and the Coulon et al. (1984) plagioclases have concentrations of 0-0.34 wt%. The crystals from this study exhibit K<sub>2</sub>O contents of 0.003-0.279 wt%.

#### **4.4.4 Ba, Pb, La and Eu**

Whilst Ba and Pb are also LILE, they behave differently to Sr, Rb and K<sub>2</sub>O and show variations more similar to those seen in La and Eu (an LREE and an MREE respectively) (Figure 4-9). However, the Pb data exhibits flatter correlations when compared to the other three elements at <An<sub>70</sub>.



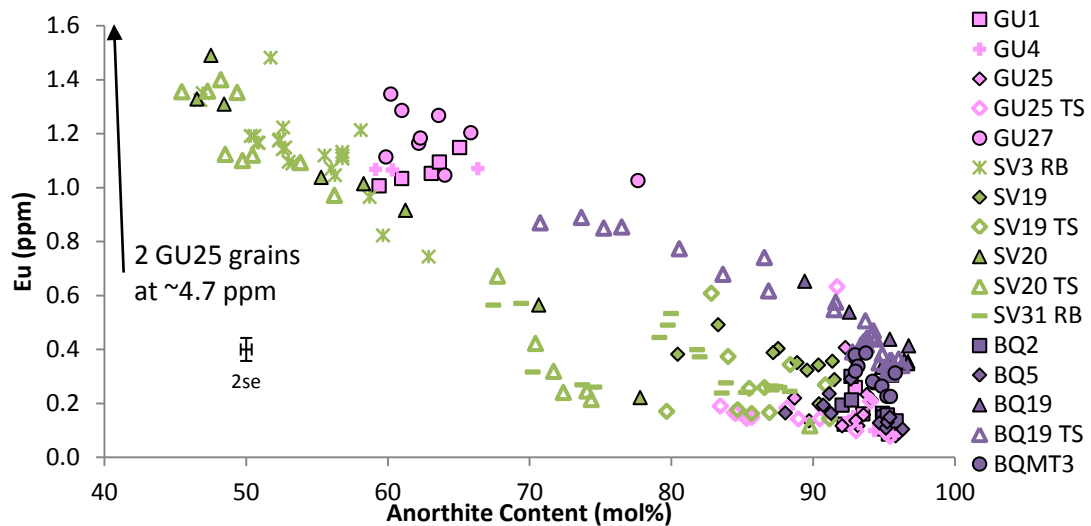


**Figure 4-9 Ba, Pb, La and Eu concentrations versus anorthite content in the analysed plagioclases in crystal mounts, thick sections and resin blocks.**

The ranges seen in La, Eu and Ba are narrower than that observed in the Sr analyses. At  $>An_{90}$ , Figure 4-8 shows the ranges of La, Eu, Ba and Pb are of similar magnitude.

There are general increases in Ba, Pb, La and Eu with decreasing anorthite content, with tight correlations observed in some host lavas. Between  $An_{90}$  and  $An_{67}$  there are two strong negative correlations. One consists of BQ19 (thick section and crystal mount plagioclases) and lies to higher concentrations of Ba, Pb, La and Eu at a given An than the other correlation comprising GU25, SV19, SV20 (both thick section and crystal mount analyses), SV31 and BQ5. Below  $An_{67}$ , there are no plagioclases from BQ19. The Guadeloupe plagioclases at  $<An_{70}$  show relatively constant concentrations of Ba, Pb, La and Eu with no real positive or negative correlation as anorthite content decrease.

The BQ2 and BQ5 plagioclases show concentrations more similar to the St. Vincent crystals at high anorthite contents and four times lower than the remaining Bequia plagioclases. All the analysed populations bar the higher An content group from the SV20 thick sections and the lower An groups from GU1 and GU4 show increasing concentrations of La, Eu, Ba and Pb as anorthite content decreases. However, n for the higher An SV20 thick section group is small. The high An SV20 group shows largely invariant concentrations of La, Eu, Ba and Pb as An content is reduced, although there is one analysis at  $An_{90}$  which exhibits lower concentrations than the remaining high An SV20 thick section plagioclases. The lower anorthite groups of

the bimodal Guadeloupe host lavas show generally positive correlations of La, Eu, Ba and Pb for GU1 and negative correlations for GU4 when compared to anorthite content.

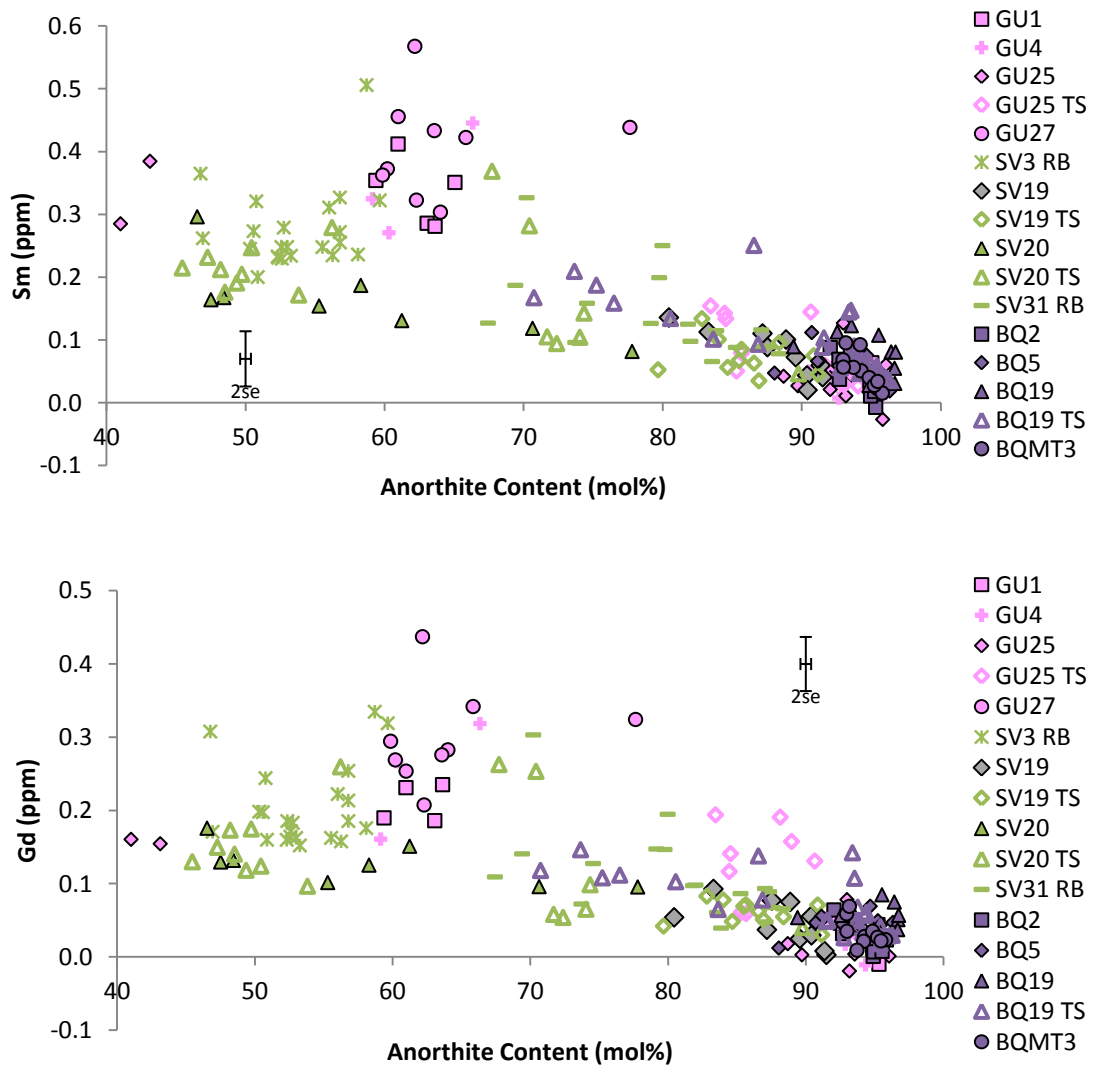
At lower anorthite contents ( $<An_{67}$ ), the Guadeloupe crystals show higher La, Eu, Ba and Pb concentrations than the St. Vincent plagioclases at a given An content, most notably in La contents where the difference between plagioclases from the two islands is up to 102% despite little variation in An content. The Eu data show higher concentrations in the Guadeloupe plagioclases than the BQ19 crystals. Although these plagioclases do not share the same anorthite contents, the previously discussed elements have all shown the highest concentrations to occur in BQ19. The SV20 thick section analyses at lower An contents show higher concentrations of La, Eu and Ba than the higher anorthite group. The two low anorthite Guadeloupe crystals show much higher concentrations than their nearest anorthite content counterparts in La, Eu and Ba but not Pb. The  $\sim An_{40}$  Pb concentrations in GU25 are comparable to the St. Vincent crystals at approximately 1.0 ppm.

Pb behaves differently at anorthite contents below  $An_{70}$  compared to Ba, La and Eu. At low anorthite contents, the Guadeloupe crystals exhibit lower concentrations than the BQ19 plagioclases (despite the lower An contents of the Guadeloupe analyses), which are more similar to those of the St. Vincent plagioclases. Also, Pb contents of the crystals at  $<An_{70}$  from GU1, GU4 and SV3 are largely invariant with decreasing anorthite content. GU27 and SV20 (crystal mounts and thick sections) show slight increases in Pb at low ( $<An_{70}$ ) anorthite contents.

Turner et al. (2003) provided Ba concentrations from two St. Vincent samples; 19.6 ppm on a single crystal from sample STV 354 (with the average anorthite content of plagioclases from this lava being  $An_{85}$ ) and 10.3 ppm on a crystal from sample WI 1A. When compared to the concentrations of Ba obtained from the analysed plagioclases of similar anorthite content from St. Vincent, the Turner et al. (2003) data, although limited, seem to agree reasonably well (with concentrations of around 15.2 ppm being expected based on an exponential trendline being fitted to the LA-ICP-MS data).

#### 4.4.5 Sm, Gd and Y

Sm, Gd are MREE, with Y behaving similarly to the HREE. With the exception of Y, these elements show more scatter and higher 2 $\sigma$  in the data than those previously discussed (Figure 4-10) as these elements are essentially incompatible in plagioclase (and have low concentrations in magmas), resulting in lower concentrations and thus greater relative uncertainties. The relative uncertainty in the Sm data is 32%, in Gd is 37% and in Y is 11%. As for the Rb data, there are negative values apparent in Figure 4-10 due to the concentrations in some crystals being below the detection limits of the LA-ICP-MS.



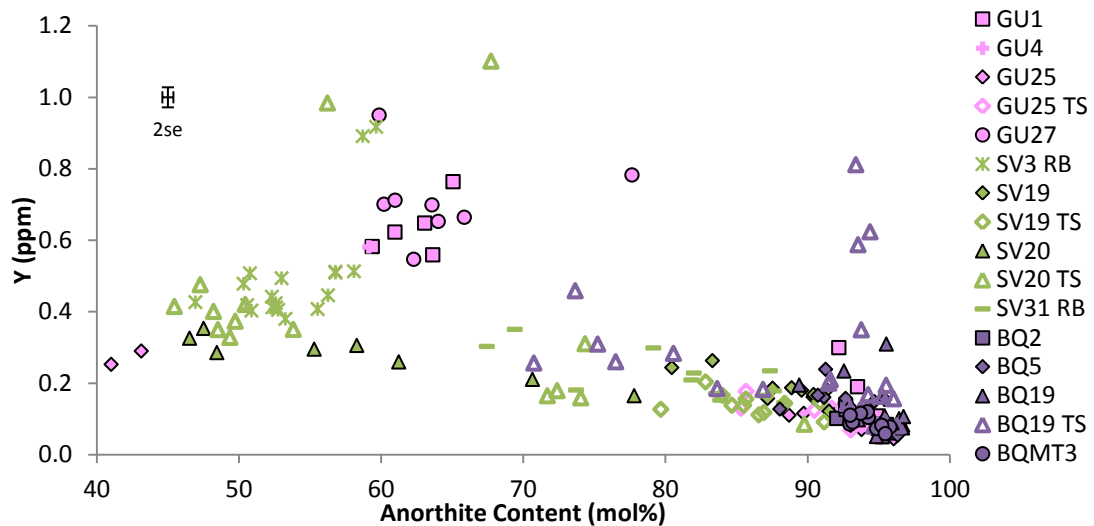


**Figure 4-10 Sm, Gd and Y concentrations in the analysed plagioclases, with Y representing the HREE contents of the Lesser Antilles plagioclases**

The MREE and Y data show similar ranges in concentration at  $>An_{90}$  to those observed for Ba (Figure 4-8). The most prominent variation between Sm and Gd and Y and those elements commented on already is that the plagioclases from all three islands exhibit comparable concentrations at  $>An_{70}$ . All the populations with anorthite contents higher than  $An_{70}$  also show negative correlations. Below  $An_{70}$  the St. Vincent plagioclases continue to exhibit negative correlations, though with more scatter than the higher anorthite crystals. The Guadeloupe analyses at  $<An_{70}$  can show large variations in MREE at similar anorthite contents (e.g. 0.27 ppm range in Sm in GU27). The two  $\sim An_{40}$  GU25 crystals show comparable concentrations to those of the An invariant St. Vincent crystals. For all three elements, the lower anorthite Guadeloupe plagioclases exhibit higher concentrations than seen  $>An_{70}$ .

The SV20 thick section analyses show relatively consistent concentrations in the lower anorthite group. The higher An group exhibits several crystals at lower Sm, Gd and Y and at least one higher concentration analysis. These higher analyses are at least 3 times higher in Sm, 5 times higher in Gd and 2 times higher in Y. These analyses may represent sampling of inclusion material or simply variations in these MREE and HREE in the rims of the crystals.

#### ***Eu Anomalies***

The Sm, Gd and Eu data for each analysed plagioclase were used to calculate the Eu anomalies for each analysis. Positive Eu anomalies are present in all the analysed

plagioclases, as expected due to the  $\text{Eu}^{2+}$  ion being able to substitute into the plagioclase structure more easily than the 3+ valence ions of the remaining REE.

Eu anomalies were constrained numerically for the analysed plagioclases using Equation 4-2, where e.g.  $\text{Eu}_N$  is the analysed concentration of the REE normalised to chondrite using the values of Nakamura (1974).

**Equation 4-2**

$$\frac{\text{Eu}}{\text{Eu}^*} = \text{Eu}_N (\text{Sm}_N \times \text{Gd}_N)^{-1/2}$$

There is a large range in  $\text{Eu}/\text{Eu}^*$  at high anorthite contents ( $>\text{An}_{90}$ ) in samples GU4 (range of 60), GU25 (42), SV19 (71), BQ2 (85), BQ19(33) and BQMT3 (39) (Figure 4-11). Below  $\text{An}_{90}$ , GU1, GU4, GU25 (thick section analyses), GU27, SV3 and SV20 exhibit increases in  $\text{Eu}/\text{Eu}^*$  as anorthite content decreases. The BQ19 thick section analyses at lower anorthite content (i.e. the rim analyses) show decreasing Eu anomalies as An contents reduce. SV19 and SV31 exhibit largely invariant  $\text{Eu}/\text{Eu}^*$  with decreasing anorthite contents.

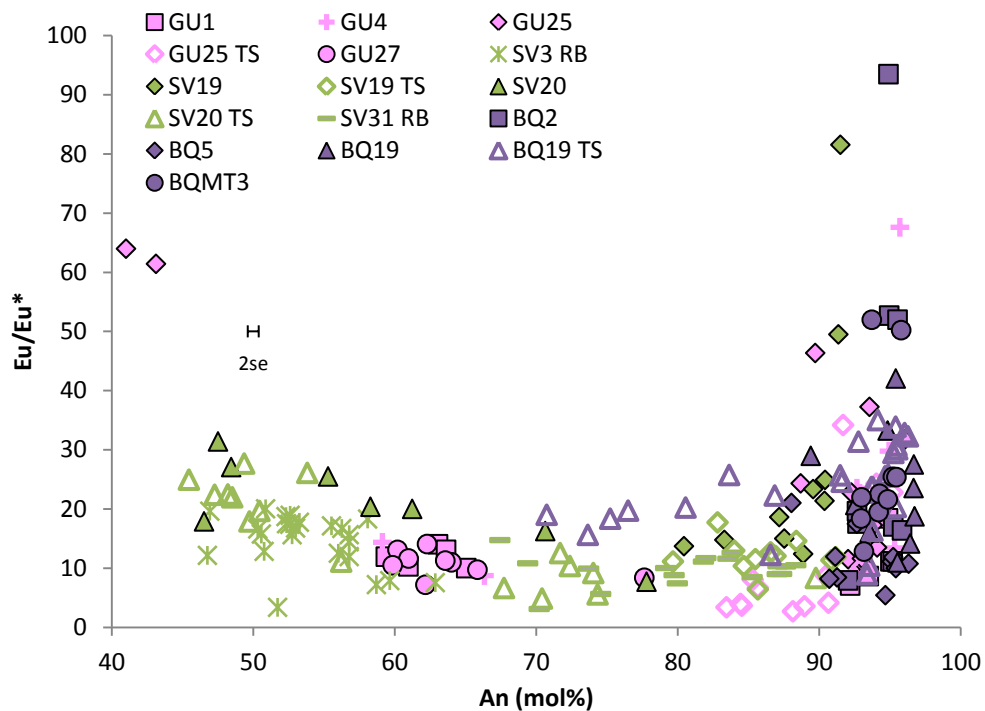


**Figure 4-11** Eu anomalies in the analysed plagioclases.

However, as discussed earlier, there are large relative uncertainties in the Sm (32%) and Gd (37%) contents measured, again due to low concentrations approaching detection limits. This has an effect on the errors on the calculated  $\text{Eu}/\text{Eu}^*$  values. As

a result, those plagioclases with higher An and consequently lower Sm and Gd have much larger errors than those at lower anorthite contents.

#### 4.4.6 TiO<sub>2</sub>

Only TiO<sub>2</sub> and Nb from the HFSE were analysed in the plagioclases, with Nb mainly being used as a measure of whether plagioclase is being sampled rather than any inclusion material (such as a melt inclusion).

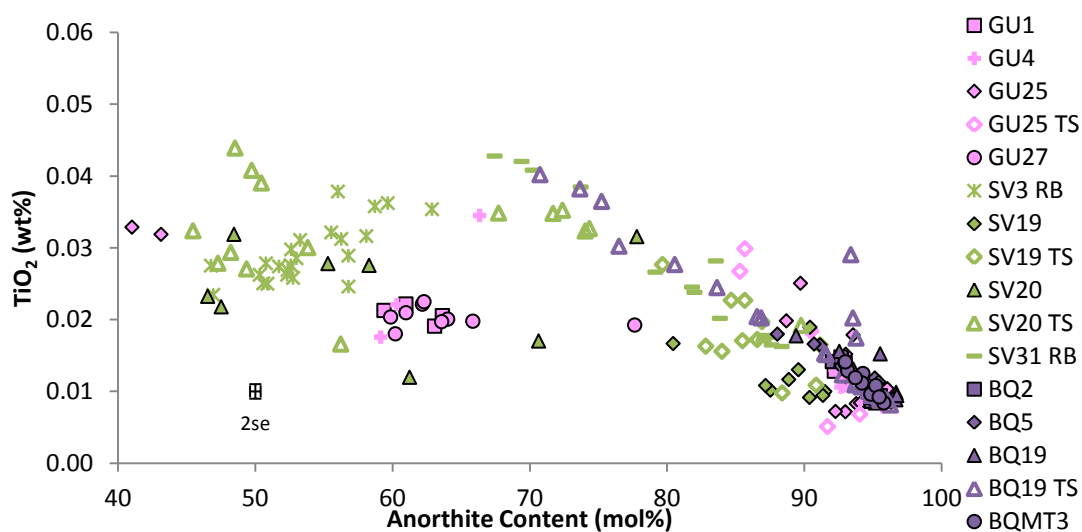


Figure 4-12 TiO<sub>2</sub> contents versus anorthite contents in the analysed plagioclases.

Plagioclases from Bequia exhibit trends of increasing TiO<sub>2</sub> as anorthite content decreases (Figure 4-12). This is particularly evident in the thick section analyses from BQ19, which show lower anorthite rims with higher TiO<sub>2</sub> than the higher anorthite cores. The other Bequia plagioclases lie on a similar correlation to BQ19 with comparable TiO<sub>2</sub> contents at a given anorthite content. The plagioclases exhibit much less variation at high anorthite contents than seen in the LILE (although one BQ19 crystal mount analysis and three thick section analyses do show higher TiO<sub>2</sub> at a given anorthite content than the remaining Bequia plagioclases).

Between An<sub>90-67</sub>, the plagioclases show a trend of increasing TiO<sub>2</sub> concentrations with decreasing anorthite contents. The SV31 crystals show similar TiO<sub>2</sub> concentrations to those seen in the Bequia plagioclases, which was not observed in the LILE data. In the latter, the St. Vincent plagioclases all showed lower concentrations of LILE, particularly at lower anorthite values (<An<sub>90</sub>). At <An<sub>70</sub> plagioclases from St. Vincent lavas shows trends of decreasing TiO<sub>2</sub> with decreasing

anorthite content. This is particularly apparent in the SV3 analyses. The thick section data from SV20 exhibit slightly higher concentrations of TiO<sub>2</sub> in the rims compared to most of the cores. In contrast to the Bequia and high anorthite St. Vincent data (SV19, SV31 and the higher anorthite group of SV20), the lower anorthite St. Vincent data show more evidence of scatter and do not follow such tight correlations.

At >An<sub>90</sub>, GU25 plagioclases show a range in TiO<sub>2</sub> contents which encompasses that observed in all the analysed crystals at a similar anorthite content. As seen in the Pb data, the lower anorthite crystals from GU25 exhibit comparable TiO<sub>2</sub> concentrations to those exhibited by the St. Vincent plagioclases at the closest An contents. The higher anorthite groups from GU1 and GU4 show comparable TiO<sub>2</sub> contents to those at a similar An content from Bequia and St. Vincent. The Guadeloupe plagioclases at higher anorthite contents shows trends of increasing TiO<sub>2</sub> with decreasing anorthite. The lower An groups from GU1 and GU4 exhibit very similar TiO<sub>2</sub> concentrations both to each other and to the GU27 crystals at approximately 0.02 wt%. In contrast to the higher An plagioclases, the lower anorthite Guadeloupe crystals show little variation in TiO<sub>2</sub> concentration with decreasing anorthite content.

In contrast to the K<sub>2</sub>O data, published values (Coulon *et al.*, 1984, Pichavant *et al.*, 2002a) for TiO<sub>2</sub> contents of Lesser Antilles plagioclases extend to higher values than those analysed in this study. No TiO<sub>2</sub> data was provided by Parkinson *et al.* (2003). Over an An range of An<sub>45-97</sub>, TiO<sub>2</sub> concentrations in plagioclases from this study range between 0.0051-0.0439 wt%, compared to 0-0.08 wt% (Pichavant *et al.*, 2002a) and 0-0.20 wt% (Coulon *et al.*, 1984) (however, only one plagioclase from the latter study is found at 0.2 wt%, with the next highest value being 0.05 wt%, meaning the higher value may be an outlier).

#### **4.4.7 MgO and Fe<sub>2</sub>O<sub>3</sub>**

There is a large range in MgO at high anorthite contents (>An<sub>90</sub>) of 0.007-0.198 wt%. However, there are 5 BQ19 thick section analyses that extend between 0.118-0.198 wt% which more than doubles the range (Figure 4-13).

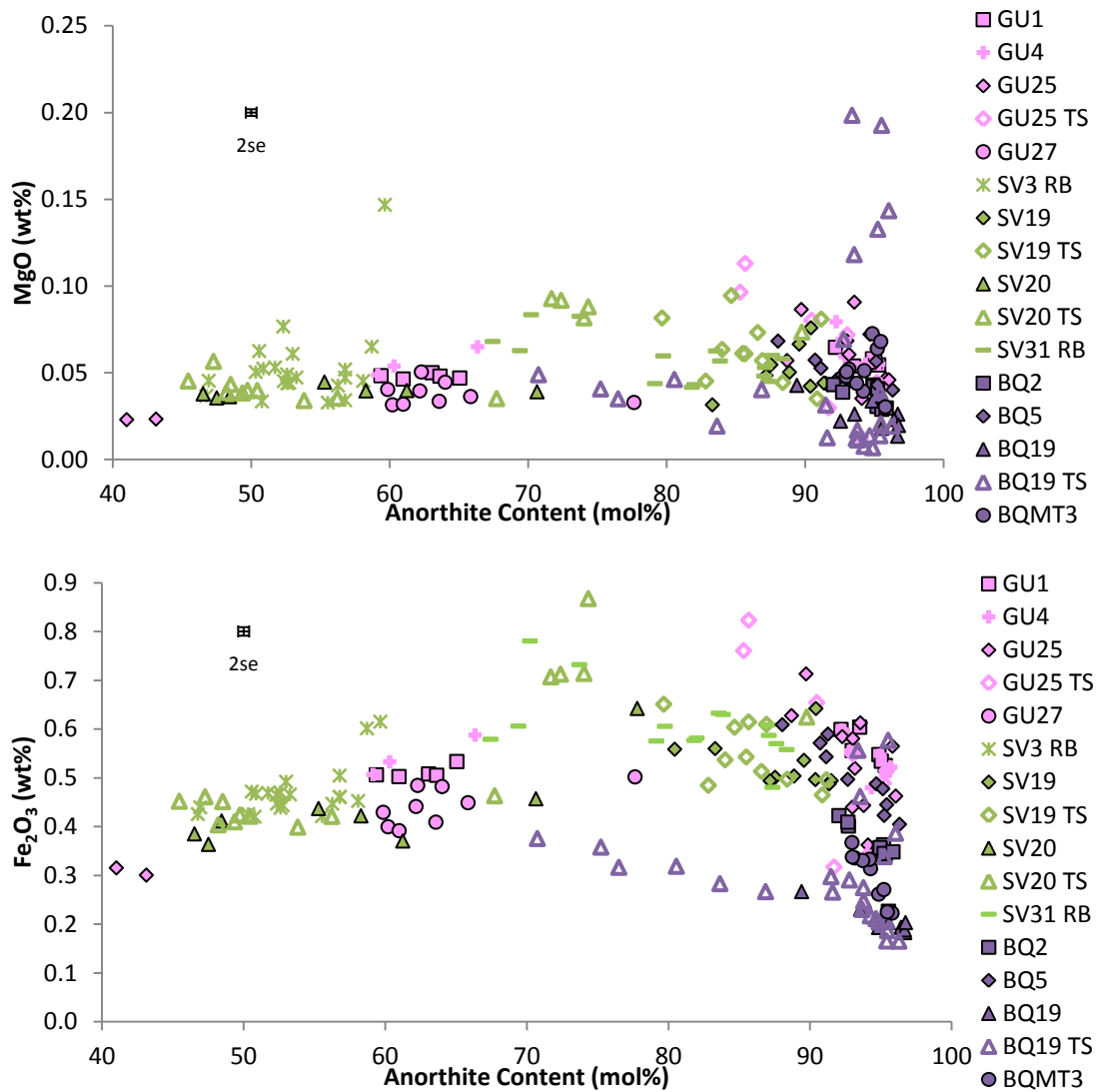


**Figure 4-13 MgO and Fe<sub>2</sub>O<sub>3</sub> concentrations in the Lesser Antilles plagioclases.**

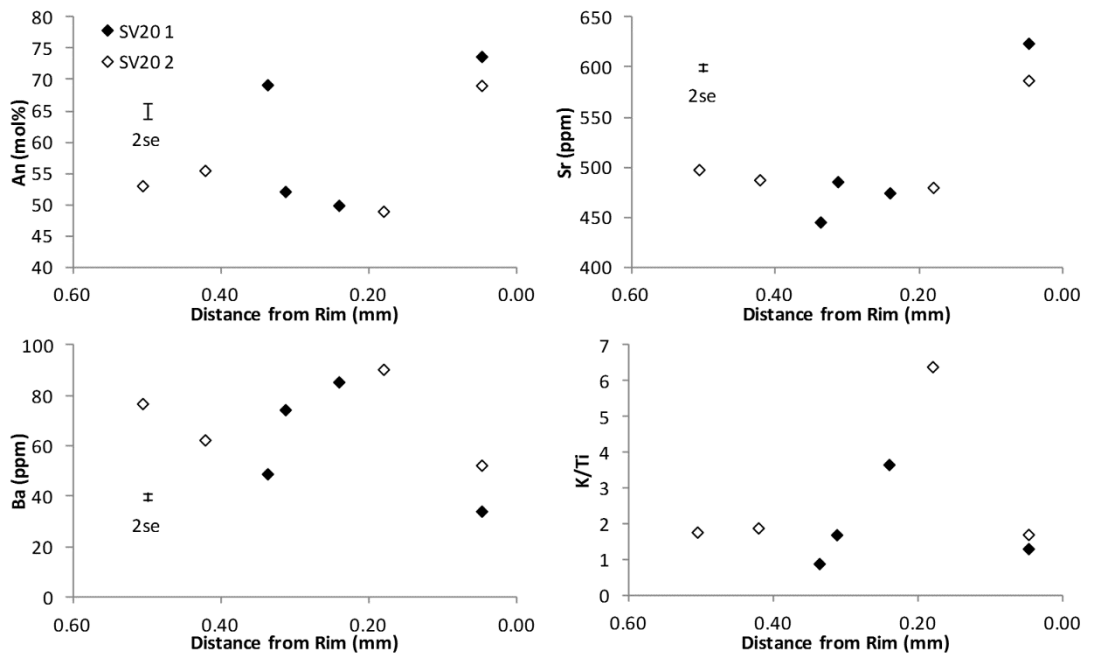
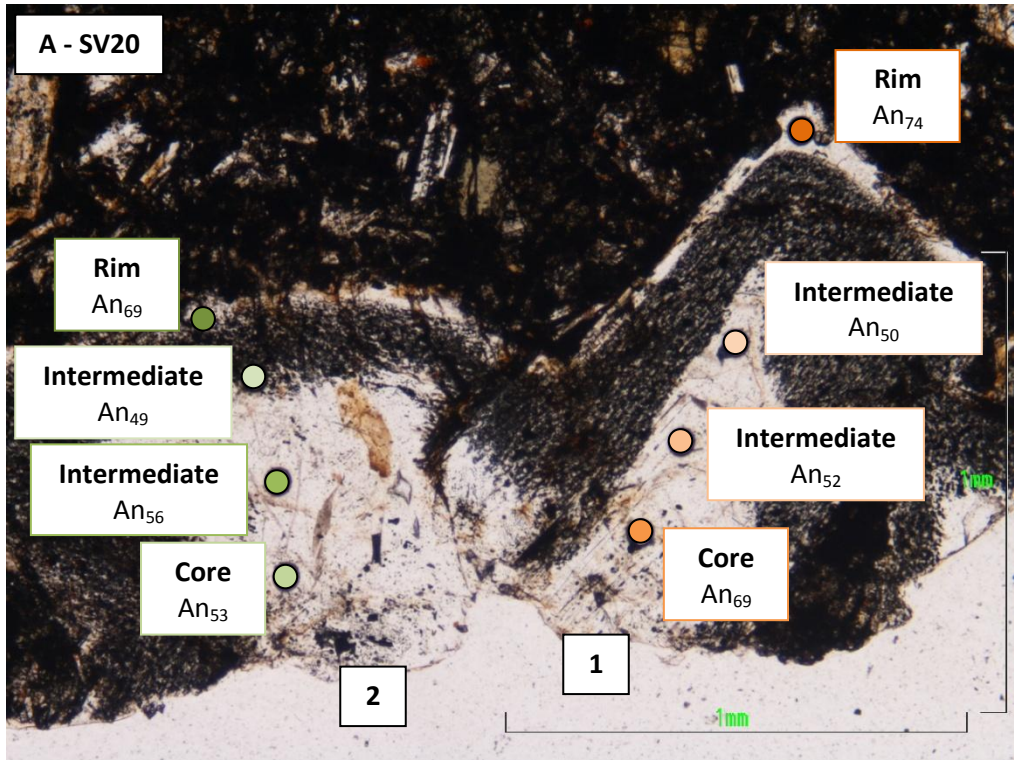
Additionally, other BQ19 crystals show the lowest MgO contents at a given anorthite content, in contrast to their normally elevated concentrations observed in the previously discussed elements. The remaining high anorthite (>An<sub>90</sub>) plagioclases from all three islands show similar ranges in MgO. The higher anorthite group of SV20 exhibits higher MgO and Fe<sub>2</sub>O<sub>3</sub> than the lower An group. This is also true for the higher anorthite groups from GU1 and GU4. Below An<sub>70</sub>, all the plagioclase populations show relatively consistent concentrations of 0.05 wt% MgO with changing anorthite content. The exceptions are the two low An content crystals from GU25 which show lower values than the St. Vincent crystals at comparable anorthite contents (at 0.023 wt%).

MgO data for Lesser Antilles plagioclases was presented by Parkinson et al. (2003), Pichavant et al. (2002a) and Coulon et al. (1984). All three studies show comparable MgO contents to the crystals analysed as part of this study at a given anorthite content. However, no MgO data for plagioclases over An<sub>91</sub> was presented. In plagioclases from this study, >An<sub>91</sub> thick section analyses from BQ19 exhibited the highest concentrations of MgO observed (up to 0.198 wt%). Plagioclase data from Parkinson et al. (2003) exhibit concentrations of <0.09-0.11 wt%, data from Pichavant et al. (2002a) show contents of 0-0.09 wt%, as do plagioclases analysed by Coulon et al. (1984). Crystals from this study below An<sub>91</sub> show MgO concentrations between 0.019-0.147 wt%.

The two low anorthite content GU25 crystals also show lower Fe<sub>2</sub>O<sub>3</sub> concentrations (0.30 wt% compared to 0.40 wt%). Fe<sub>2</sub>O<sub>3</sub> concentrations in the BQ19 thick section plagioclases are also lower than the St. Vincent crystals at constant An, with almost twice as much Fe<sub>2</sub>O<sub>3</sub> as the BQ19 analyses. There is a large range in Fe<sub>2</sub>O<sub>3</sub> at high An contents (0.17-0.61 wt%) although in contrast to the MgO data, only Bequia plagioclases are found in the lower part of the range (under 0.42 wt%). All the plagioclases between An<sub>70-90</sub> display negative correlations. However, below An<sub>70</sub>, the plagioclases show rough positive correlations.

#### **4.4.8 Spatial Variation in Plagioclase Chemistry**

In the thick sections of the St. Vincent and Bequia lavas, there are both normal and reverse zoned plagioclase crystals. Intermediate spots between the core and rim analyses were undertaken in several plagioclases from SV20 and BQ19. These intermediate analyses show that there is not always a simple transition in anorthite contents from core to rim (Figure 4-14). SV20 shows a plagioclase crystal with An<sub>69</sub> in the core, An<sub>52</sub> and An<sub>50</sub> between core and rim and An<sub>74</sub> at the rim of the crystal. Conversely in BQ19, a plagioclase exists with An<sub>95</sub> in the core, An<sub>96</sub> as an intermediate analysis and An<sub>76</sub> at the rim. Also in Figure 4-14, a ratio of K/Ti was used as a potential measure of fluid involvement. K is fluid mobile whereas Ti is fluid immobile, thus increased K/Ti ratios could suggest higher degrees of fluid involvement. The ratio was used to see if there were any perceptible differences in potential fluid involvement across the crystals in Figure 4-14.



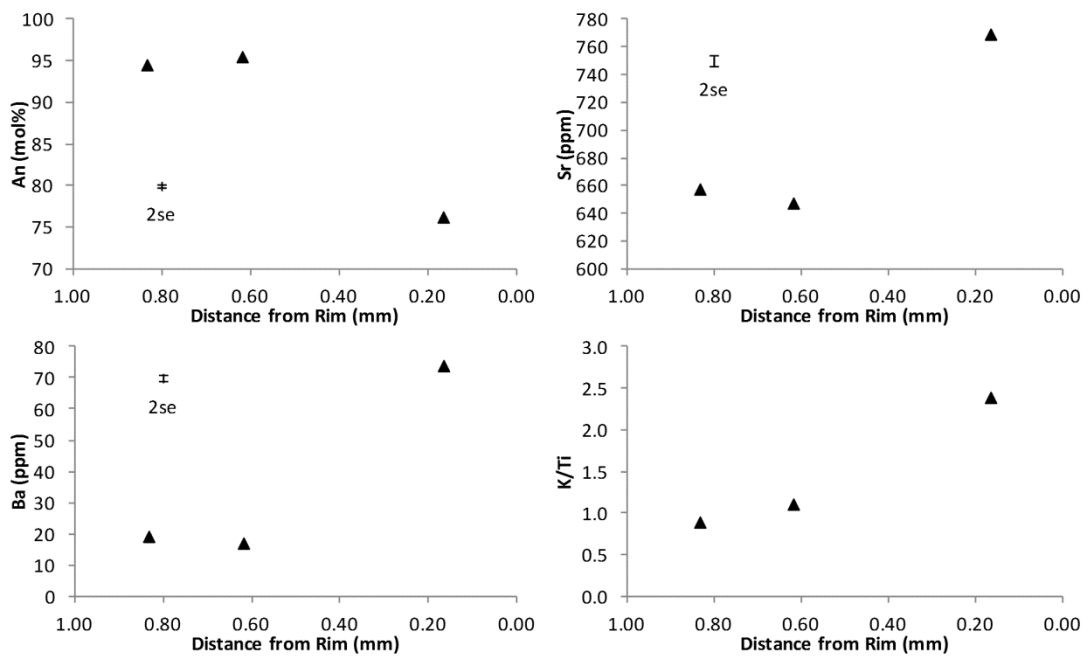
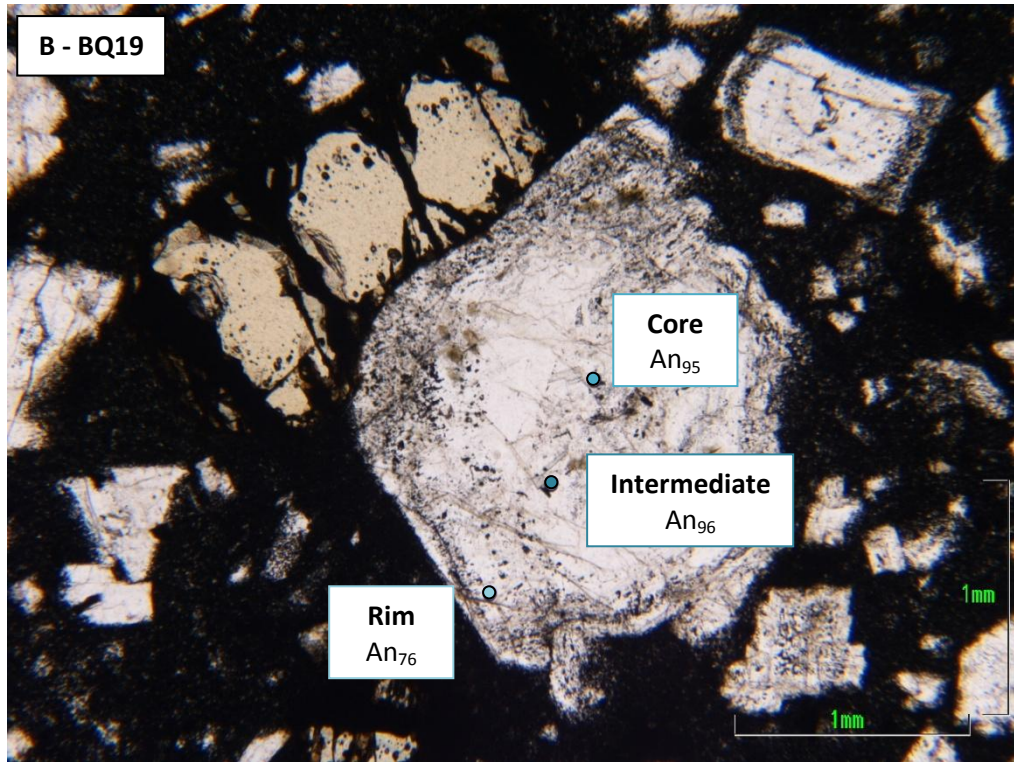


**Figure 4-14 Anorthite variation across crystals from SV20 (A) and one crystal from BQ19 (B). The laser sites are colour graded with the highest An contents being the strongest colours and the lowest An contents being the weakest shades. It can be seen that the anorthite contents do not vary smoothly particularly in the SV20 crystals. K/Ti was used as an indication of fluid involvement, with K being fluid mobile and Ti fluid immobile.**

Figure 4-14 shows that both the BQ19 crystal and the SV20 crystals have higher Sr contents at the rims. The BQ19 plagioclase has lower An at the rim but higher Ba and K/Ti than in the core. SV20 in contrast shows higher An at the rims of the

crystals, K/Ti ratios are similar to the core values and Ba concentrations are lower than those at the cores of the crystals. Given the variations across the crystals, it may be that different conditions and/or different processes are affecting the crystals as crystallisation progresses. Also, as the plagioclases from the different host lavas exhibit contrasting profiles across the crystals, it can be suggested that the conditions/procedural variations observed are different for the separate host lavas.

Table 4-5 shows the ranges in concentrations in the cores and rims of each population identified in thick section.

Element	GU25-a		GU25-b		SV19-a		SV19-b	SV20-a		SV20-b		BQ19-a		BQ19-b	
	Core	Rim	Core	Rim	Core	Rim	Rim	Core	Rim	Core	Rim	Core	Rim	Core	Rim
<b>Sr</b>	436-470	486-516	457-522	494-515	352-453	369-447	411-429	437-488	599-622	616	616-641	607-671	649-745	601-719	585-745
<b>K<sub>2</sub>O</b>	0.003-	0.006-	0.010-	0.042-	0.007-	0.017-	0.026-	0.050-	0.073-	0.019	0.074-	0.011-	0.023-	0.013-	0.013-
	0.007	0.064	0.028	0.066	0.019	0.026	0.049	0.120	0.076		0.081	0.036	0.163	0.061	0.167
<b>Rb</b>	0.004-	0.003-	0.001-	0.027-	0.004-	0.024-	0.031-	0.077-	0.081-	0.024	0.091-	0.002-	0.069-	0.025-	0.035-
	0.009	0.417	0.554	0.391	0.157	0.075	0.094	0.233	0.082		0.192	0.295	0.648	0.394	0.546
<b>Ba</b>	2.8-4.2	3.8-9.9	4.1-8.9	9.9-13.1	7.3-15.9	10.6-	12.2-	41.1-	30.7-	22.8	33.4-	15.6-	21.5-	17.8-	16.4-
						15.1	15.7	79.0	33.7		36.6	26.9	71.6	42.6	75.0
<b>Pb</b>	0.11-	0.20-	0.10-	0.21-	0.13-	0.18-	0.17-	0.93-	0.42-	0.19	0.42-	0.48-	0.64-	0.45-	0.43-
	0.14	0.27	0.40	0.35	0.46	0.39	0.27	1.14	1.03		0.70	0.84	1.76	1.62	1.63
<b>La</b>	0.09-	0.26-	0.09-	0.22-	0.18-	0.30-	0.35-	1.38-	0.80-	0.41	0.88-	0.57-	0.93-	0.61-	0.62-
	0.15	0.31	0.25	0.41	0.92	0.58	0.44	1.84	0.82		0.93	1.12	2.68	2.37	2.71
<b>Eu</b>	0.09-	0.14-	0.08-	0.14-	0.14-	0.18-	0.16-	0.67-	0.24-	0.12	0.21-	0.34-	0.44-	0.31-	0.35-
	0.21	0.63	0.19	0.19	0.61	0.37	0.17	1.12	0.42		0.32	0.55	0.89	0.74	0.87
<b>Sm</b>	0.01-	0.06-	0.03-	0.05-	0.05-	0.06-	0.04-	0.18-	0.09-	0.05	0.11-	0.04-	0.08-	0.03-	0.04-
	0.03	0.10	0.14	0.15	0.13	0.10	0.09	0.37	0.28		0.14	0.09	0.21	0.25	0.17
<b>Gd</b>	0.01-	0.05-	0.02-	0.06-	0.03-	0.05-	0.04-	0.14-	0.05-	0.04	0.06-	0.03-	0.04-	0.02-	0.03-
	0.02	0.16	0.19	0.19	0.08	0.08	0.07	0.26	0.25		0.10	0.07	0.15	0.14	0.12

<b>Y</b>	0.05- 0.09	0.13- 0.87	0.06- 0.12	0.13- 0.18	0.09- 0.20	0.11- 0.17	0.12- 0.16	0.35- 1.10	0.16- 0.18	0.09	0.16- 0.31	0.08- 0.62	0.12- 0.46	0.08- 0.59	0.08- 0.26
<b>TiO<sub>2</sub></b>	0.007- 0.010	0.005- 0.094	0.010- 0.018	0.027- 0.030	0.010- 0.016	0.016- 0.023	0.020- 0.028	0.017- 0.044	0.032- 0.035	0.019	0.033- 0.035	0.008- 0.017	0.011- 0.038	0.009- 0.025	0.009- 0.040
<b>MgO</b>	0.01- 0.05	0.03	0.04- 0.08	0.10- 0.11	0.04- 0.08	0.06- 0.09	0.06- 0.08	0.04- 0.04	0.08- 0.09	0.07	0.09- 0.09	0.01- 0.03	0.01- 0.05	0.01- 0.12	0.02- 0.19
<b>Fe<sub>2</sub>O<sub>3</sub></b>	0.34- 0.49	0.32	0.51- 0.65	0.76- 0.82	0.64- 0.50	0.51- 0.60	0.61- 0.65	0.42- 0.46	0.71- 0.71	0.62	0.71- 0.87	0.17- 0.30	0.25- 0.36	0.19- 0.46	0.21- 0.58

**Table 4-5 Core and rim ranges of the elements analysed separated by population for the thick section plagioclases. No successful analyses of cores of crystals from SV19-b were obtained. Concentrations of trace elements are in ppm and oxides are in wt%.**

## **4.5 Discussion**

The previous section has shown that plagioclase compositions in the Lesser Antilles vary substantially. This section will attempt to determine the petrologic histories of these plagioclases in order to gain a better understanding of the magmatic evolution occurring in the Lesser Antilles. Processes will be discussed in an effort to constrain the causes of the textural and compositional differences observed.

### **4.5.1 Equilibrium Plagioclases**

Anorthite contents of the plagioclases have been plotted against the whole rock  $\text{Ca}/(\text{Ca}+\text{Na}+\text{K})$  ratios of the host lavas from which they originated (Figure 4-15). A regression line was put through the data and it can be seen that few of the plagioclases plot on this trend. There are several issues when comparing mineral data to whole rock chemistry, as detailed already in Chapter 2. Particularly for the plagioclases it can be seen that there are petrographically and chemically distinct populations in the analysed host lavas (Table 4-2 and Table 4-3). Given the number of plagioclases displaying disequilibrium features of varying kinds, it seems unlikely that these plagioclases resulted from equilibrium crystallisation from the host melt. This reinforces the idea that the whole rock hosts a collection of plagioclases resulting from potentially numerous processes and sources. The whole rock then essentially represents a homogenisation of many chemical signatures without necessarily being indicative of the parental composition of any of the plagioclases. Furthermore, if processes such as accumulation have taken place, even if the plagioclases are in equilibrium with the host melt, the whole rock composition will be affected by the excess concentrations of plagioclase compatible elements. Thus comparing mineral compositions to the host rock chemistry may not be particularly useful, particularly as a test for equilibrium.

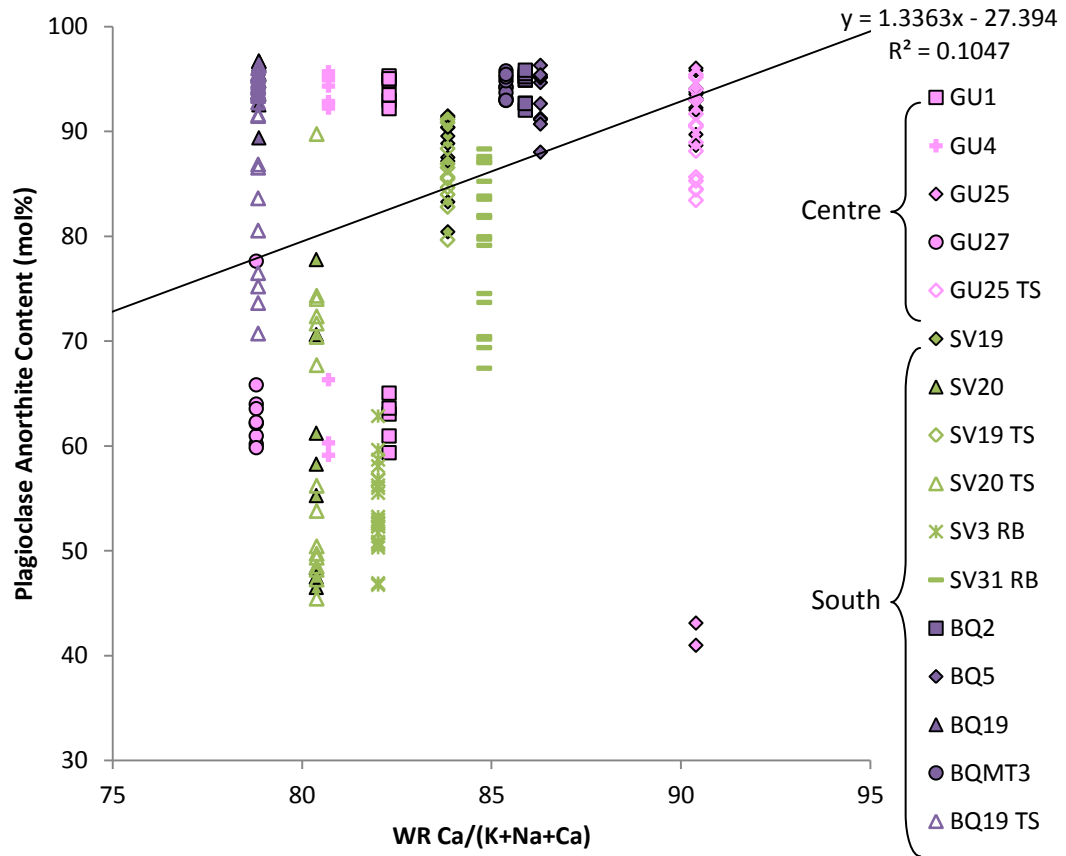


**Figure 4-15** An contents of the analysed plagioclases plotted against the Ca/K+Na+Ca ratio for the whole rocks from which they originated. Samples labelled with TS are thick section analyses, RB are resin block analyses and the remainder are crystal mounted plagioclases. The Guadeloupe samples originate from the centre of the arc and the St. Vincent and Bequia samples are from the south of the arc. The regression line shows a weak positive trend between the sampled plagioclases and the whole rock composition, although the  $R^2$  value suggests this may not be statistically robust.

In addition, there are issues in accurately constraining partition coefficients. Partitioning of Ca and Na between plagioclases and melts can be affected by the melt composition (specifically the CaO/Na<sub>2</sub>O and Al<sub>2</sub>O<sub>3</sub>/SiO<sub>2</sub> ratios), temperature and pressure (Panjasawatwong *et al.*, 1995, Ren *et al.*, 2003, Sisson & Grove, 1993, Takagi *et al.*, 2005). Therefore, in order to utilise suitable values for  $K_D^{Ca-Na}$  (Equation 4-3) it is necessary to have reasonable estimations of all these parameters.

**Equation 4-3**

$$K_D^{Plag-melt}_{Ca-Na} = \frac{(Ca/Na)_{plag}}{(Ca/Na)_{melt}}$$

It has also been suggested in the literature that anorthite contents of plagioclases can be significantly affected by water (Berndt *et al.*, 2005, Feig *et al.*, 2006, Hamada &

Fujii, 2007, Panjasawatwong *et al.*, 1995, Sisson & Grove, 1993, Takagi *et al.*, 2005). Sisson and Grove (1993) postulated that increasing water contents from 2 wt% to 6 wt% increases  $K_D^{Ca-Na}$  between plagioclases and melts from ~1.7 to ~5.5. As the Lesser Antilles is an intra-oceanic subduction zone setting, it is very likely that water will have affected Ca and Na partitioning in the plagioclases. As it is difficult to accurately constrain the conditions under which the plagioclases crystallised, it is also difficult to select suitable partition coefficients to assess whether the plagioclases are in equilibrium.

It can be seen in the thin sections of the Lesser Antilles lavas that there are disequilibrium features present in many of the analysed phenocrysts (Table 4-2 and Table 4-3), which could suggest that the plagioclases are not wholly in equilibrium with the host rocks. However, without accurate values for partition coefficients, the degree of disequilibrium cannot be quantitatively assessed easily. Additionally, not all processes producing textural differences cause accompanying chemical changes (e.g. decompression).

#### **4.5.2 Degassing and Decompression at Shallow Levels**

Degassing and decompression are both processes that take place at shallow levels in the magmatic system. Given that water solubility is dependent on pressure, it follows that degassing and decompression are related. Degassing is a release of volatiles from the system and will affect melt chemistry primarily by changing the water content, but also pH<sub>2</sub>O, changing melt composition and reducing temperature. These in turn also have an effect on partitioning of elements into the plagioclases. Decompression is a change in pressure conditions but may also influence temperature. It can lead to the generation of a pressure gradient within the magma chamber (dependent on the size, height and contrast in pressure at the top and bottom of the chamber) which can affect plagioclases resident in the host melt. Additionally, decompression in water-saturated melts of basaltic composition can prompt plagioclase crystallisation (Cashman & Blundy, 2000).

Published work (Couch *et al.*, 2003a, Couch *et al.*, 2003b) has shown anorthite contents to increase at higher pressures and higher pH<sub>2</sub>O at a given temperature. Additionally, Couch *et al.* (2003a) suggested anorthite contents increase with

increasing temperature. Anorthite contents are thought to decrease with increasing  $\Delta T$  during undercooling resulting from depressurisation and subsequent degassing Couch et al. (2003b).

Both processes produce petrographically similar sieved textures and resorption edges (Renjith, Viccaro *et al.*, 2010) and thus are difficult to distinguish through textural analysis alone.

BQ2 and BQ19 in particular show populations exhibiting fine sieve texturing towards the rims of crystals. In addition, all populations observed (with the exception of those from GU1, GU27 and BQ5) show some degree of partial resorption at the crystal edges, which is likely to be as a result of shallow degassing or decompression (Figure 4-16).

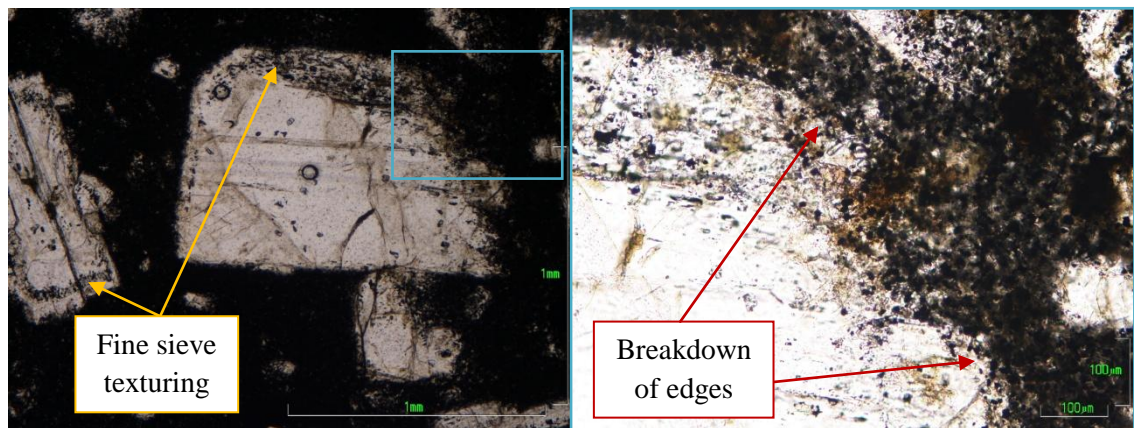


**Figure 4-16 Petrographic evidence of shallow level degassing and/or decompression in crystal BQ19-1. The blue box shows the location of the close up shown in the right hand photograph. Resorption of the crystal edges and fine sieve texturing can be seen in more detail in the larger scale image.**

Decompression during convection within the magma chamber could also produce similar textures, due to pressure changes within the chamber. Convection may cause fine sieving on ascent as pressure decreases, followed by crystallisation of equilibrium material at the top and during descent through the chamber before the cycle is repeated. There is a dependence on residence time within the chamber as more alternating zones of sieved and unsieved material will form with more convective cycles. Only a few populations within the analysed plagioclases show evidence of cyclicity within the disequilibrium features (e.g. GU25-b) and it is difficult to distinguish between convective cycling and repeated inputs of a differing magma composition using textural observations alone. More detailed sampling across the crystals (i.e. more laser sites in each transect or using electron microprobe

analysis for finer scale sampling) may shed light on which process is dominant as decompression prompted sieving should be accompanied by a drop in An contents. Introduction of a differing magma could increase or decrease An contents depending on the composition of the incoming melt.

Decompression in a water saturated system can cause a reduction in anorthite contents and thus could provide a suitable method for generating the more sodic sieve textured areas seen in some of the plagioclase populations. Decompression in a water undersaturated system would prompt the opposite effect, i.e. an increase in An contents (Viccaro *et al.*, 2010), however, as mentioned previously, it is unlikely that the Lesser Antilles system is water undersaturated, being an intra-oceanic subduction zone. Therefore, the higher anorthite rims require another method of generation, such as mixing with a more primitive melt prompting crystallisation of higher An material at the rims of crystals (section 4.5.5).

Decreases in anorthite content at the rims of the crystals would provide further evidence of prolonged degassing (Simakin & Salova, 2004). Figure 4-17 shows the variations in anorthite content between rims and cores of crystals ratioed relative to the core against % distance from the rim (calculated as in Chapter 2).

Using a ratio of  $An/An_{core}$  allows for easy identification of crystals with lower An at the rims of the crystals than the cores. SV20 is the only thick section with crystals with clearly higher An contents at the rims than in the cores. The lone SV20 rim analysis below  $An/An_{core} = 1$  is from the SV20-b population of SV20 plagioclases (Table 4-3) and is highlighted by the arrow in Figure 4-17.

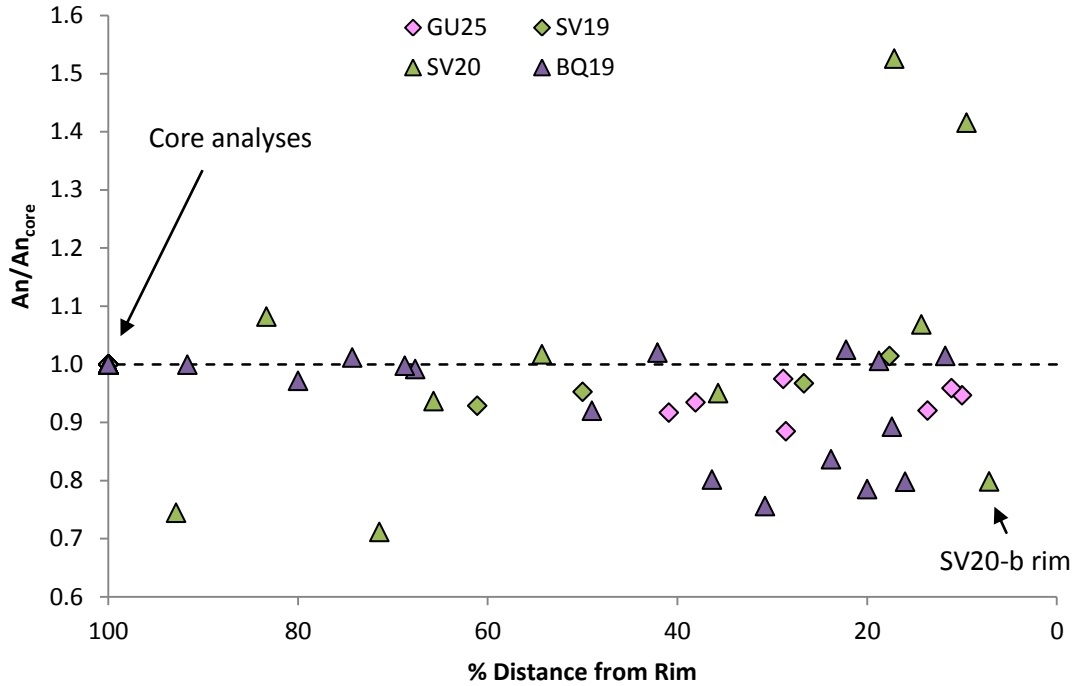


**Figure 4-17** Variations in anorthite content between cores and rims of crystals in the thick section analyses. The dashed line represents  $An/An_{core} = 1.0$ , analyses plotting below this line have lower anorthite contents than the cores of the respective crystals.

However, SV20 does show petrographic evidence of shallow level degassing/decompression, as shown in Figure 4-18. Therefore the lack of lower anorthite contents towards the rims does not preclude shallow level breakdown of the plagioclases in this lava.

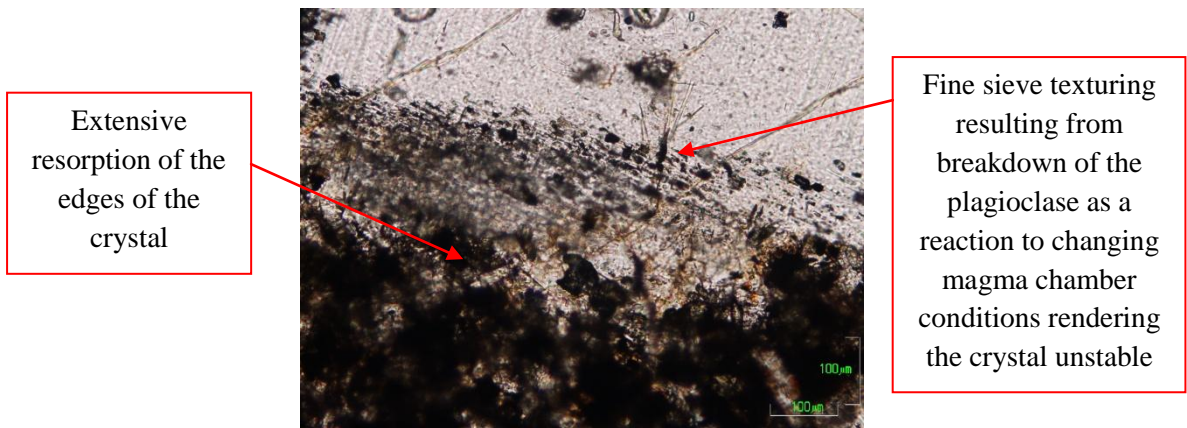


**Figure 4-18** Photograph of SV20-5 showing fine sieve texturing and breakdown and resorption of the crystal edge.

Decompression and/or degassing of the melts after plagioclase crystallisation but prior to eruption of the host lavas could explain some of the disequilibrium textures seen. It is harder to explain why some crystals would appear fresh unless they were

crystallised after any decompression/degassing or the changes in conditions were not sufficient enough to cause disequilibrium features. The third possibility is that the residence time in the host melt following any degassing/decompression event was insufficient for the features to form. The SV19 plagioclases in Figure 4-17 all belong to the fresh appearing SV19-a population (Table 4-3). It can be seen that there is little variation in these plagioclases in An contents between the cores and the rims, suggesting that any decompression/degassing events have had little effect on the chemistry of the crystals, despite petrographic indications of crystal edge resorption.

It seems likely that shallow level degassing and/or decompression played a role in the petrogenesis of nearly all of the plagioclase populations analysed, with the exceptions of GU1, GU27 and BQ5, given the petrographic and compositional evidence. However, degassing and decompression at shallow levels do not explain many of the differences (both textural and geochemical) between plagioclases from different lavas and especially differences between populations from the same lavas.

#### **4.5.3 Plagioclase Response to Magma Ascent From Depth**

Decompression of melts as they ascend through the magmatic plumbing system can cause coarse sieving in plagioclase hosted in the melts. Petrographic observation is the most effective way to establish whether decompression has occurred, particularly as heavily resorbed areas are unlikely to yield good laser analyses, due to contamination of the plagioclase by the recrystallised material.

Coarse sieving can originate due to dissolution caused by reduced plagioclase stability as the melts rise. It is then thought that as further material crystallises, trapped melt forms the characteristic sieve texturing often seen in plagioclase (Nelson & Montana, 1992, Renjith, 2013). Viccaro et al. (2010) suggested that in a water undersaturated system, the density of coarse sieving in plagioclase cores could be related to the rate of ascent. Viccaro et al. (2010) proposed that slower rates of ascent manifest as 'patchy' cores, whilst high decompression rates resulted in dissolved or resorbed cores; intermediate rates were thought to produce coarsely sieved core zones. Given that the Lesser Antilles system is unlikely to be water undersaturated, Viccaro et al. (2010) also proposed that the degrees of dissolution responsible for creating the textures would increase with increasing water contents,

for a given ascent rate. This may suggest that some of the populations observed with obvious signs of disequilibrium in the cores are formed as a result of fast to intermediate rates of magma ascent before stalling in shallow level magma chambers to allow the crystallisation of the fresher appearing rim material.

Not all of the populations exhibit coarse sieve textures. This may be a result of different populations crystallising at varying depths. Plagioclases crystallised at shallower depths may have not travelled sufficiently far to prompt formation of sieving, for example populations which appear 'fresh', such as SV19-a.

Table 4-2 and Table 4-3 provide descriptions of all the populations observed. Those with coarsely sieved or partially resorbed cores are likely to have undergone decompression during ascent (Renjith, 2013, Viccaro *et al.*, 2010). These populations include GU1-a, GU4-a, GU25-b, SV20-b and BQ5-a, which show coarsely sieved cores. GU4-b, GU4-c, GU27-c and SV31-b show some evidence of recrystallisation in the cores but to a lesser extent than the former populations. As the density of the sieving in the centre of crystals has been used in the literature to differentiate between rates of ascent (Viccaro *et al.*, 2010), the denser sieving in the first group of plagioclase populations would suggest a slower rate of ascent than those with lighter core sieving or an increased water content in those melts. Therefore the more densely sieved cores could result from an intermediate rate of decompression, whereas the less densely sieved populations may result from a slow rate of decompression (Viccaro *et al.*, 2010). In the case of GU4, rate of ascent is the control as varying water contents within the same host lava is improbable (although this assumes all the plagioclases in this host lava were crystallised from the same melt).

Geothermobarometric modelling was undertaken using the method of Putirka (2008). This model also provides an approximate hygrometer. However, by the author's own admission, the pressures calculated may not be accurate (Putirka, 2008). Whilst there are inevitably issues with using the whole rock as a proxy for the host melt composition, as discussed previously, the model can at the least provide some qualitative insights. Any analyses which did not satisfy the model's test for equilibrium were removed from the graphs. Figure 4-19 shows the temperature, pressure and water contents of the analysed plagioclases in crystal mounts, thick sections and resin blocks.

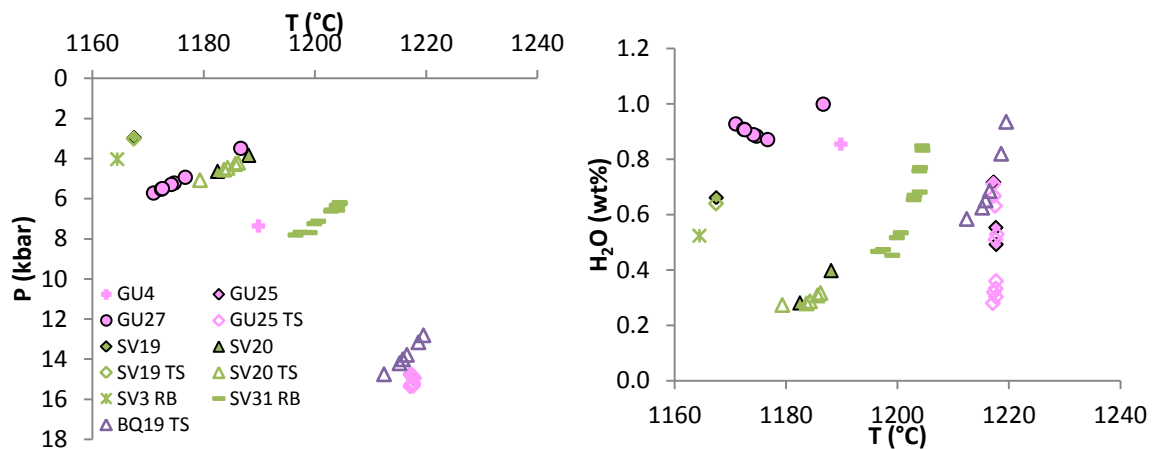


**Figure 4-19 Results from Putirka (2008) modelling using the analysed plagioclase crystals in crystal mounts, thick section and resin blocks.**

Overall there is only a temperature difference of 60°C between the hottest and coolest plagioclase crystallisation temperatures, with Putirka (2008) suggesting a possible error of between 20-30°C in the model. What is more pronounced is the differences in pressure, both between islands and between lavas from the same island. Although the pressures calculated may not be absolute, the variations appear to be significant, the error in the model being estimated at approximately 1 kbar (Putirka, 2008). The GU25 plagioclases appear to originate from the greatest depths (~16 kbar). The GU4 and GU27 crystals plot at approximately half the pressure of the GU25 crystals (4-8 kbar). The St. Vincent plagioclases indicate lower pressures, more similar to the shallower Guadeloupe crystals. The St. Vincent plagioclases appear to range from 3 kbar (SV19) to 6-8 kbar (SV31). Therefore, the model would suggest that different lavas on the islands are being produced at different depths. However, only one lava shows any real degree of bimodality, suggesting different petrographic populations are not exhibiting vastly different P/T conditions. GU27 has one crystal which appears offset from the remainder and this may represent a different population. As GU27 was sampled using separated crystals it is not possible to determine if the crystal does appear different in thin section.

In order to see if there were any obvious differences between populations in the thick sections, these were also plotted separately (Figure 4-20).

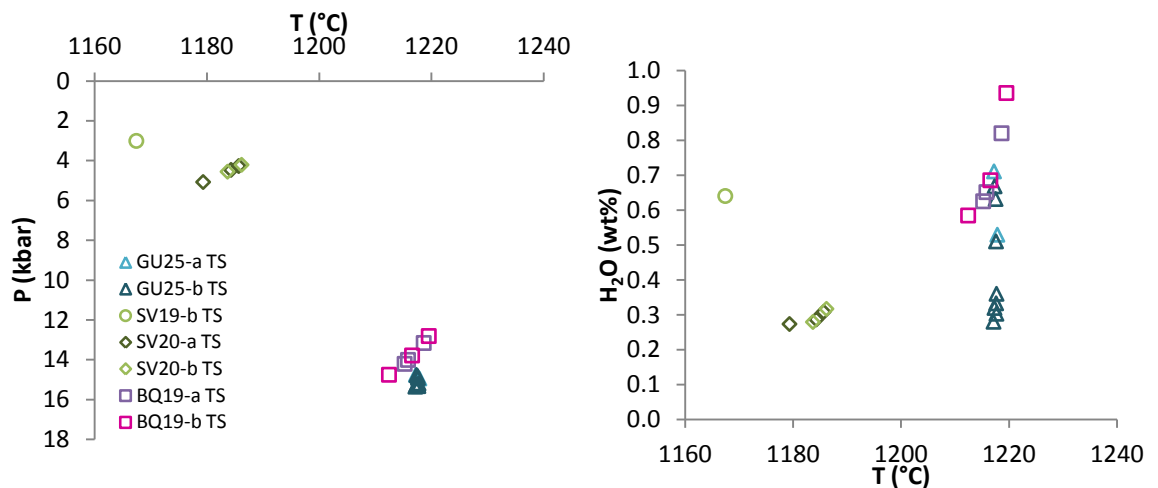


**Figure 4-20 Putirka (2008) modelling for the thick section analyses, separated by population.**

There are no apparent differences between the populations analysed, however, given the accuracy in pressure and temperature estimates from the model (Putirka, 2008) it may be that there are subtle variations which are not detectable by the model.

In terms of water content (Figure 4-19), the model suggests melt water contents of 1 wt% or less for all the analysed plagioclases. Macdonald et al. (2000) and references therein estimate water contents of between 1-2 wt% for Lesser Antilles basalts and approximately 3% for basaltic andesites. The water contents do not seem to show any real correlation with the crystallisation temperatures (or pressures) (Figure 4-19). There are large ranges in water contents at similar temperatures in some of the host lavas (e.g. GU25 and SV31). These ranges seem slightly implausible given that increasing the water content of the melt should lower the liquidus temperature (Couch *et al.*, 2003b).

Overall, whilst the geothermobarometric modelling does highlight differences between the host lavas, there is no distinct correlation between latitude and the pressure and temperature conditions of crystallisation, however, *n* is small so these interpretations are speculative. Additionally, any variations in conditions causing petrographic differences are not apparent in the model.

If the plagioclases have undergone decompression during ascent from depth rather than at shallow levels, they must have been crystallised from the melt prior to ascent to the magma chamber which was tapped during eruption. Those that do not show evidence of decompression during ascent could have crystallised at shallower levels which may not be visible in the modelling. Potential reasons for the latter include the unsuitability of using a whole rock composition as a substitute for parental melt

composition. If the modelling is qualitatively accurate, other possibilities for the differences are the entrainment of crystal cargoes or magma mixing in those lavas where populations both with and without evidence of decompression co-exist. These lavas are GU1, GU25, GU27 and SV20.

#### **4.5.4 Entrainment**

Entrainment is the incorporation of crystal cargoes into a host melt from which they were not originally crystallised. Consequently, the composition and the P/T conditions may be different in the host melt from those of the melts that crystallised the populations being entrained. These crystal cargoes may derive from several sources, the most obvious being the wall rocks of the conduits through which the melts are ascending. Other sources may include cumulate bodies and crystal mush zones at the base of magma chambers. Crystals which have been entrained in the host melt through magma mixing will be detailed in section 4.5.5.

Plagioclase populations deriving from different melts to the host melt, yet from a melt that has followed a very similar evolutionary path could be termed 'antecrysts' (e.g. Davidson et al., 2007). It is possible that the differing populations seen in some of the Lesser Antilles lavas are antecrysts crystallised from melts genetically related to the host. These crystals may then have been incorporated into the host melt further up the magmatic plumbing system. There are several permutations described by Davidson et al. (2007b) of antecryst incorporation through the magmatic plumbing system which may display different compositional characteristics (Figure 4-21). Compositionally similar cores could suggest initial crystallisation from the same melt. If the rims of the populations differ, the plagioclases may have followed differing ascent paths resulting in contrasting rim compositions. One population could then be entrained (as antecrysts) into the host melt that is responsible for crystallising the remaining plagioclase population prior to eruption. Conversely, if plagioclases form from a different parent melt to the host melt plagioclases and are then included in the host melt, the cores of the two populations may differ whilst the fresher rim material would be compositionally similar. In addition, plagioclases from the crystal mush zone at the base of a magma chamber can be entrained into the melt as it ascends through linked magma chambers, as shown by Davidson et al. (2007b).

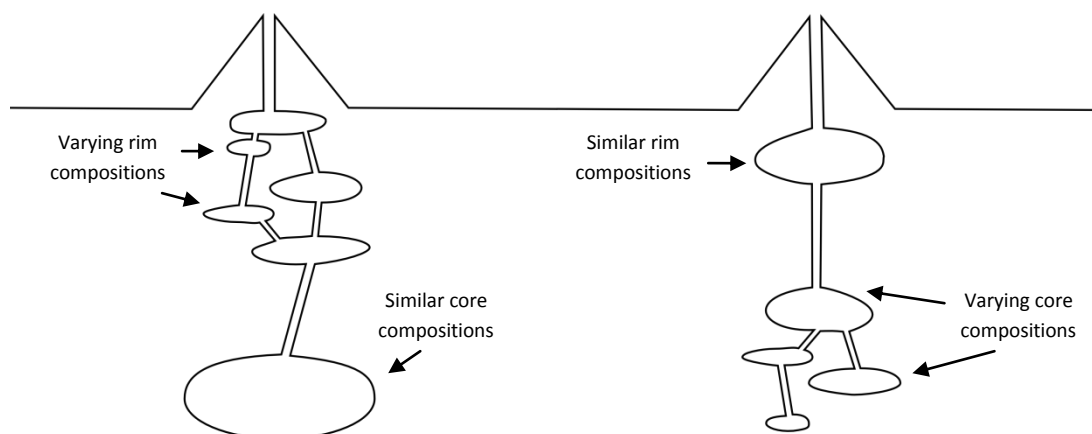


**Figure 4-21 Methods of generating compositionally different cores and rims in plagioclases through magmatic plumbing. Modified from Davidson et al. (2007).**

Incorporation of crystal cargoes is likely to produce textural features related to chemical disequilibrium in the entrained plagioclases (providing they are held in the new host melt for a sufficient period of time). Assuming that the entrained material encompasses solid crystal phases, there should be little effect on the composition of the host melt (see section 4.5.5 on magma mixing for addition of melts with solid phases). Once the antecrysts become resident in the host melt, they will no longer be in equilibrium as the host melt is unlikely to have the same composition as the melt from which the antecryst grew. Resorbed edges could be a result of residence in a melt of differing composition, as could sieve texturing. It has been suggested that fine sieve texturing can be a result of plagioclases coming into contact with a more primitive (Ca-rich) melt (Renjith, 2013, Viccaro *et al.*, 2010). The sieve texturing is caused by the dissolution of the plagioclase as it is not in equilibrium with its new host melt (Renjith, 2013, Viccaro *et al.*, 2010). The plagioclases with fresher rims could be entrained phenocrysts which have then been overgrown by plagioclase whilst resident in the host melt.

Several populations show evidence of residence in a contrasting melt to that which they were crystallised from. SV31-a shows a heavily corroded zone extending to the crystal edge. GU1-c, GU4-c, GU27-b, BQ2-a, SV3-a, SV19-b and SV20-a all show a heavily corroded/sieved region adjacent to fresher rim material (Table 4-2 and Table 4-3). In some cases this zone surrounds a fresh appearing core whereas in others the entire centre of the crystals have been resorbed (Figure 4-22).

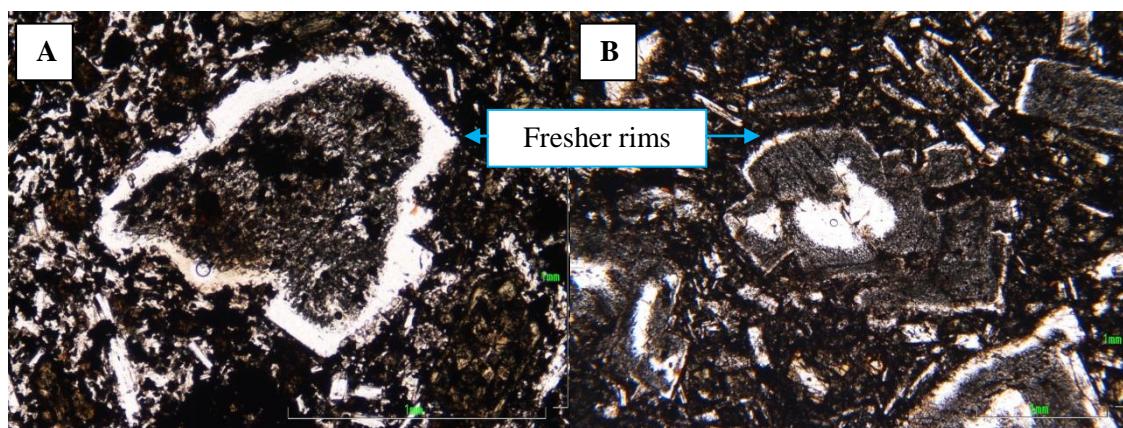


**Figure 4-22 Heavily sieved zones seen in two populations from differing lavas from St. Vincent. Photograph A shows SV19-3 and does not exhibit a fresher core region. Photograph B shows SV20-3 which has fresher material preserved in the core. Whilst the rim material appears fresher there is still evidence of some resorption of the crystal edges, possibly caused by shallow level degassing/decompression.**

These populations may represent antecrysts and not products of magma mixing as the sieving is pervasive towards the centre of crystals. Were the plagioclases to have been incorporated into the host magmas as part of a melt, the immediate conditions surrounding the crystals would be likely to be more similar to their parent melt than if they were part of a crystal cargo. In order for plagioclases included in a melt to show the degree of disequilibrium features present, the melts must have been thoroughly combined through convective mixing. Otherwise the plagioclase population would be enclosed by a melt composition similar to its parent. If the plagioclase populations were added as a crystal cargo with limited accompanying melt, they would be almost immediately in contact with a melt of different composition to that of their parent, thus prompting dissolution of the newly unstable plagioclases.

As the heavily sieved plagioclase populations show fresher rim material, this would suggest that a new phase of crystallisation has taken place after the event causing the extensive sieving. The rim material appears to be in equilibrium with the host melt as only slight breakdown of the crystal edges has occurred and this has been attributed to shallow level degassing/decompression (section 4.5.2).

As with the disequilibrium features resulting from decompression (section 4.5.3), obtaining accurate analyses of the heavily sieved material is difficult. In crystals with larger fresh rims, analyses have been undertaken in the rim material (Figure 4-23).

The populations exhibiting extensive heavily sieved zones (GU1-c, GU4-c, GU27-b, BQ2-a, SV3-a, SV19-b, SV20-a and SV31-a) will now be referred to as antecrysts based on the degree of disequilibrium pervasive throughout these populations, with the remaining populations being termed phenocrysts (as in Figure 4-23). As in Figure 4-17, the % distance from rim parameter used in Figure 4-23 is as defined in Chapter 2.

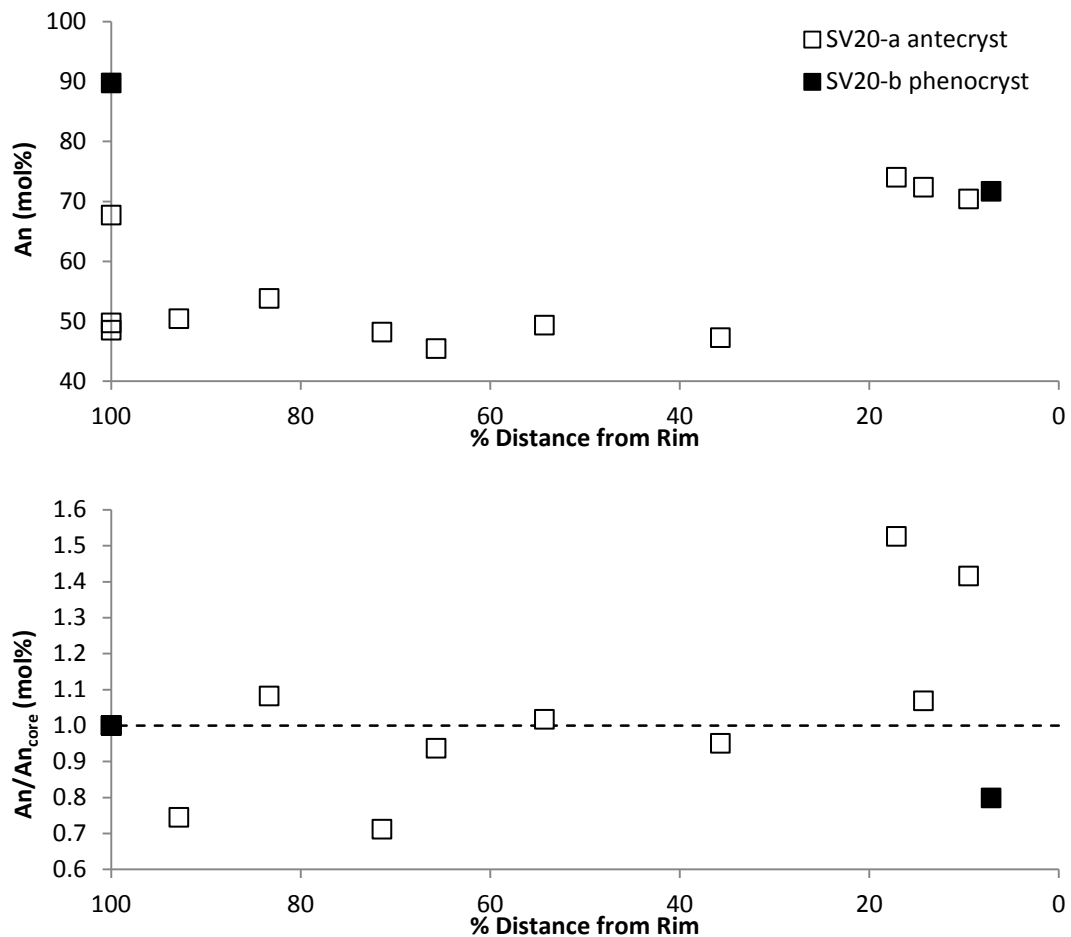


**Figure 4-23 Anorthite contents in both populations from SV20. SV20-a is the population thought to be antecrysts whereas SV20-b may originate from the host melt. The upper graph shows the absolute anorthite contents in the core and rim analyses. The lower graph shows the anorthite contents relative to the core value of each crystal.**

Figure 4-23 shows analyses from the two populations from SV20 (although n for the non-antecryst population is only 1 crystal). The upper graph shows that both populations have similar anorthite contents in the rim analyses, with the phenocryst population appearing to be normally zoned and the antecryst population displaying reverse zoning. However, the lower graph shows that when compared to the An contents of the core analyses of each crystal, the antecryst population shows an increase in anorthite at the rims. The plagioclase crystal from the second population

(potentially crystallised from the host melt) shows a decrease in anorthite content between core and rim. This could be a result of continued crystallisation and ensuing normal zoning. Given the fact that the populations have similar An contents at the rims (antecrysts  $An_{70-74}$ , non-antecryst  $An_{72}$ ), it is plausible that both populations have crystallised the rim material from the same melt, i.e. the antecrysts were resident in the host melt at the time of crystallisation of the fresher rim zones.

Figure 4-24 shows that the similarity in compositions in the rim analyses in both populations is not limited to anorthite content. Similar concentrations of compatible, LILE, HFSE and REE are seen in both populations (with an example of each being shown in Figure 4-24). The grey rectangles on Figure 4-24 represent the approximate time during the growth of the crystal when the antecryst population was entrained into the host melt (i.e. no longer crystallising material in equilibrium with the antecryst parent melt). This would suggest that at least 20% of the total material comprising the analysed crystals was crystallised after the two populations were combined in the same melt.

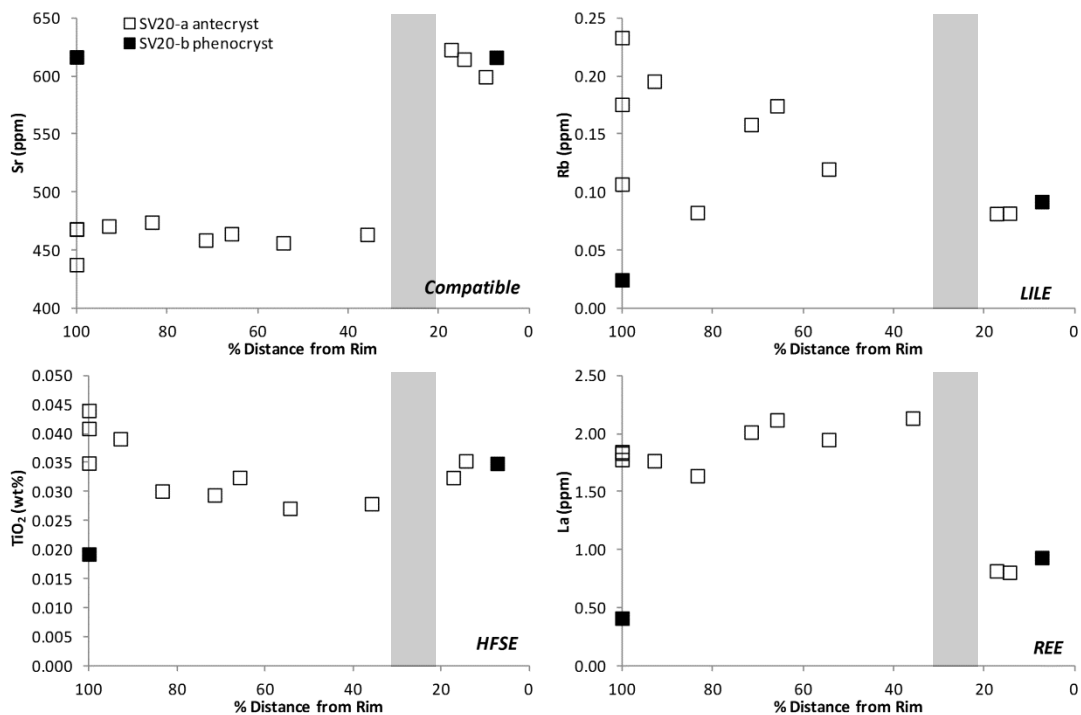


**Figure 4-24 Concentrations of a compatible, LILE, HFSE and REE element across the analysed populations in SV20. The grey rectangle shows the approximate potential point of entrainment during growth of the crystals.**

SV20 provides valuable insight into the petrogenesis of the heavily sieved populations. Based on the similar textures seen in these populations from different

lavas, it has been assumed that SV20 is a good proxy to represent all of the similar appearing crystals. As such, GU1-c, GU4-c, GU27-b, BQ2-a, SV3-a, SV19-b and SV31-a in addition to SV20-a can be classed as antecrysts that have then been incorporated into the host melt (potentially responsible for crystallising other plagioclase populations seen in these lavas). These populations all appear to be petrographically similar despite originating not only from different lavas but from different islands across the arc. The varying extent of the sieved zones could be a function of varying residence times in the final melt. Another factor may be the magnitude of compositional differences between the antecryst parent melt and the host melt. Larger contrasts in composition may result in faster and/or more extensive dissolution of the antecryst plagioclases. The entrained populations all show fresher rim material which is likely to have been crystallised from the final host melt.

#### **4.5.5 Magma Mixing and Hybridisation**

It is also worth discussing the possibility of magma mixing and ensuing hybridisation, in contrast to solely entraining crystal cargoes (although it is worth bearing in mind that there is a gradient from melt with crystals through to crystal mush through to solid). Magma mixing is the addition of a contrasting magma composition to the host melt in this case, with hybridisation referring to the combination of these two melts resulting in one hybrid composition over time. In a similar mechanism to that suggested for entrainment, it is possible that melts originating from the same or similar sources may ascend and evolve along different pathways and then potentially recombine prior to eruption (Figure 4-21).

A plagioclase that has been crystallising from a single melt over time is likely to show normal zoning as the melt around it evolves. It should be in equilibrium and thus should not display textural features resulting from chemical disequilibrium. However, if there is an injection of new magma, although the chemistry may be similar to the original chemistry of the host melt, the plagioclase will now no longer be in equilibrium with the new hybrid melt composition, causing a compositional break in the plagioclases. The normal zoning may then be mantled by new material which is in equilibrium with the hybrid melt. New plagioclases may also nucleate, forming a secondary population.

Magma mixing can also produce disequilibrium textures, for example (as previously noted) by causing dissolution of plagioclases from a more Ca poor melt mixing with a secondary melt with higher Ca contents to create fine sieve texturing (Renjith, 2013) if the original plagioclases are resident in the hybrid melt for a sufficient period of time. Further to sieve textures forming towards crystal rims (and potentially pervading inwards if residence time permits), resorption of the crystals may occur. This could lead to the core zones of crystals having more rounded edges or stepwise dissolution as the melt infiltrates along weak points (e.g. along cleavage planes).

In addition, as noted previously (section 4.5.2), varying ascent rates can produce different densities of coarse sieving (Nelson & Montana, 1992, Renjith, 2013, Viccaro *et al.*, 2010). Thus plagioclases from different melts may have already developed textural and compositional differences prior to mixing and subsequent eruption.

In contrast to entrainment of solid crystal cargoes, when magmas mix, the resulting hybrid melt has a composition different to both the component magmas (assuming a sufficient volume of material is added to the host melt to prompt a change in chemistry). The resulting composition will then be a function of the composition and volumes of the constituent magmas. As a result, any plagioclases in equilibrium with this new melt must have crystallised after mixing and it is likely any pre-existing crystal phases from either component melt will begin to develop disequilibrium features.

Further to the addition of magmas from a connected magma chamber, convective self mixing within larger magma chambers may produce similar textures. Crystals that may have equilibrated with melt compositions at the base of magma chamber may be carried to a higher level where melt composition may differ (if the melt has not completely mixed and remains slightly heterogeneous). Renjith (2013) suggested that convection within a magma chamber can also be responsible for synneusis of plagioclases, which is seen in some of the populations from the Lesser Antilles (Figure 4-25). Synneusis occurs where turbulent mixing causes the plagioclases to float together and attach along the crystal axes.

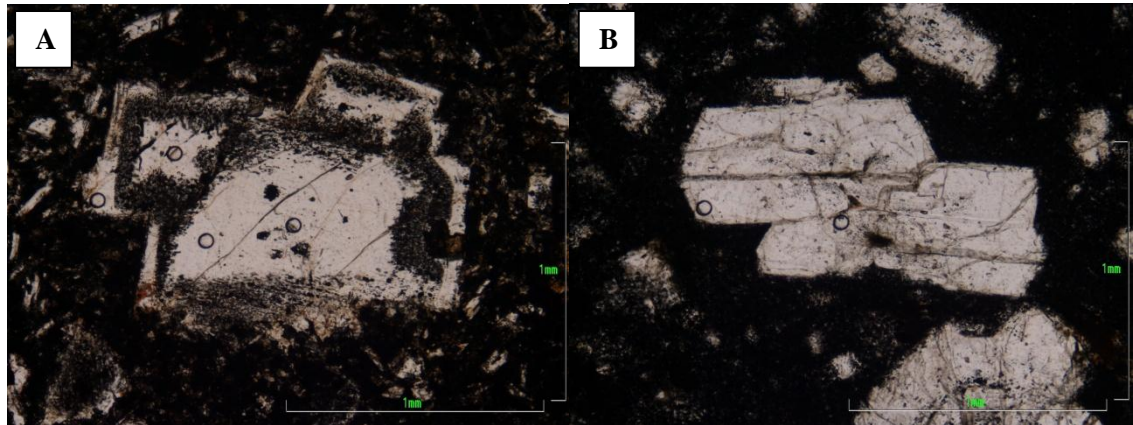


**Figure 4-25** Examples of synneusis in SV20 (A) and BQ19 (B), possibly as a result of self convective magma mixing in shallow magma chambers prior to eruption.

Given the presence of texturally and chemically different plagioclase populations in the same lava samples, magma mixing is liable to play a role in the petrogenesis of the Lesser Antilles lavas. It is needed to combine those populations that do not show signs of having been entrained (i.e. those populations that appear fresher, without extensive areas of corrosion) with populations showing disequilibrium features.

GU25-a, GU25-b, BQ2-b, BQ19-a and SV31-b appear to exhibit features resulting from mixing of magmas. These populations show a finely sieved zone(s) usually adjacent to fresher appearing material (Figure 4-26). The presence of several sieved zones is shown in Figure 4-26 in a plagioclase from the GU25-b population. Multiple sieved zones are also seen in BQ19-a. The fact that these sieve zones are seen close to the cores of the crystals in some cases suggests that this sieving is not a result of shallow decompression/degassing (section 4.5.2). Sieving resulting from the latter processes should occur much closer to the rim. Also, in order for repeated zones to form, the crystals must restabilise and crystallise new material in between events causing the disequilibrium features to form, but degassing may prompt eruption. Shallow degassing or decompression may have also occurred in the populations after magma mixing due to the resorption of edges visible.

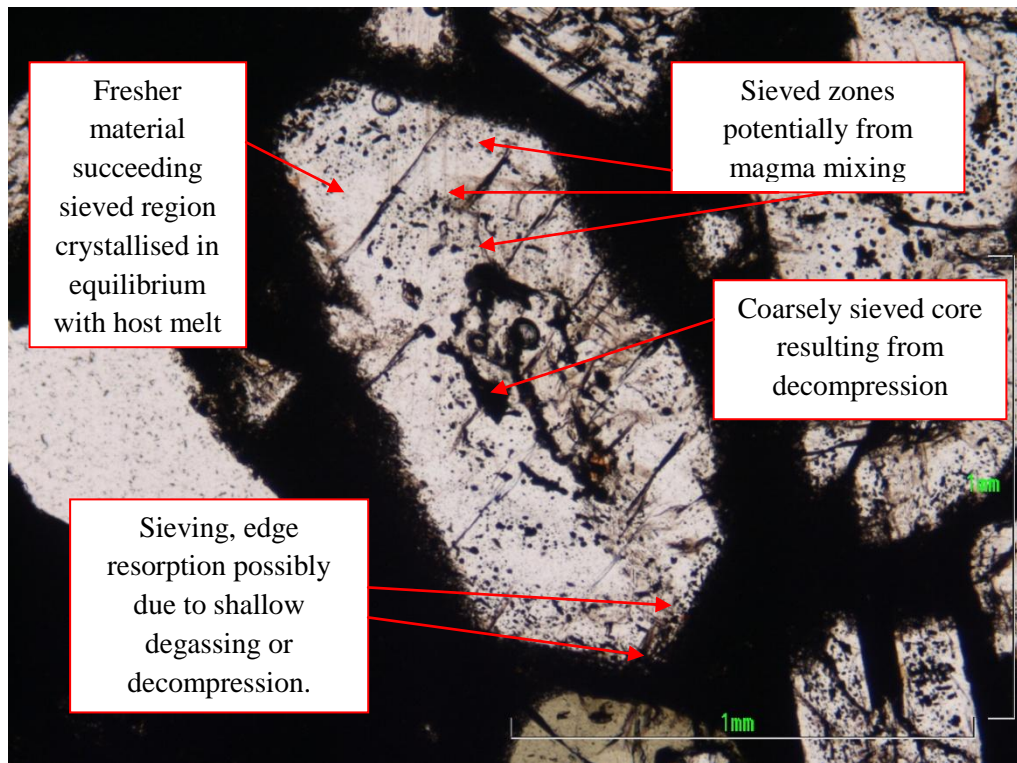


**Figure 4-26** GU25-3 which is in population GU25-b. The core shows coarse sieving (likely to be a result of decompression) followed by three finely sieved zones which may result from magma mixing.

The sieve texturing is more likely to have been caused by magma mixing with a more evolved melt in these populations, as there is little evidence of anorthite contents increasing across the crystals analysed (Figure 4-27). In addition, Figure 4-27 shows higher Sr contents across the crystals. The influx of more primitive melt would be likely to result in an increase in An content and potentially lower Sr concentrations (as the partition coefficient between plagioclase and melt for Sr increases with decreasing anorthite content, Blundy and Wood, 1991). However, the analyses nearest to the rim in both crystals shown in Figure 4-27 do not show this, being An<sub>74</sub> in BQ19-2 and An<sub>75</sub> in BQ19-11 with Sr concentrations of 745 ppm and 737 ppm respectively. Both rim analyses are situated in fresher material crystallised after the magma mixing events inferred from the fine sieve texturing (and shown as dashed lines in Figure 4-27). There are no cores with anorthite contents of approximately An<sub>75</sub> in BQ19, suggesting that the cores of the analysed crystals all crystallised before mixing occurred. The highest Sr concentration in a BQ19 core analysis is 671, at least 66 ppm lower than the Sr contents measured at the rims of the crystals in Figure 4-27. Fresh plagioclases may have nucleated from the hybrid

melt, but if these crystals are small in size they would not have been selected for LA-ICP-MS analysis.

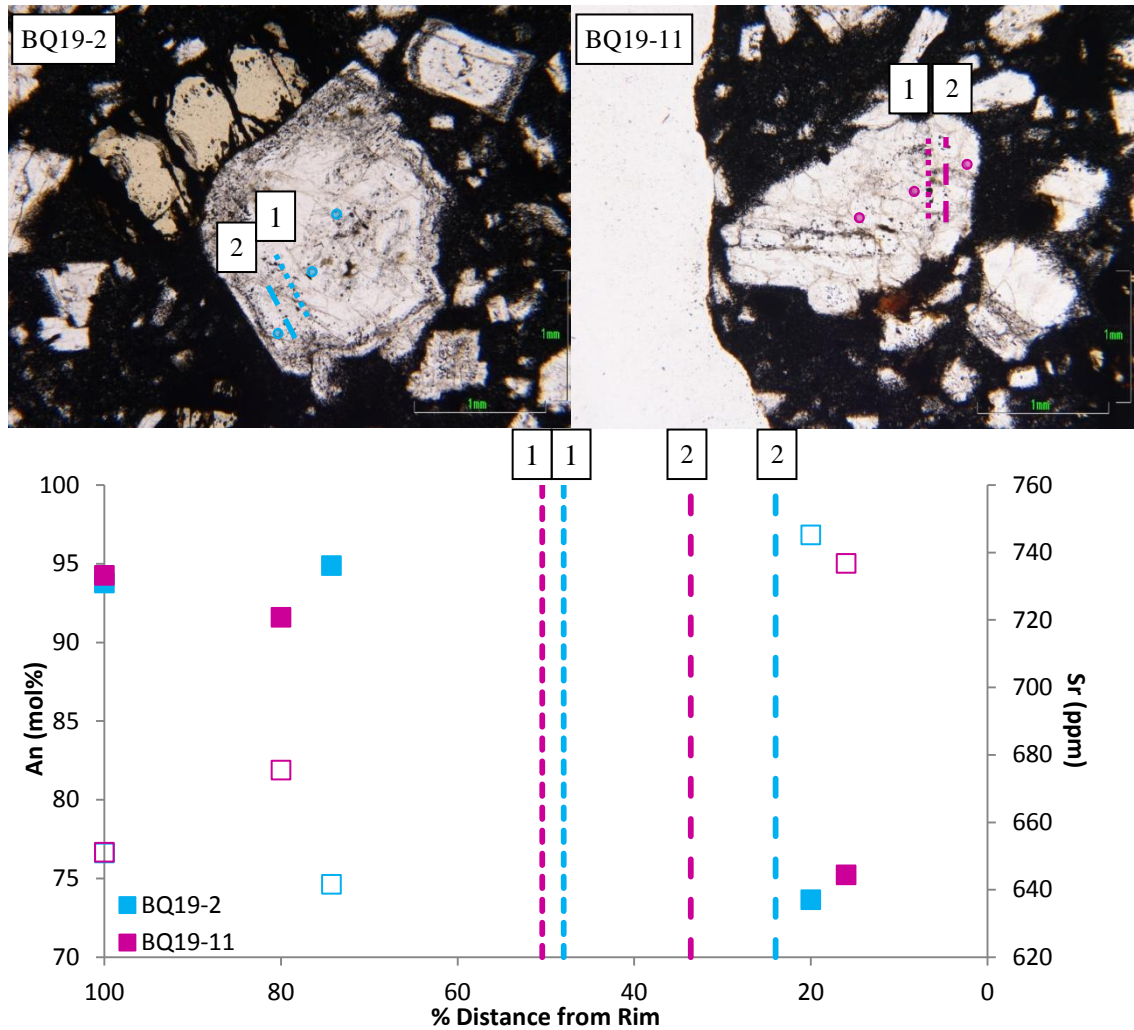


**Figure 4-27 Anorthite content (solid symbols) and Sr concentration (hollow symbols) variation across two crystals from population BQ19-a, which is thought to show evidence of magma mixing. The dashed lines on the photographs and graph represent the locations of the sieve texturing numbered in the photographs.**

The compositional and textural evidence may suggest that both GU25 populations, BQ19-a and BQ2-b were all resident in magmas to which melts were subsequently added. This would have caused instability in the resident populations, triggering dissolution and the formation of fine sieve texturing. Ensuing crystallisation after these events shows material with similar or lower anorthite contents and higher Sr concentrations, implying that the added magmas are more evolved than the host melt. Increases in rim concentrations relative to core concentrations are seen in the other analysed incompatible elements in the BQ19-2 and BQ19-11 thick section data also. It is therefore unlikely that the added melts are more primitive but insufficient

volumetrically to alter anorthite contents as this would not trigger the dissolution of the pre-existing plagioclases.

#### **4.5.6 Accumulation**

Following crystallisation, some crystals may settle from the melt to the base of the magma chamber, creating a phenocryst rich zone and concentrating the elements hosted in plagioclases, such as Sr. As a result, whole rock analyses used to provide a proxy for host melt compositions can be inaccurate if phenocryst rich samples are used. This may cause plagioclase compositions to appear out of equilibrium when compared to whole rock Ca/(Ca+Na+K) ratios, as seen in Figure 4-15.

In terms of composition and disequilibrium textures, accumulation may not result in the generation of a significantly different population of plagioclases than those remaining in the melt. It may be that the crystallisation process is 'frozen' upon settling and removal from the melt as the crystals no longer interact with the magma. However, the accumulated crystals may later be entrained into melts higher in the magmatic plumbing system as a crystal cargo within in an ascending melt (Davidson *et al.*, 2007b). At this point, the accumulated plagioclases may behave as described in section 4.5.4. Supposing any plagioclases that have settled from the melt were crystallised early, they may exhibit higher anorthite contents than later crystallising crystals.

Accumulation is required in order to generate the crystals which are entrained. However, it is unlikely that the high anorthite plagioclases analysed represent an accumulated population. For example, population BQ19-b shows some of the highest An contents in the plagioclases sampled (up to An<sub>96</sub>), but the crystals appear relatively fresh with little textural evidence of disequilibrium. Therefore another process is required to generate the high An contents.

#### **4.5.7 Melt Composition**

Aside from plagioclase, modal proportions derived from point counting (Table 4-6) in conjunction with major and trace element variations plotted against MgO (Figure 4-28) suggest that olivine and/or clinopyroxene also crystallised from the host lavas. No substantial oxide or apatite removal in the analysed lavas is apparent from the

point counting or graphs of TiO<sub>2</sub> and P<sub>2</sub>O<sub>5</sub> plotted against MgO (Figure 4-28). Fractional crystallisation will impact upon the melt composition from which the plagioclases are crystallising and thus the concentrations of elements available to be partitioned into the plagioclases.

<b>Sample</b>	<b>Plagioclase</b>	<b>Olivine</b>	<b>Clinopyroxene</b>	<b>Orthopyroxene</b>	<b>Oxide</b>
<b>GU1</b>	30.3	1.2	3.8	0	1.1
<b>GU4</b>	24.1	0	9.3	0	0.4
<b>GU25</b>	44.9	6.4	5.2	0	0.1
<b>GU27</b>	29.1	1.1	1.4	4.4	0.9
<b>SV3</b>	15.3	10.5	4.2	2.1	0.3
<b>SV19</b>	9.1	13.1	13.3	0	1.7
<b>SV20</b>	22.5	3.2	15.5	0	2.4
<b>SV31</b>	31.1	3.9	5.6	0	0.5
<b>BQ2</b>	32.3	3.9	16.6	0	0.1
<b>BQ5</b>	30.2	6.0	21.0	0	0.5
<b>BQ19</b>	43.1	2.6	2.1	0	0.5

**Table 4-6 Modal proportions of phenocryst phases in the whole rocks from which the plagioclases were analysed based on point counting data. 1500 counts per sample were used.**

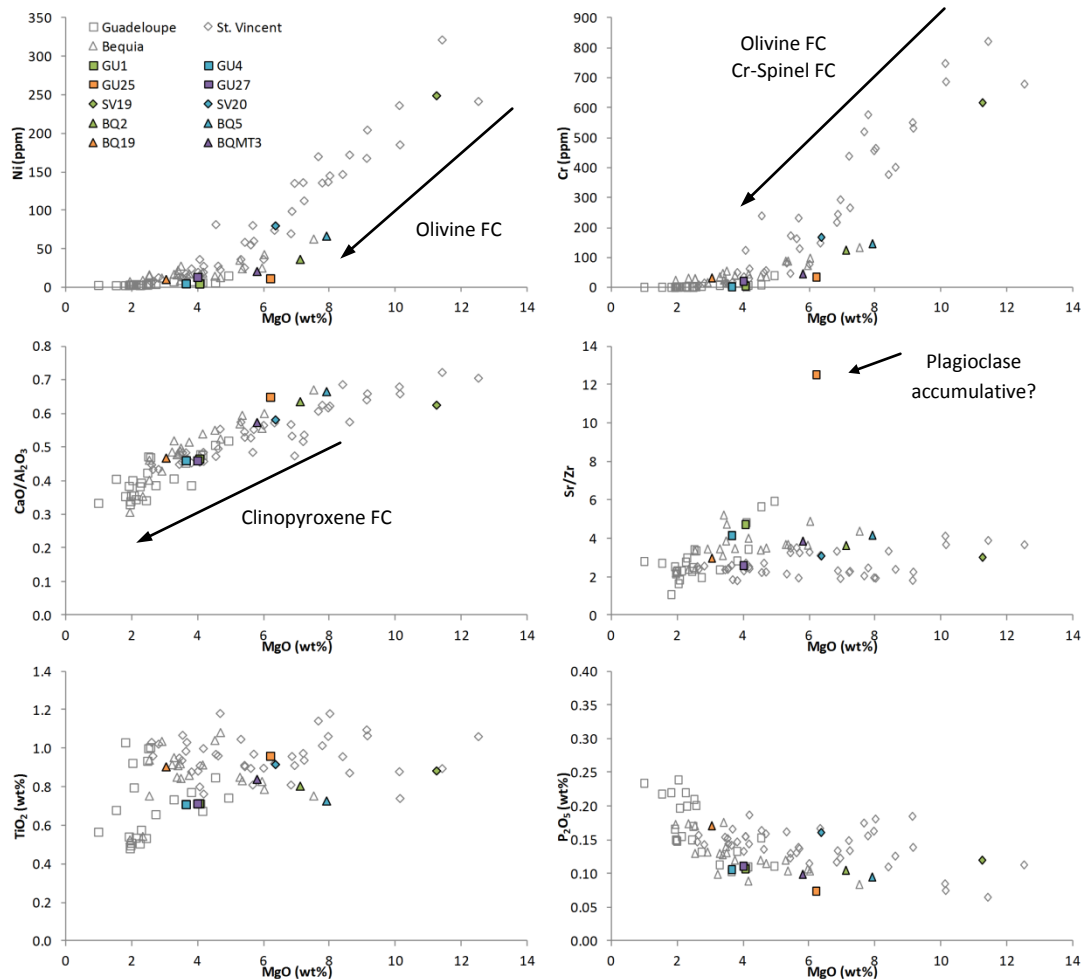


**Figure 4-28** Whole rock graphs for selected elements and element ratios against MgO content to show fractional crystallisation of olivine, clinopyroxene and plagioclase in the lavas from which the analysed plagioclases originate. Hollow grey symbols represent whole rock analyses from the same islands that the plagioclases were sampled from (squares: Guadeloupe, diamonds: St. Vincent and triangles: Bequia; Thirlwall, unpublished data). Individual sample legends are as shown in the upper left graph.

In Figure 4-6 to Figure 4-13, anorthite content is used as a proxy for the index of fractionation of the melt as MgO was used for the whole rocks. It is worth noting that anorthite contents may be affected by other variables such as water content, pressure and temperature impacting on partition coefficients between the plagioclases and melt (e.g. section 4.5.8). Increasing concentrations of the incompatible LILE and HFSE with decreasing anorthite contents are apparently consistent with melt compositions becoming more evolved (Figure 4-7, Figure 4-9, Figure 4-12). The REE plots also show similar trends in the majority of cases. However, the trends observed for Sr contents in the plagioclases may not solely be a function of evolution of melt compositions. It is widely accepted that Sr (and also Ba) should become more compatible in plagioclases with decreasing anorthite

content and therefore Sr concentrations should increase (e.g. Blundy and Wood, 1991). Below An<sub>70</sub>, this does not appear to be the case for the Lesser Antilles plagioclases (Figure 4-6). Whilst the concentrations of Sr largely decrease with decreasing anorthite content, two crystals from GU25 do not follow this trend and thus may show evidence of the effect of increased compatibility. Also, simple melt evolution does not explain the higher and lower Sr groups observed in SV20 at An<sub>71-76</sub>, given the range in Sr contents over this anorthite range (230 ppm Sr over 5 mol% An). Therefore variation in partition coefficients with anorthite content is not the major cause of changing plagioclase compositions as anorthite contents decrease. The Sr and Ba contents of the plagioclases are discussed in more detail in section 4.5.10.

Changes in melt composition caused by the fractional crystallisation of other phases are also unlikely to generate the wide ranges in some elements (e.g. TiO<sub>2</sub>, Sm and Gd in Guadeloupe, Sr and the REE in Bequia) apparent at a given anorthite content (Figure 4-6, Figure 4-10 and Figure 4-12).

Additionally, anorthite contents in the plagioclases do not steadily decrease from core to rim within crystals (e.g. Figure 4-14 and Figure 4-27), suggesting that straightforward crystallisation of the plagioclases from their host melts is too simplistic a solution for the genesis of the analysed plagioclases. This is reinforced by Figure 4-29, which shows the variations in the La/Y ratio with distance from the rim in the thick section analyses. All the populations (with the exception of SV20-b) show significant variation in the La/Y ratios across the crystals with no correlation apparent. La/Y should not be affected by fractional crystallisation and so these fluctuations cannot be explained solely by one melt evolving over time without the influence of other processes.

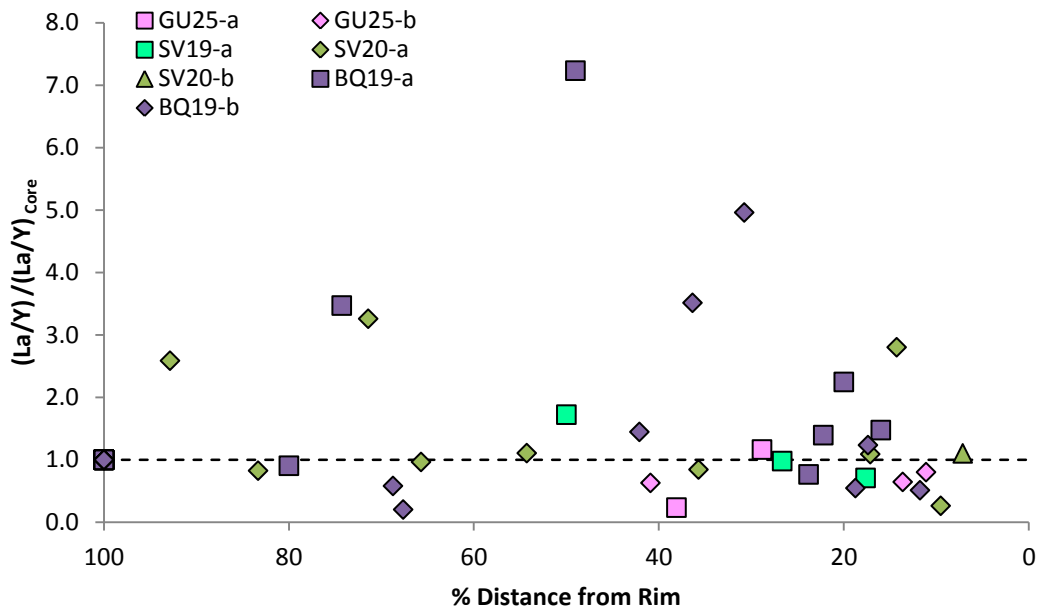


**Figure 4-29** La/Y ratios of the thick section plagioclase analyses versus % distance from the rim of the crystals.

Figure 4-14 shows that both the BQ19 crystal and the SV20 crystals have higher Sr contents at the rims. BQ19 has higher An, Ba and K/Ti (used as a potential measure of fluid involvement) at the rim than in the core, possibly suggesting an influx of fluid being responsible in the latter stages of crystallisation. SV20 in contrast shows lower An, Ba and K/Ti at the proximity of the crystal which may imply that a different process is responsible.

#### 4.5.8 Influence of Water and High Anorthite Plagioclases

Studies have shown that water contents can increase  $K_D^{Ca-Na}$  (Feig *et al.*, 2006, Sisson & Grove, 1993, Takagi *et al.*, 2005), thus producing higher An content plagioclases than would be expected using anhydrous partition coefficients. Macdonald *et al.* (2000) and references therein suggest that water contents of near primary basalts from the Lesser Antilles are between 1-2 wt%. More evolved melts are thought to have higher water contents, e.g. 3 wt% in basaltic andesites and 5-6 wt% if the melts are silicic (Macdonald *et al.*, 2000 and references therein). As the Lesser Antilles is an intra-oceanic arc it seems likely that water contents will have an effect on the chemistry of melts and ensuing mineral phases, primarily through changes in partition coefficients.

High anorthite plagioclases are common in arc basalts (Danyushevsky *et al.*, 1997, Takagi *et al.*, 2005). However, there is still some lack of understanding as to how plagioclases with high contents of anorthite are formed (Lundstrom & Tepley, 2006). As previously discussed, partitioning of Ca and Na between melts and plagioclases is variable depending on temperature and pressure conditions, the composition of the melts and the melt water contents involved. Takagi *et al.* (2005) conducted experiments in order to assess ideal conditions for crystallising high An content plagioclases ( $>An_{88}$ ) from a hydrous arc tholeiite of relatively constant composition. The authors found that pressures of between 2-3 kbar and water contents of around 5 wt% could produce plagioclases of composition up to  $An_{90}$  (with a  $K_D^{Ca-Na}$  of  $\sim 3.5$ ). Thus it appears the influx of water to the melt may play a pivotal role in generating plagioclases with a high anorthite content. Similar conclusions were reached by Sisson and Grove (1993) and Feig *et al.* (2006). Sisson and Grove (1993) calculated partition coefficients for  $K_D^{Ca-Na}$  between plagioclase and calc-alkaline melt compositions at 2 kbar for 2 wt%  $H_2O$ , 4 wt%  $H_2O$  and 6 wt%  $H_2O$  of 1.7, 3.4 and 5.5 respectively. Figure 4-30 depicts these partition coefficients in terms of the melt water content and where the analysed plagioclases plot in relation to the whole rock  $CaO/Na_2O$  ratios in order to observe whether the Sisson and Grove (1993)  $K_D^{Ca-Na}$  values are suitable for the observed Lesser Antilles plagioclase compositions.

Figure 4-30 suggests that water may not be the sole control on the high anorthite contents exhibited by many of the plagioclases. When the Guadeloupe plagioclases are considered, it can be seen that all the samples with the exception of GU27 show a wide range in observed plagioclase  $CaO/Na_2O$  ratios, extending across all the suggested water content  $K_D$  values. In addition, many of the plagioclases from Guadeloupe and in particular those from Bequia show plagioclase  $CaO/Na_2O$  ratios above those suggested using these partition coefficients at a given whole rock  $CaO/Na_2O$  ratio, possibly suggesting an even higher melt water content than 6% is required to produce the plagioclases with the highest anorthite contents.

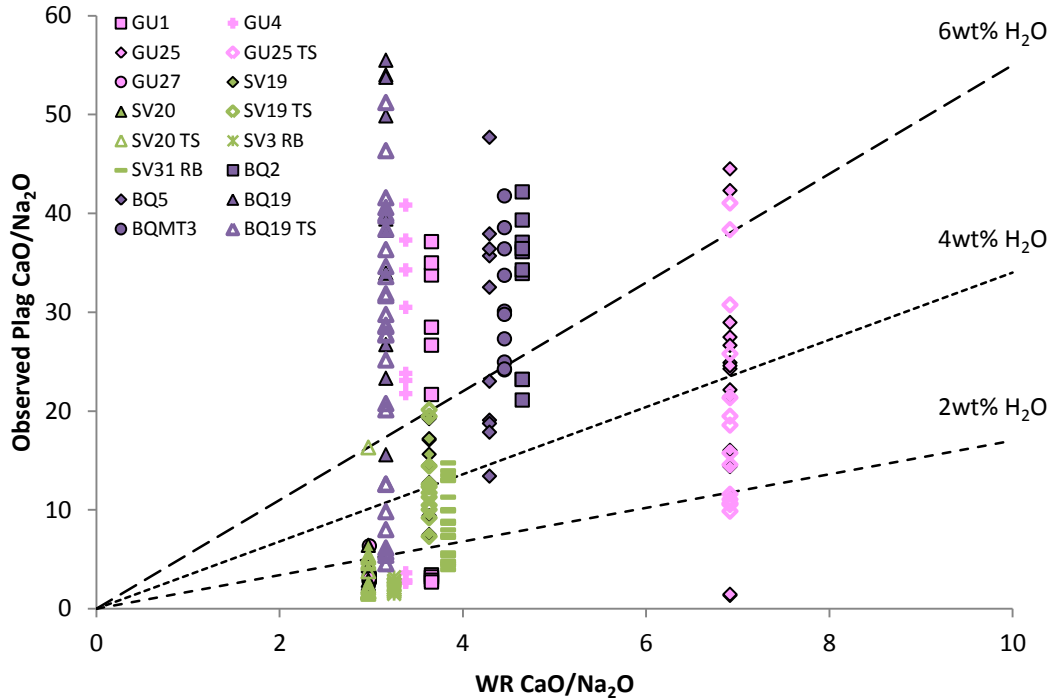


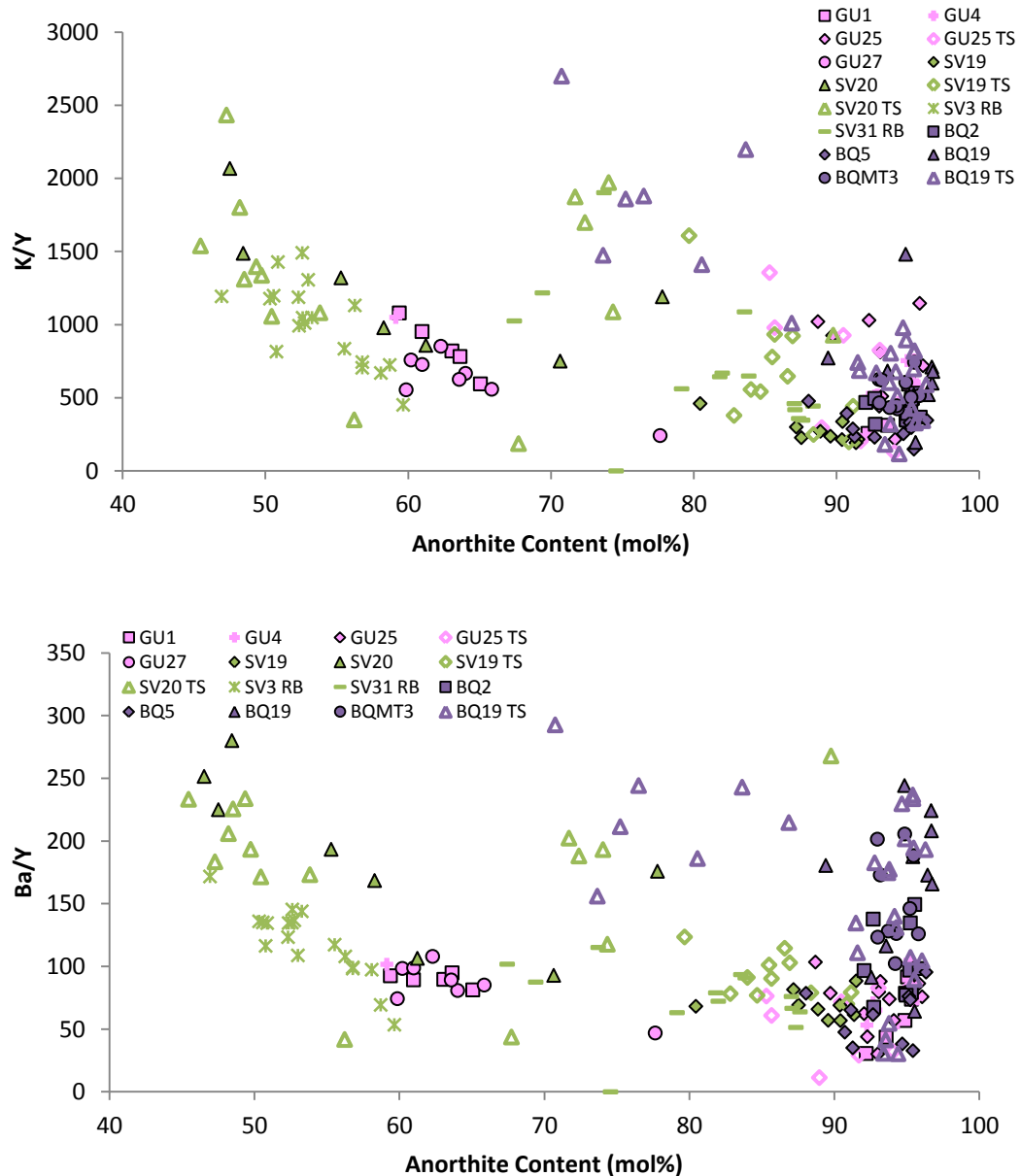
Figure 4-30 Observed analysed plagioclase compositions plotted against the whole rock (WR)  $\text{CaO}/\text{Na}_2\text{O}$  ratios from which they were sampled. Partition coefficients used are from Sisson and Grove (1993). The dashed lines represent plagioclases in equilibrium using the published  $K_D^{\text{Ca-Na}}$  for each water content, at a given whole rock  $\text{CaO}/\text{Na}_2\text{O}$  ratio.

Figure 4-30 is reliant on the use of the whole rock compositions for each host lava. As discussed previously, the whole rock compositions represent the culmination of numerous processes and populations and thus may not themselves be the parental composition of any of the minerals analysed. Therefore, any graph using whole rock compositions as an axis should be interpreted with care. Consequently, the spread in observed plagioclase  $\text{CaO}/\text{Na}_2\text{O}$  ratios seen in some lavas (such as BQ19) may be a result of plagioclases with different parental melt compositions being plotted at a single incorrect whole rock composition.

In addition, the plagioclases which seem to need excessively high magmatic water contents may be plotting at lower whole rock  $\text{CaO}/\text{Na}_2\text{O}$  compositions as a result of being hosted in a more evolved whole rock to their actual parent. Increasing the whole rock  $\text{CaO}/\text{Na}_2\text{O}$  would shift the plagioclases to the right along the x axis to be more in line with the water contents tested by Sisson and Grove (1993). Similarly, those plagioclases plotting below the 2% magmatic water line may suggest a lack of water in their parental magmas but could also indicate the whole rock  $\text{CaO}/\text{Na}_2\text{O}$  is

higher than that of the magmas responsible for crystallising the plagioclases with low CaO/Na<sub>2</sub>O.

In order to observe if there is any link between potential fluid input and anorthite content, K/Y and Ba/Y ratios for the plagioclases were used (Figure 4-31). Increased LILE/Y ratios could reflect higher melt water contents as the LILE are fluid mobile and Y is not.



**Figure 4-31 K/Y and Ba/Y ratios in the analysed plagioclases against anorthite content.**

Figure 4-31 shows that there are large ranges in particularly K/Y (117-1481, a 1165% increase) but also Ba/Y (30-268, a 793% increase) at high anorthite contents

(>An<sub>90</sub>). These crystals all have similar anorthite contents, but differing apparent fluid contributions. In addition, there are plagioclases at ~An<sub>50</sub> that show similarly high or indeed higher values for both ratios to those observed at high An (a maximum of 2433 for K/Y and 280 for Ba/Y). Comparable values are also found at approximately An<sub>70</sub>. This would suggest that there is no real relationship between high K/Y and Ba/Y ratios and high anorthite contents. Either these ratios are unsuitable proxies for relative melt fluid contents or fluid is not the sole cause of high anorthite contents in the plagioclases.

Danyushevsky et al. (1997) proposed that water contents coupled with melt Al/Si and Ca/Na ratios are both important in the formation of plagioclases with anorthite contents of >An<sub>90</sub>. Danyushevsky et al. (1997) found that high An plagioclase in arc lavas did not rely on high water contents or high Ca/Na melts alone.

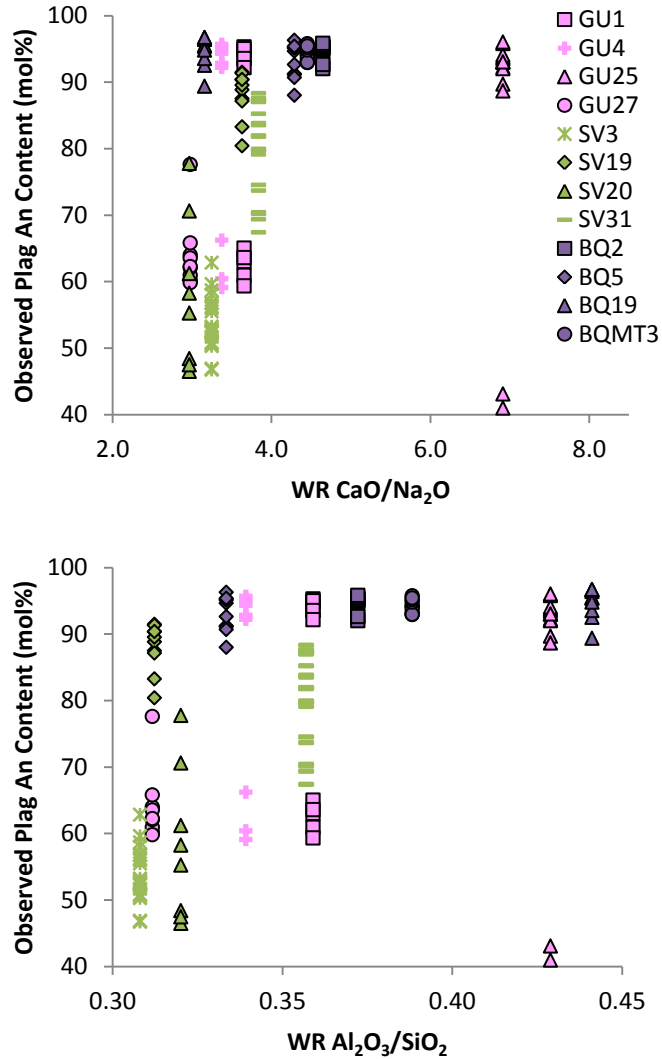
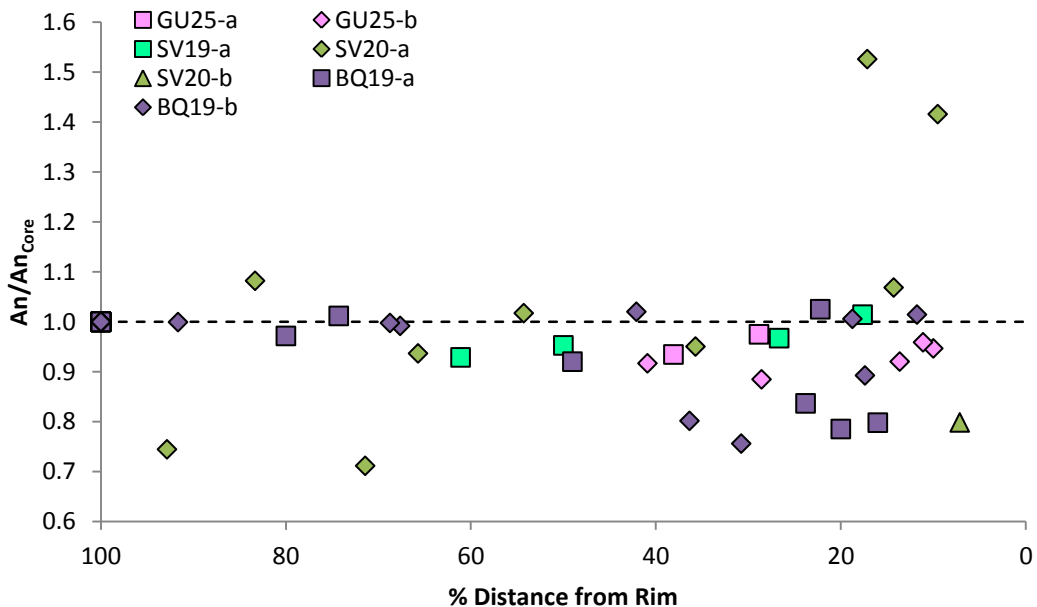


Figure 4-32 Whole rock (WR) CaO/Na<sub>2</sub>O and Al<sub>2</sub>O<sub>3</sub>/SiO<sub>2</sub> ratios (Thirlwall, unpublished data) compared to the analysed plagioclase anorthite compositions. The legend for the lower graph is as shown in the upper diagram.

Figure 4-32 shows the whole rock CaO/Na<sub>2</sub>O and Al<sub>2</sub>O<sub>3</sub>/SiO<sub>2</sub> ratios compared to the analysed plagioclase anorthite compositions. There is a large range in whole rock ratios for those plagioclases exhibiting anorthite contents greater than An<sub>90</sub> (3.16-6.91 for CaO/Na<sub>2</sub>O and 0.31-0.44 for Al<sub>2</sub>O<sub>3</sub>/SiO<sub>2</sub>) suggesting that whole rock composition is not the dominant control on anorthite content. However, as discussed previously, this assumes that the plagioclases have crystallised from the whole rock composition whereas in reality this is unlikely and parent melt compositions for differing populations may vary. Danyushevsky et al. (1997) required a CaO/Na<sub>2</sub>O ratio of over approximately 2.7 in the melt to generate plagioclases at An<sub>90</sub> and above. The Lesser Antilles plagioclases are all sampled from whole rocks with

CaO/Na<sub>2</sub>O ratios equal to or greater than 2.97 yet not all of them exhibit plagioclases with anorthite contents of An<sub>90</sub> or higher.

Lundstrom and Tepley (2006) proposed that high anorthite contents could be generated by 'diffusion-reaction' between plagioclases and partially melted gabbroic wall-rock but only in the presence of water. This study also found that the method enabled rapid changes in plagioclase chemistry with variations in melt chemistry. However, they suggest that the highest anorthite contents should be found at the cores of the plagioclases, whereas the Lesser Antilles show several crystals with higher An contents outside the core, particularly in SV20-a (Figure 4-33), potentially ruling diffusion-reactions out as a method of forming the high anorthite plagioclases observed.



**Figure 4-33 Variations in anorthite content relative to the core analysis in the plagioclase thick section data.**

A reduction in temperature has also been shown to be able to increase the potential anorthite content of the plagioclases (Takagi *et al.*, 2005). Bindeman *et al.* (1998) constructed a geothermometer based on plagioclase anorthite compositions (with a caveat that the formula has only been shown to be reliable between An<sub>40</sub> and An<sub>80</sub>). Given that the anorthite content is used to calculate temperatures this does not provide much insight into the effect of temperature on why the anorthite contents are high in the Lesser Antilles plagioclases. However, it can be used to estimate temperature ranges (in addition to Putirka, 2008, Figure 4-19) required to crystallise

the analysed plagioclases (Figure 4-34). Whilst the Bindeman et al. (1998) model suggests higher temperatures at a given anorthite content than those calculated using the Putirka (2008) method (1139-1409°C compared to 1164-1220°C), both agree that the higher anorthite content plagioclases should crystallise at higher temperatures. It appears unlikely that the high anorthite plagioclases result from crystallisation at lower temperatures.

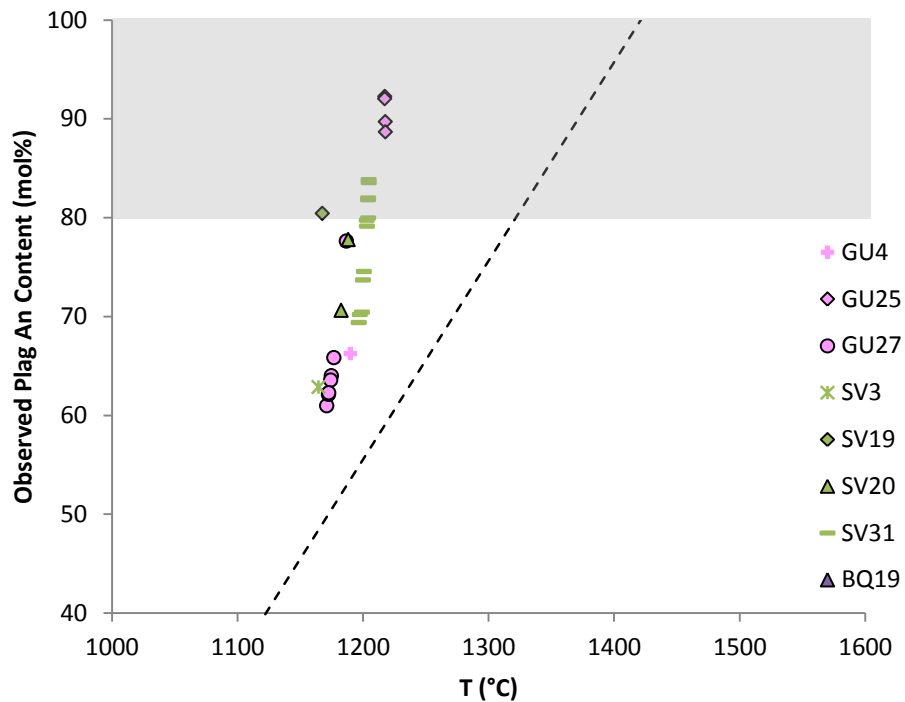


**Figure 4-34 Variations in modelled temperature with anorthite content using the Putirka (2008) and Bindeman et al. (2008) models. The Bindeman et al. (2008) model is not designed for use above An<sub>80</sub>, illustrated by the grey rectangle and is shown by the dashed line.**

In addition, Figure 4-34 shows only a range in temperature of 60°C using the Putirka (2008) method despite a range in anorthite contents of approximately 40 mol%. This would suggest that temperature is not the dominant influence on anorthite content.

It would seem that the high anorthite contents may be a result of increased water contents in the melts rather than temperature, pressure or melt composition differences. Although Figure 4-30 does not provide conclusive evidence of this, this is at least partly due to using a whole rock ratio in the model. Given that high anorthite contents are relatively common in arc lavas and Figure 4-30 shows at least some influence of increased water contents on An contents this appears a likely solution.

#### 4.5.9 Anorthite Bimodality in Guadeloupe Plagioclases

Anorthite bimodality is apparent in the Guadeloupe lavas. This bimodality could be a result of several differing processes.

Firstly, it is possible that one population of plagioclases has been accumulated. Ordinarily this would be apparent from assessing whether any of the plagioclases are in equilibrium with the whole rock chemistry. Accumulation of plagioclases would result in an increase in the whole rock  $\text{Ca}/\text{Ca}+\text{K}+\text{Na}$  ratio and thus cause the plagioclases to plot underneath the regression line in Figure 4-15. However, as discussed in section 4.4.1, there are issues with comparing mineral data to whole rock compositions. The high phenocryst proportions of modal plagioclase obtained from point counting of the thin sections (Table 4-6) allows for the possibility of accumulation, particularly in GU25 (45% modal plagioclase).

A further test for accumulation is to observe the  $\text{Sr}/\text{Zr}$  ratio of the whole rocks. Accumulation of plagioclase may be expected to be visible as a higher  $\text{Sr}/\text{Zr}$  ratio at a given  $\text{MgO}$  content (Figure 4-28) (although this ratio may also alter with variable fluid addition). However, this method works best where there are accumulative and non-accumulative samples present so as to differentiate those with elevated  $\text{Sr}/\text{Zr}$  from  $\text{Sr}/\text{Zr}$  ratios unaffected by plagioclase accumulation. It can be seen that GU25 could be plagioclase accumulative based on this criterion also (ignoring any contribution of fluid addition).

A second possibility is that there may have been a mixing event, prompting further crystallisation of plagioclase after the initial plagioclases were crystallised. A new influx of magma may result in the crystallisation of further higher anorthite content plagioclases with possible lower trace element concentrations. This assumes that the magma being input is more primitive than the host melt. The host melt may have evolved as a result of fractional crystallisation prior to the influx of the new melt. Observation of variations in anorthite content across crystals in the higher anorthite group thick section analyses may provide further insight into this (Figure 4-35). If magma mixing has occurred and prompted further crystallisation, the Guadeloupe plagioclases may show similar or higher anorthite contents at the rims than in the cores of the crystals and lower Sr contents. However, the plagioclases analysed in GU25 in thick section show lower anorthite contents at the rims than in the cores of

the crystals and higher Sr concentrations, suggesting that mixing with a more primitive melt may not be a plausible explanation.

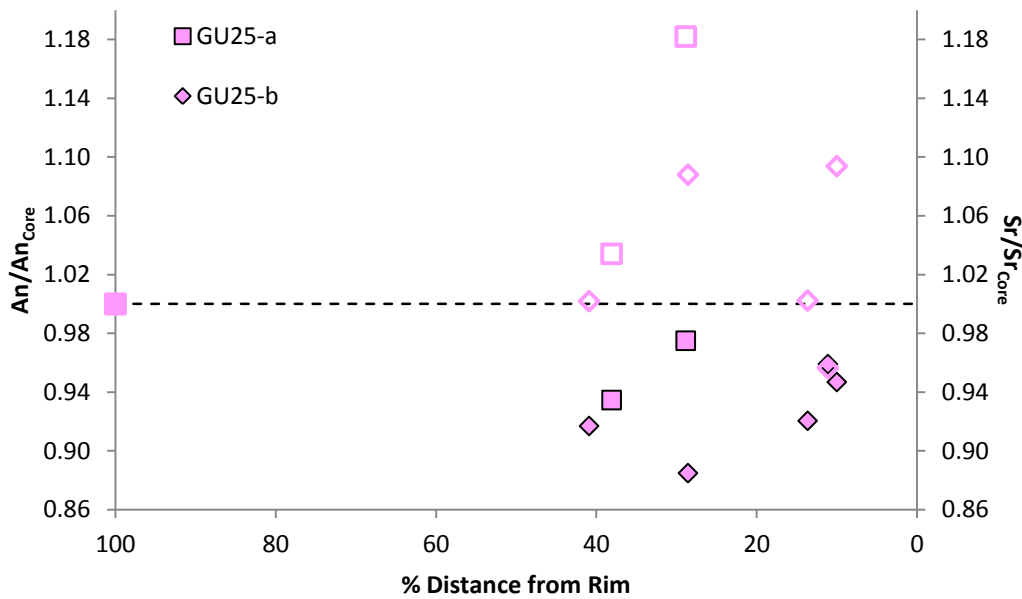


**Figure 4-35 An contents (solid symbols) and Sr concentrations (hollow symbols) ratioed to the core analyses for both GU25 populations against % distance from the rim.**

Entrainment is another possible mechanism for creating the An bimodalities seen. One population may have been included in the host melt as a result of magma mixing or from the disaggregation of a plagioclase bearing cumulate body. Entrained plagioclases would typically not be in equilibrium with the whole rock if they have been crystallised from a differing parent magma. Disequilibrium features are present in the GU25 thick section plagioclases. Two populations are present in GU25, both showing some evidence of disequilibrium and both having similar An contents. As the lower anorthite group was not sampled in the thick section analyses, it is difficult to comment on whether these crystals could have been entrained based on petrography.

Residence in a differing melt composition from which the plagioclases crystallised may result in diffusion between the melt and the phenocrysts. Thus, if new magma (with a higher concentration of incompatible elements) is introduced to the existing melt, higher concentrations of elements which are incompatible in plagioclase may be observed at the rims, although this effect may be difficult to differentiate from increases in partition coefficients with decreasing anorthite contents. Rates of diffusion differ by element. Diffusion within plagioclases is more rapid for Sr than

Ba (Cherniak, 2003). Cherniak (2003) noted similar diffusivities between the REE, with ionic radius having no real effect. However, it has been suggested that Eu should diffuse similarly to Sr as ionic charge may be important for diffusivity (Cherniak, 2003). Ca and other faster diffusing elements may have had the opportunity to fully re-equilibrate with the phenocryst plagioclases, however, higher REE concentrations in the rims of the crystals may have been preserved due to their slower diffusion rates. In the majority of crystals analysed in thick section from GU25, La concentrations are higher in the rims than in the cores of the crystals by up to a factor of 4 (Figure 4-36). Y concentrations are also higher in one crystal, with the Y data from many of the remaining crystals being contaminated by inclusion material. REE concentrations may be expected to be higher in the rims due to increasing compatibility with decreasing anorthite contents. However, the range in anorthite contents may not be large enough to prompt such large variations in La concentration between core and rim (for example in one crystal the range in An content is 6 mol% An but the La concentration varies by a factor of 2.4). This could potentially support the idea of the phenocrysts being resident in a more primitive melt.

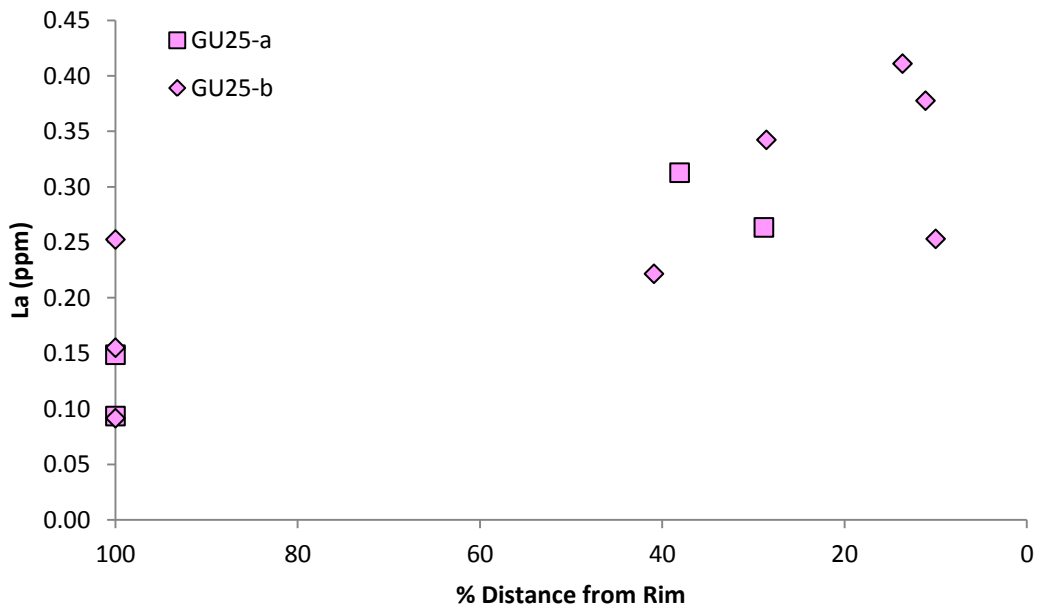


**Figure 4-36 La concentrations with % distance from rim in the GU25 thick section analyses.**

It is also possible that diffusive behaviour could have had a role to play if one of the populations was accumulated. If the lower anorthite groups were to have been

included in the melt responsible for crystallising the higher anorthite plagioclases, a similar effect may be evident.

For three of the Guadeloupe lavas (excluding GU27), the higher anorthite crystals are more numerous than the lower anorthite groups. This may suggest that the higher anorthite crystals are a product of the host melt and the lower anorthite crystals are a subsequent addition to the melt. The entrainment of crystals may also explain the numerous disequilibrium features present in the phenocrysts. However, it may also be that the lower anorthite groups crystallised from the melt following degassing, thus prompting a reduction in An contents. As discussed previously, degassing can also produce disequilibrium features in plagioclases.

#### 4.5.10 Sr and Ba Contents

The Sr contents of the analysed plagioclases are relatively constant and even decrease (with the exception of the lower anorthite group of GU25) with decreasing anorthite. This contradicts the findings of Blundy and Wood (1991), who showed that  $K_D^{Sr}$  should increase with decreasing anorthite contents. Thus if the concentration of Sr in the melt is constant, the Sr content of crystallising plagioclases should increase as anorthite content decreases. If a more mafic magma is introduced, this would be likely to increase anorthite contents and Sr concentrations of plagioclases being crystallised.

Partition coefficients were calculated based on the anorthite content of the crystals using the equations provided by Blundy and Wood (1991) in Equation 4-4 and Equation 4-5. In the following equations, R represents the universal gas constant (0.008314 kJ mol<sup>-1</sup>K<sup>-1</sup>), T is temperature in °C and  $X_{An}$  is the mole fraction of anorthite in the plagioclase.

##### Equation 4-4

$$R \times (T + 273) \times \ln D_{Sr} = 26.800 - 26.700 \times X_{An}$$

##### Equation 4-5

$$R \times (T + 273) \times \ln D_{Ba} = 10.200 - 38.200 \times X_{An}$$

Figure 4-37 shows calculated partition coefficients from Blundy and Wood (1991) against the analysed plagioclase molar anorthite contents. The partition coefficients

shown were calculated at temperatures of 500°C and 1500°C; illustrating that many of the  $[Ba]_{\text{plag}}/[Ba]_{\text{WR}}$  and  $[Sr]_{\text{plag}}/[Sr]_{\text{WR}}$  ratios (used as a proxy for partition coefficients for the analysed plagioclases) do not lie within this range of partition coefficients at a given anorthite content, despite the large temperature range. In addition, partition coefficients were calculated using temperatures provided by utilising the Bindeman et al. (1998) model for temperatures of crystallisation for plagioclases (Equation 4-6) and shown as black lines in Figure 4-37. In Equation 4-6, T is the temperature in °C,  $X_{\text{An}}$  is the anorthite content of the plagioclase,  $m = -2.04 \times 10^{-4}$  and  $n = 7.92 \times 10^{-4}$  (Bindeman *et al.*, 1998). As has been noted previously, this thermometer has only been shown to be reliable between An<sub>40</sub> and An<sub>80</sub>.

**Equation 4-6**

$$\frac{1}{T} = mX_{\text{An}} + n - 273$$

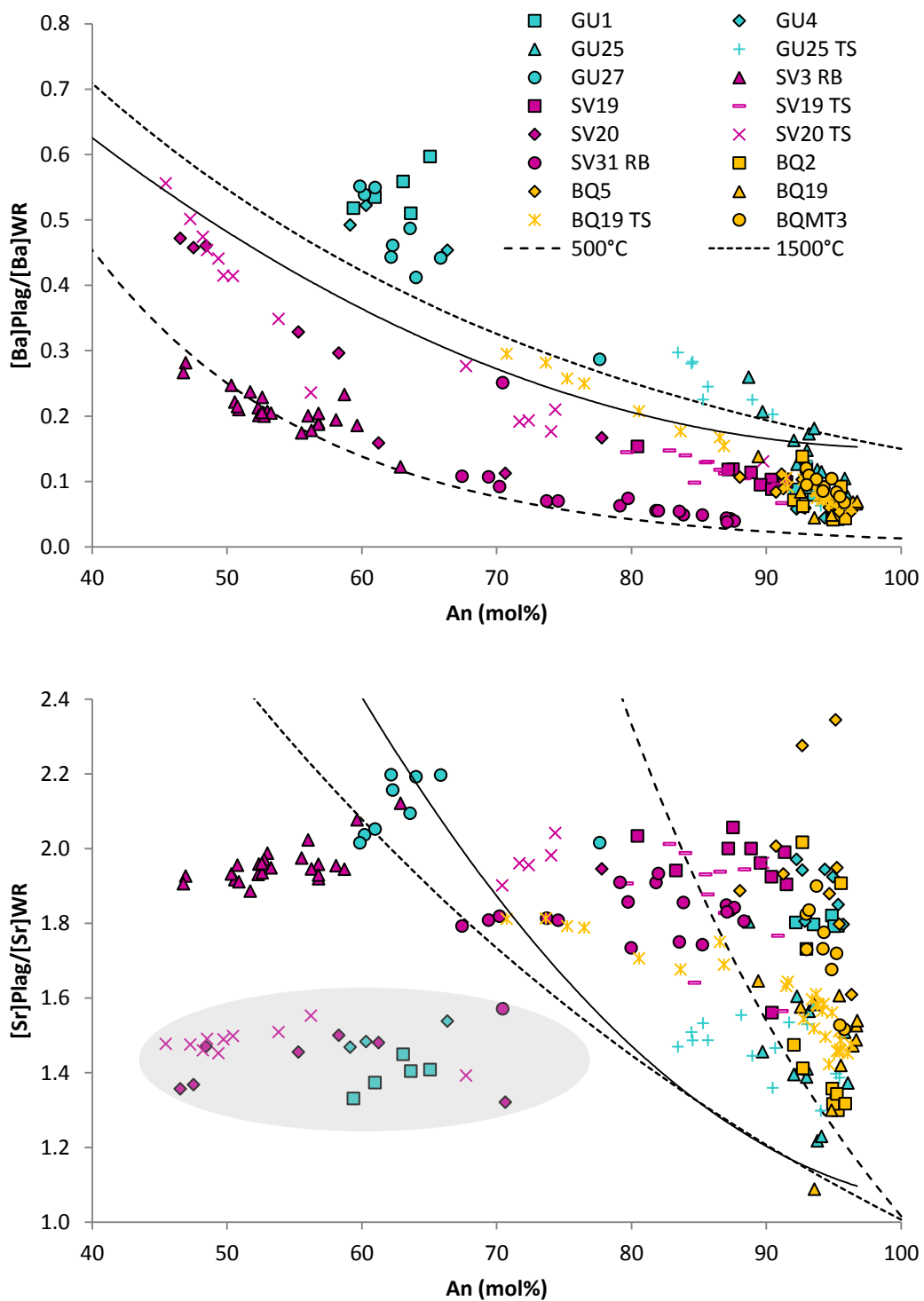


Figure 4-37 Concentrations of Ba and Sr in the analysed plagioclases ratioed with the whole rock concentrations compared to analysed plagioclase anorthite contents. The dashed black lines represent the partition coefficients calculated using Blundy and Wood (1991), with the solid black line using temperatures calculated from the analysed plagioclases using the Bindeman et al. (1998) equation. The grey ellipse shows a group of plagioclases with unexpectedly low  $[Sr]_{Plag}/[Sr]_{WR}$  at a given anorthite content.

The data show a general increase in  $[Ba]_{\text{plag}}/[Ba]_{\text{WR}}$  with decreasing An content, which is broadly consistent with the literature. Figure 4-37 shows that there is more agreement for the  $[Ba]_{\text{plag}}/[Ba]_{\text{WR}}$  ratios than for their  $[Sr]_{\text{plag}}/[Sr]_{\text{WR}}$  counterparts. In particular, SV3 and SV31 show a reasonable correlation with the 500°C Blundy and Wood (1991) model. However, the temperature estimates derived from the Putirka (2008) and Bindeman et al. (1998) models are much higher than 500°C for these samples, at around 1150°C and 1250°C respectively. The remaining St. Vincent plagioclases show trends in  $[Ba]_{\text{plag}}/[Ba]_{\text{WR}}$  that appear sub-parallel to the Blundy and Wood (1991) values at a given anorthite content. However, these again are offset from the Bindeman et al. (1998) trend. There are issues with using the whole rock concentrations, which may affect  $[Ba]_{\text{plag}}/[Ba]_{\text{WR}}$  but the Bindeman et al. (1998) temperatures are calculated solely from the plagioclase compositions. If the melts from which the St. Vincent plagioclases crystallised had lower Ba concentrations than the whole rock Ba content, this would shift the crystals upwards on Figure 4-37 and may begin to approach the trend defined by using the Bindeman et al. (1998) temperatures.

The  $[Ba]_{\text{plag}}/[Ba]_{\text{WR}}$  ratios for the BQ19 thick section analyses seem to depict a steeper gradient than those seen in the St. Vincent samples as anorthite contents decrease. The remaining Bequia plagioclases show a much smaller range in anorthite contents and thus it is difficult to ascertain if this gradient is replicated in the other lavas from this island.

The Guadeloupe plagioclases show an initial steep increase in  $[Ba]_{\text{plag}}/[Ba]_{\text{WR}}$  at high anorthite contents before shallowing at lower anorthite contents (approximately  $An_{65}$ ). In addition, the lower anorthite Guadeloupe plagioclases plot above the 1500°C Blundy and Wood (1991) partition coefficients, which again does not agree with the temperature modelling undertaken during this study. It is possible that the  $Ba_{\text{WR}}$  content used is too low (for example, if accumulation has affected the whole rock composition). A higher value would reduce  $[Ba]_{\text{plag}}/[Ba]_{\text{WR}}$  and thus the plagioclases would plot more in line with the Bindeman et al. (1998) trajectory. Adding 50 ppm Ba to the whole rock Ba concentrations would shift the plagioclases analyses to lie on the Bindeman et al. (1998) line, however, in the case of GU1, this would represent a 50% increase in whole rock Ba contents.

Little correlation between the  $[\text{Sr}]_{\text{plag}}/[\text{Sr}]_{\text{WR}}$  and Blundy and Wood (1991) models is evident for any of the host lavas. At high anorthite contents ( $> \text{An}_{90}$ ), there is a large range in  $[\text{Sr}]_{\text{plag}}/[\text{Sr}]_{\text{WR}}$  with little decrease in An content (Figure 4-37). Conversely, below  $\text{An}_{90}$ ,  $[\text{Sr}]_{\text{plag}}/[\text{Sr}]_{\text{WR}}$  remains fairly constant for most individual samples despite a large range in anorthite contents of approximately 20 mol%. Furthermore, there are a group of plagioclases (illustrated by the grey ellipse in Figure 4-37) which also exhibit largely unchanging  $[\text{Sr}]_{\text{plag}}/[\text{Sr}]_{\text{WR}}$  with anorthite content, but these are offset from the remaining plagioclases (around 0.5 lower  $[\text{Sr}]_{\text{plag}}/[\text{Sr}]_{\text{WR}}$ ). This discrepancy could suggest crystallisation from a melt with a lower Sr concentration. However, melts with sufficiently low Sr have not been documented in the Lesser Antilles. This suggests the variations observed in  $[\text{Sr}]_{\text{plag}}/[\text{Sr}]_{\text{WR}}$  with decreasing anorthite content cannot purely be explained by variations in  $K_D^{\text{Sr}}$  with An content.

Overall it would appear that the Blundy and Wood (1991) calculations, and others in the literature (Bédard, 2006, Bindeman & Davis, 2000, Bindeman *et al.*, 1998, Blundy & Wood, 1991) which suggest the  $K_D^{\text{Sr}}$  should increase as anorthite content decreases do not sufficiently explain the trends exhibited by the Lesser Antilles plagioclases. Temperature can be ruled out as a cause for the unsuitability as the Blundy and Wood (1991) calculations were performed over a range of temperatures (Figure 4-39).

Ren *et al.* (2003) noted a similar trend to that seen in the Sr contents of the Lesser Antilles plagioclases and suggested that this was a result of higher CaO contents and lower  $\text{SiO}_2$  contents in the whole rocks bearing the plagioclases in conjunction with temperature effects. When plotted against the Lesser Antilles data, it can be seen that the trend produced by the Ren *et al.* (2003) partition coefficients appears to lie sub-parallel to those exhibited by some of the samples (e.g. SV3 and SV31) (Figure 4-38). However, the Ren *et al.* (2003) samples are peraluminous silicic magmas, so there is an issue of how applicable these findings are to the Lesser Antilles lavas studied.

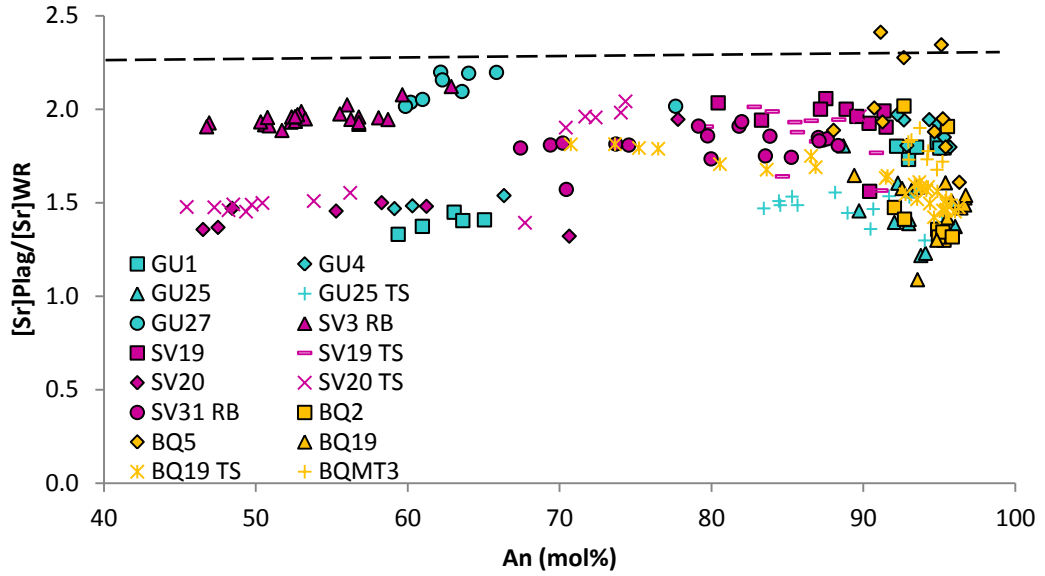


Figure 4-38 Lesser Antilles plagioclase data compared to the partition coefficient trend of Ren et al. (2003), represented by the dashed line, showing a more suitable gradient than that seen using the Blundy and Wood (1991) partition coefficient equations.

#### 4.5.11 Partition Coefficient Issues

Having established that the Blundy and Wood (1991) partition coefficients alone do not explain the Sr and Ba composition of the Lesser Antilles plagioclases, potential explanations for this were considered. The possibilities include:

- Accumulation of plagioclase phenocrysts
- Entrainment of plagioclase crystals
- Effect of water on partitioning
- Decompression/degassing of the melt

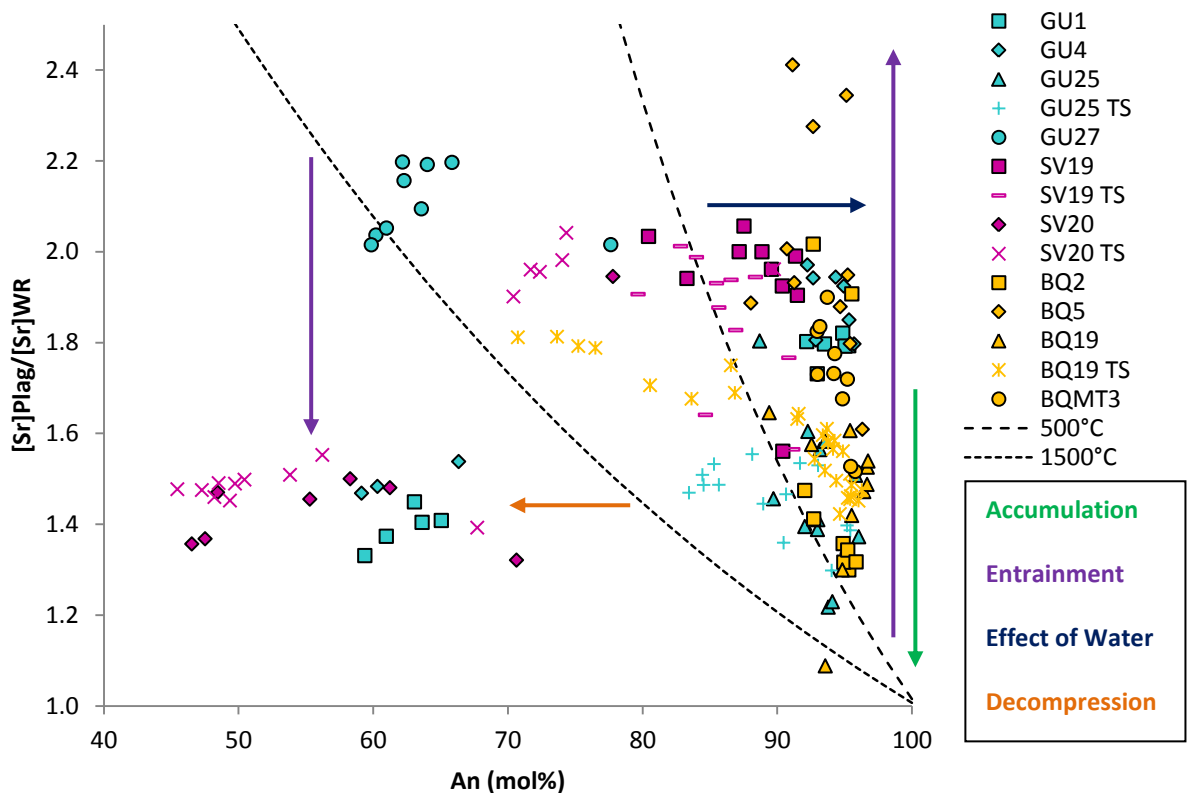


Figure 4-39  $[Sr]_{\text{plag}}/[Sr]_{\text{WR}}$  calculated for the analysed plagioclases against anorthite content. The dashed lines represent the Blundy and Wood (1991)  $K_D^{\text{Sr}}$  at 500°C and 1500°C. Annotations show the effect of possible processes affecting the system which may move the analysed crystals away from the Blundy and Wood (1991) lines. The coloured arrows and matching processes in the text box to the right indicate the direction in which the plagioclases would be shifted as a result of the processes discussed below, the length of the arrows bears no significance.

### Accumulation

If the host lavas studied had accumulated plagioclase crystals, this may cause an increase in the Sr concentration of the whole rocks. This would then cause a reduction in the  $[Sr]_{\text{plag}}/[Sr]_{\text{WR}}$  ratio at a given anorthite content (green arrow in Figure 4-39). However, accumulation of plagioclases within the melt should not produce the disequilibrium features which are seen petrographically. Accumulated plagioclases should derive from the same melt composition as the host melt. Therefore textures such as the sieving, corrosion of cores and particularly the resorbed edges should not be seen if accumulation was solely responsible for the discrepancies between  $[Sr]_{\text{plag}}/[Sr]_{\text{WR}}$  and the Blundy and Wood (1991) values at a given An content.

### ***Entrainment***

This process is capable of both increasing or decreasing the  $[\text{Sr}]_{\text{plag}}/[\text{Sr}]_{\text{WR}}$  depending on the Sr concentration of the plagioclases entrained (shown as purple arrows in Figure 4-39). This is therefore dependent on whether the melts responsible for crystallising the entrained plagioclases had higher or lower Sr contents than the host melt. However, given that Sr concentrations in plagioclases are likely to be higher than those of the whole rocks, it follows that entrainment of plagioclases would increase  $[\text{Sr}]_{\text{plag}}/[\text{Sr}]_{\text{WR}}$  in most instances.

### ***Effect of Water on Partitioning***

The Blundy and Wood (1991) model does not explicitly discuss changes in anorthite content produced by water saturation. This could cause the displacement between the Blundy and Wood (1991)  $K_D$  values and the calculated  $[\text{Sr}]_{\text{plag}}/[\text{Sr}]_{\text{WR}}$  as the anorthite contents of the plagioclases would be shifted to higher An, to the right of the Blundy and Wood (1991) lines (dark blue arrow in Figure 4-39). The Blundy and Wood (1991) model would then predict lower  $K_D$  values than required. It is possible that water saturation may affect the shape and position of the  $K_D^{\text{Sr}}$  curves in Figure 4-39 but currently their model has not been modified for hydrous melts. As discussed previously, it is thought that Lesser Antilles basaltic melts have water contents of between 1-2 wt% and basaltic andesites approximately 3 wt% (Macdonald *et al.*, 2000) (section 4.5.3).

### ***Shallow Level Decompression/Degassing***

If the anorthite compositions of the plagioclases have been reduced, this may cause the shift away from the Blundy and Wood (1991) partition coefficient line in Figure 4-39 (shown by the orange arrow), mainly for the lower anorthite plagioclases (<An<sub>70</sub>). However, for plagioclases that have already crystallised prior to decompression/degassing, there will be little to no change in the anorthite contents of the cores of the crystals (where the majority of the analyses were undertaken).

Decompression or degassing do not appear to be suitable processes to cause the  $[\text{Sr}]_{\text{plag}}/[\text{Sr}]_{\text{WR}}$  of plagioclases to be higher than the Blundy and Wood (1991)  $K_D$  values at a given anorthite content.

### ***Magma Mixing***

The introduction of melts with differing compositions may also affect  $[\text{Sr}]_{\text{plag}}/[\text{Sr}]_{\text{WR}}$  and again depends on the chemistry of the melts being input into the host. Melts with higher Sr concentrations will increase the whole rock Sr content and thus decrease  $[\text{Sr}]_{\text{plag}}/[\text{Sr}]_{\text{WR}}$ , with the reverse being true if the added melt has a lower Sr concentration. This will then produce similar effects to those resulting from entrainment (Figure 4-39). However, the host melt chemistry will be changed by the introduction of new magma, causing any subsequently crystallised plagioclases to have a different  $[\text{Sr}]_{\text{plag}}/[\text{Sr}]_{\text{WR}}$  to those predating the mixing event(s). The St. Vincent and Bequia lavas do not show evidence of bimodality in Figure 4-37 which would suggest that there are either no differences between pre- and post-mixing crystallised plagioclases or that magma mixing has not played a role in generating the observed  $[\text{Sr}]_{\text{plag}}/[\text{Sr}]_{\text{WR}}$  ratios.

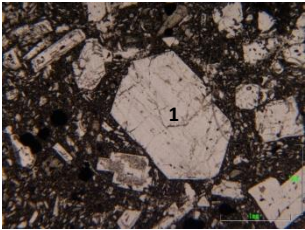
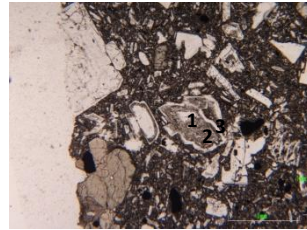
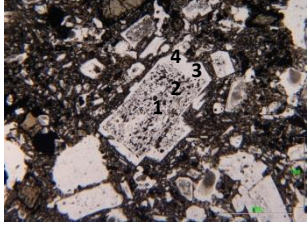
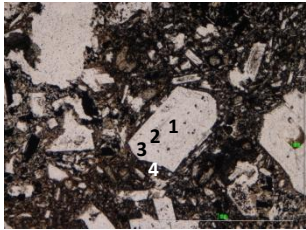
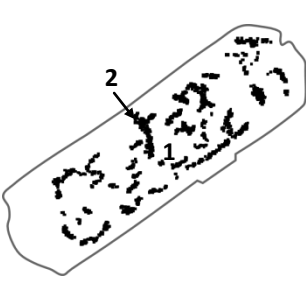
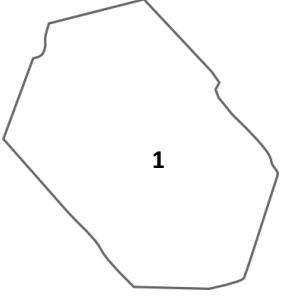
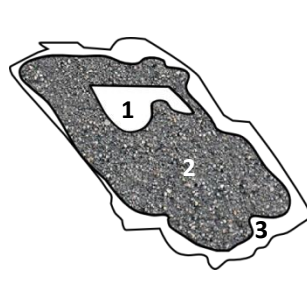
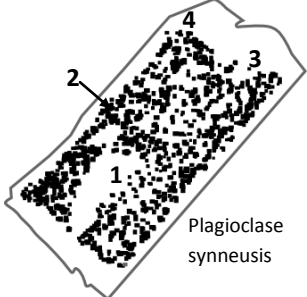
## **4.6 Conclusions**

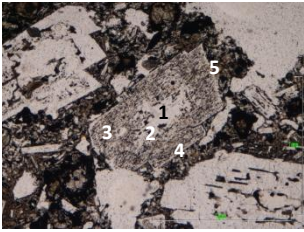
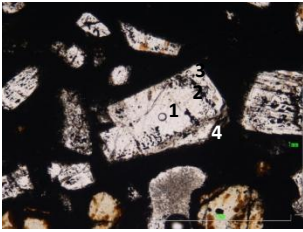
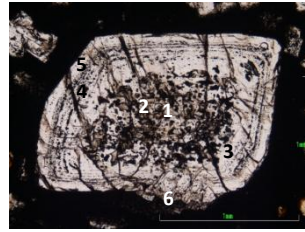
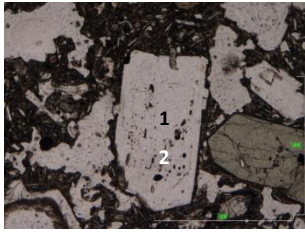
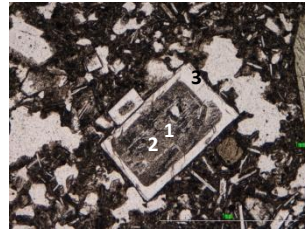
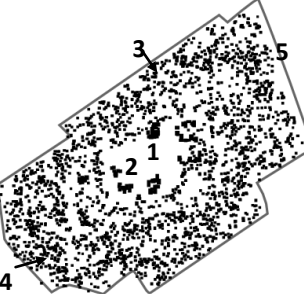
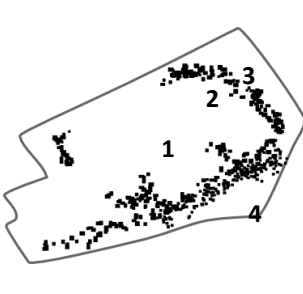
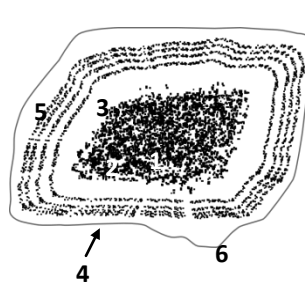
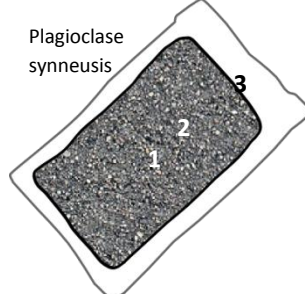
From the textural and geochemical evidence it can be observed that the Lesser Antilles host lavas analysed show at least two populations in most samples (Table 4-7). These populations are evidence of varying petrogenetic paths in the islands sampled (Figure 4-40). Some of the populations seen appear similar across two or more islands, for example GU27-b and SV19-b (heavily sieved cores) and GU1-c, SV20-a and BQ2-a (sieved zone but fresher cores) (Table 4-7). This would suggest similar plagioclase petrogenetic processes are operating across the arc from Guadeloupe in the centre to Bequia in the south.

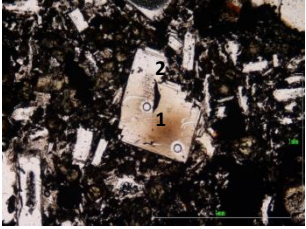
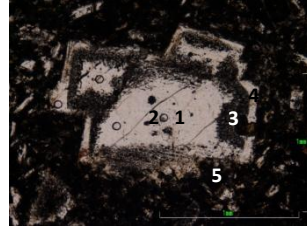
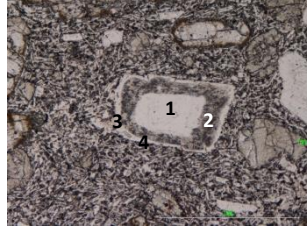
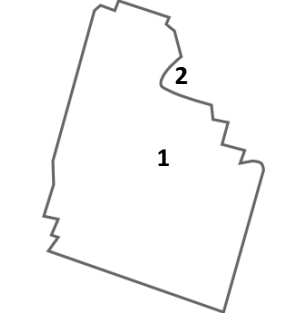
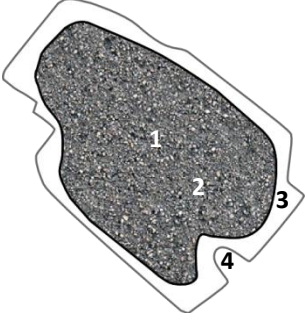
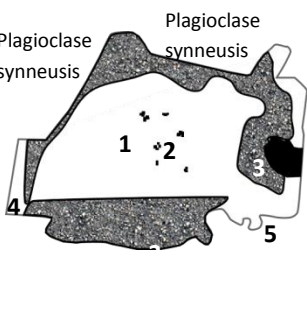
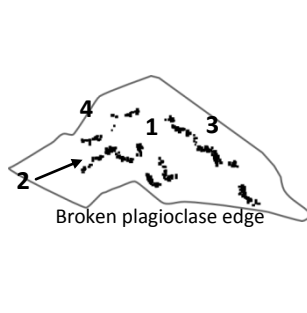
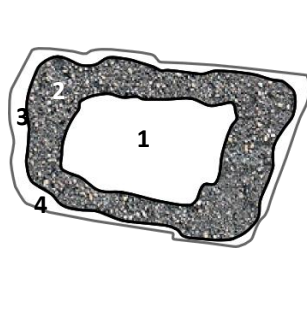
Most of the populations show evidence of shallow level degassing and/or decompression, suggesting that melts were held in a shallow level magma chamber prior to eruption in each island sampled. Entrainment and magma mixing are also prevalent. Figure 4-40 shows a schematic overview of processes occurring in the Lesser Antilles and the ensuing textures generated from them. The figure shows the processes in isolation while Table 4-7 shows which processes occur in which order for each of the observed populations.

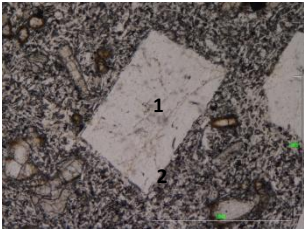
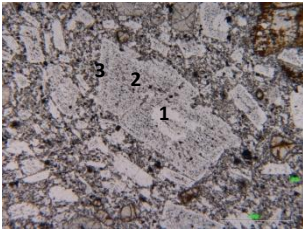
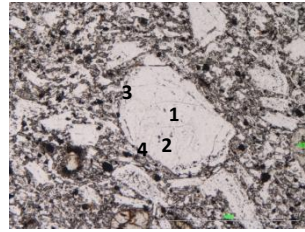
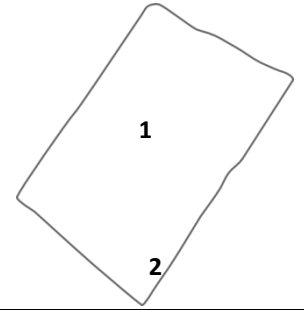
High anorthite contents are liable to be a result of increased water contents in the parent melts, a function of the intra-oceanic nature of the Lesser Antilles arc.

Bimodality in anorthite content may be a result of differing populations being analysed, although this bimodality is largely observed in the crystal mount analyses, making population identification difficult.

Population	GU1-a	GU1-b	GU1-c	GU4-a	GU4-b
<b>Photograph</b>					
<b>Schematic</b>					
<b>1</b>	Crystallisation	Crystallisation	Crystallisation	Crystallisation	Crystallisation
<b>2</b>	Decompression	Eruption	Entrainment	Decompression	Decompression
<b>3</b>	Crystallisation		Crystallisation	Crystallisation	Crystallisation
<b>4</b>	Eruption		Eruption	Shallow degassing	Shallow degassing
<b>5</b>				Eruption	Eruption
<b>6</b>					
<b>7</b>					

Population	GU4-c	GU25-a	GU25-b	GU27-a	GU27-b
Photograph					
Schematic					
1	Crystallisation	Crystallisation	Crystallisation	Crystallisation	Crystallisation
2	Decompression	Magma mixing	Decompression	Decompression	Entrainment
3	Entrainment	Crystallisation	Crystallisation	Eruption	Crystallisation
4	Crystallisation	Shallow degassing	Magma mixing		Eruption
5	Shallow degassing	Eruption	Crystallisation		
6	Eruption		Shallow degassing		
7			Eruption		

Population	SV19-a	SV19-b	SV20-a	SV20-b	SV3-a
Photograph					
Schematic					
1	Crystallisation	Crystallisation	Crystallisation	Crystallisation	Crystallisation
2	Shallow degassing	Entrainment	Decompression	Decompression	Entrainment
3	Eruption	Crystallisation	Entrainment	Crystallisation	Crystallisation
4		Shallow degassing	Crystallisation	Shallow degassing	Shallow degassing
5		Eruption	Shallow degassing	Eruption	Eruption
6			Eruption		
7					

Population	SV3-b	SV31-a	SV31-b
<b>Photograph</b>			
<b>Schematic</b>			
<b>1</b>	Crystallisation	Crystallisation	Crystallisation
<b>2</b>	Shallow degassing	Entrainment	Decompression
<b>3</b>	Eruption	Shallow degassing	Magma mixing
<b>4</b>		Eruption	Shallow degassing
<b>5</b>			Eruption
<b>6</b>			
<b>7</b>			

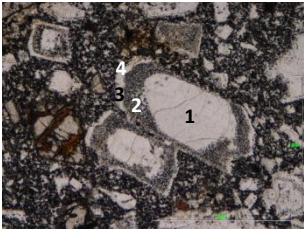
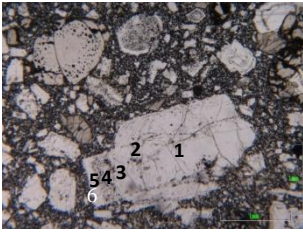
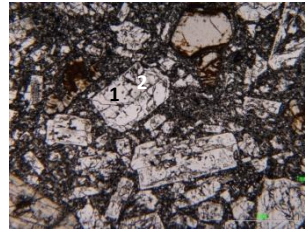
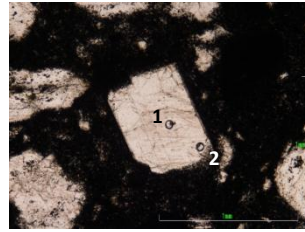
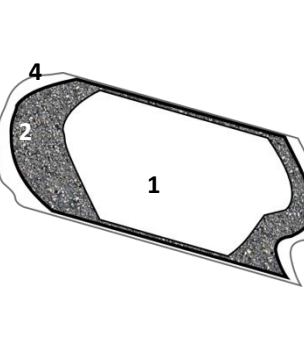
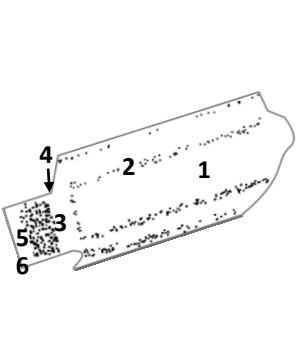
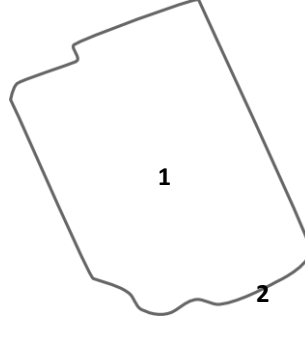
Population	BQ2-a	BQ2-b	BQ5-a	BQ19-a	BQ19-b
<b>Photograph</b>					
<b>Schematic</b>					
<b>1</b>	Crystallisation	Crystallisation	Crystallisation	Crystallisation	Crystallisation
<b>2</b>	Entrainment	Magma mixing	Decompression	Decompression	Shallow degassing
<b>3</b>	Crystallisation	Crystallisation	Eruption	Magma mixing	Eruption
<b>4</b>	Shallow degassing	Magma mixing		Crystallisation	
<b>5</b>	Eruption	Crystallisation		Magma mixing	
<b>6</b>		Shallow degassing		Shallow degassing	
<b>7</b>		Eruption		Eruption	

Table 4-7 Processes affecting each population of plagioclases identified in the thin sections analysed. Numbers on the photographs and diagrams correspond to those of the listed processes for each population and represent the order in which these processes are thought to have occurred.

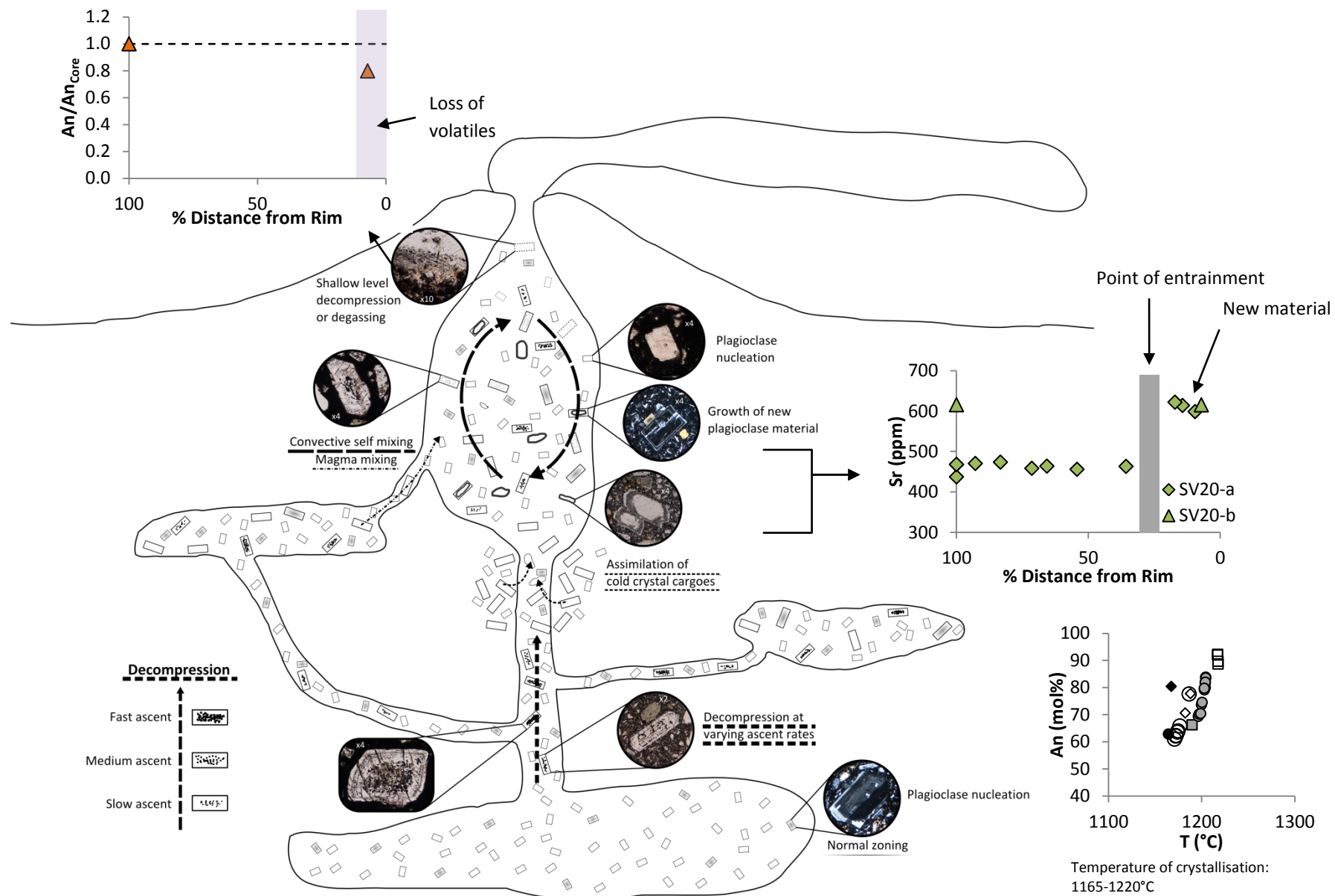


Figure 4-40 Schematic representation of processes occurring throughout the Lesser Antilles arc observed in analysed plagioclases. Temperature estimates are calculated from Putrika (2008).

## 4.7 Further Work

- Analysis of plagioclases in thick sections from more islands to broaden the range of the study and more accurately constrain any trends seen along strike of the arc.
- Sr isotopic microsampling of plagioclase zones to provide further insight into petrogenesis.
  - This would also allow easier differentiation between convective self mixing (which should not show isotopic differences) and magma mixing from separate melts (which may show isotopic differences).

---

## 5 Clinopyroxene Chemistry

---

### 5.1 Introduction

#### 5.1.1 Reasons for Analysing Clinopyroxene

Clinopyroxenes can provide useful information on magma petrogenesis. Their compositions can be used to back calculate melt chemistries from which they were crystallised. Clinopyroxene is the main repository for incompatible elements in a basaltic magma, allowing for the measurement of their concentrations at higher values than in the olivine and plagioclase analyses. In particular, partition coefficients can be estimated using the equations of Wood and Blundy (1997) for the REE. These can then be used to provide approximate rare earth element profiles for the clinopyroxene parent melts. Estimates can be made as to whether the clinopyroxenes are in equilibrium with their host melts. Clinopyroxenes not in equilibrium can indicate other processes, such as accumulation.

Furthermore, geothermobarometry calculations can be performed using the clinopyroxene compositions (Putirka, 2008 and references therein). In comparison to those methods developed for olivine and plagioclase, clinopyroxene geothermobarometry has received more attention in the literature, as detailed in the review of Putirka (2008). Geothermobarometry can be done using both the clinopyroxene and whole rock compositions as well as the clinopyroxene chemistry alone.

Zoning may be observed across crystals if the melt composition is changing during crystallisation. Clinopyroxenes from two of the host lavas studied were analysed in thick section to see if variations were apparent across individual clinopyroxenes.

As with the olivines (Chapter 2) and plagioclases (Chapter 3), clinopyroxenes were also analysed to see if any variations both within host lavas and between islands was apparent. Heterogeneities could suggest the presence of multiple populations of clinopyroxenes present in the host lavas.

### **5.1.2 Aims of Analysing Clinopyroxene in the Lesser Antilles**

The study aims to provide detailed major and trace element data for clinopyroxenes from host lavas erupted at several islands along the strike of the arc. No study comparing clinopyroxenes from this many islands across the Lesser Antilles has previously been performed. In addition, the number of trace elements analysed in conjunction with major elements is extensive compared to published studies.

#### *Aims*

- To provide a clinopyroxene dataset spanning several Lesser Antilles islands comprising an extensive range of major and trace elements.
- To perform geothermobarometric calculations using the clinopyroxene compositions to provide information on temperatures and pressures at which the minerals crystallised.
- To observe any variations both within host lavas and along arc strike in either clinopyroxene composition and/or crystallisation temperatures and pressures.
- To provide a more detailed overview of the petrogenesis of Lesser Antilles lavas in conjunction with the olivine and plagioclase datasets.

## **5.2 Host Lavas**

123 clinopyroxenes from the Lesser Antilles were analysed in the same three media as the plagioclases (Chapter 3): crystal mounts, thick sections and resin blocks. 5 islands (Guadeloupe, St. Vincent, Bequia, Carriacou and Grenada) were targeted, however only one host lava was studied from Bequia. In total, 13 host lavas were sampled although  $n$  varies between 1 and 26, where  $n$  is the number of discrete crystals (or crystal fragments) analysed. Table 5-1 shows the locations from which these host lavas were derived, the modal clinopyroxene proportions for each host lava obtained from point counting (using 1500 counts per host lava) and the numbers of crystals analysed by each method.

<b>Host Lava</b>	<b>Island</b>	<b>Modal Cpx (%)</b>	<b>Whole Rock MgO (wt%)</b>	<b>n CM</b>	<b>n TS</b>	<b>n RB</b>
<b>GU20</b>	Guadeloupe	8.2	4.93	26	-	-
<b>GU25</b>	Guadeloupe	5.2	6.20	-	2	-
<b>GU26</b>	Guadeloupe	6.3	4.53	23	-	-
<b>SV3</b>	St.Vincent	4.2	8.60	-	-	5
<b>SV20</b>	St.Vincent	15.5	6.35	-	4	-
<b>SV31</b>	St.Vincent	5.6	6.82	-	-	4
<b>BQ19</b>	Bequia	2.1	3.03	-	3	-
<b>CA3</b>	Carriacou	7.4	15.53	6	-	-
<b>CU19</b>	Carriacou	5.3	15.80	-	-	6
<b>CU28</b>	Carriacou	3.9	16.49	-	-	1
<b>468</b>	Grenada	9.7	15.96	16	-	-
<b>6103</b>	Grenada	7.4	15.28	-	-	10
<b>6259</b>	Grenada	9.4	13.10	-	-	17

**Table 5-1** Sample names and locations of the host lavas from which the clinopyroxenes were analysed. Also shown are the modal proportions of clinopyroxene in each host lava ascertained from point counting data (1500 counts per thin section) and the whole rock MgO content. **n** shows the number of clinopyroxene crystals analysed using each method, where CM are crystal mount analyses, TS are thick sections and RB are from resin blocks. It should be noted that **n** represents the number of discrete clinopyroxene crystals analysed in each host lava rather than the total number of analyses undertaken.

### **5.3 Clinopyroxene Petrography**

Thin sections of the clinopyroxene host lavas were studied. The host lavas were all porphyritic, with approximate modal proportions of each phase (olivine, plagioclases, clinopyroxene, orthopyroxene and oxides) being available in Chapter 2.

#### **5.3.1 Guadeloupe**

Clinopyroxenes from the three Guadeloupe host lavas are petrographically similar. The crystals are primarily subhedral and up to 3 mm in size in GU20, up to 5 mm in

GU25 and up to 1.5 mm in GU26. There is very little clinopyroxene apparent in the groundmass of GU25, however, it is observed in the groundmasses of GU20 and GU26. Glomerocrysts of clinopyroxene are found in both GU20 and GU26. Multiple small inclusions are apparent in some crystals, as seen in Figure 5-1.

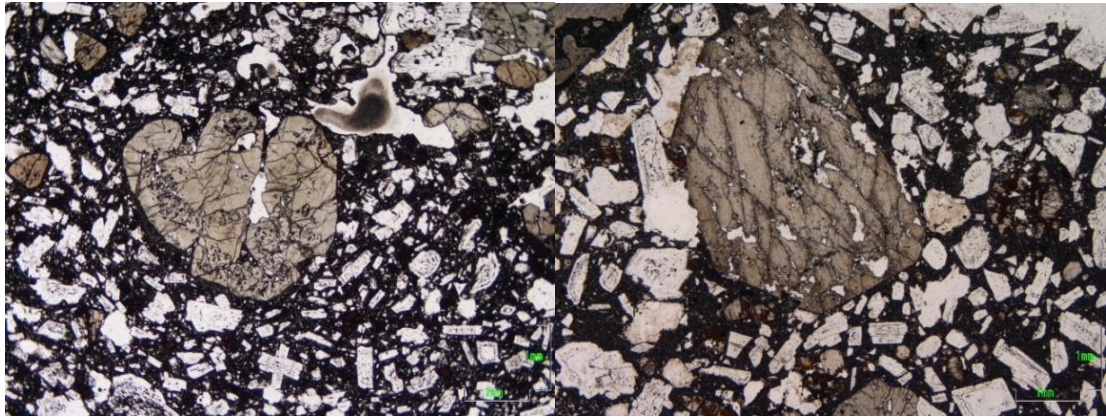


**Figure 5-1 Clinopyroxenes shown in PPL from GU20 (left hand side photographs) and GU25 (right hand side photograph).**

In addition, zoning can be observed in clinopyroxenes from GU25, such as in crystal GU25-1 (Figure 5-2).

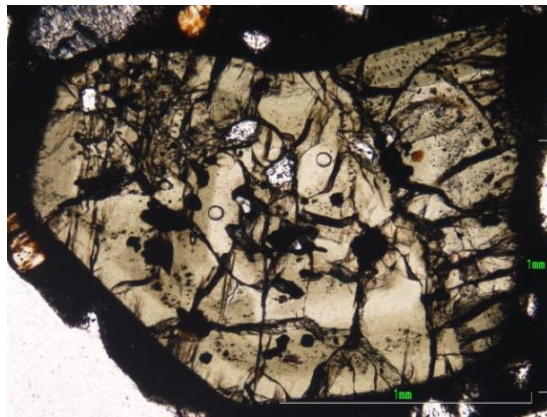


**Figure 5-2 Crystal GU25-1 shown in thick section in PPL showing zoning. The circular structures are the pits ablated during LA-ICP-MS analysis.**

### **5.3.2 St. Vincent**

Clinopyroxenes in SV20 are subhedral to anhedral, with phenocryst sizes up to 2 mm in SV3 and SV20 and up to 2.5 mm in SV31. Clinopyroxene material is also observed in the groundmasses. Inclusion material within clinopyroxenes as observed in some of the Guadeloupe crystals is also seen in the St. Vincent host lavas (Figure

5-3), particularly in SV20 and SV31. However, little evidence of zoning is apparent in thin section.

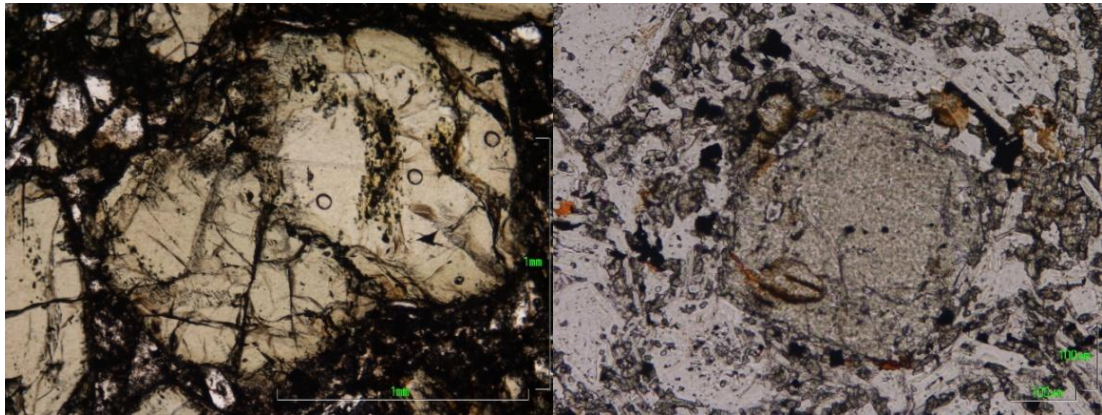


**Figure 5-3** Fine scale inclusions within a clinopyroxene from SV20 seen in PPL. Again, the circles present show the location of the LA-ICP-MS spots.

A large glomerocryst (5 mm in size) is present in the SV20 thick section, comprised of clinopyroxene crystals surrounding olivine and plagioclase crystals in the centre. Glomerocrysts are also observed in SV3 (Figure 5-4).

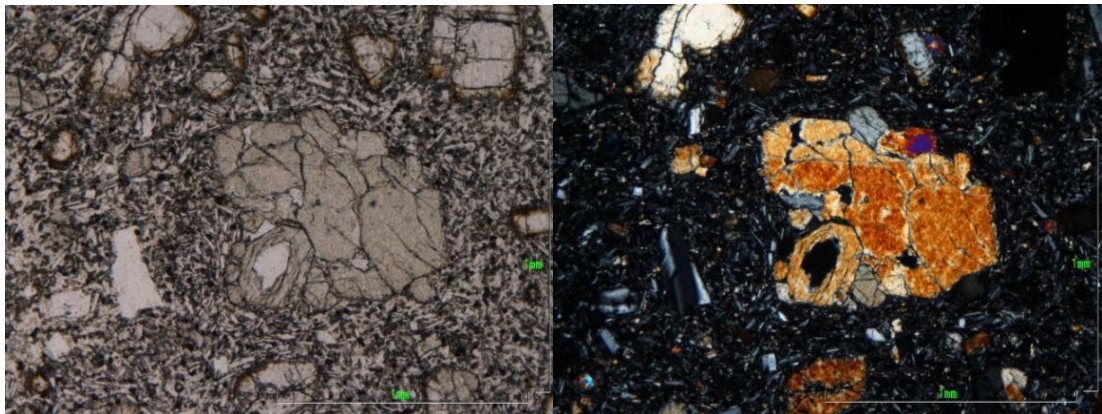


**Figure 5-4** Glomerocryst in SV3, shown in PPL in the left hand photograph and XPL in the right hand photograph.

### 5.3.3 Bequia

Clinopyroxenes from BQ19 are euhedral to subhedral and up to 3 mm in size. As for the Guadeloupe and St. Vincent host lavas, little clinopyroxene is observed in the groundmass of BQ19. Clear zoning is observed in some crystals, as seen in Figure 5-5. Small inclusions within the clinopyroxene crystals are also seen in some crystals (Figure 5-5).

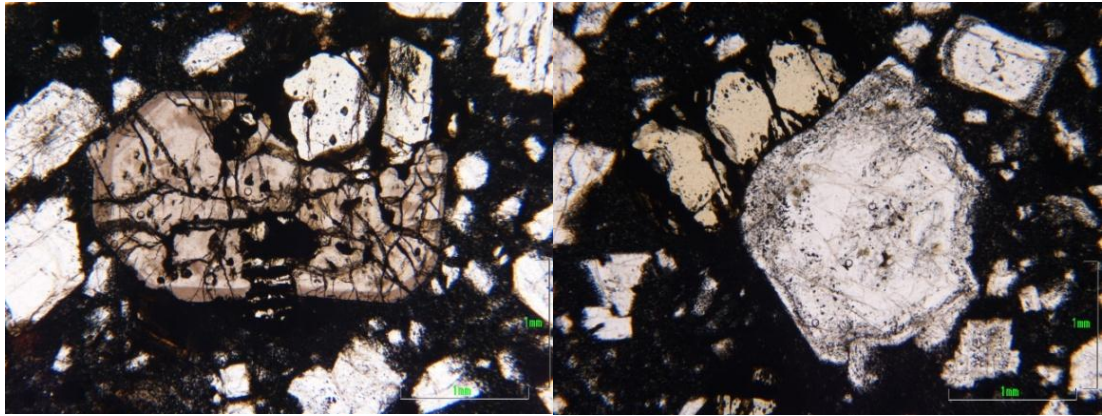


**Figure 5-5** Clinopyroxene BQ19-1 (left hand side) and another unanalysed crystal from BQ19 (right hand side) photographed in PPL. Zoning is apparent in BQ19-1 (as are the LA-ICP-MS sites). Fine scale inclusions are seen in the clinopyroxene bordering the plagioclase crystal in the centre of the right hand side photograph.

### 5.3.4 Carriacou

Clinopyroxenes from the Carriacou host lavas are subhedral to euhedral and are smaller than in many of the other host lavas, being up to 1.5 mm in size in CU19 and CU28 and up to 2 mm in CA3. Clinopyroxenes are also observed in the groundmasses of the host lavas. Fine scale inclusions are not observed, however, there are crystals in CA3 with smaller plagioclase laths within the clinopyroxenes (Figure 5-7). Glomerocrysts were observed in CU19 and CU28 (Figure 5-6).

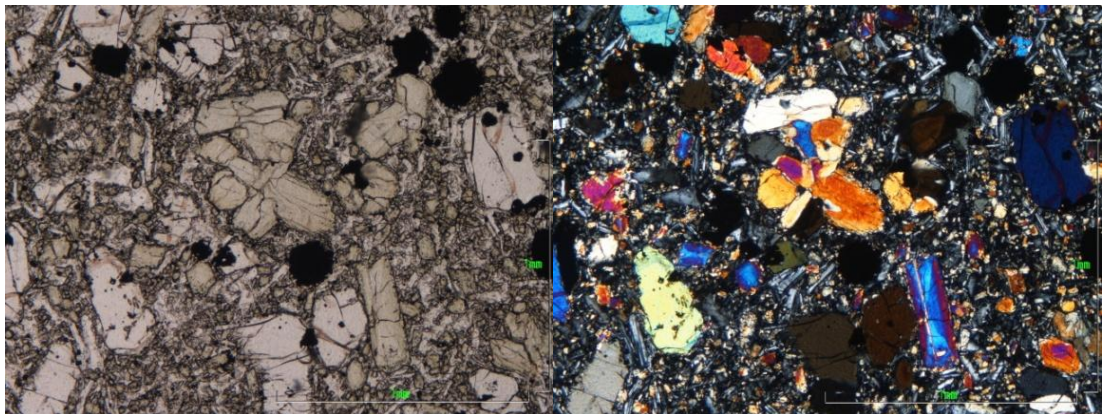


**Figure 5-6** Glomerocryst in CU28 in PPL (left hand side) and XPL (right hand side). The clinopyroxenes are small, with the overall size of the glomerocryst being less than 1 mm across in size. Also shown in the lower right quadrant of the photographs is a clinopyroxene exhibiting sector twinning in XPL.

Furthermore, there are also crystals in CA3 which show core zones which are slightly darker in PPL and show different birefringence colours in XPL when compared to the margins of the crystals.

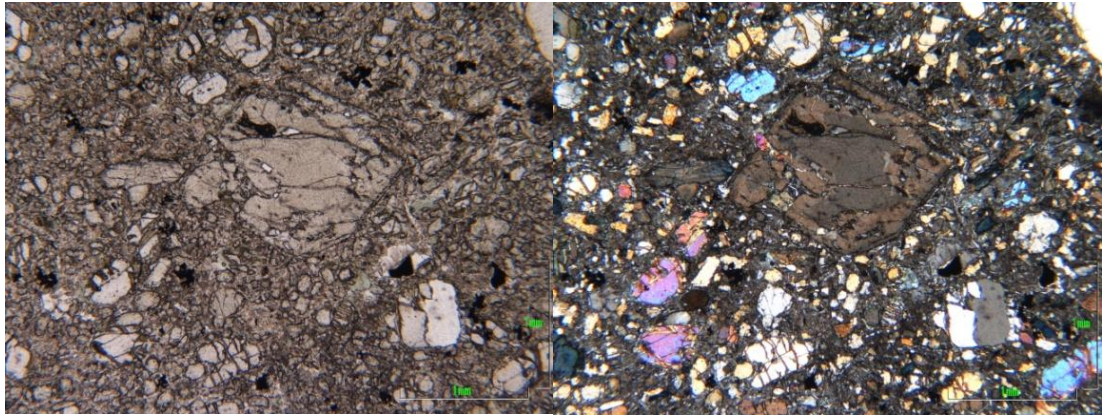


**Figure 5-7** Clinopyroxene crystal from CA3 photographed in PPL (left hand photograph) and XPL (right hand photograph). The crystal shows evidence of breaking down at the crystal margins. Zoning is also seen in the XPL photograph, with the core area showing a different birefringence colour to the outer margins. In addition, there are at least two small plagioclase laths within the clinopyroxene crystal.

### 5.3.5 Grenada

Crystals from the Grenada host lavas are subhedral to anhedral. The clinopyroxenes from 6103 are much smaller than those from the host lavas from other islands, being up to 0.5 mm in size, the clinopyroxenes in 6259 are up to 1 mm. The crystals from 468 are larger, being up to 3 mm in size. Small clinopyroxene crystals are present in the groundmass of all three host lavas. There is little evidence of fine scale inclusions within the Carriacou clinopyroxenes except in 468 (Figure 5-8). Zoning and glomerocrysts are not apparent in thin section in any of the host lavas.

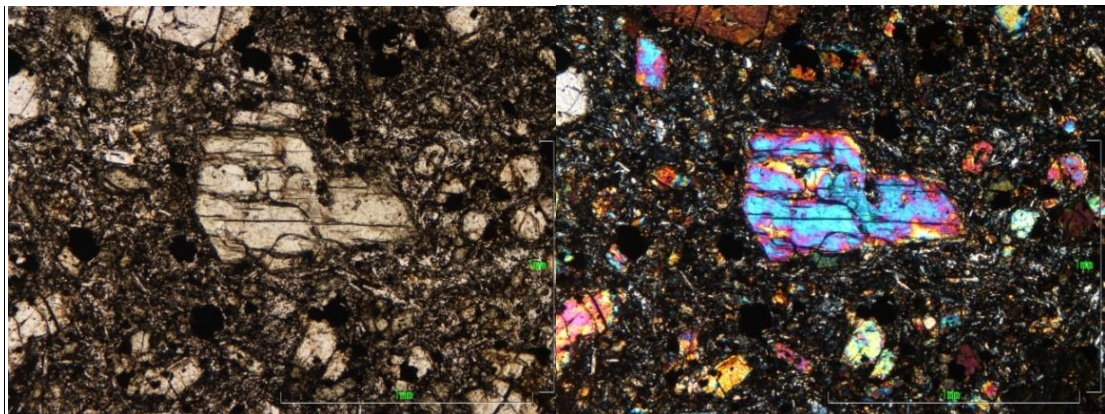


**Figure 5-8** Clinopyroxene crystal from 468 photographed in PPL (left hand side) and XPL (right hand side). Cleavage is well defined in this crystal and can be seen particularly well in PPL.

## 5.4 Clinopyroxene Chemistry

### 5.4.1 Pyroxene Quadrilateral

Endmember calculations were performed on the Lesser Antilles clinopyroxenes compositions to observe where the crystals would plot on a pyroxene quadrilateral (Figure 5-9). The Guadeloupe minerals all plot in the augite field, as do the St. Vincent clinopyroxenes. The host lavas from Bequia, Carriacou and Grenada all show crystals in both the augite and diopside fields. However, the lone clinopyroxene from CU28, 9 of 10 CU19 analyses and all of the CA3 clinopyroxenes plot as diopsides leaving only one Carriacou clinopyroxene plotting in the augite field. BQ19 shows 7 analyses in the diopside field (out of 16), the remainder being augites. Of the 16 468 clinopyroxenes, half are augite in composition and half are diopside. 9 clinopyroxenes from 6103 are augite, leaving 6 diopside clinopyroxenes. 14 of the 29 6259 analyses are augites with the remaining 15 being diopsides.

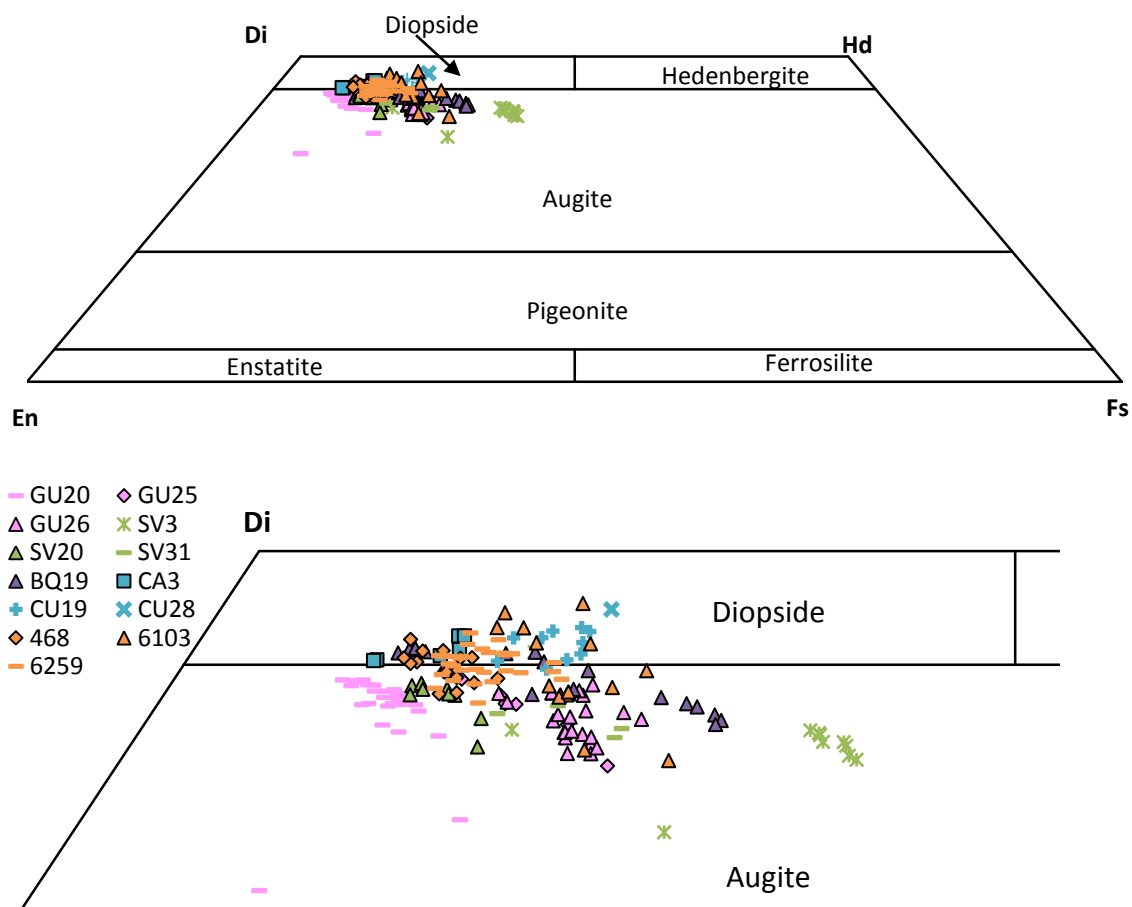


**Figure 5-9 Pyroxene quadrilateral (upper graph) and an excerpt from a pyroxene quadrilateral (lower graph) showing the locations of the Lesser Antilles clinopyroxenes after calculation of endmembers.**

### 5.4.2 Mg#

Mg# was used for the clinopyroxenes as forsterite content was used for the olivines: as an indicator of evolution of the melts from which the crystals crystallised. Figure 5-10 shows the distribution of Mg# in each host lava of all the clinopyroxene analyses.

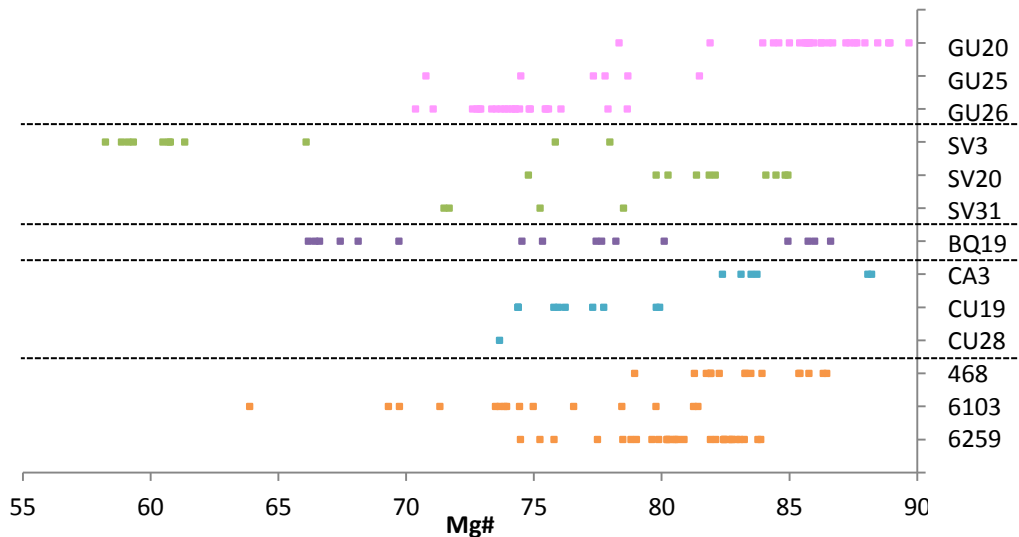


**Figure 5-10 Mg# numbers of the clinopyroxene crystals, including crystal mount, thick section and resin block analyses. Islands are ordered by latitude on the y axis. Each island is shown as a different colour.**

The total range in Mg# observed in the analysed clinopyroxene is 58-90. Ranges in the individual islands are: Guadeloupe 71-90, St. Vincent 58-85, Bequia 66-87 (although only one host lava was analysed from this island), Carriacou 74-88 and Grenada 64-86. All the islands contain clinopyroxenes with Mg#  $\geq$ 85. Bimodality in clinopyroxene Mg# is not apparent in any of the host lavas, but SV3 shows a cluster of analyses at Mg#<sub>58-61</sub>. Large ranges in Mg# are apparent in some host lavas, such as BQ19 (with a range of 20.4), SV3 (19.7) and 6103 (17.5). In contrast, CA3 and CU19 exhibit much smaller ranges (5.8 and 5.5 respectively).

The % distance from rim was calculated for the St. Vincent and Guadeloupe thick section analyses using the same method as for the olivines and plagioclases (Chapter 2). Figure 5-11 shows that there is some evidence for lower Mg# at the rims than in the cores of the clinopyroxenes.

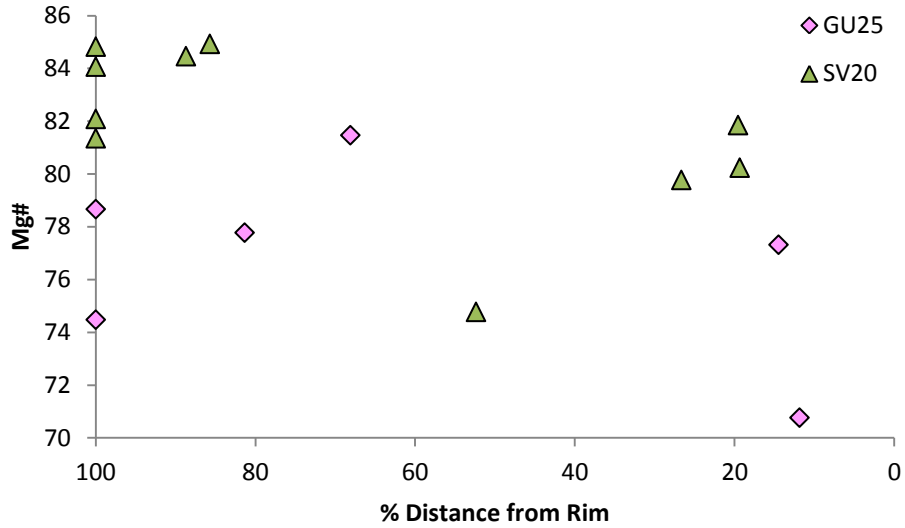


**Figure 5-11** Variation in Mg# with % distance from the rim. 100% distance from the rim indicates the core analysis.

This is more apparent when a graph of the ratio of  $Mg\#/Mg\#_{Core}$  versus % distance from the rim is used (Figure 5-12). Figure 5-12 shows that all the analyses approaching the rims of the crystals (<~25% distance from the rim) exhibit lower Mg# than their respective cores for both host lavas.

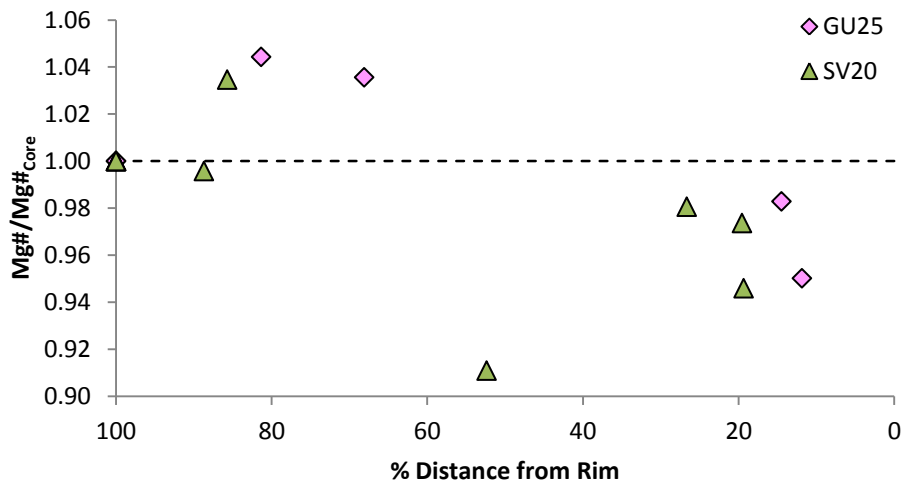


**Figure 5-12** Ratio of  $Mg\#/Mg\#_{Core}$  against % distance from the rim for the GU25 and SV20 thick section analyses. Cores plot at a  $Mg\#/Mg\#_{Core}$  ratio of 1, as indicated by the dashed line. As a result, analyses plotting above this line show a higher Mg# number than the core and those below the line have lower Mg# than the core.

### 5.4.3 CaO

CaO contents in the clinopyroxenes from all of the host lavas show positive correlations with Mg# (Figure 5-13).

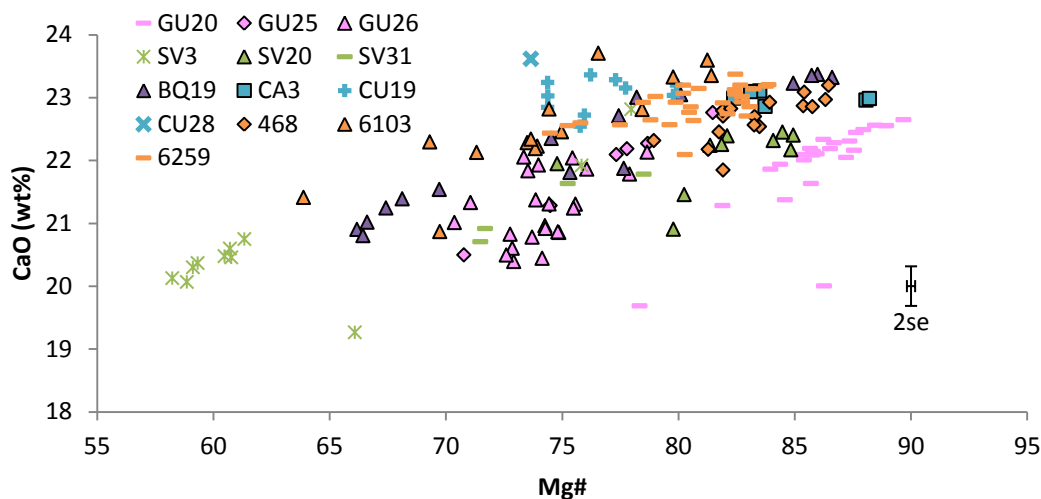


**Figure 5-13** CaO contents of the clinopyroxenes analysed from Lesser Antilles host lavas during this study. Crystal mount, thick section and resin block analyses are all shown.

In general, the Guadeloupe and St. Vincent clinopyroxenes show lower CaO concentrations at a given Mg# than the Bequia, Carriacou and Grenada crystals, particularly at Mg#>85. The crystal mount analyses from GU26 show the largest ranges in CaO content at a given Mg#, with a 2.3 wt% range at an Mg# of 73.

### 5.4.4 Al<sub>2</sub>O<sub>3</sub>, TiO<sub>2</sub> and V

The concentrations of Al<sub>2</sub>O<sub>3</sub>, TiO<sub>2</sub> and V measured in the clinopyroxenes are shown in Figure 5-14. Clinopyroxenes from some of the host lavas show positive trends whilst others show negative correlations with Mg#.

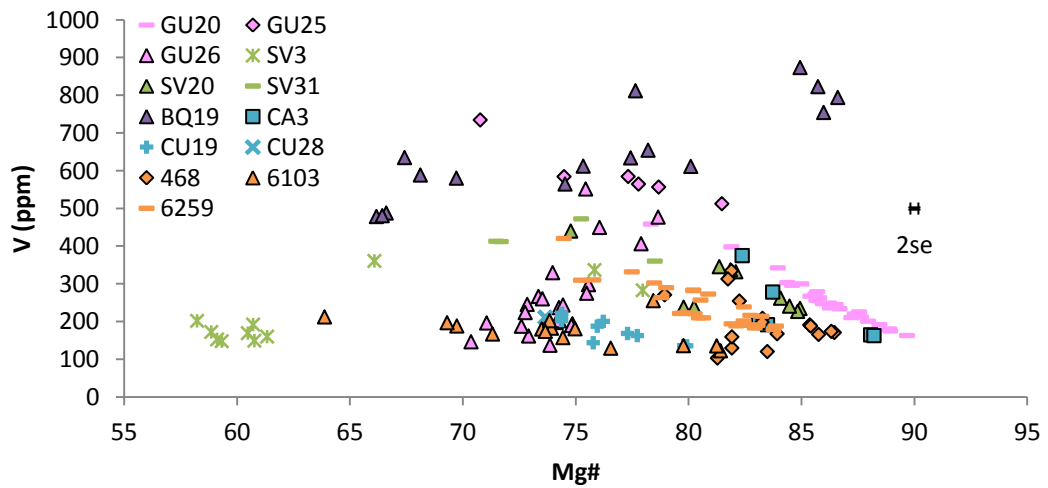
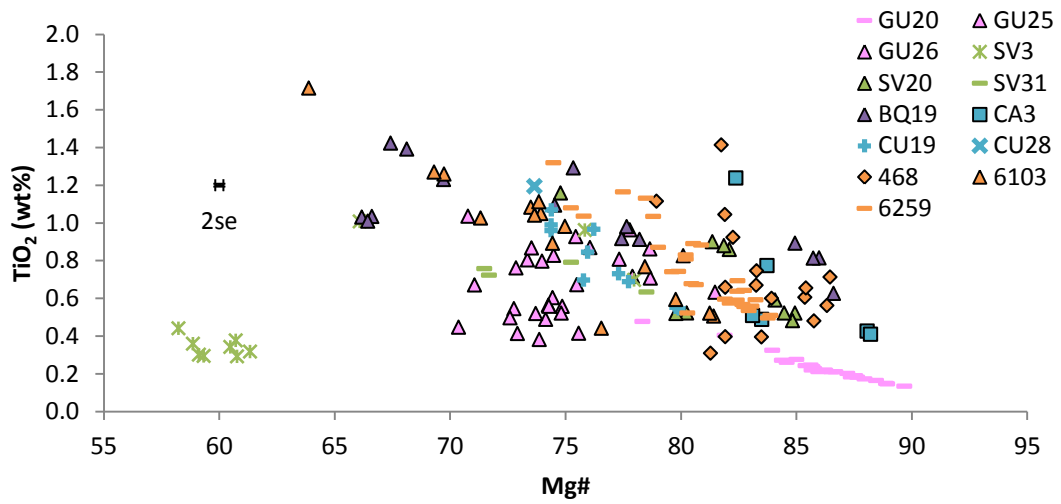
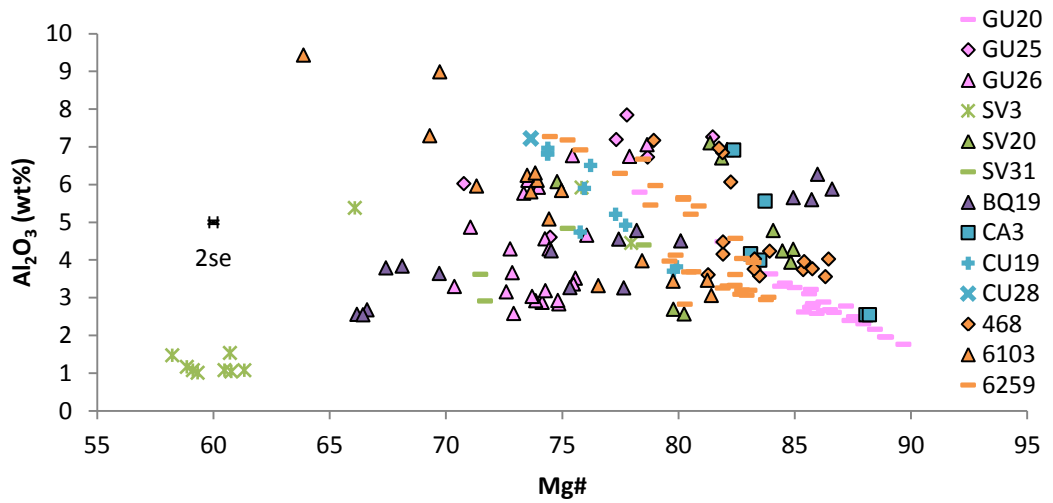


Figure 5-14  $\text{Al}_2\text{O}_3$ ,  $\text{TiO}_2$  and V concentrations in the Lesser Antilles clinopyroxenes in comparison to the Mg# of the crystals.

Clinopyroxenes from the host lavas from Guadeloupe show a strong negative correlation in GU20 and no overall correlation in both GU25 and GU26. GU20 shows the lowest concentrations at high Mg# ( $>Mg\#_{87}$ ) for both  $Al_2O_3$  and  $TiO_2$  (for V, there are CA3 crystals with lower concentrations). GU26 clinopyroxenes also show amongst the lowest concentrations of  $Al_2O_3$ ,  $TiO_2$  and V at intermediate Mg# ( $Mg\#_{70-76}$ ), although clinopyroxenes from this host lava display ranges extending to intermediate or higher concentrations at a given Mg#  $>Mg\#_{76}$ . The GU25 clinopyroxenes show the highest concentrations at a given Mg# of all the Guadeloupe crystals.

The St. Vincent clinopyroxenes also exhibit both positive (SV3) and negative (SV20) trends. However, the SV31 data show no correlation, although n for this host lavas is only 4 crystals. The SV3 crystals at low Mg# ( $<Mg\#_{65}$ ) show low concentrations of  $Al_2O_3$ ,  $TiO_2$  and V which are comparable to the contents observed at  $>Mg\#_{87}$ . The Bequia data is more variable than those from Guadeloupe. The  $Al_2O_3$  and V data show positive correlations with Mg#, whilst the  $TiO_2$  data exhibit a negative trend. For both  $TiO_2$  and V, the BQ19 crystals show amongst the highest concentrations at a given Mg#, but for the  $Al_2O_3$  data, the crystals exhibit intermediate contents, with the exception of four crystals between  $Mg\#_{85-87}$  (which show the highest concentrations of 5.6-6.3 wt% over this Mg# range).

All the host lavas from Carriacou and Grenada exhibit negative trends for  $Al_2O_3$ ,  $TiO_2$  and V. In general the clinopyroxenes from 468 and CA3 show the highest concentrations of these host lavas at a given Mg#, followed by 6103 and then 6259, CU19 and CU28. In terms of  $Al_2O_3$ , the Carriacou and Grenada crystals exhibit intermediate concentrations compared to clinopyroxene from the other islands. For  $TiO_2$ , the 468 and CA3 data show higher concentrations than most other crystals, with the exception of those from BQ19 at a given Mg#. Conversely, V is intermediate in the majority of the Grenada and Carriacou crystals, with the CU19, 6259 and some of the 468 clinopyroxenes showing the lowest concentrations at constant Mg# (in conjunction with several GU26 crystals between  $Mg\#_{70-74}$ ).

#### **5.4.5 MnO**

Figure 5-15 shows the MnO concentrations in the Lesser Antilles clinopyroxenes.

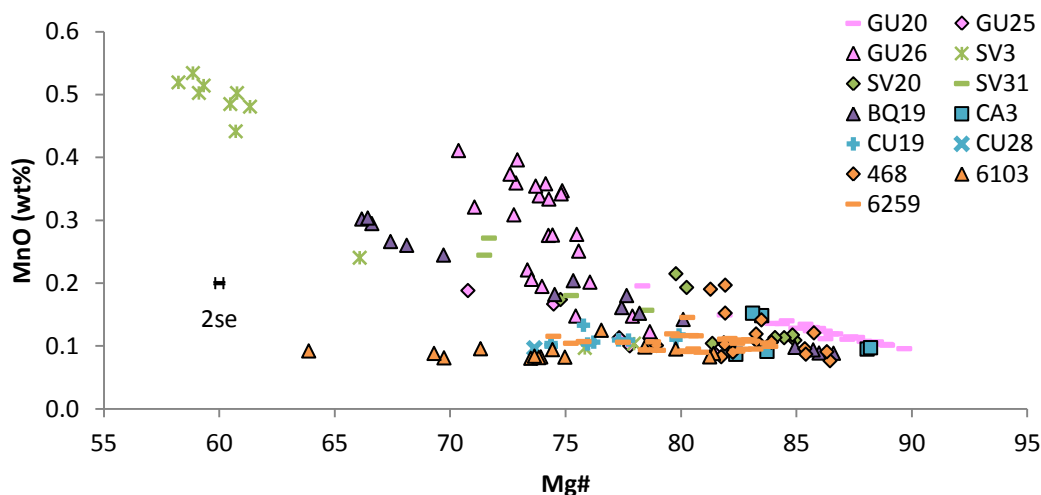


**Figure 5-15 MnO contents in the clinopyroxenes, against Mg#.**

Unlike CaO in the clinopyroxenes, the MnO data show negative correlations with Mg#. The Guadeloupe crystals show amongst the highest MnO concentrations at a given Mg#, with the exception of those analysed from GU25 (which show some of the lowest concentrations at a given  $Mg\# > Mg\#_{75}$ ). The highest MnO contents are found in clinopyroxenes from St. Vincent (up to 0.53 wt% at  $Mg\#_{59}$ ), as the crystals from SV3 show the lowest Mg#. At higher Mg# ( $> Mg\#_{75}$ ), the crystals from SV3 and SV20 show relatively constant MnO concentrations (of approximately 0.1 wt%) with decreasing Mg#. BQ19 clinopyroxenes (the only host lava analysed from Bequia) show similar MnO contents to the SV20 crystals at a given Mg#. The Grenada and Carriacou clinopyroxenes may show two trends, although it is possible that the effect is just scatter in the data (particularly for the Grenada clinopyroxenes). Above  $Mg\#_{80}$ , there are crystals from 468 and CA3 which show concentrations more similar to those observed in GU20 (and appear to show a negative trend) (Figure 5-16). However, there are also clinopyroxenes from both of these host lavas which show MnO concentrations comparable to the remaining St. Vincent, Carriacou and Grenada analyses at invariant Mg#, with little change as Mg# decreases.

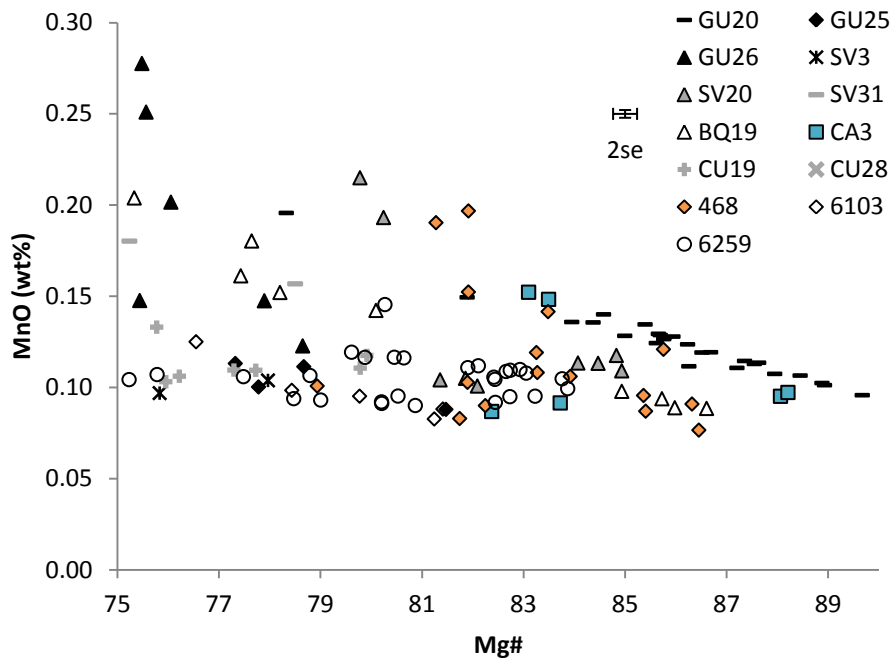


Figure 5-16 Excerpt from Figure 5-15 showing  $>Mg\#_{75}$  on the x axis. The CA3 clinopyroxenes are shown in blue and the 468 crystals are shown in orange.

#### 5.4.6 Na<sub>2</sub>O

Na<sub>2</sub>O contents of the Lesser Antilles clinopyroxenes are shown in Figure 5-17. The data for Na<sub>2</sub>O all show negative correlations with Mg#, with the exception of SV3, where the groups show relatively constant Na<sub>2</sub>O as Mg# decreases.

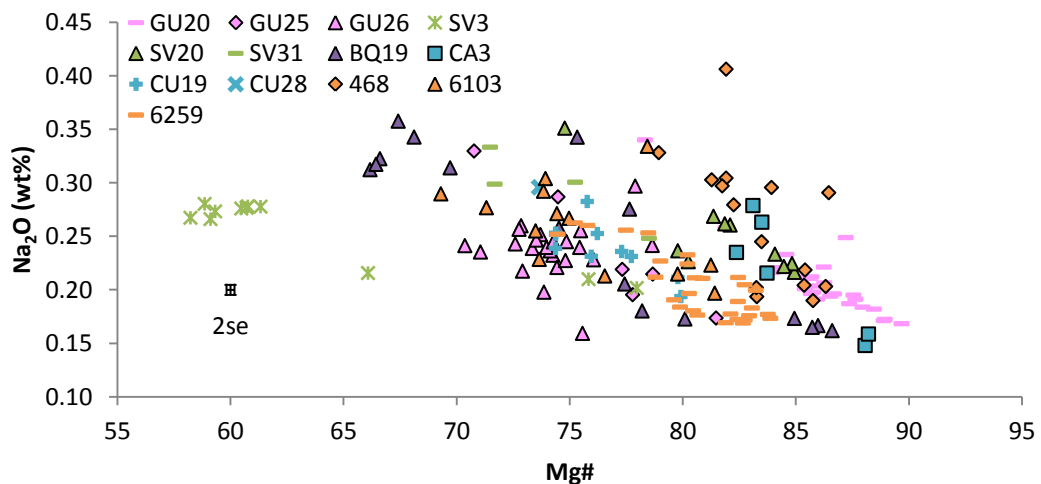


Figure 5-17 Concentrations of Na<sub>2</sub>O in the clinopyroxenes.

The Guadeloupe crystals show varying relative concentrations when compared to clinopyroxenes from other islands. At the highest Mg# ( $>Mg\#_{87}$ ), the GU20

clinopyroxenes show the highest contents (between 0.17-0.20 wt%), but as Mg# decreases, crystals from CA3 and 468 exhibit higher concentrations of Na<sub>2</sub>O. GU25 shows intermediate concentrations, whilst GU26 crystals show the lowest concentrations at a given Mg# over the range Mg#<sub>70-76</sub> (0.16-0.24 wt%). The St. Vincent clinopyroxenes above Mg#<sub>70</sub> show intermediate Na<sub>2</sub>O contents. At Mg#<sub>66</sub>, the SV3 crystal shows 0.09 wt% lower Na<sub>2</sub>O than the crystals from BQ19 with comparable Mg#. Na<sub>2</sub>O contents in the Bequia crystals are also variable when compared to those from other host lavas. At ~Mg#<sub>85</sub>, the BQ19 clinopyroxenes show the lowest concentrations (0.16-0.17 wt%), as Mg# decreases, the crystals begin to show more intermediate contents (at ~Mg#<sub>78</sub>). By Mg#<sub>70</sub>, the BQ19 crystals exhibit the highest concentrations at up to 0.36 wt% (although the number of crystals at comparable Mg# by this point has reduced).

Clinopyroxenes from Carriacou and Grenada show intermediate to high concentrations compared to the other host lavas. Crystals from CA3 and 468 have comparable concentrations, showing high contents between 0.30-0.40 wt% at Mg#<sub>81-86</sub>. The remaining Carriacou and Grenada clinopyroxenes exhibit more intermediate concentrations, being more comparable to GU25 (and also some crystals from GU26 and BQ19).

#### **5.4.7 Cr and Ni**

Cr and Ni contents in the clinopyroxenes are shown in Figure 5-18. For both of these elements, clinopyroxenes from most host lavas show positive correlations, with a negative correlation being observed in the Cr concentrations measured in the CU19 crystals. Above approximately 3000 ppm Cr there are no real correlations between Cr and Mg# in any host lava.

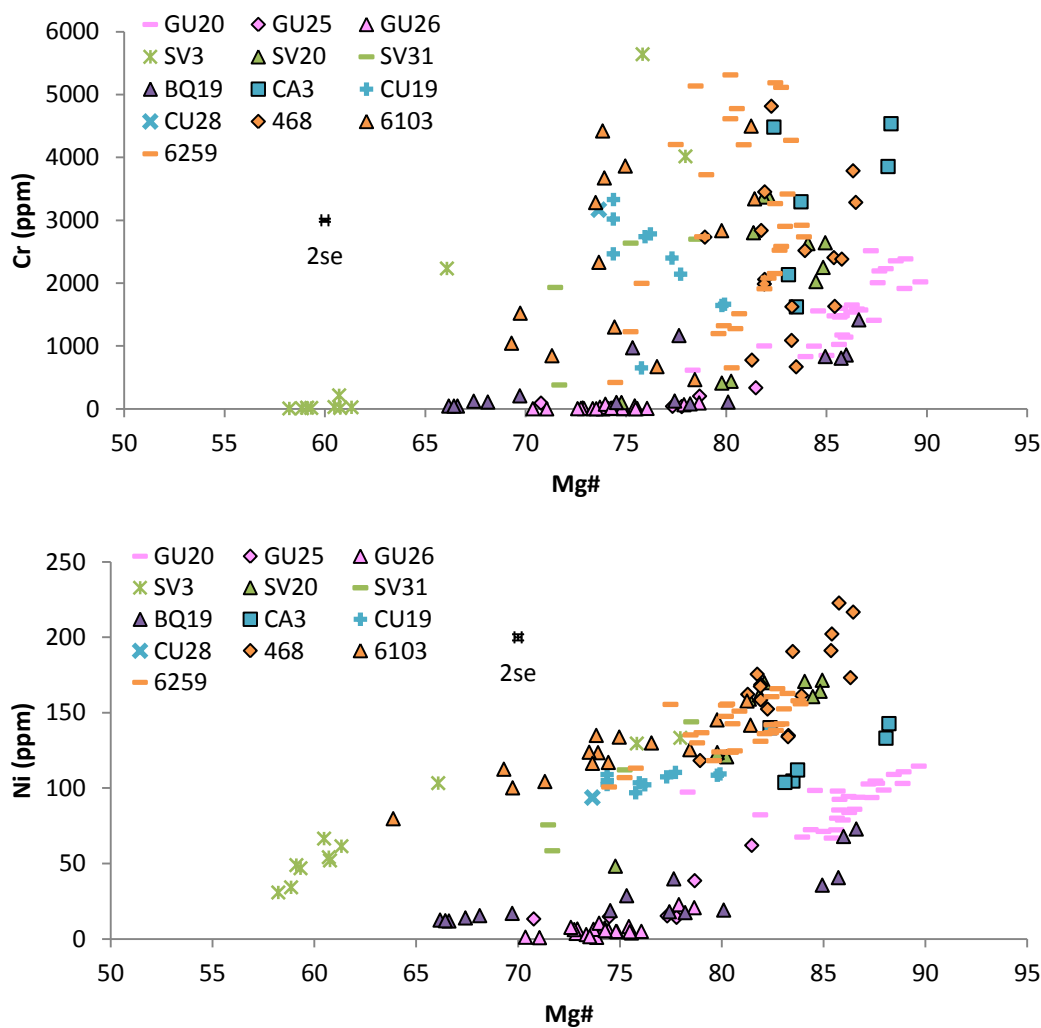


**Figure 5-18 Concentrations of Cr and Ni in the Lesser Antilles clinopyroxenes plotted against Mg#.**

The Guadeloupe and Bequia clinopyroxenes consistently show the lowest concentrations of both Cr and Ni at a given Mg#. In the case of Ni there is a significant gap between concentrations measured in clinopyroxenes from these islands and those from the remaining host lavas. Typically, the Guadeloupe and Bequia crystals exhibit 90 ppm lower contents than those from the other islands. At  $>Mg\#_{84}$ , the gap between the Guadeloupe and CA3 clinopyroxenes is much smaller at a given Mg# (with around a 25 ppm difference at  $Mg\#_{88}$ ). At  $\sim Mg\#_{70-77}$ , Ni concentrations in the Guadeloupe clinopyroxenes are less than 20 ppm, whereas crystals from St. Vincent, Carriacou and Grenada typically show contents of between 100-150 ppm Ni over this Mg# range (with the exception of three St. Vincent crystals). Both GU25 and GU26 show Cr contents up to a maximum of 350 ppm.

The St. Vincent, Carriacou and Grenada clinopyroxenes all show comparable Cr and Ni contents at a given Mg# (with the exception of the CA3 Ni concentrations). Five of the CA3 Ni contents are intermediate between the remaining St. Vincent, Carriacou (including the other CA3 analysis) and Grenada crystals (up to 22 ppm lower) and the lower Bequia and Guadeloupe clinopyroxenes (up to 24 ppm higher) at constant Mg#. In addition, the CA3 clinopyroxenes show a large range in Cr concentrations at a given Mg# of up to 2860 ppm. A range of 2826 ppm is also observed in the SV20 Cr data. The lower Mg# SV3 crystals show concentrations of Cr of 6-215 ppm at Mg#<sub>58-61</sub>.

The Grenada crystals show large ranges in concentration, particularly in Cr contents, at a given Mg#. 468 has a range of 4144 ppm at ~Mg#<sub>83</sub>, 6103 a range of 3119 ppm at ~Mg#<sub>74</sub> and 6259 a range of 4660 ppm at ~Mg#<sub>80</sub>. These ranges are larger than those observed in the Carriacou and St. Vincent crystals.

#### 5.4.8 Sc

Sc concentrations of the Lesser Antilles clinopyroxenes are shown in Figure 5-19. In general there is little correlation observed between Mg# and Sc concentrations with the exception of GU20 and SV3. Clinopyroxenes from some samples show large ranges in Sc content with little variation in Mg#, such as 468.

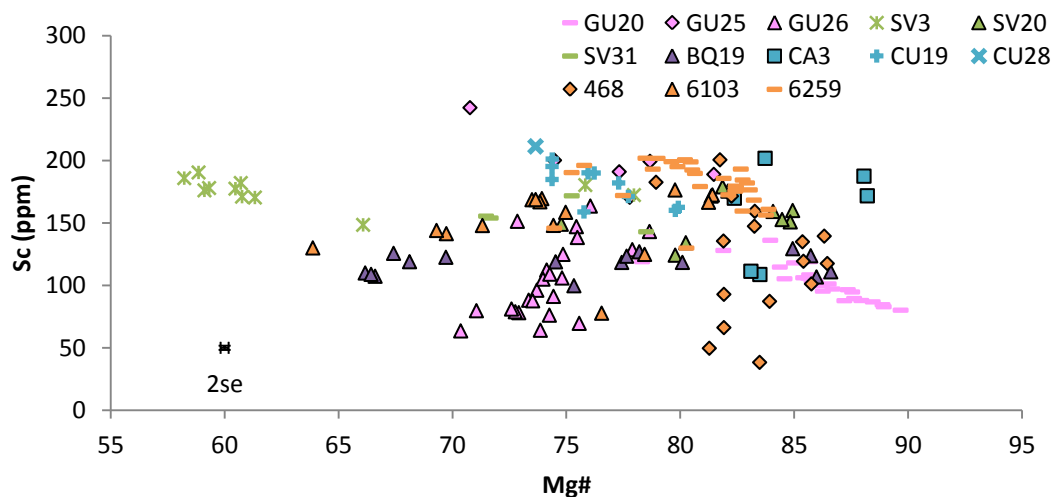


**Figure 5-19 Sc concentrations plotted against the Mg# of the Lesser Antilles clinopyroxenes.**

Clinopyroxenes from host lavas from Guadeloupe show both trends; GU20 and GU25 exhibit negative trends, whilst GU26 describes a positive trend. GU20 and

GU25 show intermediate concentrations of Sc when compared to other crystals at a given Mg# (although at  $>Mg_{87}$ , the GU20 clinopyroxenes have the lowest measured concentrations). The clinopyroxenes from St. Vincent host lavas mirror those from Guadeloupe in that SV3 and SV31 show negative trends whilst SV20 exhibits a positive trend. SV20 crystals show relatively high Sc concentrations at a given Mg# whilst those from SV31 are more intermediate in nature. The lower Mg# SV3 crystals show contents between 170-190 ppm (over a range of  $Mg_{58-61}$ ). The SV3 concentrations are relatively constant as Mg# changes, with a gradient of -0.4 when a linear regression line is applied. The BQ19 clinopyroxenes also show little change in Sc concentration as Mg# decreases, with a regression line gradient of 0.20. However, the BQ19 crystals exhibit at least 38 ppm lower Sc at a given Mg# than the SV3 clinopyroxenes.

The Carriacou host lava clinopyroxenes also show conflicting trends, CU19 exhibits a negative trend whereas the crystals from CA3 show no real correlation (only one crystal was analysed from CU28). The CA3 crystals show a large range in concentrations (e.g. 93 ppm at  $Mg_{84}$ ). Consequently some crystals show the highest contents at a given Mg# whilst others show concentrations only higher than those from 468. CU19 and CU28 contain similar Sc contents at a given Mg#. The CU19 crystals show intermediate concentrations of ~160 ppm at  $Mg_{80}$  but as Mg# decreases, the Carriacou clinopyroxenes exhibit higher contents than many of the other crystals. 6259 from Grenada shows a negative correlation, with 6103 showing a positive correlation. 468 shows no overall correlation with Mg# and exhibits a large range in concentrations (151 ppm between  $Mg_{81-82}$ ) and the lowest concentrations of any host lava between  $Mg_{81-84}$ . 6259 does not show such a wide range and in comparison to the other host lavas, the crystals exhibit amongst the highest Sc concentrations at a given Mg#. The clinopyroxenes from 6103 show more intermediate contents, being higher than those observed in the BQ19 crystals and lower than those seen in the St. Vincent clinopyroxenes.

#### **5.4.9 LREE - La, Ce and Nd**

Concentrations of La, Ce and Nd measured in the Lesser Antilles clinopyroxenes are shown in Figure 5-20. Most of the host lavas show negative correlations with Mg#, ranging from well correlated to poorly correlated.

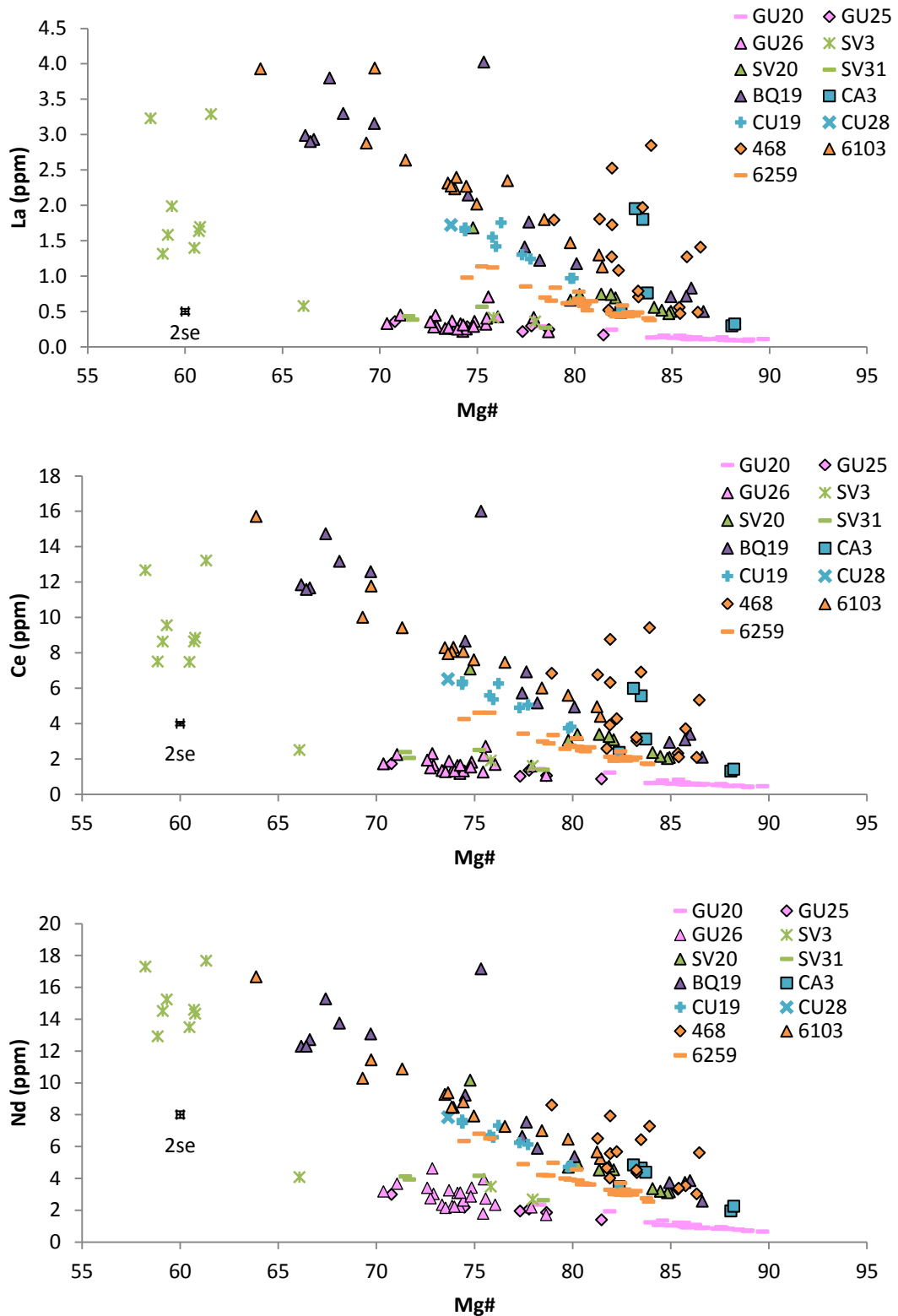


**Figure 5-20 Concentrations of the LREE in the clinopyroxenes, plotted against Mg#.**

The Guadeloupe clinopyroxenes show the lowest concentrations of LREE at a given Mg#. However, there are crystals from SV3 and SV31 with comparable concentrations at constant Mg#. At Mg#<sub>88</sub>, The GU20 clinopyroxenes exhibit 0.2

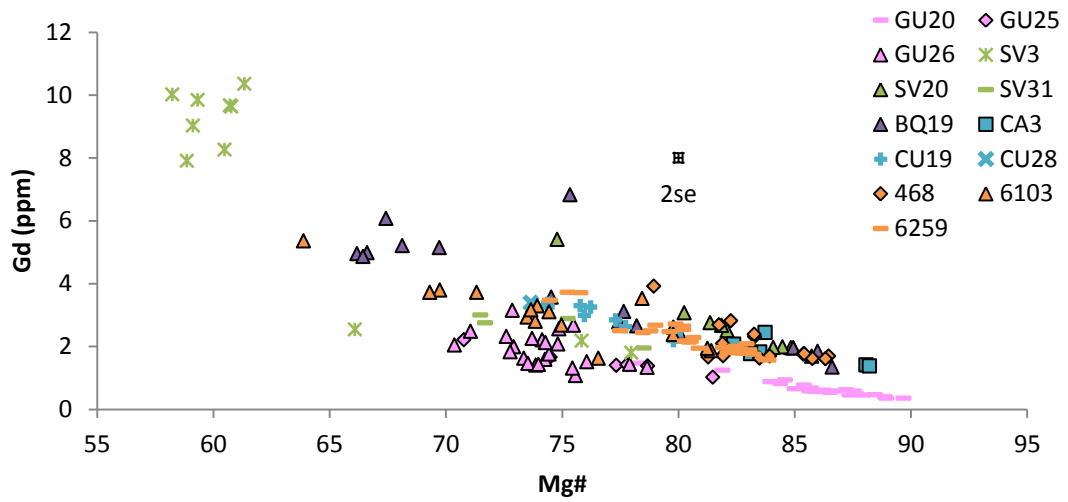
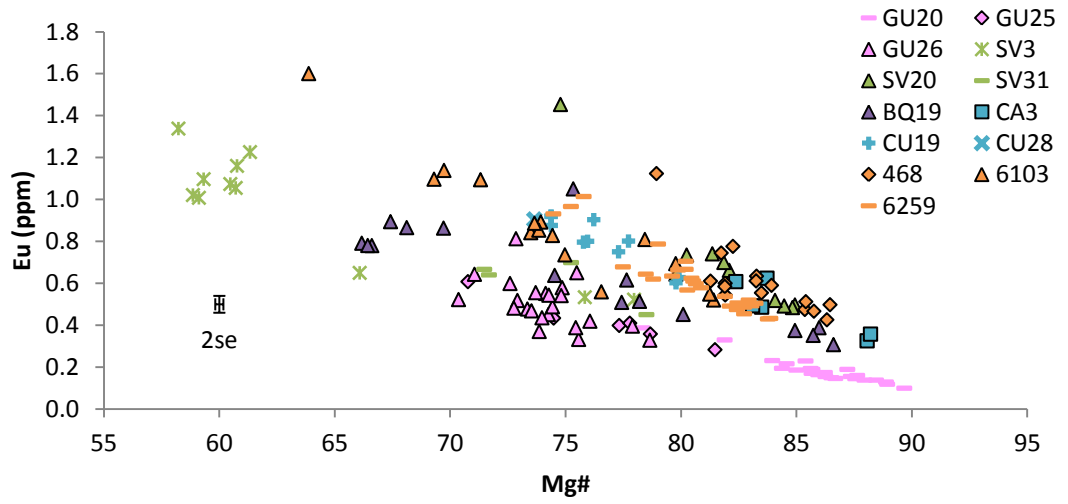
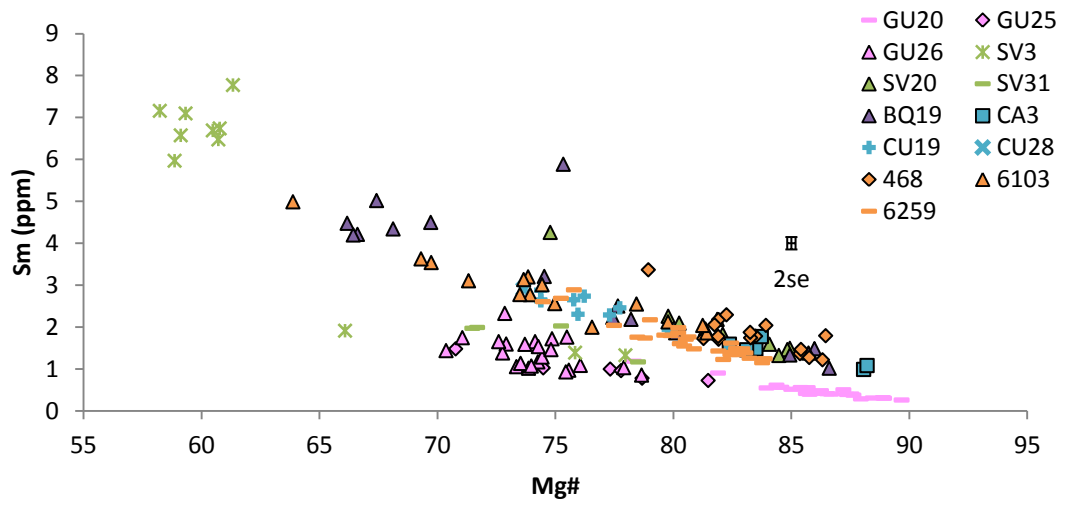
ppm lower La, 0.9 ppm lower Ce and 1.2 ppm lower Nd than the CA3 crystals. In addition, the Guadeloupe crystals show shallower gradient trends than those from the Bequia and Grenada host lavas. The aforementioned SV3 and SV31 crystals also show shallower trends. However, the lower Mg# SV3 clinopyroxenes exhibit higher concentrations of LREE than a trend based on the higher Mg# crystals would predict, exhibiting contents of 1.3-3.3 ppm La, 7.5-13.2 ppm Ce and 12.9-17.7 ppm Nd at Mg#<sub>58-61</sub>. The SV20 crystals show comparable concentrations of LREE to the CA3 and 468 clinopyroxenes, exhibiting the lowest contents at a given Mg# and slightly higher than those observed in the 6259 crystals.

The Bequia crystals show intermediate concentrations relative to SV20 and the Grenada and Carriacou clinopyroxenes at constant Mg#, although one analysis at Mg#<sub>75</sub> shows distinctly higher contents for all the LREE. This latter analysis may have been influenced by inclusion material and thus not represent clinopyroxene contents alone. The Carriacou clinopyroxenes from CU19 and CU28 also show intermediate concentrations relative to Grenada and are only slightly lower than those observed in BQ19 at invariant Mg#. The CA3 clinopyroxenes show larger ranges at constant Mg# for La (1.2 ppm at Mg#<sub>83-84</sub>, with the highest concentration being 2.6 times larger than the lowest content) and Ce (2.9 ppm, a factor of 1.9), but do not show large ranges for Nd (0.5 ppm, a factor of 1.1).

Large ranges in the LREE are also observed in the 468 clinopyroxenes. At Mg#<sub>83-84</sub>, ranges of factors between the lowest and highest values are 4 (La) and 3.1 (Ce) are shown. However, as for the CA3 crystals, the range in Nd is lower at 1.7 (despite Nd having larger absolute concentrations as a result of increased compatibility due to lanthanide contraction). The 6103 clinopyroxenes show comparable concentrations to those measured in the BQ19 crystals at a given Mg#. 6259 concentrations are slightly lower than those from SV20 at invariant Mg#.

#### **5.4.10 MREE - Sm, Eu, Gd and Dy**

As seen in the LREE, the MREE show negative correlations with Mg# for all the host lavas (Figure 5-21).



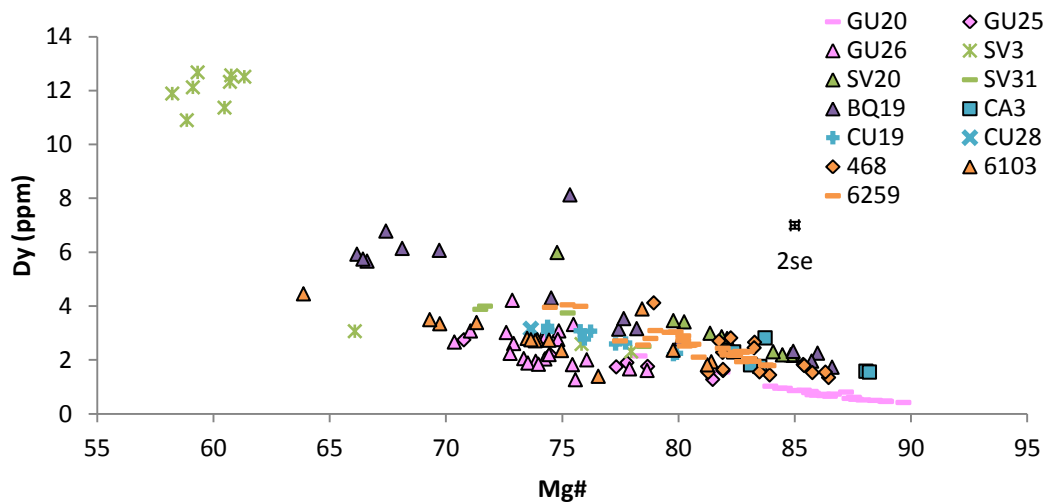


**Figure 5-21 MREE concentrations plotted against Mg# in the Lesser Antilles clinopyroxenes.**

The Guadeloupe clinopyroxenes show lower concentrations at a given Mg# than the majority of the other host lavas, as observed in the LREE. However, the Dy data show that at  $<Mg\#_{82}$ , there is more similarity between the Guadeloupe clinopyroxenes and crystals from the other host lavas. Several clinopyroxenes from GU26 in particular show similar concentrations of Dy to Grenada and Carriacou crystals at invariant Mg#. SV3 and SV31 again show comparable concentrations to the Guadeloupe crystals for Sm and Eu. Only SV3 exhibits similar contents for Gd and Dy.

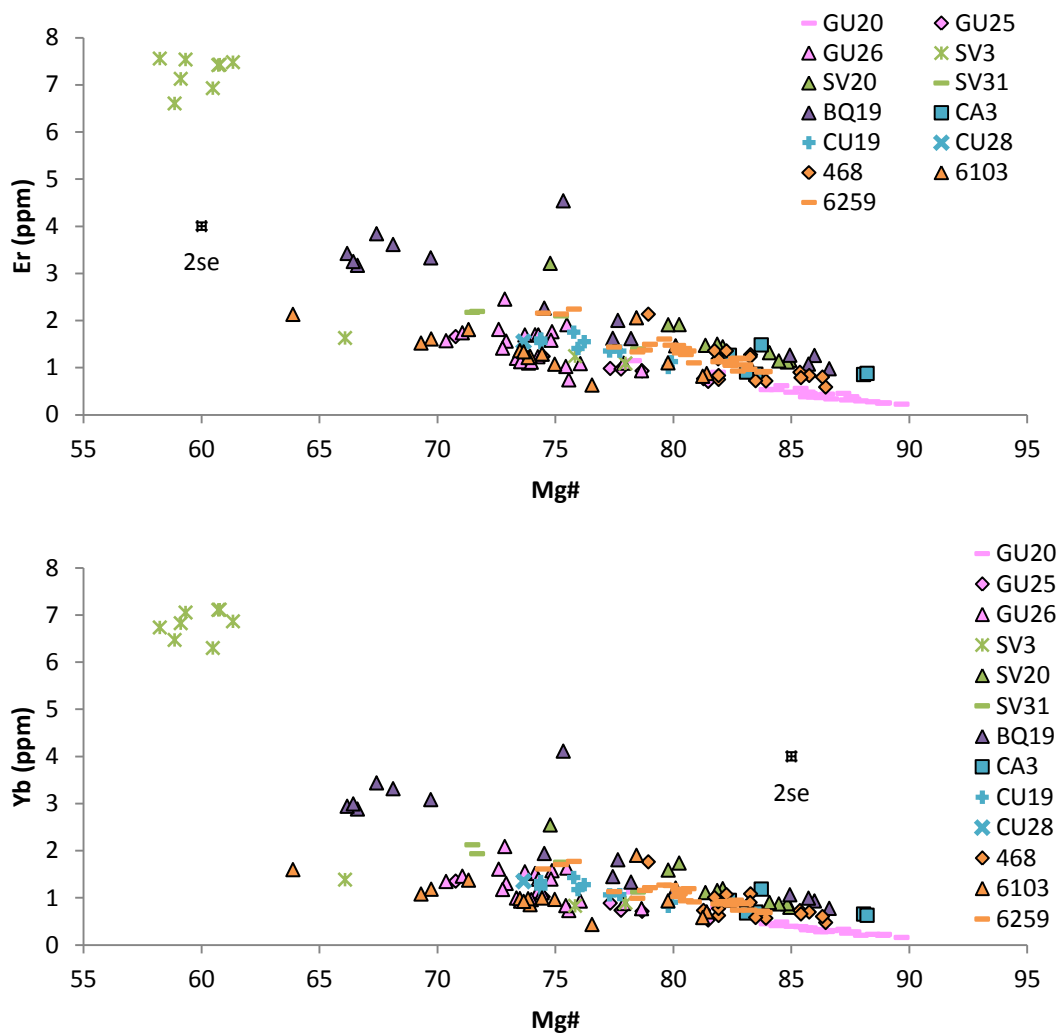
The SV20 clinopyroxenes show similar MREE concentrations to those from Bequia and Grenada. As atomic number increases, the relative concentrations of MREE in the lower Mg# SV3 clinopyroxenes also increase, resulting in the highest concentrations of Sm, Gd and Dy being measured in this group (the lower Mg# group of SV3 also shows the highest concentrations of Nd, but the values are much more comparable to those observed at higher Mg# e.g. in BQ19 and 6103). The differences in concentration between the highest non-SV3 crystal and the lowest SV3 crystal as factors are: 2.2 (0.1 ppm) for Sm, 1.9 (1.1 ppm) for Gd and 1.9 (2.8 ppm) for Dy, showing the disparity increases with atomic number in absolute terms but not as a factor.

The Bequia clinopyroxenes show very similar concentrations at a given Mg# to crystals from SV20, Carriacou and Grenada. The 468 clinopyroxenes again show the largest range in concentration at a given Mg#, as seen in the Sc and LREE data.

Additionally, the 468 crystals typically show the highest concentrations at a given Mg#.

### 5.4.11 HREE - Er and Yb and Y

HREE (including Y due to the fact it behaves similarly to the HREE) concentrations in the clinopyroxenes follow similar trends to those observed in both the LREE and the MREE (Figure 5-22). The host lavas all show negative trends between each HREE and Mg#.



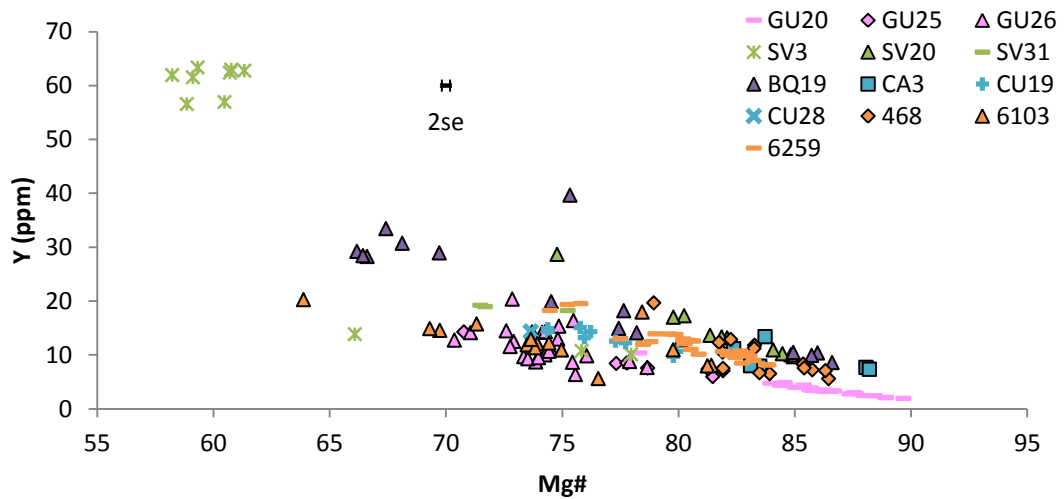


**Figure 5-22 HREE concentrations measured in the Lesser Antilles clinopyroxenes, plotted against Mg#.**

The Guadeloupe clinopyroxenes show similar trends to those seen in the Dy data, in that whilst still exhibiting the lowest contents (aside from one 6103 crystal), they show comparable concentrations to clinopyroxenes from other host lavas, such as SV3 and 6103. The lower Mg# group of SV3 again show higher HREE contents than the higher Mg# crystals from any of the other host lavas. As observed in the MREE, as atomic number increases, the discrepancy between the lowest SV3 concentrations and the highest contents in clinopyroxenes from another host lava also increases. This gap represents an increase by a factor of 2.0 (an absolute range of 2.1 ppm) for the Er data, 2.1 (2.2 ppm) for the Yb data and 2.0 (16.9) ppm for the Y data. In general, the St. Vincent, Bequia and Grenada clinopyroxenes all show comparable concentrations of the HREE at invariant Mg#. The 468 crystals do not show such large ranges at a given Mg# as in both the LREE and the MREE. Furthermore, the clinopyroxenes from 6103 show lower concentrations than the remaining Grenada clinopyroxenes at a given Mg#, being more similar to those contents measured in GU26.

***REE Plots***

Concentrations of the REE in the clinopyroxenes normalised to chondrite (Nakamura, 1974) and then plotted against atomic number are shown in Figure 5-23.

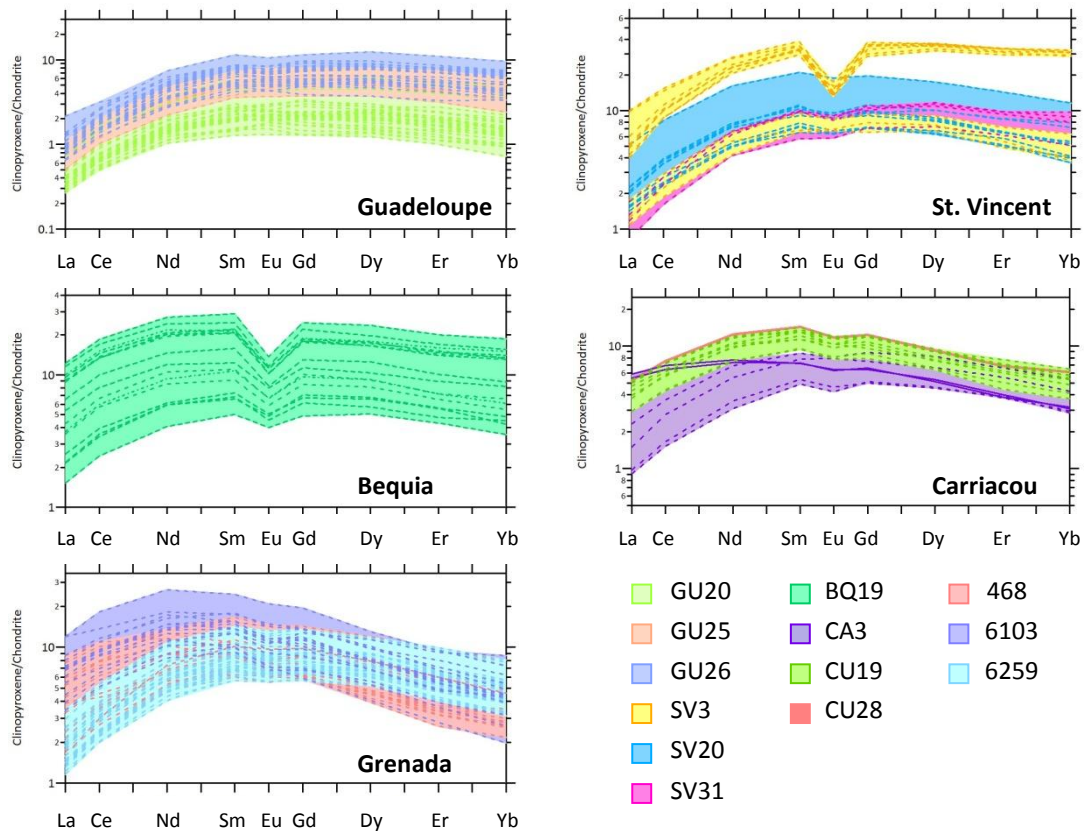


**Figure 5-23** REE profiles of the clinopyroxenes. Each graph shows a different island, with the shaded areas representing the range in concentrations normalised to the values of Nakamura (1974) with individual dashed lines representing discrete clinopyroxene analyses. The two CA3 crystals shown by solid lines on the Carriacou graph exhibit different trends to the remaining CA3 clinopyroxenes.

The BQ19 clinopyroxenes show large negative Eu anomalies (as defined in Chapter 3) (Figure 5-24). Negative Eu anomalies are also observed in the lower Mg# group of SV3 crystals and to a lesser extent in the Carriacou clinopyroxenes and Grenada. Slight negative Eu anomalies are observed in some Guadeloupe and St. Vincent clinopyroxenes. The BQ19 crystals show a positive trend between Eu anomaly and Mg# which is not seen in any of the other host lavas.

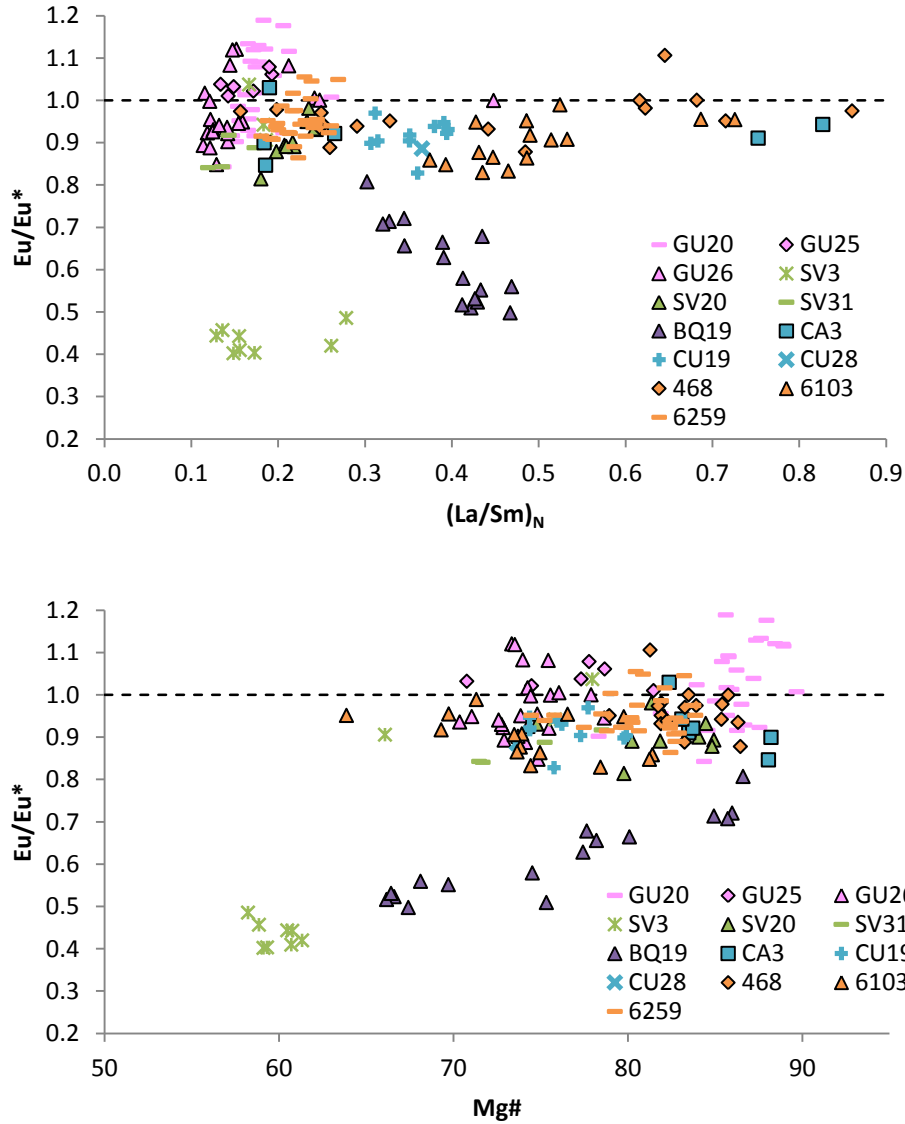


Figure 5-24 Eu anomalies in the clinopyroxenes, the upper graph shows the Eu/Eu\* ratio in relation to chondrite normalised La/Sm ratios whilst the bottom graph shows the Eu anomalies compared to Mg#. The dashed line at 1 on both graphs represents no anomaly, with those crystals below exhibiting negative anomalies and those above positive anomalies.

Figure 5-23 appears to show several broad trends. The clinopyroxenes from Guadeloupe, SV31, BQ19, CA3 (barring the two crystals depicted by solid lines in Figure 5-23, which will be discussed imminently) and to a lesser extent 6259 all show LREE depletion relative to largely flat MREE and HREE profiles, with peak normalised concentrations occurring at Sm. The MREE should be the most compatible REE in clinopyroxene, given their similarity in atomic radius to the M2 site in clinopyroxene. The two CA3 crystals which show a differing trend to their host lava counterparts show flatter LREE patterns followed by relative depletions in MREE and HREE, with peak concentrations at Nd.

The crystals from Carriacou, SV20, 468, 6103 are MREE enriched relative to the LREE and HREE, again with the highest clinopyroxene/chondrite ratio being observed at Sm.

There are two distinct groups of clinopyroxenes present in SV3 based on REE data. The group exhibiting lower concentrations exhibit clinopyroxene/chondrite ratios subparallel to those from SV20. The higher group show a pronounced depletion in Eu but otherwise show similar patterns to the lower group, albeit displaced to higher clinopyroxene/chondrite ratios. The lower clinopyroxene/chondrite group are the higher Mg# crystals from this host lava, whilst the higher clinopyroxene/chondrite group are those crystals with Mg#<sub>58-61</sub>.

#### **5.4.12 Hf and Zr**

Hf and Zr show similar relationships, as shown in Figure 5-25. All of the host lavas show negative correlations for both Hf and Zr with Mg#.

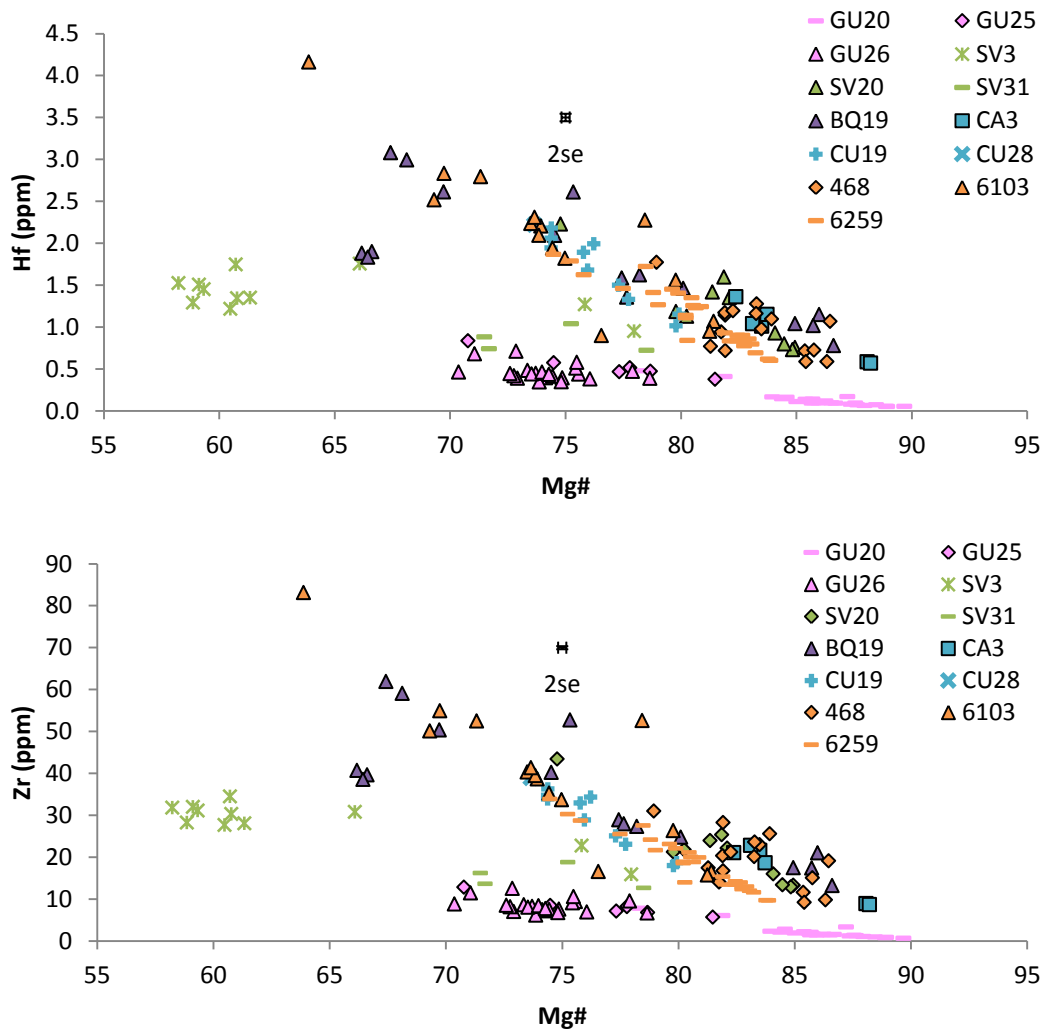


**Figure 5-25 Concentrations of Hf and Zr in the clinopyroxenes.**

The Guadeloupe clinopyroxenes show lower concentrations at a given Mg# when compared to crystals from the other host lavas (excluding SV31). At Mg#<sub>88</sub>, the Guadeloupe crystals exhibit 0.5 ppm less Hf and 7.9 ppm less Zr than the CA3 crystals. Furthermore, the trends described by the data exhibit shallower gradients than those observed in host lavas from the other islands (with the exception of SV31 and CA3).

The Bequia crystals show similar concentrations of both Hf and Zr to the St. Vincent, Carriacou and Grenada clinopyroxenes at a given Mg#. At ~Mg#<sub>66</sub>, there are 3 BQ19 crystals which show contents more comparable to the lower Mg# of SV3, particularly for Hf. These 3 crystals are 5.9 ppm and 21.3 ppm lower in Hf and Zr respectively than the closest BQ19 crystal (in terms of Mg#).

SV20 from St. Vincent and the Carriacou and Grenada clinopyroxenes all show comparable concentrations of Hf and Zr at a given Mg#. The SV31 crystals however do show lower contents more similar to those observed in the Guadeloupe crystals at  $\sim$ Mg<sub>76</sub>. The lower Mg# crystals from SV3 also show concentrations which appear lower than expected, showing 1.2-1.8 ppm Hf and 27.7-34.5 ppm Zr.

### 5.4.13 Li

Figure 5-26 shows the concentrations of Li in the clinopyroxenes. There is no overall trend between Li and Mg#, with clinopyroxenes from some host lavas showing large ranges in concentrations at a given Mg#, such as 468

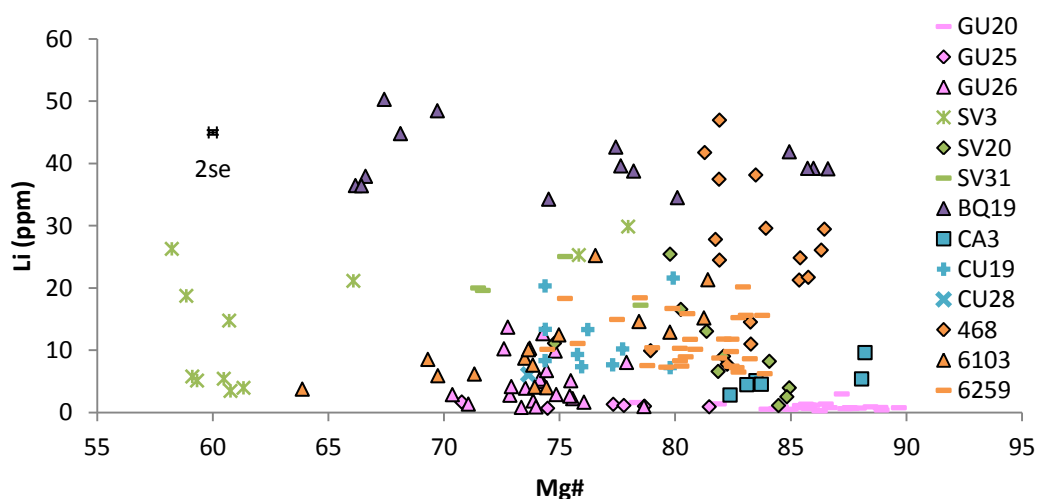


**Figure 5-26 Li concentrations in the Lesser Antilles clinopyroxenes, plotted against Mg#.**

Li concentrations in the Guadeloupe clinopyroxenes are relatively low (typically <10 ppm, up to a maximum of 14 ppm) and are the lowest at any given Mg#. GU26 shows the largest range of all the Guadeloupe host lavas with a range of 13 ppm. The St. Vincent clinopyroxenes show higher Li contents at a given Mg# (e.g. by up to 29 ppm at Mg#<sub>78</sub>) than those from Guadeloupe, with many of the crystals exhibiting similar concentrations to those from Carriacou at constant Mg#. The Carriacou crystals also show higher concentrations of Li than the Guadeloupe clinopyroxenes at a given Mg#. Whilst in many cases they are comparable to the St. Vincent crystals, the maximum concentration observed in Carriacou is 22 ppm as opposed to the 30 ppm observed in St. Vincent.

The Bequia clinopyroxenes show the highest concentrations over the entire range of Mg#. As observed for several elements previously, clinopyroxenes from Grenada (in this case from 468) exhibit some of the highest contents of Li at a given Mg#. The crystals show concentrations similar to those observed in the most Li rich Bequia clinopyroxenes between Mg#<sub>81-83</sub> (up to 47 ppm). The clinopyroxenes from 6103 and 6259 show concentrations comparable to the St. Vincent and Carriacou crystals.

#### 5.4.14 Sr

Sr contents in the clinopyroxenes show positive correlations with Mg# for clinopyroxenes from some host lavas and negative correlations for others (Figure 5-27). Host lavas with clinopyroxenes exhibiting negative correlations are GU20, SV3 and SV31. Positive correlations are shown by the remaining Guadeloupe and St. Vincent host lavas (GU25, GU26 and SV20) and the Bequia, Carriacou and Grenada host lavas. However, the positive correlation observed in GU26 has a very shallow gradient (0.02 when a linear trendline is applied).

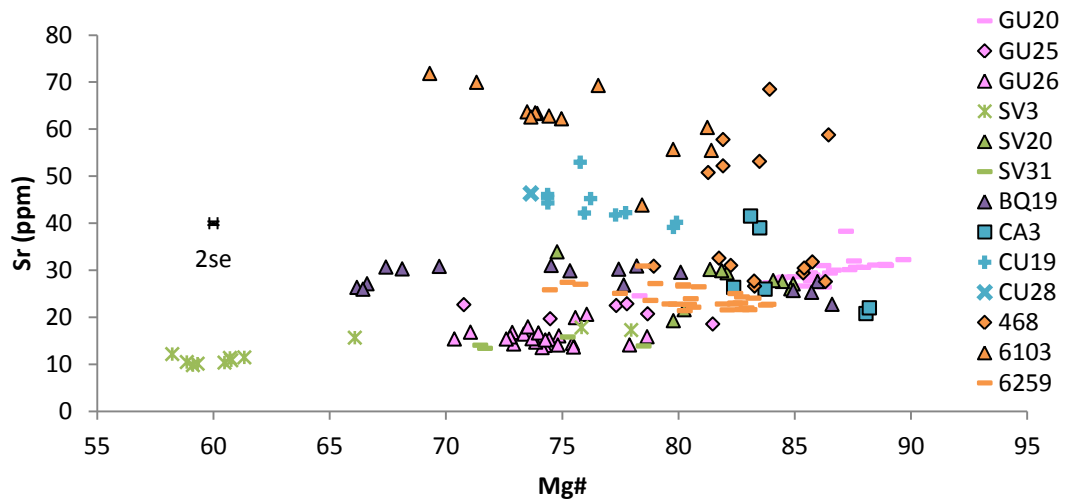


**Figure 5-27 Sr concentrations in the analysed clinopyroxenes plotted against Mg#.**

As for the CaO data, the Guadeloupe and St. Vincent clinopyroxenes show the lowest concentrations of Sr below Mg#<sub>80</sub>. In contrast to the CaO data however, many of the Carriacou and Grenada crystals show much higher concentrations of Sr at a given Mg# than those from Guadeloupe, Bequia and St. Vincent (e.g. at Mg#<sub>77</sub>, there is a 39.1 ppm difference between the highest Sr concentration in BQ19 and the crystal from 6103).

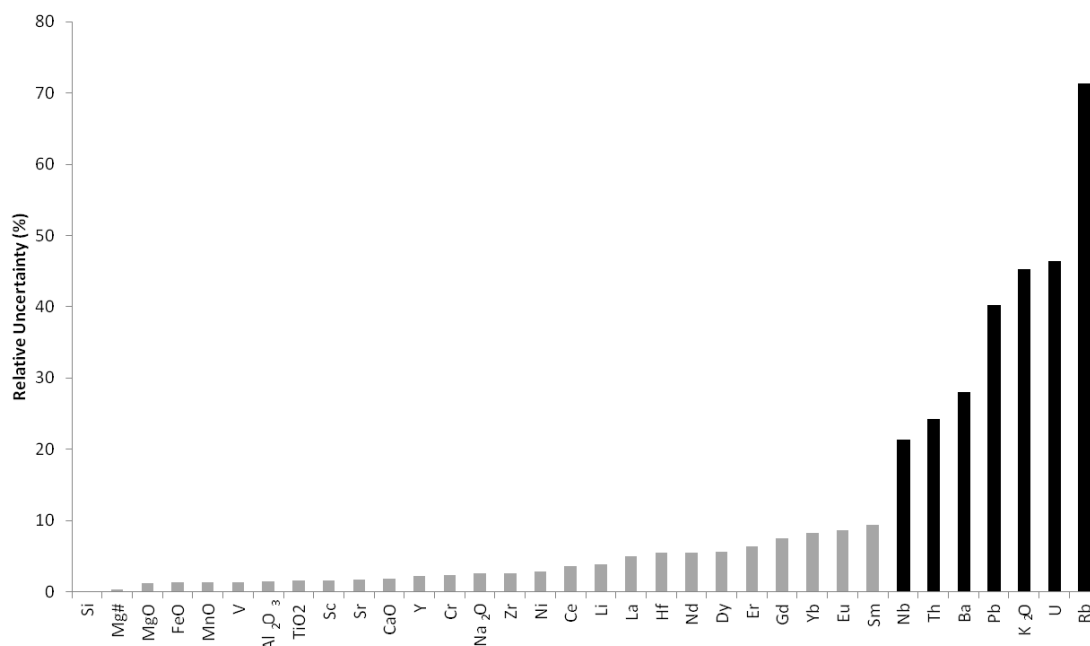
### 5.4.15 Pb, Th, U, K<sub>2</sub>O, Ba, Rb and Nb

As shown in Figure 5-29, in general the Pb, Th, U, K<sub>2</sub>O, Ba, Rb and Nb concentrations in the clinopyroxenes show negative correlations when plotted against the Mg# of the crystals, however, 2se is large. Relative uncertainty on each analysed element was calculated using Equation 5-1. In Equation 5-1, i is the element in question, average concentration is the average concentration of each clinopyroxene analysis for element i and average 2se is the average of the 2 standard errors calculated for each clinopyroxene analysis for element i.

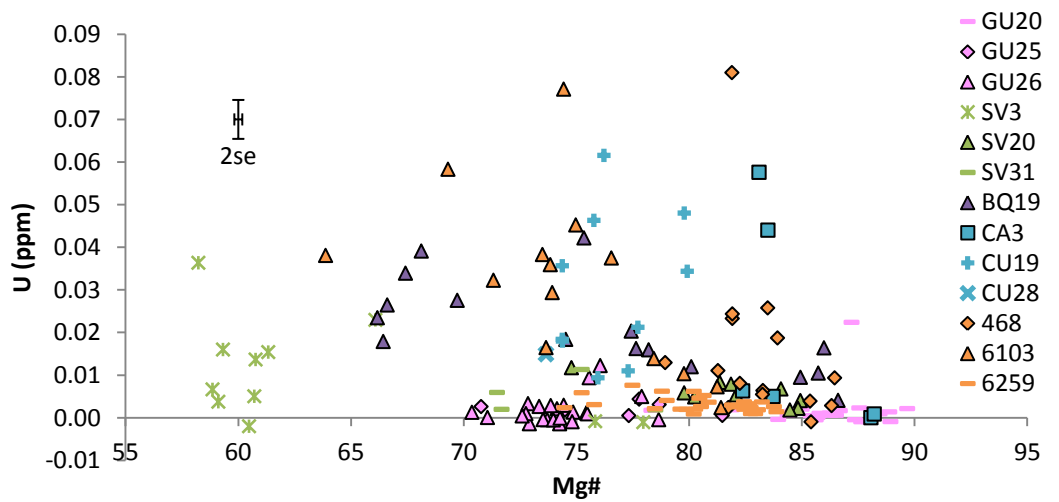
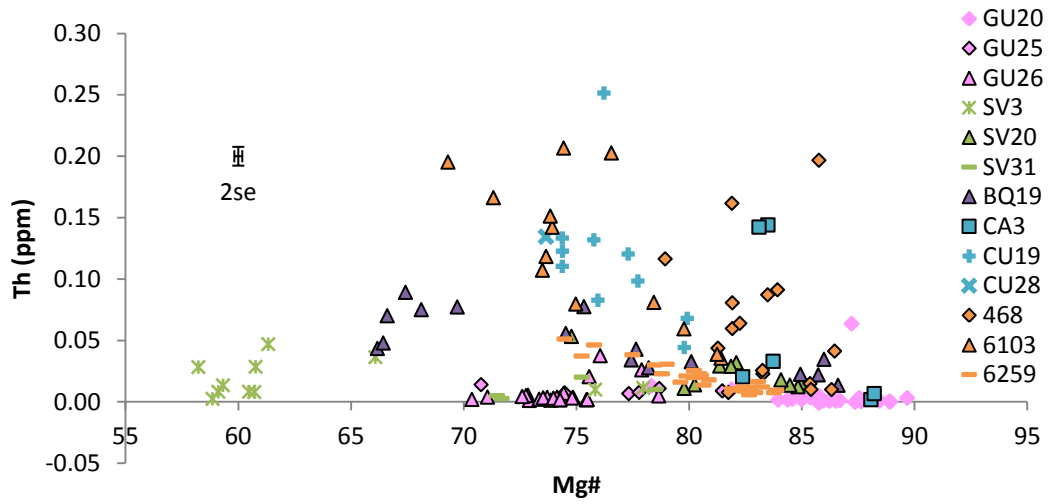
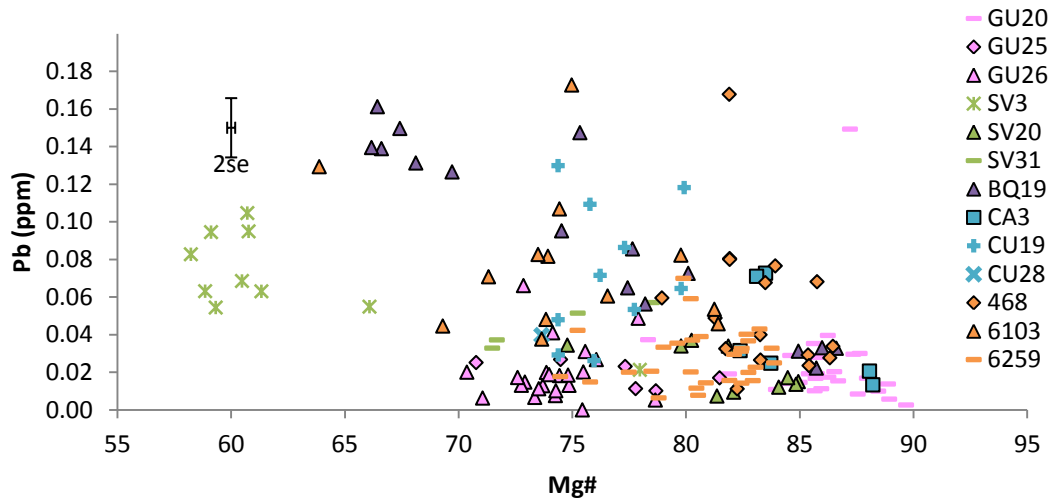
#### Equation 5-1

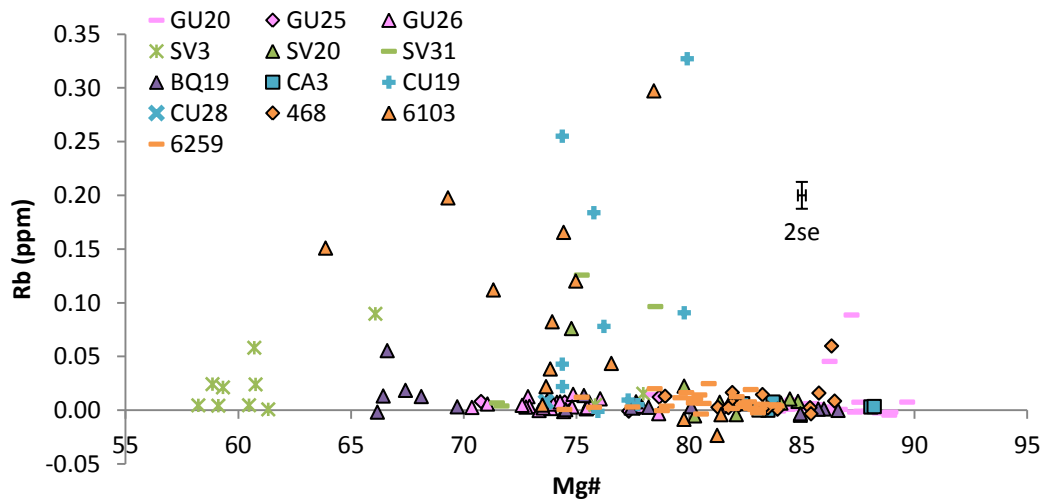
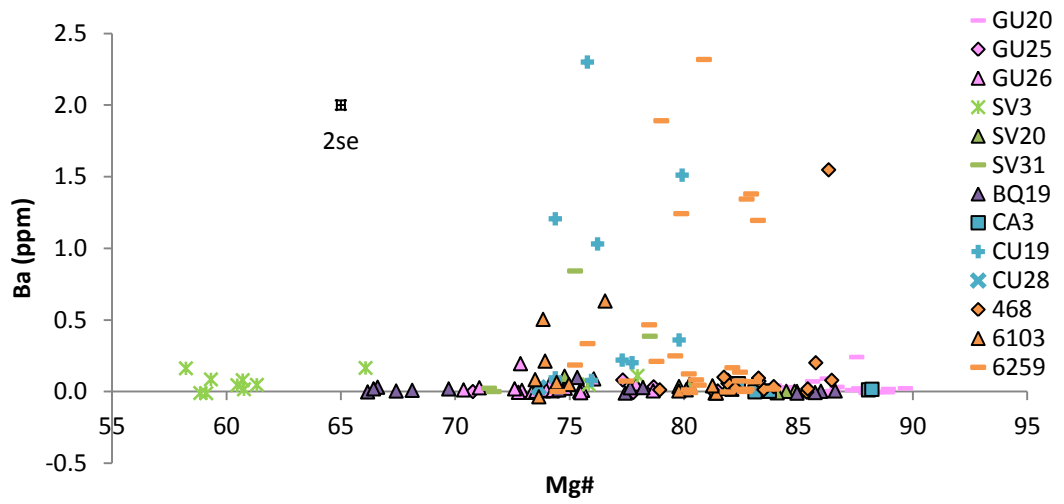
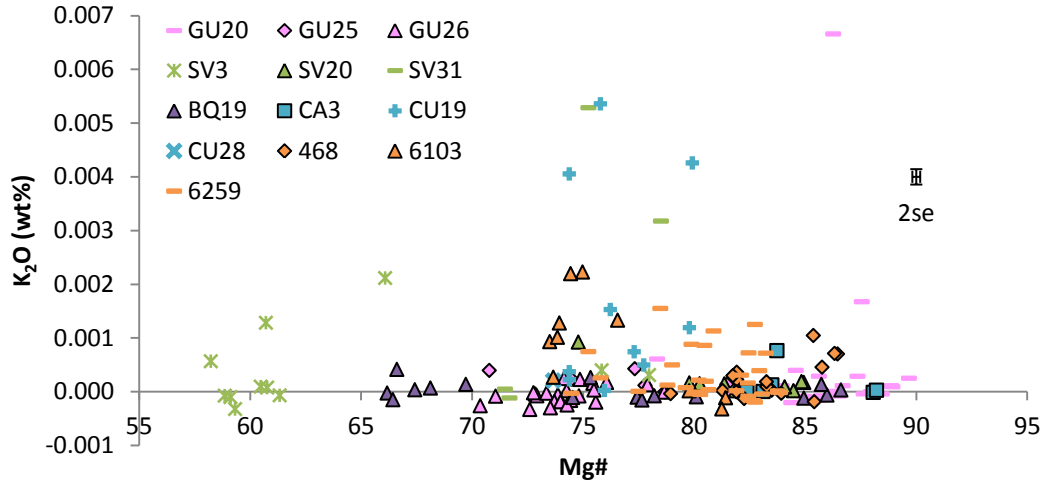
$$\text{Relative uncertainty}^i = \frac{\text{Average } 2se^i}{\text{Average concentration}^i} \times 100$$

Given the lower concentrations of some of these elements, the relative uncertainties on each are higher than the elements discussed previously (Figure 5-28). Pb, Th, U, K<sub>2</sub>O, Ba, Rb and Nb all show relative uncertainties of over 20%. In addition, there are analyses for every element with negative concentrations. As already discussed in Chapter 3, this is a result of concentrations below the detection limits of the LA-ICP-MS method. Whilst the negative values are plotted on the graphs, they will not be considered further.



**Figure 5-28 % Relative uncertainties on each oxide/element measured in the clinopyroxenes. The elements being discussed in this section of the results are coloured in black.**





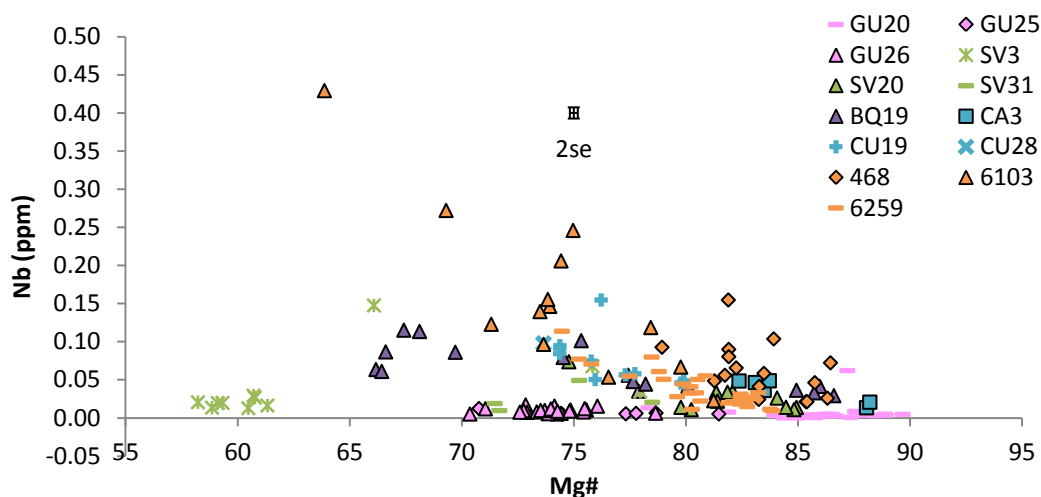


**Figure 5-29 Concentrations of Pb, Th, U, K<sub>2</sub>O, Ba, Rb and Nb in the clinopyroxenes plotted against Mg#.**

Significant scatter is seen on the plots comprising Figure 5-29, more than seen in the previously discussed elements. In general, the clinopyroxenes from 468 and 6103 from Grenada show the highest concentrations of Pb, Th, U, K<sub>2</sub>O, Ba, Rb and Nb at a given Mg#. Crystals from 6259 show intermediate concentrations at constant Mg# when compared to clinopyroxenes from the other host lavas. The Carriacou crystals show similar contents to those from Grenada. However, for some elements they exhibit similar concentrations to 6103 (e.g. Th, U, Pb and Ba) and others more closely mirror those shown by 6259 (e.g. Rb, Nb and K<sub>2</sub>O).

The lowest concentrations of Pb, Th, U, K<sub>2</sub>O, Ba, Rb and Nb are found in the clinopyroxenes from Guadeloupe at a given Mg#, with contents approaching detection limits. The St. Vincent crystals show low to intermediate concentrations. However, in most cases, the clinopyroxenes from SV3 exhibit higher contents than the other St. Vincent crystals (again this is largely a function of the SV3 crystals having lower Mg# than the clinopyroxenes from SV20 and SV31).

Clinopyroxenes from Bequia show variable concentrations compared to crystals from other islands. However, there is a group of BQ19 crystals at Mg#<sub>66-70</sub> that have very few crystals from other host lavas at similar Mg# to compare them to. The BQ19 crystals at >Mg#<sub>70</sub> show similar low K<sub>2</sub>O concentrations to the Guadeloupe clinopyroxenes (although several of the Bequia crystals show concentrations below detection limits). The U, Rb, Pb, Th, Nb and Ba data all show the BQ19 crystals to

have concentrations between the 468 clinopyroxenes from Grenada and the St. Vincent crystals.

## 5.5 Discussion

### 5.5.1 Equilibrium Clinopyroxenes

In order to ascertain if the clinopyroxenes analysed were in equilibrium with the whole rock chemistry of their respective host lavas, the Mg# of the crystals were compared to their whole rock Mg# (Figure 5-30). As the whole rock Mg# is partially dependent on the concentration of  $\text{Fe}^{2+}$  it was necessary to estimate the proportion of the total whole rock FeO which is  $\text{Fe}^{2+}$ . As for the olivine equilibrium test (Chapter 2), this was done using the ratios of Middlemost (1989), based on where the host lavas plot on a TAS diagram (Le Bas *et al.*, 1986). An  $\text{Fe}_2\text{O}_3/\text{FeO}$  ratio of 0.2 was used for basalts, 0.3 for basaltic andesites and 0.35 for the andesites (Middlemost, 1989).

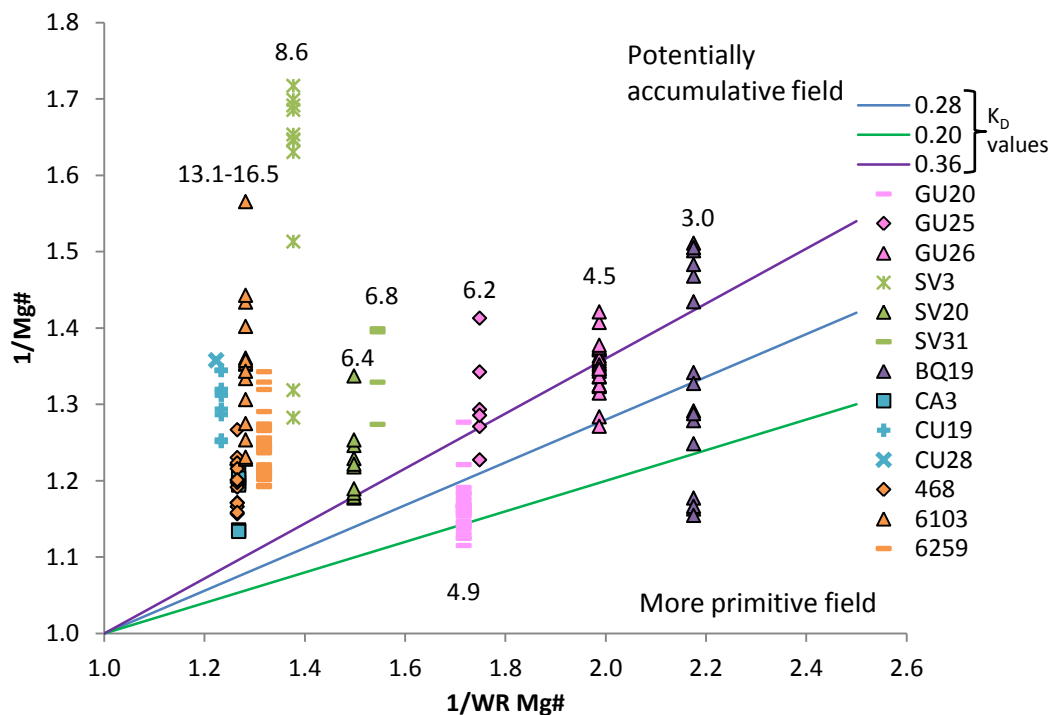


Figure 5-30  $1/\text{Mg}\#$  for each clinopyroxene analysis plotted against  $1/\text{Mg}\#$  for the respective host lava. The coloured lines show where clinopyroxenes in equilibrium with the whole rock Mg# would plot based on a partition coefficient of  $0.28 \pm 0.08$  (Putirka, 2008). The area above the upper error limit is suggested to be a potentially more accumulative field, with the area below the lower error limit being more primitive than the whole rock composition. The numbers above and below each host lava show the whole rock MgO contents.

A partition coefficient ( $K_D$ ) of  $0.28 \pm 0.08$  (Putirka, 2008) was used for Fe-Mg partitioning between clinopyroxene and melt (whole rock composition was used as an estimate for the latter), where the  $K_D$  is as defined in Equation 5-2. The lines on Figure 5-30 show where clinopyroxenes in equilibrium with the whole rock would plot, with the central line being equivalent to a  $K_D$  of 0.28 and the outer lines showing the upper and lower error limits. Consequently clinopyroxenes in equilibrium within error should plot in the area between the lines.

**Equation 5-2**

$$K_{D_{Fe-Mg}}^{cpx-melt} = \frac{(Fe^{2+}/Mg)_{cpx}}{(Fe^{2+}/Mg)_{melt}}$$

Figure 5-30 shows that at least some of the clinopyroxenes from the relatively more evolved host lavas (GU20, GU25, GU26, SV20 and BQ19) plot within the equilibrium area. The crystals from BQ19 span the entire area and also show clinopyroxenes with both higher and lower 1/Mg# ratios than anticipated to be in equilibrium. Only two analyses from both GU25 and GU26 plot above the area in equilibrium in the potentially accumulative field. In contrast, SV20 only exhibits 3 analyses in apparent equilibrium, with the majority lying to potentially accumulative 1/Mg# ratios. Only 5 of the 26 crystals analysed from GU20 appear to be in equilibrium, with the rest plotting in the potentially more primitive field. Only BQ19 and GU20 show any clinopyroxenes which are potentially more primitive than expected based on the whole rock chemistry. The clinopyroxenes from the remaining host lavas (SV3, SV31, CA3, CU19, CU28, 468, 6103 and 6259) all plot in the potentially accumulative field, i.e. with lower Mg# than predicted based on their whole rock chemistries. Some crystals from CA3 and 468 approach the upper limit of equilibrium, whilst analyses from SV3 and CU19 are the furthest removed from the hypothetical equilibrium clinopyroxenes.

If clinopyroxenes from host lavas with crystals plotting in the potentially accumulative field in Figure 5-30 are all assumed to be accumulative, a new melt composition with the clinopyroxene phenocrysts removed can be calculated. Using point counting data, the modal proportion of clinopyroxene can be estimated (Table 5-1). An average MgO and FeO for clinopyroxene from each individual host lava was then calculated. In order to calculate new melt Mg#, the MgO and FeO of the melt with clinopyroxene removed had to be calculated (Equation 5-3 and Equation

5-5). Equation 5-4 was used to calculate the proportion of the total whole rock iron oxide that is FeO. New melt Mg# was then calculated using Equation 5-6, where RMM is the relative molecular mass of the oxide in question.

**Equation 5-3**

$$New\ MgO_{melt} = \frac{MgO_{WR} - (\%_{cpx} \times average\ MgO_{cpx})}{1 - \%_{cpx}}$$

**Equation 5-4**

$$FeO_{WR} = (1 - (Fe_2O_3/FeO + Fe_2O_3)) \times FeO_{total}$$

**Equation 5-5**

$$New\ FeO_{melt} = \frac{FeO_{WR} - (\%_{cpx} \times average\ FeO_{cpx})}{1 - \%_{cpx}}$$

**Equation 5-6**

$$Mg\#_{melt} = \frac{(New\ MgO_{melt}/RMM\ MgO)}{((New\ MgO_{melt}/RMM\ MgO) + (New\ FeO_{melt}/RMM\ FeO))}$$

When the reciprocal of the new (minus clinopyroxene phenocrysts) melt Mg# is taken and used to plot the clinopyroxenes against, the potentially accumulative crystals shift along the x axis (Figure 5-31). Figure 5-31 shows the maximum effect of clinopyroxene accumulation on the melt chemistry.

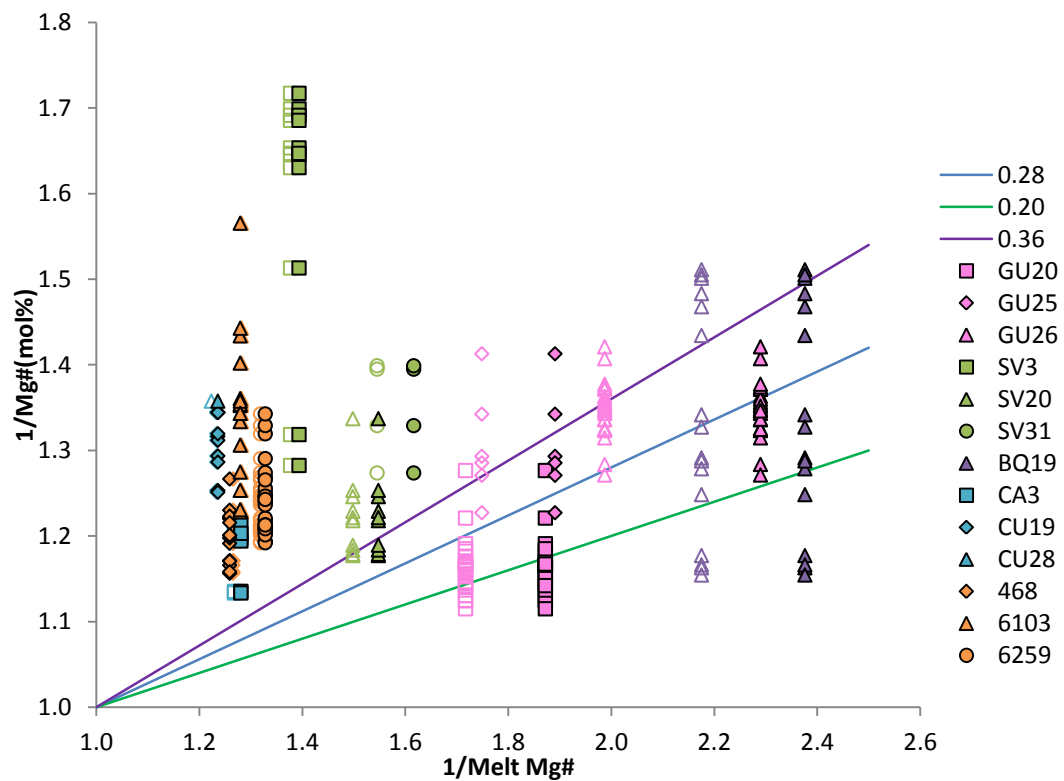


**Figure 5-31 Equilibrium graph replotted with melt Mg# if all clinopyroxene phenocrysts in the host lavas are assumed to be accumulated. Hollow symbols show 1/WR Mg# and the solid symbols show the recalculated melt Mg#.**

Figure 5-31 shows that the largest changes are observed in the more evolved lavas, such as GU26. The more primitive host lavas show little change in 1/Mg# when clinopyroxene is removed. However, removing clinopyroxene from the host melt shifts the crystals further away from the equilibrium zone rather than moving the clinopyroxenes towards equilibrium in most cases. This suggests that accumulation does not explain why the clinopyroxenes appear out of equilibrium with their respective whole rock compositions.

### 5.5.2 Clinopyroxene Geothermobarometry

Clinopyroxene compositions, often in conjunction with liquid compositions, can be used to provide estimates on the temperatures and pressures of clinopyroxene crystallisation. This therefore provides further insight into the petrogenesis of the Lesser Antilles lavas. It may provide information as to whether the pressure and/or temperature conditions of clinopyroxene crystallisation vary within individual islands or within individual host lavas.

Putirka (2008) provides an overview of clinopyroxene thermometers and barometers. The author also provides a supplementary spreadsheet to enable the calculation of temperatures and pressures using the equations provided in Putirka (2008). In order to calculate the pressures at which the clinopyroxenes crystallised, Equation 5-7 was used (Putirka & Condit, 2003), as this is suitable for hydrous systems and is suggested by Putirka (2008) to have higher precision and lower systematic error than the Nimis (1995) model.

**Equation 5-7**

$$\begin{aligned}
 P(kbar) = & -48.7 + 271 \frac{T(K)}{10^4} + 32 \frac{T(K)}{10^4} \ln \left[ \frac{X_{NaAlSi_2O_6}^{cpx}}{X_{NaO_{0.5}}^{liq} X_{AlO_{1.5}}^{liq} (X_{SiO_2}^{liq})^2} \right] \\
 & - 8.2 \ln(X_{FeO}^{liq}) + 4.6 \ln(X_{MgO}^{liq}) - 0.96 \ln(X_{KO_{0.5}}^{liq}) - 2.2 \ln X_{DiHd}^{cpx} \\
 & - 31(Mg\#^{liq}) + 56(X_{NaO_{0.5}}^{liq} + X_{KO_{0.5}}^{liq}) + 0.76(H_2O^{liq})
 \end{aligned}$$

Equation 5-8 was used to calculate the crystallisation temperatures of the clinopyroxenes (Putirka, 2008).

**Equation 5-8**

$$\begin{aligned}
 \frac{10^4}{T(K)} = & 7.53 - 0.14 \ln \left( \frac{X_{Jd}^{cpx} X_{CaO}^{liq} X_{Fm}^{liq}}{X_{DiHd}^{cpx} X_{Na}^{liq} X_{Al}^{liq}} \right) + 0.07(H_2O^{liq}) - 14.9(X_{CaO}^{liq} X_{SiO_2}^{liq}) \\
 & - 0.08 \ln(X_{TiO_2}^{liq}) - 3.62(X_{NaO_{0.5}}^{liq} + X_{KO_{0.5}}^{liq}) - 1.1(Mg\#^{liq}) \\
 & - 0.18 \ln(X_{EnFs}^{cpx}) - 0.027 P(kbar)
 \end{aligned}$$

For both equations, the whole rock compositions of the host lavas were used to represent the liquid compositions. The results of the pressure and temperature calculations using the above equations are shown in Figure 5-32.

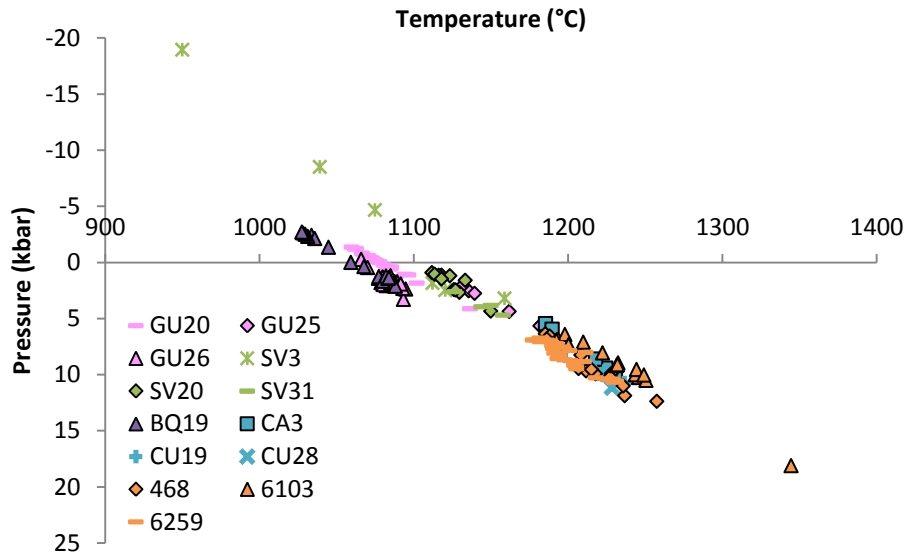


**Figure 5-32 Pressures and temperatures of crystallisation for the Lesser Antilles clinopyroxenes calculated using the equations contained in Putirka (2008).**

Given that several of the clinopyroxenes in Figure 5-32 show negative pressures, it is unlikely that the method used is entirely appropriate, at least to calculate pressures. One reason for this may again be the unsuitability of using whole rock compositions as a proxy for liquid compositions. In order to combat this, the method of Putirka (2008) (which builds upon that of Nimis, 1995) was implemented as this calculates pressures from the clinopyroxene composition alone (Equation 5-9). Whilst this method increases the precision of Nimis (1995), it does not alter the systematic error associated with the latter model with regard to hydrous systems. However, a significant source of error in using the whole rock compositions has been removed. In a similar fashion, Equation 5-10 was used for calculating temperature (Putirka, 2008, based upon the activity model of Nimis and Taylor, 2000).

**Equation 5-9**

$$P(kbar) = 3205 + 0.384 T(K) - 518 \ln T(K) - 5.62(X_{Mg}^{cpx}) + 83.2(X_{Na}^{cpx}) + 68.2(X_{DiHd}^{cpx}) + 2.52 \ln(X_{Al(VI)}^{cpx}) - 51.1(X_{DiHd}^{cpx})^2 + 34.8(X_{EnFs}^{cpx})^2$$

**Equation 5-10**

$T(K)$

$$= \frac{93100 + 544 P(kbar)}{61.1 + 36.6(X_{Ti}^{cpx}) + 10.9(X_{Fe}^{cpx}) - 0.95(X_{Al}^{cpx} + X_{Cr}^{cpx} - X_{Na}^{cpx} - X_K^{cpx}) + 0.395[\ln(a_{En}^{cpx})]^2}$$

Equation 5-10 includes the term  $a_{En}^{cpx}$ , which is the activity of enstatite in clinopyroxene, as defined in Equation 5-11 (Nimis & Taylor, 2000).

**Equation 5-11**

$$a_{En}^{cpx} = (1 - X_{Ca}^{cpx} - X_{Na}^{cpx} - X_K^{cpx}) \times (1 - 0.5(X_{Al}^{cpx} + X_{Cr}^{cpx} + X_{Na}^{cpx} + X_K^{cpx}))$$

Figure 5-33 shows the results of the temperature and pressure modelling using the clinopyroxene compositions alone.

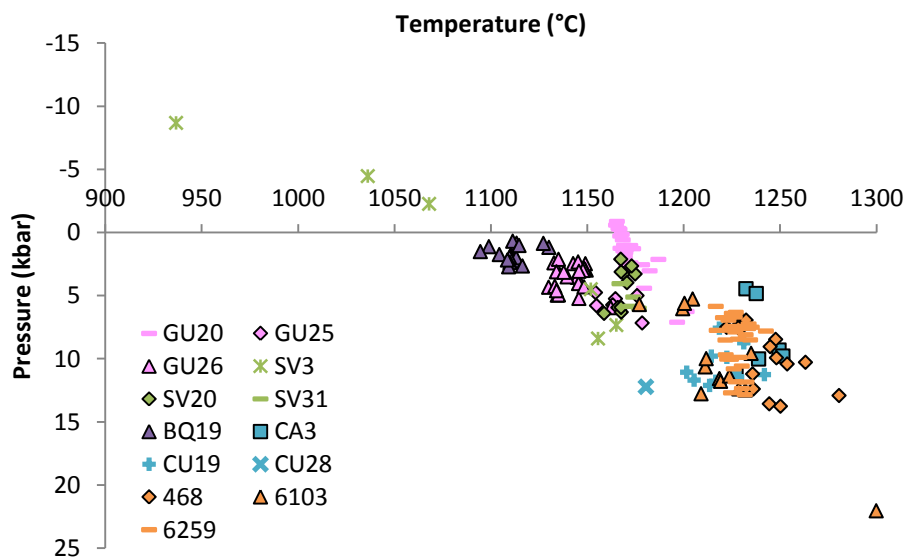


**Figure 5-33** Calculated crystallisation temperatures and pressures using equations contained in Putirka (2008), which rely solely on the compositions of the clinopyroxenes.

Although more of the clinopyroxenes show positive pressures using the Putirka (2008) method (based on the Nimis, 1995 model) than the Putirka and Condit (2003) pressure calculation, there are still several which show implausible pressures. Therefore it may be of more use to take heed of the qualitative elements of the modelling rather than the values produced.

Both Figure 5-32 and Figure 5-33 show the Grenada and Carriacou clinopyroxenes to be crystallised at the highest temperatures and the greatest depths. One clinopyroxene from host lava 6103 exhibits a much deeper signature than the remainder of the crystals at 22 kbar (and a temperature of 1300°C) on Figure 5-33. The St. Vincent clinopyroxenes show temperatures and pressures comparable to some of the Guadeloupe crystals, however, the latter island also exhibits crystals at lower temperatures and pressures. Some of the SV3 crystals show implausible

conditions on Figure 5-33 and thus are discounted, these being the crystals which exhibited lower Mg# ( $Mg\#_{59-61}$ ) than the remaining clinopyroxenes from this host lava. The Bequia clinopyroxenes show the shallowest conditions. Although the number of host lavas studied is small, there appears to be no real correlation between temperature, pressure and latitude.

Figure 5-34 shows that there is no obvious correlation between either pressure and % distance from rim or temperature and % distance from rim (using Equation 5-8 and Equation 5-10). However, it is worth noting the wide ranges in pressure calculated within the crystals.

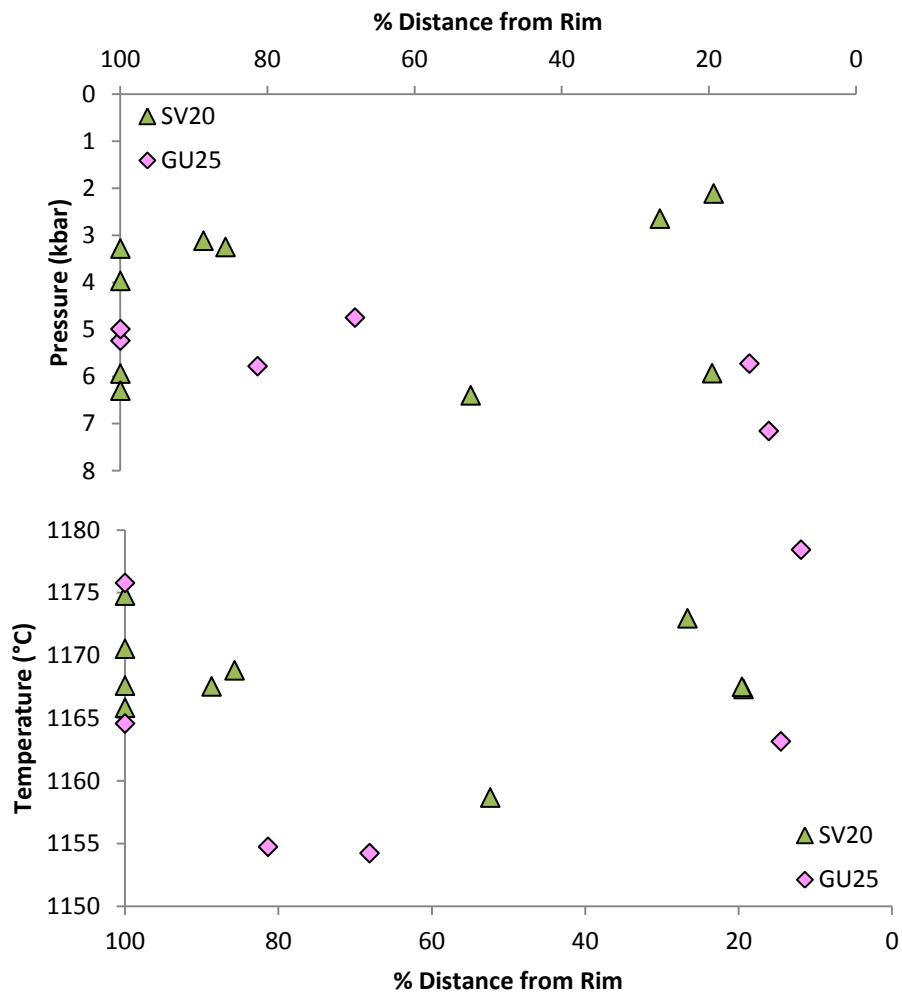


Figure 5-34 Pressure and temperature variations across crystals analysed in thick section from GU25 and SV20.

### 5.5.3 REE Partition Coefficient Calculations and Melt Back Calculation

Wood and Blundy (1997) provided a model for the calculation of REE partition coefficients, however this model is for use in anhydrous systems. Sun and Liang (2012) and references therein suggest that increasing water contents should reduce partition coefficients between clinopyroxenes and melts. Wood and Blundy (2002) agreed with this and observed that in the most hydrous examples they studied, hydrous partition coefficients are up to an order of magnitude lower than their anhydrous equivalents. Sun and Liang (2012) comment that it is still not fully understood how water influences the partitioning of REE.

The clinopyroxene melt partition coefficients were calculated using the clinopyroxene compositions along with the pressure and temperature conditions calculated in section 5.5.2. The spreadsheet provided as supplementary data by Wood and Blundy (1997) was used to calculate anhydrous  $K_D^{REE}$  after first using Equation 5-12 and Equation 5-13 (Wood & Blundy, 1997).

#### Equation 5-12

$$K_{D_{Fe-Mg}}^{cpx} = 0.109 + 0.186Mg\#_{cpx}$$

#### Equation 5-13

$$Mg\#_{melt} = \frac{K_{D_{Fe-Mg}}^{cpx} Mg\#_{cpx}}{1 - Mg\#_{cpx} + Mg\#_{cpx} K_{D_{Fe-Mg}}^{cpx}}$$

After having calculated the anhydrous partition coefficients, the hydrous partition coefficients were calculated from these values using the method provided in Wood and Blundy (2002). Firstly, the activity coefficient of  $CaMgSi_2O_6$  in the melt was calculated (Equation 5-14), where  $X_{H_2O}^{melt}$  refers to the modal proportion of water in the melt in question (2 wt%  $H_2O$  was used for the calculations Macdonald et al., 2000).

#### Equation 5-14

$$\gamma_{CaMgSi_2O_6}^{melt} = -0.3208 + \frac{0.0563}{(1 - X_{H_2O}^{melt})} + 1.8452 \times (1 - X_{H_2O}^{melt}) - 0.5807(1 - X_{H_2O}^{melt})^2$$

Wood and Blundy (2002) suggested that:

**Equation 5-15**

$$\gamma_{REEMgAlSiO_6}^{melt} = \gamma_{CaMgSi_2O_6}^{melt}$$

Using Equation 5-14 and Equation 5-15, hydrous partition coefficients can be calculated with Equation 5-16, where REE is the element of choice and again a water content of 2 wt% was used (Macdonald *et al.*, 2000).

**Equation 5-16**

$$K_D^{REE^{hydrous}} = K_D^{REE^{anhydrous}} \times \gamma_{REEMgAlSiO_6}^{melt} \times (1 - X_{H_2O}) \frac{100}{(100 - wt\%H_2O^{melt})}$$

The results of these calculations agree with the literature (Sun & Liang, 2012, Wood & Blundy, 2002), in that the anhydrous  $K_D$  values for the REE are higher than the hydrous ones. Figure 5-35 shows the average anhydrous and hydrous partition coefficients for each analysed REE during this study.

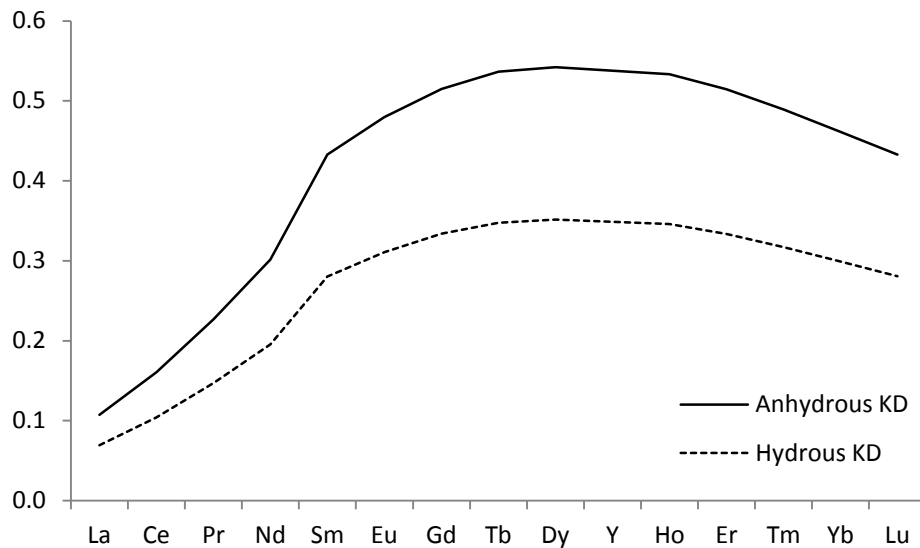


**Figure 5-35 Graph showing the average anhydrous and hydrous partition coefficients calculated from Wood and Blundy (1997) and Wood and Blundy (2002).**

After calculating the hydrous partition coefficients, approximate melt compositions were back calculated using Equation 5-17, where x is concentration and REE refers to a specific REE.

**Equation 5-17**

$$x_{melt}^{REE} = \frac{x_{cpx}^{REE}}{K_D^{REE}}$$

Figure 5-36 shows the calculated composition of a representative LREE (La), MREE (Sm) and HREE (Yb) plotted against the Mg# of the melt calculated in Equation 5-13.

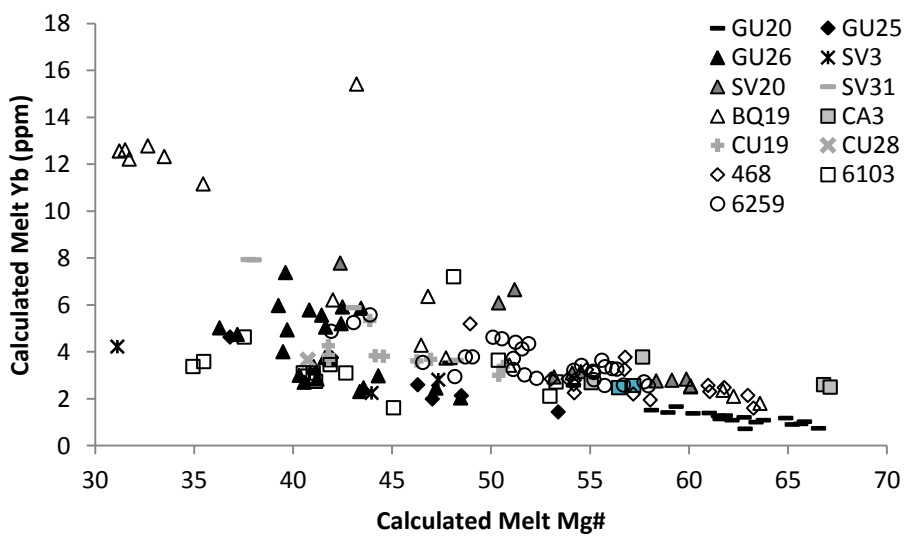
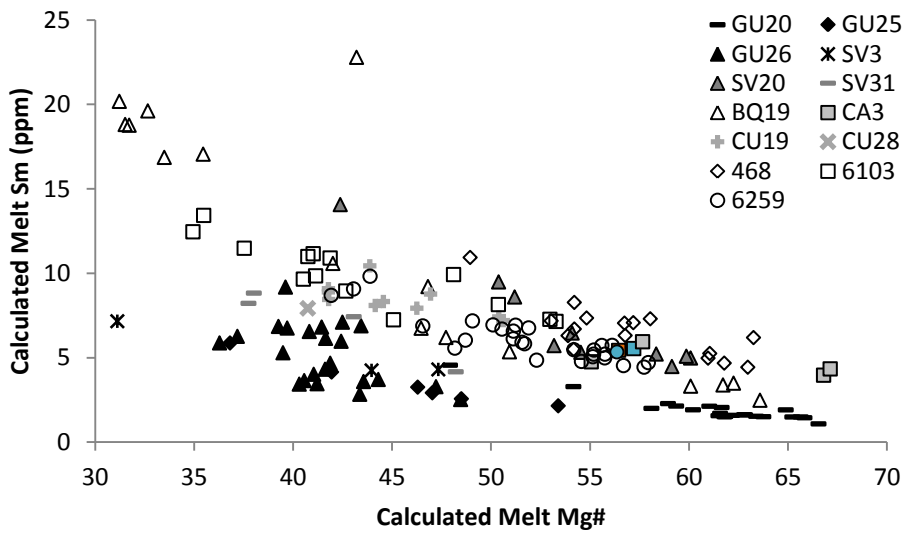
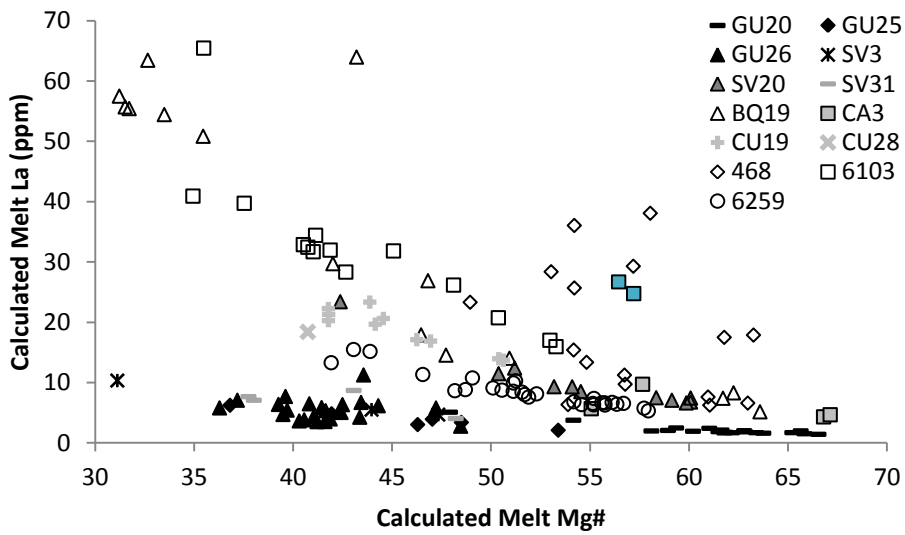


**Figure 5-36 Calculated melt compositions showing an LREE (La), MREE (Sm) and HREE (Yb). The two CA3 crystals with conflicting REE patterns to the remainder of the clinopyroxenes from this host lava are indicated by the blue squares.**

Figure 5-36 shows the Guadeloupe melts to exhibit lower REE concentrations at a given melt Mg# than those from the other islands (with the exception of several melts calculated from St. Vincent), although this effect diminishes as atomic number increases (as observed in the clinopyroxene chemistry). The Bequia melts commonly show the highest REE concentrations at low melt Mg#.

The two crystals from CA3 with distinctive REE patterns (Figure 5-23) appear to originate from a different parental composition to their counterparts from the same host lava. The two crystals show melt compositions with higher LREE at Mg#<sub>56-57</sub> than the remainder of the CA3 crystals, being more comparable with the 468 clinopyroxenes.

Unfortunately, the higher REE group from SV3 is the lower Mg# group for which the geothermobarometry provided implausible results. As such, no melt composition back calculation was possible as the method requires pressure and temperature data and thus no comparison can be made between the two groups from SV3.

## **5.6 Issues with Partition Coefficients**

The use of accurate partition coefficients requires knowledge of several parameters, such as pressure, temperature, melt water contents etc. Whilst the partition coefficients calculated from the Wood and Blundy (2002) model are among the most accurate used in any of the mineral chapters of this study (as they used calculated pressures and temperatures from the Putirka, 2008 model rather than estimates), assumptions must still be made. In this instance, in the Wood and Blundy (2002) partition coefficient calculation, estimates were regarding melt water contents, as well as any assumptions and errors that were inherited from the geothermobarometric modelling. This study is not appropriate to provide an in depth analysis of either partition coefficients provided in the literature or to make estimates of new values based on the measured data. No glass analyses were performed as, by the nature of the study, porphyritic host lavas were required to provide the minerals for analysis. Therefore, whilst partition coefficients have been used in the following

sections, it is worth considering that these may not be as accurate or suitable as desired, potentially affecting the quantitative results.

## 5.7 Melt Evolution

The effects of fractional crystallisation occurring in the host melts (and thus subsequently affecting clinopyroxene composition as a result of changes in the melt chemistry) are apparent in clinopyroxenes from several of the host lavas. Figure 5-23 shows these effects, for instance in the case of BQ19. The REE patterns are parallel and show upward translation, with accompanying increasing Eu depletions potentially indicating fractional crystallisation of the host melt. The increase in Eu depletion may suggest that plagioclase is crystallising concurrently with clinopyroxene (with Eu being less incompatible in plagioclase due to its 2<sup>+</sup> valency being more easily accommodated in the plagioclase structure). Similar patterns are observed in the GU20, GU25, GU26, SV20, SV31, CA3, CU19, 6103 and 6259 host lavas. In the case of BQ19, the highest Mg# analyses still have negative Eu anomalies, indicating that some plagioclase crystallisation occurred prior to the crystallisation of the clinopyroxenes.

Although BQ19 shows increases in REE contents towards the rims of crystals (Figure 5-37, where three different crystals analysed in thick section are shown as different colours: orange, blue and green), the degree of crystallisation required to increase the REE contents sufficiently is very large (over 80%). For example, Figure 5-37 shows an 8-fold increase in La contents in the BQ19-1 analyses and a 3.2 times increase in the BQ19-2 analyses with decreasing Mg#.

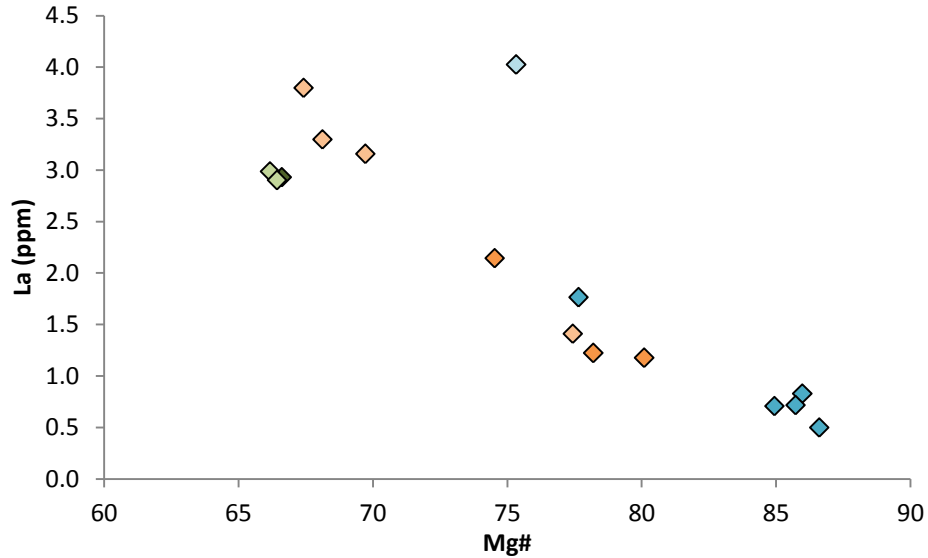


**Figure 5-37** La concentrations in clinopyroxenes from BQ19. Blue diamonds are analyses in between the core and the rims in BQ19-1, with rim analyses from this crystal being light blue. Orange diamonds are analyses intermediate between core and rim from BQ19-2, with light orange being rims. Dark green diamond is a BQ19-3 core analysis with light green being rims.

Therefore, while fractional crystallisation undoubtedly has a role to play in generating the trends between Mg# and REE contents, it cannot be the sole solution.  $K_D^{La}$  calculated from the Wood and Blundy (2002) model for BQ19 shows that for a range in Mg# of 20, the variation in partition coefficients is 92%. Given this wide range in partition coefficients at constant melt water contents, the large amount of crystallisation required may be mitigated by further variations in partition coefficients. If melt water changes, and/or the pressures and temperatures calculated using the Putirka (2008) model are inaccurate, this would alter the partition coefficients for the REE. Partition coefficients for the other analysed elements in this dataset have not been constrained during this study (section 5.6). If they vary as much as the REE partition coefficients then it would appear likely that fractional crystallisation coupled with changing  $K_D$  values with Mg# could generate the trends observed.

The two groups apparent in SV3 can also be explained to some extent by fractional crystallisation in the host melt. It would appear that the lower REE clinopyroxene/chondrite ratio group (Figure 5-23) may have crystallised first, not only because they display lower REE concentrations, but also as they exhibit higher Mg# (Mg#<sub>66-78</sub>). The higher REE group (Mg#<sub>58-61</sub>) additionally show definite depletion in Eu, which is not observed in the lower REE group. This would suggest

that the melt from which the higher REE group was crystallised had undergone a much larger degree of plagioclase crystallisation relative to the lower REE group. What is unclear is whether both groups originate from the same parent melt. Either the lower REE group crystallised first, followed by a break in clinopyroxene crystallisation (during which larger scale plagioclase crystallisation occurred) and then the higher REE group was crystallised or the two groups are derived from different parental melts. The two populations could then have been combined by entrainment or magma mixing in the magmatic plumbing system. Unfortunately, as the crystals were analysed in resin blocks, detailed textural information on the specific crystals is not available. As a result, it is not possible to determine texturally which if either population has been added to the host lava. However, given the relatively parallel nature of the REE patterns, it is feasible that both groups originated from the same parent melt or very similar melts.

## **5.8 Possible Entrainment or Magma Mixing**

The two CA3 crystals with contrasting REE profiles to the remainder from this host melt must have originated from a different source and cannot be a result of fractional crystallisation in the host melt as the REE patterns cross (Figure 5-23). Therefore, these two crystals can be identified as a separate population, meaning that the two populations must have been combined at some point in the magmatic plumbing system prior to eruption. Due to the fact that these crystals show comparable major element concentrations to the remaining crystals, the geothermobarometric modelling does not provide different pressure or temperature conditions for these clinopyroxenes. Petrographic observations are also unavailable for these specific crystals as the CA3 clinopyroxenes were analysed in crystal mounts. However, Figure 5-7 shows a phenocryst in CA3 that appears that it may have been entrained. There is obvious breakdown and resorption of the outer parts of the crystal, as well as a zone of material adjacent to the margin of the crystal visible in XPL. The latter may suggest the crystal has been resident in a melt from which it was not crystallised and has started to re-equilibrate through diffusion. Therefore, there is some petrographic evidence that entrainment of clinopyroxene has occurred in CA3. Based on the clinopyroxene data acquired alone however, it is difficult to establish which

population (if either) has been crystallised from the host melt and which has been introduced, either via magma mixing or entrainment of a crystal cargo.

Clinopyroxenes from host lavas such as 468 that show a significant amount of scatter in their concentration data at a given Mg# value may also indicate entrainment or magma mixing. Evolution of the clinopyroxenes along slightly different routes in the magmatic plumbing system could explain the large ranges at similar Mg# as different melt batches travel and evolve during ascent. Given the similar REE profiles of the 468 clinopyroxenes, it is suggested that the crystals are not xenocrysts or products of melts with significantly different compositions.

## 5.9 Depth of Melting

The relationship between chondrite normalised Dy/Yb and La/Yb has been used to provide information on the depth of melting (Thirlwall *et al.*, 1994b), with the important caveat of assuming a constant source composition. The Dy/Yb<sub>N</sub> and La/Yb<sub>N</sub> ratios for the Lesser Antilles melt compositions were back calculated from the clinopyroxene concentrations using the Wood and Blundy (1997) and the Wood and Blundy (2002) partition coefficients and are shown in Figure 5-38. Only melt compositions calculated from clinopyroxenes >Mg#<sub>70</sub> were plotted on Figure 5-38 in an effort to filter out melt compositions that may have been affected by fractionation. Thirlwall *et al.* (1994b) suggested that Dy/Yb<sub>N</sub> (degree of HREE enrichment) would be increased during melting in the garnet stability field whereas La/Yb<sub>N</sub> (LREE enrichment) is mainly controlled by melting in the stability field of spinel. Dy/Yb<sub>N</sub> can be used as a measure of depth of melting and La/Yb<sub>N</sub> as an indicator of degree of melting for a given source. Positive correlations between Dy/Yb<sub>N</sub> and La/Yb<sub>N</sub> for the melts could be explained by mixing between melts from the garnet and spinel fields.

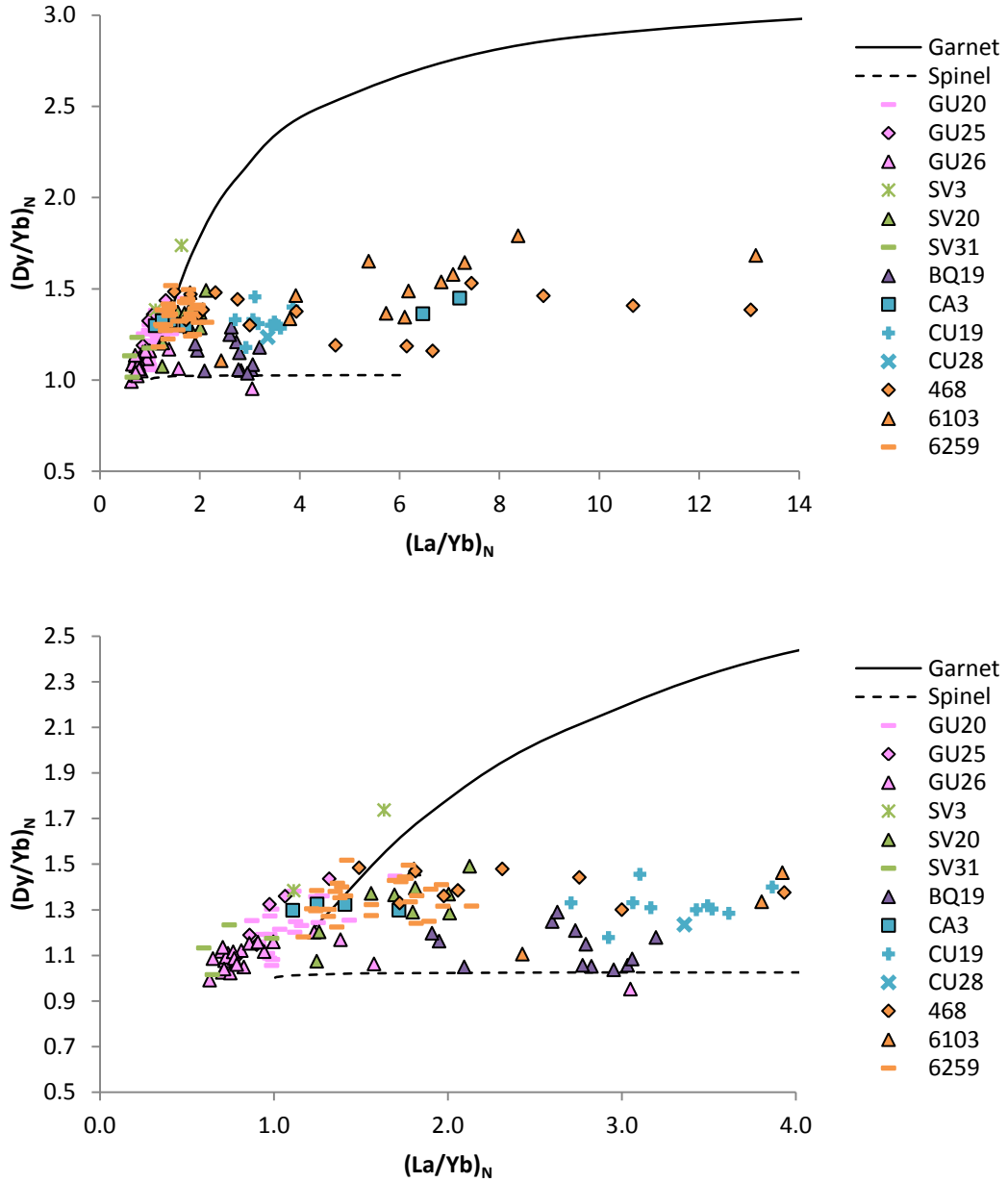


**Figure 5-38**  $Dy/Yb_N$  and  $La/Yb_N$  ratios of the melt compositions back calculated using the partition coefficients of Wood and Blundy (1997) and Wood and Blundy (2002). The upper graph shows all the compositions whilst the lower shows more detail of the lower  $La/Yb_N$  ratios.

Figure 5-38 shows many of the calculated melt compositions to have low  $La/Yb_N$  ratios, particularly in Guadeloupe where the range is 0.63-1.70 (with one outlying crystal with a ratio of 3.05). All bar one of the St. Vincent analyses also lie below a  $La/Yb_N$  ratio of 2.0. This could suggest large melt fractions in these host lavas. Melt compositions calculated from Bequia clinopyroxenes show higher  $La/Yb_N$  ratios between 1.91 and 3.31.  $La/Yb_N$  ratios in the Carriacou melts are generally below 3.65, with the notable exception of those calculated from the two crystals from CA3 which showed differing rare earth patterns to the remaining analyses from this host

lava. These latter two melt compositions have ratios of 6.46 and 7.02. This suggests that these two clinopyroxenes may have been crystallised from a lower degree partial melt than the majority of the crystals from CA3. Similar Dy/Yb<sub>N</sub> ratios observed in the CA3 melts would suggest that the depths at which melting occurred were consistent for both populations. The Grenada melts show the widest range in La/Yb<sub>N</sub> ratios, extending from 1.17 to 13.13. The range in the 6259 melts is comparable to those calculated for St. Vincent, with values between 1.17 and 2.14. 468 shows a range in La/Yb<sub>N</sub> between 1.49 and 13.03 whilst 6103 has a range of 1.63 to 13.13. This could suggest differing degrees of melting in some of the Grenada host lavas and also relatively small degrees of melt being present in both 468 and 6103.

The melt compositions from Bequia, Carriacou and Grenada all show relatively constant Dy/Yb<sub>N</sub> ratios with changing La/Yb<sub>N</sub>, as opposed to the Guadeloupe (with the exception of GU26) and St. Vincent melts which exhibit positive correlations. Lack of variation in Dy/Yb<sub>N</sub> may suggest that all of the calculated melt compositions from GU26, Bequia, Carriacou and Grenada had relatively constant depth of melting for these host lavas. Furthermore, as only a small amount of melt from the garnet stability field is required to generate positive correlations between La/Yb<sub>N</sub> and Dy/Yb<sub>N</sub>, the data may suggest that melting primarily occurred in the spinel stability field (and thus at shallower depths than the melt compositions from the remaining Guadeloupe host lavas and St. Vincent). Given the positive correlations observed in the GU20, GU25 and St. Vincent melt compositions between La/Yb<sub>N</sub> and Dy/Yb<sub>N</sub>, it appears likely that some melt from the garnet stability field has contributed to their parent melts.

These results agree somewhat with the findings of Wadge and Shepherd (1984) in that the dip of the Benioff zone is between 60-50° in the north of the arc (compared to 50-45° to the south of the arc), with the positive correlations between the La/Yb<sub>N</sub> and Dy/Yb<sub>N</sub> data showing the Guadeloupe melts to have a garnet component that is not observed in two of the southernmost islands (Carriacou and Grenada). However, it is also proposed that the Benioff zone dips to almost vertical beneath Grenada (Wadge & Shepherd, 1984) which is not seen in the La/Yb<sub>N</sub> and Dy/Yb<sub>N</sub> data.

Temperatures at the front of the downgoing slab can be much cooler than the adjacent mantle wedge (Marschall & Schumacher, 2012). As a result of this temperature difference and the drag created by the descending slab, the hotter local

mantle material convectively moves into the corner of the mantle wedge, known as corner flow (Marschall & Schumacher, 2012). Grove et al. (2009) suggested that the dip of the downgoing slab dictates the flow of the hotter material. More steeply dipping slabs allow for the hotter mantle to extend to shallower levels, prompting higher degrees of melting (Grove *et al.*, 2009). In terms of Figure 5-38, this should result in lower Dy/Yb<sub>N</sub> and La/Yb<sub>N</sub> ratios. Shallower dipping slabs may show the opposite, as the hotter mantle remains at deeper levels, prompting smaller degrees of melting. Figure 5-38 shows that the Guadeloupe data do show lower La/Yb<sub>N</sub> ratios (indicating a larger melt fraction) than most of the melts calculated from islands with shallower dipping Benioff zones (although the Guadeloupe melts do show positive correlations). They also exhibit amongst the lower Dy/Yb<sub>N</sub> ratios calculated at low La/Yb<sub>N</sub> ratios. The positive correlation may be a result of the mixing of melts originating from different parts of the mantle wedge, with a contribution from a deeper garnet stability field melt as well as a shallower spinel field component. Similar correlations are seen in the St. Vincent data, although the dip of the slab is thought to be slightly less steep under this island (Wadge & Shepherd, 1984). Given the vertical nature of the slab beneath Grenada (Wadge & Shepherd, 1984), the La/Yb<sub>N</sub> and Dy/Yb<sub>N</sub> ratios calculated for the clinopyroxene melts do not completely correlate with those suggested for steeply dipping slabs. The large ranges in La/Yb<sub>N</sub> observed in 468 and 6103 in particular cannot be explained by slab dip alone. Water contents in the mantle wedge can also have an effect on degree of melting (Gaetani & Grove, 2013) and so on La/Yb<sub>N</sub> ratios. Hydrous melting is thought to produce higher melt fractions than anhydrous melting (Gaetani & Grove, 2013). Thus the large range in the 468 and 6103 melts could represent dehydration of the wedge as melting progresses, with more hydrous melts potentially having lower La/Yb<sub>N</sub> ratios and more anhydrous melts having higher La/Yb<sub>N</sub> ratios. As the Dy/Yb<sub>N</sub> ratios remain fairly constant, there is no implication of depth changing as the melt fraction decreases. Only melts calculated from the Grenada clinopyroxenes and the two CA3 crystals with unusual REE patterns exhibit La/Yb<sub>N</sub> ratios above 4.0, suggesting that these melts are least affected by water.

The findings of the modelling are not entirely in agreement with the geothermobarometric modelling undertaken on the clinopyroxenes (section 5.5.2), which suggested that the Carriacou and Grenada crystals were crystallised at the

highest temperatures and pressures, with Bequia at the shallowest depths and St. Vincent and Guadeloupe intermediate between the latter three islands. Whilst the calculated Bequia melts do show the lowest  $Dy/Yb_N$  (and thus potentially the shallowest depths of melting), the Carriacou and Grenada melt compositions show no obvious contribution from the garnet stability field, possibly implying shallower melting depths than Guadeloupe and St. Vincent. There is a significant overlap between clinopyroxenes from different host lavas, meaning that the interpretations based on the chondrite normalised  $Dy/Yb$  and  $La/Yb$  ratios may not be particularly robust, especially in conjunction with the use of a single source composition for all the host lavas.

### 5.9.1 Comparing Back Calculated Melt Depths to Whole Rock Melt Depths

To compare the results of the melt back calculations with the whole rock compositions, the average melt  $La/Yb_N$  and  $Dy/Yb_N$  ratios were plotted on Figure 5-39 with those from the whole rocks. The whole rock analyses for GU20, GU25 and CA3 were obtained using the isotope dilution technique described in **Appendix 1**.

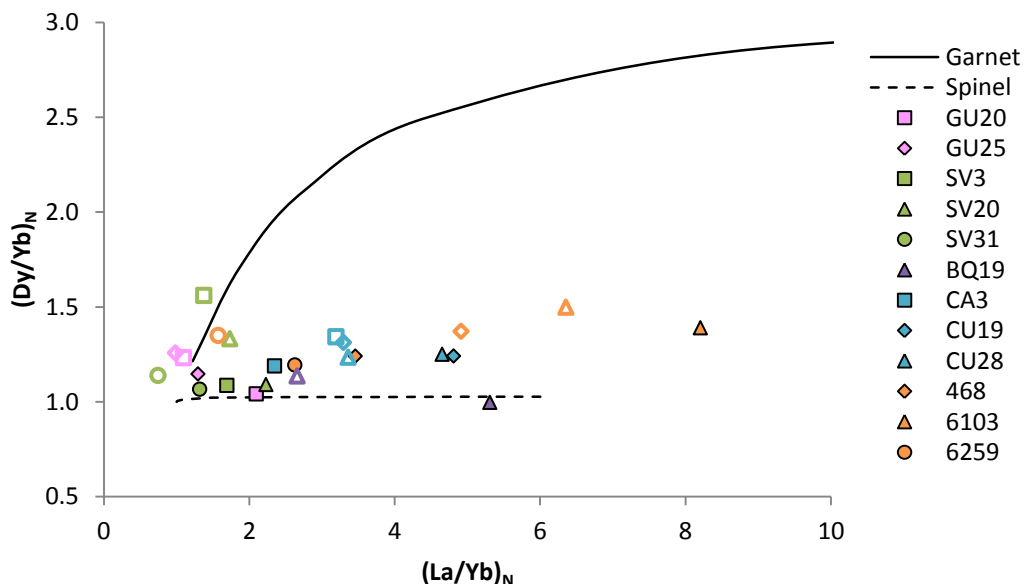


**Figure 5-39 Comparison of the average  $La/Yb_N$  and  $Dy/Yb_N$  ratios of the back calculated melt compositions (hollow symbols) with the whole rock ratios (solid symbols). The GU20, GU25 and CA3 whole rock data was obtained using the isotope dilution technique (Appendix 1). REE data not available for GU26.**

Figure 5-39 shows that with the exception of two host lavas (CA3 and 468), the back calculated melt compositions show higher Dy/Yb<sub>N</sub> ratios and lower La/Yb<sub>N</sub> ratios than the whole rocks. In general the whole rock ratios suggest shallower, smaller degree melts than the back calculated melt ratios, potentially with lower water contents. However, an alternative method of generating the differences between the whole rocks and melts is to crystallise clinopyroxene. Clinopyroxene crystallisation would decrease Dy more rapidly than La or Yb. If the back calculated melts had fractionated some clinopyroxene (and thus removed Dy preferentially to Yb) and, for example formed cumulates, this would result in the whole rock composition having lower Dy/Yb<sub>N</sub>. The Wood and Blundy (2002) hydrous partition coefficients calculated for the Lesser Antilles clinopyroxenes also show La to be much more incompatible than Yb (Figure 5-35), thus clinopyroxene removal would also increase La/Yb<sub>N</sub> ratios.

Another possibility is the formation of other REE hosting cumulate minerals, such as amphibole, removing REE from the melt. Mineral phases such as amphibole, which have been seen extensively in cumulates from across the Lesser Antilles but are not observed in the erupted products (Davidson & Wilson, 2011), could host REE at depth, meaning that they are 'missing' from the whole rock compositions and causing the decreased Dy/Yb<sub>N</sub> ratios and increased La/Yb<sub>N</sub> ratios observed in Figure 5-39. Amphibole fractionation has been shown to decrease Dy/Yb (Davidson *et al.*, 2007a). The influence of amphibole on melts whilst being absent from erupted lavas has been termed 'cryptic amphibole fractionation' (Davidson *et al.*, 2007a, Davidson & Wilson, 2011) and these authors suggest that this process has an important role to play in arc petrogenesis.

The processes discussed so far are not likely to cause the trends seen in CA3 and 468. As discussed previously, the clinopyroxene compositions (from which the melts were calculated) are not in equilibrium with the host rocks in most cases (Figure 5-30). Both CA3 and 468 plot in the potentially accumulative field but clinopyroxene accumulation is unlikely to cause the relationships between the melt and whole rock ratios for these host lavas as the remaining Carriacou and Grenada host lavas also show potentially accumulative clinopyroxene populations. However, the average value used for CA3 includes the two crystals with differing REE patterns. If these crystals are ignored, the CA3 back calculated melts and whole rock

ratios show the same relationship as the other host lavas (lower Dy/Yb<sub>N</sub> and higher La/Yb<sub>N</sub> in the whole rocks). Therefore it is possible that the two CA3 crystals represent an entrained population.

## 5.10 Conclusions

The clinopyroxene data from the Lesser Antilles show several features.

Broadly speaking the geothermobarometric modelling suggests that the clinopyroxenes originating from very south of the arc show higher temperature and pressures at the time of crystallisation to those from the other islands. However, there is no overall trend with latitude as the Bequia crystals exhibit some of the shallowest conditions despite being located to the south of St. Vincent.

Back calculated melt compositions based on the REE data show La/Yb<sub>N</sub> and Dy/Yb<sub>N</sub> data that somewhat agree with the geothermobarometric modelling. The BQ19 melts agree with the clinopyroxenes in that they originate at shallow depths. The Guadeloupe and St. Vincent melt data gives an indication of deeper melting depths than the clinopyroxene depths infer for crystallisation, with the reverse being seen for Carriacou and Grenada. Amphibole fractionation may account for these differences, as were REE to have been sequestered in the Carriacou and Grenada host lavas in this phase, the clinopyroxenes may show La/Yb<sub>N</sub> and Dy/Yb<sub>N</sub> ratios that would imply shallower melting depths. Vertical slab dip underneath Grenada may also be responsible for the apparent shallower depths (and the deeper depths for Guadeloupe and St. Vincent) as corner flow may initiate melting at lower depths. Potential differences in melt water contents affecting melt fractions and thus La/Yb<sub>N</sub> ratios may also play a role. If lower water contents are involved in the Grenada melts this could explain the wide variations seen in La/Yb<sub>N</sub>.

REE data show the presence of two populations in at least two of the host lavas (SV3 and CA3), indicating more complex petrogenesis than simple fractional crystallisation from a parent melt is occurring. This is supported by the fact that few of the clinopyroxenes from St. Vincent, Carriacou and Grenada appear to be in equilibrium with their host melts. Petrographic indications e.g. from CA3 suggest at least some of the clinopyroxenes are out of equilibrium with their host melts.

Overall, the clinopyroxene data suggest that melting and crystallisation of clinopyroxenes varies between islands. Fewer of the host lavas exhibit multiple populations than seen in the olivine and plagioclase data but this may partly be a function of the smaller number of discrete crystals analysed. It is possible that more populations exist but have simply not been sampled during this study. However, based on the data available, entrainment and/or magma mixing is likely to have occurred in at least two of the host lavas.

Conclusions by island are as follows:

Guadeloupe - Clinopyroxenes from this island show no significant evidence of plagioclase crystallisation occurring while the clinopyroxenes have crystallised. The clinopyroxenes may be in equilibrium with their host lavas, particularly in the case of GU20 and GU25. Pressure and temperature modelling puts clinopyroxene crystallisation at among the shallowest levels observed in the data in this study. The GU20 crystals show higher temperatures than the other Guadeloupe clinopyroxenes at approximately 1170°C compared to ~1140°C. Melting modelling suggests a contribution from a garnet stability field melt, which may be related to a higher slab dip than seen in other parts of the arc. Degree of melting is relatively high compared to the other Lesser Antilles data, potentially suggesting higher melt water contents.

St. Vincent - SV3 shows two populations of clinopyroxene, the higher Mg# population may have crystallised first, followed by a period of plagioclase crystallisation, followed by further clinopyroxene crystallisation (which would explain the Eu anomalies observed in the lower Mg# group but not the higher Mg# group). Geothermobarometric modelling suggest the St. Vincent clinopyroxenes crystallised at similar temperatures and pressures to the Guadeloupe crystals, with the REE melting modelling also suggesting similar conditions between the two islands. Again a garnet stability field component is suggested.

Bequia - Extensive plagioclase crystallisation is apparent before and during the crystallisation of the clinopyroxenes from the chondrite normalised REE patterns. The geothermobarometric modelling suggest that the Bequia clinopyroxenes crystallised at the lowest temperatures and among the lowest pressures of all the analysed Lesser Antilles clinopyroxene crystals. Melting modelling also shows

relatively small degree melts (compared to the Guadeloupe and St. Vincent clinopyroxenes) at shallow levels with predominantly spinel stability field melting.

Carriacou - Entrainment and/or magma mixing is apparent in CA3 with both textural evidence and two chemically distinct populations being apparent. Clinopyroxenes crystallised at greater depths than those from Guadeloupe, St. Vincent and Bequia according to geothermobarometric modelling. However, melting modelling suggests a shallower spinel stability field component (although clinopyroxenes from CA3 do show some evidence of a garnet stability field contribution). Large ranges in  $La/Yb_N$  at relatively constant  $Dy/Yb_N$  could suggest dehydration of melts during crystallisation, increasing  $La/Yb_N$  without altering the apparent depth of melting.

Grenada - Clinopyroxenes from this island do not show extensive evidence of plagioclase fractionation. Calculated pressures and temperatures of crystallisation are similar to those in Carriacou. Melting modelling also shows comparable results to the Carriacou clinopyroxenes.  $La/Yb_N$  show larger ranges than clinopyroxenes from most host lavas but not as large as those from Carriacou. Again, this may be linked to fluid input to the melt increasing as crystallisation progressed.

## 5.11 Further Work

- More clinopyroxene data is required: from the host lavas already studied, host lavas from the same islands and host lavas from islands not yet targeted.
- Further thick section analyses would be of great use to more effectively couple petrographic and geochemical data.
- Better constraint of partition coefficients would allow for more accurate melt back calculations, either in the form of a targeted study of phenocryst matrix pairs in more aphyric Lesser Antilles lavas or by more accurately constraining parameters used in existing published models. More detailed knowledge of melt water contents in particular would be highly beneficial e.g. for use in the Wood and Blundy (2002) REE partition coefficient calculations.

---

## 6 Synthesis

---

### 6.1 Introduction

So far this thesis has investigated the petrogenetic evolution of Lesser Antilles lavas using individual mineral phases. This chapter attempts to combine this information to generate a more complete model for the generation of the Lesser Antilles lavas. In addition, this section will attempt to identify variations in the source compositions and melting regimes along the strike of the arc. This will be done predominantly using new double spike Pb isotopic data acquired during this thesis which add to previous analyses (Thirlwall, unpublished data).

### 6.2 Whole Rock Pb Isotopes

High precision double spike Pb analyses (Thirlwall, 2002) were carried out on Lesser Antilles lavas from across the arc in order to provide information on source compositions, both as part of this study and by Thirlwall (unpublished data). Whole rock Pb isotopes may provide insight as to whether the mantle source is consistent along arc strike or whether this also displays regional variations. In addition the data were used to test the hypothesis of Carpentier et al., (2008).

The latter study analysed sediments from DSDP Site 144, DSDP Site 543 and Barbados (the surface expression of the accretionary prism) to try and ascertain whether the sediments being subducted beneath the arc show similar north to south geochemical variations to the lavas and why the southern islands showed unusually low  $\Delta 8/4$  ratios (where  $\Delta 8/4$  is the difference between the sample  $^{208}\text{Pb}/^{204}\text{Pb}$  and that of the Northern Hemisphere Reference Line at a given  $^{206}\text{Pb}/^{204}\text{Pb}$  ratio). Carpentier et al., (2008) found that the Site 144 sediments showed variable  $^{206}\text{Pb}/^{204}\text{Pb}$  and  $^{207}\text{Pb}/^{204}\text{Pb}$  ratios compared to the relatively constant values observed at Site 543. In addition, some of the Site 144 analyses displayed very high ratios of  $^{206}\text{Pb}/^{204}\text{Pb}$ ,  $^{207}\text{Pb}/^{204}\text{Pb}$  and  $^{208}\text{Pb}/^{204}\text{Pb}$ , coupled with low  $^{143}\text{Nd}/^{144}\text{Nd}$  ratios. The authors attributed this to the input of ancient cratonic material from the South American continent, whose influence waned with increasing latitude. In particular, a black shale unit from Site 144 (Unit 3) showed very unusual isotopic

compositions and trace element compositions, such as very low concentrations of Nd and Pb, coupled with high U contents, generating high U/Pb ratios (but normal Th/Pb). The remainder of the Site 144 data show lower trace element concentrations than those measured in Site 543 (Carpentier *et al.*, 2008). The Barbados samples also show larger ranges and lower trace element compositions than the Site 543 data.

Modelling undertaken by Carpentier *et al.*, (2008) suggested that whole rock compositions could be reproduced in the south of the arc by adding 10% of Site 144 like composition sediments (terrigenous material, carbonates and shale), whilst the northern part of the arc required 1% addition of Site 543 like material (pelagic sediment and radiolarian clays). They suggested that the extreme composition of the shale unit from Site 144 is capable of accounting for the high radiogenic Pb isotope compositions seen in the south of the arc (Carpentier *et al.*, 2008).

### 6.2.1 Pb Isotope Results

The Pb isotope data is shown in Table 6-1. Also included in the table are  $^{87}\text{Sr}/^{86}\text{Sr}$  and  $^{143}\text{Nd}/^{144}\text{Nd}$  ratios where available, measured using TIMS analysis (**Appendix 1**). Those analyses which were not performed as part of this study and constitute unpublished data from Thirlwall are indicated in the table. The unpublished data of Thirlwall also includes analyses from Redonda, St. Eustatius and Montserrat which are situated further north in the arc than any of the other analysed host lavas discussed in the previous chapters.

Sample Name	$^{206}\text{Pb}/^{204}\text{Pb}$	$^{207}\text{Pb}/^{204}\text{Pb}$	$^{208}\text{Pb}/^{204}\text{Pb}$	$^{87}\text{Sr}/^{86}\text{Sr}$	$^{143}\text{Nd}/^{144}\text{Nd}$
<b>R8202</b>	18.893	15.599	38.544	0.703221	0.513023
<b>SE8213</b>	18.948	15.637	38.645	0.703710	0.513024
<b>SE8238</b>	19.024	15.661	38.766	0.703714	0.512958
<b>SE8248</b>	18.941	15.630	38.635	0.703607	
<b>MS8207</b>	19.046	15.660	38.780	0.703550	
<b>MS8223</b>	19.004	15.652	38.732	0.703600	
<b>GU1</b>	19.181	15.677	38.883	0.703554	0.512897

Sample Name	$^{206}\text{Pb}/^{204}\text{Pb}$	$^{207}\text{Pb}/^{204}\text{Pb}$	$^{208}\text{Pb}/^{204}\text{Pb}$	$^{87}\text{Sr}/^{86}\text{Sr}$	$^{143}\text{Nd}/^{144}\text{Nd}$
<b>GU4</b>	19.187	15.683	38.904	0.703571	0.512899
<b>GU15</b>	19.253	15.700	39.006	0.703852	0.512857
<b>GU20</b>	19.095	15.659	38.787	0.703472	0.512904
<b>GU22</b>	19.168	15.685	38.898	0.703753	0.512942
<b>GU25</b>	19.157	15.660	38.809	0.703389	0.512854
<b>GU26</b>	19.214	15.691	38.939	0.703686	0.512899
<b>GU27</b>	19.211	15.697	38.963	0.703795	0.512907
<b>DM5J</b>	19.431	15.747	39.230	0.704514	
<b>DM9A</b>	19.391	15.729	39.177	0.704172	0.512791
<b>DM5DI</b>	19.420	15.739	39.206	0.704496	
<b>DM11A</b>	19.419	15.739	39.203	0.704435	0.512764
<b>DM13A</b>	19.415	15.743	39.210	0.704204	0.512769
<b>DM13C</b>	19.414	15.743	39.208	0.704205	
<b>DM15B</b>	19.427	15.745	39.223	0.704506	
<b>DM5DI</b>	19.425	15.743	39.216		
<b>DM5HI</b>	19.433	15.746	39.227		0.512786
<b>DM5K</b>	19.436	15.751	39.239		
<b>DM7A</b>	19.326	15.724	39.097		0.512745
<b>DM7B</b>	19.441	15.747	39.236		
<b>DM9A</b>	19.396	15.734	39.186		0.512791
<b>N3</b>	19.428	15.742	39.218	0.704492	0.512786
<b>DM5HI</b>					
<b>N8 DM7B</b>	19.437	15.743	39.227	0.704548	0.512775
<b>S7 DM7A</b>	19.322	15.719	39.088	0.704313	0.512745

<b>Sample Name</b>	$^{206}\text{Pb}/^{204}\text{Pb}$	$^{207}\text{Pb}/^{204}\text{Pb}$	$^{208}\text{Pb}/^{204}\text{Pb}$	$^{87}\text{Sr}/^{86}\text{Sr}$	$^{143}\text{Nd}/^{144}\text{Nd}$
<i>SV2</i>	<i>19.358</i>	<i>15.720</i>	<i>38.907</i>	<i>0.704056</i>	<i>0.513019</i>
<i>SV3</i>	<i>19.287</i>	<i>15.706</i>	<i>38.843</i>	<i>0.703830</i>	<i>0.513025</i>
<i>SV6</i>	<i>19.128</i>	<i>15.676</i>	<i>38.726</i>	<i>0.703725</i>	<i>0.513033</i>
<i>SV9</i>	<i>19.292</i>	<i>15.709</i>	<i>38.841</i>	<i>0.703779</i>	<i>0.513029</i>
<i>SV11</i>	<i>19.409</i>	<i>15.735</i>	<i>38.936</i>	<i>0.704075</i>	<i>0.513003</i>
<i>SV19</i>	<i>19.426</i>	<i>15.737</i>	<i>38.976</i>	<i>0.704347</i>	<i>0.512960</i>
<i>SV20</i>	<i>19.334</i>	<i>15.716</i>	<i>38.913</i>	<i>0.704657</i>	<i>0.512947</i>
<i>SV22</i>	<i>19.332</i>	<i>15.714</i>	<i>38.902</i>	<i>0.703989</i>	<i>0.513013</i>
<i>SV26</i>	<i>19.304</i>	<i>15.717</i>	<i>38.877</i>	<i>0.703888</i>	<i>0.512991</i>
<i>SV33</i>	<i>19.402</i>	<i>15.738</i>	<i>38.970</i>	<i>0.704034</i>	<i>0.512987</i>
<i>SV34</i>	<i>19.278</i>	<i>15.697</i>	<i>38.851</i>	<i>0.704091</i>	<i>0.512907</i>
<i>SV35</i>	<i>19.362</i>	<i>15.725</i>	<i>38.914</i>	<i>0.703997</i>	<i>0.513014</i>
<i>SV41</i>	<i>19.267</i>	<i>15.702</i>	<i>38.810</i>	<i>0.703781</i>	<i>0.513004</i>
<i>SV42</i>	<i>18.985</i>	<i>15.630</i>	<i>38.580</i>	<i>0.703574</i>	<i>0.513023</i>
<i>SV43</i>	<i>19.287</i>	<i>15.700</i>	<i>38.827</i>	<i>0.703926</i>	<i>0.513018</i>
<i>SV46</i>	<i>19.147</i>	<i>15.686</i>	<i>38.748</i>	<i>0.703767</i>	<i>0.513040</i>
<i>SV47</i>	<i>19.214</i>	<i>15.706</i>	<i>38.784</i>	<i>0.703781</i>	<i>0.512991</i>
<b>CA3</b>	<i>19.602</i>	<i>15.738</i>	<i>38.905</i>	<i>0.704640</i>	<i>0.512866</i>
<b>CA3</b>	<i>19.600</i>	<i>15.743</i>	<i>38.916</i>	<i>0.70464</i>	<i>0.512866</i>
<b>CA4</b>	<i>19.613</i>	<i>15.769</i>	<i>39.356</i>	<i>0.706504</i>	<i>0.512412</i>
<b>CA4</b>	<i>19.971</i>	<i>15.814</i>	<i>39.527</i>	<i>0.706504</i>	<i>0.512412</i>
<b>CA14</b>	<i>19.567</i>	<i>15.746</i>	<i>38.921</i>	<i>0.704757</i>	<i>0.512796</i>
<b>CU2</b>	<i>19.755</i>	<i>15.755</i>	<i>39.201</i>	<i>0.70395</i>	<i>0.513015</i>
<b>CU28</b>	<i>19.427</i>	<i>15.723</i>	<i>39.008</i>	<i>0.70559</i>	<i>0.512825</i>

<b>Sample Name</b>	$^{206}\text{Pb}/^{204}\text{Pb}$	$^{207}\text{Pb}/^{204}\text{Pb}$	$^{208}\text{Pb}/^{204}\text{Pb}$	$^{87}\text{Sr}/^{86}\text{Sr}$	$^{143}\text{Nd}/^{144}\text{Nd}$
<i>CU28</i>	<i>19.428</i>	<i>15.724</i>	<i>39.011</i>	<i>0.70559</i>	<i>0.512821</i>
<b>CU87</b>	19.564	15.751	38.999	0.70535	0.512872
<b>CU89</b>	19.345	15.736	38.898	0.7049	0.512946
<b>CU109</b>	20.029	15.799	39.488	0.70563	0.512515
<i>CU109</i>	<i>19.932</i>	<i>15.795</i>	<i>39.428</i>	<i>0.70563</i>	<i>0.512512</i>
<b>CU111</b>	19.615	15.754	38.961	0.70488	0.512821
<i>311</i>	<i>19.741</i>	<i>15.804</i>	<i>39.311</i>		<i>0.512821</i>
<i>454</i>	<i>18.657</i>	<i>15.627</i>	<i>38.358</i>	<i>0.704450</i>	<i>0.512979</i>
<i>6078</i>	<i>19.300</i>	<i>15.717</i>	<i>38.943</i>	<i>0.704930</i>	<i>0.512822</i>
<i>6103</i>	<i>19.125</i>	<i>15.695</i>	<i>38.858</i>	<i>0.704980</i>	<i>0.512828</i>
<i>6104</i>	<i>18.748</i>	<i>15.635</i>	<i>38.397</i>	<i>0.704470</i>	<i>0.513011</i>
<i>6127</i>	<i>18.934</i>	<i>15.662</i>	<i>38.565</i>	<i>0.704440</i>	<i>0.512943</i>
<i>6155</i>	<i>19.106</i>	<i>15.685</i>	<i>38.678</i>	<i>0.704460</i>	<i>0.512932</i>
<i>6157</i>	<i>19.160</i>	<i>15.694</i>	<i>38.727</i>	<i>0.704550</i>	<i>0.512923</i>
<i>6186</i>	<i>19.566</i>	<i>15.729</i>	<i>39.072</i>	<i>0.705360</i>	<i>0.512819</i>
<i>6257</i>	<i>19.432</i>	<i>15.743</i>	<i>39.020</i>	<i>0.704900</i>	<i>0.512897</i>
<i>6259</i>	<i>19.402</i>	<i>15.743</i>	<i>39.013</i>	<i>0.704730</i>	<i>0.512904</i>
<i>6264</i>	<i>18.851</i>	<i>15.641</i>	<i>38.555</i>	<i>0.704780</i>	<i>0.512954</i>

**Table 6-1 Double spike Pb data from Lesser Antilles whole rocks. Also shown are Sr and Nd isotope ratios measured on the RHUL TIMS. Analyses in italics are those of Thirlwall (unpublished data).**

The Lesser Antilles data were plotted alongside depleted MORB mantle (DMM) compositions, both that of Salters and Stracke (2004) (used by Carpentier et al., 2008) and compositions from PetDB (Figure 1-2). The PetDB data were chosen by using a latitude range between 10-20° N and a longitude range between 40-65°W to ensure the samples were from the vicinity of the Lesser Antilles. The solid black line

on Figure 6-1 represents the Northern Hemisphere Reference Line (NHRL) (Hart, 1984), as described by Equation 6-1 and Equation 6-2.

**Equation 6-1**

$$^{207}\text{Pb}/^{204}\text{Pb} = 0.1084(^{206}\text{Pb}/^{204}\text{Pb}) + 13.491$$

**Equation 6-2**

$$^{208}\text{Pb}/^{204}\text{Pb} = 1.209(^{206}\text{Pb}/^{204}\text{Pb}) + 15.627$$

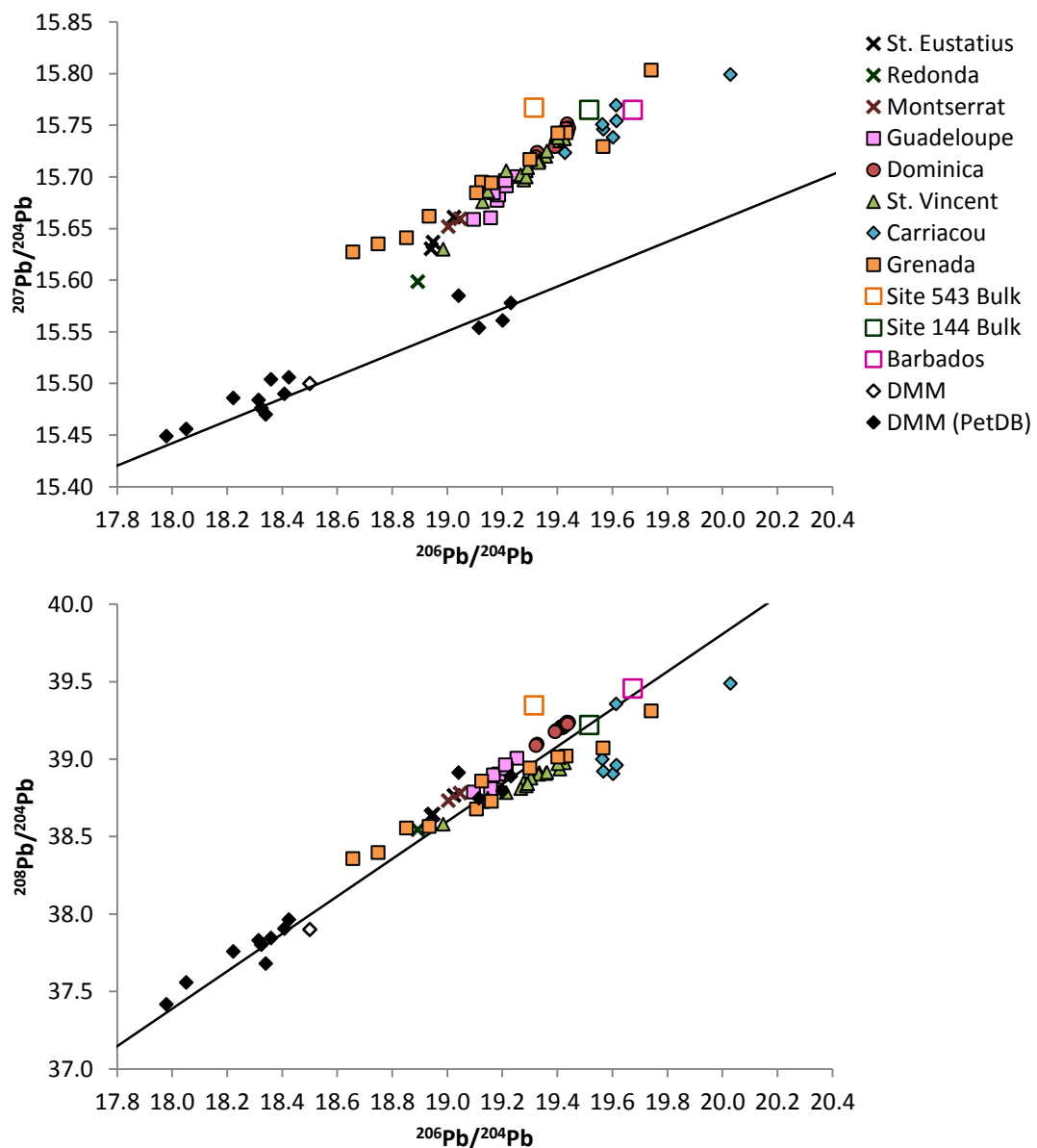


**Figure 6-1** Pb isotopic ratios of Lesser Antilles lavas compared to the DMM value of Salters and Stracke (2004), used by Carpentier et al. (2008) (hollow diamond), local DMM compositions taken from PetDb (<http://www.earthchem.org/petdb>) (solid black diamonds) and the Northern Hemisphere Reference Line (Hart, 1984) (black line). The bulk sediment compositions analysed by Carpentier et al. (2008) are shown by hollow squares.

Figure 6-1 shows that whilst the  $^{208}\text{Pb}/^{204}\text{Pb}$  ratios of the analysed Lesser Antilles whole rocks plot on or close to the NHRL, the  $^{207}\text{Pb}/^{204}\text{Pb}$  ratios are clearly offset above the line. One method of quantifying how far the whole rocks are plotting from the NHRL is the calculation of the  $\Delta 7/4$  and  $\Delta 8/4$  parameters (Hart, 1984), as shown in Equation 6-3 and Equation 6-4.

**Equation 6-3**

$$\Delta 7/4 = \left[ \left( ^{207}\text{Pb}/^{204}\text{Pb} \right)_{WR} - \left( ^{207}\text{Pb}/^{204}\text{Pb} \right)_{NHRL} \right] \times 100$$

**Equation 6-4**

$$\Delta 8/4 = \left[ \left( ^{208}\text{Pb}/^{204}\text{Pb} \right)_{WR} - \left( ^{208}\text{Pb}/^{204}\text{Pb} \right)_{NHRL} \right] \times 100$$

Figure 6-2 shows the  $\Delta 7/4$  and  $\Delta 8/4$  values of the Lesser Antilles whole rocks. It can be seen that the Carriacou data have a larger scatter in this figure than those from other islands. It is thought this may be a result of contamination of the samples, analyses were undertaken on both chips and powders, which both produced variable results.

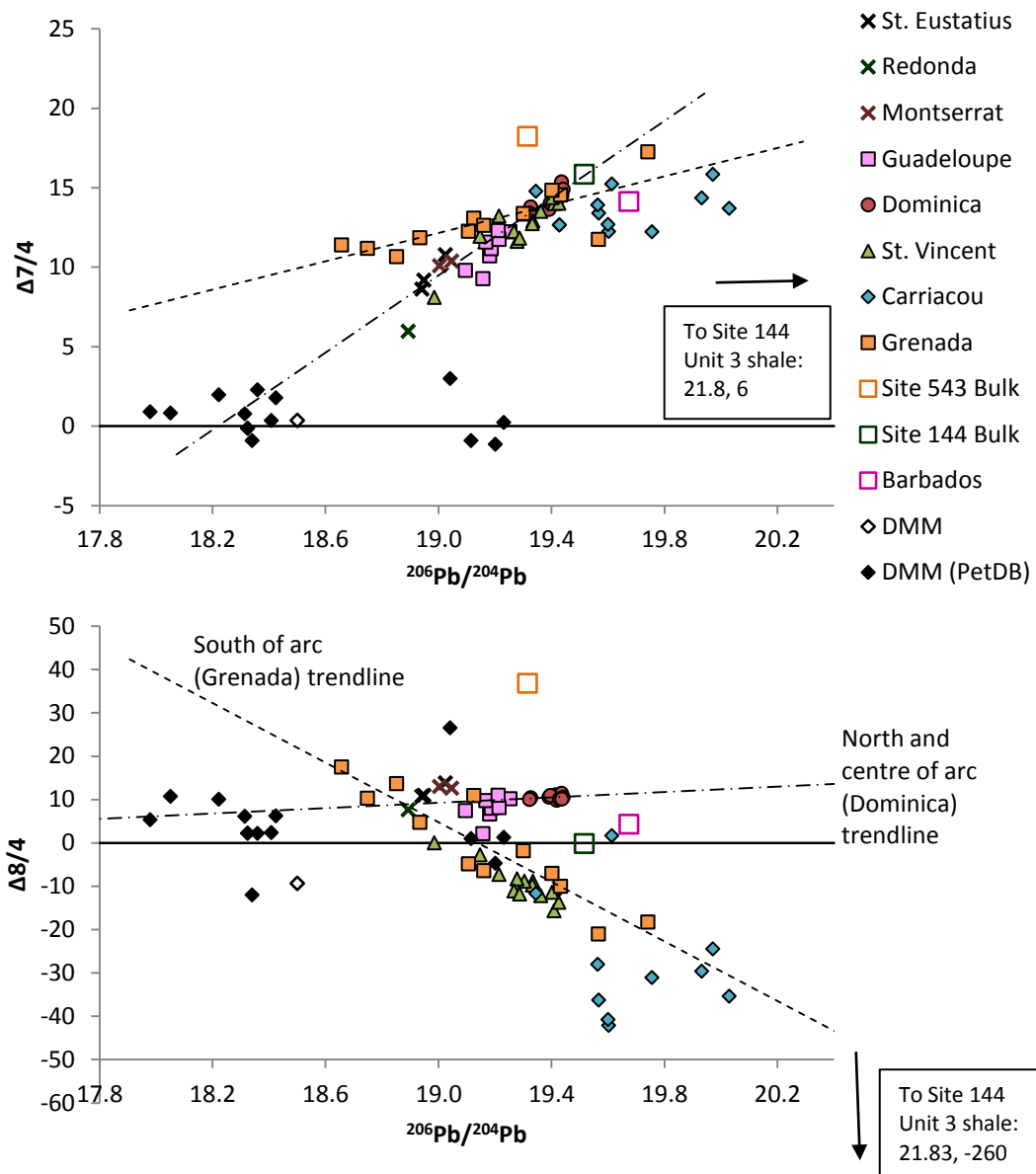


Figure 6-2  $\Delta 7/4$  and  $\Delta 8/4$  of the Lesser Antilles whole rocks. DMM (Salters & Stracke, 2004) symbols are as in Figure 6-1, as are the sediments (Carpentier *et al.*, 2008). The NHRL (Hart, 1984) is represented by a solid black line. Dashed lines represent linear regression through the Dominica (a representative island from the north and centre of the arc) and Grenada (a representative island from the south of the arc) data and are labelled on the lower graph.

Figure 6-2 also shows regression lines (ordinary least squares method) through the Dominica and Grenada data to illustrate more clearly how the Pb isotopic data vary along arc strike. These islands were chosen to represent the north and centre (Dominica) and the south of the arc (Grenada). For those islands analysed for Pb isotopes, the north and centre refers to Redonda, St. Eustatius, Montserrat, Guadeloupe and Dominica and the south comprises St. Vincent, Carriacou and Grenada. Dominica and Grenada were picked as representatives as the Dominica data showed less scatter over a similar  $^{206}\text{Pb}/^{204}\text{Pb}$  range to the Guadeloupe data and

the Grenada data covered a wide range of  $^{206}\text{Pb}/^{204}\text{Pb}$  without the contamination problems associated with the Carriacou data. The linear regressions show that both groups exhibit significantly different trends for  $\Delta 7/4$  and  $\Delta 8/4$ .

$\Delta 7/4$  values in both the south and the centre of the arc are greater at a given  $^{206}\text{Pb}/^{204}\text{Pb}$  than the NHRL and the DMM data, a feature noted in several intra-oceanic island arcs, which has been attributed to mixing with a contaminant (Carpentier *et al.*, 2008). The source differs between the north and centre of the arc and the south, with only the regression line through the northern and central islands intersecting the DMM compositions. The southern data appear to require higher  $\Delta 7/4$  at a given  $^{206}\text{Pb}/^{204}\text{Pb}$  than that of depleted mantle.

$\Delta 8/4$  values in the Lesser Antilles are also complicated. Figure 6-2 shows that the Lesser Antilles whole rocks appear to lie much closer to the NHRL on the  $\Delta 8/4$  graph than the  $\Delta 7/4$  graph. This is less common in intra-oceanic arc systems (Carpentier *et al.*, 2008).

## 6.2.2 Pb Isotope Discussion

The variations observed in  $\Delta 7/4$  and  $\Delta 8/4$  could be the result of mixing between different endmembers in the north and centre of the arc and the south of the arc, with the source endmember being that with lower  $^{206}\text{Pb}/^{204}\text{Pb}$  and the contaminant endmember having higher  $^{206}\text{Pb}/^{204}\text{Pb}$ . In both cases the source is thought to be of mantle origin, with potential contaminants being either in the form of subducted sediment or assimilated arc crust.

The northern and central islands (represented by Dominica) show increasing  $\Delta 7/4$  and to a lesser extent  $\Delta 8/4$  with increasing  $^{206}\text{Pb}/^{204}\text{Pb}$ . The linear regression based on the Dominica data intersects with some of PetDB DMM compositions which lie slightly above the NHRL between 18.0 and 18.4  $^{206}\text{Pb}/^{204}\text{Pb}$ , -1 to 2  $\Delta 7/4$  and -12 to 11  $\Delta 8/4$ . This would imply that mixing of a DMM source composition with a higher  $^{206}\text{Pb}/^{204}\text{Pb}$  and  $\Delta 7/4$  (and slightly higher  $\Delta 8/4$ ) component may explain the isotopic characteristics of these lavas. Figure 6-2 would suggest a composition between the bulk Site 543 and Barbados sediments may be suitable for the contaminant.

However, the southern islands (represented by Grenada) show differing trends, with  $\Delta 7/4$  increasing and  $\Delta 8/4$  decreasing as  $^{206}\text{Pb}/^{204}\text{Pb}$  increases. As a result, there is no

intersection with the DMM compositions, suggesting that the southern islands may require a higher  $\Delta 7/4$  and  $\Delta 8/4$  source endmember. Over a  $^{206}\text{Pb}/^{204}\text{Pb}$  range of 18.0-18.4, the southern island regression line requires  $\Delta 7/4$  values of 5 to 10 and  $\Delta 8/4$  values of between 20-35, as opposed to the -1 to 2 and -12 to 11 ranges shown by the DMM compositions. In addition, none of the bulk sediment compositions of Carpentier et al. (2008) appear to be a suitable contaminant endmember as although the southern lavas need a similarly high  $\Delta 7/4$  to the sediments, they also predominantly require a more negative  $\Delta 8/4$  composition. The only sediment composition lying to significantly low  $\Delta 8/4$  is the shale unit from Site 144 at -260. At  $^{206}\text{Pb}/^{204}\text{Pb}$  of 21.84 (the Unit 3 shale value), the southern island regression line has a  $\Delta 8/4$  value of -93, 167 higher than the -260 value of the shale (Figure 6-3).

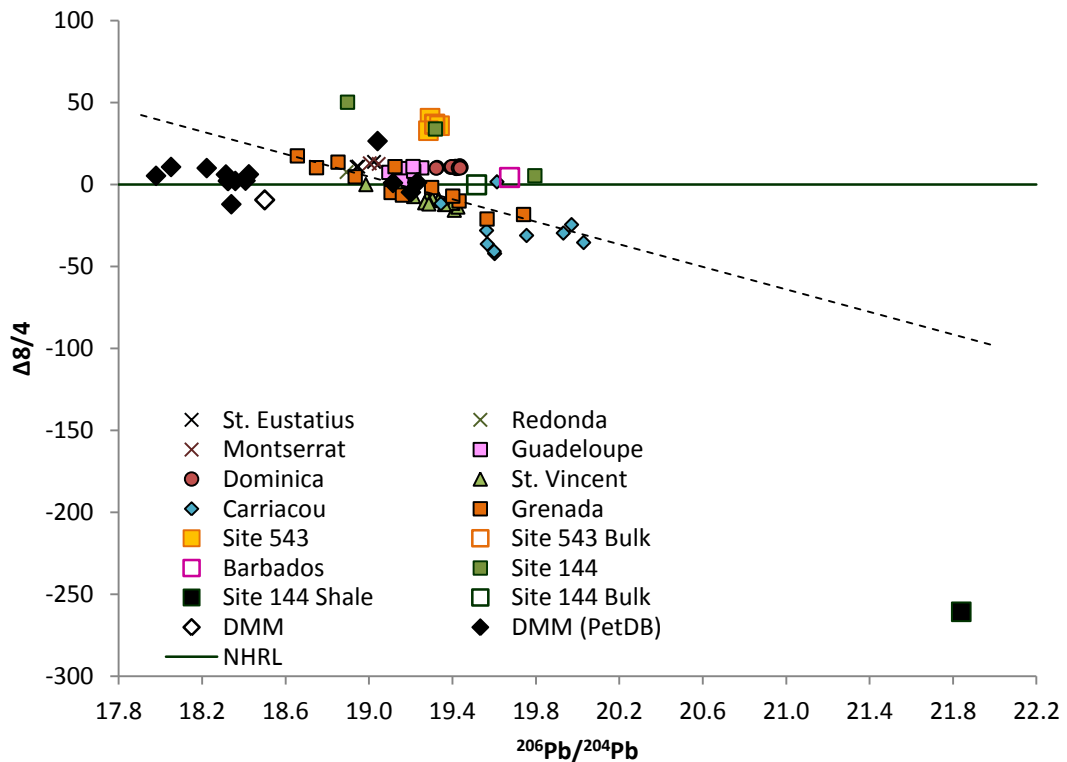


**Figure 6-3 Lesser Antilles  $\Delta 8/4$  values against  $^{206}\text{Pb}/^{204}\text{Pb}$  ratios. Also shown are both the bulk and the individual unit sediment compositions of Carpentier et al. (2008). DMM compositions are also shown (Salters & Stracke, 2004).**

These findings pose two main questions: why do the southern islands require a higher  $\Delta 7/4$  and  $\Delta 8/4$  source endmember than the northern and central islands and what contaminant endmember compositions are being mixed in to the source endmember to create the negative  $\Delta 8/4$  values?

The source endmember for the southern islands requires higher  $^{207}\text{Pb}/^{204}\text{Pb}$  and  $^{208}\text{Pb}/^{204}\text{Pb}$  ratios than that for the northern and central arc at similar  $^{206}\text{Pb}/^{204}\text{Pb}$  and therefore needs higher Th/Pb and  $\text{U}^{235}/\text{Pb}$  ratios than the northern and central arc source endmember. Possible explanations are that the southern source endmember has a crustal component or a contribution from the subducting slab (e.g. a different sediment contribution in either degree or composition) that is not seen in the north and centre of the arc (although this may not explain why  $\text{U}^{235}/\text{Pb}$  is higher than  $\text{U}^{238}/\text{Pb}$ ).

In terms of the contaminants being mixed with the mantle source, Unit 3 from Site 144 may have a greater role to play in causing the low  $\Delta 8/4$  than accounted for in the Site 144 bulk composition. The intersection between the trendline of the Grenada lavas and a line between the Site 144 bulk composition and Unit 3 may give an indication of the extra shale required to represent the sediment mixing with the southern islands (Figure 6-4). On the  $\Delta 7/4$  graph, around 7.0% extra shale is required with this figure being 7.1% for the  $\Delta 8/4$  graph. However, there are Carriacou and Grenada whole rocks with more radiogenic compositions than any of the bulk sediments.

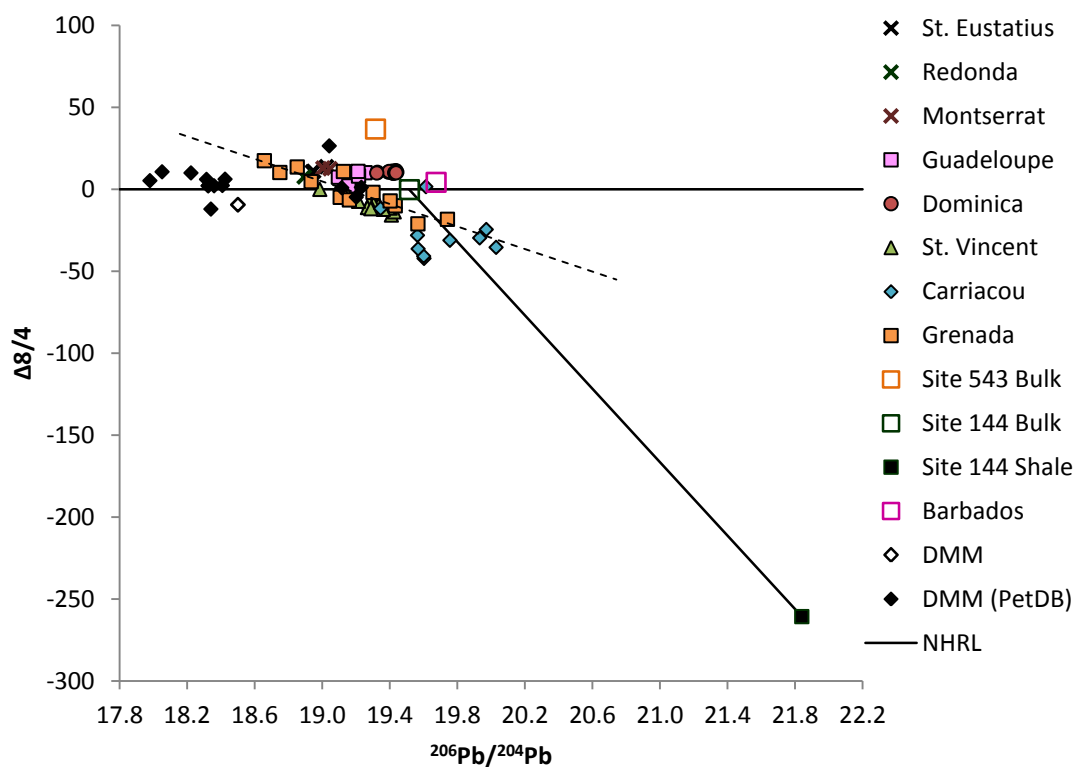


**Figure 6-4** Mixing line between Site 144 bulk sediment compositions and the shale unit from Site 144 (Unit 3) (Carpentier *et al.*, 2008). DMM data is from PetDB, with the hollow diamond representing the composition of DMM from Salters and Stracke (2004).

A similar issue was also noted by Davidson and Wilson (2011), who suggested this was one line of evidence to contradict the theory that the arc lavas are a result of simple mixing between the mantle source and sediments. The authors also proposed that differentiation of magmas whilst in the crust may also be responsible for the isotopic compositions (fractional crystallisation will not alter the isotopic composition of the magmas). Modelling by Davidson and Wilson (2011) using Pb isotopes in conjunction with  $^{87}\text{Sr}/^{86}\text{Sr}$  led them to conclude that addition of fluid and/or sediment melts was needed. Figure 6-5 shows isotopic modelling between the average composition of local DMM (averaged from the PetDB data) and the local sediments (Carpentier *et al.*, 2008, Carpentier *et al.*, 2009) together with the isotopic compositions of the Lesser Antilles lavas ( $^{87}\text{Sr}/^{86}\text{Sr}$  and  $^{143}\text{Nd}/^{144}\text{Nd}$  data from Thirlwall, unpublished data).

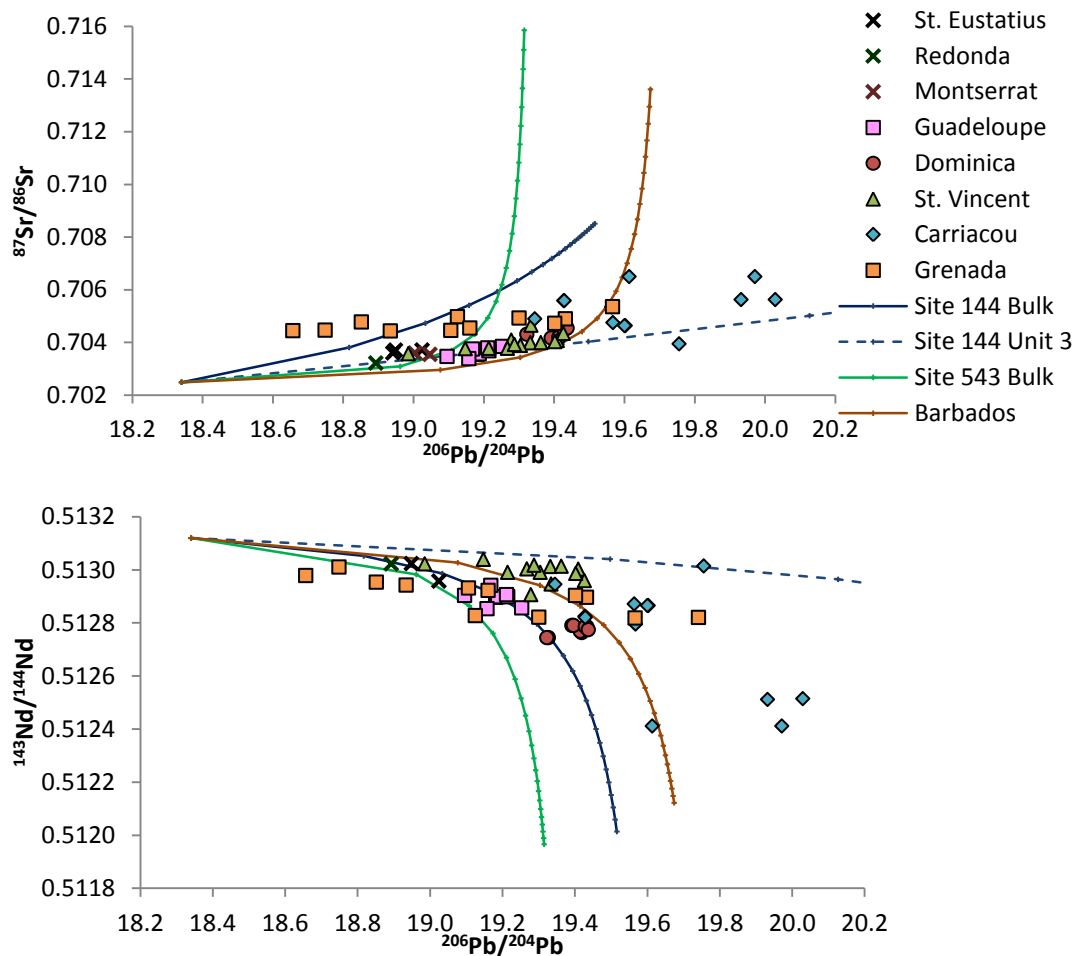


Figure 6-5  $^{87}\text{Sr}/^{86}\text{Sr}$  and  $^{143}\text{Nd}/^{144}\text{Nd}$  of Lesser Antilles lavas (Thirlwall, unpublished data) against the  $^{206}\text{Pb}/^{204}\text{Pb}$  ratios from this study and Thirlwall (unpublished data). Also shown are mixing lines between the average local DMM composition (from PetDB) and the local sediments (Carpentier *et al.*, 2008, Carpentier *et al.*, 2009). Markers on the mixing lines show 5% increments of sediment addition.

Figure 6-5 shows that for the southern arc lavas, the gradients of the correlations on both the  $^{87}\text{Sr}/^{86}\text{Sr}$  and  $^{143}\text{Nd}/^{144}\text{Nd}$  graphs are relatively flat, resembling that of the Site 144 shale unit (Unit 3) most closely. These lavas do not show hyperbolae between higher  $^{206}\text{Pb}/^{204}\text{Pb}$  ratios and lower  $^{206}\text{Pb}/^{204}\text{Pb}$  ratios, which would suggest that the Sr and Nd concentrations of the higher  $^{206}\text{Pb}/^{204}\text{Pb}$  endmember are larger than the lower  $^{206}\text{Pb}/^{204}\text{Pb}$  endmember it is mixing with, given the relatively small variation in  $^{87}\text{Sr}/^{86}\text{Sr}$  and  $^{143}\text{Nd}/^{144}\text{Nd}$ .

The results of the isotopic modelling would suggest that the theory of Davidson and Wilson (2011) is more suitable than the hypothesis put forward by Carpentier *et al.* (2008). Simple mixing between a mantle source and local sediments does not sufficiently describe the correlations within the Lesser Antilles whole rock data. The

whole rocks appear to lie closer to mixing with Barbados sediments in terms of  $^{87}\text{Sr}/^{86}\text{Sr}$  but all three sites lie near to lavas in terms of  $^{143}\text{Nd}/^{144}\text{Nd}$ .

In conclusion, whilst much more work is required in the interpretation of the data, the limited dataset generated by this study in conjunction with the unpublished work of Thirlwall would suggest that the model of Carpentier et al. (2008) is not suitable for generating the isotopic compositions observed in the Lesser Antilles data presented.

### **6.3 Synthesis of Mineral Data**

In order to provide a more rounded view of petrogenesis in the arc, the findings from each mineral phase need to be discussed together. This will enable the identification of processes that can be observed in multiple phases as well as those that are only evident in one phase. Calculated pressures and temperatures from different phases can be compared. Potential fluid involvement can also be discussed in terms of the information provided by the three analysed mineral phases. A summary of the information that can be obtained from each individual phase can also be made.

#### **6.3.1 Information from Each Phase**

##### *Olivine*

Olivine is capable of providing information on the early petrogenetic histories of the lavas as commonly this phase crystallises first from a melt. The principal contribution of the olivine data to this study is the identification of the LCO and subsequent interpretation that they represent the breakdown of cumulate xenoliths. The latter is based in part on the analysis of cumulate xenolith olivines found in host lavas from Grenada. This represents a step forward in the understanding of Lesser Antilles lava petrogenesis as previous studies have identified similar populations but attributed them to be mantle xenocrysts (Bouvier *et al.*, 2008).

##### *Plagioclase*

Plagioclase analysis provided textural and chemical information that allowed for the identification of numerous populations (at least two per host lava studied) within the

Lesser Antilles lavas. The myriad of processes recorded in these crystals allowed for an insight into how complex the magmatic plumbing systems beneath the arc are. Melts are seen to evolve along different pathways en route to the surface and magma mixing and entrainment of populations is common. Furthermore, the importance of degassing and decompression of melts at shallow levels was highlighted.

### *Clinopyroxene*

The most important contributions from the clinopyroxene data were the geothermobarometric modelling providing non whole-rock biased pressures and temperatures of crystallisation and the REE data. The latter allowed for further identification of discrete populations in the host lavas, with crystals with contrasting REE patterns to those seen in the majority of clinopyroxenes in their respective host lavas. The REE were also used to back calculate melt compositions to provide further information on potential degrees of melting, water contents and melting depth of the parent melts.

### **6.3.2 Comparison of Equilibrium Graphs**

Whilst there are obvious (and previously discussed) limitations of using whole rock data to try and ascertain if the minerals are in equilibrium with the whole rocks, equilibrium graphs can be easily compared between olivines, plagioclases and clinopyroxenes to observe if the phases show the same disparities from equilibrium in each analysed mineral within a host lava. Figure 6-6 shows the equilibrium graphs for each phase (taken from their respective chapters and reproduced here for ease of comparison, original figure numbers are listed in the figure caption).

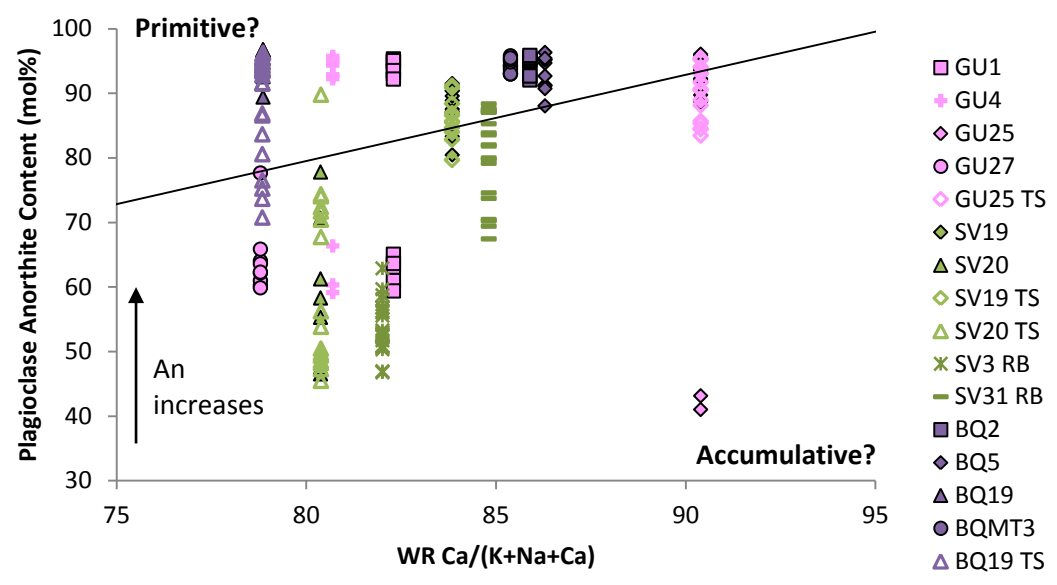
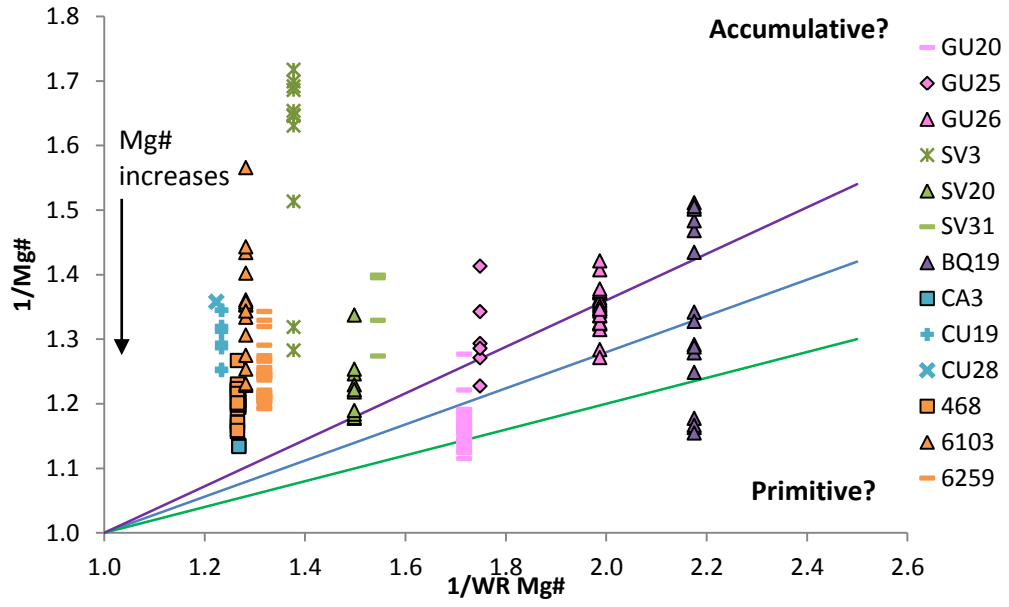
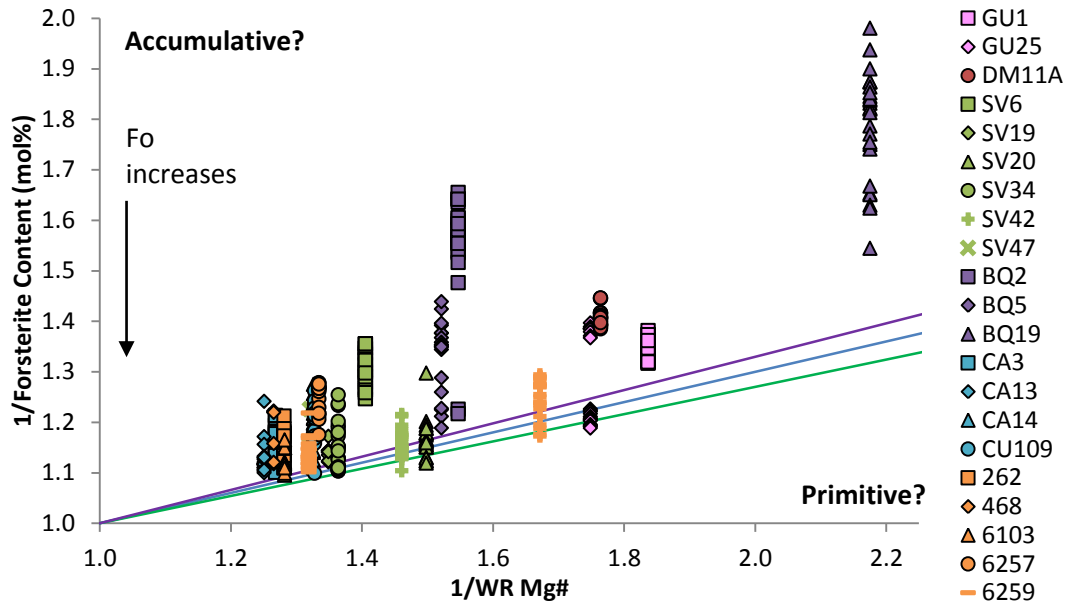


**Figure 6-6 Olivine diagram is Figure 3-28, clinopyroxene diagram is 5-30 and plagioclase diagram is Figure 4-15. It should be noted that both the olivine and clinopyroxene diagrams use the inverse of Fo content and Mg# respectively, whilst the plagioclase diagram uses actual anorthite contents. As such, the field above the line on the first two graphs represents the potentially accumulative region, whilst the field below is the more primitive region whereas the reverse is true for the plagioclase diagram.**

Of the host lavas analysed, GU25, BQ19 and SV20 are those from which olivines, plagioclases and clinopyroxenes have all been analysed. Many of the other host lavas have two analysed phases (GU1, SV3, SV19, SV31, BQ2, BQ5, CA3 and 468, 6103, 6259). The GU25 olivines and plagioclases are bimodal in terms of forsterite content and anorthite content, but not clinopyroxene Mg#. The GU25 olivines show a potentially accumulative group (the LFG) and one group lying between the equilibrium region and the more primitive field, with the plagioclases showing the same. The GU25 clinopyroxenes are either in equilibrium or potentially accumulative. The BQ19 minerals are more complex, showing potentially accumulative olivines, primitive through to accumulative plagioclases and clinopyroxenes spanning the equilibrium field. SV20 shows olivines with forsterite contents extending from the accumulative to primitive fields and potentially accumulative clinopyroxenes and plagioclases. GU1 shows both accumulative olivines and one population of accumulative plagioclases. SV3 shows accumulative clinopyroxenes and plagioclases, both the SV19 clinopyroxenes and plagioclases extend from the primitive region across equilibrium and into the accumulative field, the SV31 plagioclases also show this but the clinopyroxenes plot exclusively in the accumulative region. BQ2 shows accumulative olivines but primitive plagioclases, as does BQ5. CA3 predominantly shows accumulative olivines and clinopyroxenes. Olivines and clinopyroxenes from 468 both plot in the accumulative field, as do the crystals from 6103 and 6259, however, olivines from the latter two host lavas also extend into the equilibrium region.

There does not appear to be any distinguishable trend between plagioclases and the other mineral phases. In general if at least some of the olivines from a host lava are accumulative then at least some of the clinopyroxenes may be also but this is the only real correlation between any of the minerals. This is to be expected as olivine and clinopyroxene should crystallise over similar pressure and temperature ranges (assuming the lavas are calc-alkaline and not tholeiitic in nature) whereas

plagioclases should crystallise at shallower levels. If the melts are tholeiitic, plagioclase may crystallise before clinopyroxene.

### 6.3.3 Comparison of Calculated Pressure and Temperatures

Pressures and temperatures were calculated from both the plagioclase and clinopyroxene crystals. Plagioclase pressures and temperatures were calculated using the method of Putirka (2008) and the clinopyroxene temperatures and pressures were calculated using a combination of several methods (Nimis, 1995, Nimis & Taylor, 2000, Putirka, 2008) using the method detailed by Putirka (2008). In contrast to the clinopyroxene method, the plagioclase method required the use of the host lava composition as a proxy for melt composition. Given that the majority of the plagioclase crystals analysed within this study do not appear to be in equilibrium with their host lavas, using a whole rock composition as an approximation for the melt seems invalid in this case. However, pressure and temperature conditions were still calculated from the plagioclases to observe how they compared with those generated from the clinopyroxene method, which required no estimation of melt composition and was calculated from clinopyroxene composition alone. No pressure and temperature estimates were calculated from the olivine data.

Temperature and pressure ranges of crystallisation are shown in Table 6-2.

Island	Clinopyroxene		Plagioclase	
	Temperature (°C)	Pressure (kbar)	Temperature (°C)	Pressure (kbar)
<b>Guadeloupe</b>	1129.9-1201.5	-0.9-7.2	1171.0-1217.8	3.5-15.3
<b>St. Vincent</b>	936.7-1176.7	-8.7-8.4	1164.5-1204.5	2.8-7.8
<b>Bequia</b>	1094.5-1130.1	0.7-2.7	1212.4-1219.7	12.2-14.8
<b>Carriacou</b>	1180.4-1251.4	4.4-12.2	-	-
<b>Grenada</b>	1177.0-1299.8	5.3-22.0	-	-

**Table 6-2 Pressure and temperatures calculated for the Lesser Antilles clinopyroxenes (Nimis, 1995, Nimis & Taylor, 2000, Putirka, 2008) and plagioclases (Putirka, 2008). No plagioclases were analysed from Carriacou and Grenada.**

In general the temperature ranges between plagioclases and clinopyroxenes agree reasonably well, with the plagioclase estimates being slightly higher than those from the clinopyroxenes. Only the temperature estimates from Bequia show no overlap between phases.

The pressure estimates show a lot more variation than the temperature estimates, there is some consensus in the Guadeloupe and St. Vincent values but again the Bequia crystals show no overlap. Figure 6-7 shows a comparison between the clinopyroxene and plagioclase pressure and temperatures estimates for the same host lavas.

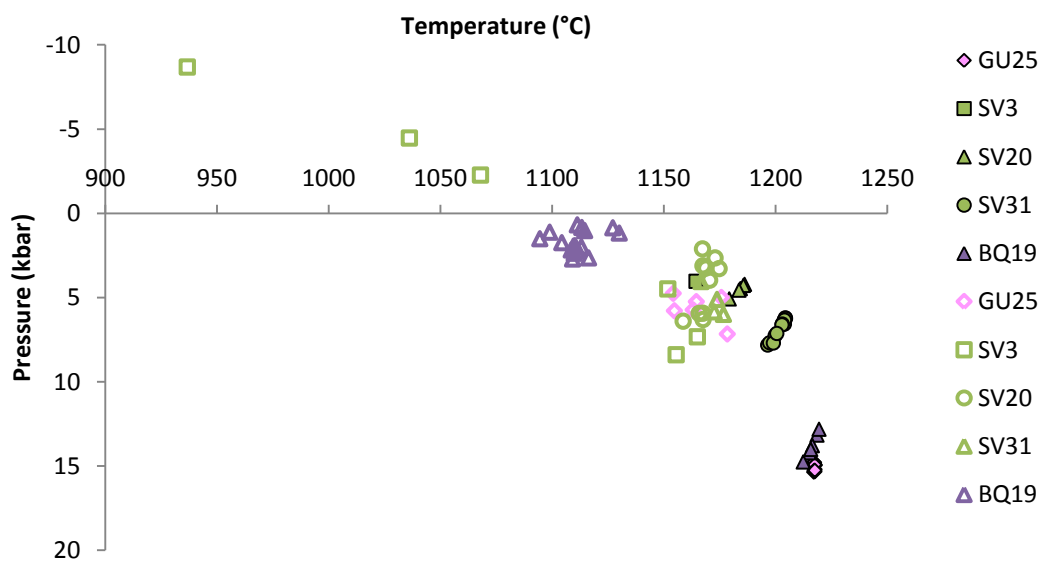


**Figure 6-7 Comparison of pressures and temperatures of clinopyroxenes and plagioclases from the same host lavas. Solid symbols are calculated from plagioclases and hollow symbols are calculated from clinopyroxenes.**

It can be seen that the plagioclase estimates have higher calculated temperatures and pressures than the clinopyroxene estimates, particularly for the Guadeloupe and Bequia host lavas. The temperatures are ~80°C higher in the BQ19 plagioclases and approximately 10 kbar higher in pressure. The GU25 plagioclases are ~40°C and approximately 8 kbar higher than the clinopyroxenes. This may suggest that the clinopyroxenes in the GU25 and BQ19 host lavas crystallised after the plagioclases. This would be in line with the crystallisation sequence of tholeiites, but the BQ19 whole rock composition plots in the calc-alkaline field on a K<sub>2</sub>O against SiO<sub>2</sub> plot (Chapter 2). However, there are issues with the plagioclase calculations using whole rock data, which introduces a significant degree of error. Thus it is hard to tell if the

plagioclase temperature and pressure differences are real or a function of the limitations of using the method with porphyritic rocks with numerous plagioclase populations.

### **6.3.4 Comparing Processes and Populations**

#### *Degassing/ Decompression at Shallow Levels*

Numerous plagioclase populations display evidence of degassing and/or decompression at shallow levels, both texturally and chemically. It is also thought that the forsterite bimodality observed in GU25 olivines is a result of volatile loss between crystallisation of the HFG and LFG, which agrees with the findings from plagioclase crystals from this host lava. The only other Guadeloupe host lavas from which olivines and plagioclases were analysed is GU1, which did not show evidence of forsterite bimodality or degassing and decompression in the plagioclases. Thus the shallow level processes involved in the petrogenesis of GU1 and GU25 must be different, or GU1 was resident for less time at shallow levels and thus was less affected by shallow level processes.

#### *Decompression During Ascent*

This is evident texturally in many of the plagioclases (as noted in Chapter 4). Whilst this process may also have affected both olivines and clinopyroxenes (as these may crystallise at greater depths than the plagioclases, particularly in those host lavas which appear to be calc-alkaline in nature), there are no clear indicators of the effects of decompression at depth in the crystals. The LCO for instance were almost certainly formed at depth prior to entrainment in the host melt and transport to the surface. More detailed petrographic studies coupled with further analysis of both olivines and clinopyroxenes in thick section may shed more light as this would permit better investigation of how compositions of the crystals change from core to rim.

#### *Entrainment*

Entrainment is apparent in both olivines (with the LCO being entrained into the host lavas after the breakdown of cumulate material) and plagioclases. REE results from

the clinopyroxenes would also suggest that there is evidence in at least two host lavas (SV3 and CA3) for the addition of discrete populations to the host melts. It is thought that the material being entrained is antecrystal rather than xenocrystal. LCO are also present in CA3 which suggests that cumulate material is present in the host lavas (olivines were not analysed from SV3). However when the CA3 clinopyroxene population is compared to the remaining CA3 crystals, there is little evidence of any other bimodality. Therefore it is not obvious that this population of clinopyroxenes is derived from disaggregated cumulate material. SV3 does exhibit three different plagioclase populations, one of which has textural evidence of being entrained and another which shows the effects of magma mixing. Thus there is evidence from another phase that entrainment and combination of melts within the magmatic plumbing system is occurring in the petrogenesis of the SV3 host lava.

Of the LCO bearing host lavas, plagioclases were analysed from SV19 and SV20 also. Both of these host lavas show plagioclase populations with evidence of entrainment. These populations differ slightly in that the SV19 crystals show no evidence of decompression on ascent from depth (although the cores are heavily sieved, making textural and chemical observations difficult) whereas the cores of the SV20 population are better preserved and show disequilibrium features in line with decompression.

### ***Magma Mixing***

Whilst the LCO crystals were added to host melts, it appears more likely that this was as a crystal cargo rather than a melt. Magma mixing was most easily observed in textural features in the plagioclases, where it is inferred that mixing would be distinguished by concentric zones of fine sieving as opposed to the broader heavily sieved areas attributed to entrainment (Figure 6-8). Fine concentric zones are thought to be associated with magma mixing as adding magma to the melt will change the composition of the material surrounding the plagioclases, potentially causing breakdown of the crystals. This breakdown exhibits as fine sieve texturing. Subsequently new plagioclase may crystallise, resulting in the fresher appearing zones. This process can repeat, either due to convection within a magma chamber or repeated influx of magma. This is differentiated from entrainment as the latter

process occurs only once, meaning concentric zoning is not viable. The sieving in entrained populations may also pervade to the centre of the crystals.



**Figure 6-8** Textural examples of magma mixing (left hand picture, crystal from GU25) and entrainment (right hand picture, crystal from SV20).

Populations showing mixing were observed in GU25 (where two of the populations showed magma mixing textures), SV31 and BQ19. GU25 and BQ19 do not show LCO in the olivines (olivines were not analysed in SV31). Therefore, given the presence of entrained crystals in many of the host lavas, coupled with the mixing of magmas in others, it appears that petrogenesis throughout the arc is not simple and that the magmatic plumbing systems are complex. Antecrysts are common, whether entrained as crystal cargoes or as a component of a melt being added in to the final host lava composition. This reinforces the fact that directly comparing minerals to whole rock data can be misleading.

### ***Different Melt Compositions***

Several of the analysed populations require differing melt compositions to the host lava as parental compositions.

### ***Olivine***

The LCO are dealt with at length in Chapter 3 and as discussed are liable to be crystallised deeper in the system as cumulates from early melts. The melts responsible for crystallising the LCO are thought to be water rich (in order to drive down CaO concentrations and potentially increase Fo contents) and it is likely the olivine crystallised alongside at least one other phase capable of reducing the CaO content of the melt, in addition to the  $Al_2O_3$ , Cr, V, Y, Yb and Sc concentrations.

This phase could potentially be either clinopyroxene or amphibole, as the elements listed are more compatible in these two phases than olivine. In addition, clinopyroxene and amphibole are prevalent in many cumulates found along the arc (Arculus & Wills, 1980, Stamper *et al.*, 2014). Amphibole fractionation will be dealt with in more detail in section 6.3.6.

### *Plagioclase*

In terms of plagioclase, multiple populations have been identified. The thick section analyses show that texturally different populations can show similar chemistries (Figure 6-9). This would suggest further that the crystals can be deemed antecrysts and not xenocrysts and have followed a different path of evolution through the magmatic plumbing system whilst originating from similar parent melts. As a result there is less evidence from the plagioclases than the olivines and clinopyroxenes for chemically distinct parent melts crystallising different populations. However, it should be noted that the number of host lavas with plagioclases analysed in thick section is small and expanding the study to include more host lavas analysed in this fashion may uncover chemical heterogeneities within the plagioclases.

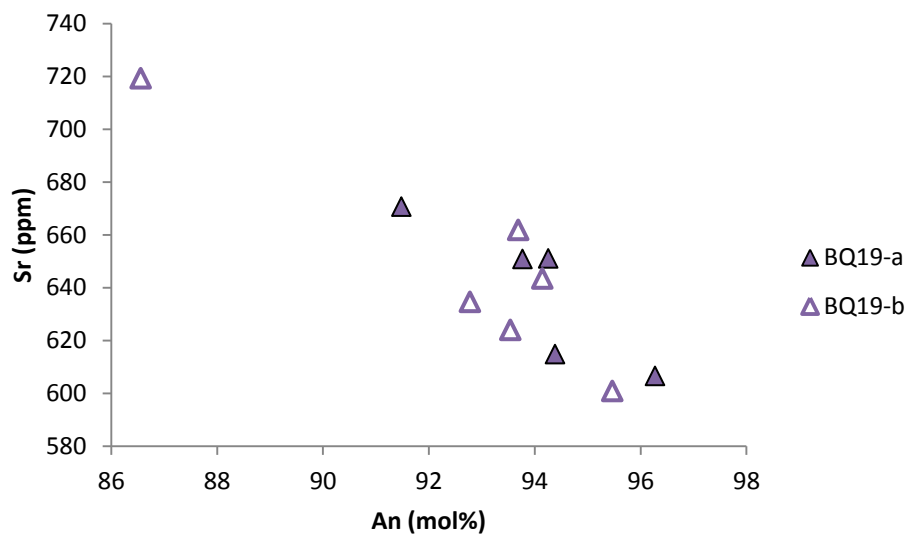


**Figure 6-9** Sr concentrations and An contents in core analyses in the BQ19-a and BQ19-b populations.

### *Clinopyroxene*

CA3 shows clinopyroxenes that require different melt compositions to produce the distinctive REE profiles observed. This is further compounded by the bimodality observed on the  $\text{La}/\text{Yb}_N$  against  $\text{Dy}/\text{Yb}_N$  graph when the back calculated melts are plotted. The crystals forming the secondary population exhibit much higher  $\text{La}/\text{Yb}_N$  than the remainder of the CA3 clinopyroxenes (Figure 6-10).

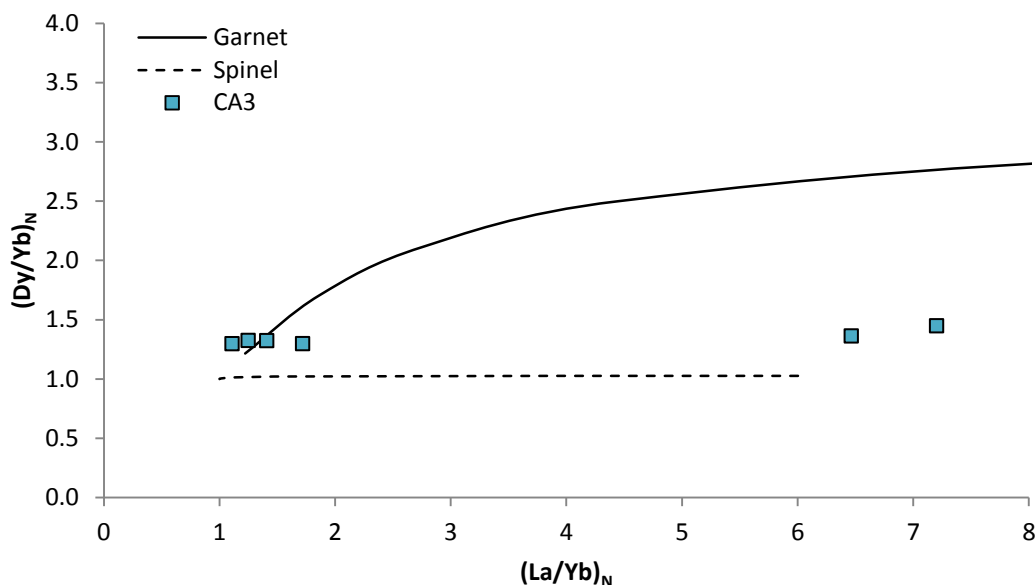


**Figure 6-10**  $\text{La}/\text{Yb}_N$  against  $\text{Dy}/\text{Yb}_N$  graph showing the bimodality observed in CA3 between the populations exhibiting differing REE profiles.

This population may originate from a smaller degree, more hydrous melt than that responsible for crystallising the remaining CA3 clinopyroxenes. There are only two crystals from the second population so any thoughts on potential compositions of the parent melt would require much more testing. Overall, the melt would require higher LREE concentrations (or a higher partition coefficient for these between melt and clinopyroxene) and slightly lower HREE contents. MREE concentrations in both populations appear comparable. The higher LREE concentrations may reflect higher fluid contents in the melt responsible for crystallising the two crystals with differing REE profiles, this is supported by higher Pb concentrations but Li contents are comparable to the remaining CA3 analyses.

### *Disaggregation of Cumulate Xenoliths*

The LCO in the olivine data are thought to result from disaggregation of cumulate xenoliths. However, no other populations have been concluded to originate from the same process. It is possible that there may be clinopyroxenes that are also originally cumulate crystals. These may either resemble clinopyroxenes from other processes too closely to be identified as a discrete population or have not been sampled during this study. The LCO are the only geochemically similar population that extends across several islands. Different populations are prevalent in the plagioclase and several of these appear to have been generated from similar processes to each other, but they do not share the chemical similarities that the LCO from different host lavas do. An example of this is the potentially entrained populations from GU21 and SV20. Texturally these populations appear similar and it is inferred that their petrogenesis is largely the same but chemically they are not related.

### **6.3.5 Effect of Fluid**

Given that the Lesser Antilles is an intra-oceanic arc setting, water is likely to play a role in the petrogenesis of the lavas. Published melt water contents for the arc range from between 1-6 wt% (Macdonald *et al.*, 2000).

In the previous chapters it has been proposed that water can increase olivine forsterite contents whilst reducing CaO concentrations, increase plagioclase anorthite contents and reduce REE partitioning between clinopyroxenes and melts. In addition, degassing at shallow levels may be responsible for creating the forsterite bimodality in GU25 olivines as well as causing crystal edge resorption in numerous plagioclase populations. Plagioclase anorthite bimodality is seen in GU1, GU4 and GU25. Both GU4 and GU25 show evidence of degassing in all their populations. This could suggest that degassing following the crystallisation of the higher anorthite content crystals could result in the lower anorthite contents of the remaining populations. This would be best observed by analysing plagioclases in thick section to couple textural observations with anorthite content measurements across crystals. Whilst this was undertaken on GU25 plagioclases, only crystals from the high anorthite group were analysed.

However, this study is unsuitable for providing estimates of the amount of water contained in the melts which crystallised the various phases studied. The closest approximation used was plotting the plagioclase CaO/Na<sub>2</sub>O ratios against whole rock CaO/Na<sub>2</sub>O before adding the various water content partition coefficient lines of Sisson and Grove (1993) (Figure 4-30). Given the wide ranges of plagioclase ratios, plotting these against a single whole rock value (and the issues that entails) produced arrays of data which extended across several of the proposed water contents. In many cases the plagioclases appeared to require a melt with more than 6 wt% water. Water contents of 6-8 wt% are only thought to contribute to silicic melts (Macdonald *et al.*, 2000). A melt inclusion study would be required to more accurately constrain the melt water contents, which is beyond the scope of this work.

### **6.3.6 Amphibole Fractionation?**

As noted by Davidson *et al.* (2007a), 'cryptic' amphibole fractionation within the arc crust can have a large impact on arc lava petrogenesis, particularly on REE concentrations. The authors propose that REE are much more compatible in amphibole than clinopyroxene. MREE in particular are more compatible than HREE (with garnet being the phase into which the HREE are most compatible). Amphibole is also capable of hosting a significant quantity of water at depth. If the amphibole becomes unstable, this water can then be released and potentially circulated back into the upper mantle (providing magnetite is present to render any hydrous melts negatively buoyant) (Davidson *et al.*, 2007a). Furthermore, if amphibole crystallisation removes water from the melt at middle to lower crustal levels, this will affect the compositions of subsequently crystallising phases (as noted in section 6.3.5). Increased amphibole fractionation will reduce water contents and thus may lead to lower forsterite, higher CaO olivines, lower anorthite plagioclases and higher REE concentrations in clinopyroxenes, depending on the amount of amphibole crystallised. Davidson *et al.* (2007a) also suggest amphibole fractionation has an effect on the La/Yb and Dy/Yb ratios of the melts, increasing the former and decreasing the latter. This may explain why in melts back calculated from the clinopyroxene data appear to show their respective trends.

Crystallising amphibole from a melt may also go some way to explain the wide range in La/Yb seen in the Grenada and Carriacou melts attributed to dehydration of

the source. Dehydration has also been postulated as a method of generating the high  $\Delta 8/4$  source seen in the southern part of the arc. However, amphibole should only accommodate the hydrogen and oxygen from water and not necessarily other fluid mobile elements.

Fractional crystallisation modelling was undertaken where amphibole and clinopyroxene were removed from the whole rock composition of 6257 from Grenada. This whole rock composition was used as LCO were identified in the olivine analyses and an amphibole composition was available for this lava (Graham, 1980). Removal of 25% clinopyroxene (that was in equilibrium with the melt at each stage of the crystallisation model) and 25% amphibole results in an olivine composition in equilibrium with the resulting melt composition with 0.10 wt% CaO and a forsterite content of Fo<sub>80</sub>, comparable to the LCO. The composition of the equilibrium olivine was calculated from the modelled melt composition by using the partition coefficients of Beattie (1994). Whilst removal of clinopyroxene and amphibole produces CaO and Fo contents comparable to the LCO, the MnO concentrations are too low and more significantly the Al<sub>2</sub>O<sub>3</sub> are far too high compared to the LCO (0.10 wt% MnO compared to a range of 0.13-0.39 wt% and 0.18 wt% Al<sub>2</sub>O<sub>3</sub> compared to a range of 0.00-0.02 wt%). Therefore, removal of these phases at the cumulate level may impact upon the composition of the LCO but cannot completely account for their chemistry.

#### **6.4 Overall Petrogenetic Model**

Using the information gained from the different mineral phases and the whole rock Pb isotopes, an overall petrogenetic model was developed for the north and centre of the arc and the south of the arc (Figure 6-11).

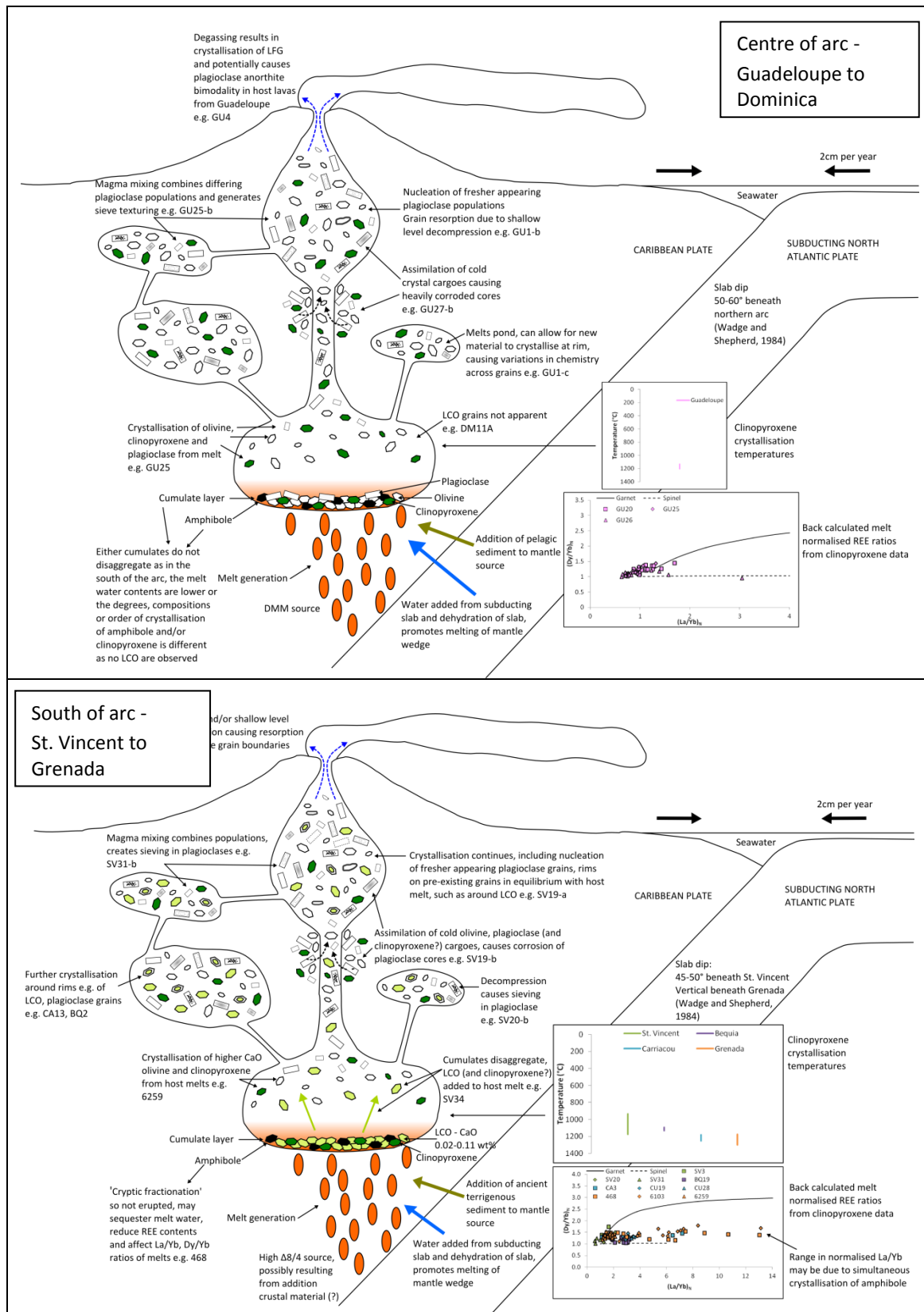


**Figure 6-11 Overall petrogenetic models for the north and centre of the arc and the south of the arc, including examples of populations which show the processes highlighted.**

---

## 7 Appendix 1 – Analytical Techniques

---

### 7.1 Sample Preparation

#### 7.1.1 Rock Crushing

A hydraulic splitter was used in order to remove any weathered surfaces from the sample rocks. Following this a jaw crusher was used to break the rock down into chips approximately 1cm<sup>3</sup> in size. Between samples, the jaw crusher and surrounding area was cleaned using a vacuum cleaner. The jaws were removed to dislodge any trapped material; the jaws were then reattached and cleaned using acetone. The chipped material was split into thirds, with a third of the material being retained as chips and the remaining two thirds being crushed into powder. The powder crushing was done using a tungsten carbide TEMA mill at 1500 rpm for 45 seconds. The powder was then stored in glass jars which had been cleaned using acetone. Between samples, the TEMA was thoroughly cleaned using acetone and water to remove all material from the previous sample. Material which could not be removed using water and acetone was eliminated by adding glass powder to the TEMA and running through the mill again before repeating the water and acetone cleaning.

#### 7.1.2 Mineral Separation

Rock chips were crushed using a steel percussive mill. This material was then sieved and separated into >1mm, 500µm-1mm, 250µ-500µm and <250µm fractions. Only the 500µm-1mm, 250µm-500µm fractions were used for analysis. Before picking, the fractions were placed into glass beakers, covered with MQ and cleaned in an ultrasonic bath. The cleaning was carried out in 10 minute periods. Between each clean, the dirty MQ was poured off and the material was rinsed with MQ before being covered again and replaced in the ultrasonic bath. This process was repeated until the water after the 10 minute cleaning run was clean. This MQ was then also poured off and the beakers placed into an oven to dry. When dry, the fractions were separated into magnetic and non-magnetic fractions using a hand magnet.

### *Picking for Double Spike Pb Analysis*

The material for double spike Pb analysis was picked under a binocular microscope from the magnetic fraction. Any anomalous material, such as fluff, was removed from the fractions. In addition, any material showing signs of alteration was also removed.

### *Picking for LA-ICP-MS Analysis*

Mineral separates (olivine, plagioclase and clinopyroxene) were picked from the non-magnetic fractions. These separated crystals were then mounted in epoxy resin blocks. When set, the blocks were polished to expose the mineral crystals at the surface ready for LA-ICP-MS analysis.

## **7.2 Thermal Ionisation Mass Spectrometry (TIMS)**

TIMS analysis was used to obtain whole rock  $^{87}\text{Sr}/^{86}\text{Sr}$  and  $^{143}\text{Nd}/^{144}\text{Nd}$  ratios. The samples were loaded on to beads which were mounted in a turret for analysis using the TIMS.

### **7.2.1 Cleaning Beakers**

Savillex beakers were used for the sample digestion. The beakers were cleaned by boiling in conc. HCl at 175°C (for >24 hours) and then again in conc. HNO<sub>3</sub> at 175°C (for >24 hours). Once cleaned, the beakers were submerged in MQ and stored until required for use. When needed, the beakers were placed in a large Pyrex beaker and covered with MQ water and boiled on a hotplate for 45 minutes. The beakers were then rinsed with fresh MQ several times. The base of each beaker was then covered with conc. HNO<sub>3</sub> and ~2ml of conc. HF was added. The beakers were sealed and placed on the hotplate at 125°C for 48 hours. Following this, the beakers were emptied and then rinsed with MQ.

### **7.2.2 Sample Digestion**

Around 0.1g of sample was weighed into the cleaned beakers and then covered with 6M HCl. The samples were then heated on the hotplate for half an hour at 180°C. When cooled, the samples were rinsed with MQ until the water coming off the

samples was clear and colourless. The base of the beaker was then covered with conc.  $\text{HNO}_3$  and approximately 2ml of conc. HF was added. The beakers were sealed and left on the hotplate for ~2 days at  $150^\circ\text{C}$  to digest. After digestion, the lids were removed and the samples evaporated to dryness for approximately 6 hours at  $125^\circ\text{C}$ . 2ml of conc.  $\text{HNO}_3$  was added to the sample beakers, which was then evaporated (in order to convert the samples to nitrate). When dry, 1ml of 8M  $\text{HNO}_3$  for Sr analysis or 2ml 10%  $\text{HNO}_3$  for Nd analysis was added to the samples. The beakers were placed on the hotplate at  $150^\circ\text{C}$  for 3 hours to redissolve the samples. After cooling, the samples were ready for the columns.

The samples were transferred to clean centrifuge tubes (which had been rinsed with MQ). The samples were then centrifuged for 5 minutes. If any solid was observed after centrifuging, the affected samples were transferred to clean, rinsed centrifuge tubes. 8M  $\text{HNO}_3$  or 10%  $\text{HNO}_3$  was then used to rinse any solid material into the second centrifuge tube before the sample was transferred back into its original beaker. The samples were then replaced on the hotplate and heated at  $150^\circ\text{C}$  overnight to digest the solid material. The centrifuging process was repeated until no solid remained in the centrifuge tubes.

The beakers were cleaned with conc.  $\text{HNO}_3$  by sealing them and placing them on the hotplate at  $150^\circ\text{C}$  for half an hour. When cool, the beakers were emptied and rinsed with MQ.

### **7.2.3 Making Columns**

Columns used for separation chemistry were made from Teflon pipette tips. The end was clipped to promote more efficient dripping.  $70\mu\text{m}$  of frits was inserted into the base of the column and pushed into place. The columns were then submerged in 10%  $\text{HNO}_3$  and observed to ensure acid was dripping through them. They were then placed in a large beaker of 10%  $\text{HNO}_3$  and left for at least 24 hours or until required.

## 7.2.4 Column Chemistry

### *Sr Chemistry*

Samples being analysed for  $^{87}\text{Sr}/^{86}\text{Sr}$  ratios and concentrations of Sr were run through columns using Sr spec resin. After pre-cleaning, 5 drops of Sr spec resin were pipetted directly into each column. Further cleaning of the columns was then undertaken with varying concentrations of  $\text{HNO}_3$  before the samples were loaded using pipettes previously rinsed in 8M  $\text{HNO}_3$ . Following elution with 8M  $\text{HNO}_3$ , the Sr fraction was collected into the cleaned original beakers in MQ. The samples were then evaporated to dryness overnight on the hotplate at  $125^\circ\text{C}$ . When cool, several drops of conc.  $\text{HNO}_3$  were added to the sample beakers before evaporating, again at  $125^\circ\text{C}$  for approximately an hour.

### *Nd Chemistry*

Nd separation was undertaken in two stages. The first stage was to run the samples through columns as for the Sr chemistry but using TRU spec resin as opposed to Sr spec resin. Pre-cleaning was undertaken in the same fashion before 0.05g of the dry TRU spec resin was weighed into the columns. The columns were then cleaned with various lower concentrations of  $\text{HNO}_3$  than used on the Sr columns before sample loading. The samples were loaded in clean pipettes (rinsed with 10%  $\text{HNO}_3$  before being used for samples) in two 1ml batches. The Nd fraction was collected into the original beakers (once cleaned) in 0.05M  $\text{HNO}_3$ . The samples were evaporated to dryness on the hotplate at  $125^\circ\text{C}$  for approximately 6 hours prior to the second stage column chemistry.

The second stage columns utilised glass anion exchange columns. 1ml of orange cocktail was used to dissolve the samples. The columns were treated with orange cocktail prior to the loading of the samples. Clean pipettes rinsed in orange cocktail were used for sample loading. Elutions were performed with both orange and yellow cocktail. The samples were then collected into the cleaned beakers and evaporated before a second pass of the second stage columns. The samples were then collected in the cleaned beakers in 10%  $\text{HNO}_3$  before being evaporated on the hotplate at  $125^\circ\text{C}$  overnight until dry.

### 7.2.5 Bead Making

Beads were cleaned of pre-existing filament material and residue by using a drill to grind off the excess metal. The correct filament material was then selected depending on the analysis to be undertaken, Re filament was used for  $^{143}\text{Nd}/^{144}\text{Nd}$  ratio analyses and Ta filament was used for  $^{87}\text{Sr}/^{86}\text{Sr}$  ratio determination. The filament was then welded into place. The beads were then placed in a Pyrex beaker, covered with MQ and boiled on the hotplate for 45 minutes. The beads were then rinsed twice with MQ. The beaker containing the beads was then placed in an oven for 12 hours to dry.

When dry, the beads were degassed at a pressure of  $<1.10^{-5}$  mbar and a current of 5A for 5 minutes, then at 3.5A for a further 5 minutes and then at 2A for another 5 minutes. The beads were then placed in a bead box. The beads were left to oxidise for at least 24 hours before any sample was loaded onto them.

### 7.2.6 Sample Loading

Samples analysed for  $^{87}\text{Sr}/^{86}\text{Sr}$  were loaded on to the prepared beads using  $\text{H}_3\text{PO}_4$  (Thirlwall, 1991b). Samples analysed for  $^{143}\text{Nd}/^{144}\text{Nd}$  were loaded using a combination of  $\text{H}_3\text{PO}_4$  and silica gel (Thirlwall, 1991a). After loading and drying of the sample, the current through the filament was increased to 2A to ensure any excess acid had been burnt off the filament.

### 7.2.7 Mass Spectrometry

The samples were analysed using the Royal Holloway VG 354 TIMS. A 16 sample turret was used, with beads loaded with standards being loaded into position 5 and 12. The pressure in the TIMS is  $10^{-7}$  mbar. The TIMS ran the samples automatically.

#### *$^{87}\text{Sr}/^{86}\text{Sr}$ Analysis*

$^{87}\text{Sr}/^{86}\text{Sr}$  isotopic ratios were analysed using a multidynamic programme, in that it uses all five collectors of the MC-ICPMS. This has the advantage of being able to correct for  $^{87}\text{Rb}$  interference. Both Sr concentrations and  $^{87}\text{Sr}/^{86}\text{Sr}$  are measured by the programme. Corrections for mass bias were made by normalisation in accordance with Thirlwall (1991a). The standard used during Sr analysis was SRM987.

### $^{143}\text{Nd}/^{144}\text{Nd}$ Analysis

$^{143}\text{Nd}/^{144}\text{Nd}$  isotopic ratios were also analysed using a multidynamic procedure. The samples were analysed as  $\text{NdO}^+$  to minimise isobaric interferences from  $\text{SmO}^+$  and  $\text{CeO}^+$ . In addition it improves the ionisation of the Nd by up to 20 times, increasing accuracy. Normalisation was carried out as outlined in Thirlwall (1991b). Dilute Aldrich was used as a standard during  $^{143}\text{Nd}/^{144}\text{Nd}$  analyses.

### 7.2.8 Standard Reproducibility

Figure 7-1 shows the reproducibility of the SRM987 and dilute Aldrich standards during the period analyses were undertaken for this study.

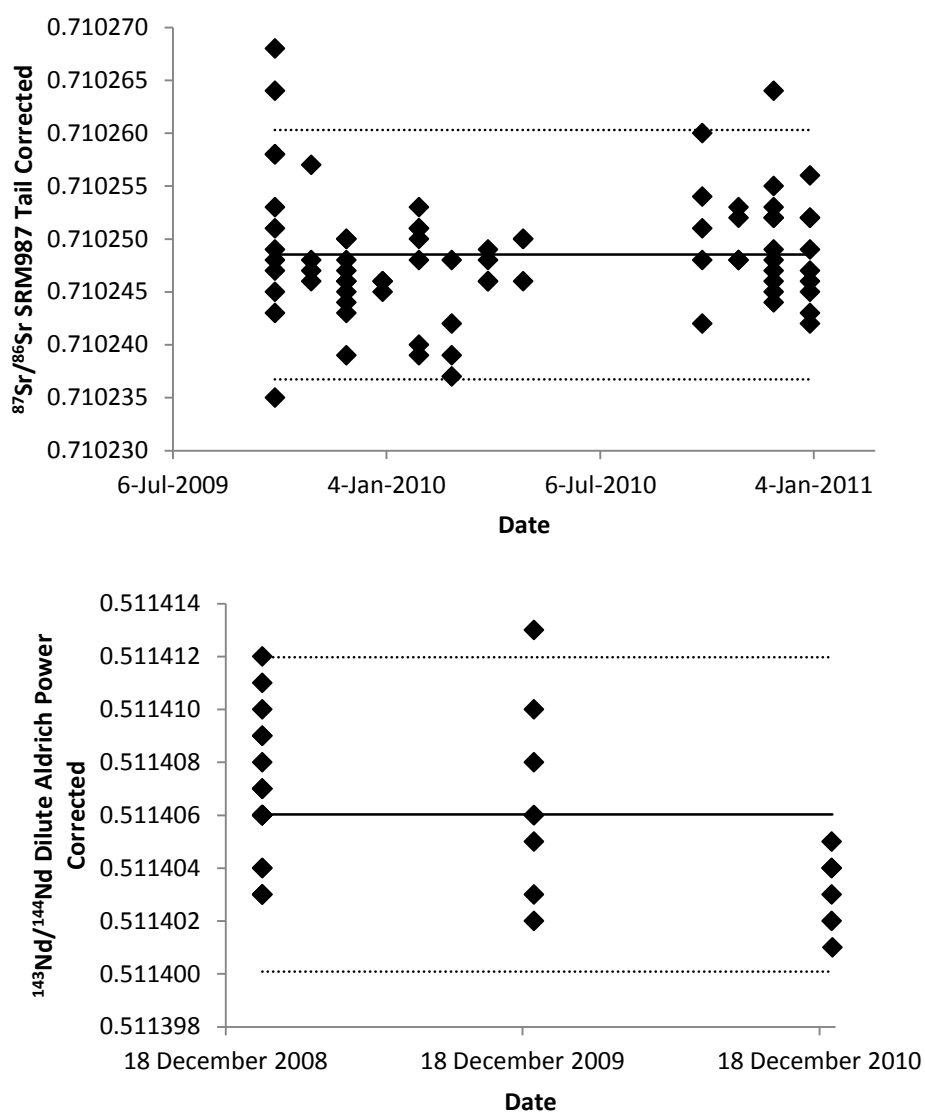


**Figure 7-1 Reproducibility of SRM987  $^{87}\text{Sr}/^{86}\text{Sr}$  and Dilute Aldrich  $^{143}\text{Nd}/^{144}\text{Nd}$  standards during the period of analysis. Solid lines represent the mean value for each standard and dotted lines represent 2sd.**

### **7.2.9 Double Spike Pb Analysis**

These analyses were carried out in order to obtain precise  $^{206}\text{Pb}/^{204}\text{Pb}$ ,  $^{207}\text{Pb}/^{204}\text{Pb}$  and  $^{208}\text{Pb}/^{204}\text{Pb}$  ratios for the whole rock samples (Thirlwall, 2002). Double spike Pb chemistry was carried out in a clean environment to try and reduce contamination. Two blanks were run in each batch of 18 to measure levels of contamination introduced during the chemistry.

#### *Cleaning Beakers*

3ml Savillex beakers were used during the double spike Pb analysis. These had been previously cleaned and blank tested. These were half filled with 6M HCl, sealed and placed on the hotplate at 120°C for 12 hours. When cool, the beakers were rinsed with MQ.

#### *Columns and Materials Preparation*

Columns and materials required for the double spike Pb chemistry (such as Pasteur pipettes and centrifuge tubes) were prepared in advance.

#### *Columns*

The columns used were Teflon pipette tips which were rinsed inside and out with MQ. The columns were then covered with NormaPur analar conc.  $\text{HNO}_3$  and put on the hotplate for >48 hours at 130°C. After cooling, the columns were rinsed with MQ. Frits were then inserted into each column. A container was filled with SB 7.6M HCl and each column was dipped in this in turn and checked to ensure the acid was dripping through the frit. The columns were then fully submerged in the acid and left to soak for >48 hours.

#### *Pipettes and Centrifuge Tubes*

The centrifuge tubes were filled with 5ml of SB 7.6M HCl. Pasteur pipettes were inserted into the centrifuge tubes and 2ml of the SB 7.6M HCl was sucked up into

the pipettes. The pipettes were then left in the centrifuge tubes and both the centrifuge tubes and the pipettes were left to soak for approximately 1 week.

### *Sample Digestion*

0.1g of sample from the magnetic fraction was weighed into each beaker. The beakers were then half filled with 6M HCl before being sealed and placed on the hotplate for 1 hour at 130°C to leach the chips. After cooling, the chips were rinsed multiple times with MQ until the MQ remained clear. 25 drops of conc. HF and 15 drops of conc. HNO<sub>3</sub> were added to the sample beakers. The beakers were then sealed and placed on the hotplate at 150°C for ~48 hours to digest the samples. The sample beakers were evaporated to dryness at 120°C for 6 hours. 20 drops of conc. HNO<sub>3</sub> were added to the dry samples, this was then evaporated off on the hotplate at 120°C for 3 hours. The samples then had 35 drops of 6M HCl added to them to convert them from HNO<sub>3</sub> ready them for the columns (which are run using HCl). The sample beakers were sealed and heated on the hotplate at 120°C for 12 hours. The sample beakers were evaporated to dryness on the hotplate at 120°C for 6 hours before 1ml of 1M HCl was added to the samples which were then replaced on the hotplate for 12 hours at 120°C.

### *Column Chemistry*

The samples were run through a set of columns using Sr spec resin and HCl. The samples were transferred from the sample beakers to the clean centrifuge tubes and centrifuged for 6 minutes prior to running. The beakers were cleaned during the running of the columns by adding 2 drops of conc. HNO<sub>3</sub>, sealing them and placing them on the hotplate at 120°C for 30 minutes. The Pb fraction was collected in 80 drops of 6M HCl. The sample beakers were then evaporated to dryness at 120°C for 6 hours. Following this, 1ml of 1M HCl was added to the sample beakers which were then replaced on the hotplate and heated at 120°C for 1 hour. After cooling, the sample solutions were passed through the columns a second time (cleaning the beakers as before during the chemistry) and the Pb fraction again collected in 80 drops of 6M HCl. The sample beakers were then evaporated to dryness at 120°C for 6 hours.

### *Mass Spectrometry*

The samples were analysed using the Royal Holloway micromass IsoProbe MC-ICP-MS used to analyse the fractions obtained during isotope dilution. Prior to analysis, 30 drops of Tl solution were added to each sample and 10 drops added to the blanks. The beakers were sealed and placed on the hotplate overnight at 100°C the night before analysis.

Two programmes were used when running the double spiked Pb samples. For the blank runs before sample was introduced, Pb2mulbk was used. For the samples themselves Pb202mul was used. Both the programmes ran multi-dynamically. After all the samples and blanks were run successfully naturally, double spike solution ( $^{207}\text{Pb}/^{206}\text{Pb}$ ) was added to the beakers. The samples and blanks were then re-run using the same programmes as before. Throughout the natural and double spiked analyses, SRM981 was used as a standard. Further information on the double spike procedure can be found in Thirlwall (2002).

### *Standard Reproducibility*

Figure 7-2 shows the reproducibility of the SRM981 standard during the period in which analyses were carried out for this study.

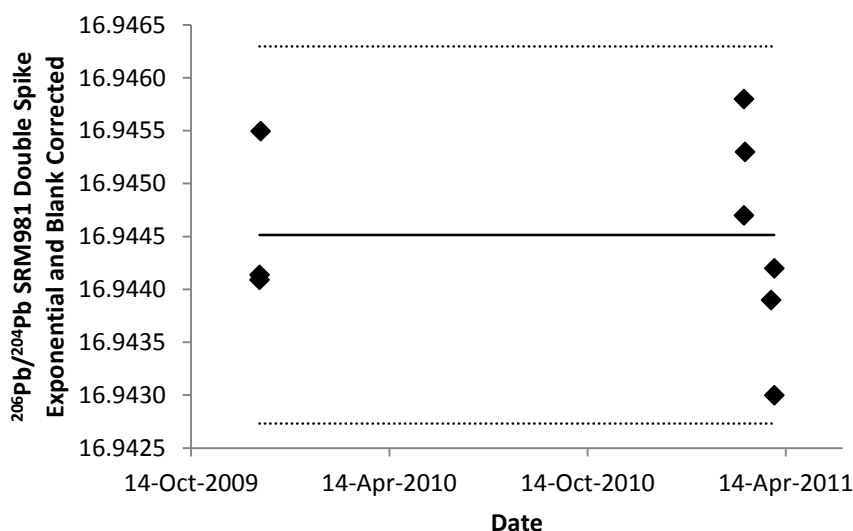


Figure 7-2  $^{206}\text{Pb}/^{204}\text{Pb}$  ratios measured on the SRM981 double spike during the period of study. Solid black line shows the mean ratio measured during the study with the dotted lines representing 2sd.

### **7.3 Laser Ablation Inductively Coupled Plasma Mass Spectrometry (LA-ICP-MS)**

Mineral analysis was undertaken on olivines, plagioclases and clinopyroxenes from various islands throughout the Lesser Antilles arc. The minerals were analysed using the LA-ICP-MS system at Royal Holloway using a new technique documented by Thirlwall *et al.*, in prep. This technique allows for the measurement of major and trace elements both on mineral separates and in-situ in polished thick sections with precision comparable to that achieved by wave dispersive electron microprobe analysis but with faster analysis times.

#### **7.3.1 Royal Holloway LA-ICP-MS System**

The laser used is a 193nm ArF excimer laser connected to a two-volume ablation cell (Mueller *et al.*, 2009). The latter utilises a combination of a  $\sim 1\text{-}2\text{cm}^3$  cell in an enclosed larger ( $380\text{ cm}^3$ ) sample cell box, the smaller cell being fixed in position relative to the imaging lens of the laser. As this inner cell is fixed, the larger sample cell box moves to position samples in differing locations for analysis under the imaging lens, eliminating any inconsistencies based on the location of the sample within the sample cell box. Another advantage of the laser ablation cell is that it allows for high sensitivities coupled with rapid washout times ( $<1\text{s}$ /order of magnitude). The ablation takes place in the presence of  $\text{He}_2$ . The ablated material is entrained as a sample aerosol in  $\text{He}_2$ , leaves the ablation cell and is then combined with Ar as a carrier gas. This then flows via a smoothing manifold (known as a 'squid') to the quadropole ICP-MS (an Agilent 7500ce/cs). The squid smoothes the signal by splitting the inflowing sample aerosol and carrier gas mixture, which then flows through ten tubes of differing lengths, before recombining it prior to arrival at the ICP-MS. Use of the squid minimises the potential for spectral skew (Schilling *et al.*, 2007) - beating and resonance effects which can adversely affect data quality. These effects can be most problematic when using the system at low frequencies.

#### **7.3.2 Tuning**

The LA-ICP-MS system was tuned prior to any analyses in order to reduce background in comparison to the signal from the materials being analysed. This was

done by ablating tracks along the NIST612 glass standard. A  $^{232}\text{ThO}/^{232}\text{Th}$  ratio of <0.3% and a  $^{232}\text{Th}/^{238}\text{U}$  ratio of >0.9 was maintained whilst trying to achieve the highest signal strength across the mass spectrum (in particular on the mid range and higher masses) (Thirlwall et al., in prep).

### ***Pulse/Analog Factors***

Software for calibrating the pulse/analog (P/A) factors from Agilent was also run on the NIST612 glass after the tuning process. The ICP-MS has a pulse collector and an analog collector; for counts under approximately 1 Mcps, the pulse collector is used. However, at intensities greater than 1Mcps, the analog collector is utilised. P/A factors are determined for every m/z being analysed to provide information on the responses of the detectors. In some instances during sample analysis there were problems when the ICP-MS switched between collectors when the threshold value was reached. Where this occurred, a correction has been applied to the data prior to further processing.

### **7.3.3 Laser Conditions and Settings**

The minerals were analysed using different conditions for the laser based on mineral type (Table 7-1). In addition, run parameters for olivines were changed between the analyses of the first olivines and subsequent olivine analyses. The initial batch of 73 olivines were not analysed for the elements Li, Sc, TiO<sub>2</sub>, V, Sr, Y, Nb, Ba and Yb. The precision of the measured Zr concentrations was vastly improved after analysis of the first batch also and thus Zr data from these runs has not been used.

<b>Mineral</b>	<b>Spot Size</b>	<b>Repetition Rate</b>	<b>Fluence</b>	<b>Delay 3</b>	<b>Delay 4</b>	<b>Ablation Time</b>
<i>Olivine</i>	74µm	8Hz	58mJ	5s	15s	7s
<i>Olivine</i>	74µm	8Hz	58mJ	20s	20s	24s
<i>Plagioclase</i>	57µm	8Hz	58mJ	18s	18s	24s
<i>Clinopyroxene</i>	57µm	5Hz	58mJ	15s	15s	20s

**Table 7-1 Laser settings used for each mineral phase analysed using the LA-ICP-MS.**

### 7.3.4 Mass Spectrometry

The ablated material was measured using the Agilent quadrupole. Integration times used in each sweep of measurement in the ICP-MS varied depending on mineral type. In addition, at the beginning of the study the methods being used were still being developed, as such, the integration times for olivine varied during the first few days of analysis. Table 7-2 shows the times each mass was measured for all the analyses undertaken.

Mineral	Integration Time (s)				
		<i>Olivine</i>		<i>Plagioclase</i>	<i>Clinopyroxene</i>
Li		0.012	0.020	0.020	0.020
Na <sub>2</sub> O				0.010	0.010
MgO	0.010	0.012	0.010	0.010	0.020
Al <sub>2</sub> O <sub>3</sub>				0.020	0.010
SiO <sub>2</sub>	0.020	0.012	0.010	0.010	0.010
K <sub>2</sub> O				0.020	0.020
CaO	0.040	0.012	0.020	0.020	0.020
Sc		0.012	0.010	0.100	0.010
TiO <sub>2</sub>		0.012	0.060	0.060	0.020
V		0.012	0.010	0.010	0.010
Cr		0.012	0.010	0.010	0.010
MnO	0.020	0.012	0.010	0.010	0.010
FeO	0.020	0.012	0.010	0.010	0.010
Fe <sub>2</sub> O <sub>3</sub>				0.020	
Ni	0.040	0.012	0.010	0.010	0.010
Rb				0.030	0.020
Sr		0.012	0.150	0.150	0.030
Y		0.012	0.060	0.060	0.050
Zr	0.020	0.012	0.150	0.150	0.020

<b>Mineral</b>	<b>Integration Time (s)</b>				
	<i>Olivine</i>			<i>Plagioclase</i>	<i>Clinopyroxene</i>
Nb	0.012	0.020	0.020	0.030	0.050
Ba	0.012	0.020	0.020	0.050	0.030
La				0.050	0.030
Ce					0.020
Nd					0.020
Sm				0.050	0.020
Eu				0.050	0.020
Gd				0.050	0.020
Dy					0.020
Er					0.020
Yb	0.012	0.100	0.100		0.020
Hf					0.050
Pb				0.050	0.020
Th					0.020
U					0.020

**Table 7-2 Integration times used for each phase. The olivine method was fine tuned during the study, as such there are several methods shown for this phase.**

### 7.3.5 Standards

In addition to the samples, standards were run throughout the analysis days, these again varied based on the minerals being analysed. NIST612 glass is a standard reference material (SRM) and was analysed for all minerals as an external standard and used to calibrate the majority of elements (with the exceptions of Fe and Mg for olivines; Fe, Mg, K, Na and Ca for plagioclases and Fe, Mg, Mn and Ti for clinopyroxenes). As an SRM the NIST612 should give inter-laboratory consistency.

Mineral specific standards were used in addition to the NIST612 glass as concentrations of the specific respective elements used for calibration in the glass standard were too low to provide precise data for calibration. Mineral standards were

also matrix matched to the phase being analysed. EPMA data is available for all the mineral specific standards analysed in conjunction with the NIST612 glass. The standards used were Smithsonian Microbeam Reference Materials, compositions for these minerals can be found in Jarosewich (2002). San Carlos olivine standards (NMNH 111312) were used for Fe and Mg in olivine analyses and as a reproducibility check on the remaining analysed elements. During plagioclase runs, both an anorthite standard (NMNH 137041) and a labradorite standard (NMNH 115900) were run, the former as an estimate of overall reproducibility and to calibrate Ca and the latter for calibration of Fe, Mg, K and Na. The labradorite standard was also used as a check on reproducibility on the other elements analysed but not used for calibration. Reproducibility for the plagioclase samples analysed appeared to be a function of anorthite content and was found to be better at higher anorthite contents. A chromian augite (NMNH 164905) standard was used during clinopyroxene analysis runs. The mineral standard was used to calibrate Fe, Mg, Mn and Ti. Again all elements were analysed and those not required for calibration purposes were used as a reproducibility check.

Detailed information about standard reproducibility using the RHUL LA-ICP-MS system for the standards used can be found in Thirlwall et al. (in prep).

### **7.3.6 Data Processing**

The raw data obtained from the LA-ICP-MS analysis had to be converted from intensities into wt% for the oxides and ppm for the trace elements. The mineral crystals were analysed in runs consisting of between 20 and 70 sample crystals and standards. Standards (NIST612 glass and mineral specific standards) were run at the beginning and end of every run and also within runs if a large number of crystals were being analysed in a given run.

#### ***Correcting for Background Intensities***

Background intensities were calculated by averaging the start of the runs (before any samples had been run) and the end of each run (after all the samples had been run) for each mass. For masses where the background intensity varied during the run, the masses were corrected for the baseline on a crystal by crystal basis, using the

background intensity recorded immediately prior to analysing the crystal for the requisite masses. The masses that were corrected on an individual basis were MgO, SiO<sub>2</sub>, CaO and MnO during the olivine runs and Na<sub>2</sub>O, SiO<sub>2</sub> and K<sub>2</sub>O during the plagioclase runs. Background intensity variation was caused by interferences on the masses, e.g. from CO<sub>2</sub>. Background correction ensures that the no effect from residual intensities measured by the LA-ICP-MS is incorporated into the data for the standards and samples.

For olivine runs, after measuring the first NIST612 glass, the background in CaO increased, however, later NIST612 analyses did not produce this effect to the same extent. The increased background was remedied by running a 'sacrificial' olivine crystal between the first NIST612 analysis and the following San Carlos standard during olivine runs. The data from this olivine was not used. Running an olivine in between the standards caused a reduction in CaO background, an effect which is not observed when running other minerals. In addition, after olivine analyses, the background was seen to be lower than the initial and final background measurements were taken (before and after the samples were run respectively).

#### ***Ratio to Si (Olivines), Si and Ca (Plagioclases and Clinopyroxenes)***

The baseline corrected data were then ratioed to the measured intensity of SiO<sub>2</sub> for olivine. For the plagioclase runs, several element (Fe<sub>2</sub>O<sub>3</sub>, MgO, CaO, Na<sub>2</sub>O, K<sub>2</sub>O and Rb) baseline corrected intensities were ratioed to SiO<sub>2</sub> and the remaining element baseline corrected intensities were ratioed to CaO. These elements were chosen as they are major constituents of the minerals thus making them suitable reference isotopes. SiO<sub>2</sub> varies less in both olivine and plagioclase than FeO and MgO (in olivine) and Na<sub>2</sub>O (in plagioclase). In addition, fractionation factors on these elements were sufficiently low to allow their use for calibration. In plagioclases, elements calibrated using the NIST612 glass rather than the matrix matched mineral standards were ratioed to CaO (with the exception of Rb which is ratioed to SiO<sub>2</sub>), due to the lower fractionation factor of CaO compared to SiO<sub>2</sub>, giving a higher estimate of internal precision (Thirlwall et al., in prep). For the clinopyroxenes, the majority of elements were ratioed to CaO, with Li, Na<sub>2</sub>O, MgO, SiO<sub>2</sub>, K<sub>2</sub>O, CaO, Cr, MnO, FeO, Ni and Rb being ratioed to SiO<sub>2</sub>. This is again due to there being sufficient concentrations of CaO and SiO<sub>2</sub> in clinopyroxene to make

them both suitable internal standards. SiO<sub>2</sub> or CaO was chosen for each element in order to minimise potential laser-induced fractionation and thus produce more accurate results.

### *Calibration to NIST612*

All calibrations were undertaken using the equations of Ludden et al. (1995) and Longerich et al. (1996) in order to convert ratioed data to concentrations either in wt% or ppm.

### *Olivine*

NIST612 glass was used to calibrate all the major and trace elements analysed during the olivine analyses with the exception of FeO and MgO (which were calibrated using the San Carlos olivine standard). NIST612 was used as the concentrations of the major and trace elements in the San Carlos olivine standard are not sufficiently high to provide a precise and repeatable calibration for the unknown samples (the elemental concentrations in the NIST612 glass are generally significantly higher than those in the San Carlos standard, with the exception of Cr and Ni).

Calibration was performed using Equation 7-1, where *x* is the element to be calibrated, *ol* represents the olivine (or standard) in question and *Given Value*<sub>NIST</sub> is the accepted published value. *Ratio to Si*<sub>NIST</sub> in the equation refers to the average of the ratio to Si of element *x* for the NIST612 standards analysed during that run.

### **Equation 7-1**

$$[x]_{ol} = \frac{\text{Ratio to } Si_{ol}^x}{\text{Ratio to } Si_{NIST}^x} \times \text{Given Value}_{NIST}^x \times \frac{\text{Calculated } SiO_{2ol}}{\text{Given Value } SiO_{2NIST}}$$

### *Plagioclase*

NIST612 glass was used to calibrate TiO<sub>2</sub>, Rb, Sr, Y, Nb, Ba, La, Sm, Eu, Gd and Pb in the plagioclases analysed; the anorthite and labradorite standards were used for the remaining elements (Fe<sub>2</sub>O<sub>3</sub>, MgO, CaO, Na<sub>2</sub>O and K<sub>2</sub>O). This is to allow some matrix matching between the standards whilst still maintaining high enough concentrations to ensure precise calibrations.

Equation 7-2 was used for the calibration in the plagioclases, notation is as for the olivine NIST612 calibration, except plag, which is the plagioclase being calibrated.

**Equation 7-2**

$$[x]_{plag} = \frac{\text{Ratio to } Ca_{plag}^x}{\text{Ratio to } Ca_{NIST}^x} \times \text{Given Value}_{NIST}^x \times \frac{Al_2O_{3plag}}{\text{Given value } CaO_{NIST}}$$

In the case of Rb, which was ratioed to Si and not to Ca, the following equation is used (Equation 7-3).

**Equation 7-3**

$$[Rb]_{plag} = \frac{\text{Ratio to } Si_{plag}^{iRb}}{\text{Ratio to } Si_{NIST}^{iRb}} \times \text{Given Value}_{NIST}^x \times \frac{SiO_{2plag}}{\text{Given value } SiO_{2NIST}}$$

*Clinopyroxene*

Li, Na<sub>2</sub>O, Al<sub>2</sub>O<sub>3</sub>, SiO<sub>2</sub>, K<sub>2</sub>O, CaO, Sc, V, Cr, Ni, Rb, Sr, Y, Zr, Nb, Ba, La, Ce, Nd, Sm, Eu, Gd, Dy, Er, Yb, Hf, Pb, Th and U were calibrated to NIST612 glass for the clinopyroxene analyses, with the chromium augite standard being used for the remaining elements (FeO, MgO, MnO and TiO<sub>2</sub>) as the concentration of these elements is lower in the NIST612 glass than in the mineral specific standard. Those elements which were initially ratioed to CaO were calibrated using Equation 7-4, notation is as for the plagioclase equations with cpx being clinopyroxene.

**Equation 7-4**

$$[x]_{cpx} = \frac{\text{Ratio to } Ca_{cpx}^x}{\text{Ratio to } Ca_{NIST}^x} \times \text{Given Value}_{NIST}^x \times \frac{\text{Assumed } CaO_{cpx}}{\text{Given value } CaO_{NIST}}$$

For those elements that were ratioed to Si, Equation 7-5 was used for calibration.

**Equation 7-5**

$$[x]_{cpx} = \frac{\text{Ratio to } Si_{cpx}^x}{\text{Ratio to } Si_{NIST}^x} \times \text{Given Value}_{NIST}^x \times \frac{\text{Assumed } SiO_{2cpx}}{\text{Given value } SiO_{2NIST}}$$

**Calibration to San Carlos**

San Carlos olivines were used to calibrated FeO and MgO in the olivine samples as the concentration of FeO and MgO in the NIST612 glass is too low to provide a suitable calibration. There may also be an interference on FeO which renders

NIST612 unsuitable for calibration of this element (Thirlwall et al., in prep). In addition to this, as the remaining elements in the San Carlos were analysed as unknowns, the San Carlos olivines also served as an external standard for checking reproducibility.

A similar equation to the calibration used for the NIST612 glass standard was used for the San Carlos standard calibration of the samples (Equation 7-6), notation as before, with Ratio to  $Si_{SC\ ol}$  being the average of the ratio to Si for element  $x$  in the San Carlos olivine data analysed during that analytical run and Given Value $_{SC\ ol}$  being the concentration of element  $x$  in the literature (Jarosewich, 2002).

**Equation 7-6**

$$[x]_{ol} = \frac{\text{Ratio to } Si_{ol}^x}{\text{Ratio to } Si_{SC\ ol}^x} \times \text{Given Value}_{SC\ ol}^x \times \frac{\text{Calculated } SiO_{2\ ol}}{\text{Given Value } SiO_{2\ SC\ ol}}$$

**Calibration to NMNH 115900**

NMNH 115900 (a USNM labradorite standard) was used in a similar role to the San Carlos olivine standard during the analysis of the plagioclase crystals, as it is matrix matched to the plagioclases being analysed. It provides a more suitable calibration for some of the elements being analysed ( $Fe_2O_3$ , MgO,  $Na_2O$  and  $K_2O$ ), in the majority of cases having a higher concentration of these elements than is present in the NIST612 glass.

The calibration calculation is shown in Equation 7-7. Notation is as detailed before, with Ratio to  $Si_{115900\ plag}$  being the average values of the ratio to Si of element  $x$  in the NMNH115900 plagioclases analysed during the run and Given Value $_{115900\ plag}$  being the accepted published value for the concentration of element  $x$  in the standard (Jarosewich, 2002).

**Equation 7-7**

$$[x]_{plag} = \frac{\text{Ratio to } Si_{plag}^x}{\text{Ratio to } Si_{115900\ plag}^x} \times \text{Given Value}_{115900\ plag}^x \times \frac{SiO_{2\ plag}}{\text{Given value } SiO_{2\ 115900\ plag}}$$

### ***Calibration to NMNH 137041***

NMNH 137041 is a USNM anorthite standard. This standard was used in the same way as NMNH 115900 for plagioclase, but only to calibrate CaO. Being an anorthite standard, NMNH 137041 has a higher concentration of CaO than both the labradorite standard and the NIST612 glass, leading to more accurate calibrations. The calibration is very similar to that given in Equation 7-7 and is shown below Equation 7-8.

#### **Equation 7-8**

$$[CaO]_{plag} = \frac{\text{Ratio to } Si_{plag}^{CaO}}{\text{Ratio to } Si_{137041\ plag}^{CaO}} \times \text{Given Value}_{137041\ plag}^{CaO} \\ \times \frac{SiO_{2\ plag}}{\text{Given } SiO_{2\ 137041\ plag}}$$

### ***Calibration to NMNH 164905***

The chromian augite standard is used to calibrate FeO, MgO, MnO and TiO<sub>2</sub> in the clinopyroxenes. As for the other mineral standards, this allows the use of a matrix matched standard for elements that are more abundant in clinopyroxene than in the NIST612 glass, improving precision. Equation 7-9 is used for calibration of those elements that were ratioed to SiO<sub>2</sub> (FeO, MgO and MnO).

#### **Equation 7-9**

$$[x]_{cpx} = \frac{\text{Ratio to } Si_{cpx}^x}{\text{Ratio to } Si_{164905\ cpx}^x} \times \text{Given Value}_{164905\ cpx}^x \\ \times \frac{\text{Assumed } SiO_{2\ cpx}}{\text{Given value } SiO_{2\ 164905\ cpx}}$$

TiO<sub>2</sub> was initially ratioed to Ca and so the equation is slightly different (Equation 7-10).

#### **Equation 7-10**

$$[x]_{cpx} = \frac{\text{Ratio to } Ca_{cpx}^x}{\text{Ratio to } Ca_{164905\ cpx}^x} \times \text{Given Value}_{164905\ cpx}^x \\ \times \frac{\text{Assumed } CaO_{cpx}}{\text{Given value } CaO_{164905\ cpx}}$$

### *Forsterite and Anorthite Contents*

The forsterite contents obtained were found to be more accurate than the anorthite contents, with 2se on the forsterite content data being between  $\pm 0.1$  and  $0.2$  mol% and 2se on anorthite contents being in the order of  $\pm 0.5$  mol%. This is due to a lower signal intensity being achieved during plagioclase analyses than for olivine analyses. In addition the plagioclase analyses suffered from higher degrees of inter-element fractionation (some elements being transferred to the plasma more easily than others), this effect does not affect Fe and Mg in the olivine analyses, rendering the forsterite content data more accurate.

### *Calculation of SiO<sub>2</sub> in Olivines*

SiO<sub>2</sub> contents in the olivines were calculated using the measured data. This was done by choosing a nominal value to start from (40.8 wt% SiO<sub>2</sub>, similar to the published SiO<sub>2</sub> content of San Carlos olivines of 40.81 wt%). This and the measured FeO and MgO contents were then used to calculate the forsterite content of the olivine for each iteration (where forsterite content is equal to  $100 \times \text{Mg\#}$  and Mg# is molar  $\text{Mg}^{2+}/(\text{Mg}^{2+} + \text{Fe}^{2+})$ ). The SiO<sub>2</sub> was then calculated using the calculated forsterite content from a regression line through wavelength dispersive olivine data from several hundred Icelandic olivines (Thirlwall, unpublished data), using a power law relationship (Equation 7-11).

#### **Equation 7-11**

$$\text{SiO}_2 = 0.0005077 \times Fo^2 + 0.0777627 \times Fo + 29.65$$

This calculated SiO<sub>2</sub> was then used to recalculate the forsterite content of each iteration of the individual olivines.

### *Calculation of SiO<sub>2</sub> and Al<sub>2</sub>O<sub>3</sub> in Plagioclases*

Plagioclase concentrations are harder to calibrate as plagioclase comprises a three component system (albite, anorthite and orthoclase) as opposed to the two end members of olivine (forsterite and fayalite). SiO<sub>2</sub> can be estimated in the plagioclases where anorthite content is thought to be greater than An<sub>20</sub> (Thirlwall et al., in prep), as the orthoclase component can be seen to roughly correlate with An

mol%. Anorthite content is 100\* molar (Ca/Ca+Na+K). The equation below (Equation 7-12) was used to calculate SiO<sub>2</sub> from the average anorthite content.

**Equation 7-12**

$$SiO_2 = -0.24825 \times An + 67.77$$

Al<sub>2</sub>O<sub>3</sub> was also calculated from the averaged anorthite content using Equation 7-13.

**Equation 7-13**

$$Al_2O_3 = -0.16188 \times An + 19.56$$

***Calculation of SiO<sub>2</sub> and CaO in Clinopyroxenes***

SiO<sub>2</sub> in clinopyroxenes is calculated in a different fashion to the other minerals due to the nature of there being multiple clinopyroxene end members. This precludes any estimation based on correlation with ratios. An alternative approach was to use the total weight oxides (Liu *et al.*, 2008). As SiO<sub>2</sub> is a major component of clinopyroxenes, the deficit between a total of 100 wt% and the sum of the other oxides gives an estimate of SiO<sub>2</sub> contents.

CaO is calculated in the same way as other elements, but the assumed CaO composition used to calibrate other analytes is the average of the calculated CaO concentrations. This in an effort to increase internal precision.

***Mean and Estimates of Uncertainty***

The overall composition of each individual crystal analysed was obtained by averaging each iteration measured for each element. In order to provide an estimate of uncertainty on the averages, 2 standard errors (2se) of each average was also calculated (Equation 7-14).

**Equation 7-14**

$$2se = 2 \times \frac{sd}{\sqrt{N}}$$

### ***Removal of Inclusion Data***

Sr, Ba and Nb in the olivine runs were mainly analysed in order to detect the presence of potential inclusions. Where significant peaks in these elements (or any of the remaining analysed major and trace elements) were observed (Figure 7-3), it was assumed to be an inclusion and not representative of the olivine chemistry. Consequently, the iterations containing data from the inclusions were removed from the data, for both the San Carlos standards and the sample olivines. Similarly, if any peaks were observed in the NIST612 glass standards, these were also removed.

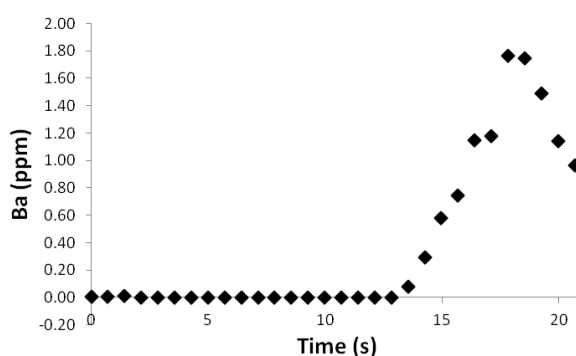


**Figure 7-3 LA-ICP-MS analysis of an olivine from BQ19 showing a significant Ba peak at the end of the analysis. The Ba peak was removed as this clearly represents included material and not the olivine itself.**

In instances where the laser went off crystal, only the iterations which were representative of the phase being analysed (glass or olivine) were used in calculating the average composition of the crystal.

For plagioclases, Pb was mainly used to detect surface contamination. Any other significant peaks in the data were also removed to try and ensure that only concentrations originating from the plagioclases (and standards) were analysed.

For clinopyroxenes, K and Ba were used as indicators of surface contamination and again the standards and the NIST612 analyses were scrutinised and any contamination was removed.

### ***Exclusion of Data Based on Total Oxides***

The respective average total oxide weights of the crystals analysed were calculated. Analyses where this total exceeded 101 wt% were excluded, crystals with an average

total oxide wt% under 98 wt% were also considered to be poor analyses and not considered further.

### ***Drift Corrections***

#### ***Olivines***

Drift corrections were performed on the olivine sample data (not the San Carlos standard data) if the San Carlos olivines were observed to be consistently different to the accepted published values or to drift during the day. All the analysed San Carlos olivine data were plotted on graphs in order of analysis and compared to the published values for each element.

Where the analysed San Carlos olivines were shown to be consistent throughout the analysis day but different to the accepted concentration for a given element, a multiplicative correction was applied to all the sample olivines in runs from that day (Equation 7-15). In Equation 7-15, x is the concentration of chosen element, ol is the sample olivine and SC ol is San Carlos olivine. Average measured<sub>SC ol</sub> is the average of all the San Carlos olivines analysed on that day for the chosen element (whether they were in the specific run being corrected or not).

#### **Equation 7-15**

$$Drift\ corrected_{ol}^x = Measured_{ol}^x \times \frac{Accepted_{SC\ ol}^x}{Average\ measured_{SC\ ol}^x}$$

In instances where the San Carlos data showed drift during a run, the sample olivines were corrected using a subtraction based correction (Equation 7-16). Notation is as above.

#### **Equation 7-16**

$$Drift\ corrected_{ol}^x = Measured_{ol}^x + Accepted_{SC\ ol}^x - (First\ measured_{SC\ ol}^x - (First\ measured_{SC\ ol}^x - Final\ measured_{SC\ ol}^x)) \times Relative\ place\ in\ run$$

Relative place in the run is defined by Equation 7-17. Olivine number and SC ol number is the number of the olivine in the analysis run, with the first analysed crystal being 1, then 2,3 etc..

**Equation 7-17**

$$\text{Relative place in run} = \frac{\text{Olivine number} - \text{First SC ol number}}{\text{Final SC ol number} - \text{First SC ol number}}$$

For any runs where both of the scenarios were present, both corrections were applied.

---

## **8 Appendix 2 – Mineral Data**

---

Mineral data is provided on a CD at the back of this thesis.



---

## References

---

- Anderson, D. L. (2006). Speculations on the nature and cause of mantle heterogeneity. *Tectonophysics* **416**, 7-22.
- Arculus, R. J. (1978). MINERALOGY AND PETROLOGY OF GRENADA, LESSER ANTILLES ISLAND ARC. *Contributions to Mineralogy and Petrology* **65**, 413-424.
- Arculus, R. J. (1994). Aspects of magma genesis in arcs. *Lithos* **33**, 189-208.
- Arculus, R. J. & Wills, K. J. A. (1980). THE PETROLOGY OF PLUTONIC BLOCKS AND INCLUSIONS FROM THE LESSER ANTILLES ISLAND ARC. *Journal of Petrology* **21**, 743-799.
- Baker, P. E. (1984). Geochemical evolution of St Kitts and Montserrat, Lesser Antilles. *Journal of the Geological Society* **141**, 401-411.
- Beattie, P. (1994). SYSTEMATICS AND ENERGETICS OF TRACE-ELEMENT PARTITIONING BETWEEN OLIVINE AND SILICATE MELTS - IMPLICATIONS FOR THE NATURE OF MINERAL MELT PARTITIONING. *Chemical Geology* **117**, 57-71.
- Bédard, J. H. (2006). Trace element partitioning in plagioclase feldspar. *Geochimica Et Cosmochimica Acta* **70**, 3717-3742.
- Berndt, J., Koepke, J. & Holtz, F. (2005). An experimental investigation of the influence of water and oxygen fugacity on differentiation of MORB at 200 MPa. *Journal of Petrology* **46**, 135-167.
- Bezard, R., Davidson, J. P., Turner, S., Macpherson, C. G., Lindsay, J. M. & Boyce, A. J. (2014). Assimilation of sediments embedded in the oceanic arc crust: myth or reality? *Earth and Planetary Science Letters* **395**, 51-60.
- Bindeman, I. N. & Davis, A. M. (2000). Trace element partitioning between plagioclase and melt: investigation of dopant influence on partition behavior. *Geochimica Et Cosmochimica Acta* **64**, 2863-2878.
- Bindeman, I. N., Davis, A. M. & Drake, M. J. (1998). Ion microprobe study of plagioclase-basalt partition experiments at natural concentration levels of trace elements. *Geochimica Et Cosmochimica Acta* **62**, 1175-1193.
- Blundy, J. D. & Wood, B. J. (1991). CRYSTAL-CHEMICAL CONTROLS ON THE PARTITIONING OF SR AND BA BETWEEN PLAGIOCLASE FELDSPAR, SILICATE MELTS, AND HYDROTHERMAL SOLUTIONS. *Geochimica Et Cosmochimica Acta* **55**, 193-209.
- Bouvier, A.-S., Métrich, N. & Deloule, E. (2008). Slab-Derived Fluids in the Magma Sources of St. Vincent (Lesser Antilles Arc): Volatile and Light Element Imprints. *Journal of Petrology* **49**, 1427-1448.
- Bouvier, A. S., Deloule, E. & Métrich, N. (2010). Fluid Inputs to Magma Sources of St. Vincent and Grenada (Lesser Antilles): New Insights from Trace Elements in Olivine-hosted Melt Inclusions. *Journal of Petrology* **51**, 1597-1615.
- Bouysse, P. (1984). The Lesser Antilles island arc; structure and geodynamic evolution. *Initial reports of the Deep Sea Drilling Project covering Leg 78A of the cruises of the drilling vessel Glomar*

*Challenger, San Juan, Puerto Rico to San Juan, Puerto Rico, February-March 1981; and covering Leg 78B of the cruises of the drilling vessel Glomar Challenger, San Juan, Puerto Rico to Las Palmas, Grand Canary Island, March-April, 1981, 78A-78B, 83-103.*

Bouysse, P., Westercamp, D. & Andreieff, P. (1990). The Lesser Antilles island arc. *Proceedings of the Ocean Drilling Program; Barbados Ridge; covering Leg 110 of the cruises of the drilling vessel JOIDES Resolution, Bridgetown, Barbados to Bridgetown, Barbados, sites 671-676, 19 June 1986-16 August 1986* **110**, 29-44.

Brown, G. M., Holland, J. G., Sigurdsson, H., Tomblin, J. F. & Arculus, R. J. (1977). Geochemistry of the Lesser Antilles volcanic island arc. *Geochimica Et Cosmochimica Acta* **41**, 785-801.

Carpentier, M., Chauvel, C. & Mattielli, N. (2008). Pb-Nd isotopic constraints on sedimentary input into the Lesser Antilles arc system. *Earth and Planetary Science Letters* **272**, 199-211.

Carpentier, M., Chauvel, C., Maury, R. C. & Mattielli, N. (2009). The "zircon effect" as recorded by the chemical and Hf isotopic compositions of Lesser Antilles forearc sediments. *Earth and Planetary Science Letters* **287**, 86-99.

Cashman, K. & Blundy, J. (2000). *Degassing and crystallization of ascending andesite and dacite.*

Castillo, P. R. (2006). An overview of adakite petrogenesis. *Chinese Science Bulletin* **51**, 258-268.

Cawthorn, R. G., Curran, E. B. & Arculus, R. J. (1973). PETROGENETIC MODEL FOR ORIGIN OF CALC-ALKALINE SUITE OF GRENADA, LESSER ANTILLES. *Journal of Petrology* **14**, 327-337.

Chakraborty, S. (2010). Diffusion Coefficients in Olivine, Wadsleyite and Ringwoodite. *Diffusion in Minerals and Melts*, 603-639.

Chase, R. L. & Bunce, E. T. (1969). Underthrusting of the Eastern Margin of the Antilles by the floor of the western North Atlantic Ocean, and origin of the Barbados Ridge. *Journal of Geophysical Research* **74**, 1413-1420.

Cherniak, D. J. (2003). REE diffusion in feldspar. *Chemical Geology* **193**, 25-41.

Coogan, L. A., Hain, A., Stahl, S. & Chakraborty, S. (2005). Experimental determination of the diffusion coefficient for calcium in olivine between 900 degrees C and 1500 degrees C. *Geochimica Et Cosmochimica Acta* **69**, 3683-3694.

Couch, S., Harford, C. L., Sparks, R. S. J. & Carroll, M. R. (2003a). Experimental constraints on the conditions of formation of highly calcic plagioclase microlites at the Soufriere Hills Volcano, Montserrat. *Journal of Petrology* **44**, 1455-1475.

Couch, S., Sparks, R. S. J. & Carroll, M. R. (2003b). The kinetics of degassing-induced crystallization at Soufriere Hills volcano, Montserrat. *Journal of Petrology* **44**, 1477-1502.

Coulon, C., Clocchiatti, R., Maury, R. C. & Westercamp, D. (1984). Petrology of basaltic xenoliths in andesitic to dacitic host lavas from Martinique (lesser antilles): Evidence for magma mixing. *Bulletin Volcanologique* **47**, 705-734.

Danyushevsky, L. V., Carroll, M. R. & Falloon, T. J. (1997). Origin of high-An plagioclase in Tongan high-Ca boninites: Implications for plagioclase-melt equilibria at low P(H<sub>2</sub>O). *Canadian Mineralogist* **35**, 313-326.

- Davidson, J. (1985). Mechanisms of contamination in Lesser Antilles island arc magmas from radiogenic and oxygen isotope relationships. *Earth and Planetary Science Letters* **72**, 163-174.
- Davidson, J., Turner, S., Handley, H., Macpherson, C. & Dosseto, A. (2007a). Amphibole “sponge” in arc crust? *Geology* **35**, 787-790.
- Davidson, J. & Wilson, M. (2011). Differentiation and Source Processes at Mt Pelee and the Quill; Active Volcanoes in the Lesser Antilles Arc. *Journal of Petrology* **52**, 1493-1531.
- Davidson, J. P. (1986). Isotopic and trace element constraints on the petrogenesis of subduction-related lavas from Martinique, Lesser Antilles. *Journal of Geophysical Research: Solid Earth* **91**, 5943-5962.
- Davidson, J. P. (1987). Crustal contamination versus subduction zone enrichment: Examples from the Lesser Antilles and implications for mantle source compositions of island arc volcanic rocks. *Geochimica Et Cosmochimica Acta* **51**, 2185-2198.
- Davidson, J. P. (1996). Deciphering Mantle and Crustal Signatures in Subduction Zone Magmatism. *Subduction Top to Bottom: American Geophysical Union*, 251-262.
- Davidson, J. P. & Harmon, R. S. (1989). Oxygen isotope constraints on the petrogenesis of volcanic arc magmas from Martinique, Lesser Antilles. *Earth and Planetary Science Letters* **95**, 255-270.
- Davidson, J. P., Hora, J. M., Garrison, J. M. & Dungan, M. A. (2005). Crustal forensics in arc magmas. *Journal of Volcanology and Geothermal Research* **140**, 157-170.
- Davidson, J. P., Morgan, D. J., Charlier, B. L. A., Harlou, R. & Hora, J. M. (2007b). Microsampling and isotopic analysis of igneous rocks: Implications for the study of magmatic systems. *Annual Review of Earth and Planetary Sciences*, 273-311.
- Davies, J. H. & Stevenson, D. J. (1992). Physical model of source region of subduction zone volcanics. *Journal of Geophysical Research: Solid Earth* **97**, 2037-2070.
- De Hoog, J. C. M., Gall, L. & Cornell, D. H. (2010). Trace-element geochemistry of mantle olivine and application to mantle petrogenesis and geothermobarometry. *Chemical Geology* **270**, 196-215.
- Defant, M. J. & Drummond, M. S. (1990). DERIVATION OF SOME MODERN ARC MAGMAS BY MELTING OF YOUNG SUBDUCTED LITHOSPHERE. *Nature* **347**, 662-665.
- Devine, J. D. & Sigurdsson, H. (1995). Petrology and eruption styles of Kick'em-Jenny submarine volcano, Lesser Antilles island arc. *Journal of Volcanology and Geothermal Research* **69**, 35-58.
- Dohmen, R., Becker, H. W. & Chakraborty, S. (2007). Fe-Mg diffusion in olivine I: experimental determination between 700 and 1,200 degrees C as a function of composition, crystal orientation and oxygen fugacity. *Physics and Chemistry of Minerals* **34**, 389-407.
- Dunn, T. (1987). Partitioning of Hf, Lu, Ti, and Mn between olivine, clinopyroxene and basaltic liquid. *Contributions to Mineralogy and Petrology* **96**, 476-484.
- Eggins, S. M. (1992). PETROGENESIS OF HAWAIIAN THOLEIITES - .1. PHASE-EQUILIBRIA CONSTRAINTS. *Contributions to Mineralogy and Petrology* **110**, 387-397.
- Elburg, M., Kamenetsky, V. S., Nikogosian, I., Foden, J. & Sobolev, A. V. (2006a). Coexisting high- and low-calcium melts identified by mineral and melt inclusion studies of a subduction-influenced syncollisional magma from South Sulawesi, Indonesia. *Journal of Petrology* **47**, 2433-2462.

- Elburg, M. A., Kamenetsky, V. S., Arculus, R. & Thomas, R. (2006b). Low-calcium olivine crystals in subduction-related magmas: Messengers from the mantle or the magma chamber? *Geochimica Et Cosmochimica Acta* **70**, A157-A157.
- Falloon, T. J., Danyushevsky, L. V., Crawford, A. J., Meffre, S., Woodhead, J. D. & Bloomer, S. H. (2008). Boninites and Adakites from the Northern Termination of the Tonga Trench: Implications for Adakite Petrogenesis. *Journal of Petrology* **49**, 697-715.
- Farver, J. R. (2010). Oxygen and Hydrogen Diffusion in Minerals. In: Zhang, Y. X. & Cherniak, D. J. (eds.) *Diffusion in Minerals and Melts*. Chantilly: Mineralogical Soc Amer, 447-507.
- Feig, S. T., Koepke, J. & Snow, J. E. (2006). Effect of water on tholeiitic basalt phase equilibria: an experimental study under oxidizing conditions. *Contributions to Mineralogy and Petrology* **152**, 611-638.
- Ford, C. E., Russell, D. G., Craven, J. A. & Fisk, M. R. (1983). OLIVINE LIQUID EQUILIBRIA - TEMPERATURE, PRESSURE AND COMPOSITION DEPENDENCE OF THE CRYSTAL LIQUID CATION PARTITION-COEFFICIENTS FOR MG, FE-2+, CA AND MN. *Journal of Petrology* **24**, 256-265.
- Gaetani, G. A. & Grove, T. L. (2013). Experimental Constraints on Melt Generation in the Mantle Wedge. *Inside the Subduction Factory*: American Geophysical Union, 107-134.
- Garrison, J. M. & Davidson, J. P. (2003). Dubious case for slab melting in the Northern volcanic zone of the Andes. *Geology* **31**, 565-568.
- Graham, A. M. (1980). Genesis of the igneous rock suites of Grenada, Lesser Antilles. University of Edinburgh.
- Grove, T. L., Till, C. B., Lev, E., Chatterjee, N. & Medard, E. (2009). Kinematic variables and water transport control the formation and location of arc volcanoes. *Nature* **459**, 694-697.
- Hamada, M. & Fujii, T. (2007). H<sub>2</sub>O-rich island arc low-K tholeiite magma inferred from Ca-rich plagioclase-melt inclusion equilibria. *Geochemical Journal* **41**, 437-461.
- Hammer, Ø., Harper, D. A. T. & Ryan, P. D. (2001). PAST: Paleontological statistics software package for education and data analysis. *Palaeontologia Electronica* **4**, 99-107.
- Hart, S. R. (1984). A large-scale isotope anomaly in the Southern Hemisphere mantle. *Nature* **309**, 753-757.
- Hawkesworth, C. J., Gallagher, K., Hergt, J. M. & Dermott, F. M. (1993a). Trace Element Fractionation Processes in the Generation of Island Arc Basalts. *Philosophical Transactions of the Royal Society of London. Series A: Physical and Engineering Sciences* **342**, 179-191.
- Hawkesworth, C. J., Gallagher, K., Hergt, J. M. & McDermott, F. (1993b). Mantle and Slab Contributions in ARC Magmas. *Annual Review of Earth and Planetary Sciences* **21**, 175-204.
- Hawkesworth, C. J., O'Nions, R. K. & Arculus, R. J. (1979). Nd and Sr isotope geochemistry of island arc volcanics, Grenada, Lesser Antilles. *Earth and Planetary Science Letters* **45**, 237-248.
- Hawkesworth, C. J., Turner, S. P., McDermott, F., Peate, D. W. & van Calsteren, P. (1997). U-Th Isotopes in Arc Magmas: Implications for Element Transfer from the Subducted Crust. *Science* **276**, 551-555.

- Heath, E., Macdonald, R., Belkin, H., Hawkesworth, C. & Sigurdsson, H. (1998a). Magmagenesis at Soufriere Volcano, St Vincent, Lesser Antilles Arc. *Journal of Petrology* **39**, 1721-1764.
- Heath, E., Turner, S. P., Macdonald, R., Hawkesworth, C. J. & van Calsteren, P. (1998b). Long magma residence times at an island arc volcano (Soufriere, St. Vincent) in the Lesser Antilles: evidence from U-238-Th-230 isochron dating (vol 160, pg 49, 1998). *Earth and Planetary Science Letters* **163**, 413-413.
- Hellebrand, E., Snow, J. E., Hoppe, P. & Hofmann, A. W. (2002). Garnet-field melting and late-stage refertilization in 'residual' abyssal peridotites from the Central Indian Ridge. *Journal of Petrology* **43**, 2305-2338.
- Higuchi, H. & Nagasawa, H. (1969). Partition of trace elements between rock-forming minerals and the host volcanic rocks. *Earth and Planetary Science Letters* **7**, 281-287.
- Hirano, N., Yamamoto, J., Kagi, H. & Ishii, T. (2004). Young, olivine xenocryst-bearing alkali-basalt from the oceanward slope of the Japan Trench. *Contributions to Mineralogy and Petrology* **148**, 47-54.
- James, D. E. (1981). THE COMBINED USE OF OXYGEN AND RADIOGENIC ISOTOPES AS INDICATORS OF CRUSTAL CONTAMINATION. *Annual Review of Earth and Planetary Sciences* **9**, 311-344.
- Jarosewich, E. (2002). Smithsonian microbeam standards. *JOURNAL OF RESEARCH-NATIONAL INSTITUTE OF STANDARDS AND TECHNOLOGY* **107**, 681-686.
- Jurewicz, A. J. G. & Watson, E. B. (1988a). CATIONS IN OLIVINE .1. CALCIUM PARTITIONING AND CALCIUM-MAGNESIUM DISTRIBUTION BETWEEN OLIVINES AND COEXISTING MELTS, WITH PETROLOGIC APPLICATIONS. *Contributions to Mineralogy and Petrology* **99**, 176-185.
- Jurewicz, A. J. G. & Watson, E. B. (1988b). CATIONS IN OLIVINE .2. DIFFUSION IN OLIVINE XENOCRYSTS, WITH APPLICATIONS TO PETROLOGY AND MINERAL PHYSICS. *Contributions to Mineralogy and Petrology* **99**, 186-201.
- Kamenetsky, V. S., Elburg, M., Arculus, R. & Thomas, R. (2006). Magmatic origin of low-Ca olivine in subduction-related magmas: Co-existence of contrasting magmas. *Chemical Geology* **233**, 346-357.
- Kamenetsky, V. S., Sobolev, A. V., Eggins, S. M., Crawford, A. J. & Arculus, R. J. (2002). Olivine-enriched melt inclusions in chromites from low-Ca boninites, Cape Vogel, Papua New Guinea: evidence for ultramafic primary magma, refractory mantle source and enriched components. *Chemical Geology* **183**, 287-303.
- Kelemen, P. B., Shimizu, N. & Dunn, T. (1993). RELATIVE DEPLETION OF NIOBIUM IN SOME ARC MAGMAS AND THE CONTINENTAL-CRUST - PARTITIONING OF K, NB, LA AND CE DURING MELT/ROCK REACTION IN THE UPPER-MANTLE. *Earth and Planetary Science Letters* **120**, 111-134.
- Klemme, S., Blundy, J. D. & Wood, B. J. (2002). Experimental constraints on major and trace element partitioning during partial melting of eclogite. *Geochimica Et Cosmochimica Acta* **66**, 3109-3123.

- KloECKE, W. & PALME, H. (1988). Partitioning of siderophile and chalcophile elements between sulfide, olivine, and glass in a naturally reduced basalt from Disko Island, Greenland. In: Ryder, G. (ed.) *Proceedings of the Lunar and Planetary Science Conference*. New York: Pergamon, 471-483.
- Labanieh, S., Chauvel, C., Germa, A. & Quidelleur, X. (2012). Martinique: a Clear Case for Sediment Melting and Slab Dehydration as a Function of Distance to the Trench. *Journal of Petrology* **53**, 2441-2464.
- Labanieh, S., Chauvel, C., Germa, A., Quidelleur, X. & Lewin, E. (2010). Isotopic hyperbolas constrain sources and processes under the Lesser Antilles arc. *Earth and Planetary Science Letters* **298**, 35-46.
- Lambart, S., Laporte, D., Provost, A. & Schiano, P. (2012). Fate of Pyroxenite-derived Melts in the Peridotitic Mantle: Thermodynamic and Experimental Constraints. *Journal of Petrology* **53**, 451-476.
- Le Bas, M. J., Le Maitre, R. W., Streckeisen, A., Zanettin, B. & Rocks, I. S. o. t. S. o. I. (1986). A Chemical Classification of Volcanic Rocks Based on the Total Alkali-Silica Diagram. *Journal of Petrology* **27**, 745-750.
- Leat, P. T. & Larter, R. D. (2003). Intra-oceanic subduction systems: introduction. *Geological Society, London, Special Publications* **219**, 1-17.
- Leeman, W. P. & Scheidegger, K. F. (1977). OLIVINE-LIQUID DISTRIBUTION COEFFICIENTS AND A TEST FOR CRYSTAL-LIQUID EQUILIBRIUM. *Earth and Planetary Science Letters* **35**, 247-257.
- Liu, Y., Hu, Z., Gao, S., Günther, D., Xu, J., Gao, C. & Chen, H. (2008). In situ analysis of major and trace elements of anhydrous minerals by LA-ICP-MS without applying an internal standard. *Chemical Geology* **257**, 34-43.
- Longerich, H. P., Günther, D. & Jackson, S. E. (1996). Elemental fractionation in laser ablation inductively coupled plasma mass spectrometry. *Fresenius' Journal of Analytical Chemistry* **355**, 538-542.
- Ludden, J. N., Rui, F., Gauthier, G., Stix, J., Lang, S., Francis, D., Machado, N. & Wu, G. (1995). Applications of LAM-ICP-MS analysis to minerals. *The Canadian Mineralogist* **33**, 419-434.
- Lundstrom, C. C. & Tepley, F. J. (2006). Investigating the origin of anorthitic plagioclase through a combination of experiments and natural observations. *Journal of Volcanology and Geothermal Research* **157**, 202-221.
- MacDonald, G. A. (1968). Composition and origin of Hawaiian lavas. *Memoirs of the Geological Society of America* **116**, 477-522.
- Macdonald, R., Hawkesworth, C. J. & Heath, E. (2000). The Lesser Antilles volcanic chain: a study in arc magmatism. *Earth-Science Reviews* **49**, 1-76.
- Marschall, H. R. & Schumacher, J. C. (2012). Arc magmas sourced from melange diapirs in subduction zones. *Nature Geosci* **5**, 862-867.
- Mattey, D., Lowry, D. & Macpherson, C. (1994). OXYGEN-ISOTOPE COMPOSITION OF MANTLE PERIDOTITE. *Earth and Planetary Science Letters* **128**, 231-241.

- McDonough, W. F. (1991). PARTIAL MELTING OF SUBDUCTED OCEANIC-CRUST AND ISOLATION OF ITS RESIDUAL ECLOGITIC LITHOLOGY. *Philosophical Transactions of the Royal Society of London Series a-Mathematical Physical and Engineering Sciences* **335**, 407-418.
- Middlemost, E. A. K. (1989). Iron oxidation ratios, norms and the classification of volcanic rocks. *Chemical Geology* **77**, 19-26.
- Mueller, W., Shelley, M., Miller, P. & Broude, S. (2009). Initial performance metrics of a new custom-designed ArF excimer LA-ICPMS system coupled to a two-volume laser-ablation cell. *Journal of Analytical Atomic Spectrometry* **24**, 209-214.
- Nakamura, N. (1974). Determination of REE, Ba, Fe, Mg, Na and K in carbonaceous and ordinary chondrites. *Geochimica Et Cosmochimica Acta* **38**, 757-775.
- Neill, I., Kerr, A. C., Hastie, A. R., Stanek, K. P. & Millar, I. L. (2011). Origin of the Aves Ridge and Dutch-Venezuelan Antilles: interaction of the Cretaceous 'Great Arc' and Caribbean-Colombian Oceanic Plateau? *Journal of the Geological Society* **168**, 333-347.
- Nelson, S. T. & Montana, A. (1992). SIEVE-TEXTURED PLAGIOCLASE IN VOLCANIC-ROCKS PRODUCED BY RAPID DECOMPRESSION. *American Mineralogist* **77**, 1242-1249.
- Nichols, G. T., Wyllie, P. J. & Stern, C. R. (1994). Subduction zone melting of pelagic sediments constrained by melting experiments. *Nature* **371**, 785-788.
- Nimis, P. (1995). A clinopyroxene geobarometer for basaltic systems based on crystal-structure modeling. *Contributions to Mineralogy and Petrology* **121**, 115-125.
- Nimis, P. & Taylor, W. R. (2000). Single clinopyroxene thermobarometry for garnet peridotites. Part I. Calibration and testing of a Cr-in-Cpx barometer and an enstatite-in-Cpx thermometer. *Contributions to Mineralogy and Petrology* **139**, 541-554.
- Panjasawatwong, Y., Danyushevsky, L. V., Crawford, A. J. & Harris, K. L. (1995). AN EXPERIMENTAL-STUDY OF THE EFFECTS OF MELT COMPOSITION ON PLAGIOCLASE - MELT EQUILIBRIA AT 5-KBAR AND 10-KBAR - IMPLICATIONS FOR THE ORIGIN OF MAGMATIC HIGH-AN PLAGIOCLASE. *Contributions to Mineralogy and Petrology* **118**, 420-432.
- Parkinson, I. J., Arculus, R. J. & Eggins, S. M. (2003). Peridotite xenoliths from Grenada, Lesser Antilles Island Arc. *Contributions to Mineralogy and Petrology* **146**, 241-262.
- Peacock, S. A. (1990). Fluid Processes in Subduction Zones. *Science* **248**, 329-337.
- Peacock, S. M. (1996). Thermal and Petrologic Structure of Subduction Zones. *Subduction Top to Bottom*: American Geophysical Union, 119-133.
- Peacock, S. M., Rushmer, T. & Thompson, A. B. (1994). Partial melting of subducting oceanic crust. *Earth and Planetary Science Letters* **121**, 227-244.
- Pearce, J. A. & Peate, D. W. (1995). Tectonic Implications of the Composition of Volcanic ARC Magmas. *Annual Review of Earth and Planetary Sciences* **23**, 251-285.
- Petry, C., Chakraborty, S. & Palme, H. (2004). Experimental determination of Ni diffusion coefficients in olivine and their dependence on temperature, composition, oxygen fugacity, and crystallographic orientation. *Geochimica Et Cosmochimica Acta* **68**, 4179-4188.

- Pichavant, M. & Macdonald, R. (2003). Mantle genesis and crustal evolution of primitive calc-alkaline basaltic magmas from the Lesser Antilles arc. *Geological Society, London, Special Publications* **219**, 239-254.
- Pichavant, M. & Macdonald, R. (2007). Crystallization of primitive basaltic magmas at crustal pressures and genesis of the calc-alkaline igneous suite: experimental evidence from St Vincent, Lesser Antilles arc. *Contributions to Mineralogy and Petrology* **154**, 535-558.
- Pichavant, M., Martel, C., Bourdier, J. L. & Scaillet, B. (2002a). Physical conditions, structure, and dynamics of a zoned magma chamber: Mount Pelee (Martinique, Lesser Antilles Arc). *Journal of Geophysical Research-Solid Earth* **107**.
- Pichavant, M., Mysen, B. O. & Macdonald, R. (2002b). Source and H<sub>2</sub>O content of high-MgO magmas in island arc settings: An experimental study of a primitive calc-alkaline basalt from St. Vincent, Lesser Antilles arc. *Geochimica Et Cosmochimica Acta* **66**, 2193-2209.
- Plank, T. & Langmuir, C. H. (1993). Tracing trace elements from sediment input to volcanic output at subduction zones. *Nature* **362**, 739-743.
- Putirka, K. & Condit, C. D. (2003). Cross section of a magma conduit system at the margin of the Colorado Plateau. *Geology* **31**, 701-704.
- Putirka, K. D. (2008). Thermometers and Barometers for Volcanic Systems. In: Putirka, K. D. & Tepley, F. J. (eds.) *Minerals, Inclusions and Volcanic Processes*. Chantilly: Mineralogical Soc Amer, 61-120.
- Rapp, R. P., Shimizu, N. & Norman, M. D. (2003). Growth of early continental crust by partial melting of eclogite. *Nature* **425**, 605-609.
- Rapp, R. P., Shimizu, N., Norman, M. D. & Applegate, G. S. (1999). Reaction between slab-derived melts and peridotite in the mantle wedge: experimental constraints at 3.8 GPa. *Chemical Geology* **160**, 335-356.
- Ren, M. H., Parker, D. F. & White, J. C. (2003). Partitioning of Sr, Ba, Rb, Y, and LREE between plagioclase and peraluminous silicic magma. *American Mineralogist* **88**, 1091-1103.
- Renjith, M. L. (2013). Micro-textures in plagioclase from 1994–1995 eruption, Barren Island Volcano: Evidence of dynamic magma plumbing system in the Andaman subduction zone. *Geoscience Frontiers*.
- Roeder, P. L. & Emslie, R. F. (1970). OLIVINE-LIQUID EQUILIBRIUM. *Contributions to Mineralogy and Petrology* **29**, 275-&.
- Salters, V. J. M. & Stracke, A. (2004). Composition of the depleted mantle. *Geochemistry, Geophysics, Geosystems* **5**, Q05B07.
- Sato, H. (1977). NICKEL CONTENT OF BASALTIC MAGMAS - IDENTIFICATION OF PRIMARY MAGMAS AND A MEASURE OF DEGREE OF OLIVINE FRACTIONATION. *Lithos* **10**, 113-120.
- Schilling, G. D., Andrade, F. J., Barnes, Sperline, R. P., Denton, M. B., Barinaga, C. J., Koppenaar, D. W. & Hieftje, G. M. (2007). Continuous Simultaneous Detection in Mass Spectrometry. *Analytical Chemistry* **79**, 7662-7668.

- Sekine, T. & Wyllie, P. J. (1982a). SYNTHETIC SYSTEMS FOR MODELING HYBRIDIZATION BETWEEN HYDROUS SILICEOUS MAGMAS AND PERIDOTITE IN SUBDUCTION ZONES. *Journal of Geology* **90**, 734-741.
- Sekine, T. & Wyllie, P. J. (1982b). THE SYSTEM GRANITE-PERIDOTITE-H<sub>2</sub>O AT 30 KBAR, WITH APPLICATIONS TO HYBRIDIZATION IN SUBDUCTION ZONE MAGMATISM. *Contributions to Mineralogy and Petrology* **81**, 190-202.
- Simakin, A. G. & Salova, T. P. (2004). Plagioclase crystallization from a hawaiitic melt in experiments and in a volcanic conduit. *Petrology* **12**, 82-92.
- Sisson, T. W. & Grove, T. L. (1993). EXPERIMENTAL INVESTIGATIONS OF THE ROLE OF H<sub>2</sub>O IN CALC-ALKALINE DIFFERENTIATION AND SUBDUCTION ZONE MAGMATISM. *Contributions to Mineralogy and Petrology* **113**, 143-166.
- Smith, T. E., Thirlwall, M. F. & Macpherson, C. (1996). Trace Element and Isotope Geochemistry of the Volcanic Rocks of Bequia, Grenadine Islands, Lesser Antilles Arc: a Study of Subduction Enrichment and Intra-crustal Contamination. *Journal of Petrology* **37**, 117-143.
- SOBOLEV, A. V. & DANYUSHEVSKY, L. V. (1994). Petrology and Geochemistry of Boninites from the North Termination of the Tonga Trench: Constraints on the Generation Conditions of Primary High-Ca Boninite Magmas. *Journal of Petrology* **35**, 1183-1211.
- Sobolev, A. V., Hofmann, A. W., Kuzmin, D. V., Yaxley, G. M., Arndt, N. T., Chung, S.-L., Danyushevsky, L. V., Elliott, T., Frey, F. A., Garcia, M. O., Gurenko, A. A., Kamenetsky, V. S., Kerr, A. C., Krivolutsкая, N. A., Matvienkov, V. V., Nikogosian, I. K., Rocholl, A., Sigurdsson, I. A., Sushchevskaya, N. M. & Teklay, M. (2007). The amount of recycled crust in sources of mantle-derived melts. *Science* **316**, 412-417.
- Speed, R. C. & Larue, D. K. (1982). Barbados: Architecture and implications for accretion. *Journal of Geophysical Research: Solid Earth* **87**, 3633-3643.
- Stamper, C. C., Blundy, J. D., Arculus, R. J. & Melekhova, E. (2014). Petrology of Plutonic Xenoliths and Volcanic Rocks from Grenada, Lesser Antilles. *Journal of Petrology* **55**, 1353-1387.
- Stolper, E. & Newman, S. (1994). The role of water in the petrogenesis of Mariana trough magmas. *Earth and Planetary Science Letters* **121**, 293-325.
- Sun, C. & Liang, Y. (2012). Distribution of REE between clinopyroxene and basaltic melt along a mantle adiabat: effects of major element composition, water, and temperature. *Contributions to Mineralogy and Petrology* **163**, 807-823.
- Takagi, D., Sato, H. & Nakagawa, M. (2005). Experimental study of a low-alkali tholeiite at 1-5 kbar: optimal condition for the crystallization of high-An plagioclase in hydrous arc tholeiite. *Contributions to Mineralogy and Petrology* **149**, 527-540.
- Tatsumi, Y. & Eggins, S. M. (1995). *Subduction Zone Magmatism*. Cambridge: Blackwell.
- Tatsumi, Y. & Kogiso, T. (2003). The subduction factory: its role in the evolution of the Earth's crust and mantle. *Geological Society, London, Special Publications* **219**, 55-80.
- TAYLOR, R. N., NESBITT, R. W., VIDAL, P., HARMON, R. S., AUVRAY, B. & CROUDACE, I. W. (1994). Mineralogy, Chemistry, and Genesis of the Boninite Series Volcanics, Chichijima, Bonin Islands, Japan. *Journal of Petrology* **35**, 577-617.

- Thirlwall, M. F. (1991a). High-precision multicollector isotopic analysis of low levels of Nd as oxide. *Chemical Geology* **94**, 13-22.
- Thirlwall, M. F. (1991b). Long-term reproducibility of multicollector Sr and Nd isotope ratio analysis. *Chemical Geology: Isotope Geoscience section* **94**, 85-104.
- Thirlwall, M. F. (2002). Multicollector ICP-MS analysis of Pb isotopes using a 207pb-204pb double spike demonstrates up to 400 ppm/amu systematic errors in Tl-normalization. *Chemical Geology* **184**, 255-279.
- Thirlwall, M. F. & Graham, A. M. (1984). Evolution of high-Ca, high-Sr C-series basalts from Grenada, Lesser Antilles: the effects of intra-crustal contamination. *Journal of the Geological Society* **141**, 427-445.
- Thirlwall, M. F., Graham, A. M., Arculus, R. J., Harmon, R. S. & Macpherson, C. G. (1996). Resolution of the effects of crustal assimilation, sediment subduction, and fluid transport in island arc magmas: Pb · Sr · Nd · O isotope geochemistry of Grenada, Lesser Antilles. *Geochimica Et Cosmochimica Acta* **60**, 4785-4810.
- Thirlwall, M. F., Smith, T. E., Graham, A. M., Theodorou, N., Hollings, P., Davidson, J. P. & Arculus, R. J. (1994a). High Field Strength Element Anomalies in Arc Lavas: Source or Process? *Journal of Petrology* **35**, 819-838.
- Thirlwall, M. F., Upton, B. G. J. & Jenkins, C. (1994b). Interaction between Continental Lithosphere and the Iceland Plume—Sr-Nd-Pb Isotope Geochemistry of Tertiary Basalts, NE Greenland. *Journal of Petrology* **35**, 839-879.
- Tollan, P. M. E., Bindeman, I. & Blundy, J. D. (2012). Cumulate xenoliths from St. Vincent, Lesser Antilles Island Arc: a window into upper crustal differentiation of mantle-derived basalts. *Contributions to Mineralogy and Petrology* **163**, 189-208.
- Toothill, J., Williams, C. A., Macdonald, R., Turner, S. P., Rogers, N. W., Hawkesworth, C. J., Jerram, D. A., Ottley, C. J. & Tindle, A. G. (2007). A complex petrogenesis for an arc magmatic suite, St Kitts, Lesser Antilles. *Journal of Petrology* **48**, 3-42.
- Turner, S., George, R., Jerram, D. A., Carpenter, N. & Hawkesworth, C. (2003). Case studies of plagioclase growth and residence times in island arc lavas from Tonga and the Lesser Antilles, and a model to reconcile discordant age information. *Earth and Planetary Science Letters* **214**, 279-294.
- Turner, S., Hawkesworth, C., van Calsteren, P., Heath, E., Macdonald, R. & Black, S. (1996). U-series isotopes and destructive plate margin magma genesis in the Lesser Antilles. *Earth and Planetary Science Letters* **142**, 191-207.
- Van Soest, M. C., Hilton, D. R., Macpherson, C. G. & Matthey, D. P. (2002). Resolving sediment subduction and crustal contamination in the Lesser Antilles island Arc: A combined He-O-Sr isotope approach. *Journal of Petrology* **43**, 143-170.
- Vannucci, R., Tiepolo, M., Defant, M. J. & Kepezhinskas, P. (2007). The metasomatic record in the shallow peridotite mantle beneath Grenada (Lesser Antilles arc). *Lithos* **99**, 25-44.
- Viccaro, M., Giacomoni, P. P., Ferlito, C. & Cristofolini, R. (2010). Dynamics of magma supply at Mt. Etna volcano (Southern Italy) as revealed by textural and compositional features of plagioclase phenocrysts. *Lithos* **116**, 77-91.

- Wadge, G. (1984). Comparison of volcanic production rates and subduction rates in the Lesser Antilles and Central America. *Geology* **12**, 555-558.
- Wadge, G. & Shepherd, J. B. (1984). Segmentation of the Lesser Antilles subduction zone. *Earth and Planetary Science Letters* **71**, 297-304.
- Walter, M. J. (1998). Melting of garnet peridotite and the origin of komatiite and depleted lithosphere. *Journal of Petrology* **39**, 29-60.
- Watson, E. B. (1977). PARTITIONING OF MANGANESE BETWEEN FORSTERITE AND SILICATE LIQUID. *Geochimica Et Cosmochimica Acta* **41**, 1363-1374.
- Westbrook, G. K., Ladd, J. W., Buhl, P., Bangs, N. & Tiley, G. J. (1988). Cross section of an accretionary wedge: Barbados Ridge complex. *Geology* **16**, 631-635.
- Westbrook, G. K., Mascle, A. & Biju-Duval, B. (1984). Geophysics and the structure of the Lesser Antilles Forearc. *Initial reports of the Deep Sea Drilling Project covering Leg 78A of the cruises of the drilling vessel Glomar Challenger, San Juan, Puerto Rico to San Juan, Puerto Rico, February-March 1981; and covering Leg 78B of the cruises of the drilling vessel Glomar Challenger, San Juan, Puerto Rico to Las Palmas, Grand Canary Island, March-April, 1981*, **78A-78B**, 23-38.
- White, W. M. & Dupre, B. (1986). SEDIMENT SUBDUCTION AND MAGMA GENESIS IN THE LESSER ANTILLES - ISOTOPIC AND TRACE-ELEMENT CONSTRAINTS. *Journal of Geophysical Research-Solid Earth and Planets* **91**, 5927-5941.
- White, W. M., Dupré, B. & Vidal, P. (1985). Isotope and trace element geochemistry of sediments from the Barbados Ridge-Demerara Plain region, Atlantic Ocean. *Geochimica Et Cosmochimica Acta* **49**, 1875-1886.
- Wood, B. J. & Blundy, J. D. (1997). A predictive model for rare earth element partitioning between clinopyroxene and anhydrous silicate melt. *Contributions to Mineralogy and Petrology* **129**, 166-181.
- Wood, B. J. & Blundy, J. D. (2002). The effect of H<sub>2</sub>O on crystal-melt partitioning of trace elements. *Geochimica Et Cosmochimica Acta* **66**, 3647-3656.
- Workman, R. K. & Hart, S. R. (2005). Major and trace element composition of the depleted MORB mantle (DMM). *Earth and Planetary Science Letters* **231**, 53-72.
- Young, S. R., Norton, G. E., Francis, P. W., Barclay, J., Casadevall, T. J., Gardner, C. A., Darroux, B., Davies, A., Delmelle, P. & Maciejewski, A. J. H. (1998). *Monitoring SO<sub>2</sub> Emission at the Soufriere Hills Volcano: Implications for Changes in Eruptive Conditions: Geophysical Research Letters* **25(19)** 1998.
- Zhao, Z.-F. & Zheng, Y.-F. (2003). Calculation of oxygen isotope fractionation in magmatic rocks. *Chemical Geology* **193**, 59-80.
- Zheng, Y.-F. (1993). Calculation of oxygen isotope fractionation in anhydrous silicate minerals. *Geochimica Et Cosmochimica Acta* **57**, 1079-1091.
- Zheng, Y. F. (1999). On calculations of oxygen isotope fractionation in minerals. *Episodes* **22**, 99-106.